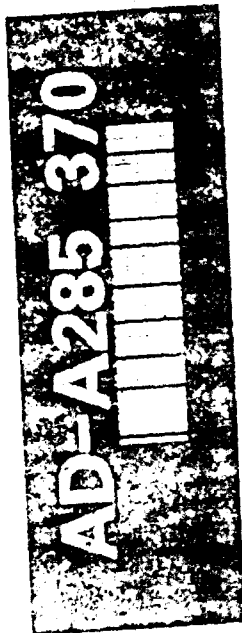


Best Available Copy

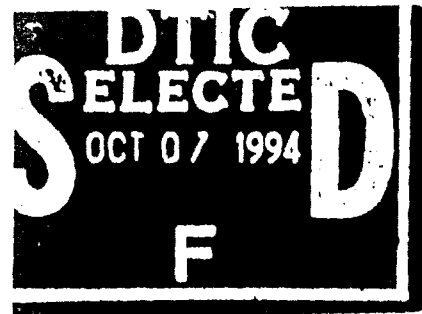


VOLUME 351

Molecularly Designed Ultrafine Nanostructured Materials



EDITED BY
Kenneth L. Gonsalves
Gan-Moong Chhow
Jongsan D. Nao
Robert C. Cammarata



This document has been approved
for public release and sale; its
distribution is unlimited.

**Molecularly Designed
Ultrafine/Nanostructured Materials**

Accession For	
NTIS CRA&I	<input checked="" type="checkbox"/>
DTIC TAB	<input type="checkbox"/>
Unannounced	<input type="checkbox"/>
Justification	
By DTIC-O	
Distribution /	
Availability Codes	
Dist	Avail and/or Special
A-1	

MATERIALS RESEARCH SOCIETY SYMPOSIUM PROCEEDINGS VOLUME 351

Molecularly Designed Ultrafine/Nanostructured Materials

Symposium held April 4-8, 1994, San Francisco, California, U.S.A.

EDITORS:

Kenneth E. Gonsalves

University of Connecticut
Storrs, Connecticut, U.S.A.

Gan-Moog Chow

Naval Research Laboratory
Washington, DC, U.S.A.

Tongsan D. Xiao

University of Connecticut
Storrs, Connecticut, U.S.A.

Robert C. Cammarata

Johns Hopkins University
Baltimore, Maryland, U.S.A.

94-31858



DTIC QUALITY INSPECTED 2



MATERIALS RESEARCH SOCIETY
Pittsburgh, Pennsylvania

This work was supported in part by the Office of Naval Research under Grant Number N00014-1-94-0067. The United States Government has a royalty-free license to reproduce this work in all copyrightable material contained herein.

Single article reprints from this publication are available through
University Microfilms Inc., 300 North Zeeb Road, Ann Arbor, Michigan 48106

CODEN: MRSPDH

Copyright 1994 by Materials Research Society.
All rights reserved.

This book has been registered with Copyright Clearance Center, Inc. For further
information, please contact the Copyright Clearance Center, Salem, Massachusetts.

Published by:

Materials Research Society
9800 McKnight Road
Pittsburgh, Pennsylvania 15237
Telephone (412) 367-3003
Fax (412) 367-4373

Library of Congress Cataloging in Publication Data

Molecularly designed ultrafine/nanostructured materials : symposium held April 4-8,
1994, San Francisco, California, U.S.A. / editors, Kenneth E. Gonsalves, Gan-Moog
Chow, Tongsan D. Xiao, Robert C. Cammarata.
p. cm. —(Materials Research Society symposium proceedings, ISSN 0272-9172 ;
v. 351)
Includes bibliographical references and index.
ISBN 1-55899-251-0
I. Nanostructure materials—Congresses. I. Gonsalves, Kenneth E. II. Chow,
Gan-Moog Chow III. Xiao, Tongsan D. IV. Cammarata, Robert C. V. Series:
Materials Research Society symposium proceedings ; v. 351.

T^418 9.N35M65 1994
620.1'1—dc20

94-26492
CIP

Manufactured in the United States of America

Contents

PREFACE	xi
ACKNOWLEDGMENTS	xiii
MATERIALS RESEARCH SOCIETY SYMPOSIUM PROCEEDINGS	xiv
PART I: SYNTHESIS AND PROPERTIES I	
THE PREPARATION, CHARACTERIZATION AND APPLICATION OF ORGANOSOLS OF EARLY TRANSITION METALS	3
Helmut Bönemann and Werner Brijoux	
SPONTANEOUS FORMATION OF Ag AND Au PARTICLES IN ALCOHOLS	9
Z.-Y. Huang, M. Quinn, G. Mills, and W. Gale	
ELECTRONIC STRUCTURE CALCULATIONS OF PURE AND OXIDIZED COPPER CLUSTERS USING JELLIUM AND MO - LCAO MODELS	15
Henrik Grönbeck, Mats Andersson, and Arne Rosén	
* NANOCOMPOSITES CONTAINING NANOCLUSTERS OF METALS OR SEMICONDUCTORS	21
Kimberly J. Burnam, Joseph P. Carpenter, Charles M. Lukehart, Stephen B. Milne, S.R. Stock, R. Glosser, and Bobby D. Jones	
* MOLECULAR PRECURSORS TO FUNCTIONAL MATERIALS	31
Norman Herron, David L. Thorn, and Richard L. Harlow	
PHYSICAL PROPERTIES OF DIAMOND-LIKE NANOCOMPOSITE FILMS	43
B. Dortman, M. Abraizov, B. Pypkin, M. Strongin, X.-Q. Yang, D. Yan, Fred H. Pollak, J. Grow, and R. Levy	
QUANTUM CONFINEMENT IN GaP NANOCLUSTERS	49
Bernhard K. Laurich, David C. Smith, and Matthew D. Healy	
PART II: SELF-ASSEMBLY AND BIOMOLECULAR ENGINEERING	
* THE CONTROL OF DNA STRUCTURE AND TOPOLOGY: AN OVERVIEW	57
Nadrian C. Seeman, Yuwen Zhang, Shou Ming Du, Hui Wang, John E. Mueller, Yinli Wang, Bing Liu, Jing Qi, and Junghuei Chen	
* POLYMERIZABLE SELF-ORGANIZED MEMBRANES: A NOVEL CLASS OF ORGANIC COMPOUNDS	67
Alok Singh, Michael Markowitz, and Gan Moog Chow	
SELF-ASSEMBLY OF INORGANIC/ORGANIC MULTILAYER FILMS	77
Astrid C. Zeppenfeld and Catherine J. Page	
PREPARATION OF NANOCOMPOSITES CONTAINING POLY(ETHYLENE OXIDE) AND MoS ₂ , TiS ₂ , OR MoO ₃	83
John P. Lemmon, Jinghe Wu, and Michael M. Lerner	
LAYERED SILICATE/POLYSTYRENE NANOCOMPOSITE	91
A. Moet, A. Akelah, A. Hiltner, and E. Baer	
LANGMUIR-BLODGETT FILMS OF CALCIUM STEARATE	97
Necesio Costa, Mark Aindow, and Peter M. Marquis	

*Invited Paper

*BIO-MIMETIC COMPOSITES	103
Jeremy Burdon, Jeffrey Szmania, and Paul Calvert	
*SELF-ASSEMBLING NANOSTRUCTURED DELIVERY VEHICLES FOR BIOCHEMICALLY REACTIVE PAIRS	109
Nir Kossovsky, A. Gelman, H.J. Hnatyszyn, E. Sponsler, and G.-M. Chow	
FREQUENCY-DEPENDENT SECOND HARMONIC GENERATION IN ACENTRIC CHROMOPHORIC SELF-ASSEMBLED NLO MATERIALS	119
Shlomo Yitzchaik, Paul M. Lundquist, Weiping Lin, David R. Kanis, Mark A. Ratner, Tobin J. Marks, and George K. Wong	
PART III: SYNTHESIS AND PROPERTIES II	
OPTICAL STUDIES OF SILICON NANOCRYSTALS IN COLLOIDAL AND SOL-GEL MATRICES	129
Howard W.H. Lee, Jeffrey E. Davis, Margaret L. Olsen, Susan M. Kauzlarich, Richard A. Bley, Subhash H. Risbud, and David J. Duval	
RARE EARTH/ORGANIC DYE NANOCOMPOSITES BY THE SOL-GEL METHOD	135
Eric P. Beschert, John D. Mackenzie, Tomoko Ohtsuki, and Nasser Peyghambarian	
NANOSIZED METAL PARTICLES BY CONTROL OF THE METAL DISPERSION DURING SOL-GEL PROCESSING	141
Ulrich Schubert, Claus Görsmann, Stefan Tewinkel, Andreas Kaiser, and Thomas Heinrich	
*NANO-SIZE SILICON WHISKERS PRODUCED BY CHEMICAL VAPOR DEPOSITION	147
Lu Shen, Youming Xiao, Ying Ma, Francis S. Galasso, Steven L. Suib, and James D. Freihaut	
RELATIONS BETWEEN STRUCTURE AND TEXTURE IN NANO-SIZED ALUMINAS	157
Dominique J. Coster, Pierre Levitz, and Jose J. Fripiat	
LAYERED SILICATE ATBN NANOCOMPOSITE	163
A. Moet, A. Akelah, N. Salahuddin, A. Hiltner, and E. Baer	
SELF-ASSEMBLY OF COBALT/BIPYRIDINE MULTILAYERS MODELED AFTER HOFMANN CLATHRATE COMPOUNDS	171
Michael A. Ansell, Astrid C. Zeppenfeld, William K. Ham, and Catherine J. Page	
BARIUM TITANIUM ALKOXIDES FOR BARIUM TITANATES: SYNTHESIS, CHARACTERIZATION, AND APPLICATIONS	177
Victor W. Day, Todd A. Eberspacher, Walter G. Klemperer, and Shurong Liang	
NANOSTRUCTURAL INVESTIGATION OF SILICA AEROGELS	183
Jue Wang, Jun Shen, Weidong Wu, and Bin Zhou	
CHARACTERIZATION OF THE INTERACTION OF HYDROGEN WITH IRIDIUM CLUSTERS IN ZEOLITES BY INELASTIC NEUTRON SCATTERING SPECTROSCOPY	189
J.M. Nicol, T.J. Udovic, R.R. Cavanagh, Z. Xu, S. Kawi, T. Mure, and B.C. Gates	
STUDIES OF NANOSTRUCTURED M50 TYPE STEEL USING X-RAY ABSORPTION SPECTROSCOPY AND NMR	195
Mahalingam Balasubramanian, Y.D. Zhang, J.I. Budnick, K.F. Gonsalves, and T.D. Xiao	

*Invited Paper

SONOCHEMICAL SYNTHESIS AND CATALYTIC PROPERTIES OF NANOSTRUCTURED MOLYBDENUM CARBIDE	201
Kenneth S. Sushick, Taeghwan Hyeon, Mingming Fang, and Andrzej A. Cichowlas	
PROCESSING OF NANOSTRUCTURED ZIRCONIA CERAMICS	207
G. Skandan, H. Hahn, B.H. Kear, M. Roddy, and W.R. Cannon	
CHEMICAL SYNTHESIS AND CHARACTERIZATION OF NANOSTRUCTURED TITANIUM ALUMINIDE	213
S.T. Schwab, P.P. Paul, and Y-M. Pan	
SYNTHESIS AND PROCESSING OF NANOGRAINED $\text{Fe-(Fe,Mo)}_6\text{C}$ COMPOSITE POWDERS	219
R.K. Sadangi, B.H. Kear, and L.E. McCandlish	
HRTEM ANALYSIS AND MAGNETIC PROPERTIES STUDY OF SURFACE OXIDIZING AND NITRIDING OF NANOCRYSTALLINE PARTICLES	227
Chi-Ming Hsu, Hong-Ming Lin, Kuen-Rong Tsai, and Pee-Yew Lee	
SYNTHESIS AND CHARACTERIZATION OF STAR POLYPEPTIDE NONLINEAR OPTICAL MATERIALS	233
Thomas M. Cooper, Weijie Su, Zbigniew Tokarski, and W. Wade Adams	
PREPARATION OF POLYPEPTIDE-DYE MULTILAYERS BY AN ELECTROSTATIC ASSEMBLY PROCESS	239
Thomas M. Cooper, Angela L. Campbell, Carol Noffsinger, Janelle Gunther-Greer, Robert L. Crane, and W. Wade Adams	
BIOMIMETIC PROCESSING OF CALCIUM CARBONATE-CHITOSAN COMPOSITES	245
Sukun Zhang and K.E. Gonsalves	
SURFACE CHEMISTRY OF NANOCRYSTALLINE CERIU OXIDE	251
Andreas Tschöpe, J.Y. Ying, K. Amonlirdviman, and M.L. Trudeau	
ORGANIC-INORGANIC SUPERLATTICES: STRUCTURAL AND OPTICAL PROPERTIES	257
Shizuo Tokito, J. Sakata, and Y. Taga	
MOLECULAR SIEVE BASED CHEMICAL SENSORS	263
Laura J. Sottile, Kenneth J. Balkus, Jr., Scott J. Riley, and Bruce E. Gnade	
SELF-ASSEMBLY OF ORIENTED METAL BISPHOSPHONATE MULTILAYERS WITH POTENTIAL NONLINEAR OPTICAL PROPERTIES	269
Grace Ann Neft, Astrid C. Zeppentfeld, Bethany Klopfenstein, and Catherine J. Page	
CHARACTERIZATION OF SILICON NANOPARTICLES PREPARED FROM POROUS SILICON	275
Richard A. Bley, Susan M. Kauzlarich, Howard W.H. Lee, and Jeffrey E. Davis	
SYNTHESIS OF LOW DENSITY MICROCELLULAR ACTIVATED CARBON SUPPORTED NANOPHASE Pt AND Pd PARTICLES AND STUDY OF ITS CATALYTIC PROPERTIES	281
Hong-Ming Lin, Ching-Shung Huang, and Chi-Ming Hsu	
EXFOLIATION OF MoS_2 CATALYSTS: STRUCTURAL AND CATALYTIC CHANGES	287
M. Del Valle, M. Avalos-Borja, J. Cruz, and S. Fuentes	

A LOW TEMPERATURE, SOLUTION PHASE SYNTHESIS OF III-V SEMICONDUCTOR NANOCRYSTALS	293
Shreyas S. Kher and Richard L. Wells	
METAL CLUSTER OXIDATION: STICKING PROBABILITIES AND IONIZATION POTENTIAL SHIFTS	299
Mats Andersson, Lotta Holmgren, John L. Persson, Thorbjörn Åklint, and Arne Rosén	
FORMATION AND PROPERTIES OF SILANE MONOLAYERS ON IRON AND ALUMINUM SURFACES	305
Maxim A. Petrunin and Andrey P. Nazarov	
MAGNETIC PROPERTIES OF NANOSIZE IRON CLUSTERS	311
E.L. Venturini, J.P. Wilcoxon, and P.P. Newcomer	
PART IV: CHARACTERIZATION AND MODELING	
* SMALL ANGLE NEUTRON SCATTERING FROM NANOCRYSTALLINE Pd AND Cu COMPACTED AT ELEVATED TEMPERATURES	319
P.G. Sanders, J.R. Weertman, J.G. Barker, and R.W. Siegel	
INTERFACIAL STRUCTURE OF ELECTRICALLY CONDUCTING ADSORBED MULTILAYERS	325
G.J. Kellogg, A.M. Mayes, W.B. Stockton, M. Ferreira, M.F. Rubner, and S.K. Satija	
DETERMINATION OF THE BOND STRENGTH BETWEEN NANOSIZED PARTICLES	331
Alfred P. Weber and Sheldon K. Friedlander	
GRAIN BOUNDARIES IN NANOPHASE MATERIALS AND CONVENTIONAL POLYCRYSTALS - ARE THEY DISTINCT?	337
S.C. Mehta, D.A. Smith, and U. Erb	
ATOMISTIC SIMULATION OF VAPOR-PHASE NANOPARTICLE FORMATION	343
Michael R. Zachariah, Michael J. Carrier, and Estela Blaisten-Barojas	
STRUCTURE AND PROPERTIES OF STRAINED CRYSTALLINE MULTILAYERS	349
J. Hoekstra, H. Yan, G. Kalonji, and H. Jonsson	
APPLICATION OF FRACTALS AND KINETIC EQUATION IN MODELLING CLUSTER AND ULTRAFINE PARTICLE SIZE DISTRIBUTIONS	355
J. Chaiken and Jerry Goodisman	
PART V: VAPOR DEPOSITION AND Si PARTICLES	
CHEMICAL VAPOR SYNTHESIS OF NANOSTRUCTURED CERAMICS	363
W. Chang, G. Skandan, H. Hahn, S.C. Danforth, and B. Kear	
CHARACTERIZATION OF NANOSCALE PARTICLES PRODUCED BY LASER VAPORIZATION/CONDENSATION IN A DIFFUSION CLOUD CHAMBER	369
M. Samy El-Shall, W. Stack, D. Hanley, and D. Kane	

*Invited Paper

GRAIN-SIZE STABILITY AND MICROHARDNESS OF COPPER-FULLERENE NANOCOMPOSITES	375
R.L. Holtz, E.V. Barrera, J. Milliken, and V. Provenzano	
FT-IR CHARACTERIZATION AND AB INITIO STUDY OF THE SURFACE SPECIES OF A NANOSIZED SiC POWDER	381
Marie-Isabelle Baraton, Sylvette Besnainou, and Lhadi Merhari	
CATALYTIC PROPERTIES OF NANOCRYSTALLINE WO _{3-x} , Pt/WO _{3-x} AND Pd/WO _{3-x} PARTICLES	387
Chiun-Yen Tung, Hong-Ming Lin, Chi-Ming Hsu, and Chao-Cheng Yang	
FACET FORMATION OF LINESHAPED SILICON MESAS GROWN WITH MICRO SHADOW MASKS	393
H. Gossner, G. Fehlauer, W. Kiunke, I. Eisele, M. Stolz, M. Hintermaier, and E. Knappek	
BLUE LIGHT EMISSION FROM SILICON ULTRAFINE PARTICLES	399
Shinji Nozaki, S. Sato, H. Ono, and H. Morisaki	
IR-VISIBLE PHOTOLUMINESCENCE STUDY OF NANOMETER-SIZE AMORPHOUS SILICON POWDER PRODUCED BY SQUARE-WAVE-MODULATED RF GLOW DISCHARGE	405
J. Costa, P. Roura, G. Sardin, J.R. Morante, and E. Bertran	
PART VI: SYNTHESIS AND PROPERTIES III	
STRUCTURAL CHARACTERIZATION OF ORDERED PHASES IN HYDROCARBON DENDRIMERS	413
Christopher J. Buchko, Atisa Sioshansi, Zhiru Xu, Jeffrey S. Moore, and David C. Martin	
A MOLECULAR APPROACH TO ULTRATHIN MULTILAYERED FILMS OF TITANIUM DIOXIDE	419
Elaine R. Kleinfeld and Gregory S. Ferguson	
A NEW PROCESS FOR PREPARING NANOSIZE CERAMIC POWDERS	425
Yong S. Zhen, Kenneth E. Hrdina, and Robert J. Remick	
THERMAL CONDUCTIVITY REDUCTIONS IN SiGe VIA ADDITION OF NANOPHASE PARTICLES	431
Nancy Scoville, Clara Bajger, Jon Rolfe, and Jan Vandersande	
MOLECULAR SIEVE THIN FILMS VIA LASER ABLATION	437
Kenneth J. Balkus, Jr., Scott J. Riley, and Bruce E. Gnade	
NANOSTRUCTURED Fe-Co CATALYSTS GENERATED BY ULTRASOUND	443
Kenneth S. Suslick, Mingming Fang, Taeghwan Hyeon, and Andrzej A. Cichowlas	
SUBWAVELENGTH LOCALIZATION OF OPTICAL MODES IN FRACTALS	449
Vladimir Shalaev, R. Botet, and M. Moskovits	
DEVELOPMENT AND CHARACTERIZATION OF ARTIFICIAL MICRO-STRUCTURES IN LONG LENGTHS OF SUPERCONDUCTING WIRE	455
P.D. Jahlonski, P.J. Lee, and D.C. Larbalestier	
AUTHOR INDEX	461
SUBJECT INDEX	465

Preface

Nanostructured materials are usually defined as having some length scale smaller than 100 nm in at least one dimension. An important subset of this group of materials is powders with particle size less than 100 nm, and polycrystalline materials, made by consolidating these powders in such a way as to retain a grain size below this limit. The choice of 100 nm stems from the fact that many physical, optical, and magnetic properties have characteristic lengths in this range. As grain or particle size is reduced below this characteristic length, the properties associated with these phenomena are radically altered. A frequently cited example is the freezing out of mechanisms for generating glissile dislocations. Another reason for expecting remarkable properties in nanostructured polycrystalline materials is the very high proportion of atoms at, or near, grain boundaries (as high as fifty percent or greater for grain sizes below five or ten nanometers). This leads, for example, to very rapid diffusion coupled with very short diffusion distances.

Nanostructured materials have been around for many years. Two examples are carbon black (for automobile tires) and TiO_2 (for white paint). The current interest in these materials dates back to the pioneering work of Gleiter and coworkers at Saarlandes on gas condensation of ultrafine particles. In this technique, the particles are precipitated from a supersaturated metallic vapor and swept by convection currents to a cold finger where they are collected. Since then, the number of methods for synthesis (as well as the number of materials synthesized) has grown steadily. They generally fall into two categories: physical and chemical. Another example of a physical method is mechanical attrition, in which a material is severely deformed in a high energy ball mill, producing an increasingly dense dislocation network which ultimately collapses into nanoscale grain boundaries. Chemical methods rely on one or more chemical reactions to form the nanoscale particles. For example, a precursor may be decomposed during passage through a hot wall reactor. In another technique, called spray conversion, water soluble precursors are spray dried to form micron-sized particles, reduced in a fluid bed reactor, and then carburized (for example) in the same reactor. In one of the most unusual methods, the chemistry is carried out in the very high temperature and pressure of a detonation front, propagating in an explosive. Nanocrystalline diamonds have been synthesized by this method with very high yield. In what is perhaps the most recent example, nanoscale particles are formed inside vesicles within artificial membranes. As suggested by the title of this symposium, nanostructured materials are being designed and synthesized from the molecule up, as envisioned by Richard Feynman many years ago.

The list of applications for nanoscale powders and "nanocrystalline" materials is enormous and keeps growing. An obvious example of the use of unconsolidated powder is in the field of catalysis, where the very large surface-to-volume ratio and altered surface chemistry leads to significant improvements in the performance of various catalysts. Another is in the fabrication of arrays of particles for use in devices based on quantum confinement. Nanoscale powders have been consolidated into nanostructured metals, intermetallics and ceramics. The use of nanoscale powders provide many advantages, regardless of whether the final product is nanocrystalline. For example, the use of nanoscale ceramic powder greatly reduces the required sintering temperature. The need for hot isostatic pressing can be eliminated. Applications for consolidated materials include: very hard, wear-resistant coatings; ceramics with improved strength and toughness; superparamagnetic materials for magnetic refrigeration; net shape forming via superplastic deformation; and transparent ceramic windows, to name only a few.

Progress in synthesis has been very rapid. Several materials, including ceramics and cermets are commercially available, in some cases in ton quantities (Co/WC). The

emphasis of research and development has been on finding ways to produce unagglomerated particles with controlled sizes and very narrow size distribution. Other important considerations are cost, scalability, and environmental impact. Progress in consolidation has been somewhat slower. This is partly due to the need to understand mechanisms of sintering, grain growth, and grain growth inhibition. Rapid progress is now being made in several areas, including oxide ceramics, cermets, ferrous alloys, and intermetallics (especially aluminides). Opportunities exist in the areas of non-oxide ceramics (especially nitrides), and ceramic matrix composites, to name only two. Progress in consolidation has enabled investigations of the mechanical properties of bulk nanocrystalline materials, as well as structure property relationships. Ultimately, it should be possible to engineer nanoscale materials from the molecule up to the macroscopic, in order to achieve specific desired properties.

The diversity of applications for nanostructured materials, combined with an explosive growth of interest and activity in this field, has led to problems of communication between various scientific communities, each with their own special needs and interests. Scientists and engineers are frequently unaware of the progress made by people from other, seemingly unrelated fields. It is vital that a dialog between different communities be established. This symposium is a major step in that direction. Previous meetings have tended to attract the same group of people. A comparison of the list of contributors to this proceeding with previous topical conferences shows the large number of "new faces." Hopefully, this is the start of a healthy trend. Ultimately, successful exploitation of nanoscale materials by industry will require the best efforts of chemists, physicists, materials scientists, chemical engineers, and even biologists, together with "real world" industrial engineers.

Lawrence T. Kabacoff
Materials Division
Office of Naval Research

May 31, 1994

Organizers' Note and Acknowledgments

This symposium brought an interdisciplinary interaction of biologists, chemists, physicists, materials scientists and engineers to address recent developments in advanced materials synthesized from molecularly designed precursors. Emphasis was placed on ultrafine microstructures and nanostructures prepared by organic, inorganic atomic and molecular clusters, and self assembly of bio/molecular precursors. The symposium covered the areas of materials synthesis, processing, characterization, modeling and properties. Of 170 abstracts received, 143 oral or poster presentations were selected. This proceedings contains 69 papers all of which were peer reviewed.

The symposium organizers would like to acknowledge the participants, speakers and session chairs for contributing to the fruitful interactions and success of this symposium, and the reviewers for refereeing the papers which appear in this proceedings. The help that was received from the dedicated staff of MRS, in organizing both the symposium and its proceedings, is also greatly appreciated. Finally, we would like to acknowledge the Office of Naval Research and the Precision Manufacturing Center of the University of Connecticut for their generous support.

Kenneth E. Gonsalves
Gan-Moog Chow
Tongsan D. Xiao
Robert C. Cammarata

June 6, 1994

MATERIALS RESEARCH SOCIETY SYMPOSIUM PROCEEDINGS

- Volume 316— Materials Synthesis and Processing Using Ion Beams, R.J. Culbertson, O.W. Holland, K.S. Jones, K. Maex, 1994, ISBN: 1-55899-215-4
- Volume 317— Mechanisms of Thin Film Evolution, S.M. Yalisove, C.V. Thompson, D.J. Eaglesham, 1994, ISBN: 1-55899-216-2
- Volume 318— Interface Control of Electrical, Chemical, and Mechanical Properties, S.P. Murarka, K. Rose, T. Ohmi, T. Seidel, 1994, ISBN: 1-55899-217-0
- Volume 319— Defect-Interface Interactions, E.P. Kvam, A.H. King, M.J. Mills, T.D. Sands, V. Vitek, 1994, ISBN: 1-55899-218-9
- Volume 320— Silicides, Germanides, and Their Interfaces, R.W. Fathauer, S. Mantl, L.J. Schowalter, K.N. Tu, 1994, ISBN: 1-55899-219-7
- Volume 321— Crystallization and Related Phenomena in Amorphous Materials, M. Libera, T.F. Haynes, P. Cebe, J.F. Dickinson, Jr., 1994, ISBN: 1-55899-220-0
- Volume 322— High Temperature Silicides and Refractory Alloys, C.L. Briant, J.J. Petrovic, B.P. Bewlay, A.K. Vasudevan, H.A. Lipsitt, 1994, ISBN: 1-55899-221-9
- Volume 323— Electronic Packaging Materials Science VII, P. Borgesen, K.F. Jensen, R.A. Pollak, 1994, ISBN: 1-55899-222-7
- Volume 324— Diagnostic Techniques for Semiconductor Materials Processing, O.J. Gilmer, S.W. Pang, F.H. Pollak, G.M. Crean, G. Larrabee, 1994, ISBN: 1-55899-223-5
- Volume 325— Physics and Applications of Defects in Advanced Semiconductors, M.O. Manasreh, H.J. von Bardeleben, G.S. Pomrenke, M. Lannoo, D.N. Lalwar, 1994, ISBN: 1-55899-224-3
- Volume 326— Growth, Processing, and Characterization of Semiconductor Heterostructures, G. Gumbs, S. Luryi, B. Weiss, G.W. Wicks, 1994, ISBN: 1-55899-225-1
- Volume 327— Covalent Ceramics II: Non-Oxides, A.R. Barron, G.S. Fischman, M.A. Fury, A.F. Hepp, 1994, ISBN: 1-55899-226-X
- Volume 328— Electrical, Optical, and Magnetic Properties of Organic Solid State Materials, A.F. Garito, A.K-Y. Jen, C.Y-C. Lee, I. R. Dalton, 1994, ISBN: 1-55899-227-8
- Volume 329— New Materials for Advanced Solid State Lasers, B.H.T. Chai, S.A. Payne, I.Y. Fan, A. Cassanho, T.H. Allik, 1994, ISBN: 1-55899-228-6
- Volume 330— Biomolecular Materials By Design, M. Alper, H. Bayley, D. Kaplan, M. Navia, 1994, ISBN: 1-55899-229-4
- Volume 331— Biomaterials for Drug and Cell Delivery, A.G. Mikos, R.M. Murphy, H. Bernstein, N.A. Peppas, 1994, ISBN: 1-55899-230-8
- Volume 332— Determining Nanoscale Physical Properties of Materials by Microscopy and Spectroscopy, M. Sarikaya, M. Isaacson, H.K. Wickramasighe, 1994, ISBN: 1-55899-231-6
- Volume 333— Scientific Basis for Nuclear Waste Management XVII, A. Barkatt, R. Van Konynenburg, 1994, ISBN: 1-55899-232-4
- Volume 334— Gas-Phase and Surface Chemistry in Electronic Materials Processing, T.J. Mountziaris, G.R. Paz-Puralt, F.T.J. Smith, P.R. Westmoreland, 1994, ISBN: 1-55899-233-2
- Volume 335— Metal-Organic Chemical Vapor Deposition of Electronic Ceramics, S.B. Desu, D.B. Beach, B.W. Wessels, S. Gokoglu, 1994, ISBN: 1-55899-234-0

MATERIALS RESEARCH SOCIETY SYMPOSIUM PROCEEDINGS

- Volume 336—Amorphous Silicon Technology-1994, E.A. Schiff, A. Matsuda, M. Hack, M.J. Powell, A. Madan, 1994, ISBN: 1-55899-236-7
- Volume 337—Advanced Metallization for Devices and Circuits—Science, Technology, and Manufacturability III, S.P. Murarka, K.N. Tu, A. Katz, K. Maex, 1994, ISBN: 1-55899-237-5
- Volume 338—Materials Reliability in Microelectronics IV, P. Borgesen, W. Filter, J.E. Sanchez, L., K.P. Rodbell, J.C. Coburn, 1994, ISBN: 1-55899-238-3
- Volume 339—Diamond, SiC and Nitride-Wide-Bandgap Semiconductors, C.H. Carter, Jr., G. Gildenblat, S. Nakamura, R.J. Nemanich, 1994, ISBN: 1-55899-239-1
- Volume 340—Compound Semiconductor Epitaxy, C.W. Tu, L.A. Kolodziejcki, V.R. McCrary, 1994, ISBN: 1-55899-240-5
- Volume 341—Epitaxial Oxide Thin Films and Heterostructures, D.K. Fork, J.M. Phillips, R. Ramesh, R.M. Wolf, 1994, ISBN: 1-55899-241-3
- Volume 342—Rapid Thermal and Integrated Processing III, J.J. Wortman, J.C. Gelpey, M.L. Green, S.R.J. Brueck, F. Roozeboom, 1994, ISBN: 1-55899-242-1
- Volume 343—Polycrystalline Thin Films—Structure, Texture, Properties and Applications, M. Parker, K. Barmak, R. Sinclair, D.A. Smith, J. Floro, 1994, ISBN: 1-55899-243-X
- Volume 344—Materials and Processes for Environmental Protection, C. Adkins, P.N. Gadgil, L.M. Quick, K.E. Voss, 1994, ISBN: 1-55899-244-8
- Volume 345—Flat Panel Display Materials, J. Batey, A. Chiang, P. Holloway, 1994, ISBN: 1-55899-245-6
- Volume 346—Better Ceramics Through Chemistry VI, C. Sanchez, M.L. McCartney, C.J. Brinker, A. Cheetham, 1994, ISBN: 1-55899-246-4
- Volume 347—Microwave Processing of Materials IV, M.F. Iskander, R.J. Lauf, W.H. Sutton, 1994, ISBN: 1-55899-247-2
- Volume 348—Scintillator and Phosphor Materials, M.J. Weber, P. Lecoq, R.C. Ruchti, C. Woody, W.M. Yen, R.-Y. Zhu, 1994, ISBN: 1-55899-248-0
- Volume 349—Novel Forms of Carbon II, C.L. Renschler, D. Cox, J. Pouch, Y. Achiba, 1994, ISBN: 1-55899-249-9
- Volume 350—Intermetallic Matrix Composites III, J.A. Graves, R.R. Bowman, J.J. Lewandowski, 1994, ISBN: 1-55899-250-2
- Volume 351—Molecularly Designed Ultrafine/Nanostructured Materials, K.E. Gonsalves, G.-M. Chow, T.D. Xiao, R.C. Cammarata, 1994, ISBN: 1-55899-251-0

*Prior Materials Research Society Symposium Proceedings
available by contacting Materials Research Society*

PART I

Synthesis and Properties I

THE PREPARATION, CHARACTERIZATION AND APPLICATION OF ORGANOSOLS OF EARLY TRANSITION METALS

HELMUT BÖNNEMANN* AND WERNER BRIJOUX
Max-Planck-Institut für Kohlenforschung, Kaiser-Wilhelm-Platz 1,
45470 Mülheim an der Ruhr, Germany

ABSTRACT

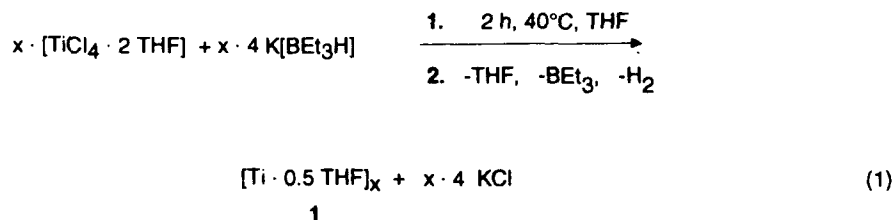
Colloidal early transition metals are of great interest in both powder technology and catalysis. We report a new process for preparing organosols of zerovalent Ti, Zr, V, Nb and Mn

INTRODUCTION

The reduction of TiCl_4 with $\text{K}[\text{BEt}_3\text{H}]$ gives an ether-soluble $[\text{Ti}(0) \cdot 0.5 \text{ THF}]_x$ which serves as a catalyst for the hydrogenation of titanium or zirconium sponges and related systems and as a powerful activator for heterogeneous hydrogenation catalysts. X-ray photoelectron spectroscopy and EXAFS analysis support the oxidation state of zero for the titanium. By analogous reduction of the THF-adducts of Zr-, V-, Nb-, and Mn-halides, the corresponding ether-soluble colloids of these early transition metals may be obtained

PREPARATION OF EARLY TRANSITION METAL-COLLOIDS

The reduction of $\text{TiCl}_4 \cdot 2\text{THF}$ or $\text{TiCl}_3 \cdot 3\text{THF}$ in THF solution with $\text{K}[\text{BEt}_3\text{H}]$ within 2h gives a brown-black solution under the evolution of H_2 from which about 90% of the precipitated KCl can be removed by filtration. After vacuum evaporation of the solvent and BEt_3 (identified by ^{11}B -NMR spectroscopy) a black residue is obtained which is extracted with THF. This THF solution is treated with pentane to give a brown-black precipitate in step 1. (Equ. 1).



After thorough drying in vacuo the pyrophoric powder 1 is obtained along with small amounts of KCl (identified by X-ray diffraction). Quantitative measurements of the gas evolved during the reduction (1 mol H₂ per mol Ti), protonolysis and cross experiments using K[BEt₃D] as the reducing agent in (1) show that the product of step 1, still has various amounts of residual hydrogen. The hydrogen is removed in vacuo to give 1 (step 2). 1 readily dissolves in THF and ether but is insoluble in hydrocarbons such as pentane. For experimental details see [1].

The IR spectrum of 1 shows intact THF coordinated to the metal core. Further characterization of 1 by X-ray diffractometry, XPS, and EXAFS [1] supports its description as colloidal titanium stabilized by complexed THF and containing residual hydrogen (Fig. 1).

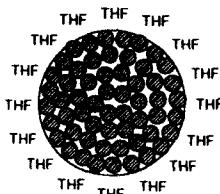
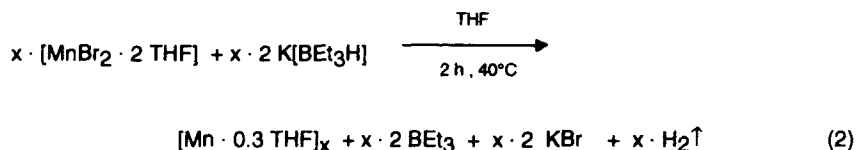


Fig 1. Ether soluble [Ti(0) · 0.5 THF]_x

The corresponding Zr-colloid was isolated by adding the THF-solution after filtration from KCl slowly to pentane, where the Zr-colloid precipitates. The workup of the V- and Nb-colloids was performed similarly. The reduction of the THF-adduct to MnBr₂ at 40°C yielded a stable, isolated [Mn · 0.3 THF]_x colloid containing typically 60% Mn.



IR and NMR data of the colloid show intact THF coordinated to Mn. There is no evidence for ether-cleavage. HRTEM showed the fringes of Mn-particles of the size 1 - 2.5 nm. An EDX-analysis of the Mn-nanoparticles showed no bromide to be present. This result confirms the assumption that colloidal Mn(0) was formed.

EXPERIMENTAL PROOFS OF ZEROVALENT COLLOIDAL TI

The protonolysis of 1 with 2N HCl provided 1.5-2 mol of H₂ per mol of titanium. Theoretically, 1.5 mol H₂ are expected for Ti⁰. This shows that in 1 Ti⁰ has various amounts of residual hydrogen.

According to the IR spectrum of **1** intact THF is coordinated to the metal center. Neither the IR nor ^1H NMR spectra give evidence of Ti-bound hydrogen. Likewise, there is no spectroscopic proof of a cleavage of THF by Ti^0 . In the X-ray diffractogram of **1** besides the reflections of the KCl impurity only a diffuse, small peak at $2\theta = 30^\circ$ is seen, the position of which matches that of the peak of amorphous titanium. The accompanying lattice distance, approximately 0.3 nm, corresponds to that in the metal. In the XPS spectrum of **1** (Fig. 2d) the Ti2p peak is found 2.3 eV higher in energy than in the spectrum of TiO_2 (Fig. 2a). Although metallic titanium as finely divided as **1** was not available for control experiments, it can be deduced from the XPS spectra (Fig. 2) that titanium in **1** is almost as reduced as titanium metal.

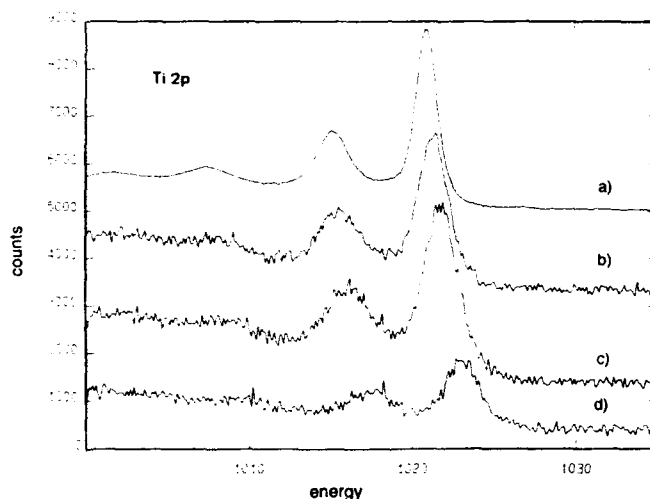


Fig. 2. XPS spectra (double peak $\text{Ti}2p_{1/2}$ and $\text{Ti}2p_{3/2}$) of a) TiO_2 , b) TiO_2 from **1**, c) a sample of **1** with an oxidized surface, d) $\text{Ti} + 0.5 \text{ THF } \mathbf{1}$. n = number of recorded pulses.

The lack of the typical broad peak between 990 and 1010 eV for **1** indicates the absence of TiO_2 (no oxidation of the sample during the measurement). As a comparison for the measured values, the curves from TiO_2 produced from **1** (Fig. 2b) and from an oxidized sample (Fig. 2c) are also displayed.

Two titanium-hydrogen compounds are known. $\alpha\text{-TiH}_x$ ($x < 0.46$) can be described as elemental titanium with incorporated hydrogen, whereas $\beta\text{-TiH}_y$ (ca. $1 < y < 2$)[2] has a CaF_2 -type structure. The radical distribution function of an initial EXAFS analysis fitted with the experimentally determined titanium phase function (of titanium metal) shows three shells of titanium for **1** with the Ti-Ti distances listed in Table 1. A hexagonal structure type similar to that of α -titanium can be deduced from

these values. The lattice is somewhat expanded [3], possibly by the included hydrogen.

The characterization of 1 up to this point supports its description as colloidal titanium stabilized by complexed THF and containing included residual hydrogen. The determination of the particle size by transmission electron microscopy has not been conducted.

The analogous reduction of $ZrCl_4$ with $K[BEt_3H]$ in THF also provided a product soluble in THF; its composition was determined to be 34.1 % C, 8.0 % H, 11.4 % O,

Table 1. Comparison of the Ti-Ti distances in 1, α -Ti and β -TiH_{1.971}

Shell	1	α -Ti ($a = 2.952$, $c = 4.689$ Å [4])	β -TiH _{1.971} ($a = 4.440$ Å [4])
1	2.96 Å	$\left. \begin{array}{l} 2.90 \text{ Å} \\ 2.95 \text{ Å} \\ 2.95 \text{ Å} \end{array} \right\} 2.925 \text{ Å}$	3.14 Å
2	4.21 Å	4.14 Å	4.44 Å
3	5.68 Å	5.85 Å	5.44 Å

3.7 % B, 5.2 % Cl, 17.9 % K, and 19.4 % Zr. The purification and closer characterization are not yet complete.

SOME APPLICATIONS OF EARLY TRANSITIONMETAL-COLLOIDS

Besides the application of 1 as dopant for noble metal hydrogenation catalysts, the colloidal $[Ti(0) \cdot 0.5THF]_x$ has been found to be a very efficient catalyst for the hydrogenation of titanium and zirconium sponges as well as for a nickel hydride battery alloy. The uncatalyzed hydrogenation of titanium or zirconium sponges using compressed hydrogen affords pressures above 100 bar and minimum reaction temperatures of 150°C. The hydrogenation of these metals under such drastic conditions, however, is associated with unwanted sintering of the materials so that the products can only be used after additional grinding. After the addition of 1% Ti (present in 1) to the metal sponges a smooth hydrogenation of titanium and zirconium is observed at low temperatures (60° - 90°C). The reaction may be carried out in THF solution, toluene suspension or in the dry state after depositing the catalyst on the surface of the samples by evaporation of the solvent in vacuo. Using a special device [5], the mass specific uptake of hydrogen depending on pressure, temperature and time was monitored automatically. Fig. 3 shows the typical course of the hydrogen uptake during the hydrogenation of a titanium sponge at 60°C catalyzed by 1% Ti in the form of 1. After a certain latent period with only negligible uptake of H₂ an abrupt start of the

catalytic hydrogenation occurs; followed by a period of rather constant H_2 -uptake (denoted as the "hydrogenation period"). Towards the end of the H_2 -uptake the reaction turns into a slow decay.

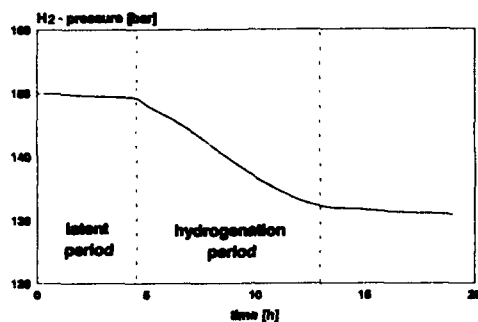


Fig. 3. Hydrogenation of Ti sponge catalyzed by 1

An inspection of Fig. 4 shows, that the mass specific hydrogenation time [min/g] detected for 1 g of titanium sponge at 100 bar H_2 in the presence of the catalyst is constant between 60° and 90°C, practically constant in THF and toluene and even in the absence of a solvent. Significant differences, however, occur with regard to the latent period. If the catalytic hydrogenation of titanium sponge is performed at very low hydrogen pressure (5 bar), a prolonged reaction time is required. In case of the $Ti(0)$ -catalyzed hydrogenation of zirconium sponge at 60°C in THF no latent period was observed.

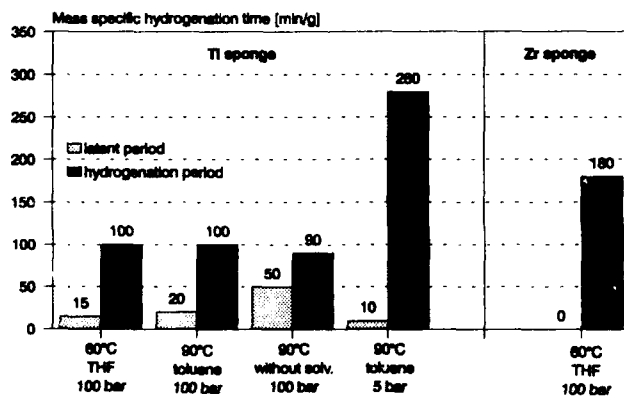


Fig. 4. Influence of temperature, solvent, and pressure in the hydrogenation of Ti and Zr sponges catalyzed by 1

A welcome benefit of the Ti(0)-catalyzed hydrogenation process is that the compact titanium and zirconium sponges break down during the H₂-uptake forming finely divided hydride powders.

X-ray diffraction of the products has provided an unambiguous identification of TiH₂ and ZrH₂. Protonolysis of the dry hydrides with 5n HCl liberates 98% of the theoretically expected amount of H₂.

An interesting application of the Ti(0)-catalyzed metal hydrogenation process is the pressureless hydrogenation of a Ni/Zr/V/Ti/Cr alloy at room temperature. The corresponding hydride of this special alloy (38.2% Ni, 24.3% Zr, 12.8%Ti 18.7%V, 6.0% Cr) is of current interest for electrochemical purposes (Nickel hydride battery). However, the hydrogenation at room temperature affords 5 bar hydrogen pressure and even under these conditions an unwanted latent period occurs. After doping the surface of the alloy with 1 wt.-% of soluble Ti(0) using **1** as the precursor, a spontaneous uptake of 0.6 - 0.7 wt.-% hydrogen is observed at room temperature without applying pressure.

REFERENCES

- 1 H. Bönemann and B. Korall, *Angew. Chem.*, 104 (1992) 1506, *Angew. Chem. Int. Ed. Engl.*, 31 (1992) 1490.
- 2 A. Chrétien, W. Freundlich, M. Bichara, *C. R. Hebd. Seances Acad. Sci.* 238 (1954) 1423.
- 3 Dr. L. Aleandri, Max-Planck-Institut für Kohlenforschung, Mülheim an der Ruhr, (1991). The X-ray absorption was recorded on the Ti K-edge (77 K) with an EXCAFS 3 spectrometer in DCI (French Synchrotron Facility in Lure) with monochromatic X-ray radiation.
- 4 S. S. Sidhu, L. Heaton, D. D. Zaubers, *Acta Crystallogr.* 9 (1956) 607.
- 5 B. Bogdanović, T. Hartwig, A. Ritter, K. Strassburger and B. Spliethoff, Abschlußbericht zum BMFT-Forschungsvorhaben Nr. 0328939 C (1991).

SPONTANEOUS FORMATION OF Ag AND Au PARTICLES IN ALCOHOLS

ZHANG,[†] M. QUINN,[†] G. MILLS,[†] AND W. GALE[‡]
[†]Department of Chemistry, Auburn University, Auburn, AL 36849
[‡]Engineering Program, Auburn University, Auburn, AL 36849

ABSTRACT

Metal particles are generated via the spontaneous reduction of Ag^+ and AuCl_4^- ions by solvent molecules that takes place in air-saturated alcoholic solutions containing hydroxide ions. Changes in the plasmon band of the Ag particles are observed when the metal particles are in contact with Ag_2O particles. The optical changes are explained in terms of surface effects of the metal particles. Larger shifts of the Au plasmon band and light scattering were observed at the initial stages of the particle formation process. These effects are explained in terms of formation of networks consisting of small metal particles. It is proposed that generation of small Au particles occurs mainly on silica surfaces, and that particle-networks are formed when small particles desorb from the surfaces.

INTRODUCTION

Small metal particles continue to receive considerable attention because of their novel physical and chemical properties.¹⁻³ For example, the optical properties of small Ag and Au particles are influenced by particle size, particle shape and surface effects.^{3,4} A convenient way to study these effects consists in using colloidal solutions of the metals.³

A simple method for the preparation of small colloidal Ag and Au particles is presented here. The general procedure is based on the instability of some metal complexes in basic alcohols, which results in the reduction of the metal ions at room temperature. The present report is centered on preparation methods, some kinetic aspects of the particle formation process, as well as characterization of colloids produced by the spontaneous reduction of Ag^+ and AuCl_4^- ions in air-saturated alcoholic solutions containing hydroxide ions.

EXPERIMENTAL SECTION

Methanol, 2-propanol, NaOH (Fisher), AgNO_3 , $\text{NaAuCl}_4 \cdot 2\text{H}_2\text{O}$ (Aldrich), and SDS (MCB) were used as received. Unless otherwise stated, all chemical reactions were performed at room temperature. Stock solutions of powdered Nafion 117 (Aldrich) containing 5% (wt) of the strongly acidic material (equivalent weight of 1,100 g/equiv.) were neutralized prior to addition to the NaAuCl_4 solutions. Suspensions of SiO_2 particles were prepared by sonicating 0.02 g of Cab-O-Sil HS-5 fumed silica (Cabot, average diameter = 8 nm) in 0.1 L of methanol. For Au colloids, 0.75 mL of a 2×10^{-2} M NaOH solution in methanol was added to about 45 mL of a methanolic solution of NaAuCl_4 and stabilizer. The volume was adjusted to 50 mL with alcohol under stirring, and the final concentrations were 10^{-4} M NaAuCl_4 , 3×10^{-4} M NaOH and 10^{-3} M SDS or 10^{-4} N Nafion. To avoid irreproducible results Au colloids were prepared in polypropylene volumetric flasks and in the absence of ambient light (the gold complex is sensitive to visible light). Colloidal Ag were prepared from 2-propanol solutions containing 2.5×10^{-4} M AgNO_3 , 5×10^{-4} M NaOH and 4×10^{-4} N Nafion. Non-neutralized Nafion was used in this case.

A Hitachi U-2000 spectrophotometer was utilized for optical absorption determinations, and the spectral changes were monitored in 1 cm quartz or Pyrex optical cells. X-ray diffraction (XRD) experiments were performed with a Siemens D5000 powder diffractometer. Transmission electron microscopy (TEM) were carried out with a JEOL 1200-EX microscope.

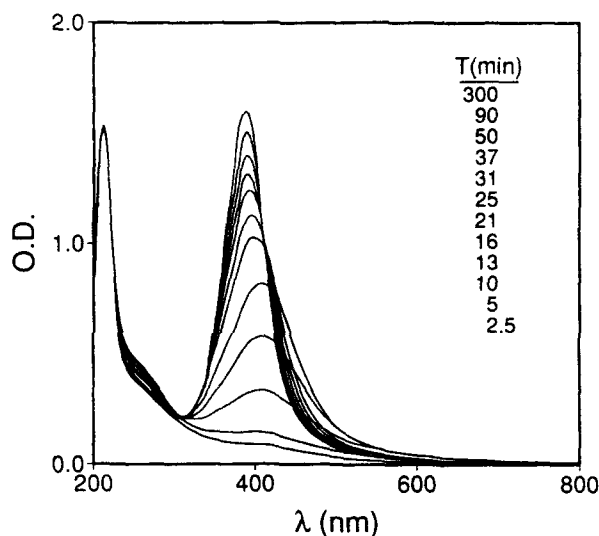


Figure 1. Evolution of the optical spectra during formation of Ag particles.

RESULTS

A bright yellow solution was slowly formed when hydroxide ions were added to an air-saturated alcoholic solution of Ag^+ ions. The evolution of the absorption spectra with time is presented in Figure 1. Between 5 and 16 min, a broad absorption centered at 410 nm developed. At longer reactions times the absorption band narrowed and shifted continuously to shorter wavelengths. The shifts in the absorption band ceased after about 5 h, at which point a narrow and strong absorption band centered at 390 nm was obtained. Afterwards, only a slow but continuous increase in the intensity of the 390 nm band was noticed. The evolution of the optical spectra was completed in about 10 hours, and the final spectra is shown in Figure 2. XRD and TEM measurements of the yellow colloid indicated that it consisted of nearly spherical Ag particles; the most frequent particle size was 4.5 nm and the statistical average particle size was 7.4 nm. Large Ag_2O particles and also a few metal particles were observed in TEM experiments with solutions prepared at -45°C . These results suggest that silver oxide is initially formed through the reaction between Ag^+ ions and OH^- ions.

Colloidal Ag particles prepared in 2-propanol with Nafion are very stable toward agglomeration or oxidation by air despite of their small size. Illumination of evacuated colloids at 290 nm or irradiation of air-saturated colloids with photons of $\lambda \geq 380$ nm produced no change in the optical spectra of the particles. However, the band centered at about 390 nm decreased in intensity and shifted to longer wavelengths with increasing time when colloids were illuminated with light of 290 nm in the presence of air (Figure 2). At irradiation times longer than 64 min the absorption decreased, but λ_{max} remained constant at about 410 nm. The decay in optical density was exponential with time and a rate constant of $4.8 \times 10^{-5} \text{ s}^{-1}$ was determined from a first order plot of the data. As shown in Figure 3, micron-size polycrystalline Ag_2O particles as well as small Ag particles were present in a colloid irradiated for 810 min.

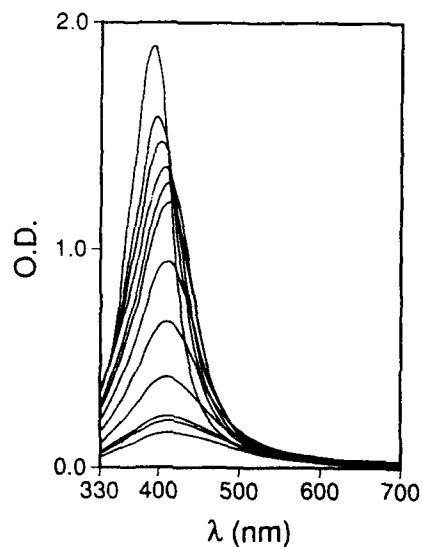


Figure 2. Spectral changes during irradiation of colloidal Ag. Irradiation times (min) from top to bottom are: 0, 7, 15, 64, 100, 180, 448, 662, 691 and 810.



Figure 3. TEM image of an Ag colloid illuminated for 810 min with 290 nm light.

Addition of hydroxide ions to an air-saturated methanolic solution of AuCl_4^- ions and Nafion resulted in a slow evolution of the absorption spectra with time, as shown in Figure 4. Broad absorption bands were observed; λ_{max} shifted initially to 590 nm and then slowly to 540 nm

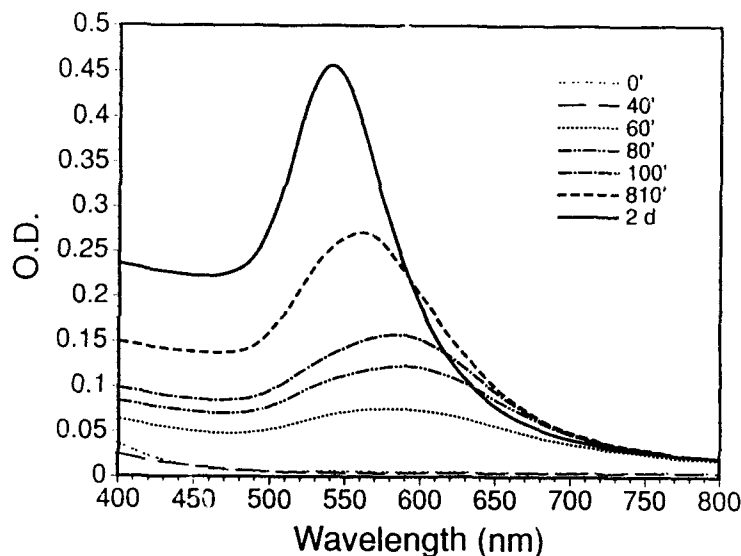


Figure 4. Spectral changes during formation of an Au colloid stabilized with Nafion.

at the later stages of the reaction. The resulting colloids were transparent and stable for several weeks. They consisted of near-spherical (faceted) metal particles with an average diameter of 57 nm (Figure 5). Our results are in good agreement with previous observations on Au particles in water ($\lambda_{\text{max}} = 536 \text{ nm}$ for $d_{\text{average}} = 60 \text{ nm}$).⁵

Shifts in λ_{max} at wavelengths longer than 500 nm similar to those shown in Figure 4 were detected in all colloid preparations. In general, a turbidity developed as the absorption bands shifted to longer wavelengths and it faded away when the bands shifted to shorter wavelengths. Changes in optical density at 560 nm were used to follow the kinetics of the initial step of the particle formation reaction. Typical results are presented in Figure 6. Curves a-c were measured in quartz cells and correspond to the changes in absorbance of solutions containing SDS, Nafion and no stabilizing agent, respectively. Au particles were formed with an apparent first-order rate constant of $k_{\text{app}} = 2 \times 10^{-2} \text{ min}^{-1}$ in SDS solutions, and with $k_{\text{app}} = 3.7 \times 10^{-2} \text{ min}^{-1}$ in solutions with Nafion.

The rate of the Au particle formation process in methanol was strongly affected by the nature of the container used to store the reacting mixture. For example, formation of particles was completed after a few hours when the basic AuCl_4^- solutions were kept in Pyrex volumetric flasks, whereas hardly any reaction was noticed after 24 h when polypropylene containers were utilized. Therefore, solutions containing the gold complex were mixed with base in polypropylene vessels and sample of the mixture was immediately transferred to optical cells where the reaction was allowed to proceed. Curve d in Figure 6 was measured using a Pyrex cell and shows the evolution of the absorbance at 560 nm with time for a solution of NaAuCl_4 , NaOH and SDS . A fast formation of particles ($k_{\text{app}} = 0.14 \text{ min}^{-1}$) followed after an induction period of 20 min. Since solutions with the same chemical composition were employed in the experiments with a quartz cell (curve a) and with a Pyrex cell (curve d), the results presented in Figure 4 indicate that the rate of metal particle formation was affected by the type of surface that is in contact with the solution.

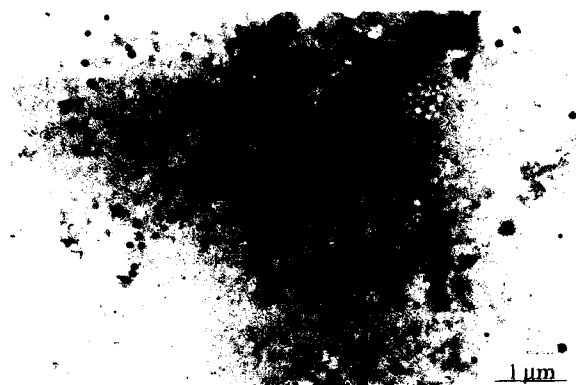


Figure 5. TEM image of an Au colloid prepared in the presence of Nafion.

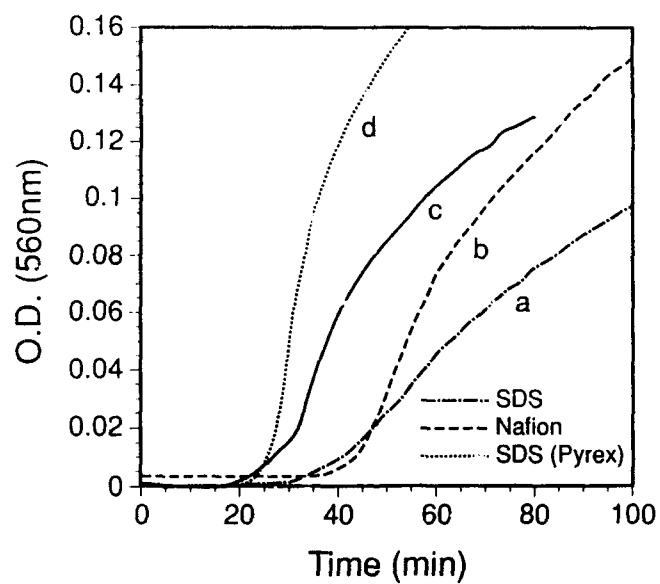


Figure 6. Evolution of the absorption at 560 nm in solutions containing 10^{-4} M NaAuCl_4 , 3×10^{-4} M NaOH and: curve a, 10^{-3} M SDS; curve b, 10^{-4} N Nafion; curve c, no stabilizer. Results were obtained using quartz cells. Curve d: 10^{-3} M SDS, measured in Pyrex cells.

DISCUSSION

The red shifts of the metal plasmon band during the formation of Ag particles can be correlated to surface effects that occur when the diameter of the metal particles is small.³ Shifts of the metal plasmon band in the opposite direction are observed during the photooxidation of the metal particles, indicating that they arise when metal and oxide particles coexist. Formation of small Ag particles on the surface of large oxide particles will result in electronic interactions between the two types of materials because Ag₂O has semiconducting properties. Thus, the surface effects of the metal particles are related to metal-semiconductor interactions. The shifts in the plasmon band of colloidal Ag are explained under the assumption that transfer of electron density from the metal to the oxide takes place when small Ag particles are formed on the surface of Ag₂O.

Very broad plasmon bands and stronger shifts of the plasmon bands were observed during the formation of Au particles. However, it is not possible to explain these effects under the assumption that they originate from surface and size effects, because smaller shifts (10 to 20 nm) are usually induced by these effects. In addition, the turbidity that develops with increasing time indicates that small Au particles formed initially react to generate species that scatter light, and that the optical effects are related to simultaneous changes in particle size and light scattering. The species that generate the optical effects may correspond to networks of weakly interacting metal particles, since it has been shown that the plasmon band of Au particles broadens and shifts to longer wavelengths when the particles form networks.^{4,5} Coalescence of the Au particles in the networks yields large metal particles with strong plasmon bands, which explains the blue shifts of the absorption bands that were observed at longer times. Since elemental gold is not formed in polypropylene or polystyrene containers it appears that metal particle formation is promoted by silica surfaces, and that the promoting effect of Pyrex is stronger than that of quartz. These observations are explained under the assumption that metal particle formation proceeds initially on top of the silica surfaces. The metal crystallites desorb from the surfaces during the early stages of growth, forming networks of small Au particles.

In conclusion, the spontaneous formation of metal particles in alcohols containing base is a simple method for the preparation of small Ag and Au particles. We have recently used this method for the deposition of thin films of these metals on Mylar supports.

Acknowledgments

We wish to thank B. Hajek for his help in XRD experiments. This work was supported by the Strategic Defense Initiative Organization's Office of Innovative Science and Technology (SDIO/TNI) through contract number N60921-91-C-0078 with the Naval Surface Warfare Center.

REFERENCES

- (1) W. P. Halperin, *Rev. Mod. Phys.* **58**, 533 (1986).
- (2) H. Gleiter, *Prog. Mater. Sci.* **33**, 223 (1989).
- (3) A. Henglein, *J. Phys. Chem.* **97**, 5457 (1993).
- (4) U. Kreibig, in Contributions of Cluster Physics to Materials Science and Technology, NATO ASI Series E, No. 104, edited by J. Davenas and P. M. Rabette, (Martinus Nijhof Publishers, Dordrecht, 1986) p. 373.
- (5) J. Turkevich, G. Garton and P. C. Stevenson, *J. Colloid Sci. Suppl.* **1**, 26 (1954).

ELECTRONIC STRUCTURE CALCULATIONS OF PURE AND OXIDIZED COPPER CLUSTERS USING JELLIUM AND MO - LCAO MODELS

HENRIK GRÖNBECK, MATS ANDERSSON AND ARNE ROSÉN

Department of Physics, Chalmers University of Technology and University of Göteborg,
S-412 96 Göteborg, Sweden.

ABSTRACT

A self consistent jellium approach to the chemisorption of molecular oxygen on copper clusters is investigated and compared with local density MO - LCAO calculations. The jellium model is found to be well suited for chemisorption studies and the results explain the main trends in the measured chemisorption properties of O₂ on copper clusters.

INTRODUCTION

One of the main objectives for research on clusters is the future prospects to use clusters in the design of new materials. Cluster assembled materials are believed to have special optical, mechanical or catalytic properties. The first step in the design of these new materials is, however, the characterization of free clusters. This has been an intense field of research during the last ten years[1].

One of the most interesting discoveries in the characterization free clusters is the existence of magic numbers first observed in the abundance spectra of sodium clusters by Knight et al.[2]. After these experiments various simple metal clusters have been reported to show magic numbers in electronic properties such as, ionization potential, electron affinity, optical response and reactivity[3]. The magic numbers are interpreted as electronic shell closings, resulting from quantized valence orbitals for electrons in an effective positive potential background constituted by the ionic cores. The self consistent spherical jellium model which almost has grown into a paradigm in cluster physics was first introduced as an appropriate cluster model by Ekardt[4]. The jellium model is simple and consequently an attractive tool that has been able to give a qualitative understanding of various experimental findings where the electronic shell structure dominates over the exact geometrical cluster configuration[5]. The original spherical model only accounts for the main trends in the size evolution of electronic properties, i.e. the abrupt property changes at cluster sizes of 8, 20, 40 atoms. To reproduce the experimental findings for also open shell clusters shape deformations of the jellium background has been introduced to model the Jahn - Teller distortion[6,7,8].

Reactivity of metal clusters is an important topic for applications in catalysis where the prospect is to obtain materials with appropriate reaction selectivity and efficiency. Regarding free clusters the reactivity has been reported to vary orders of magnitude with varying cluster size[9]. One example of cluster reactions showing a strong size dependence is the oxidation of copper clusters[10,11]. The reactivity has shown a close correlation to the jellium counting rules where the closed shell clusters with 8, 20, 40 atoms are reported to be less reactive compared with clusters having one, two or more valence electrons. Previously we

have reported on chemisorption of molecular oxygen on copper clusters using a first principle MO - LCAO approach within the local density approximation[12]. The calculations were done for clusters around the shell closing at eight atoms and indicated an electronic shell effect. The O_2 molecule was just weakly bound to the Cu_8 cluster while a strong bonding was obtained for Cu_9 . These calculations indicate that a jellium treatment of the clusters might be an appropriate approach to study the chemisorption process and we will in this work elaborate on this point and investigate how well a spherical jellium description of the copper clusters reproduce the first principle results. The comparison will be carried out for the Cu_8 and the Cu_9 clusters. In this way the two extremes of a closed and a mono valent cluster will be treated. The jellium model has previously mainly been used to describe alkali metal clusters. The extension to noble metal systems should be done with care since the hybridization of d, s and p states while forming larger aggregates is not completely clear. However, the ellipsoidal jellium model has successfully been used for the calculations of electron affinity of copper clusters[13]. The comparison of the jellium and the first principle results for the Cu_8 shell closing encouraged us to also calculate the chemisorption properties of oxygen around the shell closings at 20 and 40 atoms.

COMPUTATIONAL SCHEME

The density functional theory with the local spin density approximation[14,15] is used to transform the many - electron Schrödinger equation into a set of one - electron equations. The hamiltonian in atomic units reads,

$$h(r) = -\frac{1}{2}\nabla^2 + v_{eff}(r, \xi(r)) \quad (1)$$

Where $\xi(r)$ is the relative spin density,

$$\xi(r) = (\rho^{\uparrow}(r) - \rho^{\downarrow}(r))/\rho^{\text{tot}}(r). \quad (2)$$

The effective potential in Eq. 1, $v_{eff}(r, \xi(r))$ can be decomposed into three parts,

$$v_{eff}(r, \xi(r)) = v_n(r) + v_{ee}(r) + v_{xc}(r, \xi(r)). \quad (3)$$

The first term $v_n(r)$ represents the attractive Coulomb potential from the nuclei of the atoms, the second term $v_{ee}(r)$ is the electronic Coulomb potential due to the cluster charge density $\rho(r)$. The last term is a parameterization of the remaining electron-electron interactions for the one particle potential. For this term we have used the spin polarized formula by Gunnarsson and Lundqvist[16].

In the first principle calculations $v_n(r)$ is composed of the point charges of the constituent atoms in the cluster. The spherical jellium model approximates this part disregarding the ionic structure and uniformly distribute the charge on a sphere with a radius and a density which preserve charge neutrality. The cluster contribution to the ionic potential is thus given by,

$$v_{cluster} = \begin{cases} -\frac{Z}{r} & r \geq R \\ -\frac{Z}{R}(\frac{3}{2} - \frac{1}{2}(\frac{r}{R})^2) & r \leq R \end{cases}$$

Z is the net charge of the ionic system and R is the radius of the jellium sphere, $R = r_s Z^{1/3}$. For the Wigner Seitz radius r_s we have used the corresponding bulk value of copper 2.67

a.u.. Both in the first principle and the jellium calculations solutions to the hamiltonian is obtained by expanding wave functions in a linear combination of atomic or jellium wave functions, i.e. the LCAO approach. These wave functions are given on a numerical grid and are generated separately using a SCF-LDA code. The obtained secular equation in the LCAO approach is given a block diagonal form by applying the symmetry of the system and the matrix elements are evaluated using the three-dimensional integration scheme developed by Boerrigter et al.[17]. The eigenvalues are solved to self consistency using the density fitting method proposed by Delley and Ellis[18].

RESULTS

Fig.1a shows the one-electron eigenvalues calculated for Cu_8 and Cu_9 using the first principle MO-LCAO calculations and the self consistent spherical jellium approach, respectively. The cluster geometries used for the first principle calculations were for both cluster sizes the C_{2v} isomers. For the Cu_9 clusters this isomer is reported as the energetically most favorable[19]. The jellium description rely on the 4s electrons to completely determine the electronic properties of the cluster. Therefore we also have investigated the effect of the 3d electrons by carrying out the first principle calculations on two levels of approximation. One where the 3d electrons were included in the variational treatment and another where the 3d electrons were kept fixed as the lower lying states within the frozen core approximation. In both treatments also the 4p polarization wavefunctions were included together with an ionic basis set 4s4p of the Cu^{2+} ion to yield an increased variational freedom. In Fig. 1 the one - electron orbitals are denoted by the corresponding C_{2v} symmetry notation. For the calculations including the 3d - states only the orbitals mainly showing 4s character are

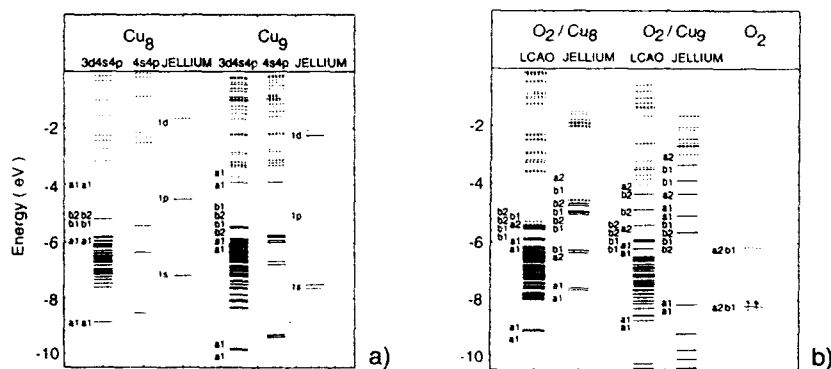


Figure 1: a) Energy level diagram for the bare clusters Cu_8 and Cu_9 . The occupied levels are represented by solid lines and the unoccupied by dashed lines. First principle results are shown at the two levels of approximation, one including the 3d states and one treating them in the frozen core approximation. The orbitals are denoted according to the C_{2v} symmetry. b) One electron energy spectrum for the oxidized clusters. The LCAO calculations represent the case of including the 3d states. To the right also the HOMO level for the free oxygen molecule is included.

indicated. In these calculations the shell structure is clearly apparent with a large HOMO - LUMO separation for Cu_8 and a high lying HOMO level for Cu_9 together with a minor HOMO - LUMO gap. The symmetry of the cluster also distribute the 4s electrons in a configuration similar to the jellium result. The exclusion of the 3d - states in the variational loop contracts the energy spectra and results in a larger separation of the one - electron orbitals corresponding to the jellium 1p state. However, it is obvious that the exclusion of the d - states just brings a minor shift to the HOMO level of the clusters and that for a qualitative understanding the 3d - states may be excluded. The spherical jellium levels are in comparison with the first principle levels shifted upwards. The absolute energies for the eigenvalues are scaled with the value of the jellium parameter r_s , which determines width and depth of the potential. Reducing the r_s value would yield absolute results in better agreement with the first principle results. However, changing the r_s value would also introduce an arbitrariness in the model removing one of the attractive features of the approach.

Knowing the electronic structure of the bare clusters we continue with an investigation of the O_2 chemisorption on the two cluster sizes. In Fig. 1b the energy level diagrams for the chemisorbed state of O_2 calculated with the jellium and the MO-LCAO approach including the 3d-electrons are shown. The bond distances between the molecule and the cluster were optimized, while the interatomic bond distance of the oxygen molecule was kept at 2.4 a.u. which corresponds to the free molecule value. Again, the notation is that corresponding to the C_{2v} symmetry. Also included in the figure are the antibonding π^* orbital levels for the free oxygen molecule. This orbital is in the free molecule half filled forming a triplet ground state. In the first principle results the chemisorption site for the Cu_8 cluster was a 'hollow' site while an 'on top' site was investigated for the Cu_9 cluster. The results obtained for Cu_8 and Cu_9 are different. For the closed shell Cu_8 cluster the interaction with the oxygen molecule breaks the high degeneracy and spin pairing of the bare cluster. The interaction is, however, not larger than that the cluster and oxygen orbitals keep their original character. The unoccupied a_2 and b_1 levels of the free molecule are shifted upwards to the HOMO level of the cluster introducing states just above the HOMO level removing the large HOMO - LUMO separation. For the Cu_9 clusters on the other hand the mixing between cluster and oxygen states is large. For example, the states originating from the 1d jellium level is for the nine atom cluster splitted over about twice the energy range compared with the eight atom cluster.

The stronger mixing can also be seen in the charge transfer from the cluster to the oxygen molecule. In our previous paper the charge transfer was analyzed using a partial density of states analysis. The net charge transfer from the cluster was found to be composed of two flows, one filling the antibonding π^* state and another resulting in less charge of the bonding π orbital. Both resulting in a weaker bond between the oxygen atoms. Using a Mulliken population analysis the charge transfer was in the Cu_8 cluster found to be 0.3 electrons for the jellium case and 0.4 for the MO - LCAO calculation. Corresponding numbers for Cu_9 were 0.7 and 0.6. These numbers clearly show the same trends. We also notice that the shift of the HOMO level due to the oxidation for the jellium and first principle results are equal, 0.2 eV for the Cu_8 cluster. This is an encouraging results since this enable us to do reliable estimations of how, for example the ionization potential will be effected by the oxidation. The corresponding change is overestimated for the Cu_9 cluster by a factor of two. This is a result of the high degeneracy of the jellium orbitals and introducing an ellipsoidal shape would decrease the discrepancy between the models. To summarize the comparison, we conclude

that the jellium model surprisingly well describes the chemisorption of the oxygen molecule. Thus, we will continue by employing the model for shell closings at larger cluster sizes.

The effect of the shell closing is mainly maintained when probing the closed shell clusters at 20 and 40 atoms together with the monovalent clusters of 21 and 41 atoms. In Fig. 2 the result of a partial density of states analysis is shown for the O_2/Cu_x systems. The chemisorption distances are optimized and the total density of states is projected on the oxygen 2p orbital. The solid line correspond to the component pointing towards the jellium sphere referred to as the 'perpendicular' component and the dashed line is the 'parallel' component. Both the occupied and the unoccupied density of states are displayed plotted with respect to the Fermi energy. The degeneracy of the levels for the free molecule is broken because of the perturbation of the jellium sphere as discussed above. We see how the splitting is much more efficient for the monovalent cluster than for the closed shell clusters. For the larger cluster sizes the cluster energy levels are closer in energy which results in a stronger mixing between these levels upon chemisorption. This will for the chemisorption result in a weaker size dependence, which clearly can be seen for the Cu_{40} and Cu_{41} clusters.

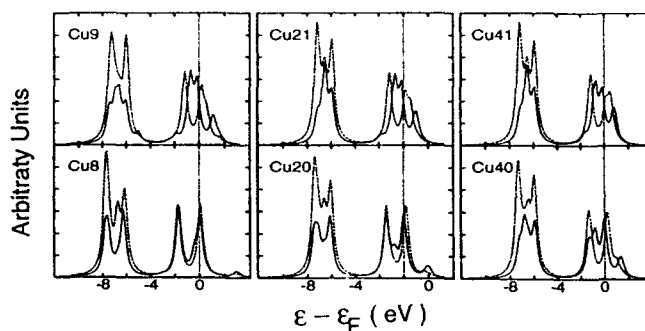


Figure 2: Partial density of states. The total density of states is projected on the two angular components of the oxygen 2p orbital. Solid line refers to the component pointing towards the jellium sphere, dashed line is the component parallel to the jellium sphere.

CONCLUSIONS

In order to analyze the reactivity of large clusters, for which first principle methods not are feasible, we have investigated the performance of the jellium model. The clusters were treated as jellium spheres and the chemisorption of molecular oxygen was studied self consistently using a MO-LCAO approach within the LSD scheme. The capability of the model was checked through a comparison with first principal calculations for the electronic shell closing at eight atoms with encouraging results. Although the spherical jellium model showed a poor performance for bare clusters due to the highly degenerated levels, the main trends in the oxidation was found to be properly described.

ACKNOWLEDGMENTS

Stimulating discussions with John L. Persson is acknowledged. Financial support was obtained from NUTEK/NFR Materials Science Consortium "Clusters and Ultrafine Particles".

REFERENCES

1. ISSPIC 6 Proceedings, Z. Phys. D **26**; ISSPIC 5 Proceedings, Z. Phys. D **19**, 20
2. W.D Knight, K. Cleminger, W. de Heer, W.A. Saunders, M.Y. Chou and M.L. Cohen, Phys. Rev. Lett. **52**, 2141 (1984)
3. W. de Heer, Rev. Mod. Phys. **65**, 611 (1993).
4. W. Ekardt, Phys. Rev. B **29**, 1558 (1984).
5. M. Brack, Rev. Mod. Phys. **65**, 677 (1993).
6. K. Cleminger, Phys. Rev. B **32**, 1359 (1985).
7. W. Ekardt and Z. Penzar, Phys. Rev. B **38**, 4273 (1988).
8. G. Lauritsch, P.G. Reinhard, J. Meyer and M. Brack, Phys. Lett. A **160**, 179 (1991).
9. A. Kaldor, D.M. Cox and M.R. Zakin, Adv. in Chem. Phys. **70**, 211 (1988).
10. B.J. Winter, E.K. Parks and S.J. Riley, J. Chem. Phys. **94**, 8618 (1991).
11. M. Andersson, J.L. Persson and A. Rosén, Nanostr. Mater. **3**, 337 (1993).
12. H. Grönbeck and A. Rosén, Comp. Matr. Sci. accepted.
13. Z. Penzar and W. Ekardt, Z. Phys. D **17**, 69 (1990).
14. P. Hohenberg, Phys. Rev. **136**, 864 (1964).
15. W. Kohn and L.J. Sham, Phys. Rev. **140**, A1133 (1965).
16. O. Gunnarsson and B.I. Lunqvist, Phys. Rev. B **13**, 4274 (1976).
17. P.M. Boerrigter, G. Te Velde and E.J. Bearendsi, Int. J. Quant. Chem. **33**, 37 (1988).
18. B. Delley and D.E. Ellis, J. Chem. Phys. **76**, 1949 (1982).
19. M.A. Nygren and P. Siegbahn, J. Chem. Phys. **96**, 7579 (1992).

NANOCOMPOSITES CONTAINING NANOCLUSTERS OF METALS OR SEMICONDUCTORS

KIMBERLY J. BURNAM*, JOSEPH P. CARPENTER*, CHARLES M. LUKEHART*,
STEPHEN B. MILNE*, S. R. STOCK**, R. GLOSSER*** AND BOBBY D. JONES***

*Vanderbilt University, Department of Chemistry, Nashville, TN 37235

**Georgia Institute of Technology, School of Materials Science and Engineering, Atlanta, GA 30332-0245

***University of Texas at Dallas, Department of Physics, Richardson, TX 75083

ABSTRACT

Neutral, low-valent complexes of transition metals or an organometallic compound of Ge are prepared containing ancillary ligands which bear silicate ester or (alkoxy)silicon functional groups. Inclusion of these molecules as dopant species in a conventional sol-gel synthesis of silica xerogels affords silica xerogels in which dopant molecules have presumably been covalently incorporated into the xerogel matrix with uniform and high dispersion. Subsequent thermal treatment of these molecularly doped xerogels under reducing or oxidizing/reducing conditions gives nanocomposites containing nanoclusters of metals or semiconductor substances. By this procedure, nanocomposites containing nanoclusters of Ag, Cu, Pt, Os, CCO_3 , Fe_2P , Ni_2P , or Ge have been prepared. Preliminary evidence for the formation of a nanocomposite containing Pt-Sn nanoclusters derived from a bimetallic molecular precursor is also presented. Characterization data for the nanocomposite materials include TEM, electron diffraction, EDS, XRD, and selected use of micro-Raman spectroscopy. These results support the hypothesis that covalent incorporation of molecular precursors containing low-valent metals into a silica xerogel can afford nanocluster phases with high dispersion, relatively small particle size, and unusual elemental composition.

INTRODUCTION

Nanocomposite materials consisting of very small particles (typically nanoscale particles having diameters less than 100 nm or, equivalently, 1000 Å) of a guest substance dispersed throughout a host matrix are a topic of intense current interest for potential applications in chemical catalysis or as magnetic, electronic, or photonic (nonlinear optical) materials [1]. Guest substances of metals or semiconductors are of particular interest for these applications.

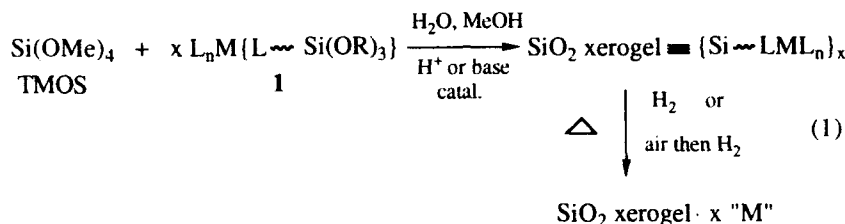
Nanocomposites containing nanoclusters of metals dispersed in a silica xerogel host matrix have been prepared by doping metal salts into a conventional sol-gel synthesis of silica xerogel followed by oxidative and reductive thermal treatments. For some metals, this procedure gives metal nanoclusters of small and quite uniform size. A more general procedure for obtaining such metal nanoclusters having a fairly uniform and monomodal particle-size distribution has been evaluated by Schubert and coworkers [2]. In this adaptation, a trialkylorthosilicate group is attached via a $\text{CH}_2\text{CH}_2\text{CH}_2$ linkage to either a NH_2 or ethylenediamine fragment. These molecules serve as bifunctional ligands. Addition of these donor molecules to a conventional sol-gel recipe in the presence of metal salts leads to complexation of the metal ion by the amine functional groups and to hydrolysis and condensation of the silicate ester functional groups with the resulting silica xerogel matrix as it is being formed. This covalent attachment of metal ion complexes to a xerogel matrix apparently gives more uniform dispersion of the metal ions throughout the xerogel. Subsequent oxidative and reductive thermal treatments results in silica

xerogels containing metal nanoclusters. Selected metal nanoclusters of the following metals (average diameter, Å, diameter range, Å) have been prepared by Schubert using this method: Ag (195, 90 - 309); Cu (39, 15 - 74); Pt (25, 8 - 42).

In this study, covalent attachment of molecular precursors to a growing silica xerogel matrix by means of bifunctional ligands is extended to include neutral, low-valent metal complexes or an organometallic compound of germanium. Such complexes are expected to be more inert toward ligand substitution than ionic amine complexes thereby affording a more uniform incorporation of molecular precursor throughout the xerogel matrix. Furthermore, precursor molecules containing low-valent metals may decompose thermally under solely reductive conditions to give nanoscale phases thus obviating the need for an oxidative thermal decomposition treatment. This latter aspect might provide synthetic control over the elemental composition of the nanocluster phase through the proper choice of precursor molecule.

EXPERIMENTAL

The overall synthetic strategy is shown in equation (1). A metal complex or compound, **1**, is



prepared containing a bifunctional ligand or substituent which bears a silicate ester (as shown) or an (alkoxy)silyl functional group. Addition of **1** to a conventional sol-gel synthesis of silica xerogel from tetramethylorthosilicate, TMOS, water, methanol and/or DMF or THF, and an acid or base catalyst gives a silica xerogel in which the dopant molecule is covalently attached to the xerogel matrix. Thermal decomposition of this doped xerogel under reducing or oxidizing/reducing conditions affords a silica xerogel containing a nanophase substance.

The bifunctional ligands used in this study include the commercially available thiols, $\text{HS}(\text{CH}_2)_3\text{Si}(\text{OMe})_3$, HSR, and $\text{HSCH}_2\text{SiMe}(\text{OEt})_2$, HSR', and the phosphines, $\text{PPh}_2(\text{CH}_2)_2\text{Si}(\text{OMe})_3$, L^A , $\text{PPh}_2(\text{CH}_2)_2\text{Si}(\text{OEt})_3$, L^B , and $\text{PEt}_2(\text{CH}_2)_2\text{Si}(\text{OEt})_3$, L^C , which were prepared according to literature procedures [3].

The molecular precursors, **1**, were prepared using published procedures or procedures reported for the preparation of analogous thiolate or phosphine complexes. These compounds include; $\text{Ag}[\text{SR}']$ oligomer [4], CuL^B_3Cl [5], $\text{Os}(\eta^6\text{-}p\text{-cymene})\text{L}^A\text{Cl}_2$ [6], *cis*- $\text{PtL}^A_2\text{Cl}_2$ [7], $(\text{HO})_3\text{SiCCO}_3(\text{CO})_9$ [8], NiL^B_4 [9], $\text{Fe}(\text{CO})_4\text{L}^A$ [10], Me_3GeSR [11], and *trans*- $\text{Pt}(\text{SnPh}_3)_2\text{L}^C_2$ [12].

Conventional sol-gel recipes were followed in the syntheses of the molecularly doped silica xerogels [13]. The xerogels were formed at room temperature using aqueous HCl as the acid catalyst or aqueous ammonia as the basic catalyst. Stoichiometries for the molar ratio of TMOS to molecular dopant complex varied from 4:1 to 100:1. Product xerogels were washed several times with alcohol prior to air drying.

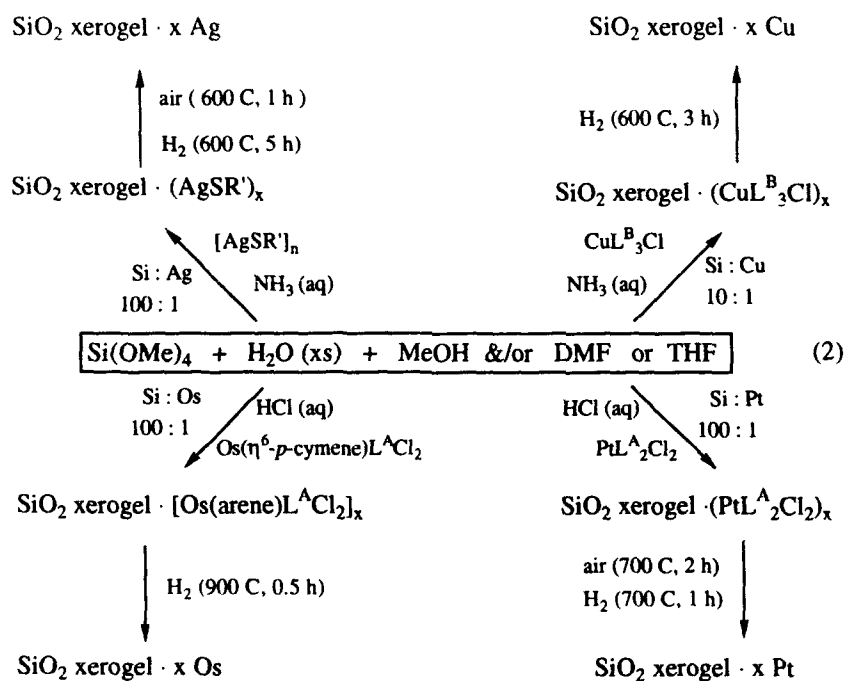
Conversion of the molecularly doped xerogels to nanocomposite materials was accomplished by placing the powdered xerogel into an alumina boat. Such samples were then introduced into a

quartz tube placed inside of a tube furnace. The atmosphere within the tube was controlled by gaseous flow of the appropriate gas. Temperatures were measured by an internal thermocouple. Specific thermal conditions are described below.

RESULTS AND DISCUSSION

Nanocomposites containing nanoclusters of metals

The synthetic conditions used for the formation of silica xerogels containing nanoclusters of Ag, Cu, Os, or Pt are shown in equation (2). TEM micrographs of typical samples of these nanocomposites are shown in Figure 1. The metal nanocluster features are highly dispersed throughout the xerogel matrix. For each sample, the presence of crystalline metal phase is confirmed by electron diffraction ring patterns. Other crystalline phases are not evident. EDS analysis reveals the presence of silicon and the appropriate metal in each sample and, within the limits of detection, the absence of any residual S, P, or Cl that was contained in the precursor complex. Histograms of the respective metal particle sizes taken from TEM images indicate monomodal particle size distributions having the following diameters (average, range): Ag (53, 30 - 120 Å); Cu (24, 15 - 35 Å); Os (27, 10 - 70 Å); Pt (38, 20 - 80 Å). XRD analysis of the Ag, Cu, and Os nanocomposites confirms the presence of crystalline metal phases with volume-weighted average particle diameters of 125 Å for the Ag nanoclusters and 55 Å for the Os nanoclusters. The presence of a small fraction of relatively large metal clusters presumably accounts for the larger



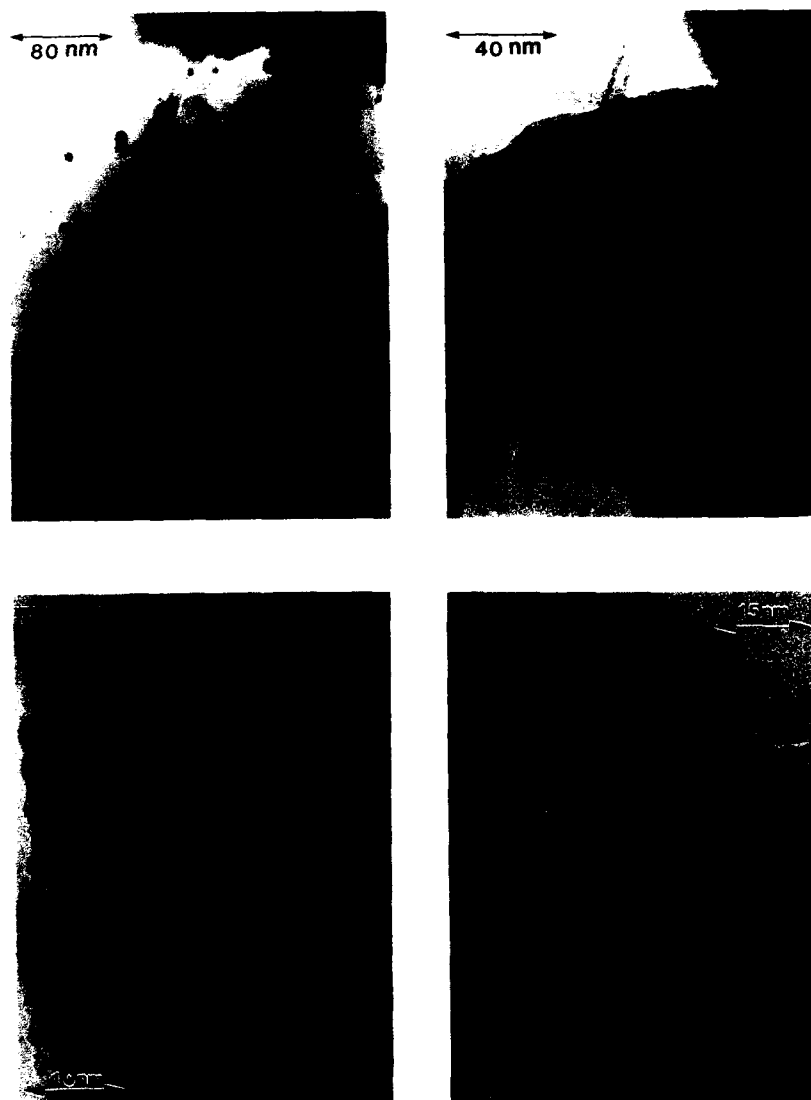


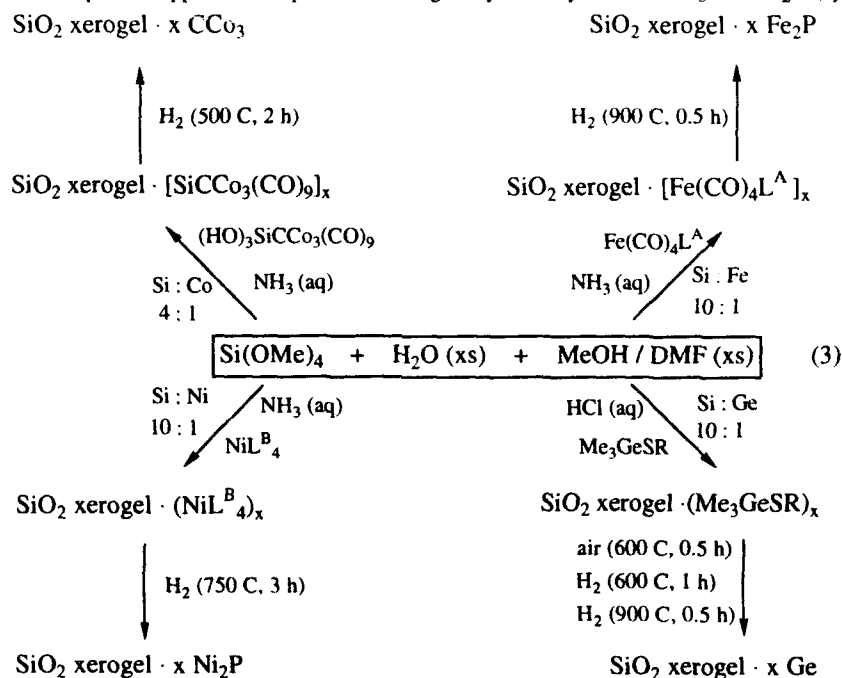
Figure 1. TEM micrographs of silica xerogel nanocomposites containing Ag (upper left), Cu (upper right), Os (lower left), or Pt (lower right) nanoclusters.

particle diameters as determined from XRD peak widths. XRD peaks of the Cu nanocomposite are too broad to give particle size measurement. A small amount of crystalline copper phosphide, Cu_3P , is also evident in the XRD scans of the Cu nanocomposite indicating that all of the phosphorus had not been eliminated from the precursor xerogel during reductive thermal decomposition. XRD analysis of the Pt nanocomposite is in progress.

In recent work by others, Gacoin and coworkers prepared Ag nanoclusters (41, 5 - 120 Å) in a sol-gel matrix using bifunctional ligands with reduction of Ag^+ ions being induced by γ -radiation [14]. Lisiecki and Pileni formed Cu nanoclusters with diameters of 14 - 35 Å by solution reduction of copper ion in reverse micelles [15]. The formation of Os particles from the thermal decomposition of silica-supported $\text{Os}_3(\text{CO})_{12}$ has been reviewed by Psaro, et al., [16]. Chaudret and coworkers produced Pt nanoclusters of 12 or 15 Å average diameter in nitrocellulose or cellulose acetate, respectively, by solution reduction of a precursor compound of Pt [17].

Nanocomposites containing nanoclusters of semiconductors

The synthetic conditions used for the formation of silica xerogels containing nanoclusters of CCo_3 , Fe_2P , Ni_2P , or Ge are shown in equation (3). TEM micrographs of typical samples of these nanocomposites are shown in Figure 2. The nanocluster features are highly dispersed throughout the xerogel matrix. For each sample, the presence of crystalline nanophase material is confirmed by electron diffraction ring patterns. Although the ring pattern for the cobalt carbide nanocomposite revealed the presence of some amount of crystalline Co_3O_4 , the other three nanocomposites appear to be pure. The single crystallinity of the CCo_3 and Fe_2P (syn-



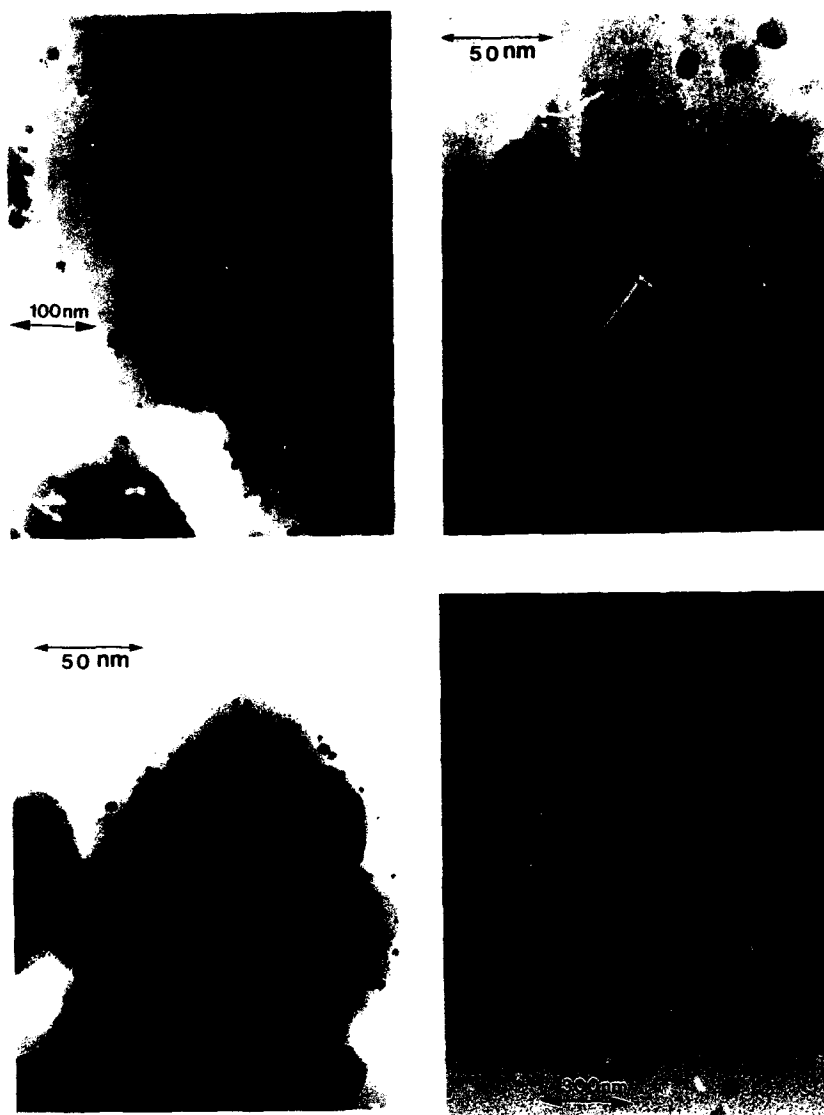


Figure 2. TEM micrographs of silica xerogel nanocomposites containing CCo_3 (upper left), Fe_2P (upper right), Ni_2P (lower left), or Ge (lower right) nanoclusters.

oarringerite) particles was determined by successful interpretation of electron diffraction spot patterns obtained from single particles. Also, TEM micrographs of individual Fe_2P particles having the correct orientation reveal hexagonal projections consistent with this hexagonal phase, and at high magnification TEM images of individual Ge particles show fringe patterns. EDS analysis reveals the presence of silicon and the other elements expected from the appropriate phase in each sample. Within the limits of detection, the EDS spectrum of the Ge nanocomposite revealed the complete absence of sulfur. Microanalysis of the CCo_3 nanocomposite gives a Si/Co atomic ratio of 4.7/1.0. Microanalytical data for the Ge nanocomposite is consistent with the approximate composition of $(\text{SiO}_2)_{15}\text{Ge}$.

Histograms of the respective particle sizes taken from TEM images indicate monomodal particle size distributions having the following diameters (average, range): CCo_3 (255, 10 - 460 Å); Fe_2P (47, 20 - 80 Å); Ni_2P (26, 15 - 40 Å); Ge (95, 35 - 155 Å). XRD analysis of the CCo_3 , Fe_2P , and Ge nanocomposites confirms the presence of the appropriate crystalline phases with volume-weighted average particle diameters of 100 Å for the Fe_2P nanoclusters and 68 Å for the Ge nanoclusters. Presumably, the Fe_2P nanocomposite contains a small fraction of relatively large crystalline particles of Fe_2P , while the Ge nanocomposite contains a relatively large fraction of small, highly crystalline Ge particles. The XRD spectrum of the CCo_3 nanocomposite reveals a predominant CCo_3 crystalline phase and the presence of crystalline Co_3O_4 . XRD analysis of the Ni_2P nanocomposite is in progress.

Micro-Raman analysis of the Ge nanocomposite shows a sharp Raman signal centered at 301 cm^{-1} corresponding to the phonon frequency of microcrystalline Ge (Figure 3). The FWHM of this peak of $13 \pm 0.5\text{ cm}^{-1}$ is consistent with Ge microcrystals having diameters of approximately 60 Å. Similar Raman signals have been reported by Fujii and coworkers for Ge nanoclusters formed by rf co-sputtering methods [18].

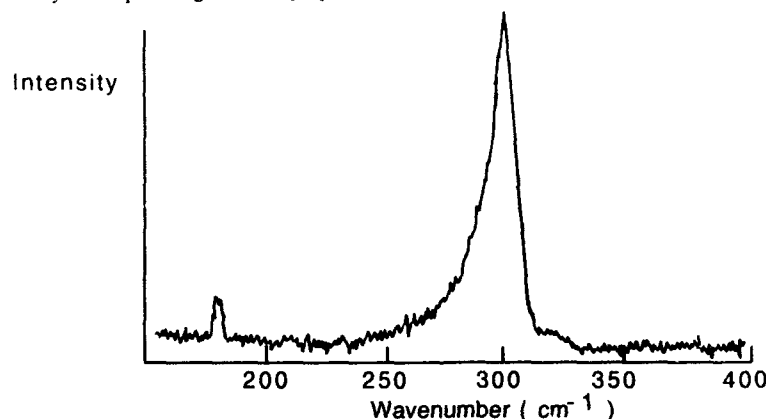


Figure 3. Micro-Raman spectrum of the Ge nanocomposite showing the phonon band of Ge.

In work reported by others, Fox and coworkers have found that CCo_3 is an effective methanol reforming catalyst [19], and thermal decomposition of cobalt oxo clusters containing $(\text{OC})_9\text{Co}_3\text{CCO}_2^-$ fragments as ligands has been used by Wolf and coworkers to prepare hydrogenation catalysts [20]. Fujii and coworkers report that Fe_2P is paramagnetic and exhibits ferromagnetism at temperatures below 217 K [21]. Particles of Fe_2P have been used by Seeger and coworkers as an ink in the fabrication of integrated circuits [22]. Ni_2P is commercially available as a chemical reagent, and Sharon and coworkers report that it has a band gap of 1.0 eV [23]. In recent work, Paine and coworkers have prepared nanocrystalline Ge embedded in SiO_2 by a hydrothermal oxidation and subsequent hydrogen reduction procedure [24].

Nanocomposite containing bimetallic nanoclusters

Very preliminary results support the hypothesis that the metal core composition of a bimetallic precursor molecule can be used to control the elemental composition of a resulting nanophase material. As shown in equation (4), a Pt-Sn molecular precursor can be covalently incorporated into a silica xerogel using bifunctional phosphine ligands. Subsequent reductive thermal treatment gives a nanocomposite containing an apparent mixture of Pt-Sn nanophases. A typical TEM micrograph of this nanocomposite is shown in Figure 4. Nanocluster features are dispersed throughout the xerogel matrix as particles having diameters in the range of 60 - 175 Å. The particulate features show either hexagonal or more spheroidal projections. Electron diffraction ring patterns confirms the presence of several Pt-Sn phases including the hexagonal PtSn 1:1 phase (niggliite). Electron diffraction spot patterns obtained from a single hexagonal nanocrystal confirm the presence of this PtSn hexagonal phase. Reduction at 750 C gives a less complex ring pattern and is consistent with the presence of PtSn and possibly a PtSn₄ crystalline phase. EDS analysis of this nanocomposite reveals Si, Pt, and Sn with no evidence of residual phosphorus from the molecular precursor. More judicious choice of thermal reductive conditions might give selective formation of the more unstable PtSn₂ phase. The use of 1:1 Pt/Sn molecular precursors to give selective formation of the hexagonal PtSn nanocomposite is currently under investigation.

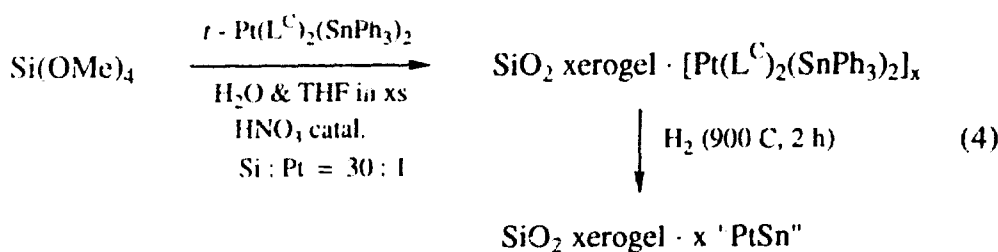


Figure 4. TEM micrograph of a "PtSn" nanocomposite showing hexagonal PtSn nanocrystals.

In work by others, Sinfelt has reviewed the importance of Pt - Sn bimetallic catalysts for reforming processes [25], and Koel and coworkers have reported the use of Pt/Sn surface alloys in catalytic reactions with acetylene [26]. An electron microdiffraction study of Pt-Sn-alumina reforming catalysts has been published recently by Srinivasan and coworkers [27].

CONCLUSIONS

Covalent incorporation of neutral precursor molecules into a silica xerogel can be accomplished through the use of bifunctional ligands or substituents and conventional sol-gel synthetic methods. Thermal decomposition of these doped xerogels under reductive or oxidative/reductive conditions gives nanocomposites containing nanoclusters of a guest phase dispersed throughout the silica xerogel matrix. In some cases, the nanophase material is obtained as smaller and more uniform particles than those prepared by related synthetic methods. The elemental core composition of the molecular precursor provides some degree of synthetic control over the elemental composition of the nanophase material. Nanoclusters of Ag, Cu, Ge, Os, or Pt are obtained from thiolate or phosphine precursor complexes. Nanoclusters of CCl_3 , Fe_2P , or Ni_2P are obtained from metal carbonyl or phosphine precursors using solely reductive thermal conditions. The formation of these latter nanophase substances indicates that this synthetic method might find application in the synthesis of nanophase materials that are difficult to prepare by other methods. A preliminary report on the use of this synthetic method is available [28].

ACKNOWLEDGMENTS

We thank Mr. W. J. Ready, Undergraduate Research Assistant, in the School of Materials Science and Engineering at Georgia Institute of Technology for his assistance in obtaining XRD measurements. Acknowledgment is made to the donors of The Petroleum Research Fund, administered by the ACS, for partial support of this research.

REFERENCES

1. G. D. Stucky, *Naval Res. Rev.* **43**, 28 (1991); G. Schmid, *Chem. Rev.* **92**, 1709 (1992); J. H. Sinfelt and G. D. Meitzner, *Acc. Chem. Res.* **26**, 1 (1993); M. L. Steigerwald and L. E. Brus, *Acc. Chem. Res.* **23**, 183 (1990); Y. Wang, *Acc. Chem. Res.* **24**, 133 (1991); H. Weller, *Angew. Chem. Int. Ed. Engl.* **32**, 41 (1993); H. Weller, *Adv. Mater.* **5**, 88 (1993).
2. B. Breitscheidel, J. Zieder and U. Schubert, *Chem. Mater.* **3**, 559 (1991).
3. V. H. Niebergall, *Makromol. Chem.* **59**, 218 (1962).
4. S. Akerstrom, *Arkiv Kemi* **24**, 505 (1965).
5. W. C. Baird, *J. Am. Chem. Soc.* **85**, 1009 (1963).
6. J. A. Cabeza and P. M. Maitlis, *J. Chem. Soc., Dalton Trans.* 573 (1985).
7. J. A. Davies, J. G. Mierzwiaik and R. Syed, *J. Coord. Chem.* **17**, 25 (1988).
8. D. Seyferth, C. N. Rudie and M. O. Nestle, *J. Organomet. Chem.* **178**, 227 (1979).

9. C. S. Cundy, *J. Organomet. Chem.* **69**, 305 (1974).
10. M. J. Therien and W. C. Trogler, *Inorg. Synth.* **28**, 173 (1990).
11. W. E. Davidson, K. Huus and M. C. Henry, *J. Organomet. Chem.* **3**, 285 (1965).
12. C. Eaborn, A. Pidcock and B. R. Steele, *J. Chem. Soc., Dalton Trans.* 809 (1975).
13. T. Adachi and S. Sakka, *J. Mater. Sci.* **22**, 4407 (1987).
14. T. Gacoin, F. Chaput, J. P. Boilot and G. Jaskierowicz, *Chem. Mater.* **5**, 1150 (1993).
15. I. Lisiecki and M. P. Pileni, *J. Am. Chem. Soc.* **115**, 3887 (1993).
16. R. Psaro, C. Dossi, A. Fisco and R. Ugo, *Res. Chem. Intermed.* **15**, 31 (1991).
17. A. Duteil, R. Queau, B. Chaudret, R. Mazel, C. Roucau and J. S. Bradley, *Chem. Mater.* **5**, 341 (1993).
18. M. Fujii, S. Hayashi and K. Yamamoto, *Jpn. J. Appl. Phys.* **30**, 687 (1991).
19. J. R. Fox, F. A. Pesa and B. S. Curatolo, U. S. Patent No. 4 632 774 (30 December 1986).
20. Z. Kalenik, B. Ladna, E. E. Wolf and T. P. Fehlner, *Chem. Mater.* **5**, 1247 (1993).
21. H. Fujii, Y. Uwatoko, K. Motoya, Y. Ito and T. Okamoto, *J. Phys. Soc. Jpn.* **57**, 2143 (1988).
22. R. E. Seeger, Jr., N. H. Morgan and J. R. Landry, Jr., U. S. Patent No 4 759 970 (26 July 1988).
23. M. Sharon, G. Tamizhmani, C. Levy-Clement and J. Rioux, *Sol. Cells* **26**, 303 (1989).
24. D. C. Paine, C. Caragianis, T. Y. Kim, Y. Shigesato and T. Ishahara, *Appl. Phys. Lett.* **62**, 2842 (1993).
25. J. H. Sinfelt, *Bimetallic Catalysis: Discoveries, Concepts, and Applications*, (Wiley, New York, 1983), pp. 130 - 157.
26. C. Xu, J. W. Peck and B. E. Koel, *J. Am. Chem. Soc.* **115**, 751 (1993).
27. R. Srinivasan, L. A. Rice and B. H. Davis, *J. Catal.* **129**, 257 (1991).
28. C. M. Lukehart, J. P. Carpenter, S. B. Milne and K. J. Burnam, *Chemtech* **23**, No. 8, 29 (1993).

MOLECULAR PRECURSORS TO FUNCTIONAL MATERIALS

NORMAN HERRON*, DAVID L. THORN AND RICHARD L. HARLOW

The DuPont Company, Central Research and Development, P.O. Box 80328, Wilmington, DE
19880-0328

ABSTRACT

The design of molecular precursors to materials for catalysis will be described. Aluminum fluoride is an important catalytic material for fluorocarbon transformations which are key to the production of CFC alternatives. Catalytic activity is closely related to the crystalline phase of the bulk AlF_3 and we show how this phase chemistry can be precisely controlled using molecular precursors to produce pure known phases and also to extend to previously unknown phases. A similar approach to vanadyl phosphate oxidation catalysts will be described where cluster chemistry can be invoked to generate isolated fragments of a catalyst's structure and then used either to explore mechanism or be used as precursors to functional catalyst materials. The underlying themes of controlled molecular precursor synthesis, resultant processability and eventual easy conversion to useful materials are emphasized throughout.

INTRODUCTION

The journey from isolated small molecule to extended bulk solid is a trek which crosses several traditional scientific disciplines and, therefore, materials in the intermediate size regime have received less attention than perhaps they merit. The realization that these intermediate materials have unique properties of their own has spurred synthetic chemists to turn more attention to the construction of molecular precursors and their subsequent conversion into larger assemblies and extended bulk solids. One early example of this approach has been the proliferation of sol-gel based ceramic syntheses where a molecular material such as tetraethylorthosilicate has been used as the fundamental building block to construct a macroscopic material - in this case silica - by simple chemical transformation. Molecule-based routes to functional materials offer the possibilities of new mechanistic understanding of their functionality and perhaps rational control over bulk properties. Equally important is the potential for exploiting new uses for traditional materials by permitting their production in non-traditional forms or phases and with possibly enhanced processability.

Our approach has been to borrow a concept long-used by organic chemists, the idea of retrosynthesis. "Given a target inorganic material, how can we design a molecule having the structural and reactivity features necessary for its eventual assembly into a desired solid-state structure? Can we learn something about the assembly process itself which may shed light on the origin of the desirable properties of the functional material? Can we use this knowledge to actually engineer the solid so as to 'tailor' new, desirable properties?" With these as the lofty goals, this contribution will briefly describe two case-histories from our own laboratory where we have tried to use these ideas to generate new materials or new understanding of traditional functional materials from the areas of catalysis (AlF_3 and vanadium phosphates).

FLUOROALUMINATE CATALYSTS AND PRECURSORS

Fluorides of aluminum are some of the most important of inorganic materials manufactured since they find use both as commodity chemicals [1] (in the aluminum industry) and as catalysts for the new "ozone benign" chlorofluorocarbon alternatives [2]. In this latter application it has become clear that the catalytic activity of AlF_3 is strongly dependent on the structural phase used [3]. This has led to extensive study of the phase chemistry of AlF_3 and an attendant folklore has evolved around the phase diagram of AlF_3 itself. Two phases are well characterized - α and β - with reliable synthetic and structural data available [4,5]. In both cases, the structures are built of octahedral $[\text{AlF}_6]$ units where all of the fluoride ions are corner-shared. The patent literature is replete with a litany of other less-substantiated claims to additional phases (e.g. γ , δ , ϵ) which may represent either impure materials or mixtures of the better characterized phases [2,6]. With this background, we began to explore the phase chemistry of AlF_3 - applying the retrosynthesis strategy described above. As our molecular precursors, we wished to explore isolated fluoroaluminate salts which could then be thermally transformed into AlF_3 itself. In order to achieve this latter goal we decided to investigate organic cation salts of the form M^+AlF_4^- (where M is an organic cation) so that simple thermal degradation could release the equivalent of MF as a volatile species leaving behind AlF_3 . On commencing this work we quickly discovered that the literature described no examples of the tetrafluoroaluminate anion which is implicit in these salts. Rather, all fluoroaluminate materials reported to that point existed as corner-shared octahedral $[\text{AlF}_6]$ species and this is true even for those materials with stoichiometries which superficially appear to contain the $[\text{AlF}_4]^-$ anion (MAlF_4 , $\text{M}=\text{K}, \text{Rb}, \text{NH}_4, \text{Ti}$ [7]). We set out to explore the existence of salts of organic cations with true tetrahedral isolated AlF_4^- anions and to investigate their utility as precursors to AlF_3 catalysts.

Reaction of trimethylaluminum or aluminum di(isopropoxide) acetoacetic ester chelate with the HF-pyridine adduct in a ratio of Al:F 1:4 was performed in pyridine solvent in a plastic container under an inert atmosphere [8]. The strongly exothermic reaction deposits a white material which is essentially insoluble in all common solvents. The microcrystalline solid has the stoichiometry

[pyridine-H]⁺.AlF₄⁻ and is produced in close to quantitative yield. M.A.S. ¹⁹F n.m.r. (broad peak at δ = -155ppm) suggests that the solid consists not of tetrahedral [AlF₄]⁻ species but rather of the ubiquitous [AlF₆] octahedral species and therefore implies extensive fluoride bridging consistent with the low solubility. This solid may, however, be rendered soluble in either acetonitrile, methylene chloride or methanol by metathesizing the pyridinium cation [8] to any of a number of other cations such as N(CH₃)₄⁺, P(Ph)₄⁺, As(Ph)₄⁺, 2,4,6-trimethylpyridinium (collidinium), 1,8-bis(dimethylamino)naphthalene.H⁺ (proton sponge, PS (Aldrich)). All of these materials (and other related cation species) can be prepared and crystallized [8,9] and all have been shown (by x-ray single crystallography) to contain the previously unconfirmed AlF₄⁻ tetrahedral anion as an isolated species. Figure 1 depicts the crystal structure of the PSH⁺ salt and lists some of the important structural data.

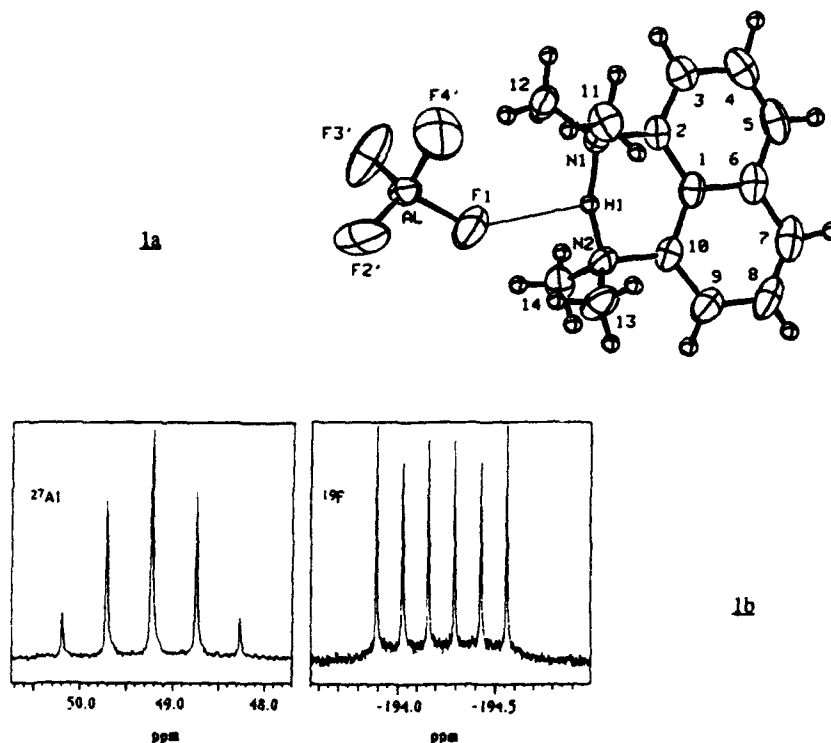


Figure 1a). Molecular structure of the salt PSH⁺.AlF₄⁻. Al-F_{av.} = 1.62(3)Å; F(1)-H(1) = 2.77Å.
b) ²⁷Al (78.31MHz) and ¹⁹F (282.78MHz) n.m.r. spectra of PSH⁺.AlF₄⁻ in d³-acetonitrile.

The accompanying ^{27}Al and ^{19}F nmr spectra of the PSH^+ material dissolved in acetonitrile categorically confirm the existence of the tetrahedral anion in solution while M.A.S ^{19}F n.m.r. shows a single very sharp peak at $\delta = -187\text{ppm}$ which turns out to be characteristic of the tetrahedral anion in the solid-state. In all cases, it appears that the tetrahedral anion has little or no propensity for interaction with the organic cations via hydrogen bonding. This is in stark contrast to octahedral $[\text{AlF}_6]$ species which almost always become involved in hydrogen bonding or bridging to avoid terminal fluoride species [8].

This wealth of new organic salts of AlF_4^- permits the investigation of their thermal "decomposition" into AlF_3 via loss of the organic cation fluoride equivalent as represented in (1).



Our intent was that the MF species would be "volatile" at moderate temperatures and would thereby allow production of AlF_3 at unprecedentedly low temperatures - perhaps allowing the preparation of hitherto unknown, metastable phases.

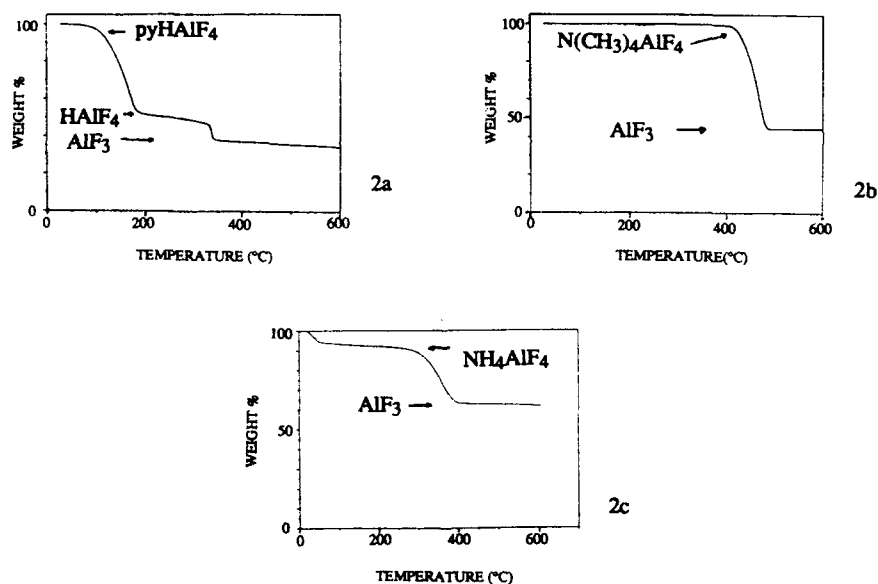


Figure 2. TGA curves of a) pyridinium. AlF_4 b) $\text{N}(\text{CH}_3)_4\text{AlF}_4$. c) $\beta\text{-NH}_4\text{AlF}_4$ (Run in N_2 at a ramp of $10^\circ\text{C}/\text{min}$. Stoichiometries calculated from weight changes are indicated on the curves).

Beginning with the original, insoluble pyridinium salt, TGA reveals two weight loss events as temperature is raised. Between 100 and 200°C pyridine is lost quantitatively leaving a material of stoichiometry HAIF_4 . At 325°C a clean, abrupt evolution of HF from this material leaves pure AlF_3 with no further weight changes up to 900°C (Figure 2a.). At this point XRD reveals it to be phase pure $\alpha\text{-AlF}_3$ with no contamination from any other material including Al_2O_3 (any phase). The new material HAIF_4 (nominally a solid acid but chemically does not appear to act as such) is crystalline as revealed by XRD (Figure 3a) and the structure is, as yet, unknown. The XRD pattern of the AlF_3 produced immediately after evolution of HF from the HAIF_4 material at 325°C (Figure 3b) reveals a major crystalline phase reminiscent of the known pyrochlore materials $\text{AlF}_x(\text{OH})_{3-x}$ ($0.4 < x < 2.07$) [10] and FeF_3 [11]. Pure AlF_3 having this structure has never been reported and so we have refined this structure using XRD data and Reitveld techniques. The new phase is designated $\eta\text{-AlF}_3$ and the structure refines very well in the pyrochlore model. The structure is depicted in Figure 4a and can be viewed as a relative of the established $\beta\text{-AlF}_3$ phase having the same nanoporous openings defined by corner-shared rings of six $[\text{AlF}_6]$ octahedra. However, where the β -phase has these openings aligned along $[001]$ of the crystal forming straight channels, the η -phase has adjacent rings tilted with respect to each other producing an undulating channel along $[110]$ of approximate diameter 2.6 Å. This undulation is imposed by the other key structural feature of the η -phase - the presence of clusters of four tetrahedrally-disposed $[\text{AlF}_6]$ octahedra. Three fluoride ions from each of the four octahedra of the cluster are corner-shared to the other three octahedra of the cluster.

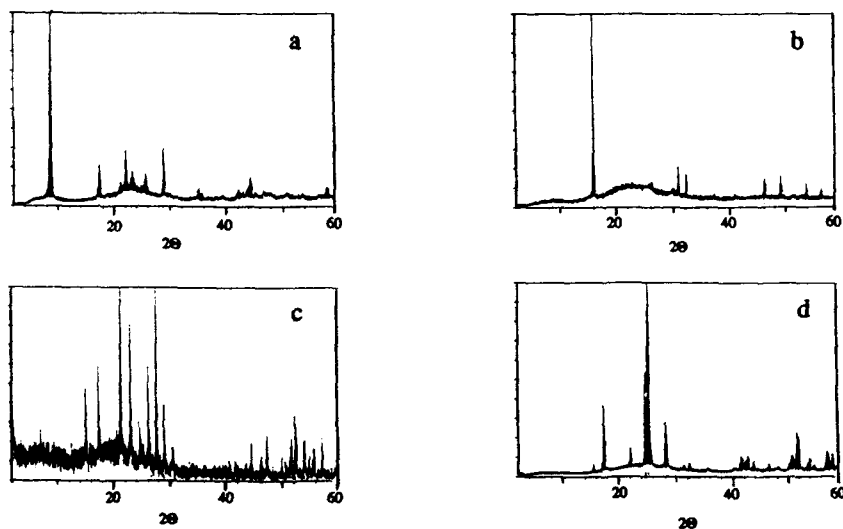


Figure 3. XRD patterns (Cu radiation) of a) HAIF_4 b) $\eta\text{-AlF}_3$ c) $\theta\text{-AlF}_3$ d) $\kappa\text{-AlF}_3$.

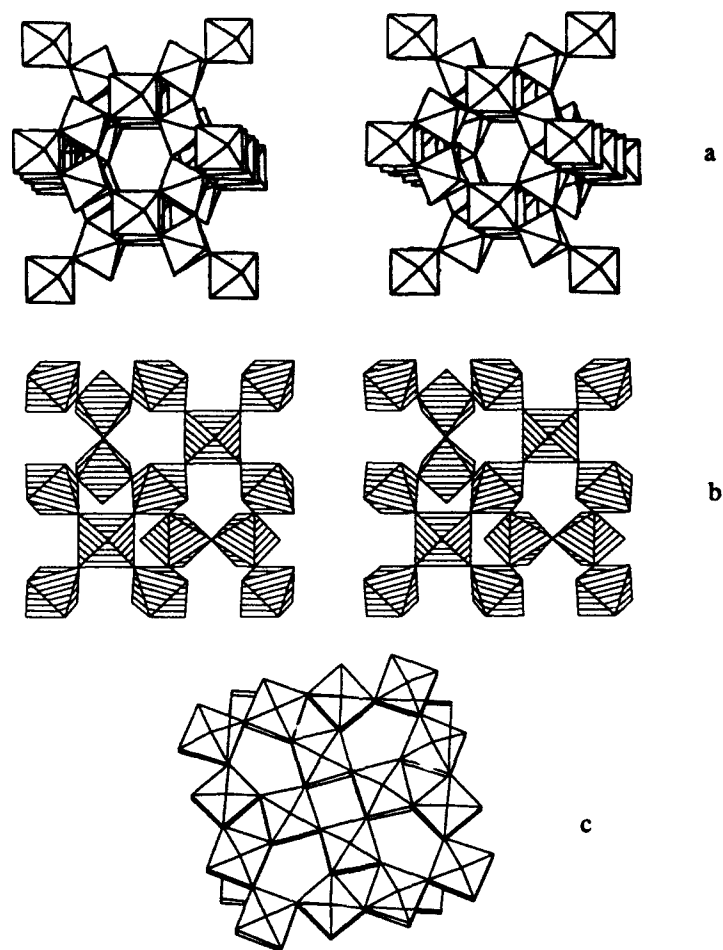


Figure 4. (a) Stereodrawing of the η - AlF_3 structure (polyhedral representation) looking nearly parallel to the $[110]$ direction to show the channels which run through the crystal. Bond length: Al-F, 1.803(1) Å. Bond angles: *cis* F-Al-F, 89.8(1)° and 90.2(1)°; Al-F-Al, 141.3(1)°. (b) Stereoview of a single "layer" (polyhedral representation) of θ - AlF_3 emphasizing the 4 and 5 rings of the linked $[\text{AlF}_6]$ octahedra. The Al-F bond lengths range from 1.738(5) to 1.862(2) Å; the *cis* and *trans* F-Al-F angles are all within 3° of 90.0 and 180.0, respectively; the Al-F-Al angles vary from 140.2(2) to 180.0°. (c) Single layer polyhedral representation of the structure of κ - AlF_3 (layers are fused perpendicular to this view by means of Al-F-Al linkages).

When the organic cation is $N(CH_3)_4^+$ [9] the thermal behavior is quite different (Figure 2b). The single weight-loss event at 450°C corresponds exactly to loss of the equivalent of $N(CH_3)_4F$. The product AlF_3 at 450°C has an XRD pattern (Figure 3c) with a major crystalline phase which could not be matched to any previously known structural phase of AlF_3 [12]. This new tetragonal phase of AlF_3 is designated the θ -phase and its structure was refined by combined XRD and neutron powder diffraction analysis. The structure is depicted in Figure 4b and again consists of corner-shared $[AlF_6]$ octahedra. The unit cell has 4 independent Al and seven independent F atoms assembled into rings of 5, 4 and 3 $[AlF_6]$ octahedra. The 5-rings form an undulating 3-D interconnected channel system around tetrahedral clusters of four $[AlF_6]$ octahedra - this latter feature being identical to that found for the η -phase described above. The microporous nature of this new phase is similar to that of the β - AlF_3 and η - AlF_3 phases.

The appearance of the material $HAIF_4$ in the preparation of η - AlF_3 was intriguing and we sought to prepare macrocrystalline samples for crystallography. One approach which suggested itself was to attempt to dissolve the pyridine H^+ . AlF_4 precursor material into some high boiling point solvent, heat it in an inert atmosphere to boil out the pyridine and allow the $HAIF_4$ material to crystallize from the cooled solution. One solvent which proved viable for this approach was formamide which was an excellent solvent for the pyridinium salt. Heating to 180°C, a concentrated solution of pyridinium salt begins to boil and fizz vigorously whereupon a clear solid begins to precipitate. On cooling, a copious white precipitate forms and may be collected for XRD. The solid is microcrystalline but the XRD is unlike the expected $HAIF_4$ phase. After detailed TGA (see Figure 2c), chemical and XRD analysis it was clear that the material was in fact of stoichiometry NH_4AlF_4 formed via attack of the fluoroaluminate upon the formamide solvent itself in a manner similar to:



However, the XRD pattern was unlike that previously reported for this ammonium salt [6] and detailed Reitveld analysis reveals the structure to be a new β -phase of this material. The structure is a layered motif wherein sheets of corner-linked $[AlF_6]$ octahedra are connected to form 3, 4 and 5 rings in a motif identical to that depicted in Figure 4c. Between these layers reside the ammonium cations. While similar to the known α -phase [6] (in that the structure is composed of sheets of corner-shared $[AlF_6]$ octahedra sandwiched with ammonium ions) the connectivity within the sheets is very different. The registry between sheets is also different and overall, the structure is very similar to the β -phase structure of $RbAlF_4$ [13]. TGA of this new phase shows a single weight loss event at 350-400°C corresponding to loss of NH_4F (Figure 2c) and the product AlF_3 has an XRD (Figure 3d) which is clean and is again a new phase which we designate κ . Detailed Reitveld analysis of the powder diffraction data reveals a structure which is depicted in Figure 4c. This structure is derived from the precursor ammonium salt by retaining the layer connectivity but eliminating ammonium fluoride from between the layers, bringing the layers into perfect registry

and then fusing the layers together via. Al-F-Al linkages. This is therefore referred to as a pseudotopotactic transformation in that the layer structure of the precursor is maintained. The structure has linear channels running through the crystal comprised of 5, 4 and 3 rings of corner shared $[\text{AlF}_6]$ octahedra.

Surface areas for the three new phases (from BET nitrogen absorption) are ~58, 64 and $19\text{m}^2/\text{gm}$ for η , θ and κ -phases respectively. Detailed, *in situ*, XRD studies of all of the known and new phases make it clear that the α -phase is the thermodynamically most stable, the β , η , θ and κ phases do not interconvert amongst themselves but rather all convert to α in the 600-700°C regime. It is further clear that the phase of AlF_3 produced in any given synthesis is apparently dictated by the temperature of synthesis but more especially by the nature of the precursor from which it is made. In our cases, we find that the intermediacy of a HAlF_4 phase seems to be required for production of the η -phase. The θ -phase can be produced from almost any decomposable organic cation which cannot proceed through a discrete HAlF_4 phase. Finally, the κ -phase is only formed in the pseudo-topotactic transformation from the new $\beta\text{-NH}_4\text{AlF}_4$ phase.

These new phases are now in the process of being tested catalytically for a wide variety of fluorocarbon transformations to determine what, if any, correlations can be made between structure/surface area and reactivity.

VANADYL PHOSPHATE MATERIALS

The partial oxidation of n-butane to maleic anhydride is a remarkable and commercially important example of heterogeneously catalyzed oxidation chemistry [14]. The catalyst preferred for this transformation is vanadyl pyrophosphate $(\text{VO})_2(\text{P}_2\text{O}_7)$ or VPO and while it is used commercially its mechanism of action is still a subject of much research [15]. In particular, this catalyst is known to use lattice oxygen atom species for incorporation into the organic molecules and the form and method of insertion of these oxygen atom species is of acute interest as is their method of regeneration from molecular oxygen. As with many catalyst materials, the exact method of preparation is critical to a high activity and selectivity material. We have adopted the molecular precursor approach to VPO to serve a dual function 1) as a method for controlled preparation of processable, dispersible or modified catalyst materials and 2) as a method for generating small, yet identifiable, pieces of the bulk VPO lattice and using these to probe the structure/reactivity characteristics of the catalyst itself.

The structure of VPO itself as a phase pure crystalline material is depicted schematically in Figure 5. Key structural features include the presence of dimeric $(\text{VO})_2$ units which lie in sheets and are coordinated by O of the pyrophosphate groups. The pyrophosphate groups lie roughly perpendicular to the sheets and link sheets together. The vanadyl groups from consecutive sheets in the structure are in approximate registry and the vanadyl oxygen atoms from each pentacoordinate

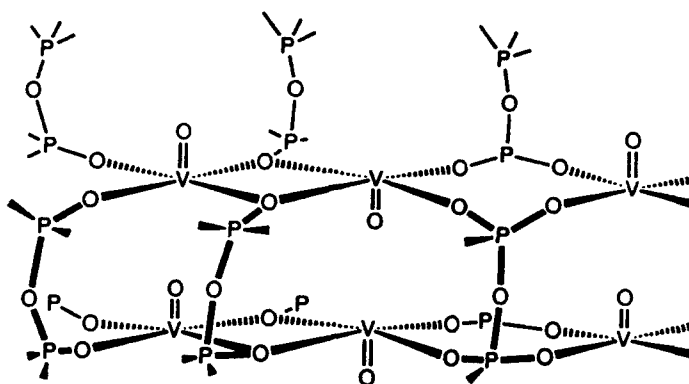


Figure 5. Schematic representation of the bulk VPO structure emphasizing connectivity (for a detailed description of the crystal structure see ref [15]).

vanadium coordinate weakly into the sixth coordination site of the vanadium in the next adjacent sheet. Finally, the dimeric $(VO)_2$ units are surrounded by eight-membered rings of $-VOPOVOPO-$ linkage. Questions about the functioning of this material and a vast pool of data exists to address those questions [15]. In this brief description we shall only consider one molecular species which models some of the structural features of VPO and which can be considered as a processable molecular precursor to 'VPO-like' species. This work is ongoing and this short description should be viewed as a progress report.

Taking vanadyl tris-isopropoxide and diethylphosphate with a minimum of acetonitrile solvent under an inert atmosphere rapidly converts the originally yellow/orange mixture to a blue/green and eventually generates a deep blue solid mass from which crystals form on standing. X-ray structural analysis of these crystals reveals that they are composed of a remarkable trimeric molecular cluster which engenders several key structural features of VPO itself, Figure 6a. The neutral cluster possesses three (VO) units where the vanadium is in the +4 oxidation state. Since the starting reagent is a vanadium +5 species, the reaction has led to internal reduction of the vanadium and concurrently some of the co-product isopropanol has become oxidized to acetone (detected by 1H n.m.r.). This is an example of the oxidizing power of phosphato co-ordinated vanadium 5+ species and may be related to the active surface species in functioning VPO catalysts. The isolated vanadyl groups are coordinated exclusively by phosphato oxygen atoms in a cyclic ring built exclusively of the eight-ring motif mentioned above. Perhaps most intriguing is the "re-entrant"

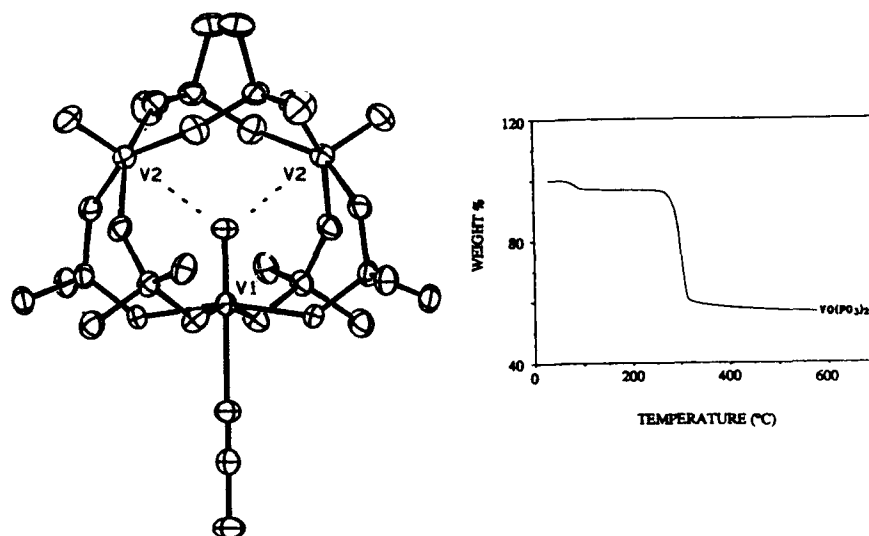


Figure 6 a) Crystal structure of the $(VO)_3((EtO)_2PO_2)_6 \cdot CH_3CN$ with the ethyl groups omitted for clarity (the central O makes contacts of $2.765(3)\text{\AA}$ with the other 2 V atoms) and b) TGA trace of its thermal decomposition in N_2 .

nature of one of the vanadyl oxygen groups [16]. In order to satisfy the apparent desire of the V^{+4} species for a ligand in their sixth co-ordination site the trimer has turned one of its oxygen atoms into the cluster interior so that it may interact with the other two vanadium sites. In so doing this vanadyl group exposes its own sixth coordination site to the molecular exterior and this Lewis acid site is coordinated by solvent acetonitrile. The $V=O \cdots V$ interaction is reminiscent of the interlayer connectivity of VPO itself (Figure 5). The cluster is very soluble in acetonitrile and exhibits interesting e.p.r behavior wherein a 22-line signal is detected at room temperature indicating that the unpaired electrons are delocalized over all three vanadium sites in the cluster [17].

Taking this solid material and heating in nitrogen in TGA reveals the expected weight losses for evolution of acetonitrile, ethanol and diethylether in successive steps at $\sim 80^\circ\text{C}$ (acetonitrile) and $\sim 300^\circ\text{C}$ (ethanol fragments) (Figure 6b) leaving a material of the stoichiometry $VO(PO_3)_2$. XRD reveals that our material is the same phase as previous preparations of this material [18] although ours is a lower temperature route to it and potentially provides a route for dispersion onto high surface area supports. Catalytic testing of this product in butane oxidation shows low but detectable activity for the pure material. The loss of acetonitrile at such a low temperature suggests also that the original trimeric cluster can be readily "activated" to generate a Lewis acid site at the

Lewis acid site at the V^{+4} site and investigations of the role of such sites in the surface chemistry of VPO with organic molecules can be probed with this molecule.

CONCLUSIONS

Examples from two catalyst material areas have shown the value of a detailed understanding of precursor chemistry and synthesis in production of new or more versatile materials. The detailed examples from the AlF_3 arena show how a wealth of new chemistry and catalyst materials can be extracted from an elaboration of the theme of designed molecular precursors. The brief description of our newer area of VPO oxidation catalyst materials reinforces the belief that molecular chemistry can directly impact materials preparation. Additionally, however, we believe that these same molecular precursors can begin to find use in augmenting the understanding of how the bulk materials function - small molecular pieces of extended structures open the possibilities for traditional solution phase and other small molecule characterizational techniques to be applied to these problems.

ACKNOWLEDGMENTS

We wish to acknowledge the outstanding technical assistance of Mr. J.B.Jensen, Ms. P.Pulcher Mr. L. Lardear and Mr. W. Marshall in performing the chemical syntheses and characterizational work described here. The collaboration of Drs. F. Davidson and C. Campbell on n.m.r . spectroscopy, Drs. J.B. Parise and J. Fernandez-Baca on powder diffraction analyses and Drs. W.E. Farneth, M. Nappa, L. Abrams and G. Jones on catalyst characterization have all been indispensable components of the work described.

REFERENCES.

1. B. Cochet-Muchy, J. Portier, in *Inorganic Solid Fluorides, Chemistry and Physics*, edited by P. Hagenmuller (Academic Press, Orlando, FL 1985), p.580.
2. F.J. Christoph and G. Teufer, U.S. Patent No. 3,178,484 (1965) and G.B. Patent No. 1,026,105 (1966).
3. D.R. Corbin and V.N.M. Rao, W/O 92/16479 (Oct 1 1992).
4. R. Hoppe and D. Kissel, *J.Fluorine Chem.* **24**, 327 (1984).
5. A. LeBail, C. Jacoboni, M. Leblanc, R. DePape, H. Duroy, J.L. Fourquet, *J. Solid State Chem.* **77**, 96 (1988).
6. F.J. Christoph and G. Teufer, U.S. Patent No. 3,178,483 (1965).
D.B. Shinn, D.S. Crocket, H.M. Haendler, *Inorg. Chem.* **5**, 1927, (1966).

7. C. Brosset, Z. Anorg. Allg. Chem. **239**, 301 (1938).
R. Losch and C. Hebecker, Z. Naturforsch. **34B**, 131 (1979).
8. N. Herron, D.L. Thorn, R.L. Harlow, F. Davidson, J. Am. Chem. Soc. **115**, 3028, (1993).
9. N. Herron, D.L. Thorn, R.L. Harlow, Inorg. Chem. **32**, 2985 (1993).
10. J.M. Cowley and T.R. Scott, J. Am. Chem. Soc. **70**, 105 (1948).
11. R. DePape and G. Ferey, Materials Research Bulletin **21**, 971 (1986).
12. After completion of this work a similar pattern and refinement of the θ -AlF₃ material was reported by U. Bentrup, Eur. J. Solid State Inorg Chem. **t.29**, 51 (1992). and in A.LeBail, J.L. Fourquet, U. Bentrup, J. Solid State Chem. **100**, 151 (1992).
13. J.L. Fourquet, F. Plet, R. DePape, Acta Cryst. **B36**, 1997 (1980).
14. P.A. Agaskar, L. Decaul, R.K. Grasselli, Catal. Letts. **23**, 339 (1994).
15. G. Centi, F. Trifiro, J.R. Ebner, V.M. Franchetti, Chem. Rev. **88**, 55, (1988).
16. Q. Chen, J. Zubieta, Angew. Chem. Int. Ed. Engl. **32**, 261 (1993).
17. B.C. Tofield, G.R. Crane, G.A. Pasteur, R.C. Sherwood, J. Chem. Soc. Dalton **1807** (1975).
18. A. Hasegawa, J. Chem. Phys. **55**, 3101, (1971).

PHYSICAL PROPERTIES OF DIAMOND-LIKE NANOCOMPOSITE FILMS

B. DORFMAN^(a), M. ABRAIZOV^(a), B. PYPKIN^(a), M. STRONGIN^(b), X.-Q. YANG^(b),
D. YAN^(c), FRED H. POLLAK^(c), J. GROW^(d) and R. LEVY^(d)

(a) International Institute of Materials and Technology, Polytechnic University, Farmingdale, NY 11735

(b) Physics Department, Brookhaven National Laboratory, Upton, NY 11973

(c) Physics Department and NY State Center for Advanced Technology in Ultrafast Photonic Materials and Applications, Brooklyn College of CUNY, Brooklyn, NY 11210

(d) Physics Department, New Jersey Institute of Technology, Newark, NJ 07201

ABSTRACT

Diamond-like nanocomposite (DLN) and metal containing DLN (Me-DLN) films, synthesized in a combined process of deposition of carbon-silicon precursor and magnetron sputtering of a metal target, have been examined by Auger electron spectroscopy, Raman and IR spectroscopy, nanoindentation and internal stress measurements. The stability of the films under ion and electron irradiation and thermal annealing has been tested.

INTRODUCTION

The development of a new class of materials, DLN, which consist of random networks of carbon and silicon have been described previously [1-3]. These materials possess a unique combination of chemical, mechanical, electronic, and superconducting properties. In this report we focus on the mechanical and electrical properties and type of carbon chemical bonding in DLN and metal containing DLN and their stability under irradiation and high temperature annealing.

EXPERIMENTAL DETAILS

The technology for DLN films has been developing since the end of the 1970s [1]. The key principles of DLN synthesis are as follows: clusterless initial beams, no collisions between atoms or radicals in the chamber, optimum initial fragmentation of C-Si precursors into low C_nH_m radicals and SiO, optimum beam energy and low substrate temperature. Several methods and precursors have been compared, but the best approximation to DLN today remains in films which are produced in a plasma enhanced co-deposition process on rf biased substrate from polyphenylmetilsiloxane $[(C_2H_5)_3SiO(CH_3C_6H_5SiO)_3Si(CH_3)_3]$ with evaporation of metals or sputtering of metal targets. The deposition regimes are presented in another paper at this conference [4]. Film thicknesses were about 1 μm .

The mechanical properties of these films were investigated using a load and displacement indentation test performed by a nanoindenter. In all cases sixteen indents were performed on each sample. The detailed description of these measurements is presented elsewhere [5]. A four probe test was used to define the surface resistivity. Measurements of the temperature dependence of the resistance were performed on DLN with Ti electrodes (deposited in 10^{-5} T vacuum) fabricated on (a) sital and (b) $<001>$ p-Si ($p \approx 5 \times 10^{15} \Omega\text{-cm}$). The stress measurements were performed using a two laser beam system calibrated by Flexus 2-300. The difference in substrate curvature was used to calculate the film stress from the Stoney equation [6]. Auger spectra were taken in an UHV chamber with a 3 keV, 30 mA electron beam for

excitation. Standard phase-sensitive detection methods with a 2 V peak-to-peak modulation voltage were used [7]. The sputtering was performed by means of a 4 keV Ar beam. The Raman and IR spectroscopy experimental setup and results are presented in [4].

EXPERIMENTAL RESULTS

Mechanical Properties

Adhesion

DLN and Me-DLN films showed good adhesion (tested by tape pull) on various metals and plastics. The rating for tape adhesion per ASTM D3359, Method B were 5B and 3B for DLN on high density polyethylene and Teflon (tested at Buffalo Testing Laboratories, Buffalo, NY), respectively. The DLN film also was used as an intermediate layer to glue the teflon band to steel by epoxy. High adhesion was proved both by pull test and high frequency ultrasound measurements (tested in Lorex Industries, Inc., Poughkeepsie, NY).

Elastic Modulus and Hardness

Presented in Table I are the elastic moduli (EM) and hardness (H), together with their 1σ standard deviation, for DLN and various Me-DLN films. The TiN-DLN and Zr-DLN materials possess the highest E and H among the films studied. For these samples the ratio $H/E \approx 0.1$. It should be mentioned that standard Knoop measurements show 3-4 times higher hardness than nanoindentation [8]. The values of EM and H of DLC films obtained by nanoindentation are in the range 40-130 GPa and 5-15 GPa, respectively, [8,9] which is close to our experimental data.

Stress

Hard diamond-like carbon (DLC) films possess high compressive stress (usually more than 1 GPa) [10], whose origin is still not clear. The stress was found to be dependent on hydrogen concentration [11] or the energy of ion beam [10]. The internal stress in as-deposited DLN films is also compressive but in the range of 200-350 MPa. The stress in Me-DLN films does not depend on sheet resistance (ρ_s) for Pt, Cr, and Pd but for Zr, W, Cu, and Ta it increases when ρ_s decreases. For example, in the case of Zr-DLN the change in stress from 0 to -1100 MPa corresponds to a decrease in ρ_s from 470 Ω/\square to 4 Ω/\square [5].

Electrical properties

The electrical resistance of DLN films can be varied over 15-17 orders of magnitude, i.e., from that of wide band-gap semiconductors to that of amorphous metals [2]. Values of ρ , in the DLN films of the present study were found to lie in the range 10^{12} - 10^{14} Ω/\square . The I-V characteristics of the DLN on *p*-doped Si showed a strong rectifying effect when a positive voltage was applied to the film [12]. The independence of the breakdown voltage (600-900 V) on the film thickness (30-300 nm) suggests that the properties of the Si depletion layer also must be taken into account.

Table I. Sheet resistance, elastic moduli and hardness of as-deposited films.

Material	Sheet Resistance (Ω/\square)	Elastic Modulus (GPa)	Standard Deviation (GPa)	Hardness (GPa)	Standard Deviation (GPa)
DLN	10^{13}	84.0	4.0	6.3	0.4
Ti-DLN	90.2	98.9	5.2	8.1	0.7
TiN-DLN	6.0	184.5	19.0	17.7	3.9
W-DLN	8.9	123.5	11.1	9.6	1.6
W-DLN	320.0	86.7	7.0	8.6	1.3
Hf-DLN	76.1	109.0	5.9	8.9	1.1
HfN-DLN	90.1	138.8	7.3	11.3	1.0
Cr-DLN	0.4	160.5	12.9	8.9	1.4
Zr-DLN	2.8	192.7	8.8	20.7	1.7
ZrN-DLN	69.6	131.7	7.1	9.8	0.6

Thermal stability

Thermal stability is a main problem of amorphous DLC films. In the annealing study of Grill et al [13] the internal stress of DLC decreased considerably after annealing in vacuum at 390°C but annealing at 440-490°C reduced the stress from 1.5 GPa to practically zero. No hydrogen effect on the stress change was observed in this report. Probably this stress reduction is related to an sp^3 to sp^2 transformation. The lengths of the C-C bond in sp^3 and the C=C bond in sp^2 are 0.154nm and 0.142nm, respectively. According to Koidl et al [14] the thermal decomposition of a-C:H is caused by a loss of chemically bonded hydrogen and resulting dangling bonds rearrange by forming sp^2 bonds. Graphitization is reflected in the changes of the DLC properties, particularly the drastic increase of the electrical conductivity (two orders of magnitude at 350°C in [14]). For comparison, thermal annealing in air (2 hrs at 350°C + 2 hrs at 400°C) decreased the DLN stress by 10% and by 25% after 1 hr annealing at 500°C in

Table II. Electrical and mechanical properties of annealed Me-DLN films.

Material	Sheet Resistance (Ω/\square)	Elastic Modulus (GPa)	Standard Deviation (GPa)	Hardness (GPa)	Standard Deviation (GPa)
Cr-DLN	0.4	145.3	7.4	7.0	0.7
TiN-DLN	6.0	179.7	17.2	18.0	3.9
Zr-DLN	2.4	168.6	12.4	17.1	3.4

vacuum.

Shown in Fig. 1 is the temperature dependence of ρ_s of DLN/sitall [heating (●) and cooling (○)]. For comparison purposes we also show the data for the sitall substrate alone [heating (■) and cooling (□)]. From the DLN/sitall results one can see that high temperatures cause an increase in ρ_s of the DLN film. Obviously, the change in resistivity cannot be caused by graphitization but rather by an increase in the sp^3/sp^2 ratio or/and oxidation.

Listed in Table II is the influence of thermal annealing in vacuum (1 hr at 400°C + 1 hr at 500°C) on ρ_s , EM and H of some of the Me-DLN films presented in Table I. The sheet resistance, ρ_s , of the studied films remained relatively constant as did EM and H of the TiN-DLN film. However, the EM and H of the Cr-DLN and Zr-DLN films decreased by 10-15%.

Stability to irradiation

Pd-DLN films with room temperature $\rho_s = 3, 5, 10$ and $500 \Omega/\square$ were studied by means of AES. In Fig. 2 we present the differentiated carbon KLL (C-KLL) AES of the $3 \Omega/\square$ sample (a) as-deposited, (b) after ion etching and after electron beam exposure for (c) 10 min, (d) 180 min, (e) 240 min and (f) 300 min. Complete AES data of these and some other films will be published elsewhere [15]. For comparison purposes Fig. 3 shows the AES data of (a) natural diamond, (b) flame synthesized diamond, (c) graphite and (d) DLC obtained by Ravi et al [16]. One can see that the carbon on as-deposited Pd-DLN is in a graphite state. Argon sputtering creates considerable change in the fine structure of the C-KLL spectrum which appears to be very similar to flame synthesized diamond and consists of a mixture of sp^3 and sp^2 with sp^3 dominant. During long time exposure to electron irradiation the C-KLL peak transforms back to the graphite-like structure. That is, the intensity of the fine structure peak located at a lower energy increases over the peak closest to the primary C-KLL peak. Following ion sputtering restores again "more diamond" appearance. In our experiment the spot from the ion beam is considerably bigger than that of electron beam so the sputtered surface not exposed to electron irradiation remained unchanged. It is well known that under ion or electron irradiation as well as thermal annealing graphitization of diamond and DLC films occurs [17]. Pd-DLN films have showed increase in sp^3/sp^2 ratio, i.e., the opposite behavior under ion bombardment. Research is ongoing to determine the role of argon sputtering. The evolution of the C-KLL spectra under electron irradiation is probably caused not by radiation damage but electron stimulated growth of the carbon layer on the film surface (vacuum in the chamber was 5×10^{-8} - 5×10^{-9} T). This conclusion is supported by the complete disappearance of the peaks of other elements (Pd, Si, O) present in the Auger spectra after a long exposure to electron irradiation [15].

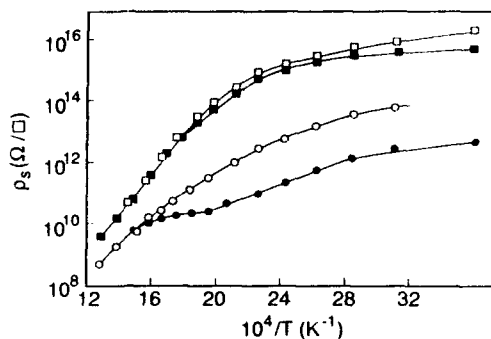


Fig.1 Temperature dependence of the sheet resistance, ρ_s , of DLN/sitall [heating (●) and cooling (○)] and the sitall substrate alone [heating (■) and cooling (□)].

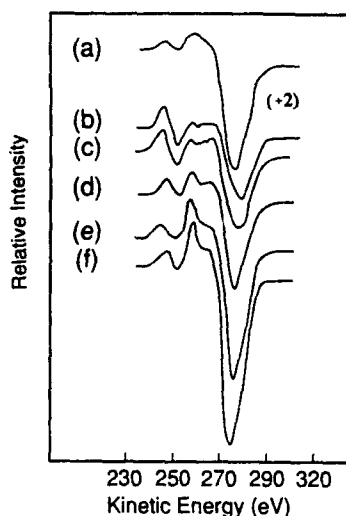


Fig. 2 The C-KLL spectra of (a) as-deposited Pd-DLN, (b) after ion etching and after electron exposure for (c) 10 min, (d) 180 min, (e) 240 min and (f) 300 min.

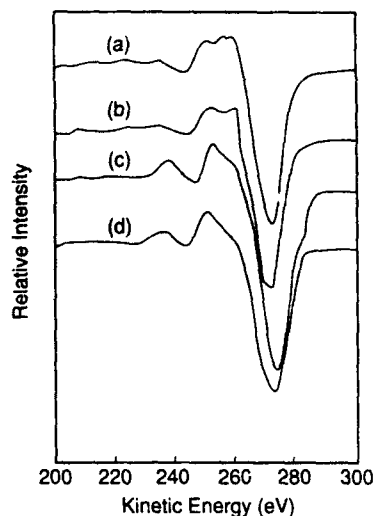


Fig. 3 AES spectra of (a) natural diamond, (b) flame synthesized diamond, (c) DLC and (d) graphite.

DISCUSSION

The obtained data can be explained on the basis of the following model. The DLN structure is composed of two random networks tied with weak Van der Waals forces: a carbon network, mainly in the form of sp^3 "diamond-like bonds" and a silicon "glass-like" network. This results in a purely amorphous structure. No Si-C bonding has been detected by FTIR, Raman, XPS or other techniques. The C-network is chemically stabilized by hydrogen and the Si-network by oxygen. These networks form an ideal matrix for the introduction of additional atomic or molecular species. Indeed, Raman spectroscopy measurements for both DLN and Me-DLN (metal: W, Zr, Pt) films showed the same broad peak centered at 1500 cm^{-1} typical for diamond-like carbon [4]. Also, no additional peaks in the FTIR spectra were observed in Me-DLN compared to pure DLN. An XPS study of Zr-DLN films established that no carbidization occurs after annealing at 400°C and no change was found on Zr-DLN IR spectra after annealing at 600°C [5]. These results probably support the idea that metallic atoms are placed in the matrix nanopores. Therefore, the implantation of a soft metal increases the hardness of relatively hard DLN without formation of carbides. The qualitative picture of mutual stabilization of interpenetrating atomic-scale filaments is presented in [2]. In such a structure the special thermodynamic properties of the mesoscopic forms of carbon come into play, i.e., the critical size of the graphite nucleus is 39 atoms and while that of diamond is only 14 atoms. Therefore,

the multi-network DLN structure prevents graphite formation even at high temperatures while the sp^3 bonded clusters can be formed at relatively low temperature.

CONCLUSIONS

Amorphous DLN materials possess a unique combination of high E and H, low stress and good adhesion to various substrates. The addition of soft metal increases both E and H of the initially hard matrix. In contrast to diamond and DLC, argon sputtering increases the sp^3/sp^2 ratio and thermal treatment increases the electrical resistance. Data obtained are explained as a result of multi-network formation which prevents graphitization under various treatments.

ACKNOWLEDGMENTS

We wish to thank Dr. V. Lopatin and Dr. D. Sirota for measurements of the resistance and adhesion. The authors BD, MA, MS, X-QY acknowledge the support of US Department of Energy contract DE-AC02-7600016 and CRADA #C-93-01. DY and FHP acknowledge the support of the New York State Science and Technology Foundation through its Centers for Advanced Technology program.

REFERENCES

1. B. Dorfman, B. V. Kozeikin and V. V. Sevastyanov, *Microelectronica*, 11(4)(1982)349 (in Russian).
2. B. Dorfman, *Thin Solid Films*, 212(1992)267.
3. B. Dorfman et al, *Thin Solid Films*, 212(1992)274.
4. B. Dorfman, M. Abraizov, F. H. Pollak, D. Yan, M. Strongin, X.-Q. Yang and Z. Y. Rong, to be published in Vol. 349 of the *Mat. Res. Soc. Symp. Proc.* (1994).
5. B. Dorfman, M. Abraizov, B. Pypkin, J. Grow, R. Levy, S. Mukhopadhyay and S. Nourbash, to be published in *Thin Solid Films*.
6. I. E. Sneddon, *Int. J. Eng. Sci.*, 3(1965)47.
7. Handbook of Auger Electron Spectroscopy, edited by L. E. Davis et al (Physical Electronics Industries, Inc., Eden Prairie, MN, 1976) p. 3.
8. X. Jiang, K. Reichelt and B. Stritzker, *J. Appl. Phys.*, 66(1989)5805
9. C. J. McHargue in Applications of Diamond Films and Related Materials, edited by Y. Tzeng, M. Yoshikawa, M. Murakawa and A. Feldman (Elsevier, Amsterdam, 1991) p. 113.
10. D. Nir, *Thin Solid Films*, 146(1987)27.
11. M. Rubin, C. B. Hopper and N. H. Cho, *J. Mater. Res.*, 5(1990)2538.
12. B. Dorfman and M. Abraizov, private communication.
13. A. Grill, V. Patel and B. Meyerson, *J. Mater. Res.*, 5(1990)2531.
14. P. Koidl, C. Wild, R. Locher and R. Shan in Diamond and Diamond-Like Films and Coatings, edited by R. Clausing et al. (Plenum Press, New York, 1991) p. 243.
15. P. Asoka-Kumar, B. Dorfman and M. Abraizov, to be presented at the 41st National Symposium of the American Vacuum Society, October, 1994, Denver, CO.
16. K. Ravi, C. Koch, H. Hu and A. Joshi, *J. Mater. Res.*, 5(1990)2356.
17. Y. Mizokawa, T. Miyasato, A. Nakamura, K. Geib and C. Wilmsen, *J. Vac. Sci. Technol.*, A5(1987)2809.

QUANTUM CONFINEMENT IN GaP NANOCCLUSERS

BERNHARD K. LAURICH*, DAVID C. SMITH**, and MATTHEW D. HEALY**

* Electronic Materials and Device Research,

** Chemical Science and Technology,

Los Alamos National Laboratory, Los Alamos, NM 87545

ABSTRACT

We have prepared GaP and GaAs nanoclusters from organometallic condensation reactions of $E[\text{Si}(\text{CH}_3)_3]_3$ ($E = \text{P, As}$) and GaCl_3 . The size of the as synthesized clusters is 10 Å to 15 Å. Larger clusters of 20 Å to 30 Å size were obtained by thermal annealing of the as grown material. X-ray diffraction and transmission electron microscopy confirm the high crystalline quality. A lattice contraction of 6.7% could be seen for 10 Å sized GaAs clusters. The clusters are nearly spherical in shape. Optical absorption spectra show a distinct line which can be assigned to the fundamental transition of the quantum confined electronic state. The measured blue shift, with respect to the GaP bulk absorption edge is 0.53 eV. As the cluster is smaller than the exciton radius, we can calculate the cluster size from this blue shift and obtain 20.2 Å, consistent with the results from X-ray diffraction of 19.5 Å for the same sample.

INTRODUCTION

III-V semiconductor nanoclusters have attracted growing interest in recent years because of their structural, electronic, and optical properties.[1] Clusters in the size regime of a few nanometers show a crystalline structure, their electronic properties, however, are very different from those of bulk semiconductors.[2] The quantum confinement of the charge carriers leads to distinct electronic levels, having an energy higher than the bandgap of the bulk material (blue shift). Due to the long coherence length of the charge carriers in semiconductors, e.g. an excitonic Bohr radius of 12.4 nm in GaAs, the electronic and optical properties are strongly influenced by the cluster size.[3] The behaviour of quantum confined systems has been studied in semiconductor quantum wells, wires, and dots, fabricated by molecular beam epitaxy and electron beam lithography. Studies on nanoclusters, down to a few nanometers, have been done mostly with II-VI semiconductors.[4] There are few reports on the synthesis of III-V semiconductor clusters.[5-8] This study focuses on the synthesis, and the structural and optical properties of III-V semiconductor clusters in the 1 nm regime.

EXPERIMENT

We have fabricated GaP and GaAs nanoclusters using the organo-metallic condensation reaction:



Synthesis of **GaP**: GaCl₃ was dissolved in acetonitrile (MeCN) and P(SiMe₃)₃ was added, immediately producing a yellow solution. The reaction was heated to reflux for 16 hrs, producing an orange turbid solution. The solvent was removed to yield an orange solid, which can be redissolved in acetonitrile. Synthesis of **GaAs**: As(SiMe₃)₃ which was prepared via a published method,[9] was suspended in MeCN and GaCl₃ was added resulting in the immediate formation of a yellow-orange precipitate. The reaction mixture was heated to reflux and filtered to give a reddish solid. The alternate use of diethyl ether as solvent yielded a orange solid. Thermal annealing was performed under dynamic vacuum. Outgassing was observed and the samples darkened in colour proportionally to the annealing temperature. X-ray diffraction measurements were performed with a Siemens D 5000 diffractometer with a CuK α source (1.54 Å) using a curved germanium monochromator to obtain an instrument resolution of 0.03 deg, combined with the high intensity necessary for small powder samples. The samples were contained in a sealed cell with beryllium window.

RESULTS AND DISCUSSION

We have used X-ray diffraction to determine the lattice constant and the cluster size. III-V semiconductors have a Zincblende structure. The strongest diffraction peaks are [111], [220], and [311]. The latter two strongly overlap if the linewidth exceeds a few degrees. Figure 1 shows a X-ray diffraction spectrum of a annealed GaP cluster sample with the [111], [220], and [311] reflections marked. The sharp lines are caused by the beryllium window and the sapphire plate which holds the powder in place. It should be noted that there are no diffraction peaks indicating other crystalline phases, e.g. of oxides. The effect of annealing the clusters is shown in figure 2, comparing as grown GaAs clusters with an annealed sample. Note the strong shift in the peak position. The as grown GaAs clusters of 9 Å size show a lattice contraction with a lattice constant 6.7% smaller than the bulk one, whereas the annealed, larger clusters of 32 Å size have the bulk lattice constant, similar to clusters grown by molecular beam epitaxy.[10] This shows the effect of surface tension. The cluster size was determined by a Warren-Averbach analysis and using the Scherrer formula. No correction for particle shape was done. As shown in table 1, the values obtained by both methods agree. As synthesized material and samples annealed at lower temperatures (350 C or below)

exhibit a Gaussian lineshape, a sign of a narrow size distribution. Samples annealed at higher temperature, such as the GaAs annealed at 500 C a more Lorentz type lineshape.

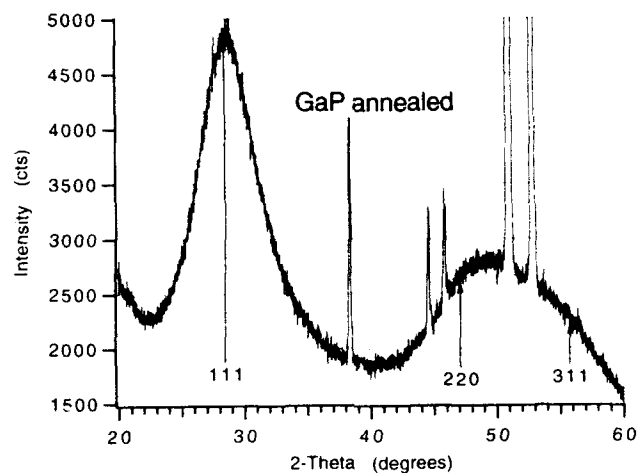


Figure 1: X-ray diffraction spectrum of annealed GaP nanoclusters with a size of 19.5 Å.

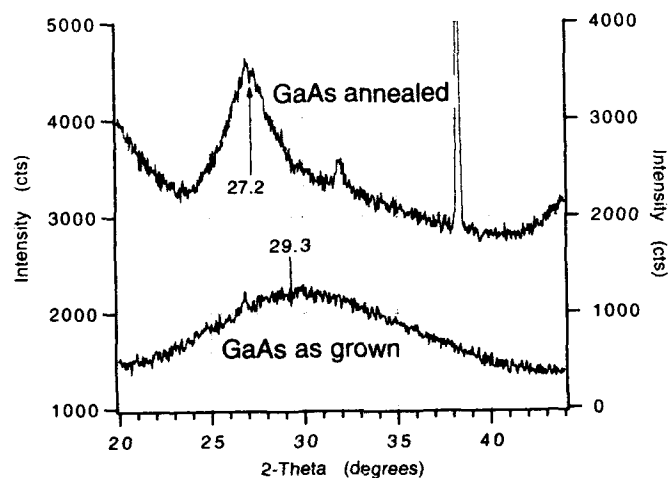


Figure 2: X-ray diffraction spectra of as synthesized 9 Å GaAs nanoclusters (bottom) and 32 Å GaAs clusters annealed at 500C (top).

	a (Å)	$\Delta \frac{a_{\text{cluster}}}{a_{\text{bulk}}}$	l (Å)		Line shape
			Scherrer / Warren-Averbach		
<u>GaP</u> as grown	5.26	-3.5%	11.5	-	Gauß
annealed (350°C, 20h)	5.40	-1%	19.5	18.5	Gauß
<u>GaAs</u> as grown	5.275	-6.7%	9.0	10	Gauß
	5.51	-2.5%	12.0	-	
annealed (500°C)	5.68		32	30	Pseudo-Voigt

Table 1: Lattice constant and cluster sizes of GaP and GaAs nanocrystallites

In order to obtain a verification of the crystallinity and the size of the clusters we performed transmission electron microscopy. Figure 3 shows a cluster of annealed GaP. The lattice planes can be clearly seen.

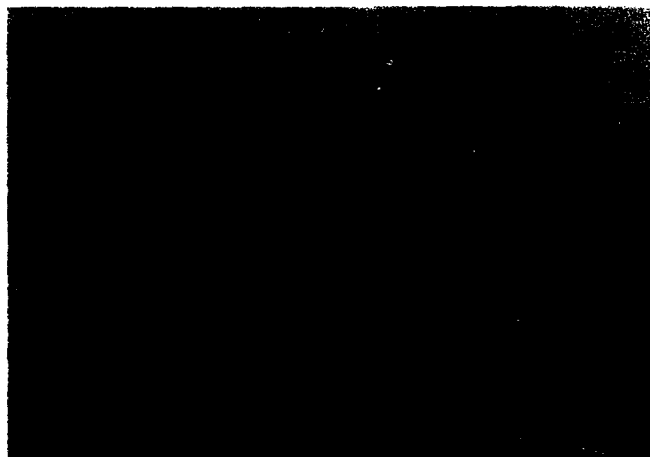


Figure 3: TEM image of a GaP nanocluster with a larger size.

Measuring a number of clusters, we obtain a typical size of 19 Å, a maximum size of 23 Å and a minimum size of 15 Å, confirming the narrow size distribution suggested by the Gaussian X-ray lineshape. The clusters have a nearly spherical shape, and they appear to be only weakly faceted. A thin shell covering the crystalline cluster can be seen in figure 3. As the clusters were prepared by a chemical reaction in a solution, the residual reaction products, Cl and $\text{Si}(\text{CH}_3)_3$, can chemically bond to the surface, saturating the dangling bonds which a bare surface would have. This surface layer seems to prevent the oxidation of the clusters. This effect is similar to efforts to coat II-VI semiconductor clusters.[11]

We have performed optical absorption measurements using an UV-visible absorption spectrometer. The as grown material, GaP and GaAs, showed an absorption edge blue shifted with respect to the bulk, but without distinct structure. The annealed GaP exhibits a distinct line in the absorption spectrum, that can be assigned to the lowest electronic level caused by the quantum confinement of the charge carriers; see figure 4.

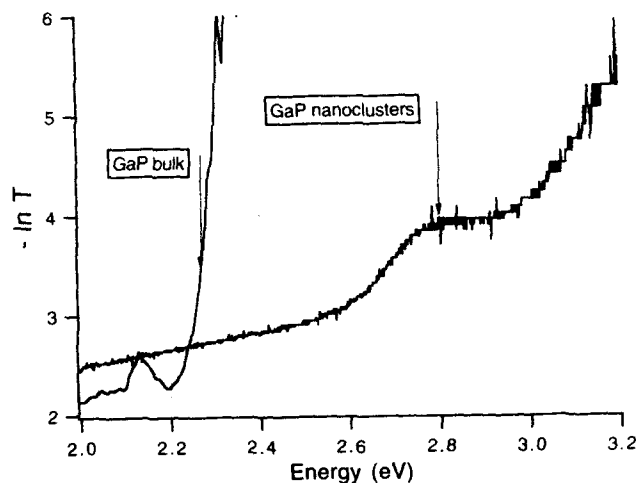


Figure 4: Optical absorption spectrum of GaP nanoclusters (same material as in figure 1). The GaP bulk absorption edge is included to show the blue shift.

This spectrum is similar to absorption spectra reported for II-VI semiconductor clusters.[12] We measured the position of the absorption line as 2.80 eV, resulting in a blue shift of 0.53 eV with respect to the bulk absorption edge at 2.27 eV. As the cluster size is smaller than the excitonic Bohr radius, we can use the following equation for 3- dimensional charge carrier confinement:[6,13]

$$\Delta E(\text{eV}) \approx \frac{\hbar^2 \pi^2}{2 R^2 (\text{nm}^2)} \left(\frac{1}{m_c} + \frac{1}{m_v} \right)$$

This results in a cluster size of 20.2 Å, in good agreement with the X-ray diffraction and the TEM results. Note that the blue shift is a sensitive function of the cluster size. From the width of the absorption line we can estimate a cluster size distribution from 17 Å to 23 Å.

CONCLUSION

We have shown, that GaP and GaAs nanoclusters can be fabricated by organometallic synthesis with high crystalline quality in the size regime of 10 Å to 30 Å. They seem to be coated with a chemically bonded shell of the residual reaction products, inhibiting oxidation. Calculating the particle size from the measured blue shift of 0.53 eV using the function for 3-dimensional charge carrier confinement gives 20.2 Å, consistent with the structural measurements. This gives clear experimental evidence for a quantum confinement of carriers in these GaP nanoparticles.

ACKNOWLEDGEMENT

The authors thank John A. Samuels for support with the synthesis and for valuable discussions.

REFERENCES

1. H. Uchida, C.J. Curtis, P.V. Kamat, K.M. Jones, and A.J. Nozik, *J. Am. Chem. Soc.* **96**, 1157 (1992).
2. L.J. Brus, *J. Phys. Chem.* **90**, 2555 (1986).
3. A.L. Efros, and A.I. Efros, *Sov. Phys. Semicond.*, **16**, 772 (1982).
4. M.L. Steigerwald, and L.E. Brus, *Acc. Chem. Res.* **23**, 183 (1990).
5. E.K. Byrne, L. Parkanyi, and K.H. Theopold, *Science*, **241**, 332 (1988).
6. M.A. Olshavsky, A.N. Goldstein, and A.P. Alivasatos, *J. Am. Chem. Soc.* **112**, 9438 (1990).
7. R.E. Treece, G.S. Macala, and R.B. Kaner, *Chem. Mater.*, **4**, 9 (1992).
8. S.R. Aubuchon, A.T. McPhail, R.L. Wells, J.A. Giambra, and J.R. Bowser, *Chem. Mat.* **6**, 82 (1994).
9. G. Becker, G. Gutekunst, and H.J. Wessely, *Z. Anorg. Allg. Chem.* **462**, 113 (1980).
10. C.J. Sandroff, J.P. Harbison, R. Ramesh, M.J. Andrejco, M.S. Hedge, D.M. Hwang, C.C. Chang, and E.M. Vogel, *Science*, **245**, 391 (1989).
11. Y. Wang, N.J. Herron, *J. Phys. Chem.*, **95**, 525, (1991).
12. N.F. Borrelli, D.W. Hall, H.J. Holland, and D.W. Smith, *J. Appl. Phys.*, **61**, 5399 (1987).
13. L.E. Brus, *J. Chem. Phys.*, **79**, 5566 (1983).

PART II

Self-Assembly and Biomolecular Engineering

THE CONTROL OF DNA STRUCTURE AND TOPOLOGY: AN OVERVIEW

NADRIAN C. SEEMAN, YUWEN ZHANG, SHOU MING DU, HUI WANG, JOHN E. MUELLER, YINLI WANG, BING LIU, JING QI AND JUNGHUEI CHEN
Department of Chemistry, New York University, New York, NY 10003 USA

ABSTRACT

The control of structure on the nanoscale relies on intermolecular interactions whose specificity and geometry can be treated on a predictive basis. DNA fulfills this criterion, and provides an extremely convenient construction medium: The sticky-ended association of DNA molecules occurs with high specificity, and it results in the formation of double helical DNA, whose structure is well known. The use of stable branched DNA molecules permits one to make stick-figures. We have used this strategy to construct in solution a covalently closed DNA molecule whose helix axes have the connectivity of a cube: The molecule has twelve double helical edges; every edge is two helical turns in length, resulting in a hexacatenane, each of whose strands corresponds to a face of the object. We have developed a solid-support-based synthetic methodology that is more effective than solution synthesis. The key features of the technique are control over the formation of each edge of the object, and the topological closure of each intermediate. The isolation of individual objects on the surface of the support eliminates cross-reactions between growing products. The solid-support-based methodology has been used to construct a molecule whose helix axes have the connectivity of a truncated octahedron. This figure has 14 faces, of which six are square and eight are hexagonal; this Archimedean polyhedron contains 24 vertices and 36 edges, and is built from a 14-catenane of DNA. Knotted molecules appear to be the route for cloning DNA objects. It is possible to construct three knotted topologies, as well as a simple cyclic molecule from a single precursor, by control of solution conditions. Control of both branching and braiding topology is strong in this system, but control of 3-D structure remains elusive. Our key aim is the formation of prespecified 2-D and 3-D periodic structures for use in diffraction experiments. Another application envisioned is scaffolding for the assembly of molecular electronic devices.

CONTROL OF STRUCTURE ON THE NANOMETER SCALE

All scientists who devise new formulations of matter would relish structural control on the molecular scale comparable to that enjoyed by craft workers on the macroscopic scale.¹ The ability to join, couple or weave two molecules together to produce a structure with the same certainty enjoyed by a carpenter, a plumber or a garment worker, would increase greatly the efficiency of materials scientists, chemists, and molecular biologists. These ends have been sought by chemists on the molecular (Angstrom) scale for years; new arrangements of atoms on this scale sometimes produce new chemical properties, due to subtle features of the charge density distribution in the product. Chemists have learned that it is not as straightforward to create structures from molecules as it is from macroscopic objects: They must rely on intrinsic propensities of precursor molecules, because there are no nails, screws, or threads available to form bonds between atoms. Furthermore, the laws of physics do not permit all conceivable arrangements of atomic nuclei to produce stable compounds; for example, carbon-carbon bonds 0.5 or 1.8 Å long are not available as structural components. Nevertheless, when they are successful, chemists generate products in parallel on a scale that is almost unimaginably vast in the macroscopic world: Reactions involving a gram of a simple compound of molecular weight 600 generate roughly 10^{21} product molecules.

The nanometer scale is used by biological systems to build their structural components. The globular protein components of the microtubules and microfilaments that form the

architectural basis of the cell are typically a few nanometers in dimension. The nanometer scale appears to be the smallest macroscopic scale, in that there are no evident principles that prevent the fabrication of any structural arrangements not forbidden by the impenetrability of matter. Of course, care must be taken to avoid unfavorable interactions, such as the juxtaposition of like charges. Likewise, it is important to remember that the large number of molecules involved in nanoscale systems are subject to the laws of chemical equilibria: Target structures must be sufficiently favorable that byproducts do not result². It is easier to fashion new structures derived from biological components on the nanometer scale, because the components can associate by means of weak interactions, such as hydrogen bonds and van der Waals forces, rather than by covalent bonds. On this scale, it is unlikely that new chemical properties will arise, because the chemical features of the constituent residues are already fairly well fixed. However, the re-orientation and juxtaposition of well-defined macromolecular elements can lead to new functionality on this scale. In much the same way that a given piece of metal can be fashioned to form a paperweight, a key, a spring, or a chair without altering its internal structure, new functions can be derived from new shapes on this scale. Indeed, Medawar has suggested that the evolution of new kinds of biochemicals predates the divergence of plants and animals³; nevertheless, the reorganization of the existing biochemicals has led to the diversity of eukaryotic life.

Self-Assembly is a Route to Nanometer Scale Construction

It is most natural to imagine assembling structures piece by piece, in the same way that a house or an automobile is built. The movement of atoms by scanning tunneling microscopes (STM) exemplifies this top-down approach to nanotechnology; the constructions of a corporate logo⁴ and an atomic switch⁵ by these techniques are dramatic examples of this methodology. These top-down methods enjoy the advantage of lacking undesirable cross-reactivities between the large numbers of components found in a chemical reaction. Nevertheless, the efficiency of top-down methodology for interfacing with the nanometer scale is inherently low: A single STM is used by an individual investigator to construct one object.

The structural components in biological systems often self-assemble spontaneously. In fact, self-assembly appears to be the most effective means for achieving structural goals on the nanometer scale. In self-assembling systems, complementary surfaces form cohesive structures. Microtubules and microfilaments are examples of nano-scale systems that self-assemble to grow in one-dimension, and the capsid proteins of simple viruses form self-assembled two-dimensional (icosahedral) surfaces. Many biological macromolecules can be induced to self-assemble into three-dimensional crystals, although these are not common within the cell. Complementary surfaces are the key common elements in each of these processes.

We have exploited the self-assembly properties of DNA. The complementary nature of DNA structure makes it an ideal molecule to use in nanoscale construction. We have used branched DNA molecules to form stick-polyhedra, and we have exploited the self-complementary features of single-stranded molecules to form a variety of knotted molecules. We will show below that by means of a solid-support-based synthetic methodology, it is possible to combine self-assembly with molecular isolation on the nanometer scale to achieve the level of control characteristic of the top-down approaches: We have been able to assemble DNA molecules whose helix axes have the connectivity of a truncated octahedron.

DNA Molecules Self-Assemble

For the past decade, we have used the self-assembly of DNA molecules as a convenient way to achieve control over the structure of matter on the nanometer scale. DNA is the molecule that offers the most predictable *intermolecular* associations known. The double helical molecule invariably forms in compliance with the complementarity rule that adenine (A) pairs with thymine (T) and that guanine (G) pairs with cytosine (C). The biotechnology industry is predicated in part on the reliability of this type of association. Other forms of association are possible in the absence of complementary partners, but complementarity appears to prevail if it is one of the competitive alternatives. Under conventional conditions, the product of this

association is a right-handed double helix approximately 20 Å in diameter with a pitch about 34 Å, containing about 10 nucleotide pairs per turn. Two DNA molecules with single-stranded overhangs, called 'sticky ends' will cohere, and can be linked covalently by DNA ligases⁶.

DNA Can Be a Branched Molecule

The apparent drawback to engineering DNA molecules for structural purposes is that naturally occurring DNA is a linear molecule, in the sense that its helix axis is unbranched. Thus, the ligation of linear DNA corresponds to the concatenation of line segments that can produce longer lines, circles or knots. However, DNA need not always be linear. It is possible to design *synthetic* sequences that self-assemble to form branched molecules called 'junctions'. Junctions are designed by minimizing the sequence symmetry of the strands and maximizing Watson-Crick base pairing of the target complex, so that the branched structure will actually form under convenient solution conditions⁷⁻⁹.

Molecular Associations Between Branched Molecules Can Be Directed by Sticky Ends

The sticky-ended ligation of DNA fragments⁶ is the fundamental reaction of biotechnology. The combination of branched DNA molecules with sticky ends provides building blocks that can be assembled⁷ into multiply-connected stick-figures and networks¹⁰. All the edges of these figures consist of double helical DNA. Thus, one can imagine designing and building complex structures from branched DNA molecules. The concept of self-assembly among branched molecules is illustrated in Figure 1, which shows a 4-arm junction with sticky ends arranged to form a quadrilateral.

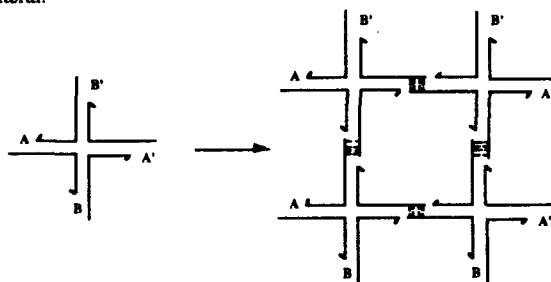


Figure 1. Formation of a Quadrilateral from a Junction with Sticky Ends. A is a sticky end and A' is its complement. The same is true of B and B'. Four of the monomers on the left are complexed in parallel orientation to yield the structure on the right. DNA ligase can close the gaps left in the complex. The complex has open valences; it could be extended to form a 2-dimensional lattice by the addition of more monomers.

Connectedness

A key concept in the assembly of DNA stick-figures is *connectedness*¹⁰, which is the number of edges of a closed object or a lattice that meet at a vertex; the number of arms of the junction at a given vertex limits the maximum connectedness of that vertex. Thus, 3-connected objects and lattices can be built with 3-arm junctions, and 4-connected structures can be built with 4-arm junctions. Junctions with 3-6 arms have been constructed and characterized^{9,11,12}. It is important to recall, however, that the assembly of individual objects into larger constructs, such as clusters and periodic arrays, requires junctions containing arms that can be used for connections between objects. For example, Figure 2 shows two periodic arrays. The one on the right is a 6-connected array corresponding to the edges of space-filling cubes, which are themselves 3-connected objects. The array on the left is the 5-connected space-filling array formed by 4-connected octahedra at the corners of 3-connected truncated cubes. Each of these

lattices is shown acting as a host for a guest macromolecule.

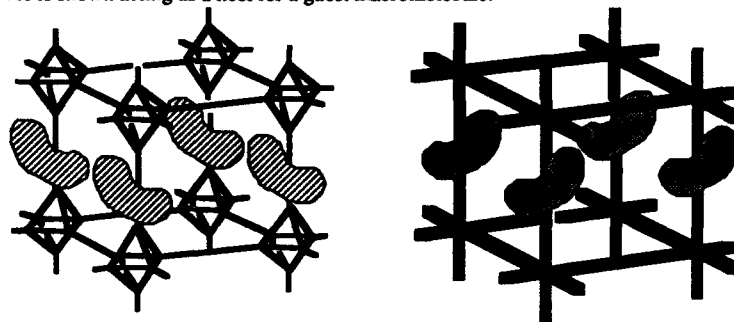


Figure 2. Five-Connected and Six-Connected Networks Acting as Hosts for Macromolecular Guests. The simplest conceptual network, the 6-connected cubic lattice, is shown on the right side of this drawing. Macromolecular guests, represented as shaded kidney-shaped objects, have been added to four unit cells. Note that if the guests are all aligned in the parallel fashion shown, the entire material will be a crystalline, and it will be possible to determine the structure of the guests by crystallography.

MOLECULAR ASSEMBLY USING BRANCHED DNA COMPONENTS

Branched Junctions Are Not Rigid, But Specific Sticky Ends Can Produce Target Structures

In practice, junctions are flexible over the 1-100 hr periods used for ligation^{11,13}. It is reasonable to expect the short double helical edges of each object to be torsionally and flexurally stiff, because the persistence length of DNA has been estimated to be between 450 Å and 2500 Å^{14,15}. However, the 'valence angles' between the double helical edges of each object are not fixed. When a 3-arm or 4-arm junction is oligomerized to yield oligolaterals with two helical turns between branch points, it forms a series of cyclic products: trimers, tetramers, pentamers and so on^{11,13}. Thus, the angles flanking a DNA branch point are variable, in contrast to the local geometry near a covalently bonded atom. Hence, a junction is more closely analogous to an octopus, whose flailing arms are separated by a variety of angles, than to a starfish, whose arms rarely appear to deviate substantially from pentagonal symmetry.

Although their flexibility implies that oligomerization of individual junctions is unlikely to be a useful way to generate target polygons, unique sticky-ends can be used to direct the assembly of particular junctions into target structures. We have tested this approach by assembling a specific quadrilateral from four branched DNA molecules¹⁶. The sticky ends on each junction are unique, so the process is directed synthesis, rather than oligomerization.

The Construction of a Platonic Solid, a DNA Cube

The most exciting prospects for this system entail the assembly of multiply-connected objects in 3-D. We have exploited the flexibility of branched DNA to construct from 3-arm junctions a molecule whose helix axes have the connectivity of a cube¹⁷. A schematic of the 3-dimensional, 3-connected object is shown in Figure 3. The object is shown as a cube, but the angles between the edges are uncharacterized. It contains 12 edges that consist of double helical DNA. Whereas every edge contains 20 nucleotide pairs of DNA, we expect that their lengths will be about 68 Å. Each of the edges contains a unique site for recognition and cleavage by a restriction endonuclease, thereby enabling us to establish the validity of the synthesis. The synthesis of the cube-like object has been demonstrated by breaking it down to standard catenanes¹⁸ whose electrophoretic properties are known.

There is an integral number of turns in each edge, so every face of the cube corresponds to a single cyclic strand. Therefore, the object in Figure 3 is a complex catenane of 6 single-

stranded cyclic molecules, each doubly linked to its four nearest neighbors. The catenated nature of the strands in Figure 3 highlights an important point about double helical DNA: The braiding of the strands about the helix axis is a critical structural and topological property of any DNA molecule. For example, the strands in the cube can be separated from nicked failure products by electrophoresis under denaturing conditions, because the catenane holds together, but nicked molecules separate into individual strands¹⁷. The twisting of DNA strands about each other implies that closed structures will be complex catenanes, and materials constructed from this medium can contain polycatenated mesh substructures, much like chain mail.

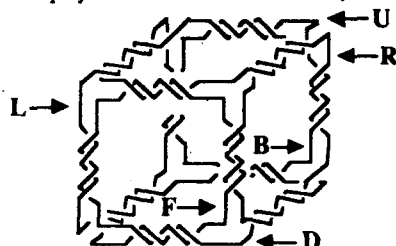


Figure 3. A DNA Molecule Whose Helix Axes Have the Connectivity of a Cube. The molecule consists of six cyclic strands that have been catenated together in this particular arrangement. They are labeled by the first letters of their positions, Up, Down, Front, Back, Left and Right.

A Solid-Support Based Synthetic Methodology

The synthesis of the cube was performed in solution. This led to numerous problems, arising from the combination of (i) the flexibility of the branched junctions, (ii) the difficulty of separating products from catalysts, reactants and byproducts, and (iii) the differences between the optimal concentrations for intermolecular addition reactions and for intramolecular cyclization reactions. Control of DNA ligation in solution derives solely from the ability to phosphorylate sticky ends in a selective fashion. This is insufficient control for the synthesis of complex objects, so we have developed a new methodology that is more effective¹⁹.

This procedure is based on the use of a solid support, which permits convenient removal of reagents and catalysts from the growing product. Each ligation cycle adds a component that creates a covalently-closed, topologically-bonded intermediate. This feature permits exonuclease digestion of incompletely ligated edges, thereby purifying the growing object during synthesis. A single edge of an object can be formed at a time. Control derives from the restriction endonuclease digestion of hairpin loops that form each side of the new edge. The isolation of growing objects on the support also removes the problem of cross-reactions between growing product molecules. Sequences are chosen to destroy restriction sites when the edge forms. In principle, the component added to the growing construct can be a junction, a polygon, a group of polygons, a polyhedron, or an array of polyhedra.

The Construction of an Archimedean Solid, a Truncated Octahedron

In order to analyze the solid-support methodology, we have constructed a truncated octahedron from DNA²⁰. This Archimedean solid contains six squares flanking its four-fold symmetry axes, and eight hexagons that surround its 3-fold symmetry axes. There are two turns of DNA per edge, so each of the 14 faces corresponds to a single cyclic strand. Thus, the final object is a complex 14-catenane. The truncated octahedron is a 3-connected figure, but the molecule has been constructed from 4-arm junctions; thus each vertex is associated with another arm that could be used to join polyhedra, although this has not been done. The extra arms are all hairpins within the strands that correspond to the square faces. The entire molecule contains 2550 nucleotides, and has a molecular weight ca. 790 kd.

In this construction, the objects added to the support are squares and square groupings, as indicated in Figure 4. The figure contains six squares and eight hexagons. The object has been constructed by doing two intermolecular additions to a square attached to the support. In the first addition, a tetrasquare complex is added, and in the second addition, the final square is added. The structure on the lower left of Figure 4 is a heptacatenane hexasquare complex. The square strands are already intact in this construct, and the hexagons are all formed from the outer strand. The hexagons result from successive intramolecular closures of the sticky ends associated with the restriction enzyme site pairs, S1-S1'...S7-S7'. Whereas the molecules are

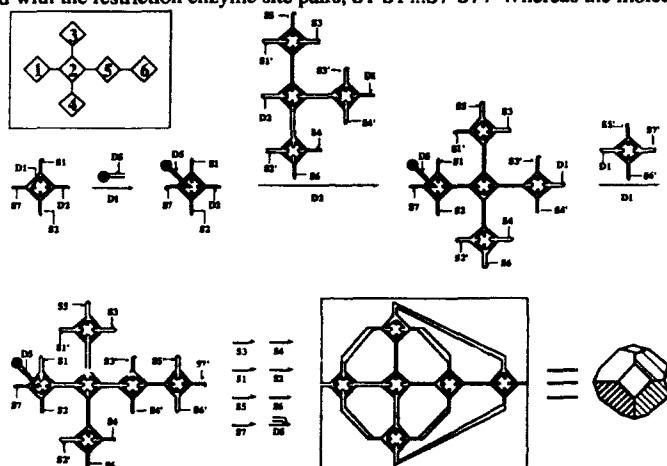


Figure 4. *The Synthetic Scheme Used to Synthesize the Truncated Octahedron.* The boxed diagram in the upper left indicates the numbering of individual squares. Each square in the rest of the diagram is shown with its restriction sites indicated. Symmetric restriction sites are named 'S', indicated in pairs, with one member primed; restriction sites cut distally are named 'D'. Arms that will eventually combine to form edges are drawn on the outside of each square, and exocyclic arms are drawn on the inside of the square. A reaction is indicated by a line above a restriction site: This means that the restriction enzyme is added, protecting hairpins are removed and then the two sticky ends are ligated together. The product is shown in two forms. On the left, the S1-S6 closures are shown as triple edges, to emphasize their origins; the two strands of the edge formed by the S7 closure are separated to maintain the symmetry of the picture. On the right, a slightly rotated front view of a polyhedral representation of a truncated octahedron is shown without the exocyclic arms; the 432 cubic symmetry of the ideal object is evident from this view.

isolated from each other on the support, it is possible to expose this group of sticky ends successively by using symmetrically-cleaving restriction enzyme pairs that recognize six nucleotide pairs each. Although the initial sites are destroyed after ligation, four-base cutting sites remain, for analytical purposes. The final step in the synthesis involves releasing the structure from the support and annealing it shut with a hairpin. The synthesis is demonstrated in two stages: First, by showing that all six cyclic strands corresponding to the square molecules are in the heptacatenane, and second, by digesting the final product to the tetracatenanes that flank each square. This second stage of proof has been performed for five of the squares, but the molecule lacks restriction sites for square #6.

SINGLE-STRANDED KNOTS: THREADING DNA

An intimate relationship exists between catenanes and knots²¹: Removal of a node by switching strands, yet maintaining local symmetry and strand polarity (sometimes called

forming a zero node), converts a catenane to a knot, and a knot to a catenane (Figure 5). This relationship is important here, because it appears that cloning these DNA structures will be most readily achieved by getting single-stranded DNA molecules to fold up into complex knots, whose restriction will lead to the desired stick figures²². It is not possible to clone branched structures directly, because a single round of replication will reduce a branch to linear duplexes.



Figure 5. Interconversions of Knots and Catenanes by Switching Strands at a Node. The structure shown on the left is a 5_1 knot. The strand direction is indicated by the arrowheads appearing along the strand. When the two strands entering the lower node on the right exchange outgoing partners, the node disappears, and a 'zero node' is introduced²¹. This converts the knot to a catenane, shown in the middle; the two linked cycles are drawn so as to retain their shapes, but they are drawn with pens of different thicknesses. The lower left node of the catenane undergoes a strand switch, and the structure is converted to a trefoil knot, illustrated on the right. The trefoil knot is one strand, so it is drawn with one pen.

Nevertheless, it is possible, in principle, to make an entire structure from a single strand, as illustrated for a dodecahedron in Figure 6. The key to this strategy is to add an extra external

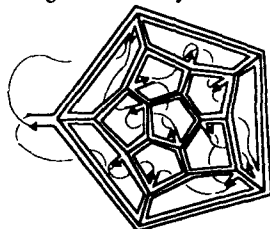


Figure 6. A Single-Stranded Representation of a Pentagonal Dodecahedron. A pentagonal dodecahedron is illustrated with twelve exocyclic arms, in a Schlegel diagram. This is a 2-D representation of a 3-D object in which the central polygon is closest to the reader, the polygons removed from the center are distorted and further behind in the page, and the outer polygon is at the rear of the figure. The Schlegel diagram of the dodecahedron is shown in the thickest lines. Flanking these are lines that represent the double helical DNA corresponding to each edge of the dodecahedron. Each of the twelve pentagons contains an exocyclic double helical arm, with one strand terminating in an arrowhead, indicating the 5'→3' polarity of the strand. In addition, each of the individual faces has been connected to a neighboring face through the exocyclic arms and very thin connecting strands, so that the entire representation is a single long strand. The structure shown would need to be cleaved in order to fold. Each exocyclic double helical segment would contain a restriction site, to allow it from connecting DNA upon formation of the structure. No topological representation is made here; connecting DNA lies behind the polygonal DNA for clarity.

arm for every strand; for molecules whose edges only contain an integral number of helical turns, this corresponds to an extra arm per face. The external arms are connected to form the complex knotted structure shown. The sequence of such a single-stranded molecule could be cloned. Whereas one needs external arms on a polyhedral structure to form a lattice, the target structure will have restrictable external arms.

We have explored the possibilities for threading knots experimentally. A DNA molecule can be synthesized containing the sequence $X-T-Y-T-X'-T-Y'-T$, where X and Y correspond to one helical turn, X' and Y' are their Watson-Crick complements, respectively, and T is dT_n linker. When cyclized, the strand yields a trefoil knot with negative nodes (3_1^-), because the nodes formed by ordinary right-handed B-DNA correspond to negative topological nodes²³. However, there is a left-handed form of DNA, Z-DNA²⁴, that is formed by special sequences, under the control of solution conditions²⁵. One can choose for both X and Y

sequences capable of forming Z-DNA under different conditions. Figure 7 shows that mild Z-promoting conditions will produce an amphichiral figure-8 (4_1) knot (in methylated DNA), containing two positive nodes and two negative nodes, but strong Z-promoting conditions

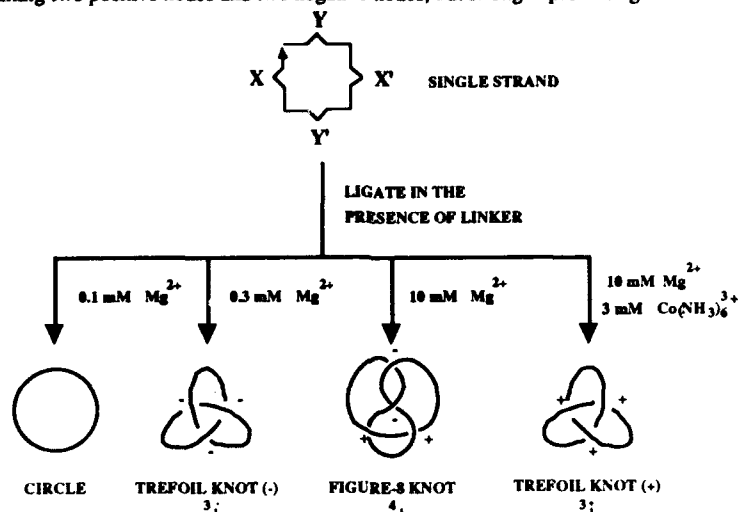


Figure 7. The Synthetic Scheme Used to Produce Four Target Topologies. The top of this scheme indicates the molecule from which the target products are produced. The four pairing regions, X and its complement X', Y and its complement Y' are indicated by the bulges from the square. The 3' end of the molecule is denoted by the arrowhead. The 3' end is between helical domains, and therefore requires a linker complementary to the 3' and 5' ends of the strand. The molecular topologies are shown at the bottom.

will produce a trefoil knot with positive nodes (3_1^+)²⁶. The circle of the same sequence can be prepared by ligating in an ionic strength too low to support knot formation. Altering the

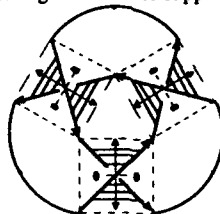


Figure 8. The Relationship Between Nodes and Antiparallel B-DNA Illustrated on a Trefoil Knot. A trefoil knot is drawn with negative nodes. The path is indicated by the arrows and the very thick curved lines connecting them. The nodes are formed by individual arrows drawn at right angles to each other. Each pair of arrows forming a node defines a quadrilateral (a square in this figure), which is drawn in dotted lines. Double-arrowheaded helix axes are shown perpendicular to these lines. The two-fold axis that relates the two strands is perpendicular to the helix axis; its ends are indicated by lens-shaped figures. The two-fold axis intersects the helix axis and lies halfway between the upper and lower strands. The DNA shown base paired at each node corresponds to half a double helical turn.

solution conditions after a knot has been closed creates a molecule under stress. In the presence of DNA topoisomerase I, which lacks an energy source, the molecule will convert to the topological species most favored by solution conditions²⁷. The shortest knots of a given motif

are likely to contain the greatest amount of stress. We have ascertained that the shortest 3_1 - and 4_1 -two-domain knots readily made contain about 80 nucleotides, although molecules as short as 70 or 66 nucleotides yield traces of knotted material²⁸.

There is a general relationship between the nodes of DNA molecules and the nodes of single-stranded DNA knots: A half-turn of duplex DNA can be used to generate a node in a knot^{29, 30}. Figure 8 illustrates this point with a trefoil knot built from a branched junction. The three nodes of the knot shown are formed by perpendicular lines, whose polarity is indicated by arrowheads. The nodes act as the diagonals of a square, which they divide into four regions, two between antiparallel arrows and two between parallel arrows. The transition from topology to nucleic acid chemistry can be made by drawing base pairs between strands in the antiparallel regions. The axes of the helices are drawn perpendicular to the base pairs. A trefoil knot has been constructed recently from a the branched junction motif³¹.

MOLECULAR TARGETS FOR DNA ASSEMBLY

The Directed Assembly of Periodic Matter

A key use envisioned for DNA arrays⁷ is to function as macromolecular zeolites, serving as hosts for globular macromolecular species, as an aid in crystallographic structure determination. This application is illustrated in Figure 2. The rate-determining step in macromolecular crystallography is the preparation of adequate crystals. The ability to assemble periodic arrays of cages that contain ordered guests would help solve that problem. Intracage orientation might be accomplished through binding the guest by site-specific fusion domains. The assembly of periodic lattices is likely to be difficult: One can control the synthesis of an individual object by minimizing sticky-end symmetry, but symmetry minimization cannot be used to build a crystal, since the lattice inherently contains translational symmetry.

Scaffolding to Direct the Assembly of Other Macromolecules

The medical and commercial importance of DNA has resulted in convenient technology for the synthesis³² and modification³³ of DNA. There are also natural mechanisms by which drugs, particular proteins, or other DNA strands recognize and bind to specific sites on DNA. These methods may ultimately be used to attach molecular electronic components to DNA molecules³⁴. The self-assembly of the DNA molecules could thereby direct the assembly of these other components. We have suggested that a crystalline array of this sort could act as a biochip, in which the DNA plays a structural role³⁴. The scaffolded threading of polymeric species has also been suggested²⁹.

CONCLUDING COMMENTS

Structure and topology are key properties in DNA molecules. DNA molecules whose helix axes meet at branch points can be used to construct multiply-connected stick figures. The construction of a truncated octahedron demonstrates that this type of topological control is now well in hand. Likewise, achieving the level of control necessary to generate four different knotted (or unknotted) topologies from a single strand of DNA indicates that braiding topology is also under reasonably good control today. The next stages in DNA construction are periodic DNA lattices and more complex knots: The former will enable many applications, such as diffraction studies and long-range scaffolding, and the latter be useful in cloning structures and in testing the relationship between half-turns of DNA and nodes in knots. The greatest stumbling block for the construction of lattices is the lack of rigid junctions with fixed 'valence' angles. It is possible that the 'bulged' junctions reported recently by Leontis and his colleagues³⁵ will be of use in this context. The construction of more complex knots awaits technologies that can be applied to direct characterization of their topologies. Developments in scanning probe microscopy³⁶ and optics³⁷ may lead the way in this direction.

ACKNOWLEDGMENTS

This research has been supported by grants N00014-89-J-3078 from the Office of Naval Research and GM-29554 from the NIH. The support of Biomolecular Imaging on the NYU campus by the W. M. Keck Foundation is gratefully acknowledged.

REFERENCES

1. Drexler, K.E., Proc. Natl. Acad. Sci. (USA) **78**, 5275-5278 (1981).
2. Seeman, N.C., Nanotechnol. **2**, 149-159 (1991).
3. Medawar, P.B., The Art of the Soluble, (Methuen & Co., London 1967), p. 48.
4. Eigler, D.M. and Schweizer, E.K., Nature (London) **344**, 524-526 (1990).
5. Eigler, D.M., Lutz, C.P. and Rudge, W.E., Nature (London) **352**, 600-603 (1991).
6. Cohen, S.N., Chang, A.C.Y., Boyer, H.W. and Helling, R.B., Proc. Natl. Acad. Sci. (USA) **70**, 3240-3244 (1973).
7. Seeman, N.C., J. Theor. Biol. **99**, 237-247 (1982).
8. Seeman, N.C., J. Biomol. Str. & Dyns. **8**, 573-581 (1990).
9. Kallenbach, N.R., Ma, R.-I. and Seeman, N.C., Nature, **305**, 829-831 (1983).
10. Wells, A.F., 3-D Nets and Polyhedra (John Wiley & Sons, New York, 1977).
11. Ma, R.-I., Kallenbach, N.R., Sheardy, R.D., Petrillo, M.L. and Seeman, N.C., Nucl. Acids Res. **14**, 9745-9753 (1986).
12. Wang, Y., Mueller, J.E., Kemper, B., Seeman, N.C., Biochem. **30**, 5667-5674 (1991).
13. Petrillo, M.L., Newton, C.J., Cunningham, R.P., R.-I. Ma, Kallenbach, N.R. and Seeman, N.C., Biopolymers **27**, 1337-1352 (1988).
14. Hagerman, P.J., Ann. Rev. Biophys. & Biophys. Chem. **17**, 265-286 (1988).
15. Hustedt, E.J., Spaltenstein, A., Kirchner, J.J., Hopkins, P.B. and Robinson, B.H., Biochem. **32**, 1774-1787 (1993).
16. Chen, J.-H., Kallenbach, N.R. and Seeman, N.C., J. Am. Chem. Soc. **111**, 6402-6407 (1989).
17. Chen, J. and Seeman, N.C., Nature (London) **350**, 631-633 (1991).
18. Chen, J. and Seeman, N.C., Electrophoresis **12**, 607-611 (1991).
19. Zhang, Y. and Seeman, N.C., J. Am. Chem. Soc. **114**, 2656-2663 (1992).
20. Zhang, Y. and Seeman, N.C., J. Am. Chem. Soc. **116**, 1661-1669 (1994).
21. White, J.H., Millett, K.C., and Cozzarelli, N.R., J. Mol. Biol. **197**, 585-603 (1987).
22. Seeman, N.C., DNA and Cell Biology **10**, 475-486 (1991).
23. Mueller, J.E., Du, S.M. and Seeman, N.C., J. Am. Chem. Soc. **113**, 6306-6308 (1991).
24. Wang, A.H.-J., Quigley, G.J., Kolpak, F.J., Crawford, J.L., van Boom, J.H., van der Marel, G. and Rich, A., Nature (London) **282**, 680-686 (1979).
25. Behe, M. and Felsenfeld, G., Proc. Natl. Acad. Sci. (USA) **78**, 1619-1623 (1981).
26. Du, S.M., Stollar, B.D., and Seeman, N.C. (1994) (unpublished).
27. Du, S.M., Tse-Dinh, Y.-C., and Seeman, N.C. (1994) (unpublished).
28. Wang, H., Du, S.M. and Seeman, N.C., J. Biomol. Str. & Dyns. **10**, 853-863 (1993).
29. Seeman, N.C., Molecular Engineering **2**, 297-307 (1992).
30. Seeman, N.C., J. Chen, S.M. Du, J.E. Mueller, Y. Zhang, T.-J. Fu, H. Wang, Y. Wang, and S. Zhang, Synthetic DNA Knots and Catenanes, New J. Chem. **17**, 739-755 (1993).
31. Du, S.M. and Seeman, N.C., Biopolymers **34**, 31-37 (1994).
32. Caruthers M. H., Science **230**, 281-285 (1985).
33. Eckstein, F., Oligonucleotides and Analogues (IRL, Oxford, 1993), pp. 49-313.
34. Robinson, B.H. and Seeman, N.C., Prot. Eng. **1**, 295-300 (1987).
35. Leontis, N.B., Hills, M.T., Piatto, M., Malhotra, A., Nussbaum, J. & Gorenstein, D.G. (1993), J. Biomol. Str. & Dyns. **11**, 215-223.
36. Karrasch, S., Hegerl, R., Hoh, J.H., Baumeister, W., and Engle, A., Proc. Natl. Acad. Sci. (USA), **91**, 836-838 (1994).
37. Bilderback, D.H., Hoffman, S.A. and Thiel, D.J., Science **263**, 201-203 (1994).

POLYMERIZABLE SELF-ORGANIZED MEMBRANES: A NOVEL CLASS OF ORGANIC COMPOUNDS

ALOK SINGH, MICHAEL MARKOWITZ, AND GAN MOOG CHOW

Center for Bio/Molecular Science and Engineering, Code 6900, Naval Research Laboratory,
Washington DC. 20375-5348

ABSTRACT

Molecular Self-assembly of amphiphilic phospholipid molecules (containing a hydrophobic acyl chain and a hydrophilic phosphate group attached to glycerol backbone) and other amphiphiles offers a versatile approach to form ordered structures. Stabilization of lipid microstructures by polymerization renders them useful for practical applications in the areas ranging from controlled release technology to template mediated synthesis of metals. Our efforts are focussed on the development and use of polymerizable diacetylenic phospholipids and their microstructures as template for chemical synthesis. The surface of vesicles and lipid microcylinders (0.5 μm dia.) is made reactive by chemically modifying the hydrophilic region of phospholipids. Lipids with chemically reactive sites were incorporated into lipid membranes predominantly formed from charge neutral lipids and used for binding metal ions and growing fine metal particles.

INTRODUCTION

Multidisciplinary approaches may often provide efficient solutions to technologically important problems by virtue of maintaining a balance of efforts to address the issues involved. Synthesis of micron and sub-micron particles, composites, and ordered growth and pattern formation during crystallization are the examples of successful implications of these approaches [1-3]. In addition, the hierarchical approach (progression in increased complexity) similar to that observed in nature is getting attention in the fabrication of advanced materials [4]. By combining these two strategies - multidisciplinary and hierarchical - it is possible to emulate nature's architecture by designing materials that are optimized for their ultimate functions on every scale, from molecular to macroscopic.

Phospholipids are amphiphilic molecules, which means that each molecule contains both hydrophobic and hydrophilic segments. Phospholipids are common building blocks for cell membranes and fulfill a number of vital basic cell membrane functions [5]. Synthetic phospholipids, particularly phosphatidylcholines, have received considerable attention because of their ability to produce a variety of morphologies including vesicles - spherical structures consisting of an aqueous core surrounded by single or multiple bilayers with dimensions on the micron to sub-micron scale. Figure 1 shows the structures formed by spontaneous self-organization of phospholipids in the presence of aqueous medium. The amphiphilic nature of phospholipid molecules leads them to orient in such a way that the polar headgroups remain in contact with surrounding aqueous medium while the hydrocarbon segments are segregated from water. Vesicles have been the subject of extensive investigations because of their usefulness as models for biological membranes and in the development of applications that utilize their membrane properties e.g., encapsulation and controlled release, functional incorporation of proteins, and signal transduction. However, the problem of long term stability of membrane structures restricted their utility and led to the development of new strategies to stabilize membranes. In particular, polymerization has emerged as a promising strategy for stabilizing bilayer membranes. Polymerization strategy is versatile because it stabilizes membranes by crosslinking the lipid monomers only after they have attained a particular morphology. Other methods reported for membrane stabilization include the use of proteins, sugars, and cholesterol in the preparation of lipid membranes.

In this article, we will discuss the results of our research efforts which began with stabilization of vesicles by polymerization. Results obtained during the course of these investigations have led to the development of reactive membranes that are, a) suitable for carrying out reactions at the membrane interface as well as inside of the closed bilayer structures, and b)

easy to modify to achieve transport of ions.

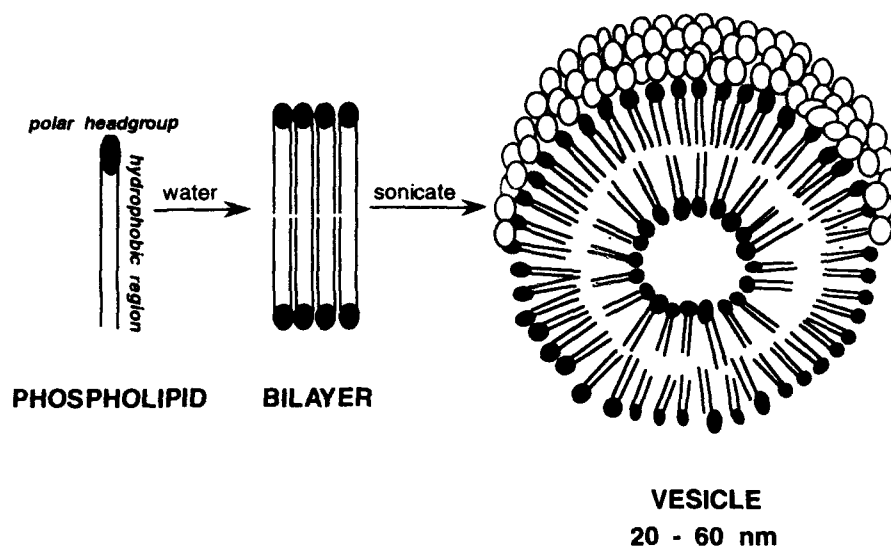


FIGURE - 1

STABILIZATION OF VESICLES FROM POLYMERIZABLE PHOSPHOLIPIDS:

Use of polymerizable phospholipids in stabilization schemes represents a pristine strategy for lipid bilayer stabilization because the scheme doesn't rely on the addition of an extra component to the lipids. The polymerizable phospholipids in monomer form exhibit physical properties that are similar to their non-polymerizable analogues. The added capability of polymerizable lipid monomers is their ability to stabilize membranes by crosslinking with their next neighbor lipids [6-9]. The polymerizable functionalities have been incorporated both in the headgroup region and to the acyl chains. A variety of polymerizable groups have been tried to achieve membrane stability [10]. Of all the polymerizable groups, diacetylenic group has been the most studied because of the thermochromic behavior of polydiacetylenes and ability of diacetylenes to influence membrane morphology [11-12]. Figure 2 shows the chemical structures of polymerizable phospholipids used in our vesicle studies.

Polymerized vesicles produced by incorporating methacryloyloxy monomer in the acyl chain of a phosphatidylcholine (1) and irradiating with UV showed reduced permeability and enhanced stability against chemical and physical perturbations that included mild ultrasound agitation, phospholipase A₂ catalyzed hydrolysis, and freeze drying - redispersion cycle [13,14]. The following method for the polymerized - vesicle preparation demonstrates that the technique is straightforward and the polymerization step is very simple to follow.

Typically, 2 mg of polymerized phospholipid (1) was dissolved in chloroform and coated on the walls of a glass tube with the aid of a stream of nitrogen. Traces of solvent were removed under vacuum (5 hrs.), and the lipid was hydrated in water (2 mL) which was warmed up in a water bath (80 °C) for 10 minutes. Vortex mixing produced multilamellar vesicles (vesicles with many bilayers) which were converted to a clear solution of small unilamellar vesicles by ultrasound agitation (50 °C) for one hour. The dispersion was then irradiated with ultraviolet light (254 nm) for 30 minutes to produce polymerized vesicles. The polymerization was monitored by thin layer chromatography. The polymerized lipid stayed at the origin of the TLC plate. The vesicle morphology was confirmed by transmission electron microscopy.

Polymerized lipid membranes were originally thought to be attractive candidates for pharmaceutical applications e.g., inhibition of fungal growth [15,16]. On the other hand, a large number of studies are reported concerning non-medical related studies such as, protein reincorporation, sensors, interfacial interactions and use of vesicles as reaction cages [17-21].

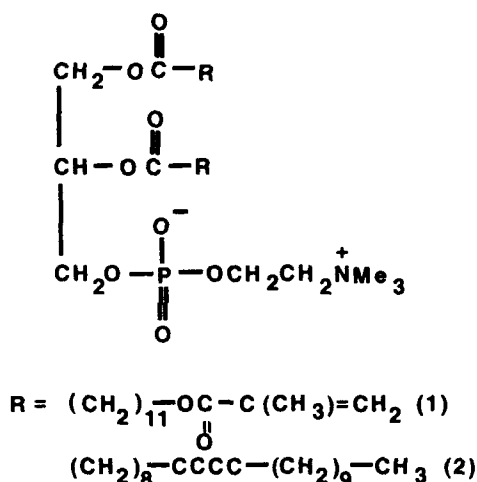


FIGURE - 2

DIACETYLENIC PHOSPHOLIPIDS MEMBRANES:

Phosphocholine Membrane: The diacetylenic moiety was incorporated in the acyl chains of a phospholipid to stabilize the vesicles by photo-polymerization [7-9]. But, the diacetylenic lipids turned out to be quite unique since their dispersions from 2 produced hollow cylindrical structures or tubules (Figure 3) in addition to the vesicles [12,22]. Lipid tubules formed from diacetylenic phosphocholines have a fixed internal diameter of ~0.5 µm. The length of the tubules is, however, process dependent. Experimentally, the tubules have been produced by two separate routes; the liposomal route (thermally grown) and the solution route (solvent grown) using an alcohol/water solvent system. Both methods have advantages and limitations but, tubule formation

from ethanol/water is easy, straight forward, less time consuming, and less dependent on sample purity. Two techniques to fabricate tubules are described in the following paragraphs. The simple operation demonstrates the effectiveness of self-assembling route for making complex structures.

For the preparation of tubules via thermal vesicular route, 4 mg poly-crystalline **2** was hydrated in 2 mL distilled water by incubating at 50°C for an hour. Lipid was dispersed by occasional vortex mixing during incubation period. Small unilamellar vesicles were produced by sonication at 50°C using a sonifier with a cup-horn attachment. Sonication was continued until dispersion with constant turbidity was produced (usually 45 minutes to one hour). The small vesicles then cooled down to room temperature and then maintained at 4°C till the dispersion turned into thick gel. The gel was then slowly heated to above the phase transition temperature of the dispersion ($T_m = 43.1^\circ\text{C}$) followed by slow cooling ($> 0.5^\circ\text{C}/\text{min}$) of the dispersion to room temperature. This cooling cycle produces uniform sized tubules in high yield.

The second procedure for the preparation of tubule is the solvent method. The diacetylenic lipid was dissolved in ethanol containing 30% water (concentration 0.5-1.0 mg/mL). The turbid solution was warmed to ensure complete dissolution of lipid in the solvent system. The clear solution was slowly cooled to room temperature. An increase in turbidity indicates the formation of tubules. This method produces high yields of tubules. Once the tubules are produced they are stable enough to withstand the dialysis step that follows to exchange alcohol with water.



FIGURE - 3

A large number of studies have been conducted to understand the mechanism of tubule formation. Important information on tubule structures was collected by implementing various techniques including X-ray analysis [23,24] and Raman spectroscopy [25]. Reported mechanisms for tubule formation didn't fully account for all the reported tubule properties [4]. In a recent report, however, experimental evidence is provided that the tubules are the result of chiral molecular architecture and that the helices are the common precursor for the tubules prepared by either technique [26].

For technological applications, it is necessary that the tubules should retain their morphological integrity during physical and chemical perturbation. Diacetylenes do not polymerize efficiently in organized assemblies [27]. Ultra violet irradiation (254 nm) of the tubules (solvent or thermally grown) cross-linked the diacetylenes available only on the outer surface of tubules as evidenced by the generation of deep red color due to conjugated polydiacetylenic polymer backbone. About 60 % monomer phospholipid was recovered from the polymerized tubules by a

simple methylene chloride extraction. The inefficient polymerization of the tubules forced a search for alternate methods of tubule stabilization. The strategy of incorporation of a second polymerizable group at the end of the acyl chains was implemented successfully. In this approach polymerization was initiated after the lipid was transformed into tubules [28]. Alternatively, the stabilization of tubules by coating its surface with metals through electroless metallization proved to be the best option [29]. This method utilized the ability of quaternary amine of phosphocholine headgroup to bind the tin-palladium catalyst. The bound catalyst has been used in the metallization of tubules with a variety of metals including copper, nickel, permalloy, cobalt etc. Metallized tubules, due to their size and stability, were studied in the interests of developing a variety of technological applications [4].

Electroless metallization of tubules with copper was accomplished as follows. To a 2 mL aqueous dispersion of thermally or solvent grown tubules (from 4 mg phospholipid) an equal volume of Pd/Sn colloid (MacDermid Co., Waterbury, CT) was added and the contents were gently mixed. After two minutes, the solution was removed after gentle centrifugation that separated the tubules from the medium. The brown colored, palladium coated tubules were washed several times with water. To these tubules 0.1 M HCl was added (pH 4.0) to oxidize the tin shell and expose the palladium catalyst. The oxidation was further accelerated by bubbling oxygen into the dispersion. Then 5 mL of copper bath Metex 9027 (MacDermid, containing cupric chloride and a reducing agent) was added. After about three minutes evolution of gas was observed and the color of the dispersion turned from brown to black. The reaction was then quenched by repeated centrifugation, removal of supernatant, and resuspension of the tubules in water. The metallized tubules are mechanically strong and withstand freeze drying step with retention of morphological features.

Hydroxyalkanol Membrane: The tubules produced from diacetylenic phosphocholines have two major drawbacks from an application points of view. One drawback was the fixed diameter of tubules which was independent of both the acyl chain length as well as the position of diacetylene in the chain [4,10]. The second drawback related to the low quality of metal coating due to the presence of tin oxide produce during metallization. Also, the acceleration step involved bubbling of oxygen at pH 4.0 which caused the tubules to break. To overcome these drawbacks we explored the possibility of designing and synthesizing alternate materials that would form tubules. We focussed on those diacetylenic lipids that could be produced by adopting simple synthetic routes. Phospholipase D mediated transphosphatidylation of lipids is a simple, one step method that can replace choline ($-\text{CH}_2-\text{CH}_2-\text{N}^+\text{Me}_3$) with a molecule that contains primary alcohol group. For convenience we replaced the choline moiety with $-(\text{CH}_2)_n-\text{OH}$ (Figure- 4) [30]. These lipids produced the tubules in the presence of metal ions while in the absence of metal ion no tubule was observed. By selecting the appropriate hydroxyalkanol group, metal ion, pH of the dispersion medium, and the ionic strength of the buffers, Markowitz et al. [31] were able to produce tubules of varying diameter. The strategy of making tubules using bivalent metal ions was extended to the use of palladium ion which not only produced the tubule structure but also acted as catalyst for electroless metallization. Following this strategy electroless metallization of cobalt, nickel, and gold was achieved [32,33] (Figure- 5). This metallization method did not metallize charge-neutral phosphocholines because the palladium ion did not bind to the surface.

Tubule Formation The lipid tubules were prepared by thermal cycling of the lipid dispersion. A thin film of the lipid 3 was hydrated above the melting transition of the lipid (51°C) in 0.2 M acetate buffer (pH 5.6) containing a small volume of palladium-complex solution. The final concentration of lipid in the dispersion was 2 mg/mL and that of the palladium complex was 1 mM. The molar ratio of lipid to metal ion was 2.6:1. The volume of palladium complex solution added to the buffer solution was less than 2% of the buffer solution. The mixture was sonicated at 80°C for 10 min and then allowed to gradually cool to room temperature. The dispersion was kept at 4°C for 3 hrs and then, reheated to 80°C and kept at this temperature for 30 min. The dispersion was then allowed to gradually cool to room temperature ($< 1^\circ/\text{min}$) to produce lipid tubules.



72

dissolved in 50 mL of water were then added. The dialyzed tubule dispersion was diluted with five times its volume of water and then an equal volume of the metal plating solution was added. The plating was allowed to continue until hydrogen evolution stopped (about 2 hours) and metallized microstructures settled at the bottom of the bath. The metallized microstructures were then washed three times with water. For long term storage, the tubules were washed twice with acetone and were kept stored under acetone.

Mixed Phospholipid membranes: Since the metallization protocol described in the preceding section doesn't work on charge-neutral lipids, we utilized this property for metallization of selective sites on lipid surfaces. Vesicles were formed from a mixture of charged and zwitterionic phospholipids 2 and 3. Palladium ion was then added. The palladium ion was able to bind to the negatively charged phospholipid but not to the charge-neutral phospholipid. Addition of a gold metal plating bath for electroless plating resulted in the selective metallization of the vesicle (figure-6) [i.33,34]. Electron diffraction analysis demonstrated that fine gold polycrystalline particles were deposited on the vesicle surface. It has been observed that the best results are achieved only if both the negatively charged and charge-neutral phospholipids were polymerized in the membrane. With vesicles formed from mixtures of polymerizable phospholipid 2 and non-polymerizable lipid 4, the vesicles were not stable to the metallization procedure. In addition to phospholipid polymerizability, the headgroup structure of the phospholipid was an important factor in the metallization of the vesicle. Phospholipids with a sterically unhindered headgroup such as phosphatidic acid caused uncontrolled metallization while vesicle membranes containing relatively more sterically hindered phosphohydroxyethanol headgroup were metallized at a manageable rate. A simple alteration of this system has provided the means to synthesize metal particles exclusively on the outer or inner side of the vesicles [35]. The vesicles were formed in the presence of palladium ions. As a result, both the inner and outer vesicle membranes contain bound palladium ion. After removing the palladium ions on the exterior membrane by the addition of the tetrasodium salt of EDTA, the gold plating bath was added. Because of the polymer boundaries in the polymerized vesicles, the metal cations were able to diffuse across the bilayer membrane thereby providing the capability to carry out the synthesis of metal nanoparticles within the vesicles. Using this strategy, we produced unagglomerated gold nanoparticles within the vesicles (figure 7) [36].

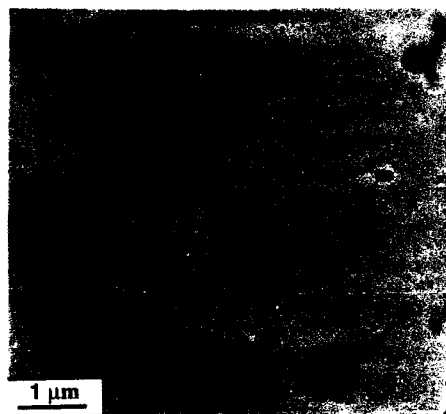


FIGURE - 6

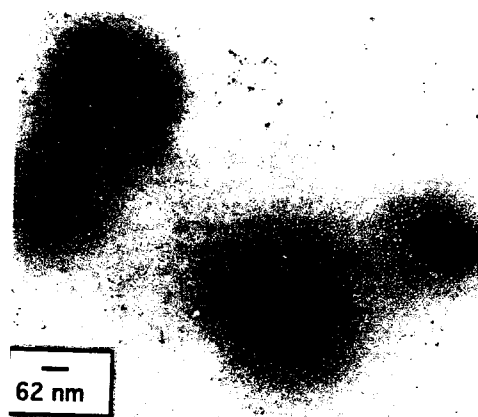


FIGURE - 7

SUMMARY

The results presented in this article clearly demonstrate the technological potential of polymerized membranes. New applications evolved while exploring the properties of polymerizable lipids. It is worth noting that the membrane approach was originally adopted to design and construct vesicles for controlled release studies. It has finally led to the capability to perform chemistry in a constrained environment and to study nucleation and growth of nanoparticles at membrane interface.

ACKNOWLEDGEMENTS

We thank Dr. Paul Schoen for his valuable comments. Financial support from the Office of Naval Research is gratefully acknowledged.

REFERENCES

1. Chow, G. M., Markowitz, M. A., and Singh, A., JOM, **45**, 62 (1992).
2. Heuer, A. et al., Science, **255**, 1098 (1992).
3. Alper, M., MRS Bulletin, **17**(11), 53 (1992).
4. Schnur, J. M., Science, **262**, 1669 (1993).
5. Bangham, A. D., Standish, M.M., and Watkins, J. C., J.Biol.Chem., **13**, 238 (1965).
6. Regen, S. L., Czech, B., and Singh, A., J. Amer. Chem. Soc., **102**, 6638 (1980).
7. Johnston, D. S., Sanghera, S., Pons, M., and Chapman, D., Biochim. Biophys. Acta,

602, 57 1(1980).

8. Hub. H., Hupfer, B., Koch, H., and Ringsdorf, H., *Angew. Chem. Int. Ed. Engl.*, **19**, 938 (1980).
9. O'Brien, D. F., Klingbiel, R. T., and Whitesides, T. H., *J. Polym. Sci., Polym. Lett. Ed.*, **19**, 95 (1981).
10. Singh, A. and Schnur, J. M. Polymerizable lipids in Phospholipids Handbook, (G.Cevc, Ed.) Marcel Dekker, NY 1993, p 233.
11. Singh, A., Thompson R. B., and Schnur, J.M., *J. Amer. Chem. Soc.*, **108**, 2785 (1986).
12. Yager, P., and Schoen, P. E., *Mol. Cryst. Liq. Cryst.*, **106**, 371 (1984).
13. Juliano, R. L., Regen, S. L., Singh, M., Hsu, M. J., and Singh, A., *Biotechnology*, **1**, 882 (1983).
14. Regen, S. L., Singh, A., Oehme, G., and Singh, M., Biochim. Biophys. Res. Commun., **101**, 131 (1981).
15. Mehta, R., Hsu, M. J., Juliano, R. L., Krause, H. J., and Regen, S. L., *J. Pharm. Sci.*, **75**, 579 (1986).
16. Krause, H. J., Juliano, R. L., and Regen, S., *J. Pharm. Sci.*, **76**, 1 (1987).
17. Ligler, F. S., Fare, T. L., Seib, K.D., Smuda, J. W., Singh, A., Ayers, M. E., Dalziel, A. and Yager, P., *Med. Inst.* **22**, 247 (1988).
18. Fare, T. L., Singh, A., Seib, K. D., Smuda, J. W., Ahl, P. L., Ligler, F. S., Schnur, J. M., in Molecular Electronics (Felix T. Hong, Ed.), Plenum Publishing Corporation, New York, 1989, p 305.
19. Dalziel, A. W., Georger, J., Price, R. R., Singh, A., and Yager, P., in Membrane Proteins, (Steven C. Goheen, Ed.), Bio-Rad Laboratories Pub., 1986, p. 643.
20. Ahl, P. L., Price, R., Schmuda, J., Gaber, B. P., and Singh, A., *Biochim. Biophys. Acta*, **1028**, 141 (1990).
21. Yager, P., *Biosensors* **2**, 363 919860.
22. Yager, P., Schoen, P. E., Davies, C., Price, R., and Singh, A., *Biophys. J.* **48**, 899, (1985).
23. Rhodes, D. G., Blechner, S. L., Yager, P., and Schoen, P. E., *Chem. Phys. Lipids*, **49**, 39 (1988).
24. Blechner, S. L., Morris, W., Schoen, P.E., Yager, P., Singh, A., Rhodes, D. G., *Chem. Phys. lipids*, **58**, 41 (1991).
25. Schoen, P. E., Nagumo, M., and Singh, A., *Chem. Phys. Lipids*, **69**, 251 (1994).
26. Schnur, J. M., Ratna, B., Selinger, J. V., Singh, A., Easwaran, K. R. K., and Jyothi, G., *Science*, **264**, 945 (1994).
27. Peek, B. M., Callahan, J., Namboodiri, K., Singh, A., and Gaber, B. P.,

Macromolecules, **27**, 292 (1994).

28. Singh, A., and Markowitz, M. A., New J. Chem., **18**, 377 (1994).
29. J.M. Schnur, P.E. Schoen, J. M. Calvert, J. H. Georger, and R. Price, Metal Clad Lipid Microstructures, US Patent # 4,911,981, March 27, 1990
30. Singh, A., Markowitz, M. A., and Tsao, Li-I, Synth. Commun., **22**, 2293 (1992).
31. M. A. Markowitz, J. M. Schnur and A. Singh, Chem. Phys. Lipids, **62**, 193 (1992).
32. M. A. Markowitz, S. Baral, S. Brandow and A. Singh, Thin Solid Films, **224**, 242 (1993).
33. A. Singh, Michael Markowitz and S. Baral, A simple process for producing metallized vesicles and tubules, Navy Case No. 74,204, 1993, US Patent pending.
34. Markowitz, M. A., Chow, G.-M., Baral, S., and Singh, A. in Metallized Plastics IV, (K. L. Mittal, Ed.), Marcel Dekker, 1994, accepted.
35. Markowitz, M. A., Chow, G.-M., and Singh, A., Navy Case No. 76,030, 1994
36. Markowitz, M. A., Chow, G.-M., and Singh, A., Langmuir, 1994, submitted

SELF-ASSEMBLY OF INORGANIC/ORGANIC MULTILAYER FILMS

ASTRID C. ZEPPEFELD and CATHERINE J. PAGE
University of Oregon, Department of Chemistry, Eugene, Oregon 97403

ABSTRACT

In order to investigate the influence of substrate functionalization on the subsequent self-assembly of multilayer films, multilayers composed of alternating hafnium and 1,10-decanediylbis(phosphonic) acid (DBPA) have been grown on three different substrates. Substrates studied include gold wafers functionalized with 4-mercaptobutylphosphonic acid, silicon wafers functionalized using a hafnium oxychloride solution, and silicon wafers coated with an octadecylphosphonate LB-template layer. The nature of these films is probed using ellipsometry and grazing angle x-ray diffraction. These studies indicate that the overall order and the individual layer thickness can vary substantially from sample to sample and depend strongly on the initial surface functionalization prior to multilayer growth.

INTRODUCTION

The research effort in the preparation and characterization of self-assembled multilayer films has increased rapidly in recent years.¹⁻⁶ Interest in these materials arises in part from the variety of physical properties which could be incorporated by rational design and synthesis of such microstructures. By assembling a material one molecular (or atomic) layer at a time, layers with conducting, magnetic, luminescent or nonlinear optical properties can be assembled with control of order and spacing between layers. The advantage of multilayer film synthesis via self-assembly compared to other methods lies in the relatively easy, straight-forward preparation methods and the mechanical and thermal stability of the films due to strong ionic and/or covalent bonds between the layers.

We are currently investigating hafnium 1,10-decanediylbis(phosphonate) (Hf-DBP) multilayer films, which are structurally analogous to the prototype zirconium-DBP self-assembled films first reported by Mallouk and coworkers.^{7,8} These films can be prepared by alternate adsorption of hafnium (or zirconium) ions and bisphosphonic acid molecules from aqueous solutions onto a substrate bearing an appropriate reactive functionality.

The main objective of this investigation was to study the influence of the substrate and the initial surface functionalization on the overall quality, reproducibility and structural characteristics (e.g. thickness and density) of the multilayer films. We therefore used two different substrates, commercial silicon wafers and very smooth vapor deposited gold substrates. The silicon wafers were primed with two different "anchor" layers, a hafnium layer and a preassembled octadecylphosphonate Langmuir-Blodgett (LB) template layer capped with zirconium.^{9,10} The hafnium functionalization reaction (using aqueous HfOCl_2 solution) is not fully understood, although we presume it involves adsorption of a very thin hydrous hafnium oxide layer (2-8 Å by ellipsometry) onto the native silicon oxide surface of the wafer.¹¹ This functionalization is analogous to that reported by Mallouk et al.¹² using zirconium oxychloride solution to functionalize fumed silica (Cab-o-Sil) for growth of Zr-DBP multilayers. In this case, the authors report that multilayers grown on the zirconium-functionalized Cab-o-Sil appear to be better ordered and more crystalline than Cab-o-Sil functionalized with a silanol phosphonate. In accord with their result we have also found that multilayer films are of better quality if prepared using hafnium- or zirconium-functionalized silicon.

The organic LB-template^{9,10} on silicon consists of a zirconium-capped octadecylphosphonate

LB-layer transferred onto a silicon wafer rendered hydrophobic by self-assembly of a monolayer of octadecyltrichlorosilane. This LB-template provides a surface layer of zirconium with very low roughness, high order and consistent density.^{9,10} The gold surface was functionalized with 4-mercaptopbutylphosphonic acid, an anchor which is reported to give well ordered primer layers with a high surface density of phosphonate moieties.⁸

Multilayer films prepared on these substrates were characterized by ellipsometry and grazing-angle x-ray diffraction. Ellipsometry has been used widely for the determination of layer thicknesses of thin films,^{5,13,14,15} and also of self-assembled metal-bisphosphonate films.^{9,1,7,8} However, a main disadvantage of this technique lies in the fact that the correctness of the calculated film thickness relies on the proper choice of the refractive index for both the substrate and the film. Unless the substrate is very reproducible (as is the case for silicon wafers), the refractive index of the substrate has to be calculated for every particular sample from the ellipsometry parameters Δ and Ψ of the bare substrate.¹⁶ The main problem, however, lies in the choice of the refractive index of the multilayer film. Generally, the refractive index of the film is not known, and is usually estimated to be the same as for the bulk compound. Using the bulk value for the index in the calculation of film thicknesses implies exactly the same properties (structure, density etc.) of film and bulk compound, which may not be the case. In addition, slight variations in the film density from sample to sample, as may result from variations in the substrate or the surface functionalization, can only be reliably detected if the exact refractive index of each particular film is known.

The use of grazing angle x-ray diffraction is still rather uncommon in thin film investigations, although this method allows the direct measurement of multilayer film thicknesses and does not require any assumptions about the properties of the sample.¹⁷ This technique is exploited in these studies to accurately assess film thicknesses as a function of multilayer growth, and to compare multilayers grown on the substrates described above. We compare ellipsometry measurements with grazing angle x-ray diffraction in order to assess the refractive indices of our films.

EXPERIMENTAL

Materials: Hafnium oxychloride octahydrate was used as obtained from Teledyne Wah Chang Albany. 1,10-Decanediybisphosphonic acid (DBPA) was prepared by the Michaelis-Arbuzov reaction using 1,10-dibromodecane and triethyl phosphite.⁸ 4-Mercaptopbutylphosphonic acid was provided by Prof. Thomas E. Mallouk (Pennsylvania State University).⁸ In all experiments deionized water purified to a resistivity of 18 M Ω -cm with a Barnstead Nanopure II was used.

Substrates and surface functionalization: Single crystal silicon wafers of 76 mm in diameter with polished 100 faces were obtained from Silicon Quest. Prior to hafnium functionalization the wafers were rinsed for 10 min. with trichloroethylene, 10 min. with 2-propanol and 15 min. with ultrapure water. The wafers were then immersed in a 5 mmolar aqueous solution of HfOCl_2 and heated to 50°C for 1½ - 4 days. The preassembled LB template was provided by Professor Daniel R. Talham and Houston Byrd (University of Florida).^{9,10} It was prepared by transferring an octadecylphosphonic acid monolayer via the LB-technique onto a with octadecyltrichlorosilane functionalized silicon substrate. An additional monolayer of Zr^{4+} was then added by self-assembly. The wafers as obtained were rinsed with ultrapure water prior to multilayer deposition. Flame-annealed gold substrates, prepared by thermal evaporation of ca. 2000 Å of gold onto glass substrates precoated with ca. 20 Å chromium, were provided by Dr. Peter Zeppenfeld (Kernforschungszentrum Jülich, FRG). The gold substrates were rinsed with methanol and ultrapure water, then immersed in a 1 mmolar solution (80% water, 20% methanol) of 4-mercaptopbutylphosphonic acid for 72 hrs at room temperature.

Multilayer deposition: Hf-DBP multilayers were grown on the functionalized substrates by alternate immersion of the wafers in a 5 mmolar aqueous solution of HfOCl_2 for 4-6 hrs. and in a 1.5 mmolar aqueous solution of DBPA for 6-12 hrs. A 15 min. rinse with ultrapure water was performed after each immersion step. The dipping sequence was started with the HfOCl_2 solution in the case of the gold samples and with the DBPA solution in case of the other samples, in accordance with the respective surface

functional group of the substrate.

Instrumentation and measurements: Ellipsometric measurements were done with a Rudolph Research Thin Film Ellipsometer 43603-200E using a tungsten halogen light source, a 632 nm filter light source and an incident angle of 70 degrees. Film thicknesses were calculated from the measured Δ and Ψ values with a program from Rudolph Research using $n = 3.858 - 0.018i$ as the refractive index for Si and $n = 1.462$ for SiO_2 . The refractive indices of the gold substrates were calculated for each particular sample from the Δ and Ψ values measured for the bare substrate, using standard equations.¹⁸

Low angle x-ray diffraction was done on a Scintag XDS-2000 θ - θ powder diffractometer using Cu K α radiation. The diffraction experiment measures the interference of x-rays reflected from the air-film interface and the film-substrate interface. The resulting diffraction pattern shows several "beats", each corresponding to a different order of interference.¹⁹ The position of the beats is given to a first approximation by the Bragg equation $n\lambda = 2d\sin\theta$ (d = total film thickness). In order to take into account index of refraction effects however, the layer thickness is not calculated directly from the absolute peak positions. Instead, the position $\sin^2\theta$ of each beat maximum is plotted versus n^2 , the square of the corresponding order. After a linear regression fit to the data, the layer thickness is obtained from the slope, which corresponds to $(\lambda^2/4d^2)$.^{17,19}

RESULTS

The Hf-DBP multilayer growth on gold surfaces was monitored by ellipsometry measurements. Fig. 1 shows a plot of film thickness versus number of layers for a gold sample derived from ellipsometry data. The film thickness was calculated using various values for the film refractive index in the range $1.45 \leq n_{\text{film}} \leq 1.60$. No matter which value is chosen, the data show a constant increase in layer thickness after each additional layer added, as can be seen by the straight lines in Fig. 1. However, the slopes of the lines, corresponding to the average thickness per layer, depend strongly on the value of the refractive index. An average layer thickness as high as 23.3 Å results when using $n_{\text{film}} = 1.45$ as refractive index, whereas a layer thickness of 18.1 Å is obtained when using $n_{\text{film}} = 1.60$. This example shows clearly the need of an independent method to determine layer thicknesses. Unfortunately, to date no grazing angle x-ray diffraction has been detected from the multilayer films grown on gold. This is probably due to the high critical angle for total reflectance of gold (26.3°). The multilayer film diffraction, which is usually seen in the region $0.5^\circ \leq \theta \leq 2.0^\circ$ is most likely masked by the high intensity of the total reflectance x-ray beam. Therefore no independent information could be obtained about the exact layer spacing of the multilayer or about the proper value for the refractive index.

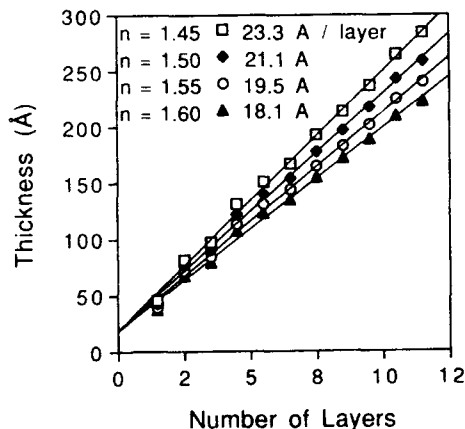


Figure 1. Film thickness versus number of Hf-DBP layers deposited onto functionalized gold determined by ellipsometry using various film refractive indices (1.45, 1.50, 1.55, 1.60). The solid lines are a linear regression fit to the data; the slope of the straight lines is given in the left corner.

For the Hf-DBP multilayers grown on silicon surfaces (e.g. on Hf- and LB-template-covered samples) data from both diffraction and ellipsometry experiments were obtained. Figs. 2 and 3 show the total film thickness as derived from both methods plotted versus the number of Hf-DBP layers. A constant increase in layer thickness with every additional layer added can clearly be seen in all plots indicating the regular multilayer growth on these substrates.

The average layer spacing of the multilayer films is given by the slopes of the straight lines shown in Fig. 2 and 3. The spacings obtained by x-ray diffraction, which are not dependent on any assumption about the film properties, are 16.8 Å/layer for the film grown on the LB-Template and 18.1 Å/layer for the film grown on the Hf-functionalized silicon (Hf-Si) wafer.

Figure 2. Film thickness versus number of Hf-DBP layers deposited onto Hf-functionalized silicon determined by ellipsometry (solid squares) and grazing angle x-ray diffraction (open squares). The ellipsometry data is fit using a film refractive index $n_{\text{film}} = 1.49$. The solid lines are a linear regression fit to the data; the fit parameters are given in the left corner.

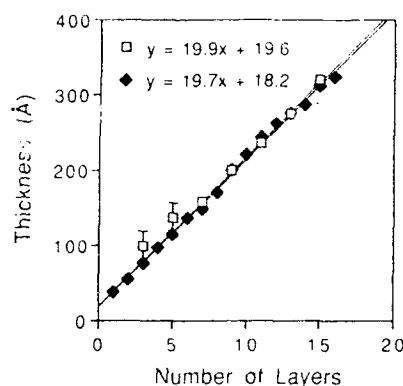
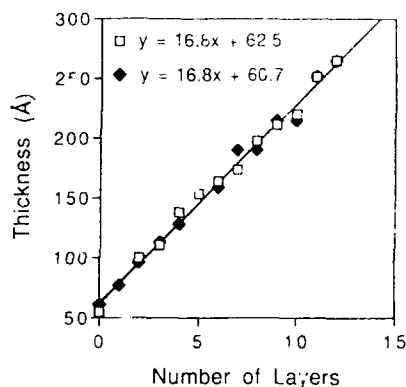


Figure 3. Film thickness versus number of Hf-DBP layers deposited on LB-template covered silicon determined by ellipsometry (solid squares) and grazing angle x-ray diffraction (open squares). The ellipsometry data is fit for a film refractive index $n_{\text{film}} = 1.57$. The solid lines are a linear regression fit to the data; the fit parameters are given in the left corner.



The layer spacing calculated from the ellipsometry data depends strongly on the value for the refractive index as shown above. We therefore fitted the refractive index to give layer thicknesses which closely match the layer thickness determined by grazing angle x-ray diffraction. In fitting the ellipsometry data, a close match in the slopes of the x-ray data in the plots of Figs. 2 and 3 (corresponding to the average layer thickness) was attempted rather than a close match to the absolute values for the layer thickness. This procedure was chosen because the uncertainty in the determination of *absolute* layer thicknesses is considered much higher for both ellipsometry and diffraction measurements than is the uncertainty associated with the determination of the

average thickness increase per layer. A close match was found for a refractive index of 1.57 for the multilayer grown on the LB-template and 1.49 for the layer grown on the Hf-Si.

An average layer spacing of about 16.8 Å/layer and a refractive index of about 1.57 for multilayers grown on the LB-template could be confirmed by layer experiments on a second LB-template substrate. These values are also close to the preliminary values we determined for the bulk Hf-DBP compound which are 16.7 Å/layer and $n_{\text{film}} = 1.545$, respectively. However, multilayers grown on Hf-functionalized wafers show a substantial variation in layer spacing from sample to sample. Most layer spacings range between 18 Å/layer and 20 Å/layer, although spacings as low as 15 Å/layer and as high as 21 Å/layer have also been observed. However, for all films grown on Hf-anchored silicon a good match between ellipsometry and diffraction data is always obtained using a comparatively low refractive index within the narrow range $1.48 \leq n_{\text{film}} \leq 1.50$, independent of the average layer spacing of the particular sample.

DISCUSSION

All layer experiments, done on various substrates and anchor layers, show consistent incremental layer growth of Hf-DBP multilayers. Thus, the different substrates investigated here all provide suitable surfaces for uniform multilayer growth. The average layer spacing, however, is found to be strongly dependent on the initial surface functionalization. Compared to the layer spacing of about 16.7 Å for bulk Hf-DBP, layer spacings of the multilayers grown on the hafnium-functionalized silicon are generally larger (18-20 Å). From other studies, the density of multilayers grown on Hf-Si is estimated to be approximately 75% that of the bulk Hf-DBP.¹⁹ This observation is consistent with the observation reported here that the refractive index of multilayers grown on Hf-Si is consistently lower than that of the bulk (≈ 1.49 of the film compared to 1.545 of the bulk Hf-DBP).

The large variation in layer spacing observed for multilayers grown on Hf-anchored silicon is most likely due to variation in the hafnium functionalization of the substrates. In order to understand and optimize the functionalization reaction we have investigated a variety of reaction conditions and have characterized functionalized wafers by ellipsometry and AFM microscopy. These investigations show that the thickness and roughness of the Hf-anchor layer increases substantially with increasing reaction temperature ($>50^\circ\text{C}$) and reaction time, possibly due to precipitation of colloidal hydrous hafnium oxide similar to that observed for zirconium oxychloride solutions.¹¹ Although we did not observe any formation of precipitate in our HfOCl_2 solutions, we assume that the Hf-anchor layer consists of a rather undefined layer of hydrous hafnium oxide. Ellipsometry measurements indicate that this layer is generally 2-8 Å thick. Properties such as roughness, thickness and density of this anchor layer are likely to vary considerably from sample to sample, and may account for the observed variation in layer thicknesses of the multilayer films.

Although no exact layer spacing could be determined for the multilayers grown on gold, the value for the refractive index is most likely in the range $1.50 \leq n_{\text{film}} \leq 1.57$, which would yield an average layer thickness of 19-21 Å, which is significantly larger than the bulk layer spacing, and comparable to that of the multilayers grown on Hf-Si substrates.

A possible explanation for layer thicknesses larger than the bulk layer spacing could lie in the tilt angle of the phosphonate alkyl chains, which may differ between the multilayer films and the bulk material. In bulk Zr-DBP, which should be similar to bulk Hf-DBP, this tilt angle is about 31° with respect to the surface normal.¹⁹ In this case the phosphonate carbon bond is oriented nearly perpendicular to the plane of metal ions. A much smaller tilt angle for the multilayer film would result in a larger layer spacing and could (at least in part) explain the high layer spacings observed here. A smaller tilt angle would require the bisphosphonate alkyl chain to orient nearly perpendicular to the plane of Hf-ions, which in turn would preclude binding of all three oxygens of a phosphonate group to the plane of hafnium ions. Alternative phosphonate-metal binding involving only two of the phosphonate oxygens has been proposed by Talham and coworkers and

is reported for some bulk metal phosphonate materials.⁹ Assuming perpendicular orientation of the alkyl bisphosphonate moiety would suggest an individual layer thickness of ≈ 19 Å. This layer thickness is closer to the larger values obtained for Hf-functionalized silicon and gold substrates.

A smaller alkyl chain tilt angle in the film compared to the bulk could simply be due to the (stepwise) preparation method. It is also possible, however, that the density of binding sites on the initial surface determines (at least in part) the tilt angle. By this argument, one would predict that a high density of initial binding sites might produce a denser packing of the alkyl chains, thus forcing the alkyl chains to orient more perpendicular to the surface. One would further predict on this basis that the films grown on the LB-templates should have the largest average layer thickness, since the LB-template presents a close-packed array of zirconated phosphonates at the surface, and should therefore have the highest surface binding site density. This, however, is contrary to our observations, since the average layer spacing for the multilayers grown on the LB-template is smaller than for those grown on the other substrates, and is nearly identical to that of bulk Hf-DBP (16.8 vs 16.7 Å, respectively). From these observations, we conclude that larger layer thicknesses do not necessarily correlate with denser packing of bisphosphonate alkyl chains. Larger layer thicknesses are more likely to correlate with increased roughness of the surface functionalization and/or increased disorder in the alkyl chains.

ACKNOWLEDGMENT

We thank Professor Daniel Talham and Houston Byrd (University of Florida) for providing the LB-templates and Dr. Peter Zeppenfeld (Kernforschungszentrum Jülich, FRG) for providing the gold substrates. Financial support by the German Research Foundation is gratefully acknowledged. Acknowledgment is also made to the donors of the Petroleum Research Fund, administered by the ACS for partial support of this research.

REFERENCES

1. H. C. Yang, K. Aoki, H.-G. Hong, D. D. Sackett, M. F. Arendt, S.-L. Yau, C. M. Bell, T. E. Mallouk, *J. Am. Chem. Soc.* **115**, 11855 (1993)
2. H. E. Katz, G. Scheller, T. M. Putvinski, M. L. Schilling, W. Wilson, C. E. D. Chidsey, *Science* **254**, 1485 (1991)
3. L. A. Vermeulen, M. E. Thompson, *Nature* **358**, 656 (1992)
4. M. B. Dines, P. M. DiGiorgio, *Inorg. Chem.* **20**, 92 (1981)
5. M. D. Porter, T. B. Bright, D. L. Allara, C. F. D. Chidsey, *J. Am. Chem. Soc.* **109**, 3359 (1987)
6. L. Netzer, J. Sagiv, *J. Am. Chem. Soc.* **105**, 674 (1983)
7. H. Lee, L. J. Kepley, H.-G. Hong, T. E. Mallouk, *J. Am. Chem. Soc.* **110**, 618 (1988)
8. H. Lee, L. J. Kepley, H.-G. Hong, S. Akhter, T. E. Mallouk, *J. Phys. Chem.* **92**, 2597 (1988)
9. H. Byrd, J. K. Pike, D. R. Talham, *Chem. Mater.* **5**, 709 (1993)
10. H. Byrd, S. Whippo, J. K. Pike, J. Ma, S. E. Nagler, D. R. Talham, *Chem. Mater.* **5**, 709 (1993)
11. A. Clearfield, *Inorg. Chem.* **3**, 146 (1964)
12. H.-G. Hong, D. D. Sackett, T. E. Mallouk, *Chem. Mater.* **3**, 521 (1991)
13. S. R. Wasserman, G. M. Whitesides, Ian M. Tidswell, B. M. Ocko, P. S. Pershan, J. D. Axe, *J. Am. Chem. Soc.* **111**, 5852 (1989)
14. J. Rühe, V. J. Novotny, K. K. Kanazawa, T. Clarke, G. B. Street, *Langmuir* **9**, 2383 (1993)
15. R. G. Nuzzo, F. A. Fusco, D. L. Allara, *J. Am. Chem. Soc.* **109**, 2361 (1987)
16. H. G. Tompkins, *A User's Guide to Ellipsometry*, (Academic Press, Inc., San Diego, 1993), p. 36
17. B. Lengeler, *Mikrochimica Acta* **1**, 455 (1987)
18. H. Kiessig, *Annalen der Physik* **10**, 769 (1931)
19. A. C. Zeppenfeld, S. L. Fiddler, W. K. Ham, B. J. Klopfenstein, C. J. Page, submitted to *J. Am. Chem. Soc.*

PREPARATION OF NANOCOMPOSITES CONTAINING POLY(ETHYLENE OXIDE) AND MoS₂, TiS₂, OR MoO₃

JOHN P. LEMMON*, JINGHE WU**, AND MICHAEL M. LERNER**

*Current address: Ostrath, Sylvania, Hawes St. Tawanda, PA 18848

**Department of Chemistry and Center for Advanced Materials Research, Oregon State University, Corvallis, Oregon 97331-4003

ABSTRACT

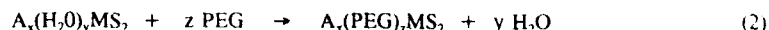
Single-phase nanocomposites containing montmorillonite, MoS₂, MoO₃ or TiS₂ with poly(ethylene oxide) are obtained by the exfoliation of the layered solid, adsorption of polymer, and subsequent precipitation of solid product. Aqueous solutions can be employed for all syntheses except PEO/TiS₂, which is prepared from lithiated TiS₂ in an N-methyl formamide (NMF) solution. X-ray diffraction indicates that the resulting solids increase in basal-plane repeat by approximately 4 or 8 Å, consistent with the incorporation of a single or double layer of polymer between the inorganic layers. Reaction stoichiometries and elemental analyses provide compositions for the single-phase products.

METHODS FOR GENERATING POLYMER-CONTAINING NANOCOMPOSITES

The incorporation of poly(ethylene glycols) or poly(ethylene oxide) by smectite clays has been known for several decades.¹ More recently, novel materials derived from polyethers and other low-dimensional solids, including oxide,²⁻⁵ chalcogenide,^{6,8} and MPS,⁹ lattices have also been described. In each case, a significant increase in the interlayer spacing is observed, indicating that oligomers or polymers are incorporated within the galleries. Interest in the incorporation of polymers within inorganic hosts stems from the potential mechanical, structural, and electrical properties of organic/inorganic nanocomposites.¹⁰ This work will describe nanocomposites derived from PEO with a variety of layered structures, as summarized in Table I.

Topotactic Methods

Layered ternary chalcogenides of the transition metals, A_xMCh₂ (A = alkali metal; M = Ti, Nb, Ta; Ch = S, Se, Te) spontaneously incorporate water or polar organic molecules to form stable compounds with solvated cations. Exchange reactions can also be utilized to expand the chemistry of these materials. An example is the incorporation of the oligoether poly(ethylene glycol) by exchange of water in the hydrated lithium salt:



A topotactic mechanism for the above reaction, in which the intersheet galleries expand or contract but the solid retains its two-dimensional character should usually be ineffective for the introduction of high-molecular-weight polymers due to the slow diffusion of macromolecules into

the galleries. It should be noted, however, that recent work utilizing elevated temperatures shows some promise for this method of obtaining nanocomposites.⁵

Table I. Layered nanocomposites containing PEO

<i>PEO Nanocomposite</i>	<i>Host</i>	<i>Basal Spacing (Å) Nanocomposite</i>	<i>Expansion</i>
PEO/Na-montmorillonite	9.6	17.7*	8.1
		13.7	4.1
Li _{0.1} (PEO) _{10.1} MoS ₂ ^b	6.5	14.5	8.0
Mo _{0.3} (PEO) _{0.8} TiS ₂	6.0	14.2	8.2
Li _{0.1} (PEO) _{0.9} MoO ₃	8.1	16.0	7.9
		12.7	4.6
Li ₁ (PEO) ₇ MoSe ₂	7.3	15.2	7.9

*Boldface indicates excess polymer employed in synthesis.

^bStoichiometry of PEO indicates moles of monomer repeat (C₂H₄O)

An alternate route to polymer-containing nanocomposites involves the *in situ* polymerization of monomeric intercalants, and the preparation of materials such as poly(styrene) / MoS₂,¹¹ poly(aniline) / V₂O₅,¹² and poly(aniline) / MoO₃¹³ have been reported. As a variant of this method, Nazar and coworkers¹⁴ have reported the incorporation of a water-soluble precursor into MoO₃ by the exfoliation / adsorption method, followed by the *in situ* thermal polymerization.

Exfoliation / Adsorption Method

Single-sheet colloids can be obtained by chemical oxidation of the lithiated metal disulfides.¹⁵ Morrison and co-workers^{11,16} have demonstrated that a colloidal suspension of single-sheet MoS₂ can incorporate molecular organics, organometallic complexes, or other complex cations when the single-sheets are restacked. The general method is simple: layered compounds are reduced, rapidly re-oxidized by hydrolysis to form a stable colloid, and then interacted with a soluble polymer and the solid product precipitated from the solution.

PEO / Na-montmorillonite Nanocomposites

Polymer composites with smectite clays are produced by the exfoliation / adsorption method, although no special techniques are required to prepare the colloid (which is directly obtained by the dissolution of the clay).

The variation of polymer / clay stoichiometry shows that polymer/montmorillonite ratios of 0.15 and 0.30 g/g provide single-phase products with sharp diffraction peaks and several higher-order (00 l) reflections. Peak widths indicate ordered domains of 150 Å (approximately 10 layers) along the stacking direction for these products. Least-squares fits to these data yield lattice spacings of 13.73(4) Å and 17.65(4) Å. At stoichiometries richer in polymer than 0.30 g/g an admixture of the 17.7 Å phase and crystalline PEO is obtained.

The polymer conformation in these nanocomposites raises significant fundamental issues and will also govern important physical properties. Two models which may be considered are a helical conformation similar to that observed in crystalline PEO, or an adsorbed polymer layer on the clay surfaces. The formation of a 13.6 Å phase involves a gallery expansion of 4.0 Å, which sterically limits the polymer conformation to approximate a single adsorbed layer between the clay surfaces. The 17.7 Å phase displays twice the gallery expansion and also twice the polymer content of 13.6 Å phase, and therefore is consistent with the incorporation of two such polymer layers. This architecture can be derived from the coalescence of colloidal clay sheets with adsorbed polymer layers on both surfaces. The similarity of complexes prepared from PEO and an amorphous copolymer PEM, $[\text{OCH}_2(\text{OCH}_2\text{CH}_2)_m]_n$, is also significant in that the helical conformation is disrupted in PEM.

The 4 Å and 8 Å gallery expansions are also similar with those obtained when oligomeric (PEG) or small-molecule ethers such as ethylene glycol are incorporated into montmorillonite. This coincidence is reasonable if each of these species adopts an adsorbed-layer conformation within the galleries.

Nanocomposites prepared with stoichiometries between 0.15 and 0.30 g/g do not produce a sharp (001) peak, but show highly asymmetric peak profiles. When physical mixtures of the single-layer (0.15 g/g) and double-layer (0.30 g/g) phase are ground together at ambient temperature, two sharp peaks corresponding to the discrete phases are obtained, but a broad diffraction profile of intermediate repeat spacing appears upon annealing this mixture at 100 °C for two days. These patterns therefore appear to correspond to homogenous nanocomposites of intermediate composition (0.15 - 0.30 g/g) which are a solid solution of the single and double-layer phases.

Li₁PEO₂MoS₂

The powder diffraction data from the nanocomposites prepared via exfoliation / adsorption in aqueous media using excess PEO indicate single-phase products. Basal-repeat spacings obtained increase slightly with higher polymer content, and range from 14.2 to 14.6 Å. Peak widths indicate stacking coherence lengths in the range of approximately 200 - 400 Å (20 - 25 unit repeats). At low polymer stoichiometries, a broad peak associated with restacked MoS₂ appears.

The distance between Mo planes in these nanocomposites is 8.0 - 8.3 Å greater than in LiMoS₂. This expansion, similar to that obtained by insertion of poly(ethylene glycol) or PEO into MS₂ or montmorillonite, suggests that a polymer bilayer is incorporated into the intersheet region.

The polymer conformation within the galleries cannot be determined directly from diffraction studies, and a helical polymer conformation, as in crystalline PEO, cannot be excluded by steric arguments. Since the favorable energy of polymer adsorption will decrease dramatically once monolayer coverage of the sheet surfaces is complete, a bilayer within the galleries (resulting from monolayer coverage of each sheet face) is reasonable. Elemental analyses for C, H, and Li for reactions indicate that the polymer stoichiometry for single-phase products can vary between 1.0 and 1.3 moles of monomer repeat to MoS₂. The polymer / MoS₂ ratio found in the product depends on the mixing stoichiometries utilized in the nanocomposite syntheses. The change in polymer content found for these products indicates a higher packing density of polymer within the disulfide galleries. This explanation is consistent with the reproducible change in relative peak intensities and slight increase in c-repeat distance with polymer content.

The overall stoichiometry was found to be close to $\text{Li}_{0.12}(\text{PEO})_x\text{MoS}_2$ for all three samples, which reflects a negative charge on MoS_2 sheets similar to that present in the hydrated lithium salts. The lithium stoichiometry ($x \approx 0.1$) is consistently similar to that obtained for hydrates prepared under similar conditions. Electrical measurements indicate a semimetallic conductivity and thermal response, which are again consistent with negatively-charged MoS_2 layers.

Thermal and Chromatographic Analyses

A simultaneous DTA / TGA scan of the nanocomposite is provided in Figure 1. The absence of a melting endotherm at 60 °C indicates that no crystalline PEO phase occurs in the product. An exotherm near 310 °C arises from degradation of the polymer and the associated weight loss of 27 %, due to volatilization of the decomposition products, closely corresponds to the polymer content within the nanocomposite. X-ray diffraction of the nanocomposite after heating to 450 °C shows only a restacked MoS_2 phase.

An additional exotherm between 125 and 255 °C is not associated with any significant sample weight loss. In order to further explore this transition, ambient-temperature X-ray diffraction pattern of a single pellet of the nanocomposite following heating at 200 °C in an Ar atmosphere for 3 - 6 hrs show an indicate an irreversible loss of sample order. After six hours, the material appears entirely disordered by X-ray diffraction. Subsequent heating of the pellet above 400 °C under inert conditions for several hours to remove the polymer component regenerates crystalline MoS_2 . The disordered phase must therefore contain MoS_2 sheets without a coherent stacking arrangement. The driving energy for this process may be provided by the thermally-activated rearrangement of adsorbed polymer. The potentially high electroactive area for the disordered phase make it an attractive candidate for electrochemical applications.

GPC data on polymer extracted from the nanocomposites indicates that the polymeric component of these materials is not degraded into low-molecular-weight fragments, although the results of crosslinking and scission are evident. The extracted polymer from $\text{Li}_{0.12}\text{PEO}_{1.4}\text{MoS}_2$ contains significant molecular weight components centered at 450,000 and 20,000 Da. After heat treatment to form the unstacked nanocomposite, the extracted polymer has a single peak centered at 45,000 Da. In these samples, only 10 - 50% of the total polymer component can be extracted into an organic solution for analysis.

$\text{M}_x\text{PEO}_y\text{TiS}_2$

The exfoliation / adsorption process can probably be extended to other layered disulfides (TaS_2 , WS_2 , and NbS_2) or dichalcogenides. For example, we have recently obtained results with MoSe_2 indicating single-phase nanocomposites are readily prepared by methods described above.

Some target compounds, however, are not amenable to processing in aqueous solution. A notable example is TiS_2 -containing nanocomposites; TiS_2 is susceptible to hydrolysis under acidic conditions, and forms a stable hydrate in aqueous base. The charge-storage properties of TiS_2 , generally as the anode in a solid-state Li cell, naturally leads to interest in the preparation and characterization of a single-phase polymer/ TiS_2 nanocomposite.

A recent communication notes that the addition of a solution of PEO with sodium perchlorate in acetonitrile to an aqueous colloid of TiS_2 will produce a nanocomposite (7). Our results indicate that the PEO/TiS_2 nanocomposite can be obtained from aqueous media, but a single-phase product is not readily obtained.

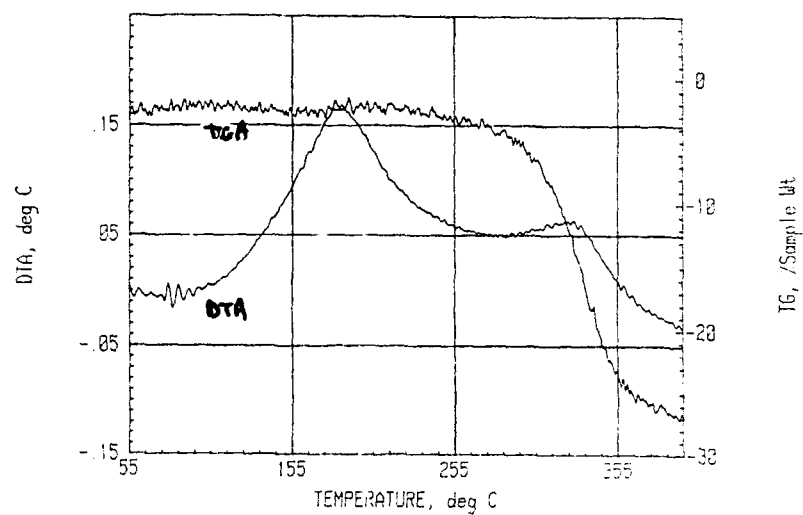


Figure 1

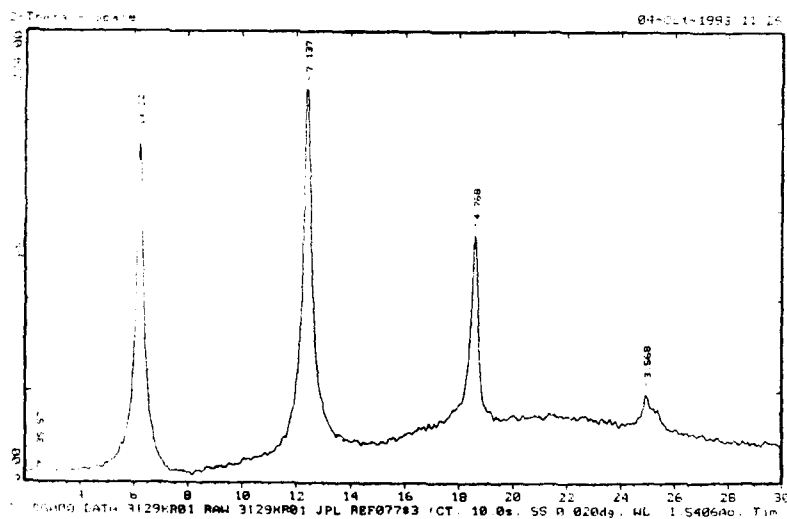


Figure 2

Exfoliation in N-Methyl Formamide (NMF)

The exfoliation of TiS_2 and other disulfides in NMF has been known for some time. Two phases can be obtained by the interaction of MTiS_2 with NMF; $\text{M}_x(\text{NMF})_y\text{TiS}_2$ ($\text{M} = \text{Li}, \text{Na}$), with $c\text{-repeat} \approx 13.7 \text{ \AA}$, and $(\text{RNH}_2)_x(\text{NMF})_y\text{TiS}_2$, containing $\text{CH}_3\text{NH}_2\text{CHO}^+$ (RNH_2^+) cations, with $c \approx 19.5 \text{ \AA}$. The relative abundance of the metal and RNH_2^+ -containing products is pH dependent, with the latter predominating when the reaction is carried out under acidic conditions. Similarly, the insertion of NMF has been reported for other lithium and transition metal disulfides. Optimal conditions for the synthesis of $\text{PEO} / \text{TiS}_2$ are found in a basic NMF solution using excess PEO (which can be washed away from the desired product). In this way, single-phase products are reproducibly prepared. A representative diffraction pattern is provided in Figure 2.

The products obtained in this manner do not contain a large component of the molecular solvent within the galleries. Elemental analysis allow for a maximum ratio of NMF to monomer repeat near 0.1 mol/mol. Unlike the NMF-intercalated products, these nanocomposites do not lose a significant fraction of weight during DSC scans through the boiling point of NMF (185 °C).

The powder diffraction data for the single-phase products obtained provide a basal-plane repeat of 14.2 Å. Peak widths for the (00l) set provide a stacking coherence length of 300 Å (approximately 20 repeat units). The absence of a diffraction peak at $d = 5.7 \text{ \AA}$ indicates that the product is devoid of unreacted TiS_2 , and the absence of a melting exotherm at 60 °C in the DSC trace shows that no crystalline PEO phase occurs in the nanocomposite.

The distance between Ti planes in the nanocomposite is 8.0 - 8.2 Å greater than in LiTiS_2 . This expansion suggests that a polymer bilayer has been incorporated into the intersheet region. Elemental analyses indicate a product stoichiometry of $\text{Li}_{0.02}\text{Na}_{0.25}(\text{PEO})_{0.79}\text{TiS}_2 \cdot 0.09\text{NMF}$; the notation $(\text{PEO})_n$ refers to n moles of the monomer repeat unit ($\text{CH}_2\text{CH}_2\text{O}$). The overall cationic content is consistent with other similar compounds which retain the composition $\text{A}_x(\text{solv})_y\text{TiS}_2$ ($x \approx 0.3$), and reflects the partial re-oxidation of the TiS_2^{1-} sheets through interaction with solvents. The polymer content is somewhat less than that obtained with $\text{PEO} / \text{MoS}_2$ nanocomposites.

Thermal and Electrical Measurements

Thermal analysis of the nanocomposite reveals a broad endotherm between 90 and 140 °C. This endotherm is also observed with unreacted TiS_2 . A sharper endotherm is observed at 180 °C and could be associated with the minor NMF component in the product. Both TiS_2 and the nanocomposite are unstable to loss of sulfur above 220 °C.

Electrical measurements on pellets pressed from powders indicate a semimetallic conductivity and thermal response; the conductivity of the nanocomposite somewhat less than the pure TiS_2 . The bulk conductivity for the partially reduced sheets, $\text{TiS}_2^{0.3-}$, is expected to increase significantly relative to TiS_2 ; however, the reduced crystalline order in the nanocomposites and the incorporation of a large fraction of electronically-insulating polymer between the sheets should decrease the conductivities of these pellets.

$\text{Li}_x\text{PEO}_y\text{MoO}_3$

Li_xMoO_3 rapidly exfoliates during sonication in aqueous solution, and the nanocomposite with PEO is easily obtained. The extent of lithiation in the Li_xMoO_3 employed (i.e. x in Li_xMoO_3) was not evaluated quantitatively in our studies, other studies indicate that the maximum value for x by these methods may be less than 0.5. Complete exfoliation results only for the most highly reduced salts, when the anhydrous lithiated compounds show a basal-plane expansion of at least 1 Å relative to MoO_3 . The nanocomposites prepared by the exfoliation/adsorption method expand by approximately 8 Å when excess PEO is employed: the stacking repeat of 8.2 Å in Li_xMoO_3 is increased to 15.9 - 16.5 Å. A 4.4 Å expansion is observed, however, when the PEO content is limited to 0.1 g/g Li_xMoO_3 . These data are consistent with adsorbed bilayers or monolayers of PEO between MoO_3 sheets.

Elemental analysis of the products provides a Li/MoO₃ mole ratio of 0.25. The nanocomposite rapidly reforms a colloid when placed in aqueous solution, so the products cannot be washed to remove excess polymer. Some products therefore contain excess PEO; in this case scanning calorimetry of the products indicates a sharp exotherm near 60 °C corresponding to a bulk PEO melting transition. Single-phase products are obtained by careful control of the PEO / MoO_3 and solvent ratios. Elemental analyses for Li, C, and H in the single-phase products provides a stoichiometry of $\text{Li}_{0.25}\text{PEO}_{0.93}\text{MoO}_3 \cdot 0.06\text{H}_2\text{O}$. Thermal analyses of the products show an irreversible exotherm, associated with polymer decomposition, at 320 °C.

Acknowledgments

The authors gratefully acknowledge supporting grants from the National Science Foundation (DMR-9157005) and the AlliedSignal Foundation.

References

1. *The Formation and Properties of Clay-Polymer Complexes*; Theng, B. K. G., Ed.; Elsevier: New York, NY, 1979.
2. Aranda, P.; Ruiz-Hitsky, E. *Chem. Mater.* **1992**, *4*, 1395.
3. Wu, J.; Lerner, M. M. *Chem. Mater.* **1993**, *5*, 835.
4. Liu, Y.-J.; DeGroot, D.C.; Schindler, J. L.; Kannewurf, C.R.; Kanatzidis, M.G. *Chem. Mater.* **1991**, *3*, 992.
5. Vaia, R. A.; Ishii, H.; Giannelis, E. P. *Chem. Mater.* **1993**, *5*, 1694.
6. Lemmon, J.; Lerner, M. *Chem. Mater.* **1994**, *6*, 207.
7. Ruiz-Hitsky, E.; Jimenez, R.; Casal, B.; Manriquez, V.; Santa Ana, A.; Gonzalez, G. *Adv. Mater.* **1993**, *5*, 738.
8. Bissessur, R.; Kanatzidis, M. G.; Schindler, J. L.; Kannewurf, C. R. *J. Chem. Soc., Chem. Commun.* **1993**, 1582.
9. Lagadic, I.; Léaustic, A.; Clément R. *J. Chem. Soc., Chem. Commun.* **1992**, 1396.

10. Stucky, G. D. In *Progress in Inorganic Chemistry*; Lippert, S. J., Ed.; Wiley & Sons Inc.: New York, NY, 1992; Vol. 40.
11. Divigalpitiya, W. M.; Frindt, R. F.; Morrison, S. R. *J. Mater. Res.* **1991**, *6*, 1103.
12. Liu, Y.-J.; DeGroot, D.C.; Schindler, J.L.; Kannewurf, C.R.; Kanatzidis, M.G. *J. Chem. Soc., Chem. Commun.* **1993**, 593.
13. Bissessur, R.; DeGroot, D.; Schindler, J.; Kannewurf, C.; Kanatzidis, M. *J. Chem. Soc., Chem. Commun.* **1993**, 687.
14. Nazar, L. F.; Zhang, Z.; Zinkweg, D. *J. Am. Chem. Soc.*, **1992**, *114*, 6239.
15. Murphy, D. W.; DiSalvo, F. J.; Huil, G. W.; Waszczak, J. V. *Inorg. Chem.* **1976**, *15*, 17.
16. Divigalpitiya, W. M. R.; Frindt, R. F.; Morrison, S. R. *Science* **1989**, *246*, 369.

LAYERED SILICATE/ POLYSTYRENE NANOCOMPOSITE

A. MOET, A. AKELAH*, A. HILTNER AND E. BAER

Department of Macromolecular Science, Case Western Reserve University
Cleveland, OH 44106-7202

* Department of Chemistry, Tanta University, Tanta, Egypt

ABSTRACT

Nano-composites have been prepared from Na^+ and Ca^{++} montmorillonite (MMT) in a polystyrene matrix via chemical intercalation. Vinyl monomer-g-MMT was prepared by exchanging the mineral cation by vinylbenzyl trimethylammonium chloride, thus rendering the mineral organophilic and forming polymerizable moieties directly bonded to the lamellar surface of the mineral. Styrene was added and polymerized by free radical in selected solvents. The ratio of mineral to the bound polymer ranged from 0.3 to 1.25 (by weight) depending on the initial mineral concentration in the feed and on the solvent used. The mineral domains in the composite, measured from suspension cast film fall in the range of 150 nm to 400 nm. Measured from compression molded samples, the domains were ca. 50 nm which is much smaller than the mineral aggregate and comparable to that of the primary particle of the mineral. WAXD disclosed that the d (001) spacing of MMT in the composite ranged from 1.7 to 2.5 nm suggesting that the mineral aggregates (ca. 10 μm) were dissociated into individual layers then reassembled into lamellar nanoclusters.

INTRODUCTION

Concurrent with the recent surge in the preparation of nanoscale materials, nanostructured composites based on hybrids of polymers and smectic clay minerals, mostly montmorillonites, are emerging with the prospect of solving recognized limitations of fiber composites and filled polymers. Montmorillonite nanocomposites of nylon 6 [1-5], polystyrene [6,7] and rubber [8,9] have been described in the recent literature. Like other multiphase materials, successful development of this class rests on two basic principles: chemical continuity and morphological hierarchy. From a chemical point of view, these systems may be considered as clay-polymer complexes [10] and are based on physical or chemical intercalation. In both cases, it is suggested that a limited quantity of the polymer resides within the interlamellar spacing as evidenced by d (001) measurements. In the chemical intercalation approach [6,8,9,11], the polymer is chemically bonded to the ionic sites at the internal surfaces of the lamellae through an ion exchange process. Physical intercalation [12,13], which has been also called "direct intercalation" [7], involves mixing clay or its organophilic derivative with a polymer in the melt. The organophilic treatment of MMT facilitates the adsorption of the polymer into the interlamellar spacing but does not assure effective bonding.

Undoubtedly, ionic bonding of the polymer to the internal surface of the clay lamellae provides chemical continuity from which higher levels of stability may derived. Indeed, a polystyrene/ montmorillonite composite prepared by the physical intercalation approach [7] has been noted to deintercalate by suspending the composite in toluene. On the other hand, the

polystyrene in a similar composite (PS/MMT), prepared by the grafting approach [6], remained chemically bonded to the mineral after extensive solvent treatment. Since *intercalation* is a common attribute of all three methods, it is instructive to categorize the hybrids prepared by chemical intercalation as "mineral-polymer grafts".

The morphological hierarchy of this class of composites stems from the lamellar assembly of the mineral into primary particles which constitute the native aggregate [14]. It is also known that MMT swells and disaggregates by the action of certain liquids then reverts back to its aggregated character. Thus, regardless of the type of bonding, intercalation does not necessarily give rise to a nanoscale morphology [11, 13]. Morphological evolution of MMT-polymer hybrids remains ambiguous and appears to depend on thermodynamic and kinetic factors which dictate the balance between forces of dispersion and aggregation. Realizing that materials derive their properties from their chemical stability and morphological hierarchy, this paper describes a method for the preparation of PS-g-MMT and provides evidence to its nanostructured character. A companion paper provides detailed chemical and morphological analysis of another nanocomposite: MMT-g-ATBN [8].

PROCEDURES

The concept underlying our method of preparing the grafted PS intercalate rests on two basic steps [6]. The first comprises the preparation of the onium salt of an appropriate vinyl monomer which is subsequently bonded to the mineral interlayer by ion exchange. The second step involves a routine polymerization reaction. Thus, a suspension of 25 grams of MMT (Na or Ca) in 1 liter of water was stirred overnight. To the stirred, cooled (0-5 °C) suspension, an aqueous (30 mmol) solution of vinylbenzyl trimethylammoniumchloride (I in Fig. 1) in 100 ml water was added drop wise. After 3 hours, a white precipitate (II) was filtered, washed and dried. To a prescribed mixture of MMT-g-monomer and solvent a predetermine volume of styrene monomer and AIBN initiator are added. The mixture was then heated to 80 °C while being stirred, for 5 hours, at the end of which the Poly(styrene-g-montmorillonite) (III) was precipitated in methanol, washed and dried in vacuum at 100 °C for several hours. Figure 1 presents a scheme to describe the preparation procedure and Table I specifies the composition of five different preparations of PS-g-MMT. The polymerization reaction was carried out in acetonitrile (MeCN) and toluene whose amounts (in ml) are reported in parentheses.

Table I. Composition of polymerization recipes.

CODE	MMT-g-MONOMER per 100 ml styrene	SOLVENT (ml)
A	5	MeCN (40)/Tol (60)
B	10	MeCN (125)
C	10	MeCN (125)/THF (125)
D	25	MeCN (200)/Tol (200)
E	50	MeCN (400)/Tol (400)

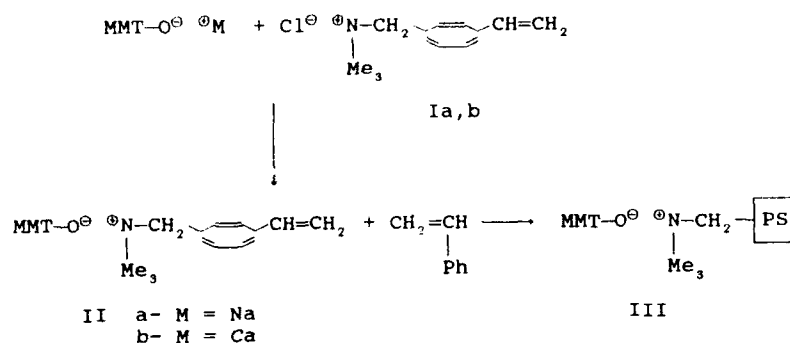


Figure 1. Schematic illustration of the preparation procedure

The material produced by the scheme outlined above (III) was characterized systematically to define the evolving nanostructure. The interlamellar structure which includes the stability of the ionic bonding and the nature of polymer packing between the lamellae has been examined by elemental analysis, FTIR and WAXD. The morphological hierarchy was elucidated using SEM and TEM.

RESULTS AND DISCUSSION

Elemental and FTIR analyses of the MMT-monomer intercalate (II) and the MMT-polymer were used to ascertain the chemical structure of the monomer and the stability of the ionic bond [6]. WAXD of the MMT-monomer gave rise to an interlamellar spacing of $d(001) = 1.5$ nm in both the Na and Ca montmorillonites. This increase amounts to a swelling in the interlamellar spacing of 0.54 nm which suggests bimolecular packing of the vinyl monomer in (II) if horizontal alignment is assumed. It was also ascertained that the exchange of the inorganic cation was complete and that the cation exchange capacity of the MMT-monomer was similar to its original value [6].

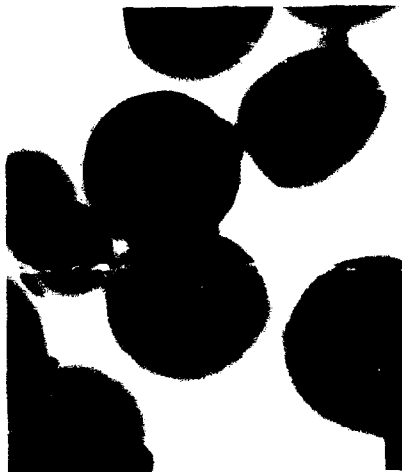
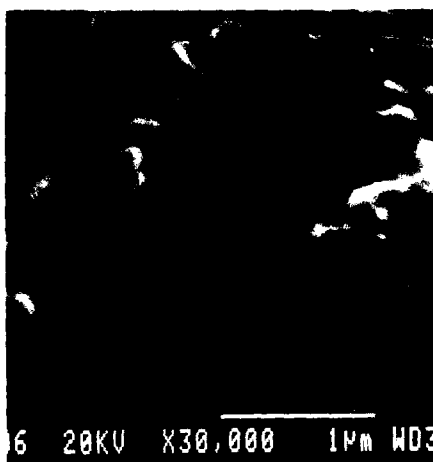


Figure 2. TEM of suspension cast film

A recent US patent [15] described a similar procedure to prepare PS/MMT composite containing only 5.3% MMT. The patent narrates that the X-ray diffractometry of this

composite material gave no peak attributable to the (001) plane of MMT. This indicates, the patent disclosed, that the *individual layers* of MMT were uniformly dispersed in the polymer. Similar claims were examined in another publication [8]. The present study established that it is possible to carry out polymerization recipes containing up to 50% MMT (Table I). In this regard, it is useful to note that intercalation of MMT involves two interrelated phenomena: namely, swelling and disaggregation.

TEM micrography of a thin film fabricated from THF suspension of a crude composite preparation (E) is shown in Fig. 2. The product appears to be comprised of mineral-rich spheres, in which the polymer is bound to the mineral, evenly dispersed in a polymer matrix. The spheres in Fig. 2 range in diameter from 150 nm to 400 nm. This observation leads into two worthwhile consequences. One is that the spherical clusters of Fig. 2 can not be perceived to undergo unlimited swelling upon molding. On the other hand, this morphology indicates the feasibility of extracting the mineral-rich domains from the polymer matrix by centrifuge treatment of the suspension to obtain a composite with higher MMT content.



SEM examination of a compression molded sample of preparation E (Table I) is exhibited in Fig. 3. The presence of nodular submicroscopic domains (ca. 50 nm) in Fig. 3-a implies that the spherical clumps of Fig. 2 are plausibly assemblies of smaller domains. Related phenomenon has been observed in ATBN-g-MMT [8]. Mapping the surface of the specimen imaged in 3-a for Si at the same magnification (Fig. 3-b) unveils that MMT domains in the molded specimen probably maintain a wide size distribution, of which the nodular entities of Fig. 3-a are the largest, and that they are homogeneously dispersed.

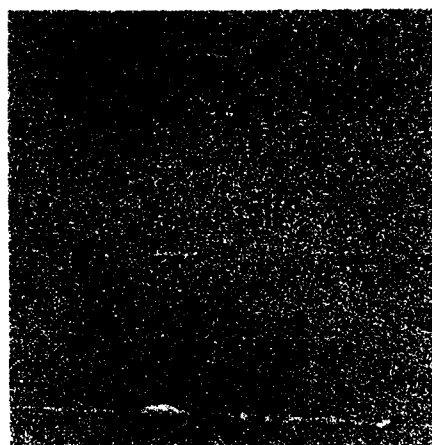


Figure 3. SEM micrograph (a) and Si mapping (b) of 50% MMT composite.

Table II summarizes the results of the separation experiment. The Table also includes

the interlamellar spacing measured before and after extraction. Further extraction of unintercalated PS was found possible at elevated temperature [16].

Table II. Extraction Results

Code	Extr. PS, %	MMT 1 g (PS)	d (00) Crude	d (001) Extr
A	80	0.31	20.3 Å	22.9/11.2 Å
B	79	0.91	24.5 Å	21.7 Å
C	75	0.67	22.2 Å	18.9 Å
D	42	0.77	18.1 Å	17.1/10.1 Å
E	10	1.25	17.2 Å	20.8/10.6 Å

Considering the data in Tables I and II, it is noted that the interlamellar activity in these polymerizations depends on the solvation power of the used solvent and the fraction of II in the polymerization recipe. Typical WAXD behavior of our preparations are shown in Fig. 4 for samples containing (a) 5% and (b) 50% MMT. Apparently, two diffracting species exist in these samples, one of which exhibit d (001) of about 10 Å, is perhaps associated with unreacted mineral. The majority of the material exhibits interlayer diffraction of 2.1 nm and 1.7 nm for the 5% and 50% composites, respectively. Quantitative TEM analysis indicated that the spacing between the MMT layers in the composite exhibits a wide distribution ranging from 3 nm to 20 nm with an average of about 6 nm [16].

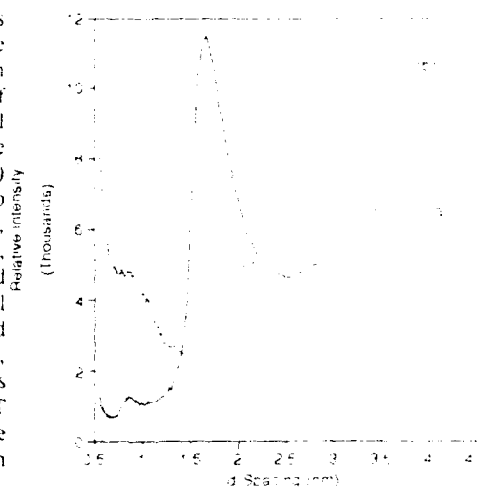


Figure 4. WAXD of two composites containing 5% (a) and 50% (b) MMT

CONCLUSIONS

A method to prepare PS-g-MMT composites containing more than 50% MMT is disclosed. It entails two steps; preparation of a chemically intercalated monomer which is then polymerized with styrene. The amount of polymer contained within the interlamellar spacing of MMT, as detected from WAXD, appears to reflect multimolecular packing whose magnitude depends on the preparation conditions. MMT in the composite predominates as clusters in the order of ca. 50 nm which are homogeneously dispersed within the matrix.

ACKNOWLEDGEMENTS

This research was supported, in part, by ARO, grant No. DAA LO # 92 G 0241. The authors wish to thank Dr. Vasily Topolkaraev for his assistance in the measurements and for useful discussions. We are also indebted to ECC America, Inc. for providing montmorillonite samples.

REFERENCES

1. A. Okada, M. Kawasumi, T. Kurauchi and O. Kamigaito, *Polymer Preprints*, **28**, 447 (1987).
2. Y. Fukushima and S. Inagaki, *J. Inclusion phenomena*, **5**, 473 (1987).
3. Y. Kurauchi, A. Okada, M. Kawasumi, T. Kurauchi and O. Kamigaito, *Clay miner.*, **23**, 27 (1988).
4. A. Usuki, M. Kawasumi, Y. Kojima, A. Okada, T. Kurauchi and O. Kamigaito, *J. Mater. Res.*, **8**, 1174 (1993).
5. A. Usuki, M. Kawasumi, Y. Kojima, A. Okada, T. Kurauchi, and O. Kamigaito, *J. Mater. Res.*, **8**, 1179 (1993).
6. A. Moet and A. Akelah, *Materials Letters*, **18**, 97 (1993).
7. R. A. Vaia, H. Ishii and E. P. Giannelis, *Chem. Mater.*, **5**, 1694 (1993).
8. A. Moet, A. Akelah, N. Salahuddin, A. Hiltner and E. Baer, *Proceedings Mater. Res. Soc.*, San Francisco, April 4-8, 1994.
9. Y. Kojima, K. Fukumori, A. Usuki and T. Kurauchi, *J. Mater. Sci. Lett.*, **12**, 889 (1993).
10. B. K. G. Theng, *Formation and properties of Clay-polymer Complexes*, Elsevier, New York (1979).
11. P. Kelly, A. Akelah, S. Qutubuddin and A. Moet, *J. Mater. Sci.*, in press (1994).
12. M. T. Bryk, A. Sh. Goikhman, I. E. Skobets and F. D. Ovcharenko, *Kolloidnyi Zhurnal*, **45**, 1043 (1983).
13. A. Moet, S. Qutubuddin and P. Kelly, "Anti-shrink Agent for Plastic Moldings". Final Report, The Edison Materials Technology Center, Dayton, OH, October 1990.
14. J. Mering, *Trans. Faraday Soc.*, **42**, 205 (1946).
15. US Patent No. 4,889,885, December 26, 1989.
16. V. Topolkaraev, private communications.

LANGMUIR-BLODGETT FILMS OF CALCIUM STEARATE

NECESIO COSTA, MARK AINDOW AND PETER M. MARQUIS,
School of Metallurgy & Materials and Dental School, The University of Birmingham, Edms
Road, Edgbaston, Birmingham, B15 2TT, United Kingdom.

ABSTRACT

The Langmuir Blodgett (LB) Process has been shown to be an appropriate method for use in mimicking of biological processes for producing engineering materials such as bioceramics. The main advantages of this approach are that the layers form at low temperatures, that they are fully dense and that the process of densification is by infiltration rather than by sintering. Moreover, biological hard tissues are self-assembled to perform certain functions; the architecture being controlled by an epitaxial organic matrix. Clearly, if this process can be understood in detail then it is possible that LB films may be used to replicate this architecture for engineering purposes.

Atomic Force Microscopy (AFM) and X-ray diffraction (XRD) have been used to study and characterise LB films of calcium stearate obtained by the repeated dipping into and withdrawal of a (001) Si wafer from a subphase containing calcium ions and using stearic acid as the surfactant. Contact-mode AFM images of the film surface have been used to measure the thickness of the LB layers and to reveal the nature and distribution of defects in the film. The measured thickness of the calcium stearate layers is about 2.5 nm; a value consistent with that obtained by XRD, but smaller than the length of an individual calcium stearate molecules.

INTRODUCTION

Recently, the design of new materials on the atomic and molecular level for practical applications has been investigated in detail. The Langmuir Blodgett process has been suggested to be one of the most appropriate methods for the production of well-ordered two dimensional arrays. The Langmuir Blodgett process consists of the transference of a preformed monolayer onto a solid substrate. The process consists of amphiphilic compounds being spread at air-water interfaces and a monomolecular layer being formed. Upon compression of the monolayer, the molecules are oriented at the interfaces. The compressed monolayer is transferred onto a solid substrate via its immersion into, and withdrawal from, the subphase. Fig. 1 shows a schematic drawing illustrating the various stages of the Langmuir Blodgett Process. Three different stages are identified: spreading, film compression and deposition.

Characteristics such as film stability, a low-defect structure with molecular-scale features and the fact that the process is "designable" fulfil the technological requirements of a method for the production of: piezoelectric and pyroelectric thin films; organic thin films for photoelectric information conversion; organic thin films for optical information storage and organic thin film for biomimetic process.

In this work the Langmuir Blodgett process has been used as a biomimetic process to produce a material with similar structure to that in the shell of a mollusc. Mollusc shells are biological hard tissues which have well-ordered crossed lamellar microstructures. Their strengths are comparable with those of many common engineering ceramics. The main idea of this project is to produce a biomimetic surface in the form of a LB film and to investigate how

such surface films will modify crystallisation behaviour. As a prelude to this, thickness measurements were carried out on calcium stearate LB films. The evaluation of this parameter is of vital importance in any study of LB films and such measurements are the focus of the present paper.

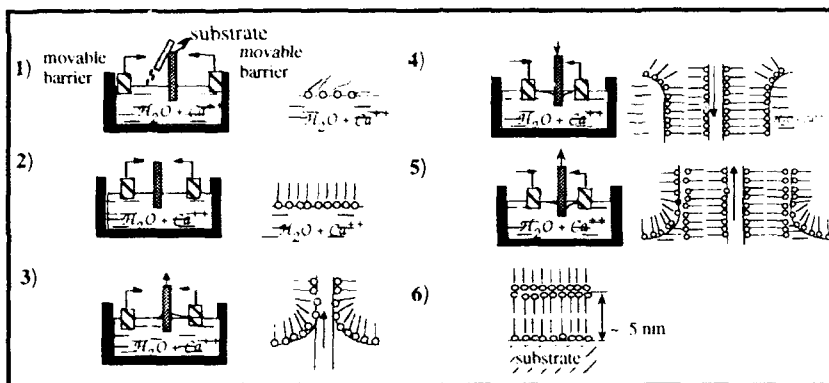


Fig. 1 - Schematic drawing of the Langmuir Blodgett process; 1-spreading; 2-compression; 3, 4 & 5 - deposition of 1st, 2nd and 3rd layers; 6-final film structure.

MATERIALS AND EXPERIMENTAL APPROACH

The surfactant used in this study was a 5×10^{-3} M solution of stearic acid ($\text{C}_{17}\text{H}_{35}\text{COOH}$) in chloroform and the subphase was a pH10 in solution of calcium hydroxide ($\text{Ca}(\text{OH})_2$) in double distilled water (0.102 g/l). The surfactant solution was deposited onto the subphase using a micro syringe fitted with a metal needle. The substrates used were, polished wafers of semiconductor grade silicon with a nominal surface orientation of (001). The wafers cleaned and degreased by washing with detergent, rinsing with deionised water in an ultrasonic bath and then rinsing in isopropyl alcohol.

The Langmuir-Blodgett trough used was a double rigid barrier type unit constructed of PTFE, with a paper Wilhelmy plate. The surfactant solution was introduced into the middle of the trough and the chloroform was allowed to evaporate until only pure surfactant remained on the subphase. The surface pressure was measured using an infrared detector which was calibrated against the isotherm curve determined for the system in separate experiments. The barriers close until the surface pressure between the surfactant molecules reaches a specific target value. The surface pressure is maintained at this target value by direct computer control of the barriers. The target value is chosen such that the surfactant molecules are close enough to enable the substrate to be coated by immersion into the subphase. After each layer is deposited, the target pressure is re-established before producing the next layer. Since the Si substrates used are hydrophilic, they were immersed in the subphase before spreading the surfactant mixture. In order to allow drainage of the aqueous subphase solvent from the film, the withdrawal speed chosen was lower than the critical speed for film deposition. Between deposition of the first and second layers, the wafers were allowed to drain for 1 hour such that

more of the water was eliminated from the film.

X-ray diffraction was used to determine the thickness of the LB film "monolayers". The diffraction studies were carried out using a Philips PW 1380 horizontal diffractometer with a graphite crystal monochromator controlled by a DACO-MP controller. The $\text{K}\alpha$ line from a Cu target, which produces X-rays with a characteristic wavelength of 0.1452 nm, was used. The film thickness were obtained by assuming that, since the scattering of X-rays from carbon and hydrogen atoms is very small compared to that from the heavier metal ions, the lattice spacing (normal to the film) measured by X-ray diffraction for simple fatty acids corresponds to the distance between adjacent planes containing metal ions. Thus the d-spacing can be calculated for each pair of layers.

Film thicknesses were also determined by contact-mode AFM using a Digital Instruments Nanoscope II scanning probe microscope with a microfabricated Si_3N_4 cantilever with a force constant of 0.06Nm^{-1} and scanning at 4kHz. Images were obtained by scanning under conditions of constant height with a net tip force in the region of 10-100 pN. Since the AFM gives quantitative measurements of surface geometry, layer thicknesses can be calculated by measuring the vertical displacement between adjacent regions on stepped LB multilayers.

RESULTS

Cracks were generated in the LBF during examination in a low vacuum SEM (LVSEM) and a typical region is shown in Fig. 2. Despite the relatively high background pressure which the LVSEM maintains, evaporation of water or more volatile components from the sample can still occur. We note that, whilst simple ageing of the films can produce similar effects, films such as the one shown in Fig. 2 were only produced 1 hour before examination and thus this is not likely to be the cause of the cracks in the present case.

It is interesting to note that multilayers consisting of 15 or more layers did not crack when viewed under LVSEM. One possible explanation for this behaviour is that it may be related to increasing film disorder, small environmental changes (e.g. in temperature and pressure) can cause defects on the multilayers. According to Allara et al¹ layers can peel off the substrate after reaching 10 nm (approx. five layers) as a consequence of an increase in film disorder. However using purer reagents² and with alternative reaction and bonding schemes^{3,4} this problem has been solved and uniform intact films of over 100 nm thickness are readily achievable.



Fig. 2 - AFM images of cracks on the surface of a 40 layers of calcium stearate LB film. (a) two dimensions (b) 3-dimensions.

The thickness of the layers were then measured using X-ray diffraction and AFM and these measurements were compared with the thicknesses which would be expected for ideal LBFs.

Since the atomic scattering amplitudes for X-rays from carbon and hydrogen atoms are much smaller than those of the heavier metal atoms, the X-ray diffraction patterns from LBFs are dominated by the arrangement of these latter atoms. Thus the main diffraction peaks from the films corresponds to the distances between adjacent planes containing metal atoms. A typical scan is shown in Fig. 3, and up to ten orders of such (001) reflections can be identified. The direct beam has a divergence which swamps the detector at angles below 1° , thus the (001) peak is not accessible but (002) and higher order are clearly visible. There is some suggestion of subsidiary oscillations in the tails of the (002) peaks; similar features have also been observed by Pomerantz et al^{5,6} who used a diffractometer with excellent collimation and monochromaticity, under computer control and with counting times of about 5 min per point to measure the fine structure of the diffraction pattern. It was shown that, the tails of the Bragg peaks are modified by an envelope function giving pronounced maxima and minima for films which consist of small numbers of monolayers.

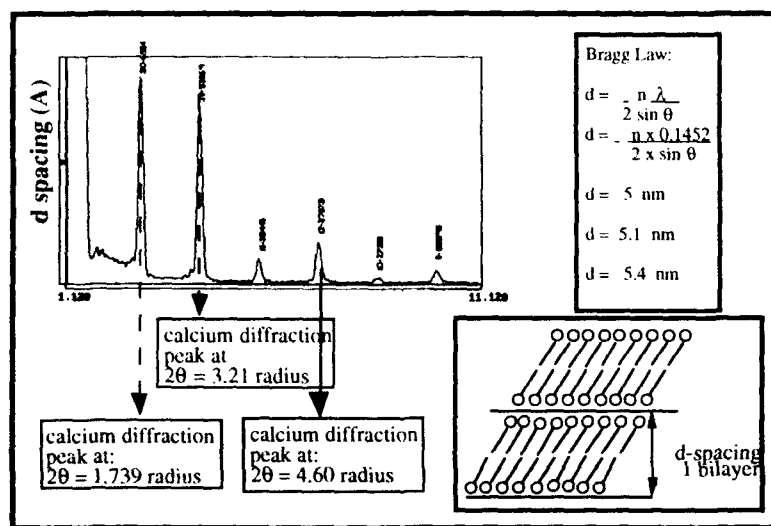


Fig. 3 - X-ray Diffraction results for calcium stearate Langmuir Blodgett multilayer.

The monolayer thicknesses determined for the calcium stearate is around 3 nm. This value is comparable with the value of 2.75 nm which would be expected on the basis of atomic structure models using standard values for interatomic distances and atomic radii (Fig. 4).

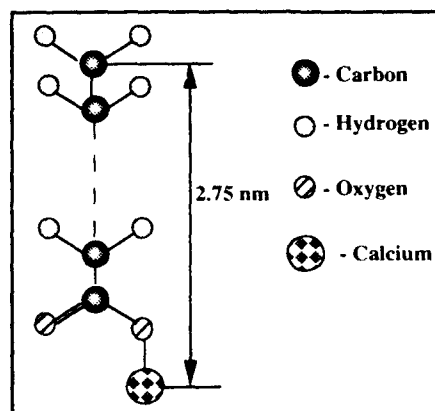


Fig. 4 - Atomic Structure of calcium stearate.

To verify these X-ray results, measurements of film thicknesses were also obtained using AFM. Fig. 5 shows an AFM image obtained from a test structure whereby a step of 9 monolayers has been deposited onto one side of a continuous 20 monolayer film. The height of the step was measured as 21.77 nm which corresponds to 9 monolayers as expected and yields a layer thickness of 2.41 nm.



FIG. 5 - Cross sectional section of a Calcium stearate LB Film.

Thus there is a small but consistent discrepancy between the measured thickness of the monolayers and that which would be expected on the basis of atomic models. If this discrepancy does not arise because the atomic radii and/or interatomic distances in the molecule are different from the standard values used, then one possible explanation is that the calcium stearate molecules are inclined to the substrate thereby producing a thinner layer.⁷

The use of those three thicknesses (theoretical, X-ray, and AFM values) also could indicate the type of structure obtained. X-rays diffraction measurements showed that the spacing of metal cations were nearly twice the thickness of a single layer, confirming the head-to-head, tail-tail arrangement (Y-type structure). X-type multilayers are expected to have

a different structure than Y-type. The methyl groups of one layer should be adjacent to the carboxyl groups of the next layer on the basis that the deposition occurs only during the immersion sequences of the dipping operation. However, Holley⁸ and Ehlert⁹ have shown that the spacing of the metal cations is essentially the same in both x- and y-type multilayers. This indicates that the orientation of the molecules must overturn during the building of the x-type multilayers.

CONCLUSIONS

The thickness of calcium stearate LB film has been determined to be 2.5 nm. It is consistent with values obtained using different techniques (AFM, X-ray diffraction). A small discrepancy (theoretical value = 2.75 nm and experimental calculation = 2.5 nm) has been found in relation to the theoretical value and the value obtained experimentally. It has been proposed that this discrepancy could arise due to tilting of the molecules in the film away from the substrate surface normal.

REFERENCES

1. H. O. Finklea, L. R. Robinson, A. Blackburn, B. Richter, D. Allara and T. Bright, *Langmuir* **2**, 239 (1986).
2. R. Maoz, L. Netzer, J. Gun and J. Sagiv, *Journal de Chimie Physique et de Physico-Chimie Biologique* **85**, 1059 (1988).
3. M. D. Porter, T.B. Bright, D.L. Allara and C.E.D. Chidsey, *J. Am. Chem. Soc.* **109** 3559 (1987).
4. H. Lee, L.J. Kepley, H.G. Hong, S. Akhter, T.E. Mallouk, *J. Phys. Chem.* **92**, 2597 (1988).
5. M. Pomerantz, *Thin Solid Films* **152**, 165 (1987).
6. M. Pomerantz, F. Dacol and Segmuller, *Phys. Rev. Lett.* **40**, 246 (1978).
7. N.G. Costa, Mphil Thesis, The University of Birmingham, 1994.
8. C. Holley and S. Bernstein, *Phys. Rev.* **52**, 525 (1937), **49**, 403 (1936).
9. R. C. Ehlert, *Journal of Colloid Science*, **20**, 387 (1965).

ACKNOWLEDGEMENTS

The authors would like to thank the Conselho Nacional de Pesquisa - Brazilian Government for the financial support of this research project and the School of Metallurgy and Materials at The University of Birmingham for providing the facilities. We would also like to express their gratitude to Dr. Ziad for the many discussions on the Langmuir Blodgett Process and for providing us with the facilities to carry out the X-ray analytical work at The University of Manchester.

BIO-MIMETIC COMPOSITES

JEREMY BURDON, JEFFREY SZMANIA AND PAUL CALVERT,
Department of Materials Science and Engineering, University of Arizona, Tucson AZ, 85721.

ABSTRACT

The properties of bone, as a polymer reinforced with nanometer-sized ribbon-shaped crystals of mineral, are compared with the properties of synthetic polymer composites. Bone does show some superiority to existing composites. The improvements can be attributed to the microstructure. Methods for reproducing this structure in a synthetic material are discussed.

INTRODUCTION

Mineralized biological tissues show a range of properties from slightly reinforced polymer through tough composite to ceramic. Bone particularly stands out as having a good combination of stiffness, strength and toughness when compared to equivalent synthetic materials. The main components of bone, collagen and hydroxyapatite, have properties that are typical of other tough polymers and minerals, respectively. Hence we must look to the microstructure as the source of the good properties.

This paper will provide a brief comparison of bone and composites, will identify the key aspects of the structure and then will discuss synthetic efforts to duplicate these structures and properties. Bone will be compared to short fiber reinforced composites which are moldable, roughly isotropic materials. Much better properties can be obtained with continuous fiber reinforcement but at the cost of expensive processing methods and poor properties in at least one direction. The challenge is to extend these good properties into moldable materials.

BONE AND COMPOSITES

Bone has an elastic modulus in the range of 20-30 GPa, about 10 times that of collagen or synthetic resins, table 1. This increase is achieved by reinforcement with 40-50 vol% of hydroxyapatite ribbons which have a thickness of a few nanometers and a high aspect ratio. Various theories can be used to predict composite moduli from composition [1] and bone seems to be in the range expected for the known component moduli, volume fraction and particle shape.

Particle-filled composites generally show a decrease in strength and a rapid decrease in toughness with increasing particle content. Fiber-filled composites get stronger but also less tough [2]. Properties are very dependent on the aspect ratio of the fibers which is generally limited to a range from 10-50 by the processing conditions. Glass fibers are typically 10 μ m in diameter and standard processing equipment will break fibers with lengths in the millimeter range. Finer fibers are undesirable because they would be a health hazard during handling. In addition normal mixing procedures, which randomize fiber orientations, limit the fiber volume fraction to the percolation threshold. This is around 40 vol% at an aspect ratio of 10 and 10 vol% at 50 [3].

Dense bone has a strength of 150 MPa, measured in tension parallel to the length and an

extension to break of 10%. Some equivalent composites are also shown in table 1. It can be seen that bone is distinguished by a large extension to break. It has also a large work of fracture. The characteristics which must contribute to these fracture properties include: high aspect ratio particles combined with a high packing density. There is no *a priori* reason to expect the small particle thickness to be an advantage since composite theory predicts a decrease of work of fracture with decreasing particle size at constant volume fraction and aspect ratio [4].

This rather counterintuitive conclusion arises in essence from the fact that the energy to pull out a fiber will vary as the critical length squared multiplied by the diameter, while the number of fibers in a cross-section depends on the diameter squared. The result is an energy that increases as the first power of size.

Two other aspects of bone structure may be important. Little is known about the nature of the hydroxyapatite-collagen interface. Presumably the bonding is quite good as it is in good synthetic systems. It is possible that the helical structure of collagen allows some specific energy-absorbing mechanism to operate at the interface during fracture. Such a mechanism has been observed during the fracture of mollusc shells [5]. In addition it has been suggested that the large extension to break of bone is due to microcracking which may follow specific planes within the Haversian or lamellar structure and so reflect structure on the 10-100 micron scale [6]. Bone has a very clear hierarchical structure [7,8] and it may well be that part of the reason for this is to control fracture by including weak planes. Different bone types do show different fracture behavior.

INORGANIC-ORGANIC HYBRIDS

Inorganic-organic hybrids have been studied for about 10 years by several groups and the general pattern of mechanical properties is now becoming clear. The addition of the inorganic phase stiffens glassy polymers in line with composite theory. The change in modulus does depend on morphology in that a material formed with a continuous inorganic network is stiffer than one with an continuous organic phase and inorganic particles. There is a much more marked increase in modulus above the glass transition (figure 1).

The mechanical strength in compression does increase, as for many particulate composites, but there is generally a decrease in tensile strength and in toughness, especially at high particle contents [9,10]. To date there is no clear sign of special properties arising from the nanometer scale of the inorganic filler except the effect of rubber modulus and an increase in degradation temperature for acrylic polymers [11].

Based on current knowledge of organic-inorganic hybrids and the preceding discussion of bone, there are two obvious routes for achieving better nanoscale composites. Firstly the reinforcing particles should have an elongated shape rather than being spherical. This needs to be achieved without paying a penalty in packing density. Secondly weak planes should be built into the structure to control failure; a similar mechanism is being tested by incorporating weak interfaces in ceramics [12]. The possibility of building into the matrix special structures with high work of fracture should also be explored.

ELONGATED PRECIPITATES

We have previously shown that elongated inorganic oxide precipitates could be formed in amorphous polymers by drawing the polymer during the precipitation process. The resulting

elongated particles had aspect ratios comparable to the draw ratio of the polymer, which could be controlled by changing the drawing temperature and rate [13].

Since this drawing process limits the composite to the form of fibers or films, we investigated methods of impregnating polymers with metal alkoxides to form elongated precipitates. Solid polymer sheets such as polyethylene terephthalate can be impregnated with silicon alkoxides and then steam treated to form a harder, silica-reinforced, surface layer [14]. This process is very dependent of selecting an alkoxide with a good solubility parameter match to the polymer, in order to get good swelling.

We attempted to use a similar swelling process with oriented polymer films to produce elongated reinforcement. It appears that the more limited swellability of oriented films makes this very difficult. However we were able to get good swelling of a two-phase mixture of polymethylmethacrylate and polyvinylidene fluoride. These two polymers are miscible in the melt but polyvinylidene fluoride crystallizes and so segregates from the amorphous polymethylmethacrylate [15]. When films are formed from solution, this segregation occurs on a large scale (10 μ m), from the melt the separation is on a very fine scale (10-100nm). On swelling with titanium alkoxides and hydrolysis, the acrylic polymer takes up alkoxide and is converted to a titania-reinforced composite [16].

When drawn, swollen with alkoxide and then hydrolysed, solvent-cast films show elongated aggregates of titania in the polymer (figure 2).

Another approach to the formation of elongated particles is to precipitate an inorganic crystalline material with an elongated crystal habit. This is essentially what occurs in bone. For an oxide, or other true ceramic, reinforcement it will be necessary to prevent formation of amorphous gel particles prior to crystallization. It is not yet clear how this can be achieved rapidly but recent experiments with concentrated surfactant systems point toward this [17].

CRYSTALLINE MATRIX POLYMERS

A further approach to control the particle morphology is to use a crystalline polymer matrix rather than an amorphous polymer. The lamellar morphology of crystalline polymers should redistribute the alkoxide to the interlamellar amorphous regions during crystallization. Subsequent hydrolysis should lead to titania particles in layers between the polymer crystals. In addition the toughness of crystalline polymers is related to the ability of chains to pull out of the lamellae during yielding and this toughness may be carried over into the composites.

To investigate a system of this type polypropylene was melt blended with titanium butoxide and extruded. After extrusion the film was treated with boiling water for 24 hours to precipitate the titania. In the melt the alkoxide is compatible with the polymer. Visual observation of the extrusion shows two transitions. At around 100°C the polymer appears to crystallize to become opalescent. At around 40°C the film becomes much more opaque; we believe that this is due to phase separation of the alkoxide, possibly induced by secondary crystallization of the polypropylene [18].

Initial samples were very weak and brittle. The spherulite size was much increased in the presence of the alkoxide. A coupling agent (triisostearylitanium alkoxide, Kenrich Corp.) and a nucleating agent (potassium benzoate) were added. This reduced the spherulite size and increased the toughness.

Dynamic mechanical measurements showed an increase in tensile modulus from 1.3 GPa to 2.2 GPa with 9% titania. There was a large decrease in the loss modulus. The tensile yield strength showed an initial small increase from that of pure polypropylene (14 MPa) and then a

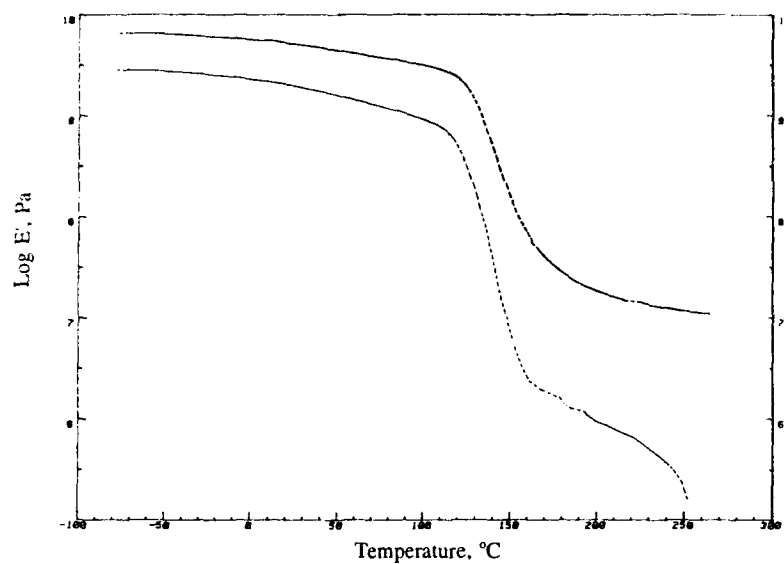


Figure 1: Storage Modulus of PMMA-(22 vol%) Silica hybrid composite and pure PMMA



Figure 2: Titania Particles formed by alkoxide swelling and hydrolysis of a PVF2-PMMA polymer blend (PVF2-PMMA)

drop to 9 MPa at 9% titania. Scanning electron microscopy of fracture surfaces in samples containing high levels of titania showed that there was a titania-rich region at the spherulite boundaries that tended to embrittle the polymer. Small angle x-ray scattering showed only nanometer-sized titania particles.

This first attempt to combine *in situ* reinforcement with the lamellar morphology of a crystalline polymer has shown that such systems can be formed by normal polymer melt processing methods. The elastic properties follow those that could be expected for a composite. The fracture properties seem to be dominated by morphology at the whole spherulite scale rather than at the lamellar scale and this needs to be controlled if the intrinsic behavior of this type of structure is to be studied.

Polypropylene is probably not the ideal polymer for this type of reinforcement, but it does have the merits of a low melting point and absence of any reaction with the titanium alkoxide, to which most esters would be vulnerable.

CONCLUSIONS

There is reason to believe that stiff, tough materials can be made by *in situ* reinforcement, but they have not been made yet. It is probable that locally aligned, elongated reinforcing particles will be necessary. It may also be necessary to add toughening structures on the scale of a few microns.

REFERENCES

1. L.A. Utracki and T. Vu Khanh in Multicomponent Polymer Systems, I.S.Miles and S. Rostami (eds), Longman, London, 1992
2. J.L. Kardos in International Encyclopedia of Composites, Volume 5, S.M.Lee, ed., VCH Pubs, 1991
3. J.V. Milewski and H.S. Katz, Handbook of Reinforcements for Plastics, Van Nostrand Reinhold, NY 1987
4. D. Hull An Introduction to Composite Materials, Cambridge University Press, 1981
5. M. Sarikaya, K. Gunnison, M. Yasrebi and I. Aksay, MRS Symposium Proc. **174** 109-116 (1990)
6. J. Currey, The Mechanical Adaptations of Bones, Princeton, 1984
7. E. Baer, A. Hiltner and R.J. Morgan, Physics Today **45** 60 (1992)
8. S.A. Wainwright, W.D. Biggs, J.D. Currey and J.M. Gosline, Mechanical Design in Organisms, Arnold, London, 1976
9. B.M. Novak, M.W. Ellsworth and C. Verrier, Amer. Chem. Soc. PMSE Preprints **70** 266 (1994)

10. C.J.T. Landry, B.K. Coltrain and B.K. Brady, *Polymer* **33** 1486 (1992)
11. J.D. Mackenzie *Amer. Chem. Soc. PMSE Preprints* **70** 380 (1994)
12. S. Baskaran, S.L. Nunn, D. Popovic and J.W. Halloran, *J. Amer. Ceram. Soc.* **76** 2209 (1993)
13. J.Burdon and P.Calvert, *Mater.Res.Soc.Symp.(Hierarchically Structured Materials)* **255** 375-383 (1992)
14. J.L.Lombardi and P.Calvert, *Mat. Res. Soc. Symp.* **286** 309-314 (1993)
15. T. Nishi and T.T. Wang, *Macromolecules* **9** 603 (1976)
16. J.Burdon and P.Calvert, *Mat.Res.Soc.Symp.* **286** 315-320 (1993)
17. S. Mann, presented at *Amer. Chem. Soc. San Diego*, 1994
18. P.D.Calvert and T.G.Ryan, *Polymer* **25** 921 (1984)

SELF ASSEMBLING NANOSTRUCTURED DELIVERY VEHICLES FOR BIOCHEMICALLY REACTIVE PAIRS

NIR KOSSOVSKY,^{*} A. GELMAN,^{*} H.J. HNATYSZYN,^{*} E. SPONSLER^{*} AND G.-M. CHOW^{**}

^{*}Biomaterials Bioreactivity Characterization Laboratory, Department of Pathology and Laboratory Medicine, University of California, Los Angeles, 90024-1732

^{**}Center for Bio/Molecular Science and Engineering, Code 6900, Naval Research Laboratory, Washington, DC 20375

ABSTRACT

Intrigued by the deceptive simplicity and beauty of macromolecular self-assembly, our laboratory began studying models of self-assembly using solids, glasses, and colloidal substrates. These studies have defined a fundamental new colloidal material for supporting members of a biochemically reactive pair.

The technology, a molecular transportation assembly, is based on preformed carbon ceramic nanoparticles and self assembled calcium-phosphate dihydrate particles to which glassy carbohydrates are then applied as a nanometer thick surface coating. This carbohydrate coated core functions as a dehydroprotectant and stabilizes surface immobilized members of a biochemically reactive pair. The final product, therefore, consists of three layers. The core is comprised of the ceramic, the second layer is the dehydroprotectant carbohydrate adhesive, and the surface layer is the biochemically reactive molecule for which delivery is desired.

We have characterized many of the physical properties of this system and have evaluated the utility of this delivery technology *in vitro* and in animal models. Physical characterization has included standard and high resolution transmission electron microscopy, electron and x-ray diffraction and ζ potential analysis. Functional assays of the ability of the system to act as a nanoscale dehydroprotecting delivery vehicle have been performed on viral antigens, hemoglobin, and insulin. By all measures at present, the favorable physical properties and biological behavior of the molecular transportation assembly point to an exciting new interdisciplinary area of technology development in materials science, chemistry and biology.

INTRODUCTION

Self-assembly, broadly defined as the spontaneous fabrication of multi-component molecular structures, is the elegant mechanism by which most complex biological molecules achieve their ultimate form. Self-assembly, at the biological level, is the inevitable consequence of fundamentally weak electron interactions between complex macromolecules. The deceptive simplicity and beauty of macromolecular self-assembly, as exists in nature, has prompted many commercial concerns and research laboratories to experiment with "biomimetic process."

At the commercial level, industry has experienced financial success with applications of self-assembly principles in polymerase chain reaction. In the biomedical arena, several pharmaceutically oriented biotechnological applications of self-assembly including liposomes and virus-like particles are in development and some are already in clinical trials. On the

experimental level, investigators have successfully produced a variety of self-assembly products such as microlithographed bio-patterns, triple helical DNA, DNA cubes, nanotubules and cage compounds.¹ Neural networks and bio-optico-electronic devices are among the envisioned applications.

Challenged by problems of molecular conformation at interfaces, our laboratory has studied models of self-assembly using solids, glasses, and colloidal substrates for the past six years. These studies have defined a fundamental enabling platform for the safe transportation of biochemically active molecules.² Among the applications of this safe molecular transportation assembly are: vaccines, artificial blood, drug delivery and gene therapy.

This article reviews the principles of self-assembly, nanobiology, and the challenges of maintaining the activity of biologically reactive pairs. The convergence of these principles into a single delivery vehicle with a variety of biological applications is described.

PRINCIPLES OF SELF-ASSEMBLY

Synthetic products are *self assembling* if the constituent parts assume spontaneously prescribed structural orientations in two or three dimensional space. The study of such processes has traditionally been called *supramolecular chemistry*, *macromolecular association phenomena* or *nanotechnology*, and the products have been called *smart materials*.³ In aqueous biological environments, the assembly of macromolecules is governed basically by three physicochemical processes: the interactions of charged groups, dehydration effects and intrinsic structural stability.

Interactions between charged groups

Most biological and synthetic surfaces are charged due to constituent chemical groups or adsorbed ions from the biological milieu. The interactions of charged groups such as amino-, carboxyl-, sulfate-, and phosphate-groups, facilitate the long range approach of self assembling subunits. The long range interaction of constituent subunits, beginning at around 15 nm, and their gradual attraction to an energy minimum that exists at a distance of approximately 3 nm, is the necessary first phase of self-assembly.

Natural self assembling structures that are favored by the existence of strong interactions of charged groups include crystal lattice formation and bone mineralization. Charged groups also play a role in stabilizing tertiary structures of folded proteins.⁴ Biotechnological applications of self-assembly based on charged group interactions include the analytically useful technique of forming cadmium arachidate bilayers to study the dielectric constants of protein layers, frictional slippage between bilayers, and other parameters of biological membranes.

Hydrogen bonding and dehydration effects.

Hydrogen bonds arguably constitute the most important molecular interaction in self assembling structures. Molecules that form hydrogen bonds are hydrophilic, and these molecules confer a significant degree of organization to the surrounding water molecules.⁵ Hydrocarbons and other molecules that are hydrophobic are incapable of forming hydrogen

bonds with the surrounding water. Nevertheless, their repulsion of water also imparts a great deal of organization to the surrounding environment. The organized water decreases the overall level of entropy of the surrounding medium. Because organized water is thermodynamically unfavorable, molecules tend to "welcome" the opportunity to shed the surrounding water, or dehydrate, in favor of assembling with one another.⁶ This step is the primary driving force of self-assembly in the typically aqueous biological milieu, and accounts for interactions among surfaces and macromolecules that may intuitively appear to be unlikely. While charge effects begin long range at 15 nm, dehydration effects soon take over. Dehydration effects and the associated entropic drive continue to favor surface adsorption to approximately the 3 nm intermolecular distance where steric, double layer and electrostatic repulsion forces begin to reverse the process.⁷

In nature, hydrogen bonds are largely responsible for base pair matching in double stranded nucleic acids, codon-anticodon matching in transfer RNA, stabilization of RNA cloverleaf structure via base pair matching, and stabilization of secondary protein structures such as α -helices and β -sheets. The premier biotechnological application to date has been exploitation of the polymerase chain reaction process.

Intrinsic structural stability

The structural stability of proteins in the biological environment is determined by two competing groups of forces. There are denaturing forces created by the interactions between charged groups and hydrogen bonds largely external to the molecule and there are conformationally stabilizing van der Waals forces largely internal to the molecule. The van der Waals forces, most often experienced by the relatively hydrophobic molecular regions that are shielded from water, play a subtle but critical role in maintaining molecular conformation during self-assembly.

Molecules that are "hard" and relatively stable are less likely to be deformed during self-assembly. The associated minimal change of the Gibbs free energy, a consequence of molecular denaturation to an energetically more favorable state enables the interaction to be relatively reversible. "Softer" molecules, however, are particularly vulnerable to the biophysical forces of self-assembly, and the energy minima assumed upon conformational denaturation tend to preclude reversal.

NANOSCALE BIOLOGY

Although we live in a three dimensional world, most of our sensory experiences with matter involve perceptions of only the very few surface layers of molecules. Our two-dimensional cognition of a three dimensional environment is a primary consequence of the fact that most chemical and biophysical interactions between materials and the biological environment, of which we are an integral part, occur at surfaces. While colloidal materials and nanoscale processes have not generally considered to be in the realm of the biological sciences, even a cursory view of the biological world yields a vision resplendent with things nano.

In our world, surfaces rule. Surfaces are physically unique environments with mechanical, chemical and electrical properties derived from the electron clouds of the atoms comprising them. Three dimensional matter that is comprised primarily of surfaces, better known as a

colloid, is the chief operator. Introduced by Thomas Graham in 1861, a colloid is any particle, droplet, molecule, or otherwise designated form of matter whose linear dimension is somewhere between 1 nm and 1 μ m. Indeed, Man* himself is a complex animated colloid representing the interfacial activities of the four forms of matter: gas, liquid, glass and solid. Self assembled from Leibnitzian monads† of almost unimaginable variety, man is a testimony to the awesome inherent properties of colloids and nanoparticles.

BIOCHEMICALLY REACTIVE PAIRS

Biochemical phenomena consist of binary interactions between pairs of molecules. Common names for such biochemically reactive pairs include but are not limited to immunological pairs, ligand-receptor pairs, enzyme-substrate pairs, drug-receptor pairs, catalyst-reactant pairs, catalyst-substrate pairs, absorbate-absorbent pairs, adsorbate-adsorbent pairs, and toxin-ligand pairs. On a molecular level, nearly all biochemical phenomena between such pairs involve the spatial recognition of one molecule by another, and such recognition serves as the means by which energy and information are transmitted, products are generated, responses are initiated and complex biological structures are built.

The process of spatial recognition implies both regioselective and stereoselective interactions among biochemically reactive pairs. One member of a biochemically reactive pair, constrained by fundamental biophysical laws, may interact with the other member of a biochemically reactive pair if and only if both members are physically conformed within some bounded set of possible spatial arrangements and if both members have their respect interactive regions unencumbered. The environment within which biochemically reactive pairs interact affect greatly the process of spatial recognition. Environments that constrain spatial mobility or encumber molecular regions may, depending on the degree of constraint and the resulting spatial conformation, either promote or inhibit biochemically reactive pair interactions.

An example of the former is surface activation of synthetic chemical reactions in a process known as "solid phase synthesis." Solid phases, either as solid glassy polymers, crystalline materials, or complex macromolecular polymers have been features of synthetic biochemistry since the early 1960's. Their use was advanced largely by Merrifield⁸ for facilitating peptide synthesis and for which he received the Nobel Prize for Chemistry in 1984. They became widely popular because the solid-phase method offered simplicity, speed, avoidance of intermediate isolation, and automation. The principal limitation in the widespread use of solid phases has been the empirical observation that only a few surfaces were effective biochemically reactive pair interaction promoters.

It is impractical to list the many examples of environmental constraints that affect biochemically reactive pair interactions, but it is reasonable to acknowledge that such

* The term "Man" is used here in the generic sense as a more linguistically palatable form of *H. Sapiens*.

† Metaphysical theory of matter developed in the late 17th century and stimulated, in part, by organic microscopic entities that had been discovered recently following Leeuwenhoek's (1632-1723) invention of the microscope. Although the theory argues for the non-interaction of substances, it nevertheless entails rudimentary allusions to the conservation of energy and to the principle of least action - elements that are used today to describe colloidal and macromolecular phenomena.

constraining conditions include but are not limited to temperature, salinity, surface chemistry, solution dielectric constant, osmolarity, concentration of competitive species, gas partial pressures, electric fields, and magnetic fields.

CHALLENGES OF MOLECULAR DELIVERY

Molecular delivery is the Holy Grail of the biomedical sciences. Delivery, to the extent that molecules would be stabilized for greater activity and targeted for greater specificity, offers the promise of greatly improving such fields as vaccines, drugs therapy and even gene therapy. A host of chemical reactions that tend to destroy polypeptides and other labile biochemically active molecules might be prevented with adequate surface immobilization (Table 1).⁹ Consequently, vaccines might not have to be boosted because they would last longer, and their immunoprotective properties might be enhanced. Drugs might be more effective with fewer side effects if they were targeted. And most significantly, gene therapy might be possible on a practical level without the need for surgery.

TABLE 1	Stability Problems in Bulk Solutions [†]	Potential Advantages of Surface Immobilization
<i>Rationale for using delivery vehicles in the biomedical community.</i>	<ul style="list-style-type: none"> • Hydrolysis • Oxidation • Deamidation • Phosphorylation • β-elimination • Racemization • Glycation 	<ul style="list-style-type: none"> • Stability (protection against the processes described to the left) • Cellular or Organ Targeting

Unfortunately, the marriage of biological sciences with materials science has been rocky. Nanoscaled members of a biologically reactive pair, when immobilized onto a surface that alters dramatically aspects of their environmentally constrained conformation, tend to assume novel conformations that may render the members either biochemically inactive or antigenically irrelevant. Since the primary driving force in non-covalent interactions between aqueous dispersions of macromolecules and surfaces is dehydration, the possibility that dehydroprotectants might solve the challenge of surface-facilitated molecular delivery was assessed.

Previous work published in the agricultural and microbiological literature identified carbohydrates, specifically disaccharides, as potentially effective dehydroprotectants. In the early 1940's, Lewis¹⁰ showed that a 40% sucrose solution exhibited a substantial stabilizing effect on the viability of ergot producing *Claviceps purpurea* when inoculated on host rye. This empirical observation acquired biophysical mechanistic support from Crowe et al.¹¹ Briefly, they suggested that certain sugars may replace the water around polar residues in membrane phospholipids and proteins thereby maintaining their integrity in the absence of water. It is a phenomenon that has been utilized by nature to protect anhydrobiotic organisms such as fungal spores, yeast cells, and cysts of brine shrimp against desiccation. It appears that

[†] Adapted from F. Franks, *Bio/technology*, 12, 253 (1994).

sugars are capable of preserving the structure and function of both membrane bound and soluble proteins in the absence of water.

The family of sugars that exhibit dehydroprotectant properties are largely mono-, di-, and oligosaccharides, and their ability to do so correlates with their ability to form glasses.¹² Working with the model disaccharide trehalose, Green and Angell concluded that the trehalose/water system passes into the glassy state and thereby arrests all long-range molecular motion.¹³ Denaturation is thus impeded. The glass transition temperatures of the most common natural dehydroprotectants, trehalose and sucrose, are 79°C and 70°C respectively.

The empirical observations of Lewis coupled with the explanations offered by Crowe suggest that disaccharides and related poly-OH oligomers with comparable glass transition temperatures may function as dehydroprotectants for surface immobilized members of a biochemically reactive pair. Studies of the secondary structure of dehydrated molecules immobilized on disaccharide films¹⁴ and the results obtained in various biomedical applications tend to confirm these principles.

APPLICATIONS

Macromolecules representing a variety of classes of biochemically reactive pairs have been studied in our laboratory following immobilization on surface modified nanocrystalline materials. Examples of applications include vaccines, synthetic blood, and drug delivery vehicles. The basic self-assembling synthetic units are rather similar among the applications, yet the consistent observation is that the conformation and or biological activity of the immobilized molecule is preserved.

Materials and Methods

The delivery vehicles, as self-assembled through non-covalent interactions, consist of three layers: a solid phase core to provide a nidus for surface immobilization, a surface modifying layer of the glassy disaccharide cellobiose,⁵ and an outer layer consisting of a member of a biochemically reactive pair (Table 2). For the solid phase, ceramic materials were used because ceramics are the most structurally regular materials in existence. Being crystalline, the high degree of order in ceramics ensures that any surface modification will have only a limited effect on the nature of the atoms deep to the surface and thus the bulk properties of the ceramic will be preserved. Also, the high degree of order of ceramics ensures that the surfaces will exhibit high levels of surface energy which will favor the binding of the disaccharide surface film.

The two most commonly used ceramic cores have been carbon (diamond) and calcium-phosphate dihydrate (brushite). The diamond has been used primarily for vaccine applications, while the degradable brushite has been used for applications where substantial quantities of biochemically active material would be expected to be administered.

A typical process for producing clean diamond cores and coating them with cellobiose begins with 1 gram quantities of diamond powder [General Electric, Worthington, OH] which are cleaned by 400 Watt sonication at 4°C [Branson, Danbury, CT] in 12 N HCl for 16 hours

⁵ The glass transition temperature of the disaccharide used by us, cellobiose, is 77°C.

and washed with ultrafiltered water until the pH is near 7. The resultant opaque dispersions are layered over glass plates and baked in a vacuum oven for 2 days at 185 C. Dried diamond is then rehydrated once more and acid washed as previously described. Activated diamond

TABLE 2	STRUCTURAL POSITION	CHEMISTRY	FORM OF MATTER
<i>Composition of the three layer molecular transportation assembly</i>	Core	Ceramic formed from metal oxides or carbon (diamond)	Solid (crystal)
	Surface Coating (stabilizer-dehydroprotectant)	Disaccharide (sugar)	Glass
	Outer Biochemically Active Molecule	Variable	Colloid

dispersions in ultrafiltered deionized water are adjusted to 1.0 mg/ml and then introduced to 250mM cellobiose [Sigma, St. Louis, MO] and lyophilized for 24 hours. Unadsorbed cellobiose is removed by ultrafiltration dialyses against sterile water in a 100 kd nominal molecular weight cutoff stir cell [Filtron, Northborough, MA] at room temperature.

The addition of the third layer, consisting of a biochemically reactive pair member, is tailored to the solubility properties of the molecule of interest.

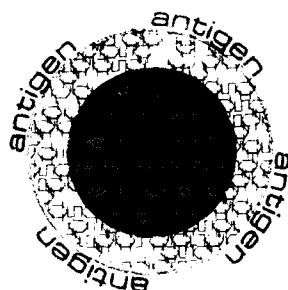
Experimental Results

To date, we have immobilized antigens to produce viral decoys (Figure 1) as vaccinating agents,¹⁵ hemoglobin to produce red blood cell surrogates,¹⁶ and insulin to test the drug delivery concepts.¹⁷ The diamond based viral decoys, comprised of immobilized viral outer envelope proteins, most recently from HIV, tend to range in size from 30 to 100 nm and exhibit a broad range of properties that indicate preserved conformation of the adsorbed viral proteins. They exhibit the same ζ -potential as whole virus, react with monoclonal antibodies directed at whole virus, and evoke both antibody and cellular immunity in test animals comparable to the reactions evoked by whole virus. Specifically, the decoys exhibit the same size, same surface charge, are recognized by conformationally specific and non-specific monoclonal antibodies, are recognized by HIV positive human serum, evoke antibody responses with the same magnitude and western-blot profile as HIV, and evoke cellular immunity.

The red cell surrogates, comprised of degradable calcium phosphate cores, exhibit comparable molecular oxygen binding cooperatively relative to whole blood, and can be dispersed in solutions that have an effective hemoglobin concentration of 10g/dl. Specifically, the red cell surrogates exhibit the Bohr effect, have a solution pH 7.4, 80nm size, 10 g/dl hemoglobin solution concentration, p50 26-32 torr, Hill coefficient 2.2, Osm 230 mOsm and viscosity .0352 Poise.

The drug delivery applications, again using the degradable ceramic cores with immobilized insulin, show *in vivo* biological activity that is as intense and slightly prolonged relative to insulin without the benefit of being immobilized.

FIGURE 1



The molecular transportation assembly consists of three distinct layers. The core is a ceramic solid that provides a crystalline high surface energy nidus for the subsequent self-assembly of a glassy layer of carbohydrates that then act as molecular stabilizers for the adsorbed biochemically active layer. Shown in the example is the composition of an HIV decoy (vaccine) fabricated from a ceramic diamond core, cellobiose, and HIV envelope antigenic proteins.

CONCLUSION AND SUMMARY

Self-assembly is a natural process that serves as the basis for most forms of life. In natural self-assembly systems, small changes in molecular conformation are necessary, as exemplified by the changes observed during successful antibody-antigen interactions.¹⁸ More substantial conformational alterations induced by surface immobilization in synthetic systems can be controlled by applying another natural principle -- disaccharide induced molecular stabilization.

One biotechnological application of the above consists of surface modified nanocrystalline ceramics as an enabling platform for the safe delivery of a wide range of biochemically active molecules. The interdisciplinary approach we have taken, combining materials science, surface chemistry, and biology, has yielded a promising technology that may define principles useful in a broad range of human endeavors.

ACKNOWLEDGEMENTS

The authors acknowledge the contribution of the many members of the Biomaterials Bioreactivity Characterization Laboratory to developing the technologies described herein. Special thanks are extended to Gold team leaders Ed Mena, Anhtu Nguyen, Samir Rajguru and Mariel Torres, and to Rina Shah, Anh D.D. Chung, J. Zemanovic, J. Crowder, C. Sukiassians, A. Festekian and C. Hacker. The molecular transportation assembly and related applications are subject to patents issued and pending to the Regents of the University of California, and are optioned to Structured Biologicals International, Inc., an affiliate of the sole research sponsor, Structured Biologicals, Incorporated, Toronto.

REFERENCES

- ¹ J-M. Lehn, *Science* **260**, 1762 (1993); *Angew. Chem. Int. Ed. Engl.* **27**, 89 (1988); G.M. Whitesides, J.P. Mathias, C.T. Seto, *Science* **254**, 1312 (1991); N. Kossovsky, D. Millett, A. Gelman, E. Sponsler and H.J. Hnatyszyn, *Bio/Technology*, **11**, 1534 (1993); J.M. Schnur, presented at the 1994 MRS Spring Meeting, San Francisco, CA, 1994 (unpublished).
- ² N. Kossovsky and R. Bunshah, *U.S. Patents* #5,178,882 (12 Jan 1993); # 5,219,577 (15 June 1993); and Australian Patent # 638,841 (7 June 1993); and patents pending.
- ³ W. Burchard, *TRIP* **1**, 192 (1993).
- ⁴ A.L. Lehninger, *Biochemistry*. (Worth Publishers, Inc, New York, 1975); B.T. Nall and K.A. Dill, *Conformations and Forces in Protein Folding*. (American Association for the Advancement of Science, Washington, D.C., 1991).
- ⁵ J.N. Israelachvili, *Intermolecular and Surface Forces*. (Academic Press, New York, 1985).
- ⁶ G.C. Kreshech and I.M. Klotz *Biochemistry* **8**, 8 (1969); W. Norde and J. Lyklema, in *The Vroman Effect*, edited by C.H. Bamford, S.L. Cooper, and T. Tsuruta (VSP, Utrecht, 1992).
- ⁷ W. Norde, presented at the American Chemical Society 207th National Meeting, San Diego, CA, 1994 (unpublished).
- ⁸ G. Barany and R.B. Merrifield, in *The Peptides*, Vol 2, edited by E. Gross and J. Meienhofer (Academic Press, New York, 1979).
- ⁹ F. Franks, *Bio/technology* **12**, 253 (1994).
- ¹⁰ R.W. Lewis, *J Am Pharm Assoc*; **37**, 511 (1948); U.S. Patent No. 2,402,902 (1945); Y.H. Loo and R.W. Lewis, *Science*; **121**, 367 (1955).
- ¹¹ J.H. Crowe, *Am Nat*, **105**, 563 (1971); *Biochim Biophys Acta*; **947**, 367 (1988).
- ¹² H. Levine, L. Slade, *BioPharm* 1992 (May) 36-40.
- ¹³ J.L. Green and C.A. Angell, *J Phys Chem*; **93**, 2880, (1989).
- ¹⁴ N. Kossovsky, A. Nguyen, K. Sukiassians, A. Festekjian, A. Gelman and E. Sponsler, *J Colloid Interface Sci.* IN PRESS (1994).
- ¹⁵ N. Kossovsky, A. Gelman, E.E. Sponsler, D. Millett, *J Applied Biomaterials*, **2**, 251 (1991); N. Kossovsky, E. Sponsler, A. Gelman, S. Rajguru, M. Torres, H.J. Hnatyszyn, K. Ly, E. Mena, N. Rosales and J. Yu, presented at the American Chemical Society 207th National Meeting, San Diego CA, 1994 (unpublished).
- ¹⁶ N. Kossovsky, A. Gelman, E.E. Sponsler, *Artific Cells, Blood Substitutes and Immobiliz Biotech*, IN PRESS (1994); N. Kossovsky, A. Gelman, E. Sponsler, S. Rajguru, M. Torres, presented at American Chemical Society 207th National Meeting, San Diego, CA, 1994 (unpublished).
- ¹⁷ H.J. Hnatyszyn, N. Kossovsky, A.E. Gelman, J. Crowder, J. Zemanovic, R. Shah, A. Chung and S. Rajguru, In preparation; N. Kossovsky, H.J. Hnatyszyn, A. Gelman, J. Crowder, M. Pham, S. Rajguru, R. Shah, A. Chung, J. Zemanovic, presented at the American Chemical Society 207th National Meeting, San Diego, CA, 1994 (unpublished).
- ¹⁸ J.M. Rini, U. Schelze-Gahmen and I.A. Wilson, *Science* **255**, 959 (1992).

FREQUENCY-DEPENDENT SECOND HARMONIC GENERATION IN ACENTRIC CHROMOPHORIC SELF-ASSEMBLED NLO MATERIALS

SHLOMO YITZCHAIK, PAUL M. LUNDQUIST[†], WEIPING LIN[†], DAVID R. KANIS, MARK A. RATNER^{*}, TOBIN J. MARKS,^{*} AND GEORGE K. WONG^{†*}

Department of Chemistry, Physics and Astronomy[†] and the Materials Research Center, Northwestern University, Evanston, Illinois 60208-3113 (USA)

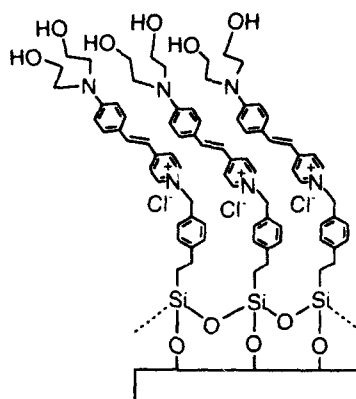
ABSTRACT

An attractive and challenging approach to the construction of robust, thin film materials with large second-order optical nonlinearities is the covalent self-assembly of aligned arrays of high- β molecular chromophores into multilayer superlattices. In this paper, we describe the dispersion of second harmonic generation (SHG) in a self-assembled (SA) monolayer containing a stilbazolium chromophore. The frequency-dependent measurements were performed on 25 Å thick monolayers on glass using a tunable (0.4-2 μm) light source based on optical parametric amplification (OPA). The SHG spectrum contains a clear two-photon resonance at $\hbar\omega = 1.3\text{eV}$. The maximum in the second-order susceptibility coincides with a low energy chromophore-centered charge-transfer excitation at 480 nm. The experimental SHG dispersion values compare favorably with theoretical results computed using a sum-over-states (SOS) formalism. However, the measured values exhibit a somewhat broader band response than the theoretical curve, and the origin of this behavior is discussed.

INTRODUCTION

A new approach to the construction of second-order nonlinear optical (NLO) materials was recently reported from our laboratory (Scheme I).¹ This method involves the covalent self-assembly of intrinsically acentric multilayers of high- β chromophores on inorganic oxide substrates. Such robust thin film superlattices exhibit high second harmonic generation (SHG) efficiencies with $\chi_{zz}^{(2)}$ values for 25 Å thick monolayers of $5\text{--}7 \times 10^{-7}$ esu at $\hbar\omega = 1.17$ eV. This level of response is higher than in conventional inorganic oxides such as LiNbO_3 and is comparable to the most efficient poled polymers and acentric Langmuir-Blodgett films.^{2,3} In addition, the self-assembled thin films⁴ are thermodynamically equilibrated systems which do not require an external aligning electric field to establish an acentric environment. This represents a major advance over poled NLO polymers where inducing and completely stabilizing net chromophore alignment remains a daunting challenge.^{2,3} In this contribution, we provide detailed information on the frequency-dependent second-order optical nonlinearity of a stilbazolium monolayer, focusing on the origin of the broader experimental width of the nonlinear spectra as compared with the theoretical prediction.

Scheme 1



Construction of Self-Assembled Thin Films.

The procedure for the present molecular self-assembly process (Scheme 1) has been reported in detail elsewhere.¹ In summary, clean glass substrates are immersed in a toluene solution of 1-chloromethyl-4-(2-trichlorosilylethyl)benzene (coupling agent) at room temperature for 36 h, and the resulting monolayers are air-cured at 115 °C for 30 minutes. Chromophore deposition is carried out by immersion of these functionalized substrates in toluene at 100 °C for 72 hours. Evolution of the surface structures is monitored by contact angle measurements which repeat in the sequence: original glass surface, 15°; coupling agent monolayer, 74°; chromophoric monolayer, 46°; and are in accord with expected surface wettabilities; by XPS - the original signal at 205 eV for Cl_{2p} (benzylic chlorine) of the coupling agent shifts to 203 eV (chloride) and a signal at 400 eV for N_{1s} appears upon quaternization; by U'V-Vis spectroscopy which reveals large shifts in λ_{max} upon quaternization (from 390 to 490 nm); by polarized second harmonic generation (*vide infra*), and also by grazing angle X-ray reflectivity. These films are insoluble in common organic solvents and most acids, and can only be removed by etching with HF solution or by diamond polishing.

RESULTS AND DISCUSSION

Sample preparation

Stilbazolium-based self-assembled monolayers were assembled on both sides of a fused silica slide, and the film was subsequently removed from one side with a 20% HF solution to avoid interference effects in the dispersion measurement. Figure 1 shows the angular-dependent SHG signal for the sample before and after removal of the monolayer from one side. The $\chi_{zzz}^{(2)}$ value at 1064 nm of 5×10^{-7} esu remains unchanged after the etching treatment, as evident from

the 4 fold decrease of the SHG. The chromophore tilt angle from the surface normal was determined by fitting the angular dependent SHG signal envelope to eq (1)⁵. As expected, the

$$\frac{\chi_{zzz}^{(2)}}{\chi_{xx}^{(2)}} = 2 \cot^2 \bar{\psi} \quad (1)$$

tilt angle $\bar{\psi} = 42 \pm 2^\circ$ remains unchanged before and after removing the film from one side of the substrate. The chromophore number density, N_s , on the surface is computed by the use of eq (2)^{1a} where β_{zzz} is the calculated magnitude (9.4×10^{-28} esu) of the hyperpolarizability

$$\chi_{zzz}^{(2)} = N_s (\cos^3 \bar{\psi}) \beta_{zzz} \quad (2)$$

component along the chromophore long axis (which is comparable to the estimated experimental value³ 8.3×10^{-28} esu) yielding $N_s = 3 \times 10^{14}$ molecules/cm².

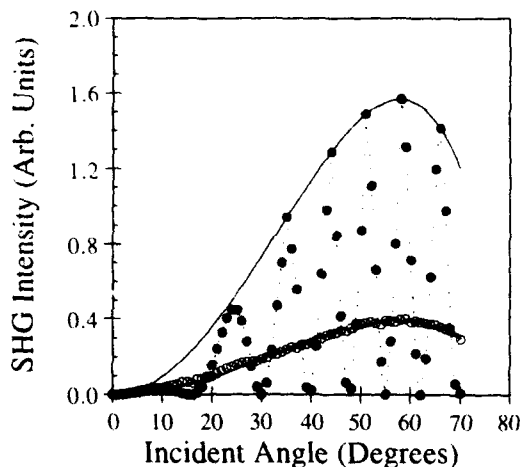


FIGURE 1. SHG intensity ($I_{pp}^{2\omega}$) as a function of fundamental beam incident angle of a glass slide having a self-assembled stilbazolium monolayer on either side (full circles) and after etching one side with 20% HF solution (open circles). The experimental data are fitted to eq. 2 (full lines). As a guide to the eye, the data from the double sided sample are connected with a dotted line.

Frequency-dependent $\chi^{(2)}$ measurements

An Optical Parametric Amplifier (OPA), the construction and operation of which is described elsewhere,^{1e} was used to provide a tunable light source. SHG measurements on the self-assembled films were performed over the fundamental range 800-1600 nm. In these films, the ratio $\chi_{zzz}^{(2)}/\chi_{xx}^{(2)}$ was found to be 2.7, resulting in maximum SH intensities for incident angles

near 60°. Data were collected at this angle. $\chi^{(2)}$ for the self-assembled films was obtained by using measured values for the linear absorption α , calculating quartz coherence lengths, l_c , from refractive index data, and using the literature $\chi_{\text{quartz}}^{(2)}$.

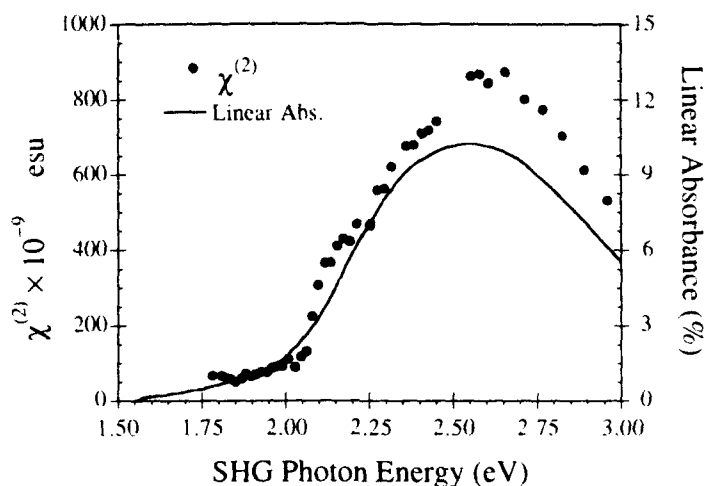


FIGURE 2. SHG photon energy dependence of $\chi^{(2)}$ for a self-assembled film derived from stilbazolium chromophore (SHG uncertainties <6%) and the linear absorption spectrum ($\lambda_{\text{max}} = 480$ nm).

As seen in Figure 2, the output signal of the second-order response (2ω) closely follows the linear absorption spectrum, with the film $\lambda_{\text{max}} = 480$ nm ($2\omega = 2.6$ eV) corresponding to the resonant $\chi_{\text{max}}^{(2)} = 9 \times 10^{-7}$ esu, an exceptionally large value for organic thin films². The off-resonance values ($\sim 10^{-7}$ esu) may also prove useful for device applications.

Theoretical considerations

The frequency-dependent second-order nonlinear susceptibility spectrum resembles the linear absorption band. The deviation from an identical line shape is due to the different dispersive nature of the real and imaginary part of the susceptibility, the presence of nonresonant background, and multiphoton absorption bands. For SHG this can be expressed by eq (3)^{6,7} where ω_L is the laser fundamental frequency and ω_j and Γ_j are the center and the width at half height of the j -th band. A_j contains induced dipole moment and oscillator strength terms.

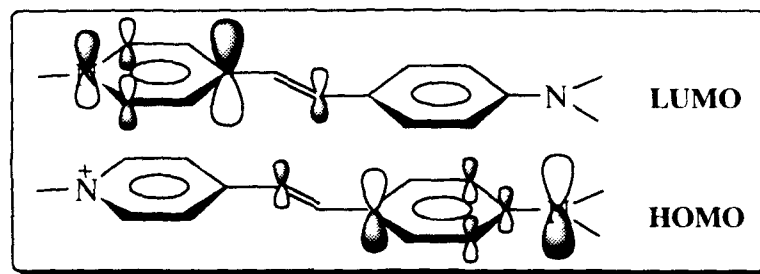
$$\chi^{(2)}(-2\omega; \omega, \omega) \propto \sum_j \frac{A_j}{(2\omega_L - \omega_j + i\Gamma_j)(\omega_L - \omega_j + i\Gamma_j)} \quad (3)$$

In our investigation, the origin of the β dispersion was investigated using a reliable sum-over-states formalism for calculating the elements of the chromophore hyperpolarizability tensor as a function of fundamental frequency⁸⁻¹⁰ to aid in interpretation, we can use the approximate two level form: eq (4), and relating the absolute values of β to $\chi^{(2)}$ by eq. (2).

$$\beta(-2\omega;\omega,\omega) = \frac{3e^2}{2} \frac{\hbar\omega_{ge} f_{ge} \Delta\mu_{ge}}{[\hbar\omega_{ge}]^2 - (\hbar\omega)^2} \frac{1}{[\hbar\omega_{ge}]^2 - (2\hbar\omega)^2} \quad (4)$$

The sum-over-states expansion indicates that a single chromophore-centered charge-transfer excitation (Scheme II) along the dipole moment direction, from the stilbazolium highest occupied molecular orbital (HOMO) to lowest unoccupied molecular orbital (LUMO, $\lambda_{CT} = 472$ nm), dominates the response. The associated oscillator strength is substantial ($f = 1.12$)

Scheme II



with a pronounced dipole moment change ($\Delta\mu_{ge} = 17$ D). The functional form of the curves can be further investigated using the two-level model,^{13,14} where the response is assumed to originate from one excited state (e) in the perturbative expansion of β . The nonresonant background, $\chi^{(2)}_{NR}$, containing the contribution from all states far from resonance, is neglected here. However, the resonant part, $\chi^{(2)}_R$, will contribute a real and an imaginary part to $\chi^{(2)}$. The imaginary part will maximize at the resonance frequency, where the real part goes through a sign change.

The response ($\beta(-2\omega;\omega,\omega)$) is described by eq. (4), where f_{ge} is the oscillator strength, $\hbar\omega_{ge}$ is the energy of the charge-transfer optical excitation between the ground state (g) and the excited state (e), and the $\Delta\mu_{ge}$ is the difference in dipole moment between the two states. This formula predicts a pair of resonances for each input frequency ω : one at the fundamental frequency ($\hbar\omega$) and the other at twice the incident frequency ($2\hbar\omega$). The two-photon resonance is the origin of the 1.3 eV (960 nm) feature in Figure 3. The relationship also predicts anti-resonant behavior at ω and 2ω ; however, in this experiment the sign (phase) of $\chi^{(2)}$ is not measured.

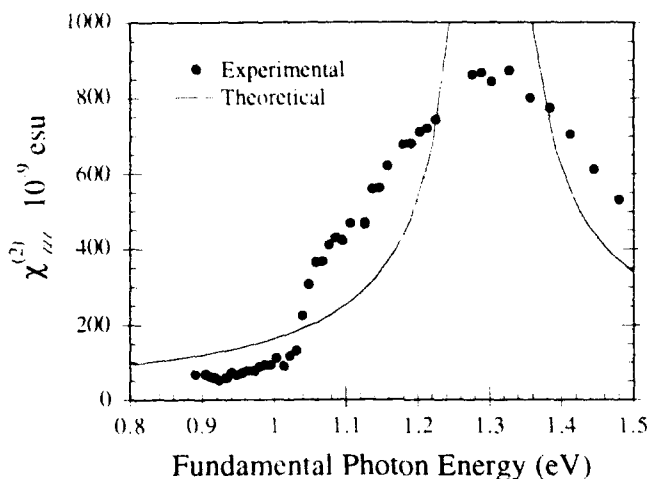


FIGURE 3. Experimental and theoretical fundamental photon energy dependence of $\chi_{zz}^{(2)}$ for a self-assembled film derived from stilbazolium chromophore (SHG uncertainties <6%).

Agreement between the experimental $\chi^{(2)}$ profile and the computed response is quite good. However, the experimental results exhibit a somewhat broader $\chi^{(2)}$ response with a shoulder at 1.06 eV, compared with a narrower bandwidth and an infinite maximum for the theoretical response. This mismatch is partly due to the neglect of the complex nature of β near resonance. Here the damping term ($i\Gamma_{eg}$) in the imaginary part ($\omega_{eg} + i\Gamma_{eg}$) is necessarily neglected because of the complexity in predicting its value theoretically.

CONCLUSIONS

An OPA and accompanying instrumentation for the highly expedient measurement of the frequency-dependence of $\chi^{(2)}$ in thin film materials has been demonstrated. This technique has been applied to chromophoric self-assembled stilbazolium-chromophore films and the results indicate that $\chi^{(2)}$ resonance enhancement is operative in these structures. However, the high off-resonance values of $\chi^{(2)}$ are encouraging for exploring the use of these materials in waveguide applications. The two-level model predicts the observed trends in the dispersion. A further improvement of the model by introducing the parameters to account for the width of the dispersion curve is underway. Experiments involving device applications are also in progress, as well as extension of the OPA instrumentation to include broader frequency ranges and SHG phase information.

Acknowledgments This research was supported by the NSF-MRL program through the Materials Research Center of NU (Grant DMR9120521) and by the Air Force Office of Scientific Research (Contract 93-1-0114).

REFERENCES

1. (a) S. Yitzchaik, S.B. Roscoe, A.K. Kakkar, D.S. Allan, T.J. Marks, Z. Xu, T. Zhang, W. Lin and G.K. Wong, *J. Phys. Chem.* **97**, 6958 (1993).
 (b) A.K. Kakkar, S. Yitzchaik, S.B. Roscoe, F. Kubota, D.S. Allan, T.J. Marks, W. Lin and G.K. Wong, *Langmuir* **9**, 388 (1993).
 (c) L. Li, M.A. Ratner, T.J. Marks, C. Zhang, J. Yang and G.K. Wong, *J. Am. Chem. Soc.* **112**, 7389 (1990).
 (d) S.B. Roscoe, S. Yitzchaik, A.K. Kakkar, T.J. Marks, W. Lin and G.K. Wong, *Langmuir* -in press.
 (e) P. Lundquist, S. Yitzchaik, T. Zhang, D.R. Kanis, M.A. Ratner, T.J. Marks and G.K. Wong, *Appl. Phys. Lett.* - in press.
2. (a) S.R. Marder, J.E. Sohn and G.D. Stucky (Eds.) Materials for Nonlinear Optics: Chemical Perspectives, ACS Symposium Series 455, American Chemical Society, Washington, DC (1991).
 (b) P.N. Prasad and D.J. Williams, Introduction to Nonlinear Optical Effects in Molecules and Polymers, Wiley, New York (1991).
3. G.J. Ashwell, R.C. Hargreaves, C.E. Baldwin, G.S. Bahra, C.R. Brown, *Nature* **357**, 393 (1992).
4. A. Ulman, An Introduction to Ultrathin Organic Films, Academic Press, New York, (1991), and references therein.
5. T.G. Zhang, C.H. Zhang and G.K. Wong *J. Opt. Soc. Am. B* **7**, 902 (1990).
6. G.C. Schatz and M.A. Ratner, Quantum Mechanics in Chemistry, Prentice-Hall (1993) p.297.
7. (a) R. Yam, G. Berkovic, *Langmuir* **9**, 2109 (1993).
 (b) W.M.K.P. Wijckoon, Z.Z. Ho, M.W. Mull, G.G. Padmabandu, W.M. Hethrington, *J. Phys. Chem.* **96**, 10450 (1992).
 (c) D.A. Higgins, M.B. Abrams, S.K. Beyerly, R.M. Corn, *Langmuir* **8**, 1994 (1992).
8. D.R. Kanis, M.A. Ratner and T.J. Marks, *Chem. Mat.* **3**, 19 (1991).
9. D.R. Kanis, M.A. Ratner and T.J. Marks, *Int. J. Quantum Chem.* **43**, 61 (1992).
10. D.R. Kanis, M.A. Ratner and T.J. Marks, *Chem. Rev.* **94**, 195 (1994).
11. T.F. Heinz, H.W.K. Tom, and Y.R. Shen, *Phys. Rev. A*, **28**, 1883 (1983).
12. T.G. Zhang, C.H. Zhang, and G.K. Wong, *J. Opt. Soc. Am. B* **7**, 902 (1990).
13. J.L. Oudar, *J. Chem. Phys.* **67**, 446 (1977).
14. J.L. Oudar and D.S. Chemla, *J. Chem. Phys.* **66**, 2664 (1977).

PART III

Synthesis and Properties II

OPTICAL STUDIES OF SILICON NANOCRYSTALS IN COLLOIDAL AND SOL-GEL MATRICES

HOWARD W. H. LEE¹, JEFFREY E. DAVIS², MARGARET L. OLSEN¹, SUSAN M. KAUZLARICH³, RICHARD A. BLEY³, SUBHASH H. RISBUD⁴, AND DAVID J. DUVAL⁴

¹Lawrence Livermore National Laboratory
Livermore, CA 94550

²Department of Applied Science, University of California,
Livermore, CA 94550

³Department of Chemistry, University of California,
Davis, CA 95616

⁴Division of Materials Science and Engineering, University of California,
Davis, CA 95616

ABSTRACT

We studied the optical properties of silicon nanocrystals incorporated into colloidal and sol-gel matrices. The silicon nanocrystals are produced by ultrasonic dispersion of porous silicon layers. We report results on the dependence of the photoluminescence (PL) spectra with excitation intensity. The PL shows a blue peak (at ~ 415 - 460 nm) and a red peak (at ~ 680 nm). This PL spectrum shows a remarkable dependence on the excitation intensity. As the intensity is increased, the blue peak grows at the expense of the red. A model is suggested for this behavior. We also report on the excitation intensity dependence and the emission wavelength dependence of the PL decay at low (1 kHz) and high (82 MHz) repetition rates of optical excitation. When low repetition rate excitation is used, the PL decay times are all exponential, short (ns), and appear to vary little with emission wavelength. This sharply contrasts with what is observed in porous silicon. With high repetition rate excitation, both red and blue peaks show long (100's ns) and short (ps-ns) lifetime components. We contrast the different optical properties of these silicon nanocrystals with that observed in porous silicon.

INTRODUCTION

The discovery by Canham in 1990 that porous silicon (PS) efficiently emits visible light [1] has initiated intense worldwide research into the mechanism for the light emission. Numerous models for the luminescence mechanism has been proposed and has been described in various review articles [2]. Many of these models have been refuted in some form or another. Though a complete understanding of the mechanism for efficient light emission from PS is still lacking, the consensus has leaned strongly toward quantum confinement as being at least partly responsible. The important role of surface states as recombination centers in the luminescence process has also been proposed [3]. To investigate the mechanism and to understand how quantum confinement, surface states, etc. may affect the luminescence of PS, we studied monodispersed and aggregated Si nanocrystals incorporated into colloidal and sol-gel matrices as simpler systems that are easier to characterize. These Si nanocrystals also offer an interesting light emitting system for study and provide new and different options for Si-based optoelectronics and photonics.

We performed various optical studies on the dynamics and spectroscopy of these nanocrystalline Si systems, which include: the dependence on emission wavelength and excitation intensity of the time-resolved PL decay, and the dependence on excitation intensity of the PL spectra. Many of our results differ from that observed in porous Si and in other nanocrystalline Si systems. We also observe for the first time, an interesting dependence of the PL spectra with excitation intensity. Our results are discussed in terms of the insights they offer into the light emitting process. Finally, we point out the usefulness of using different excitation repetition rates in studying systems such as these where there is a broad distribution of lifetimes.

EXPERIMENTAL

These nanocrystals were made from PS and the synthetic procedure is described in detail elsewhere [4]. The nanocrystals were incorporated into various organic solvents as colloidal suspensions and into TEOS sol-gel matrices. The procedure for this incorporation is also described in detail elsewhere [4,5]. Optical excitation was provided by several sources: (1) the ~100 fs, 82 MHz output from a self-modelocked Ti:sapphire laser was frequency-doubled with an appropriate KDP crystal to give output varying from 355-400 nm, (2) the ~150 fs, 1 kHz output from a Ti:sapphire regenerative amplifier was frequency-doubled to give 400 nm output, and (3) a Xe arc lamp. A photomultiplier tube (1.5 ns resolution) and a synchroscan streak camera (5 ps resolution) were used to detect the PL decay. The spectra were recorded with a 0.25 m or 0.5 m monochromator and an intensified optical multichannel analyzer. All spectra were calibrated and corrected with NIST-traceable spectral calibration lamps.

RESULTS AND DISCUSSIONS

Except for where noted, the results we obtained in colloidal and sol-gel matrices were qualitatively similar. Therefore, we will discuss the results in general terms and address particular matrices only where appropriate. The fact that we see similar optical properties in these different matrices indicates that their physics depend on the inherent properties of the Si nanocrystals. The nanocrystals do not interact strongly with these hosts.

We began by studying the optical properties of the PS from which the Si nanocrystals were made. We found the PL lifetimes, variation of lifetimes with emission wavelength, and emission spectra of the starting porous silicon samples to be consistent with what is generally observed for porous silicon. In particular, the decays are nonexponential in the microsecond regime, the red luminescence dominates the blue (if any), and the lifetime decreases monotonically with higher emission energy.

Detailed discussions of the synthesis and physical characterization of the Si nanocrystals are given elsewhere in this volume [4]. We briefly discuss a few pertinent results. High Resolution Transmission Electron Microscopy (HRTEM) in Ref. [4] shows both aggregates of and monodispersed crystalline particles. Cluster sizes range from 7 to 40 nm. Individual nanocrystals range in size from 2-10 nm. It is difficult to determine whether these nanocrystals exist as aggregates in the solvent or whether they aggregate when prepared for TEM analysis. It is likely that they exist both in monodispersed and aggregated form in the matrix. HRTEM also show a thin amorphous shell surrounding the nanocrystals. In addition, the IR spectra show peaks corresponding to various Si-O bond vibrations and an absence of Si-H vibrations. This indicates that the hydrogen passivation has been replaced by oxygen passivation. It has been shown that oxygen passivation can lead to efficient light emission as well as with hydrogen. The observation of C-H stretches in the IR spectra points to the presence alkyl groups. This is discussed in greater detail in Ref [4]. Thus, the picture that emerges of the nanocrystals is one where there is an inner silicon crystalline core covered with a layer of SiO_x and possibly alkyl groups attached to the outer oxide layer.

Typical photoluminescence spectra of Si nanocrystals in a colloidal and in a sol-gel matrix taken with low excitation intensity are shown in figure 1. Our spectra differs from that observed in PS and other Si colloids [6] in that our PL spectra show predominantly a strong and broad blue emission peaked near 415-460 nm, along with a weaker red luminescence peak near 680 nm. The red peak is similar to that observed in PS. The large Stokes shift for the red peak suggests that the emission originates from highly relaxed carriers. On the other hand, the blue emission may result from nonthermal carriers or from bandedge recombination. We will later present evidence that the blue and red peaks arise from different processes and species.

The blue peak in figure 1 resembles the blue peak observed at early times in time-resolved PL studies on as-prepared PS and PS oxidized to varying degrees[7]. In those studies, the as-prepared PS emission spectrum shows a blue peak at 460 nm at early times (~10 ns), which evolves to a red peak at 680 nm at longer times (~100 ns). If the oxidation level of the PS is

increased, the red peak diminishes, until, at high oxidation levels, only the blue peak is observed. The weaker red peak in our studies also resembles the red peak observed in these studies. With intermediate levels of oxidation, Ref. [7] observes both blue and red peaks coexisting at long times. This is similar to our spectra taken at low excitation intensities and suggests that our Si nanocrystals have a similar level of oxidation. This may be the result of limited ambient exposure of our samples and perhaps extensive ultrasonication treatment.

Figure 2 shows the dependence of the photoluminescence decay on the emission wavelength for the case of an acetonitrile colloid. Low repetition rate excitation (1 kHz, inter-pulse period = 1 ms) with 400 nm, ~150 fs laser pulses was used. Similar results are obtained in the sol-gel. The PL decays are exponential and nearly identical for all emission wavelengths. The decay times vary from 4.2-5.1 ns after deconvolution. This result is contrary to what is observed in PS and in other nanocrystalline Si systems. There, nonexponential PL decays are observed and the lifetimes of the red emission are microseconds and increases at longer wavelengths. We also varied the excitation intensity by a factor of 63 to study the effect on the emission decay and to assess the contribution from nonlinear processes such as bi-molecular kinetics or Auger-type processes. We found that the excitation intensity has little effect on the functional form of the decay at long times where the influence of the impulse response function of the photomultiplier is absent. This suggests that carrier density does not affect the PL decay. It is difficult, however, to draw conclusions near $t = 0$ due to the width of the impulse response function of the detection system (~1.5 ns).

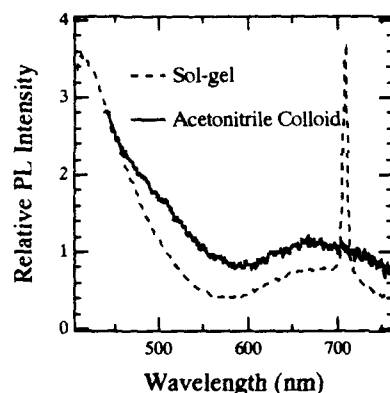


Figure 1. Photoluminescence spectra of Si nanocrystals in an acetonitrile colloid and in TEOS sol-gel matrix. The sharp peak at 710 nm is due to laser light.

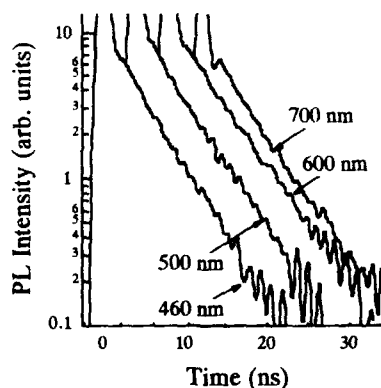


Figure 2. Dependence of photoluminescence decay on emission wavelength of Si nanocrystals in acetonitrile colloid. Low repetition rate excitation (1 kHz) was used.

If we repeat the experiment at a higher repetition rate (82 MHz, inter-pulse period ~ 12 ns), different results are observed. The data is shown in figure 3 and was taken with a synchroscan streak camera (resolution ~5 ps). We point out that excitations with lifetimes greater than the inter-pulse period are manifested as non-zero baselines, which are observable at $t < 0$. The longer the lifetime, the higher the baseline. Processes with lifetimes shorter than the inter-pulse period will appear essentially unaltered. By varying the inter-pulse period, different dynamics within the distribution of relaxation times exist. This is useful in studying systems where a broad distribution of relaxation times exist. Figure 3 clearly shows nonzero baselines indicating long-lived contributions to the ns PL decays observed in figure 2. The long-lived component may not be observable in figure 2 because of its small contribution and the lower repetition rate used. The long-lived component comprises only a small fraction of the decay and can be seen in figure 3 because of the accumulation effect possible with higher repetition rates. The long-lived

components behave the same within two spectral regions ranging from 450-550 nm and from 600-700 nm. These two regions coincide with the spectral regions for the blue and red PL peaks in figure 1. For the blue emission peak, the baselines are small and identical, indicating the same long-lived component. In contrast, the decays for the red emission peak have substantial baselines that increase with longer emission wavelengths. This indicates the contribution of very long-lived components with lifetimes that increase with longer emission wavelengths. It is conceivable that this corresponds to the microsecond-decaying red component observed in PS and other Si nanocrystalline systems.

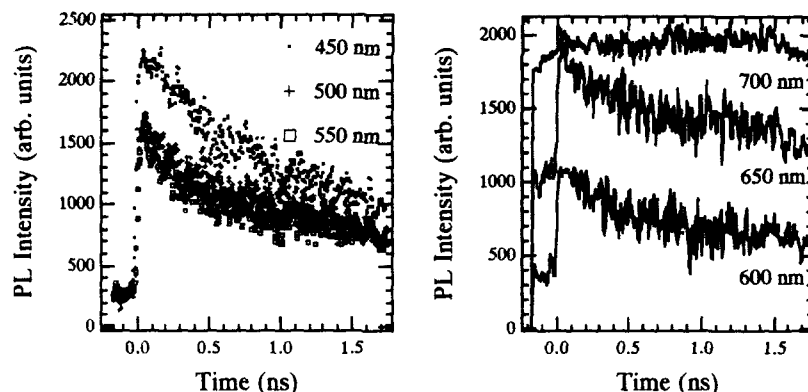


Figure 3. Dependence of the photoluminescence decay on emission wavelength for an acetonitrile colloid. High repetition rate excitation (82 MHz) was used.

Analysis of the data in figure 3 shows that the fast component of the decays can be fit to a variety of functional forms including exponential, bi-exponential, and stretched exponential. The ambiguity arises because of the short time scan and the signal-to-noise ratio. If bi-exponential decays are assumed, the fast components have time constants ranging from 120-290 ps and 1-2 ns, except for the decay at 450 nm. There, a bi-exponential fit gives 730 ps and 1.1 ns.

The data in figure 3 suggest that the blue and red emission originate from different processes. Our data show that the lifetimes within the blue peak change little with emission wavelength. This result would argue against quantum confinement being directly responsible for the blue emission. It has been suggested that this behavior is what would be expected from molecular species or extremely small inclusions of Si in an oxide matrix [7]. In contrast, the long lifetime component of the red emission increases as the emission wavelength increases. This can be interpreted within a variety of models such as quantum confinement, dispersive radiative tunneling between distributions of localized states, or recombination limited by carrier transport.

It is evident that our PL decay data is different than what is typically observed in PS and other nanocrystalline Si systems. Our data show that the predominance of the PL decay is exponential, occurs in ns, and is similar for all visible wavelengths. Long-lifetime components are present, but their contribution is small and discernible only with high repetition rates. It has been suggested that the microsecond lifetimes observed in PS and its increase with emission wavelength arise from nonradiative processes [8]. This involves the tunneling of carriers from confined zones toward more extended and less passivated regions where nonradiative recombination can occur. This model correctly predicts the PL lifetime variation with emission wavelength in PS. Though we observe long lifetime components that have similar wavelength dependencies, their contribution is small. This may be the result of the limited spatial extent of our nanocrystalline system, which fundamentally differentiates it from PS. As suggested by the HRTEM, the Si nanocrystals are either monodispersed or aggregated into small clusters of nanocrystals. As a result, tunneling into more extended and less passivated regions is limited. Most of the recombination occurs within a

single nanocrystal. Our observation of similar ns PL decays throughout the visible suggests that the recombination within the nanocrystal core may be via localized states in which transport of carriers is the limiting process.

Figure 4 shows the dependence of the PL spectra with the excitation intensity, where we have normalized the spectra to the height of the blue peak. The excitation consisted of 400 nm ~150 fs pulses. The range of excitation intensities extends from $<1 \text{ mW/cm}^2$ continuous wave to $\sim 319 \text{ MW/cm}^2$ peak intensity. A definite change in the spectra is seen. Increasing the excitation intensity increases the proportion of the blue peak at the expense of the red peak. This effect is not permanent and is reversible. There is no discernible shift in peak positions, as would be expected from a radiative tunneling mechanism between localized states. The spectral changes only involve the red and blue peaks. There is no smooth spectral transition that would involve, for example, a green peak. The red peak coincides with what is widely reported for the luminescence from PS. Figure 4 demonstrates that the states responsible for the blue and red emission can be accessed from each other.

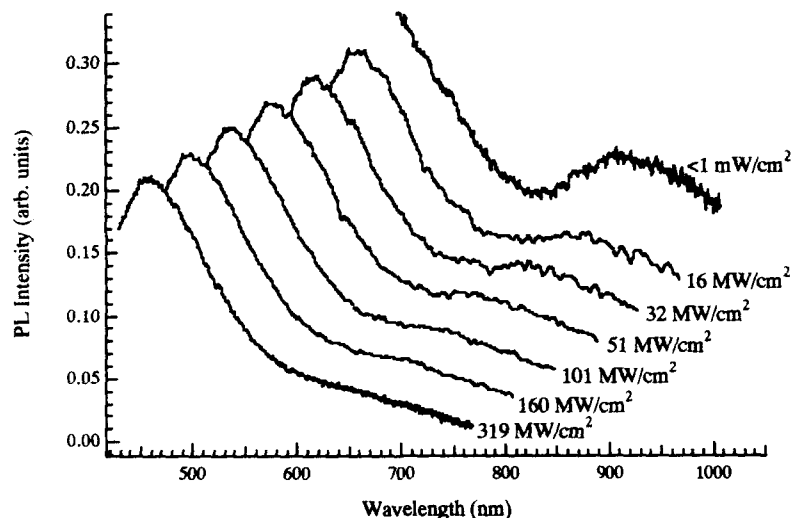


Figure 4. Dependence of PL spectra on the excitation intensity. The spectra have been offset to allow comparison.

We suggest the following model for the intensity-dependent PL spectra. Our data show that the blue transition has a faster emission rate than the red transition. Furthermore, carrier excitations can transfer between the states involved in the blue and red emissions. As a result, the states involved in the blue emission will behave as "sinks" for carrier excitations. This is because a higher percentage of excitations reaching the states involved in the blue emission will radiatively relax than in the red emission due to the faster blue emission rate. Since the red emission has slower rates, and since interchange between states involved in each transition can occur, this provides a method to "sink" excitation from the red to the blue emission. Therefore, at high excitation intensities, the states involved in the red emission will effectively saturate because of the lower emission rate. Consequently, as the excitation intensity increase, more and more emission will originate from the states involved in the blue emission. Within this model, the fast PL decay observed in figure 3 may possibly be interpreted as the transfer time from states responsible for red emission and states responsible for blue emission. This model is similar to the observation in

donor-acceptor pair recombination processes in which the peak of the emission shifts to higher energies as the excitation intensity increase [9].

As discussed above, it has been suggested that the blue luminescence originates from molecular Si species since the PL decays are exponential and the luminescence lifetimes are short and show little dependence on emission wavelength. It is also possible that the blue emission arises from extremely small Si crystallites imbedded in an oxide host. Small crystallites are required to account for the ns lifetime. This could occur during oxidation just before the Si is totally consumed and transformed into SiO_2 . This possibility has also been raised by others [7,10]. In support of this, it has been observed that only the blue peak will persist at high levels of oxidation [7]. This possibility is problematic to verify because of the difficulty in detecting small numbers of Si atoms in whatever structural form.

In summary, we observe red and blue PL peaks in Si nanocrystals in colloidal and sol-gel matrices similar to that observed in PS although with a greater proportion of the blue peak. Our results suggest that these peaks originate from different processes within different species, and that carrier excitations can interchange between the states responsible for the two emissions. Previous work showed that the peaks can dynamically evolve from one into another. We show that evolution of the peaks can occur by varying the excitation intensity. Our results also show that the predominance of the ns PL decay is exponential at all emission wavelengths, though there is a small contribution from long-lived components. The decay of the blue emission does not depend on the PL wavelength, though a small and wavelength-independent long-lived component is present. The decay of the red emission has a contribution from a wavelength-dependent long-lived component and a contribution from a fast-decaying component. It is suggested that the blue emission originates from Si molecules, or extremely small Si crystallites imbedded in an oxide host. Quantum confinement cannot directly account for the blue emission. Our results also suggest that recombination occurs predominantly within the nanocrystal core via localized states in which transport of carriers is the limiting process. Finally, there is no evidence for intensity-dependent decays, indicating that the PL dynamics are not carrier density dependent.

ACKNOWLEDGMENT

This work was performed under the auspices of the U. S. Department of Energy by Lawrence Livermore National Laboratory under contract No. W-7405-ENG-48 and supported in part by the National Science Foundation (DMR-9201041).

REFERENCES

- [1] L. T. Canham, *Appl. Phys. Lett.*, **57**, 1046(1990).
- [2] See, for example, *Mat. Res. Soc. Symp. Proc.* 298, (1993) or *J. Lumin.*, vol. **57**, 1993.
- [3] F. Koch, V. Petrova-Koch, and T. Muschik, *J. of Lumin.*, **57**, 271(1993).
- [4] R. A. Bley, S. M. Kauzlarich, H. W. H. Lee, J. E. Davis, *Mat. Res. Soc. Symp. Proc.*, This volume; S. Berhane, S. M. Kauzlarich, K. Nishimura, R. L. Smith, J. E. Davis, H. W. H. Lee, M. L. S. Olsen, L. L. Chase, *Mat. Res. Soc. Symp. Proc.* 298, 99(1993).
- [5] D. J. Duval, S. H. Risbud, Z. A. Munir, B. J. McCoy, *Mat. Res. Soc. Symp. Proc.* 298, 109(1993).
- [6] K. A. Littau, P. J. Szajowski, A. J. Muller, A. R. Kortan, and L. E. Brus, *J. Phys. Chem.*, **97**, 1224(1993); W. L. Wilson, P. F. Szajowski, and L. E. Brus, *Science*, **262**, 1242(1993).
- [7] D. I. Kovalev, I. D. Yaroshetskii, T. Muschik, V. Petrova-Koch, and F. Koch, *Appl. Phys. Lett.*, **64**, 214(1994) and references therein.
- [8] J. C. Vial, A. Bsiesy, F. Gaspard, R. Herino, M. Ligeon, F. Muller, R. Romestain, and R. MacFarlane, *Phys. Rev. B*, **45**, 14171(1992).
- [9] R. A. Street, *Hydrogenated Amorphous Silicon*, (Cambridge University Press, Cambridge, 1991).
- [10] C. Delerue, M. Lannoo, and G. Allan, *J. Lumin.*, **57**, 249(1993).

RARE EARTH/ORGANIC DYE NANOCOMPOSITES BY THE SOL-GEL METHOD.

Eric P. Bescher*, John D. Mackenzie*, Tomoko Ohtsuki* and Nasser Peyghambarian*,

*Department of Materials Science and Engineering, University of California Los Angeles, Los Angeles CA 90024

*Optical Sciences Center, University of Arizona, Tucson AZ 85721

ABSTRACT

This paper describes the processing of rare-earth/organic dye composites fabricated via three different sol-gel routes. In the first approach, low hydroxyl ormosil matrices were fabricated via reaction of a methyl-modified silicon halide with tertiary alcohol and subsequently doped with erbium iodide and a near-infrared dye. In the second approach, gels were made from tetramethoxysilane and doped with erbium complexes and dyes. In the third approach, a hybrid siloxane method was used. No Er^{3+} luminescence at 1.55 μm was observed in any of the three cases, mainly due to the strong absorption of the matrices centered around 1.4 μm . Fluorescence of Er^{3+} in the visible was observed in the first matrix, but no dye luminescence was detected. Dye luminescence was observed in the second type matrix, along with some reabsorption of the dye luminescence by Er^{3+} . In the third approach, neodymium exhibited optical activity in the near infrared, as well as the dye.

INTRODUCTION

Within the last few years, it has become apparent that the low processing temperature of sol-gel is an important advantage of the technique. Innovative hybrid organic-inorganic materials may now be processed, combining species within a solid matrix that would not have coexisted with conventional processing techniques. The prospects for synthesis of innovative materials with unique properties are indeed very exciting. For example, gels have been extensively investigated as matrices for a variety of organic moieties such as organic laser dyes, saturable absorbers, complexing agents, enzymes, proteins, photochromes, molecules with large optical non-linearities, polymeric chains, etc.[1].

Gels have also been explored as possible hosts for optically active inorganic species such as lanthanides[2]. Therefore, it seemed interesting to study the combination of both optically active organic and inorganic species within the same matrix, a combination which only the sol-gel process allows. Such a material could have interesting properties, for example in terms of energy transfer between both species. The strong absorption of organic dyes over a wide spectrum range could have technological advantages as sensitizer of Er^{3+} , which has a small absorption cross-section at near-infrared wavelengths. An increase in Tb^{3+} luminescence due to co-doped Coumarin was observed by Genet et al in thorium phosphate gels [3].

In this work, we investigate three matrices for rare-earths and organic dyes in terms of luminescence quenching and dye stability. Three approaches were selected for matrix processing: non-hydrolytic ormosils, rare-earth complex doped gels, and mixed siloxanes gels.

GEL PREPARATIONS

Non hydrolytic gels

Non-hydrolytic ormosils were processed in a Schlenk line under nitrogen according to a technique described elsewhere [4]. Methyltrichlorosilane was reacted with tertiary butanol (Aldrich Chemicals). The solution was doped with anhydrous erbium iodide (99.99%, Aldrich Chemicals) prior to gelation, as well as with IR 125 and HITC in dimethyl sulfoxide (DMSO, Aldrich Chemicals). Gels were cast in glass vials and dried at room temperature under nitrogen.

Er-complex doped gels

Erbium(fod) was obtained from Aldrich. The matrix material was processed by mixing tetramethoxysilane (1 mole) with methanol (4). Dimethyl aminopyridine (0.01 mole) dissolved in water (4 moles) was added dropwise. The solutions were doped with Er complex and the infrared dye dissolved in ethanol. The gels were cast in glass vials were dried at room temperature

Mixed siloxanes

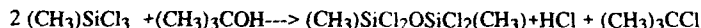
A modification of a method described by Koslova et al [7] was used. Methyl-diethoxysilane (MDES, Petrarch Chemicals, 1 mole) was mixed with water (1 mole). Rare earth (Nd,Er) methoxyethoxides in methoxyethanol were purchased from Gelest. The methoxyethoxides were refluxed with Zr-n-propoxide (Fluka, 1 to 9 molar ratio) before being added to the prehydrolyzed MDES solution. The dyes in ethanol were added after the evolution of H₂ gas subsided. The solution was coated onto a glass substrate several times in order to obtain films of about 100 micrometers thickness.

HITC, DTTC and IR 125 infrared dyes were obtained from Exciton.

RESULTS AND DISCUSSION

Low hydroxyl Ormosils

The reaction of tertiary alcohols with silicon halides has been previously described [5]. Whereas the reaction of silicon halides with primary or secondary alcohols leads to the formation of silicon alkoxides, the case of tertiary alcohols is somewhat different. The formation of a Si-O-Si network follows the overall reaction



through cleavage of an O-R bond rather than the Si-O bond. This effect stems from a strong donor effect stabilizing a carbocation in t-butanol. Our preliminary research has indicated that the reaction proceeds even if one chlorine is substituted by a methyl. Non-reactive CH₃ groups decrease the possibility of OH bond formation through reaction with the atmosphere, increase the hydrophobicity of the matrix, and allow the processing of materials with tailorable mechanical properties. The properties of the matrix are described in greater detail elsewhere [4]. The IR spectra in the region of OH vibration shows a drastically reduced OH concentration compared to conventional materials (Fig.1).

Er³⁺ luminescence was observed in a low-hydroxyl CH₃SiO_{1.5} around 550 nm when pumped at 488 nm (Fig.2). However, no infrared luminescence was observed with 800 nm pumping.

Luminescence of the infrared dye could not be observed in these materials. This was ascribed to the acidity of the matrix which damaged the dye. Attempts to backfill the dried gel with the dyes in an ethanol solution failed because of the hydrophobicity and pore size of the matrix.

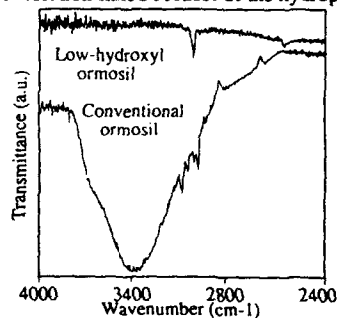


Figure 1- FTIR spectra of conventional (Vinyltriethoxysilane) and non-hydrolytic Ormosils

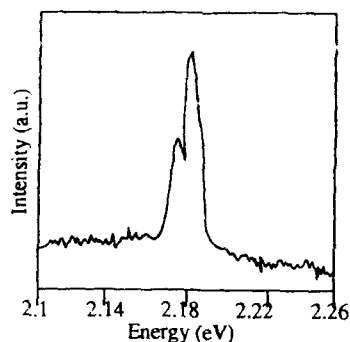


Figure 2. Luminescence of Er^{3+} in a low hydroxyl $\text{CH}_3\text{SiO}_{1.5}$

Rare-earth complexes-doped gels

Europium complexes have been reported to exhibit luminescence in the visible in sol-gel matrices [6]. This behavior is linked to the shielding effect of the large ligands surrounding the trivalent rare-earth which render the $4f$ electrons less sensitive to surrounding OH (Figure 3). It appeared interesting to investigate the optical properties of Er complexes in gels. Because acidity is detrimental to dye stability, the gels were catalyzed with dimethylaminopyridine. The solutions gelled in 12 minutes. Owing to the presence of DMAP, the infrared dyes remained stable in the matrix for several weeks.

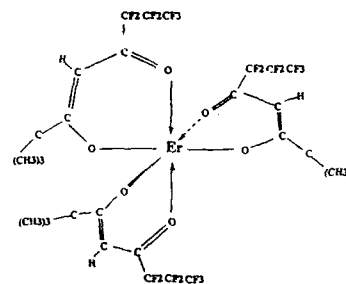


Figure 3- Er (fod) complex

Figure 4 shows the emission spectrum of DTTC with a dip at 800 nm ascribed to reabsorption of the dye luminescence by the rare-earth.

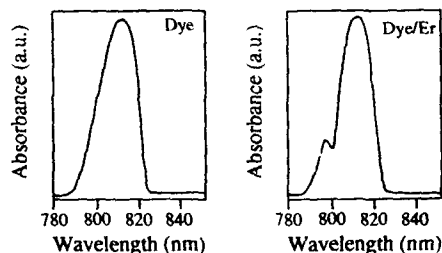
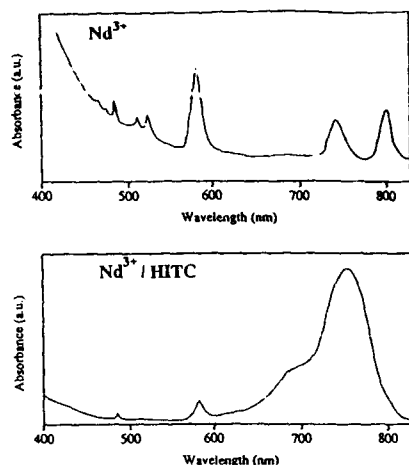


Figure 4- Reabsorption of dye luminescence by Er^{3+} at 800 nm.



Hybrid siloxanes have been shown to be promising materials for rare-earth luminescence, in part because the matrix may be tailored to be hydrophobic and expel luminescence-quenching water molecules [7]. They also have the advantage of not requiring acid catalysis, to which near-IR dyes are greatly sensitive. In zirconia-catalyzed siloxanes, the color of IR dyes remains unchanged, blue-green, indicating a greater stability in these matrices than in conventional acid-catalyzed gels. Figure 5 shows the absorption spectrum of Nd^{3+} -doped ormosil for a Nd^{3+} concentration of ca. 10^{21} Nd^{3+}/cc . The absorption lines are broad, which is characteristic of a disordered material. When the Nd^{3+} /HITC dye composite gel was excited at 800 nm Nd^{3+} luminescence was observed with the broad band luminescence from HITC (Fig.6). However, the luminescence from HITC decreased during the measurement due to the photodegradation of the dye molecule.

Figure 5- Absorption of Nd^{3+} -doped and HITC/ Nd^{3+} doped siloxanes

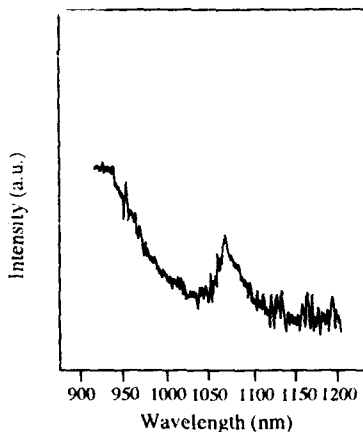


Figure 6. Luminescence spectrum of Nd^{3+} co-doped with HITC. The broad luminescence is from HITC.

The relatively weak luminescence of Nd^{3+} indicates a decrease in lifetime of the $^4\text{F}_{3/2}$ state due to concentration quenching.

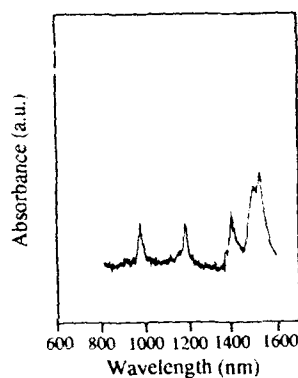


Figure 7 -Absorption of the Er^{3+} -doped mixed siloxane matrix in the near IR.

It is noteworthy that under pumping at 800 nm, luminescence of Er^{3+} doped materials was not observed at 1.55 micrometers. During our investigation on the causes of this behavior, we measured the near IR absorption characteristics of the gels, and noticed two absorption peaks centered at 1.19 and 1.4 μm due to matrix absorption, in addition to Er^{3+} peaks at 980 nm and 1550 nm (Fig.7). Similar peaks were observed for Nd^{3+} doped materials but they are sufficiently away from 1.06 microns to not affect Nd^{3+} luminescence. It is particularly interesting to note that these peaks were also observed in the case of the non-hydrolytic gels and Er-complex doped gels with even stronger absorption, which seems to indicate that they could be related to overtones of CH_3 vibrations.

CONCLUSIONS

Three different routes were explored for the fabrication of rare earth-organic dye composites as the host matrices to investigate optical activities of rare-earth and organic dye composite system in the near infrared region. No Er^{3+} luminescence was observed in all three cases mainly due to the strong absorption of the matrices centered around 1.4 μm . In low hydroxyl $\text{CH}_3\text{SiO}_{1.5}$ Ormosils, the low OH concentration allowed fluorescence of the dye in the visible but the acidity of the matrix was detrimental to the stability of the dye. In erbium complex/ IR dye composites, reabsorption of dye luminescence by the rare-earth was observed. In hybrid siloxanes, both Nd^{3+} and dye showed luminescence in the near IR. The hybrid siloxane was shown to be a promising system to investigate the properties of Nd^{3+} and dye in the near IR.

REFERENCES

- 1-Sol-Gel Optics II (1992) Proceedings, Volume 1758, Ed. J.D. Mackenzie
- 2-E.J.A. Pope and J. D. Mackenzie, J. Am. Ceram. Soc., Vol 76, No. 5 (1993), pp.1325-1328.
- 3- M. Genet, V. Brandel, M.P. Lahalle, E. Simoni, , SPIE Vol 1328 Sol-Gel Optics (1990) pp.194-200
- 4-S.K. Yuh, E. Bescher, and J.D. Mackenzie, Mat. Res. Soc. Symp. Proc
- 5-R.J. P. Corriu, D. Leclercq, P. Lefevre, P.H. Mutin and A. Vioux, , J. Non-Cryst. Solids, 146 (1992) 301-303.
- 6-L.R. Matthews and E.T. Knobbe Materials Research Society Symp. Proc. Volume 286, 1993, pp.259-264
- 7-N.I. Koslova, B. Viana and C. Sanchez, J. Mater. Chem 3(1) 1993, pp.111-112

ACKNOWLEDGMENTS

The authors wish to acknowledge the support of the Air Force Office of Scientific Research, Tom Erstfeld Program Director.

NANOSIZED METAL PARTICLES BY CONTROL OF THE METAL DISPERSION DURING SOL-GEL PROCESSING

ULRICH SCHUBERT^{*,+}, CLAUS GÖRSMANN^{*}, STEFAN TEWINKEL^{*}, ANDREAS KAISER^{**} AND THOMAS HEINRICH^{**}

^{*}Institut für Anorganische Chemie der Universität, Am Hubland, D-97074 Würzburg

^{**}Fraunhofer-Institut für Silicatforschung, Neunerplatz 2, D-97082 Würzburg, Germany

ABSTRACT

The previously developed method to prepare highly dispersed metals in SiO₂ by sol-gel processing of metal complexes containing alkoxysilyl-substituted ligands was extended to the preparation (i) of bimetallic particles in SiO₂ and (ii) of highly dispersed metals in TiO₂.

INTRODUCTION

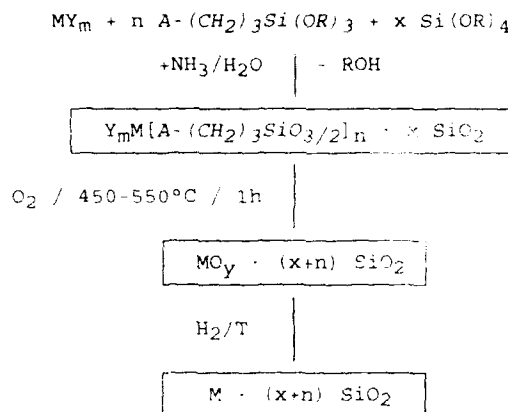
Contrary to conventional methods for the preparation of highly dispersed metals [1] on oxidic supports (impregnation, precipitation), the sol-gel process [2] allows the preparation of nanosized metal particles with narrow particle size distributions and adjustable metal loadings. The inherent advantages of this process can additionally be exploited, such as the tailoring of the microstructure of the oxide matrix, or the preparation of sols with a defined rheology suitable for coatings.

The key to control the metal particle size is the maximum dispersion of the metal precursor during the sol-gel step. Anchoring of the metal precursor to the support via Si-O-M links (M = transition metal) was very successful in several cases [3,4]. We developed a more general method of anchoring metal complexes to gels, by using the readily available compounds (RO)₃Si-X-A. Instead of linking the metal atom to the silicate network by an oxo bridge, organic groups are used. The group A is an organic function capable of coordinating to metal atoms. X is a chemically inert spacer, for instance a (CH₂)_n chain. The link M-A-X-Si is easily chemically adjusted to the requirements of a particular metal or to particular reaction conditions.

The dispersed metals were prepared by a three-step procedure, as previously reported [5,6] (Scheme 1). In the first step a solution of a metal salt, a silane of the type A(CH₂)₃Si(OR)₃ (A = NH₂, NHCH₂CH₂NH₂, CN, [CH₃(O)C]₂CH, etc.) and Si(OR)₄ was processed by the sol-gel method. The functional organic groups of the starting silane coordinate to the metal ions, and the resulting metal complexes are anchored to the silicate matrix during sol-gel processing. Aggregation of the metal ions is thus prevented. By the M:Si ratio of the starting

⁺ New address: Institut für Anorganische Chemie der Technischen Universität Wien, Getreidemarkt 9, A-1060 Wien, Austria

compounds the later composition of the composite is determined. In the second step the metal complex-containing gels are dried and then heated in air to oxidize all organic moieties. Due to the high dispersion of the metal ions in the first step, small metal oxide particles are formed, which are then reduced to metal particles having diameters of a few nm.



Scheme 1: Preparation of highly dispersed metals in SiO_2 via organo(alkoxy)silanes (A = functional group to bind the metal ion; X = spacer; Y = counterion).

The metal particle size mainly depends on the kind of metal, the reaction conditions, the nature of the organic anchoring group, and for some metals also on the metal loading [5]. The obtained metal particles are highly dispersed and homogeneously distributed *throughout* the SiO_2 matrix. They are not agglomerated, and their diameters are very small and uniform, even in the materials with high metal loadings. The particle size distributions are very narrow.

Bimetallic particles [7] on inorganic supports are conventionally prepared by the same methods as monometallic particles. However, we do not know about any attempts to prepare bimetallic particles by the sol-gel method. Several investigations showed that the kind of metal precursors and the reaction conditions have a pronounced influence on the composition of bimetallic particles. A close contact between the different metals during all stages of the preparation process generally favours the formation of truly bimetallic particles.

We report two extensions of this method: the preparation of bimetallic particles in SiO_2 and of highly dispersed metals in ceramic matrices other than SiO_2 .

RESULTS AND DISCUSSION

Bimetallic particles

We applied the $(\text{RO})_3\text{Si-X-A}$ method (Scheme 1) to mixtures of two different metal ions. The composites $\text{CuRu} \cdot 30 \text{ SiO}_2$ and $\text{Pd}_z\text{Ni}_{(1-z)} \cdot 15 \text{ SiO}_2$ (for different Ni : Pd ratios) were

prepared from the corresponding metal acetates or acetylacetonates, $(\text{EtO})_3\text{Si}(\text{CH}_2)_3\text{-NHCH}_2\text{CH}_2\text{NH}_2$ and $\text{Si}(\text{OEt})_4$ by the same procedure as the monometallic composites. Very small metal particles with narrow size distributions were again obtained: the mean particle diameter (determined by TEM) was 1.6 nm for $\text{CuRu} \cdot 30 \text{ SiO}_2$. A bimodal particle distribution was found for $\text{Pd}_2\text{Ni}_{(1-z)} \cdot 15 \text{ SiO}_2$ (mean diameters 5 nm and 17 nm) [8] as for monometallic $\text{Ni} \cdot y \text{ SiO}_2$ composites in an intermediate range of y (2 - 5.5).

Ni and Pd form solid solutions for any Ni/Pd ratio. Therefore, the particle composition can be determined from the f.c.c. lattice constants, obtained by electron diffraction (the electron probe being focused on individual particles). Since the presence of Ni allows thermomagnetic investigations, the metal particle composition (from the Curie temperatures) and the metal particle diameter (from the experimental FMR intensity) were independently determined. Both methods gave a sufficiently good agreement for both size and composition of the alloy particles [8].

The smaller particles had about the nominal composition while the larger particles were richer in Pd. By simulation of the FMR powder spectra a third, Pd-rich, composition was identified (for $\text{Pd}_2\text{Ni}_{(1-z)}$ with $z \geq 0.3$) [8]. To balance the starting composition, there has to be additional nickel in the bulk of the material. Since these nickel species were neither seen by electron diffraction nor by FMR spectroscopy, they must be nickel silicate species. Incomplete reduction of the less noble metal is not unusual for bimetallic metal particles on solid supports.

CuNi composites having the overall composition $\text{Cu}_{0.6}\text{Ni}_{0.4} \cdot (x+n) \text{ SiO}_2$ were prepared as the PdNi alloy particles, starting from the metal acetates, 5 molar equivalents $(\text{EtO})_3\text{Si}(\text{CH}_2)_3\text{-NHCH}_2\text{CH}_2\text{NH}_2$ (n in Scheme 1) and 0 to 10 molar equivalents of $\text{Si}(\text{OEt})_4$ (x in Scheme 1). Ni and Cu also form solid solutions for any ratio. The appearance of shoulders on the X-ray diffraction peaks of the composites indicate an inhomogeneous alloy formation and the presence of at least two alloy compositions. Satisfactory fits were obtained by using two analytical Pearson VII functions combined with a least squares optimization algorithm [9]. The average alloy compositions were then calculated from the obtained lattice constants. One phase was richer in Ni than the nominal composition, but the fraction of Ni changed with the metal loading. The composition was $\text{Cu}_{0.45}\text{Ni}_{0.55}$ for $x = 0$, and $\text{Cu}_{0.15}\text{Ni}_{0.85}$ for $x = 10$. Intermediate compositions were found for intermediate x . A second phase was Cu-rich, but the fraction of Ni also increased with increasing x ($\text{Cu}_{0.9}\text{Ni}_{0.1}$ for $x = 0$, and $\text{Cu}_{0.6}\text{Ni}_{0.4}$ for $x = 10$). In order to balance the starting composition, there has to be additional copper. Since Cu is more easily reduced than Ni, we suppose that there were additional Cu particles (or Cu-rich alloy particles) which were too small to be detected by XRD.

Only triclinic CuO (tenorite) and cubic NiO (bunsenite) were found as crystalline components after the oxidation step by XRD. This is not surprising owing to the low mutual miscibility of the oxides. The crystallite diameters of the oxide particles (between 15 and 30 nm) were calculated with Scherrer's formula from the half-widths of the X-ray reflections.

To find out how the alloy particles develop, we performed in situ reduction experiments in a high-temperature diffractometer. The metal oxide-containing composite was uniformly distributed on a Pt foil, and heated from 100 to 250°C in 10° steps under an atmosphere of 10 vol% H_2 and 90 vol% N_2 . Diffractograms were taken in certain intervals (Figure 1).

The reflections at 35.6° and 38.8° are assigned to CuO, the reflections at 37.3° and 43.3° to NiO. A reflection of metallic Cu coincides with the 43.3° reflection of NiO. CuNi

alloy particles cause reflections between 43.3° (100% Cu) and 44.6° (100% Ni), depending on their composition.

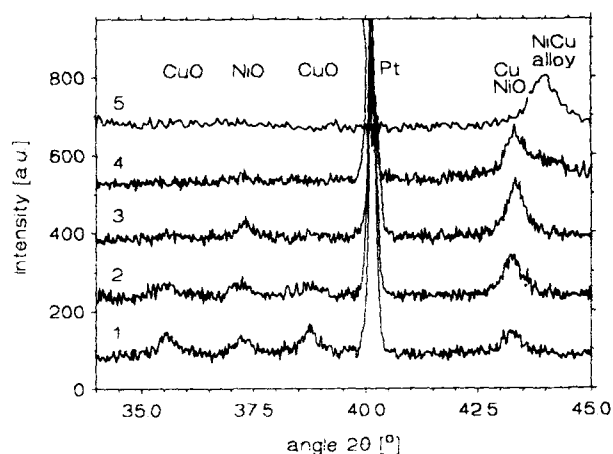


Figure 1. Reduction of $(\text{Cu}_{0.6}\text{Ni}_{0.4})\text{O} \cdot 6 \text{SiO}_2$ by H_2 / N_2 (1:9) in a HT-XRD experiment. Trace 1: 120°C , 10 min. Trace 2: 150°C , 10 min. Trace 3: 150°C , 120 min. Trace 4: 200°C , 10 min. Trace 5: 500°C , 120 min, pure H_2 .

CuO was first reduced upon treatment with H_2 , as seen by the weakening of the CuO reflections and an increase in intensity of the 43.3° peak starting at 150°C (trace 2). NiO was only reduced above 200°C (trace 4). While the reflection at 37.3° disappeared, a shoulder at 43.9° developed. Since no reflection of pure Ni was observed, the reduced nickel is immediately alloyed. Similar results were also found for CuNi particles on silica, prepared by impregnation or coprecipitation methods [10]. Relatively homogeneous alloy particles (average diameter $16 \pm 5 \text{ nm}$) were only obtained if the composite was held at 500°C for 2 h in a pure H_2 atmosphere (trace 5).

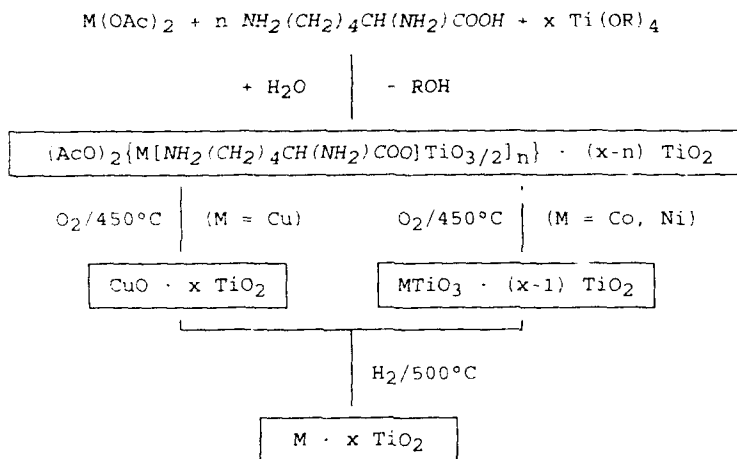
The low miscibility and the different reducibilities of the two metal oxides act against a homogeneous alloying of the two metals. When the metal loading is low, the Cu particles (which are formed first) are more segregated from each other and from the NiO or Ni particles. The longer diffusion pathways obviously impede the effective formation of an alloy. This results in the formation of Ni -rich alloy particles along with (undetected) highly dispersed Cu (or Cu -rich alloy). At higher temperatures alloying is of course more effective.

The results obtained so far with bimetallic particles in SiO_2 show that the intimate mixing of the two metals during sol-gel processing is not sufficient to maintain a close contact during the oxidation and reduction step. Therefore, future efforts have to be focussed on optimizing the calcination step to obtain a better homogeneity in the oxide stage.

Metal / TiO₂ Composites

The general approach for the preparation of metal/SiO₂ composites shown in Scheme 1 is also suitable for the preparation of highly dispersed metals in other oxide matrices, such as Al₂O₃, TiO₂ or ZrO₂. Since Al-C-, Ti-C- or Zr-C bonds are not hydrolytically stable, the grouping M-A-X-E (E = Al, Ti, Zr etc.) must have another chemical composition as for E = Si.

When metal alkoxides are reacted with carboxylic acids or β-diketones, part of the alkoxide groups is substituted by carboxylate or β-diketonate groups. Upon addition of water the remaining alkoxy groups are preferentially hydrolyzed, while coordination of the carboxylate or β-diketonate group is retained. We have previously shown that *functional* carboxylic acids or β-diketones can also be used [11]. Diamino acids turned out to be particularly suitable for the preparation of metal/ceramic composites.



Scheme 2: Preparation of highly dispersed metals in TiO₂ from metal acetates by using lysine to coordinate the metal ions and to bind the obtained metal complexes to the TiO₂ gel.

One oxygen atom of the carboxylate unit and the α-amino group chelate the hydrolyzable metal alkoxide moiety (E(OR)_p) [12], while the terminal amino group coordinates to the metal ions. With lysine, H₂N(CH₂)₄CH(NH₂)COOH, well-defined aminocarboxylate complexes of the type H₂N(CH₂)₄CH(NH₂)COO(E(OR)_p) were obtained upon reaction with Ti(OR)₄ (R = Et, Pr, Bu). Zr(OPr)₄ or Al(OBu)₃. The amino end of these modified alkoxides reacted with metal salts as primary amines to give the ammine complexes {M[NH₂(CH₂)₄CH(NH₂)COO(E(OR)_p)]_n}^{m+}. These complexes are employed as precursors for sol-gel processing, similar to the silicon compounds {M[NR₂(CH₂)₃Si(OR)₃]}^{m+}. The preparation of the metal/ceramic composites (Scheme 2 for metal/TiO₂) is basically the same as for metal/SiO₂ (Scheme 1).

When calcination in air is carried out at 450°C, the organic groups are completely removed, and an anatase matrix is formed. Oxidation temperatures higher than 550°C result in the appearance of rutile. With copper as the transition metal, CuO particles are formed, as in the silicate system. Contrary to this, the titanates $MTiO_3$ are formed starting from cobalt or nickel acetate. Reduction with H_2 at 500°C results in highly dispersed metals, independent of the composition in the oxide stage (Scheme 2). From the line broadening in the XRD spectra, average particle diameters of 12 nm were calculated for $Co \cdot 6 TiO_2$, 9 nm for $Ni \cdot 6 TiO_2$, and 21 nm for $Cu \cdot 4 TiO_2$.

CONCLUSIONS

Our method for the preparation of highly dispersed metals on oxidic supports by using organic ligands for coordination of metal ions and for anchoring the metal complexes during sol-gel processing, which was previously developed for monometallic particles on SiO_2 , appears to be very general. It can also be applied to control the metal particle size distribution in bimetallic particles. By proper modification of the organic spacer group the metal dispersion on ceramic materials other than SiO_2 can be controlled as well.

ACKNOWLEDGEMENTS

This work was supported by the Deutsche Forschungsgemeinschaft and the Fonds der Chemischen Industrie.

REFERENCES

1. W. Romanowski, Highly Dispersed Metals (Ellis Horwood Publ., Chichester, 1987).
2. C.J. Brinker, G. Scherer, Sol-Gel-Science, the Physics and Chemistry of Sol-Gel Processing (Academic Press, Boston, 1990).
3. Selected articles: K. Tohji, Y. Udagawa, S. Tanabe, A. Ueno, J. Am. Chem. Soc., **106**, 612 (1984). H. Tamagawa, K. Oyama, T. Yamaguchi, H. Tanaka, H. Tsuiki, A. Ueno, J. Chem. Soc. Faraday Trans. I, **83**, 3189 (1987).
4. Selected articles: T. López, M. Villa, R. Gómez, J. Phys. Chem., **95**, 1690 (1991). T. López, P. Bosch, M. Morán, R. Gómez, J. Phys. Chem., **97**, 1671 (1993).
5. B. Breitscheidel, J. Zieder, U. Schubert, Chem. Mater., **3**, 559 (1991).
6. U. Schubert, B. Breitscheidel, H. Buhler, C. Egger, W. Urbaniak, Mat. Res. Soc. Symp. Proc., **271**, 621 (1992).
7. J.H. Sinfelt, Bimetallic Catalysts (J. Wiley, New York, 1983).
8. W. Mörke, R. Lamber, U. Schubert, B. Breitscheidel, submitted to Chem. Mater.
9. S.A. Howard, R.L. Snyder, Mat. Sci. Res., **19**, 57 (1984).
10. S.D. Robertson, S.C. Kloet, W.M.H. Sachter, J. Catal. **39**, 234 (1975).
11. U. Schubert, H. Buhler, B. Hirle, Chem. Ber., **125**, 999 (1992). H. Buhler, U. Schubert, Chem. Ber., **126**, 405 (1993).
12. U. Schubert, S. Tewinkel, F. Möller, unpublished crystallographic results.

NANO-SIZE SILICON WHISKERS PRODUCED BY CHEMICAL VAPOR DEPOSITION

Lu Shen,¹ Youming Xiao,¹ Ying Ma,¹ Francis S. Galasso,¹ Steven L. Suib^{1,2,3*} and James D. Freihaut⁴

¹U-60, Department of Chemistry, University of Connecticut, Storrs, CT 06269-3060

²Institute of Materials Science, University of Connecticut, Storrs, CT 06269

³Department of Chemical Engineering, University of Connecticut, Storrs, CT 06269

⁴United Technologies Research Center, Silver Lane, East Hartford, CT 06108

ABSTRACT

Sponge type deposits composed of nanometer sized Si whiskers were formed on Davisil (porous SiO_2) gel substrates by chemical vapor deposition (CVD) using methyltrichlorosilane (MTS) as a precursor and H_2 as carrier gas. The diameters of the fine whiskers are estimated to be 100 nm or smaller from SEM observations. XRD analyses revealed that the coatings formed at 800 and 900°C contained microcrystalline Si and the Auger analysis indicated the existence of free carbon. The surface area of the coated Davisil was approximately $189 \pm 5 \text{ m}^2/\text{g}$, as obtained from BET measurements. The coatings were also applied on several other substrates, such as AlN and low surface area ($< 224 \text{ m}^2/\text{g}$) silica gel, with the same coating conditions. On these substrates, highly porous Si has also been observed on AlN substrates, and nonporous, half sphere shaped coatings were observed on low surface area silica gel substrates.

INTRODUCTION

In recent years the syntheses and properties of submicrometer ($100 \text{ nm} < \text{diameter} < 1 \mu\text{m}$) and nanoscale ($1 \text{ nm} < \text{diameter} < 100 \text{ nm}$) particles have aroused tremendous interest.¹⁻⁶ Both submicrometer and nanoscale particles find wide applications in different areas, such as catalysis, ceramics, electronics, optical devices. Nanophase titania (TiO_2) is a better catalyst than conventional forms of titania in removing

*To whom all correspondence should be addressed.

sulfur⁷. Nanophase ceramics can be more ductile than traditional ceramics at low temperature¹, and nanophase metals can be much harder than large grained metals. Polymer composite consisting of nanosize iron oxide particles have unusual optical and magnetic properties.⁷ It is also possible to make quantum dots and quantum wells by manipulation of nanoscale materials which can control the movement of single electrons which can result in new developments in the electronics industry.⁸ Various synthetic methods have been developed to make ultrafine particles including physical vapor deposition (PVD),⁹⁻¹⁰ solution methods (sol-gel process, solvated metal atom dispersion),¹¹⁻¹³ mechanical milling of solid phases, and self-assembling methods.¹⁴

In this study, chemical vapor deposition methods were employed to deposit ultrafine porous silicon on different substrates. It has recently been discovered that porous silicon can emit visible light.¹⁵⁻¹⁷ This is a very important discovery since it demonstrates that silicon has the potential to be used as photoelectronic material. Nanostructured materials usually have very large surface areas, thus porous nanoscale silicon also has the potential applications in photocatalysis.

EXPERIMENTAL

1. Chemical vapor deposition of Si (or SiC):

The deposition of Si was conducted at atmospheric pressure at temperatures between 800°C and 1100°C. Methyltrichlorosilane (MTS) was used as the precursor with H₂ as the carrier gas. The flow rate of H₂ was varied from 21 mL/min to 72 mL/min and the deposition time used varied from 40 min to 1 hour. The substrates used in this study are Davisil porous silica gel (grade 6461, 35-60 mesh, pore sizes are 15 nm, Aldrich Chemical), AlN (lab made) and low surface area silica gel (28-200 mesh, Fisher Scientific).

2. Characterization:

Scanning electron microscopy (AMRAY, 1810D) was employed to investigate the morphologies of the coatings and to estimate the sizes of

the particles or whiskers. The structure and the crystallinity of the coatings as well as the substrates were studied by X-ray diffraction using a Scintag PDS 2000 diffractometer with a monochromatic X-ray beam and scintillator. Cu K α radiation was used at a current of 40 mA and a voltage of 45 kV. X-ray photoelectron spectroscopy (XPS) and Auger electron spectroscopy (AES) were used to study the chemical compositions of the coatings. The surface areas of the coated materials were measured by the BET method using N₂ as the adsorbant.

RESULTS AND DISCUSSION

1. Deposits on Davisil (porous SiO₂) gels.

XRD studies indicate that as-received Davisil (SiO₂) gel is amorphous, and remains amorphous even after being heat treated at 900°C in air for 40 min. Several experiments were designed to explore the optimum experimental conditions to form nanometer sized Si whiskers on Davisil substrates. In atmospheric pressure CVD reactors, the major variables are: deposition temperature, flow rates of reactants and the deposition time.

It was found that the reaction temperature was critical for the formation of Si whiskers. A H₂ flow rate of 19-80 mL/min and a deposition time of 5-60 min were used and the deposition temperature was varied from 700°C to 1050°C. No deposition was formed at 700°C while at 800°C and 900°C, Si whiskers were formed on the surface of Davisil gels with few particles (Fig. 1a & 1b). The diameters of whiskers formed at 800°C were estimated to be less than 100 nm by the SEM observation. The diameters of whiskers formed at 900°C, however, ranged from 100 nm or less to about 500 nm.

At higher temperatures, 1000 and 1050°C, almost no Si whiskers were formed as can be seen in the scanning electron micrographs (Fig. 1c).

The XRD data indicate that the deposits formed at 800°C and 900°C on Davisil contained crystalline silicon (Fig. 2a & 2b). The deposits formed at 1000°C and 1050°C, however, were amorphous as revealed by the XRD data (Fig. 2c & 2d). The X-ray line broadening calculation



Fig. 1. Scanning electron micrographs of Si deposits on Davisil at (a) 800°C, (b) 900°C, (c) 1000°C and (d) 1050°C.

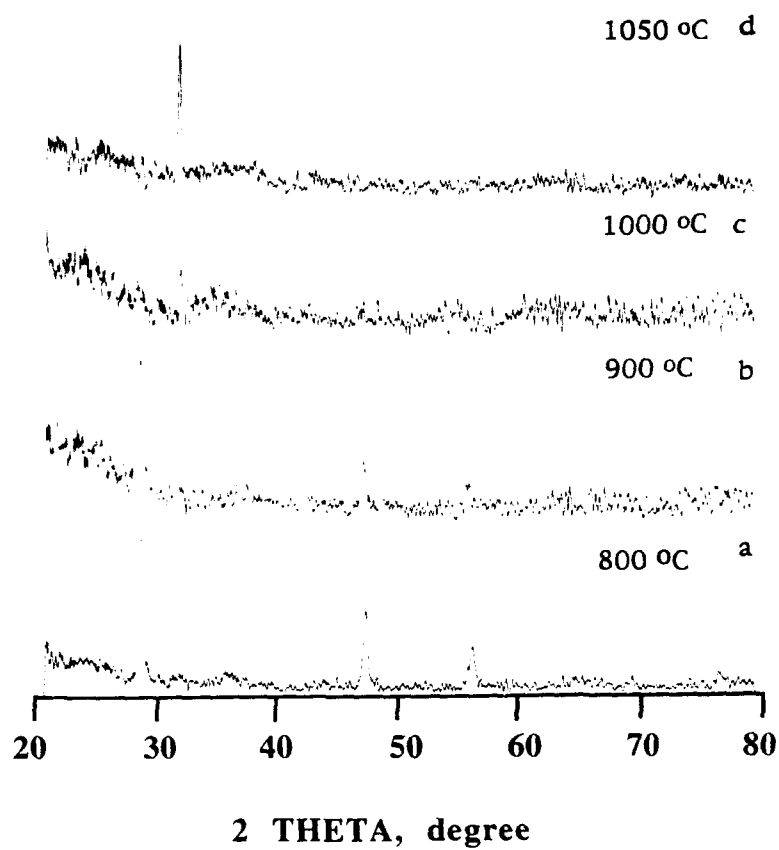


Fig. 2. X-ray diffraction of (a) Si deposits on Davisil at 800°C; (b) Si on Davisil at 900°C; (c) Deposits on Davisil at 1000°C and (d) deposits on Davisil at 1050°C.

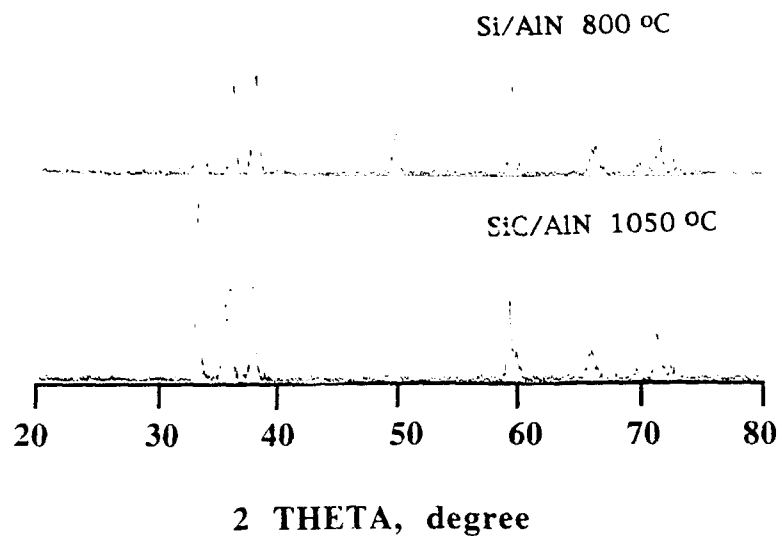


Fig. 3. X-ray diffraction of (a) SiC deposits on AlN at 1050°C and (b) amorphous Si deposits on AlN at 800°C.

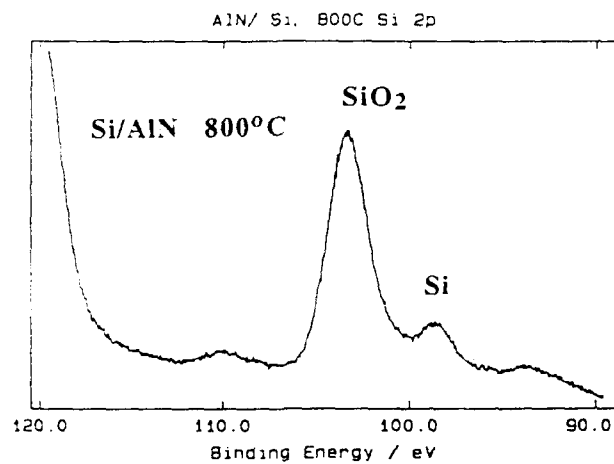


Fig. 4. XPS detailed scan of Si 2p peak from Si coated AlN at 800°C showing the existence of elemental Si.

indicates that the Si whiskers formed at 800 and 900°C has particle sizes ranged around 120 Å.

The flow rate of H₂ with MTS and the deposition time also have a direct impact on the formation of Si whiskers. It was found that at high flow rates and long deposition times, amorphous particulate form of deposits are produced.

The surface area of as-received Davisil is 224 m²/g, and it decreased to 185 m²/g after being heated in flowing N₂ at 900°C for 40 min. The surface area of whisker Si coated Davisil was 189 m²/g which is evidently close to that of heated Davisil. All the surface area measurements were conducted on the same BET apparatus.

2. Deposits on other substrates.

In order to study the effect of substrates on the formation of Si whiskers, several different materials such as AlN and low surface area SiO₂ gels were used as substrates. The coating conditions were kept the same as that for coatings on Davisil.

The deposits formed at 1050°C on AlN substrate contained microcrystalline β-SiC (Fig. 3a) which is evidence by the split of peaks. However, the deposits formed at 800°C on AlN substrates were amorphous (Fig. 3b) since all the peaks correspond to AlN with no noticeable peak splitting. XPS studies showed the existence of Si on the surface of coated AlN (Fig. 4). The deposits formed on AlN at 800 and 1050°C both appeared to be porous, even though they may not be in a whisker form (Fig. 5a & 5b) but in a particulate form.

On low surface area silica gel, which has much higher density than Davisil, half spherical Si particles (with approximately 3 μm radius) were formed on the surface as shown in Fig. 6. The deposits were amorphous. On these silica gels, evidence of whisker or porous deposits was not observed.

XRD and XPS studies suggested that at lower temperatures (800-900°C) amorphous or nanosized crystalline Si were formed. However, at high temperatures (>1000°C) amorphous or crystalline β-SiC were formed. This is in accord with the phase diagram reported by Veltri et al.¹⁸ which showed that at atmospheric pressure, Si is formed at temperatures below 1000°C while SiC is formed at higher temperatures.

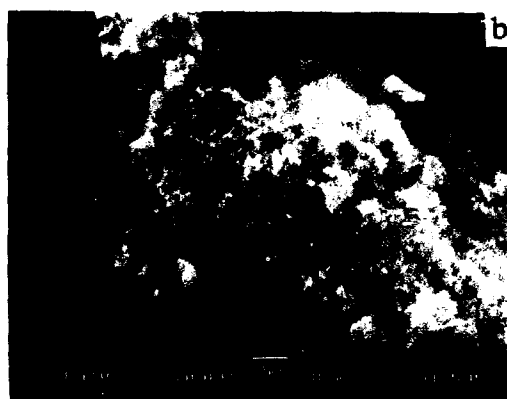
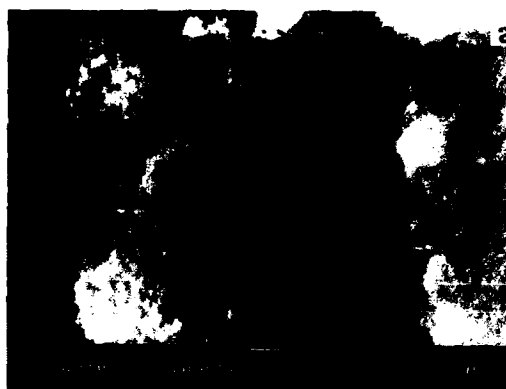


Fig. 5. Scanning electron micrographs of (a) Si coated AlN at 1050°C and (b) SiC coated AlN at 800°C.



Fig. 6. Deposits on low surface area SiO_2 gels showing the solid half-spherical deposits, no porous deposits were found.

The XRD data also indicated that it is more difficult to form β -SiC on Davisil than on AlN substrates.

CONCLUSIONS

Sponge type Si, which is composed of nanometer and submicron size whiskers, was formed on Davisil (porous SiO_2 gels) at 800 to 900°C by CVD using methyltrichlorosilane (MTS) as a precursor. SEM data suggest diameters $< 1 \mu\text{m}$ and XRD data suggest an average diameter of 123 Å for Si whiskers on Davisil. The coated Davisil has a surface area of 189 m^2/g , which is very close to its original surface area (224 m^2/g). The same deposition conditions resulted in solid half-sphere filled types of coatings on low surface area SiO_2 gels. At temperatures above 1000°C, solid particles were formed on Davisil. However, porous but crystalline β -SiC was formed on AlN substrates with a deposition temperature of 1050°C. Whisker formation may result from kinetic and steric constraints due to the porous nature of Davisil.

REFERENCES

1. G. S. Chen, C. B. Boothroyd, and C. J. Humphreys, Appl. Phys. Lett. **62**(16), 1949(1993).
2. K. Tsai and J. L. Dye, Chem. Mater. **5**, 540(1993).
3. R. W. Cahn, Nature, **348**, 389(1990).
4. J. Y. Yang, J. B. Benziger and H. Gleiter, Phys. Rev. B. **48**(3), 1830(1993).
5. J. Yu and W. P. Halperin, Phys. Rev. B. **47**(23), 15830(1993).
6. J. Karch, R. Birringer and H. Gleiter, Nature, **330**, 556(1987).
7. R. Dagani, C&EN, Nov. 23, 18, 1992.
8. R. Dagani, C&EN, Mar. 22, 20, 1993.
9. I. Uno, T. Kasuga, S. Nakayama and A. J. Ikushima, J. Am. Ceram. Soc. **76**(2), 539(1993).
10. W. B. Philips, E. A. Desloge and J. G. Skofronick, Appl. Phys. **39**, 3210(1997).
11. A. M. Kazakos, S. Komarneni and R. Roy, J. Mater. Res. **5**, 1095(1990).
12. S. Komarneni, Y. Suna and R. Roy, J. Am. Ceram. Soc., **69**, C155 (1986).
13. K. J. Klabunde, Y. X. Li and B. Tan, Chem Mater, **3**, 30(1991).
14. G. Chow, M. A. Markowitz and A. Singh, J. Mater. Nov., **62**(1993).
15. H. Takagi, H. Ogawa, Y. Yamazaki, A. Ishizaki and T. Nakagiri, Appl. Phys. Lett. **56**, 2379(1991).
16. A. G. Cullis and L. T. Canham, Nature **353**, 335(1991).
17. L. T. Canham, Appl. Phys. Lett. **57**, 1046(1990).
18. Veltri et al., J. Am. Ceram. Soc., **72**, 478(1989).

RELATIONS BETWEEN STRUCTURE AND TEXTURE IN NANO-SIZED ALUMINAS

DOMINIQUE J. COSTER*, PIERRE LEVITZ** AND JOSE J. FRIPIAT*

* University of Wisconsin-Milwaukee and Laboratory for Surface Studies, P.O. Box 413 Milwaukee, WI 53211

**CNRS- CRMD, rue de la Ferollette, 45071 Orleans Cedex 2, France

ABSTRACT

Alumina xerogels were prepared by a two step hydrolysis in non-aqueous media. This synthesis produced high surface area materials with controlled amount of pentacoordinated aluminum. The effect of heat treatment and of the preparation procedure on the physical characteristics of the powder was determined by nitrogen adsorption and X-Ray diffraction, whereas the aluminum coordination was studied by ^{27}Al MAS NMR. The pore size distribution and the pentahedral aluminum content (up to 700°C) are closely related to the degree of condensation of the prehydrolysed oligomer species.

INTRODUCTION

In the present work, we carry out with the investigation of aluminum alkoxides ($\text{Al}(\text{OR})_3$) hydrolysis at low water to aluminum ratios ($r = \text{mole H}_2\text{O} / \text{mole Al}$). The results obtained earlier are briefly summarized and the improvement are discussed.

In our previous work [1], $\text{Al tri-}i\text{-sec-butoxide}$ solution in *sec*-butanol was hydrolysed by a limited amount of water ($0.7 \leq r \leq 1.4$) in presence of urea and/or ammonium chloride. After freeze-drying and subsequent drying at 85°C, the gel were calcined between 550°C and 750°C. An accurate monitoring of the hydrolysis conditions allowed us to generate solids with controlled amounts of penta-coordinated aluminum (Al^{5+}). A detailed ^{27}Al magic angle spinning (MAS) NMR study (structure) combined with nitrogen adsorption isotherm (texture) had evidenced memory effect during the thermal treatment. Knowing the degree of octahedral condensation (octahedral aluminum (Al^{6+}) chemical shift) in the gel, it was possible to predict the amount of Al^{5+} in the aluminas calcined at 550°C. The alumina texture could also be traced down to the gel. A large concentration of Al^{5+} in the aluminas, and thus reduced polymerization of the octahedra in the gels, was correlated to a narrow pore size distribution and small pore diameter (4-5nm). The metastability of the Al^{5+} species toward water was also demonstrated. The specific role of urea and ammonium chloride was unclear.

In the present work, we improve the sol-gel route. A more complete hydrolysis of the $\text{Al tri-}i\text{-sec-butoxide}$ is achieved by increasing the hydrolysis ratio. The yield of the reaction is considerably improved whereas the nature of the alumina is unchanged. We also focus our effort to control and vary the pore size distribution over a wider range.

The results are discussed in terms of Al^{5+} content and porosity and are related to reaction mechanisms. The surface properties of some of these aluminas are reported elsewhere [2].

MATERIALS AND METHODS

The Al tri-*sec*-butoxide (Aldrich, Milwaukee) is diluted with *sec*-butanol to an aluminum molar concentration of 0.43M. The hydrolysis is induced at two stages, namely before (pre-hydrolysis) and after (post-hydrolysis) an aging period of three days at 80°C, under continuous stirring. The pre-hydrolysis consists in a rapid water addition to reach $r=0.7$. The sol was then aged. Different gels were obtained depending on the post-hydrolysis ratio and subsequent treatments. In fact the post-hydrolysis is a base-catalysed process. Either 0.7, 1.4, 2.8 mL of aqueous ammonium hydroxide solution (28-30% NH_3 in weight) diluted in 100 mL of *sec*-butanol is added to 100 mL of pre-hydrolysed sol and stirred vigorously for 5 minutes. The final hydrolysis ratio r is either 1.65, 2.60 or 4.50. Then the gels are processed into different ways, either the solvent is evaporated to dryness in an oven at 70°C (gel processing II) or the gel is centrifuged, washed three times with fresh *sec*-butanol, then freeze-dried overnight and finally dried at 80°C for 24 hours (gel processing I). In one variant, the pre- and post-hydrolysis are combined into a one step hydrolysis followed by gel processing of type I. Finally, one set of sample was prepared starting with Al ethoxide (Janssens, Bruxelles, Belgium) in ethanolic solution. The pre-hydrolysis and final r ratio are 0.7 and 2.90 respectively.

The gels were subsequently calcined at 550, 600, 650, 750°C for twenty hours. The oven temperature was increased from room temperature to the final temperature at a rate of 150°C per hour. The samples will be named according to the experimental procedure (Table I). For instance, gel A calcined at 550°C will be called A550.

CHARACTERIZATION TECHNIQUES

The ^{27}Al MAS NMR spectra of the gel (before calcination) and alumina (after calcination) were recorded at 130.3 MHz and a spinning rate ca 12-14 KHz. Single pulse excitation using 9.5 μsec (15°) pulses and a delay time of 50 msec was used.

The complete nitrogen adsorption-desorption isotherms were recorded after outgassing at 300°C for at least 2 hours, using the Omnisorb 100 (Coulter Co.) in static mode. The pore size distribution is obtained from the desorption isotherms, using the Barret et al. [3] algorithm and assuming cylindrical pore shape.

Carbon and nitrogen analysis were carried out and X-ray (Cu K α) diffractograms were recorded on some samples.

RESULTS AND DISCUSSION

The main information concerning the gel processing, the thermal treatment and the physico-chemical characterization are summarized in table I. As it was demonstrated before [1], the Al content is a valuable parameter to probe the sample thermal evolution and will be correlated to reaction mechanism and physical properties. Thus it will play a major role in the discussion.

Table I. Summary of the experimental procedure and of the sample characteristics

GeI ID	Final r	Process	Firing Temp (°C)	Surface Area (m ² /gr)	Total Pore Vol (mL/gr)	% Pore Vol $\phi < 6$ nm	%Al ^{IV}	%Al ^{VI}
A	2.60	I ⁽²⁾	550	339	0.376	93.8	42.9	39.3
			650	286	0.258	91.1	37.7	18.8
			750	142	0.221	92.2	29.9	2.0
B ⁽¹⁾	2.60	I	550	380	0.345	85.7	29.9	28.6
			700	200	0.298	91.6	35.8	5.9
			750	142	0.221	92.2	29.9	2.0
C	4.50	I	550	344	0.712	55.9	32.7	27.4
			650	251	0.534	54.5	27.5	2.5
			750	193	0.424	51.3		
D	1.65	II	550	304	0.627	45.9	36.1	28.7
			750	167	0.522	25.8		
			750	167	0.522	25.8		
E	2.60	II	550	324	0.882	28.1	34.2	17.0
			600	367	0.903	33.2		
			750	185	0.730	17.4		
F	2.60	X ⁽³⁾	550	305	0.888	28.2	26.3	9.3

(1) Al(OR)₃ = Al ethoxide

(2) See text

(3) One step synthesis

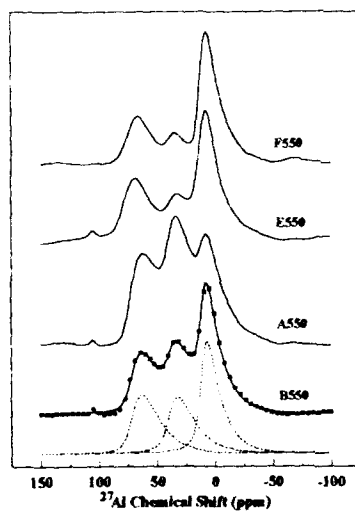


Fig.1 ²⁷Al MAS NMR spectra of selected samples calcined at 550°C. Bottom: simulation of B550 spectrum; dotted lines are the individual contributions, the solid line is the sum, the solid squares correspond to the experimental data.

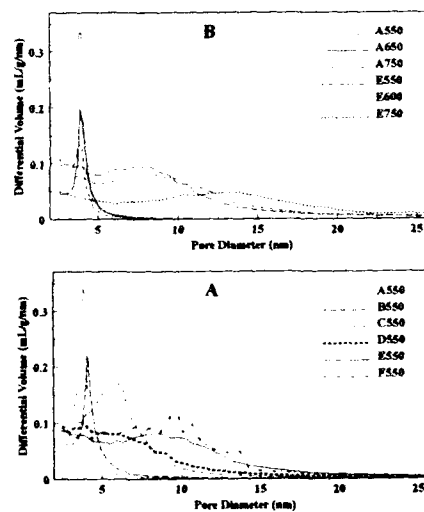


Fig.2 Pore size distribution of samples A-E calcined at 550°C (A). Comparison of Samples A and E calcined between 550°C and 750°C (B).

Our goal was to produce Al^{V} rich aluminas and to simplify the former procedure. First of all, the reaction yield has been improved considerably. 85 to 100% of the aluminum alkoxide is hydrolysed and is ultimately transformed to aluminas whereas the yield was as low as 30% in the procedure reported earlier. Accordingly the gels contain less carbon: this is about 10% in weight compared to more than 30% before.

The ^{27}Al MAS NMR spectra of a typical transition aluminas show two resonance at 65 and 8 ppm corresponding to aluminum in tetrahedral (Al^{IV}) and octahedral (Al^{VI}) position respectively. The ratio of the two peak is 1 to 2 as expected in a spinel-like structure. For the aluminas produced by this sol-gel, there is in addition a contribution at 35 ppm (Fig. 1) assigned to pentacoordinated aluminum.

The Al^{V} concentration increases with increasing calcination temperatures and reaches a maximum around 450-550°C. Then it decreases and almost disappears upon calcination at or above 750°C. It is worth mentioning that the few Al^{V} remaining after calcination at high temperature are concentrated at the surface. The intimate modifications encountered by the sample during thermal treatments are depicted when deconvoluting the ^{27}Al MAS NMR spectra. Without going into the details of the deconvolutions procedure [4], the following facts are observed. The gel is a relatively homogenous and well-organized (at the local scale) material. The resonances are narrow and can be simulated with low quadrupolar coupling constant (QCC), narrow distribution of quadrupolar parameters and reduced overall broadening. Calcination at 550°C maximizes the disorder and increases the line widths. This can be accounted for by increasing the width of the QCC distribution as well as the overall broadening. At 750°C, the material starts to reorganize, as it is evidenced by the decrease in line width and the appearance of some X-ray diffraction lines (vide infra). If one compares the samples at 550°C, a consistent trend is observed; as the Al^{V} content increases the width of each individual line (Al^{IV} , Al^{V} , Al^{VI}) increases also. Thus the Al^{V} appears in highly disordered structures.

It is also evident that the Al^{V} concentration is controlled by the experimental procedure. Large pre-hydrolysis ratios inhibit the Al^{V} formation [1,5], so that r must be kept around 0.7 during the aging period to obtain high yield of pentagonal species. The post-hydrolysis ratio is also a critical parameter. Using the gel processing I, r can be increased up to about 3 without altering the gel properties; only the reaction yield is improved. Over a final hydrolysis ratio of 3, the Al^{V} content starts decreasing (compare sample A550 and C550). The two gel processing (I and II) give some interesting insight into the sol chemistry. In fact method I corresponds to a rapid hydrolysis. The ammonium hydroxide solution is added and reacts for 5 minutes. Then most of the unreacted water is washed away and finally the traces of water left are frozen during the freeze-drying step. Thus the hydrolysis proceeds for a short period of time and the freeze drying procedure prevents the gel to agglomerate and/or condense further. On the opposite, method II allows for an extended condensation and removal of the alkoxide residues. It is worthwhile to remember that the hydrolysis rate constant is 4 to 5 order of magnitude larger than the condensation rate constant in the $\text{Si}(\text{OR})_4$ and $\text{Ti}(\text{OR})_4$ systems [6,7]. It is likely that procedure I isolates the hydrolysed products with limited condensation, whereas condensation between partially hydrolysed oligomers is expected for procedure II. We also conducted an acid-catalysed reaction where the ammonium hydroxide was replaced by HCl 6N. The product shows large amount of Al^{V} but the surface area was rather low (200 versus 300 m^2/gr). These observations confirm the fact that base-catalysed condensation leads to highly branched polymeric species. For the one step hydrolysis (sample F), the pre- and post-hydrolysis are combined and followed by the gel processing of type I. Al^{V} is almost absent showing the importance of the pre-hydrolysis and of the aging period. It is possible that the first reaction produces a well-dispersed sol that acts as "seed" for the second hydrolysis.

All the results discussed up to now were obtained starting with the Al tri-*sec*-butoxide. This

alkoxide already contains Al^{IV} [8] thus a legitimate question can be raised. Is the Al^{IV} observed for the calcined powder related to the nature of the alkoxide? Is the alkoxide the chemical precursor? To answer this question, we produced a gel equivalent to sample A but using the Al ethoxide. The precursor is solid and contains less than 5% of Al^{IV} and Al^{III} . As it can be seen (Fig. 1, Table I), the Al ethoxide leads also to Al^{IV} rich alumina. Without overlooking the influence of the alkoxide nature and of the solvent on the hydrolysis and condensation reaction, one can conclude that Al^{IV} is produced even though it is not present in the alkoxide. Al^{IV} depends on the degree of condensation of the structural (tetrahedral and octahedral) elements. Misfits in the condensation would produce Al^{IV} .

The pore size distributions of each sample calcined at 550°C and of sample A and E activated between 550 and 750°C are displayed in figure 2A and 2B respectively. The total pore volume and the surface area are summarized in table I. At a constant calcination temperature the different samples have similar specific surface area, whereas the porosity is deeply affected by the hydrolysis ratio and the gel processing, as also observed for the Al^{IV} yield. Thus it is not surprising to find a relationship between porosity and aluminum coordination. As the Al^{IV} content decreases, the pore volume increases (Fig. 2A and table I) and because the surface area is more or less constant, larger pores are developed. If samples A550 and B550 are compared, it seems that a low r ratio (2.6) tends to produce a structure with a very narrow pore distribution centered at 4 nm. Increasing r to 4.50 (sample C550) generates a solid with a poorly defined porosity centered around 6 nm. Long condensation periods (procedure II, sample D550 and E550) or too short a reaction time (sample F550) produces large but badly defined pore volume. The pore size distribution in gels calcined at increasing temperature shows (fig 2 B) an interesting feature. Even though the specific area drops by as much as 50%, a sample with narrow pores tends to preserve its pore structure. When the pores are larger at the origin, they become still bigger at higher calcination temperature (sample E). The pore size distribution is a good probe to follow the thermal evolution of the powder and evidence a textural memory up to at least 750°C.

The influence of the Al^{IV} concentration in the gels calcined at 550°C on their thermal evolution is shown in figure 3. The surface stability is the surface area left at 750°C expressed in % of the surface measured at 550°C. The crystallinity is the ratio of the width at half maximum intensity to the maximum intensity of the X-ray reflection at $2\theta=46^\circ$. In fact, γ -alumina X-ray pattern is observed. It is clear that sintering and recrystallization are favored by a higher contents in Al^{IV} as true for any surface defect [9].

Finally, it would have been interesting to compare the structural and textural information reported above to small angle X-ray scattering data. Only one sample (sample 111A in ref. 1, fresh and calcined at 550°C) similar to sample A was studied. Both the fresh and calcined powders exhibit an extended Porod region, $I = \text{const} \cdot Q^{-4}$ with a Porod slope $\alpha=4$. Such a behavior would indicate that the gel and the corresponding alumina are non-fractal [6], e.g. the mass fractal dimension is 3 and the surface is Euclidian. The scattering function shows a nice correlation peak near $r = 0.006 \text{ nm}^{-1}$ and a correlation length $\approx 10 \text{ nm}$. High resolution transmission electron microscopy of the sample calcined at 550°C reveals aggregates of small pseudo-spherical particles 2 nm diameter looking like quasi-linear strings of beads separated by voids with average width of 3 nm. These voids are forming slit-shaped pores, the average distance between their centers being on the order of 8 nm.

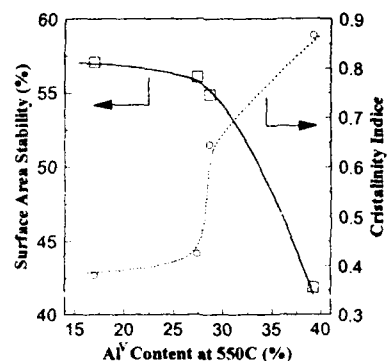


Fig.3 Surface area stability (left) and powder crystallinity at 750°C (right) versus the Al³⁺ content at 550°C. For details refer to text. The lines have no particular meanings.

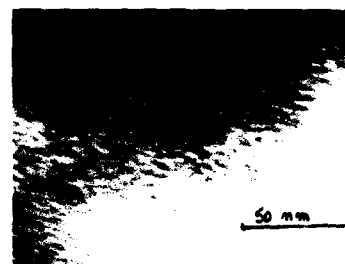


Fig.4 Transmission electron microscopy of sample A550.

ACKNOWLEDGMENT

This work was supported by DOE Grant DOE-FG02-90ER1430 DC thanks the Laboratory for Surface Studies for a travel award. We like to thank Dr. G. Pacheco-Malagon and A. Garcia-Borques, Materials Dept., Polytechnic Institute of Mexico, Mexico D.F. for the TEM picture.

REFERENCES

1. D. Coster and J.J. Fripiat, *Chem. Mater.*, **5**, 1204 (1993).
2. D. Coster, V. Gruver, A. Blumenfeld and J.J. Fripiat in *Better Ceramics through Chemistry VI*, (Mater. Res. Soc. Proc.) in press.
3. E.P. Barret, L.G. Joyner and P.H. Halenda, *J. Am. Chem. Soc.*, **73**, 373 (1951).
4. D. Coster, A. Blumenfeld and J.J. Fripiat, *J. Phys. Chem.* (submitted).
5. R.A. Sinclair, M.L. Brostrom, W.B. Gleason and R.A. Newark (Mater. Res. Soc. Symp. Proc. Vol. 271, Pittsburgh, PA, 1992) pp. 27-32.
6. C.J. Brinker and G.W. Scherer, *Sol-Gel Science* (Academic Press, New York, 1990) chapter II and references therein.
7. G. Orcel and L. Hench, *J. Non-Cryst. Sol.*, **79**, 177 (1986).
8. O. Kriz, B. Cazensky, A. Fusek and S. Hermanek, *J. Magn. Res.*, **60**, 375 (1984).
9. T.E. Wood, A.R. Siedle, J.R. Hill, R.P. Skarjune and C.J. Goodbrake in *Better Ceramics through Chemistry IV*, edited by B.J.J. Zelinski, C.J. Brinker, D.E. Clark and D.R. Ulrich (Mater. Res. Soc. Proc. Vol. 180, Pittsburgh, PA, 1990) pp. 97-116.

LAYERED SILICATE/ATBN NANOCOMPOSITE

A. MOET, A. AKELAH*, N. SALAHUDDIN, A. HILTNER AND E. BAER

Department of Macromolecular Science, Case Western Reserve University
Cleveland, OH 44106-7202

* Department of Chemistry, Tanta University, Tanta, Egypt

ABSTRACT

Composites of amine terminated butadieneacrylonitrile (ATBN) and montmorillonite (MMT) were prepared by ion exchange between the onium salt of the polymer and the interlamellar cation of the mineral following two different preparation approaches. The first carried out the ion exchange in situ and used dioxane, a better solvent for the polymer, and the second administered the onium salt to MMT using dimethylsulfoxide (DMSO). Elemental analysis and IR spectroscopy indicated that all the ionic sites of the mineral have been occupied by polymer end groups. The $d(001)$ spacing and the span between the internal lamellar surface were only expanded to about 14 Å and 5 Å, respectively, suggesting horizontal packing of the polymer molecules. TEM of microtome sections prepared from compression molded composites revealed that the lamellae, laminated with polymers assembled into multiplets of about 5 nm for both preparations. The multiplets clustered into mineral rich domains whose average size was 250 nm for the DMSO preparation. Finer clusters (70 nm) were obtained by the first method. This three fold decrease in the average domain size was attributed to the strong solvation power of dioxane in the binary solvent and to the locale of ion exchange.

INTRODUCTION

Interest in the properties of complexes of organic molecules with layered silicate minerals [1] has been driven by a remarkable level of inherent activity. The crystalline structure of this class comprises two dimensional crystalline regularity (layers or lamellae) superposed without any regularity except for a constant separation and held together by relatively weak forces. Even though activity of various cationic species have been studied [2], the bulk of the literature is focused on Na and Ca montmorillonites [3], perhaps due to their natural abundance. Several technologies have been developed on basis of organophilic montmorillonites prepared by ion exchange or adsorption of small organic molecules into the interlamellar spacing [4-9]. The swelling characteristics of montmorillonites have been recently exploited to effect shrinkage control of concrete/polymer mixtures [10], nylon 66 [11] and epoxy compounds [12]. The structural and morphological characteristics of montmorillonites have been used to prepare polymer/clay nanocomposites including nylon 6 [13-17] and polystyrene [18,19]. A recent U.S. patent [20] describes fifteen examples of composite materials based on the intercalation of vinyl monomers, prepolymers or functional polymers with smectic clay minerals. In all, but few reports [15,17,18,21,22] nanostructure was concluded from WAXD measurements of the interlamellar $d(001)$ spacing, neglecting the fact that interlamellar expansion is possible without disaggregation of the mineral [11,12]. More recently, Usuki and coworkers reported a TEM micrograph denoting the nanostructure dispersed into a rubber compound [21,22]. In view of the fact that the properties of structured materials arise from their morphological organization, this paper pursues the morphological hierarchy of ATBN-g-MMT and examines the effect of the

ion exchange method on the evolution of the nanostructure in an attempt to elucidate the "rules" by which this evolution occurs. A companion publication [23] continues to clarify yet another issue in the preparation of montmorillonite/polymer hybrids. That is the significance of chemical and physical bonding in these materials.

EXPERIMENTAL PROCEDURE

The clay mineral used in this study was Na-montmorillonite (colloid BP) from Southern Clay Products, Inc. (Gonzales, Texas) with cation exchange capacity (CEC) of 114.8 m.eq/100 g. The polymer, amine-terminated butadiene acrylonitrile (Hycar® ATBN, 1300x16) with Brookfield viscosity of 2×10^5 mPa.s at 27°C and a glass transition temperature of -51° C was obtained from BF Goodrich, Specialty Polymers & Chemicals Division (Cleveland, OH). Using GPC with polystyrene as a reference, the number average molecular weight was found to be 1.09×10^3 and the weight average was 7.34×10^3 which gives rise to a polydispersity of 6.75.

The general idea underlying the preparation of MMT chemical intercalates follows the simple rules of ion exchange [4]. In our case, the amine end groups of the polymer chains were converted into the corresponding onium salt which was then caused to exchange with the interlayer cation of the mineral. The exchange process was achieved step-wise or simultaneously. The Toyota's approach uses 1:1 ratio of dimethylsulfoxide and water, aided by intensive mechanical stirring, to swell the polymer and transform its end groups to the onium salt by adding HCl. This salt suspension is added to montmorillonite dispersion in water [22]. Realizing the limitation of this approach, another was devised according to which dioxane, a better solvent for ATBN, was used to dissolve the polymer and as a co-swelling agent for MMT. In the latter method, the salt transformation took place in the vicinity of the dispersed mineral layers. The products obtained from the two procedures are then compared at the various levels of phase organization.

The analytical strategy was devised to examine the nature of bonding between MMT and ATBN in the reaction product and to investigate the evolving morphology of the composite. This task was achieved by a battery of tests including elemental analysis, wide angle X-ray diffraction (WAXD), fourier transform infrared spectroscopy (FTIR), scanning electron microscopy (SEM) and transmission electron microscopy (TEM).

RESULTS

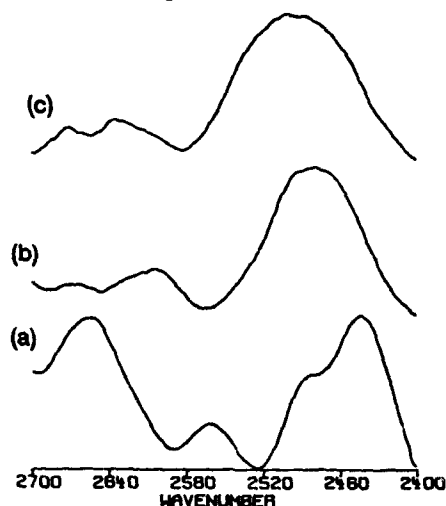
To probe the nature of the interaction between the ATBN polymer and montmorillonite our results are presented on three levels. At the ionic level, elemental analysis and FTIR established that the polymer has accessed all the interlayer charge sites and that the functionalized chain ends have been ionically bonded to the layers. Diffraction measurements gauged the polymer packing between mineral layers. Finally, microscopic evidence was used to construct the morphological hierarchy of the composite. Where appropriate, comparison will be made between the products obtained from the two preparations.

Intercalation Reaction

Quantitative analysis of C, H, N and Na in the reaction product provides evidence of the efficiency of ion exchange and the MMT content in the composite. The Na content (<0.08%)

is equivalent to that arising from Na_2O implying that all ionic sites in MMT were exchanged with the onium salt of the polymer. A polymer-to-clay ratio of about 1.5 (by weight) was calculated from the C and N content. Additional evidence for the intercalation of ATBN with MMT was obtained from FTIR spectroscopy. The terminal amine of the polymer used in this investigation (ATBNX16) is N-aminoethylpiperazine. The halide salt of this secondary amine shows four characteristic IR bands in the region from 2700 cm^{-1} to 2400 cm^{-1} , specifically at 2655 cm^{-1} , 2550 cm^{-1} , 2495 cm^{-1} and 2440 cm^{-1} as shown in Fig. 1 (a).

Figure 1. FTIR of:
(a) ATBN salt,
(b) composite of the dioxane preparation and
(c) composite of the DMSO preparation.



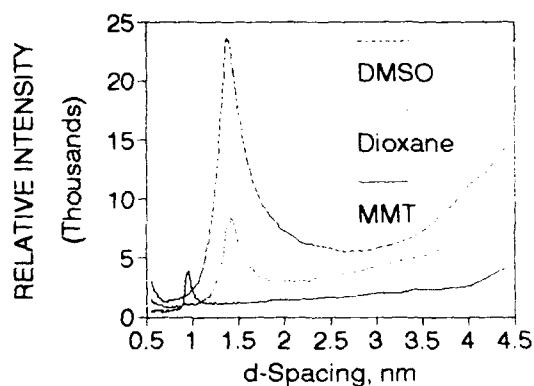
These observed bands are similar to those reported in earlier literature [24]. Secondary amine salts show bathochromic shift in the order hydrochloride, hydrobromide, hydroiodide [25]. The shift in our case (spectra b and c) is higher than that which was reported for hydrochloride [25] implies that the onium salt of ATBN must be intercalated with a more electronegative moiety, i.e., metal oxide. The broadening of the characteristic bands of the two intercalates (b and c) is apparently related to intermolecular interaction.

Interlamellar Structure

It has been shown above that the polymer chains must have accessed the inter-lamellar spacing of the mineral giving rise to a polymer/mineral intercalate by ion exchange. The amount of polymer residing within the interlayer spacing can be estimated by WAXD. Figure 2 shows typical WAXD traces of MMT and ATBN-MMT (compression molded samples) obtained from both preparations. The interlamellar spacing is 9.6 \AA for MMT and 14.1 \AA for both preparations. Realizing that the Na ion (ca. 0.3 \AA [9]) has been replaced by ATBN and subtracting the thickness of the silicate layer (two halves = 0.93 nm) from the observed d (001) spacing (1.41 nm) produce the thickness of the polymer layer within [26]. The corresponding value is 0.49 nm for both preparations. This value is slightly less than a bimolecular layer ($2 \times 2.8\text{ \AA}$) and might be considered to represent the mean thickness of a buckled and folded macromolecular chain, in which approximately half of the segments of each chain is in contact

with the surface. The interlamellar packing deduced here is similar to that observed in grafted styrenic monomer [18] and is lower than that observed in MMT-g-PS [18] MMT-g-epoxy [12] and nylon 6-g-MMT [15-17].

Figure 2. WAXD of MMT and composites from dioxane and DMSO preparations.



Morphological Evolution

The WAXD evidence presented above indicates that the aluminosilicate lamellae, 9.6 Å each, are laminated by a polymer layer of about 5 Å. The method of preparation does not appear to play a major role at the lamellar level. The elementary building block of the composite, in both preparations, is probably a pair of mineral lamellae and the enclosed polymer layer which add up to about 2.5 nm. This elementary building block may erect an agglomerate of a micro scale [12] or a nanostructure [18]. Detailed TEM analysis of suspension cast film and microtome sections prepared from molded specimens are reported in another publication [27]. In this section, we present a few illustrations for the morphological hierarchy.

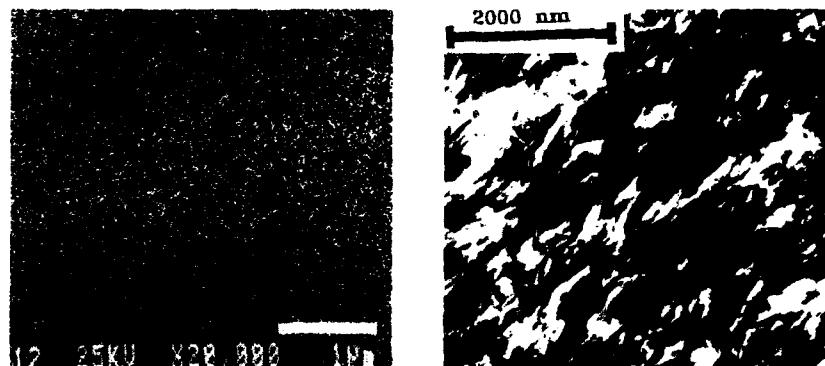


Figure 3. (A) Dispersive X-ray mapping for Si, and (B) TEM micrograph of microtome section prepared from compression molded sample.

The uniformity observed in an image of Si mapping (Fig. 3A) indicates that the mineral domains are submicron in size and are homogeneously dispersed (on this scale) in the polymer matrix. Figure 3B displays a TEM image exhibiting mineral-rich clusters. The clusters appear ellipsoidal (70 nm x 300 nm). That the super assembly of MMT occurs through lamellar planes draw the attention to examine morphological evolution of the thickness. The histograms of Fig. 4 provide a clear distinction between the morphology obtained from our preparation method (dioxane) and that of Toyota (DMSO). Our approach yields a narrower domain size distribution (average 70 nm) as compared to the Toyota approach (average 250 nm). Higher magnification of the clusters (Fig. 5) shows that they are assemblies of layered materials (lamellar multiplets), and are not a continuous dispersion of MMT lamellae as promoted by Toyota publications [15,17].

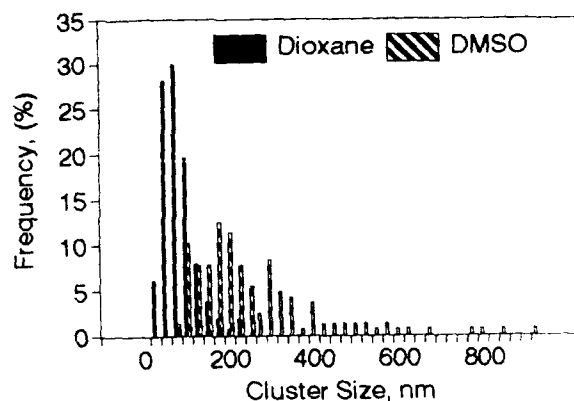


Figure 4. Histograms of cluster size distribution

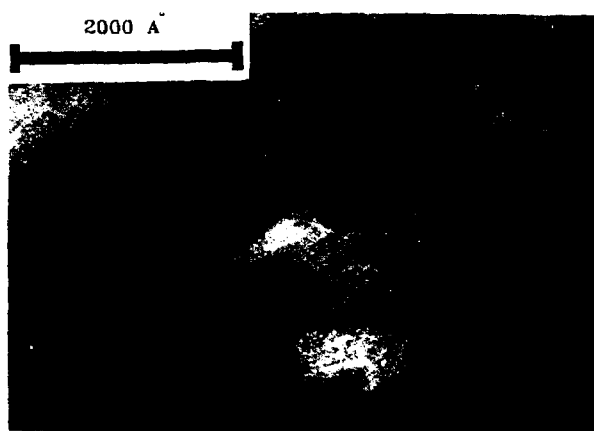


Figure 5. TEM micrograph showing the assembly of mineral multiplets within the cluster.

DISCUSSION

Montmorillonite-polymer nanocomposites, like other structured materials, derive their properties from their morphology. Because these are multiphase materials, chemical continuity between the phases, i.e., the nature of bonding between the polymer and MMT, plays a significant role in forging their durability. Chemical continuity of the interphase has been established from elemental analysis, FTIR spectroscopy and TGA analysis [27]. The succeeding discussion considers relevant characteristics of MMT, attempts to construct a hierarchical model for ATBN-g-MMT and examines the validity of the idea that increased $d(001)$ alone is a sufficient evidence to demonstrate that a polymer-MMT intercalate is a nanocomposite.

The various levels of organization in montmorillonite include: *Primary particles* (ca. 10 nm) consisting of stacks of parallel elementary sheets (lamellae) with an average of about 10 sheets per particle, *micro-aggregates* (ca. few hundreds nm) formed by the association of several primary particles which are nearly parallel and joined together laterally and *aggregates* (0.1 to 10 μm) comprising a large number of primary particles and micro-aggregates. Early evidence suggests that the swelling and plasticizing of MMT are due to increasing interparticle spaces rather than to expansion of individual primary particles [3]. Thus, MMT appears to undergo two interdependent processes during intercalation; *swelling* of the interlamellar spacing and *disaggregation*. Lastly, it should be kept in mind that most intercalation reactions with polymers are brought about in a binary aqueous mixture. Montmorillonite literature [28] indicates that certain binary liquid mixtures exert more effective intercalation than others. Thus, the role of the intercalating medium should not be overlooked.

Examination of the basics presented above in association with the findings introduced in the results section would aid in elucidating the organizational behavior of MMT as it becomes intercalated with the polymer. A summary of the measurements made on various scales by WAXD and image analysis of TEM results [27] is tabulated below.

Table I, Average Domain Size (nm)

Domains	Dioxane	DMSO
Cluster	71.0	245.0
Multiplets	5.2	4.3
Multiplet spacing	11.0	11.4
$d(001)$ spacing	1.4	1.4

One notes that lamellar multiplets (few lamellae) appear to represent the elementary constituents of the mineral rich domains in the composites, regardless of the method of preparation. The significant reduction in the cluster size and distribution (Fig. 4) is most likely related to the dual effect of the better solubilization of the dioxane and the local ion exchange in the dioxane method. An observation of significance is that the average spacing between the multiplets falls in the range of 11 nm. The assembly of the mineral layers into multiplets and the ability of the multiplets to diffract X-rays offers an alternate interpretation to the notion of "disappearance" of the interlayer spacing from WAXD measurements [15,17,20].

It is widely believed that a nanocomposite status could be conferred on MMT-polymer intercalates if the d (001) spacing is sufficiently increased. For example, in their patent [20], Toyota's researchers disclose that the X-ray diffractometry of ATBN-g-MMT indicates that the (001) plane of MMT has disappeared and the layers of MMT *are uniformly dispersed* in the liquid butadiene (i.e., ATBN). The patent further narrates that the MMT in the complex has a silicate interlayer distance greater than 80 Å. In another publication [22], a TEM micrograph related to that of Fig. 4 was erroneously used to conclude that the silicate layers are dispersed on the molecular level. In addition, earlier report [15,17] used TEM micrographs comparable to those of Fig. 5 to assume that the MMT is dispersed as *single layers* in the polymer matrix leading the authors to conclude "unlimited swelling". However, recent WAXD measurements [29] shows that interlamellar spacing remains in the range of 13.7 Å after intercalative polymerization of ϵ -caprolactone from which the authors sketch a schematic diagram bearing the basic idea of our model [27]. That is, the reactively small interlamellar spacing does not represent the whole picture of the composite which should better be understood in terms of a morphological hierarchy.

CONCLUSIONS

Within the scope of the preceding analysis of the two ATBN-g-MMT preparations, the following conclusions are reached:

- (1) Ion exchange between the interlayer cations of MMT and the onium salt of ATBN gives rise to a chemically intercalated composite.
- (2) The polymer intercalation produces an interlamellar expansion of about 5 Å which suggests polymer packing either as a bimolecular layer or as a buckled and folded chain.
- (3) A morphological hierarchy based on WAXD and quantitative analysis of TEM observations suggests that multiplets of laminated mineral lamellae are assembled to form mineral-rich clusters.
- (4) An intercalating medium containing dioxane, a good solvent for the polymer, is found to produce smaller cluster domains in comparison with those obtained in a weaker solvent.

ACKNOWLEDGEMENTS

This research was supported, in part, by ARO, grant No. DAA LO #92-G-0241. N.S. acknowledges the scholarship support of the Cultural and Educational Bureau of Egypt. The authors wish to thank L. Pulliam and A. Seibert of BF Goodrich for providing well characterized ATBN samples and for useful discussion. We are also indebted to T. Brennan of Southern Clay Products, Inc. for providing montmorillonite samples.

REFERENCES

1. C. R. Smith, *J. Am. Chem. Soc.*, **56**, 1561 (1934).
2. M. T. Bryk, A. Sh. Goikhman, I. E. Skobets and F. D. Ovcharenko, *Kolloidnyi Zhurnal*, **45**, 1043 (1983). Translated, Plenum Publishing (1984).
3. J. Mering, *Trans. Faraday Soc.*, **42**, 205 (1946).
4. B. K. G. Theng, "The Chemistry of Clay-Organic Reactions", Adam Hilger, London (1974).
5. T. R. Jones, *Clay Miner.*, **18**, 399 (1986).
6. C. Kato, K. Kuroda and H. Takahara, *Clays Clay Miner.*, **29**, 294 (1981).
7. D. H. Solomon and M. J. Rosser, *J. Appl. Polym. Sci.*, **9**, 1261 (1965).

8. D. H. Solomon and J. D. Swift, *J. Appl. Polym. Sci.*, **11**, 2567 (1967).
9. D. H. Solomon and B. C. Loft, *J. Appl. Polym. Sci.*, **12**, 1253 (1968).
10. E. Haque, and C. D. Armeniades, *Polym. Eng. Sci.*, **26**, 1524 (1986).
11. A. Moet; S. Qutubuddin and P. Kelly, "Anti-shrink Agent for plastic Moldings", Final report, The Edison Materials Technology Center, Dayton, OH, October, 1990.
12. P. Kelly, A. Akelah, S. Qutubuddin and A. Moet, *J. Mater. Sci.*, **29** (1994).
13. A. Okada, M. Kawasumi, T. Kurauchi and O. Kamigaito, *Polym. Preprints*, **28**, 447 (1987).
14. Y. Fukushima and S. Inagaki, *J. Inclusion Phenomena*, **5**, 473 (1987).
15. Y. Fukushima, A. Okada, M. Kawasumi, T. Kurauchi and O. Kamigaito, *Clay Miner.*, **23**, 27 (1988).
16. A. Usuki, M. Kawasumi, Y. Kojima, A. Okada, T. Kurauchi and O. Kamigaito, *J. Mater. Res.*, **8**, 1174 (1993).
17. A. Usuki, Y. Kojimai, M. Kawasumi, A. Okada, Y. Fukushima, T. Kurauchi and O. Kamigaito, *J. Mater. Res.*, **8**, 1179 (1993).
18. A. Moet and A. Akelah, *J. Mater. Lett.*, **18**, 97 (1993).
19. R. A. Vaia, H. Ishii and E. P. Giannelis, *Chem. Mater.*, **5**, 1694 (1993).
20. A. Usuki, et.al, *US Pat*, 4,889,885 (1989).
21. A. Okada, K. Fukumori, A. Usuki, Y. Kojima, N. Sato, T. Kurauchi and O. Kamigaito, *Polym. Preprints*, **32**, 540 (1991).
22. Y. Kojima, K. Fukumori, A. Usuki, A. Okada and T. Kurauchi, *J. Mater. Sci. Lett.*, **12**, 889 (1993).
23. A. Moet, A. Akelah, A. Hiltner and E. Baer, "Layered Silicate/PS Nanocomposite" Paper No. V4.2, this symposium.
24. R. A. Heacock and L. Marion, *Can. J. Chem.*, **34**, 1782 (1956).
25. C. Bernadette and C. Sandorfy, *Can. J. Chem.*, **36**, 1181 (1958).
26. A. Blumstein, *J. Polym. Sci.*, **3**, 2653 (1965).
27. A. Akelah, N. Salahuddin, A. Hiltner, E. Baer and A. Moet, *Chem. Mater.*, in press.
28. A. D. Wilson and H. J. Prosser, "Developments in Ionic Polymers", Elsevier Applied Science, New York (1986).
29. P. B. Messersmith and E. P. Giannelis, *Chem. Mater.*, **15**, 1064 (1993).

SELF-ASSEMBLY OF COBALT/BIPYRIDINE MULTILAYERS MODELED AFTER HOFMANN CLATHRATE COMPOUNDS

MICHAEL A. ANSELL, ASTRID C. ZEPPENFELD, WILLIAM K. HAM AND
CATHERINE J. PAGE*

Department of Chemistry, University of Oregon, Eugene, OR 97403

ABSTRACT

Progress has been made towards the development of inorganic-organic multilayered films modeled after Hofmann clathrate compounds. Cobalt-bipyridine multilayers were grown layer by layer on a silicon substrate. The resulting films were characterized using ellipsometry, grazing angle X-ray diffraction, Auger electron spectroscopy and EPMA (Electron Probe Micro-Analysis). Results indicate that moderately well ordered layers have been synthesized, but cross-linking with $M(CN)_4^{2-}$ ($M = Ni, Pd, \text{ or } Pt$) to simulate the model structure does not significantly occur.

INTRODUCTION

Self-assembled multilayers have attracted considerable interest recently because of the potential for controlling orientation, individual layer composition and properties, and the overall supramolecular architecture of layered assemblies on surfaces. Many potential applications have been considered for such materials, including use as active components in nonlinear optical devices,^{1,2} stable charge-separated assemblies,³ and as materials with selective responses for sensor applications.^{4,5} Zirconium-bisphosphonate self-assembled multilayers^{6,7} are currently under intense investigation for all of these applications.^{2,3,5} This system provides well-ordered multilayer films made of organic and inorganic layers that are robust and relatively easy to prepare.

Other systems are desired in order to increase the number of potential applications and to expand the types of chemistry available for building multilayer structures. The Hofmann-type clathrate⁸ model structure (Figure 1) is a member of well characterized class of bulk materials which also consist of alternating organic and inorganic layers. Each inorganic layer is made of a square net of alternating octahedral and square planar metal centers cross-linked by bridging cyanide molecules. The square planar metal site is generally occupied by a d^8 metal ion (Ni^{2+} , Pd^{2+} , or Pt^{2+} , for example) coordinated to the carbon end of four bridging cyanides. The octahedral site can be occupied by a variety of transition metal ions (Co^{2+} in the present case), and this metal center is coordinated to the nitrogen end of four cyanides and to two diamines. The diamines comprise the organic layers and serve to connect the inorganic layers. The square planar metal cyanide complex acts to cross link the material within the inorganic layer, providing order and stability. If this system could be adapted to allow self-assembly of a thin film based on this structure, it would provide an attractive alternative to the zirconium-bisphosphonate system. Some work in this direction with a ruthenium-bipyridine-nickel cyanide system has been recently reported.⁹

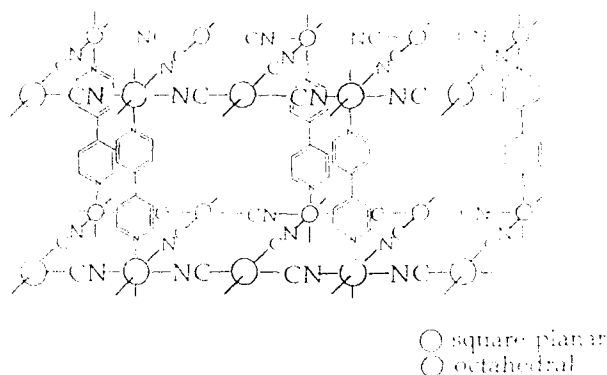


Figure 1: An example of the Hofmann-type clathrate structure.

The strategy for self-assembly of systems modeled after Hofmann-type clathrate materials adopted here involves the following steps. A flat silicon substrate is functionalized with an anchor molecule bearing a trimethoxysilyl group on one end (which will presumably form a covalent Si-O-Si linkage with the silicon substrate), and an amine functionality at the other. Divalent metal ions (Co^{2+}) are then bound to the amine-terminated surface. Mimicking the model compound, this step is followed by incorporation of the square planar complex ion $\text{M}(\text{CN})_4^{2-}$ into the Co^{2+} layer. The final step to complete the layer involves binding a diamine (bipyridine) monolayer to the remaining coordination sites of the Co^{2+} ions. 4,4'-Bipyridine was chosen because its rigid, bulky structure may help to impart order to the material. The process can be repeated by cycling through each of the above steps to produce multilayers. Results pertaining to the synthesis and characterization of the thin films prepared by this general sequence are presented below. Specific systems reported here include those using Co^{2+} , bipyridine, and each of the square planar complexes: $\text{Ni}(\text{CN})_4^{2-}$, $\text{Pd}(\text{CN})_4^{2-}$ and $\text{Pt}(\text{CN})_4^{2-}$. A control system which was prepared using only Co^{2+} and bipyridine (without a square planar complex) is also reported.

EXPERIMENTAL

Materials. Potassium tetracyanoplatinate(II) trihydrate and 4,4'-bipyridine were purchased from Aldrich and used as received in 10mM aqueous solutions. $\text{CoCl}_2 \cdot 6\text{H}_2\text{O}$ was purchased from Baker and used in a 10mM solution in acetone. Potassium tetracyanopalladate(II) and potassium tetracyanonickelate(II) were prepared^{10,11} from the respective dichloride salts and potassium cyanide and used in 10mM aqueous solutions.

Polished prime grade (100) silicon wafers used as the substrate were purchased from Silicon Quest. The anchor molecule, 3-aminopropyltriethoxysilane (APS), was purchased from Aldrich. Wafers were cleaned prior to use as substrates by rinsing successively in trichloroethylene for 10 minutes, isopropanol for 15 minutes and under flowing ultrapure water for 20 minutes.

Substrate functionalization. Wafers were functionalized using a modified procedure similar to that used by Goss et al¹² and Katz et al¹³. Clean wafers were submerged in a refluxing 1% (v/v) APS /ethanol (200 proof) solution for ten minutes, rinsed with ethanol, dried with flowing N₂, and placed in a 105°C oven for eight minutes. The wafers were returned to the refluxing solution and the cycle was repeated three times.

Preparation of Multilayers. All reactions were carried out in solution under ambient pressure and temperature. Samples were placed in the cobalt, K₂M(CN)₄, and bipyridine solutions for 20, 20, and 40 minutes respectively and rinsed for ten minutes under flowing water purified to a resistivity of 17-18 MΩ-cm with a Barnstead E-pure system after each step in the preparation.

Ellipsometry was done using a Rudolph Thin Film Ellipsometer 43702-200E with a tungsten-halogen light source and a 632 nm filter. Thicknesses were calculated using DaFIBM (version 2.1) provided by Rudolph, assuming an index of refraction of 3.858-0.013i for the silicon substrates. Grazing angle X-ray diffraction was measured using a Scintag XDS-2000 θ - θ powder diffractometer.

Auger Electron Spectroscopy (AES) was performed with a 2.8 keV electron beam in a UHV chamber at 10⁻⁷ to 10⁻⁸ torr.

RESULTS AND DISCUSSION

Samples prepared as described above were analyzed using a number of techniques to determine the resulting composition and structure. No single technique yet exists allowing one to completely characterize nanoscale thin films, but several techniques can be used in combination to obtain a fairly good picture of the resulting materials.

Ellipsometry is an optical technique commonly used to determine film thicknesses.¹⁴ Changes in the amplitude and phase of elliptically polarized light reflected from a surface or thin film are measured. If the refractive index of the film is known, then the film thickness can be calculated.

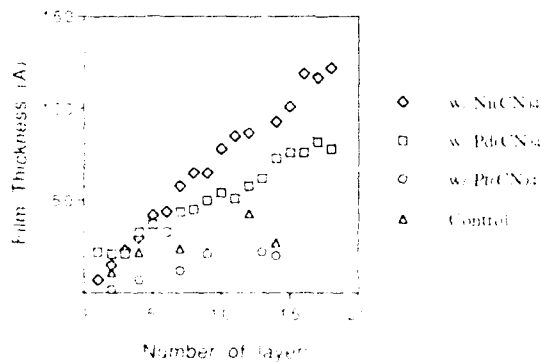


Figure 2: Layer thickness vs. number of layers for Co/bipyridine multilayers

Ellipsometry data for multilayer growth of Co^{2+} - $[\text{Ni}(\text{CN})_4]^{2-}$ -bipyridine (Co-Ni-bpy), Co^{2+} - $[\text{Pd}(\text{CN})_4]^{2-}$ -bipyridine (Co-Pd-bpy), Co^{2+} - $[\text{Pt}(\text{CN})_4]^{2-}$ -bipyridine (Co-Pt-bpy) and a control Co-bpy system are shown in Figure 2. The film thicknesses were calculated assuming a refractive index of 1.50 for all films. This value is chosen because hafnium- and zirconium-bisphosphonate films have indices in this range, and it is an appropriate choice given that the index for these materials is not known. Different values of the index in the range 1.45-1.60 give similar thicknesses.

Figure 2 shows that in each case film growth is occurring in the early stages, but except for the case of the Co-Ni-bpy sample, layer growth becomes very irregular after the first few layers. The consistency of layer growth is best for the Co-Ni-bpy system, but becomes noticeably worse for the Co-Pd-bpy system, and the Co-Pt-bpy system shows no advantage over the control Co-bpy sample. In the case of the Co-Ni-bpy system, uniform layering appears to continue to ~18 layers. Thus the square planar $\text{M}(\text{CN})_4^{2-}$ complex apparently influences the degree of order in these films, and also the ability to continue layer growth beyond the first several layers.

Grazing angle X-ray diffraction (Figure 3) shows fringes due to interference between reflections of x-rays from the front and back of a film.¹⁵ Film thickness is determined using the Bragg Equation:

$$n\lambda = 2d\sin\Theta \quad (1)$$

where d is the total thickness of the film, n is the order of reflection of interference, λ is the x-ray wavelength and Θ is in degrees. The total layer thickness for the 19-layer Co-Pd-bpy sample is calculated to be 91.2 Å. By dividing simply by the number of layers the average layer thickness is 4.8 Å/layer. This number is deceptive though, because our studies show that layer thickness is larger for the first several layers and decreases

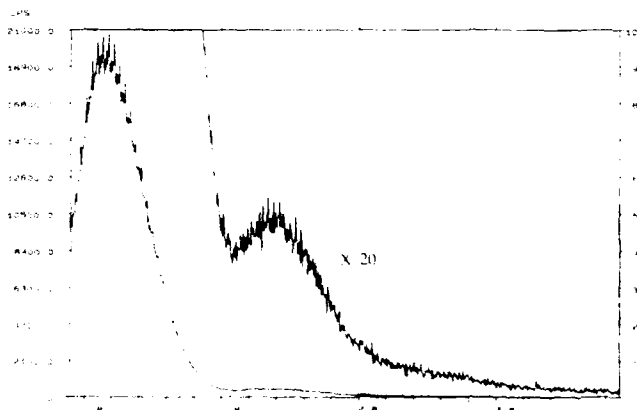


Figure 3: Grazing angle x-ray diffraction of a 19 layer Co-Pd-bpy multilayer.

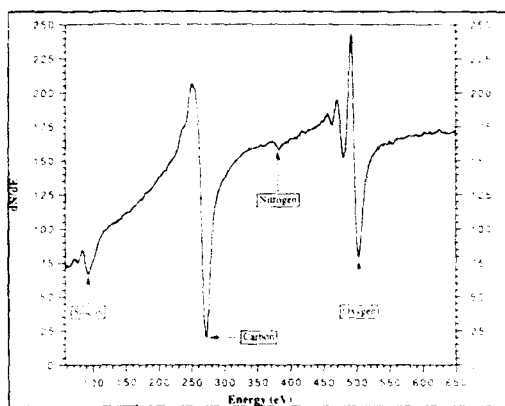


Figure 4: Auger Electron Spectroscopy data of Co/bipyridine multilayers prepared without a cross-linking metal cyanide complex.

steadily with additional layering. This indicates that the overall disorder is increasing with increasing numbers of layers.

Auger Electron Spectroscopy (AES)¹⁶ was performed on 2-layer Co-bpy, Co-Ni-bpy, Co-Pd-bpy, and Co-Pt-bpy samples. This technique was used to qualitatively determine the elemental composition of each of the films. Each of the resulting spectra were very similar. The silicon peak is a result of the substrate and the anchor molecule. A carbon peak is expected, indicating the presence of the anchor molecule and/or bipyridine. The oxygen peak could be due to the silicon oxide layer, hydroxide coordinated to a metal center, or solvent (water or acetone) trapped in the film. It is probably a combination of two or more of these factors. The nitrogen peak is small and similar in each of the samples, including the control prepared without a cyanide complex. This indicates that the metal cyanide complex is probably not present in the resulting film. However, Auger electrons are easily absorbed below a surface, so x-ray photoelectron spectroscopy (XPS) may be a more conclusive probe for nitrogen.

Electron probe microanalysis (EPMA) was used to analyze Co-Ni-bpy and Co-Pd-bpy samples for cobalt, nickel, and palladium. Cobalt was found in each case, but nickel and palladium were not detected in respective samples. This supports the conclusion that Co is incorporated into the materials, but the nickel, palladium, or platinum cyanide complexes are not permanently bound in the films, although they may participate indirectly in film growth.

In summary, we have prepared novel organic-inorganic multilayered thin films consisting of moderately well-ordered layers of cobalt and bipyridine grown from an amine-functionalized silicon surface. Efforts to incorporate metal cyanide complexes into the layered matrix have so far been unsuccessful, but the metal complex has been shown to be a significant factor in the successful preparation of multilayer films. Experiments are underway to investigate the effects of varying the bridging ligands and

organic constituents of the system in order improve the structural properties of these unique materials.

ACKNOWLEDGMENT

Acknowledgment is made to the donors of the Petroleum Research Fund, administered by the ACS, for the partial support of this project (#26158-ACS). Support from the U.S. Department of Education Graduate Assistance in Areas of National Need for MAA and support from the German Research Foundation for ACZ is gratefully acknowledged. We thank Derek Gragson of the U of O for the AES and Michael Shaffer of the U of O for the EPMA.

REFERENCES

1. D. Li, M.A. Ratner, T.J. Marks, C. Zhang, J. Yang, G.K. Wong, *J. Am. Chem. Soc.* **112** (20), 7389 (1990).
2. H.E. Katz, G. Sheller, T.M. Putvinski, M.L. Schilling, W.L. Wilson and C.E.D. Chidsey, *Science* **254**, 1485 (1991).
3. L.A. Vermeulen, J.L. Snover, L.S. Sapochak, and M.E. Thompson, *J. Am. Chem. Soc.*, **115** (25), 11767 (1993).
4. I. Rubinstein, S. Steinberg, Y. Tor, A. Shanzer, J. Sagiv, *Nature* **332**, 426 (1988).
5. D. Rong, Y.I. Kim, H.G. Hong, J.S. Krueger, J.E. Mayer, T.E. Mallouk, *Coord. Chem. Rev.* **97**, 237 (1990).
6. H. Lee, L.J. Kepley, H.G. Hong, T.E. Mallouk, *J. Am. Chem. Soc.* **110**, 618 (1988).
7. H. Lee, L.J. Kepley, H.G. Hong, S. Akhter, T.E. Mallouk, *J. Phys. Chem.* **92**, 2597 (1988).
8. K.A. Hoffmann, *Z. Anorg. Allg. Chem.* **15**, 204 (1897).
9. C.M. Bell, S.W. Keller, V.M. Lynch and T.E. Mallouk, *Mater. Chem. and Phys.* **35**, 225 (1993).
10. W.C. Fernelius and J.J. Burbage, in *Inorganic Synthesis Vol. II*, edited by W.C. Fernelius (McGraw-Hill Book Co., Inc., New York, 1946), p. 227.
11. J.H. Bigelow, in *Inorganic Synthesis Vol. II*, edited by W.C. Fernelius (McGraw-Hill Book Co., Inc., New York, 1946), p. 245.
12. C.A. Goss, D.H. Charych, and M. Majda, *Anal. Chem.* **63**, 85 (1991).
13. H.E. Katz, M.L. Schilling, C.C.D. Chidsey, T.M. Putvinski, R.S. Hutton, *Chem. Mater.* **3**, 699 (1991).
14. H.G. Tompkins, *A User's Guide to Ellipsometry*, 1st ed., (Academic Press Inc., Boston, 1993), p. 19.
15. B. Lengeler, *Mikrochim. Acta* **I**, 455 (1987).
16. A. Ulman, *An Introduction to Ultrathin Organic Films*, 1st ed. (Academic Press, Inc., Boston, 1991), p. 77.

BARIUM TITANIUM ALKOXIDES FOR BARIUM TITANATES: SYNTHESIS, CHARACTERIZATION, AND APPLICATIONS

VICTOR W. DAY,* TODD A. EBERSPACHER,* WALTER G. KLEMPERER** AND
SHURONG LIANG**

*Department of Chemistry, University of Nebraska, Lincoln, NE 68588

**Beckman Institute for Advanced Science and Technology and Department of Chemistry,
University of Illinois, Urbana, IL 61801

ABSTRACT

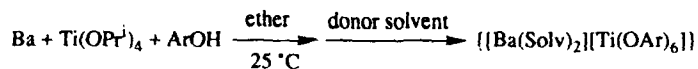
Several new crystalline bimetallic alkoxide precursors for barium titanates processing have been prepared: $\{[\text{Ba}(\text{Solv})_2][\text{Ti}(\text{OAr})_6]_2\}$ (1) (Solv = coordinated solvent molecule, Ar = aryl group), $[\text{Ba}(\text{CH}_2\text{OHCH}_2\text{OH})_4(\text{H}_2\text{O})][\text{Ti}(\text{OCH}_2\text{CH}_2\text{O})_3]$ (2), $\text{Ba}[\text{Ti}_2(\text{OR})_9]_2$ (3) (R = methyl, ethyl, and n-propyl), and $[\text{Ba}(\text{BzOH})\text{Ti}_2\text{O}(\text{OBz})_8]_2$ (4) (Bz = benzyl). These precursors have been characterized by elemental analysis, IR, NMR, and single-crystal X-ray diffraction techniques. Compound 1 is well-suited for sol-gel processing of BaTiO_3 powders and thin films under a variety of conditions. The facile preparation of 2 using relatively inexpensive starting materials makes it a viable alternative for the synthesis of BaTiO_3 fine powders. Both compounds 3 and 4 are fairly moisture-sensitive; hydrolysis of these precursors under acidic conditions affords the formation of gels instead of precipitates. The reactivity of 3 toward hydrolysis can be tailored by varying the alkyl group.

INTRODUCTION

Barium titanates are important electronic ceramic materials. For example, barium titanate (BaTiO_3) is a widely used dielectric material in the manufacture of multilayer capacitors [1], and BaTi_4O_9 , $\text{Ba}_2\text{Ti}_9\text{O}_{20}$, and $\text{BaTi}_5\text{O}_{11}$ have found applications in microwave communication due to their high dielectric constants and low dielectric loss [2]. Recent investigations have focused on the preparation and processing of high quality materials through wet chemical routes such as coprecipitation and sol-gel processing [3]. In order to obtain materials with improved properties, an understanding of the chemistry involved in these processes is desirable. As a first step in this direction, we and others [4] have sought to prepare fully characterized, single-source precursors for different barium titanate materials. In this paper, we report the synthesis, characterization, and properties of several new barium titanium alkoxides suitable for this purpose.

$\{[\text{Ba}(\text{Solv})_2][\text{Ti}(\text{OAr})_6]\}$

Solvated barium titanium alkoxides $\{[\text{Ba}(\text{Solv})_2][\text{Ti}(\text{OAr})_6]\}$ (1) can be prepared from barium metal, titanium isopropoxide, and phenol in appropriate solvents at ambient temperature according to the following equation:



All operations are carried out under an inert atmosphere using Schlenk and dry box techniques. As an example, reaction of barium metal with one equivalent of $\text{Ti}(\text{OPr}^i)_4$ (Pr^i = isopropyl) and excess phenol in ether at room temperature yields a yellow powder. After recrystallization of the powder from a DMF/ether solution, a yellow complex, $\{[\text{Ba}(\text{DMF})_2]_2[\text{Ti}(\text{OC}_6\text{H}_5)_6]_2\}$, is obtained in analytically pure form; the overall yield is 73% based on barium.

The solid-state structure of $\{[\text{Ba}(\text{DMF})_2]_2[\text{Ti}(\text{OC}_6\text{H}_5)_6]_2\}$ has been determined using single crystal X-ray crystallography, and its metal-oxygen core structure is shown in Figure 1. It is a molecular dimer in which two $[\text{Ti}(\text{OC}_6\text{H}_5)_6]^{2-}$ groups are linked by two $[\text{Ba}(\text{DMF})_2]^{2+}$ units through doubly and triply bridging OC_6H_5 ligands. Each DMF ligand is coordinated to barium through its carbonyl oxygen atom. The metal-oxygen core structure approximates D_{2h} symmetry: the two Ba atoms, two Ti atoms, and four doubly-bridging OC_6H_5 oxygen atoms are virtually coplanar.

Several derivatives have also been prepared under similar conditions using different Ar groups and solvents. These compounds have been characterized by elemental analysis as well as IR and NMR spectroscopy. All of these compounds are fairly moisture-sensitive. By varying the solvent molecule (Solv) and the alkoxy group (OAr), it is possible to tailor the properties of the precursor to specific needs. For example, letting $\text{Ar} = \text{C}_6\text{H}_4\text{CH}_3$ instead of C_6H_5 or $\text{Solv} = i\text{PrOH}$ instead of DMF renders the molecule highly soluble in hydrocarbon solvents.

The $\{[\text{Ba}(\text{Solv})_2][\text{Ti}(\text{OAr})_6]\}$ molecules are well-suited for sol-gel processing of BaTiO_3 under a variety of conditions. Nanocrystalline barium titanate powders and thin films have been prepared using these precursors.

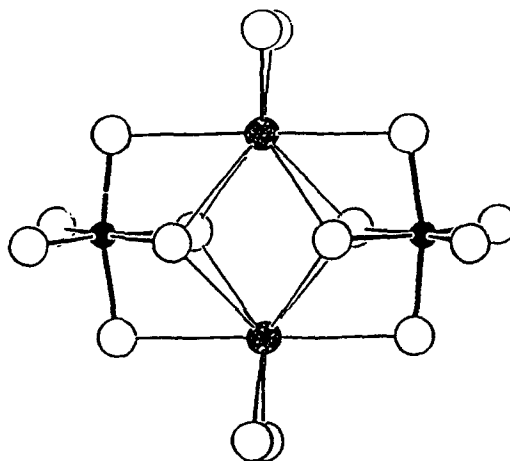
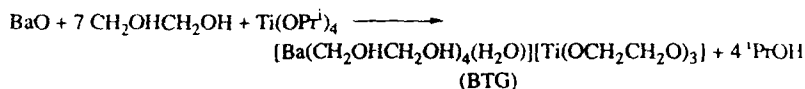


Figure 1. The metal-oxygen core of $\{[\text{Ba}(\text{DMF})_2]_2[\text{Ti}(\text{OC}_6\text{H}_5)_6]_2\}$ structure. Titanium atoms are represented by small filled circles, barium atoms by heavily shaded circles, and oxygen atoms by large open circles. Carbon, hydrogen, and nitrogen atoms are not shown.



Technical grade BaO fine powder reacts exothermically with ethylene glycol to form a slightly cloudy suspension. Rapidly addition of one equivalent of $\text{Ti}(\text{OPr}^i)_4$ to the suspension accompanied by vigorous stirring yields analytically pure $[\text{Ba}(\text{CH}_2\text{OHCH}_2\text{OH})_4(\text{H}_2\text{O})][\text{Ti}(\text{OCH}_2\text{CH}_2\text{O})_3]$ (barium titanium glycolate or BTG) as a white crystalline precipitate in 95 %



yield. This compound exhibits moderate moisture-sensitivity. Upon exposing BTG to the air for a few hours, absorption of water has been observed. Nevertheless, preparation and manipulation of BTG can be quickly carried out in the air with little difficulty. BTG is only poorly soluble in ethylene glycol at room temperature and is virtually insoluble in the commonly-used organic solvents we have tested. It has been characterized by elemental analysis, IR spectroscopy, and single crystal X-ray crystallography.

The solid-state structure of BTG consists of discrete $[\text{Ba}(\text{CH}_2\text{OHCH}_2\text{OH})_4(\text{H}_2\text{O})]^{2+}$ cation and $[\text{Ti}(\text{OCH}_2\text{CH}_2\text{O})_3]^{2-}$ anion (Figure 2). Three bidentate $[\text{OCH}_2\text{CH}_2\text{O}]^{2-}$ ligands are octahedrally coordinated to the Ti^{4+} center in the anion. In the cation, a water molecule and four ethylene glycol molecules are coordinated to a nine-coordinate Ba^{2+} cation.

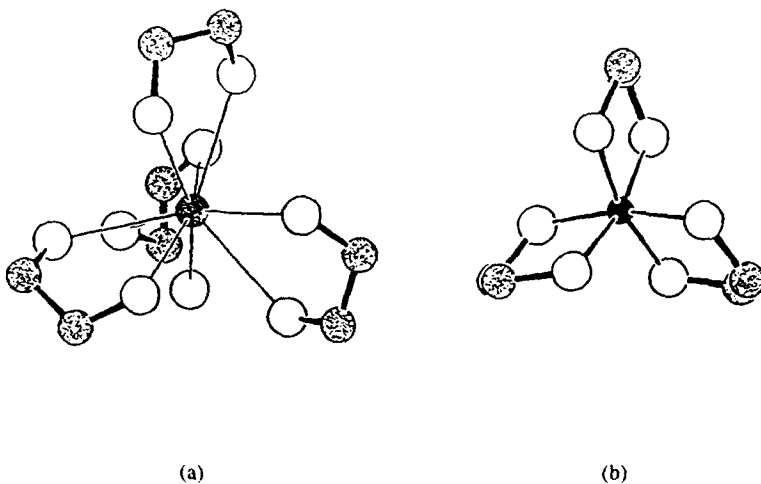
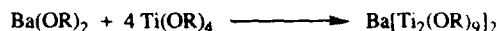
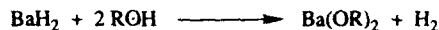


Figure 2. The structures of (a) the $[\text{Ba}(\text{CH}_2\text{OHCH}_2\text{OH})_4(\text{H}_2\text{O})]^{2+}$ cation and (b) the $[\text{Ti}(\text{OCH}_2\text{CH}_2\text{O})_3]^{2-}$ anion in crystalline $[\text{Ba}(\text{CH}_2\text{OHCH}_2\text{OH})_4(\text{H}_2\text{O})][\text{Ti}(\text{OCH}_2\text{CH}_2\text{O})_3]$. The titanium atom is represented by a small filled circle, the barium atom by a heavily shaded circle, oxygen atoms by large open circles, and carbon atoms by lightly shaded circles. Hydrogen atoms are not shown.

The poor solubility of compound 2 in commonly-used solvents precludes study of its hydrolysis behavior and application for sol-gel thin film deposition. Nevertheless, its facile preparation using relatively inexpensive starting materials makes it a viable alternative for the manufacture of BaTiO₃ fine powders.

Ba[Ti₂(OR)₉]₂

The synthesis of Ba[Ti₂(OR)₉]₂ (3) (R = methyl, ethyl, and n-propyl) is carried out by reacting BaH₂ with the appropriate alcohol followed by addition of the corresponding titanium alkoxide according to the following equations:



Compounds 3 were isolated as crystalline precipitates which are highly soluble in hydrocarbon solvents. The structure of the *n*-propoxide Ba[Ti₂(OPrⁿ)₉]₂ has been determined and is shown in Figure 3. In this structure, two [Ti₂(OR)₉]⁻ are linked by a Ba²⁺ cation through doubly and triply bridging alkoxy ligands to form a molecular complex. The same structure has recently been reported by Turevskaya, *et al.* for the Ba[Ti₂(OEt)₉]₂ molecule [4e]. The reactivity of 3 toward hydrolysis can be tailored by varying the alkyl group. Replacing R = ethyl by *n*-propyl, for example, dramatically decreases reactivity of 3 toward hydrolysis. Hydrolysis of 3 (R = ethyl) with excess amounts of water affords the formation of a white precipitate; in the presence of a catalytic amount of strong acid, however, a transparent gel is obtained.

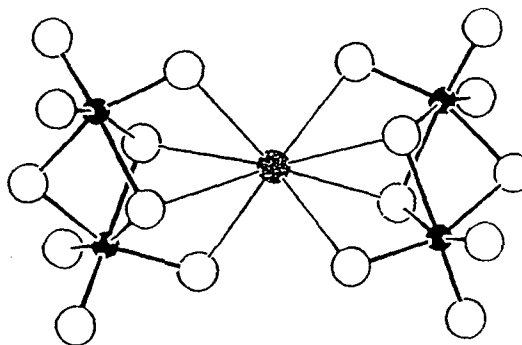
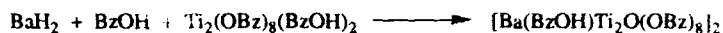


Figure 3. The metal-oxygen core of Ba[Ti₂(OPrⁿ)₉]₂ structure. Titanium atoms are represented by small filled circles, the barium atom by a heavily shaded circle, and oxygen atoms by large open circles. Carbon and hydrogen atoms are not shown.



$[\text{BaTi}_2\text{O}(\text{OBz})_8(\text{BzOH})]_2$ (Bz = benzyl) (**4**) is prepared by first reacting BaH_2 with excess BzOH and then adding a solution of $\text{Ti}_2(\text{OBz})_8(\text{BzOH})_2$ in benzene. Compound **4** is



isolated as analytically pure white crystals and has been characterized by NMR and IR spectroscopy. The solid-state structure of **4** is shown in Figure 4, in which two $[\text{Ti}_2\text{O}(\text{OBz})_8]^{2-}$ units are linked by two $[\text{Ba}(\text{BzOH})]^{2+}$ groups. This complex is also fairly moisture-sensitive. Hydrolysis of **4** yields a precipitate immediately, whereas a transparent gel is formed in the presence of a strong acid.

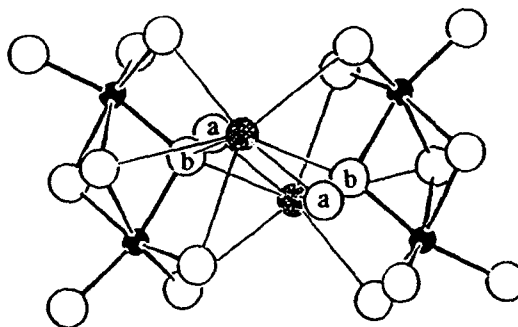


Figure 4. The metal-oxygen core of $[\text{Ba}(\text{BzOH})\text{Ti}_2\text{O}(\text{OBz})_8]_2$ structure. Titanium atoms are represented by small filled circles, barium atoms by heavily shaded circles, and oxygen atoms by large open circles. The alcohol oxygen atoms are labeled as O_a , oxide oxygen atoms as O_b , and the alkoxide oxygen atoms remain unlabeled. Carbon and hydrogen atoms are not shown.

To summarize, various alkoxide ligands have been employed to prepare barium titanium alkoxides with Ba:Ti ratios of 1:1, 1:2, and 1:4. These precursors exhibit physical and chemical properties that are well-suited for processing barium titanates under various conditions. We are currently investigating and optimizing these conditions.

ACKNOWLEDGMENTS

This work was supported by the United States Department of Energy, Division of Materials Science under Contract DE-AC02-76 ER01198. We are also grateful to Professor David A. Payne of the Department of Materials Science and Engineering at the University of Illinois for helpful discussion.

REFERENCES

1. J. M. Herbert, *Ceramic Dielectrics and Capacitors*, (Gordon and Breach Science Publishers, New York, 1985).
2. (a) T. Negas, G. Yeager, S. Bell, N. Coats, and I. Minis, *Am. Ceram. Soc. Bull.* **72**, 80 (1993).
(b) T. Negas, G. Yeager, S. Bell, and R. Amren, *NIST Special Publication 804-21* (1991).
3. P. P. Phule and S. H. Risbud, *J. Mater. Sci.* **25**, 1169 (1990).
4. (a) E. P. Turevskaya, N. Ya. Turova, and A. V. Novoselova, *Dokl. Akad. Nauk SSSR* **242**, 883 (1978). (b) K. W. Kirby, *Mater. Res. Bull.* **23**, 881 (1988). (c) J.-F. Campion, D. A. Payne, H. K. Chae, J. K. Maurin, and S. R. Wilson, *Inorg. Chem.* **30**, 3244 (1991). (d) A. I. Yanovsky, M. I. Yanovskaya, V. K. Limar, V. G. Kessler, N. Ya. Turova, and Y. T. Struchkov, *J. Chem. Soc., Chem. Commun.* 1605 (1991). (e) E. P. Turevskaya, M. I. Yanovskaya, V. K. Limar, and N. Ya. Turova, *Zh. Neorg. Khim.* **38**, 609 (1993). (f) Y. Suyama and M. Nagasawa, *J. Am. Ceram. Soc.* **77**, 603 (1994).

NANOSTRUCTURAL INVESTIGATION OF SILICA AEROGELS

JUE WANG, JUN SHEN, WEIDONG WU AND BIN ZHOU

Tongji University, Pohl Institute of Solid State Physics, Shanghai, CHINA

ABSTRACT

Silica aerogels are sol-gel derived nanostructured materials with high porosities up to 99.8%. The nanostructures of silica aerogels are investigated by BET, SEM, SAXS techniques. A typical fractal structure is found especially for base-catalyzed aerogels. That is the aerogels are made of particles of size a , these particles form the branching and interconnecting networks up to an average cluster size ξ . At length scales above ξ , the material is an homogeneous assembly of such clusters; between a and ξ , the structure is fractal. Meanwhile, the effects of catalysis and aging on the structures are investigated and discussed. The reasons why SCD technique should be used are also deeply discussed.

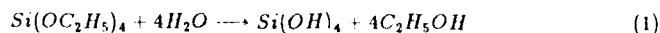
INTRODUCTION

Silica aerogels are sol-gel derived solid materials with porosities from about 80% to 99.8%[1]. The high porosity is achieved via supercritical drying(SCD) technique. It differs markedly in structure and appearance from other low density materials such as feather, cotton, sponge or insulating foams. The nanoporosity, i.e., the porosity in the nanometer region, which is typical of aerogels endows them with numerous special properties such as low index of refraction, small Young's modulus, low acoustic impedance, low thermal conductivity, excellent accessibility of inner surface and so on. Interest in aerogels is growing progressively, more and more applications have been realized[2]. There is also an upsurge in basic research on aerogels[3,4]. Scientists started to make and investigate aerogels with fractal structure, to derive the density of states of aerogels or to measure their low temperature thermal conductivity or heat capacity. Almost all of the special properties are due to their nanoporosity, therefore, the investigation of nanostructure of aerogels is a hot spot of material science as well as condensed matter physics.

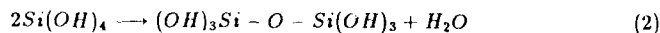
PREPARATION

Sol-gel process

The silica aerogels are prepared through sol-gel process from TEOS. The sol-gel process, i.e., the hydrolysis and polycondensation of organosilicon precursors denotes the transition of a system of colloidal particles in a solution into a disordered, branched, continuous network interpenetrated by a liquid of water, alcohol etc. It can be described by two reaction steps, hydrolysis of TEOS by addition of water and a catalyst:



and the silicic acid condenses by expelling water:



The sol-gel process is quite different under different catalyst conditions because the reaction rates of hydrolysis and condensation are quite different under different PH values. Therefore, the nanostructure of aerogels derived is quite different[5]. Normally, under acidic conditions, hydrolysis is completed before condensation starts, the slow condensation reaction of the silicic acid monomers leads to the formation of polymer-like silica chains, resulting in a weakly cross-linked, low density network. While under basic conditions, hydrolysis is the limiting step, i.e. whenever a monomer is hydrolyzed, it condenses

rapidly. This behavior leads to the growth of comparatively dense, colloidal particles; their final size depends on the temperature and on the PH value of the solution. The catalysts used are normally hydrochloric acid and ammonia solution, the main purpose is to regulate the PH value.

Drying process

The gel, still embedded in the solvent, which consists mainly of alcohol with some water and catalyst, is called an alcogel. The drying process consists in eliminating the interstitial liquid phase, when an alcogel is dried under ambient condition, the following sequence of events is observed: progressive shrinkage and hardening, stress -development and fragmentation. This is due to the capillary forces. While a liquid evaporates from a porous material the solid phase is subjected to forces due to capillary phenomena at the solid-liquid-gas interface. The capillary pressure Δp of a cylindrical capillary of radius r and a liquid having a wetting angle θ is:

$$\Delta p = p_r = \frac{2\gamma \cos \theta}{r} \quad (3)$$

where γ is the surface tension. In a drying gel there are capillary pores and gases of different sizes and shapes. Fig.1 shows variations of Δp as a function of r for water with $\gamma = 0.0729 \text{ N/m}$ and ethanol with $\gamma = 0.0224 \text{ N/m}$ (the wetting angle taken was $\theta = 0$). Obviously, while the pore size is about several nanometer, the capillary force is extremely large.

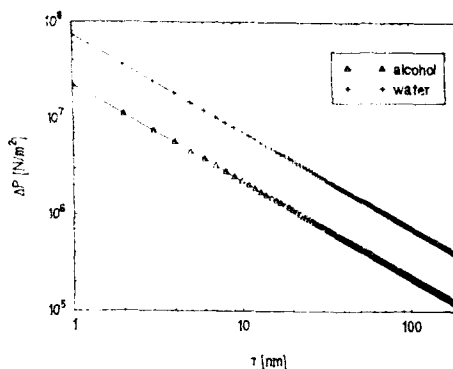


Fig.1 The capillary pressure Δp of cylindrical capillary of radius r for water and ethanol.

The size of pores of an alcogel is about 1nm to 100nm. In the first stage of drying, the volume shrinkage is equal to the volume of water lost by evaporation. This keeps the fluid meniscus at the surface of the gel body as shown in fig.2(a). This stage continues till the solid skeleton attains certain strength. In this situation, the volume shrinkage rate no longer maintains the fluid meniscus at the surface; the liquid tries to flow to the surface of the gel to avoid the more energetic solid/vapour interface(fig.2(b)). This is the first falling rate period. Usually crack occurs during this period. In the last stage of drying, called the second falling rate period, the funicular distribution of water inside the pores becomes pendular. Now the liquid transport is only by diffusion of vapour from the interior(fig.2 (c)). Normally fragmentation occurs during this period because numerous

meniscus are turned in much smaller pores now (fig.3). The dried gels obtained here are called xerogels.

In order to avoid shrinkage and cracking, i.e. to preserve the structure of the wet state, the most efficient way is to remove the solvent supercritically [6] during which the liquid-vapor phase transition is avoided. In this experiment, the supercritical drying (SCD) is performed near ambient temperature using liquid carbon dioxide which has a low critical temperature ($T_c = 31.0^\circ\text{C}$, $P_c = 73.9\text{bar}$) for safety purpose. Therefore, the pore liquid must be exchanged for liquid carbon dioxide before drying; this is carried out in an autoclave. A complete solvent exchange may require a long time depending on the sample size. Fig.4 is the pressure in the autoclave vs. time during a normal SCD. It also shows the whole SCD process. The dried gels derived through SCD are called aerogels. The density of aerogels derived here varies from 60kg/m^3 to 400kg/m^3 depending on the preparation conditions.

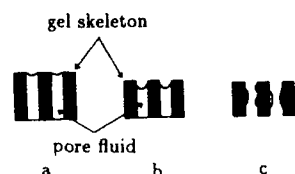


Fig.2 Three different stages of drying: (a) constant rate period. (b) first falling rate period and (c) second falling rate period. alcogel.

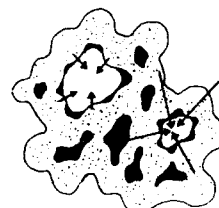


Fig.3 Capillary forces during drying of alcogel.

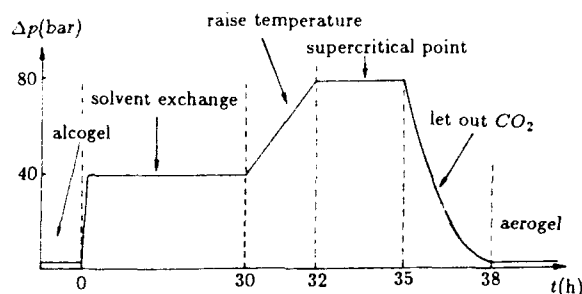


Fig.4 The pressure in the autoclave vs. time during SCD.

STRUCTURE INVESTIGATION

BET and XRD

BET-adsorption/desorption is a wide-spread technique for determining the specific surface area of porous materials. The BET used here is a Micromeritics FlowSorb II 2300. The experimental results show that the specific surface of the aerogels derived here is very high, it varies from $200\text{m}^2/\text{g}$ to $600\text{m}^2/\text{g}$. Normally, the lower the density, the higher the specific surface. Therefore aerogels are materials with high porosity. Also, XRD spectra show no character peaks for SiO_2 crystal, aerogels are composed of non-crystalline silica.

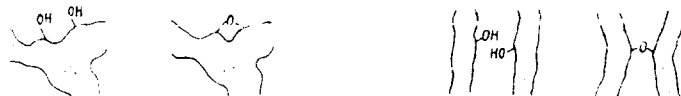
SEM

SEM can yield a direct image of the structure. Morphological features such as particle shapes, particle arrangements, etc., can be recognized. Quantitative estimates for pore or particle sizes can be obtained, although the derivation of size distributions is rather laborious. Fig.5 is SEM photographs of aerogels derived from different preparing conditions; (a) is a typical aerogel from acidic condition while (b) is typically from basic condition, the other conditions are same. Obviously, the size distribution of pores of (a) is relatively narrow (10~50nm) while that of (b) is quite wide(10~300nm). This is due to the different sol-gel process as well as the syneresis during aging and SCD.



(a) (b)
Fig.5 SEM photographs of aerogels derived from different conditions

After gelation the gel-body ages, sol particles and small clusters in the solution attach to the spanning cluster and extend the gel network. Moreover, all the condensation reactions(Eq.2) that caused gelation, continue; even continue during the SCD process. The syneresis is usually caused by condensation between neighbouring silanol groups[7] (fig.6). For base-catalyzed gels, most of the condensing groups are located on neighbouring surfaces which causes less shrinkage and expulsion of water (fig.6(a)). While for acid-catalyzed gels which have a flexible polymerlike network, most of the condensing groups are located on neighbouring branches or chains (fig.6(b)), shrinkage is particularly extensive and the pore size thus is limited considerably.



(a) (b)
Fig.6 Condensation between neighbouring silanol groups

SAXS

Small angle X-ray scattering(SAXS) is known to be one of the most powerful non-destructive techniques to explore the structure of aerogels. SAXS experiments in aerogels often give evidence of three regimes, corresponding to three different structural ranges[8]. At small q values, the crossover between a nearly q -independent intensity and a power-law behaviour $I(q) \propto q^{-D}$ reflects the existence of an homogeneous structure at large

Table 1: Size distribution of particles derived from Fig.7

Gyration radius(nm)	Diameter(nm)	Ratio
1.897	4.897	0.511
4.344	11.215	0.333
7.670	19.803	0.084
9.916	25.602	0.046
15.876	40.993	0.021
22.211	57.348	0.005

scales and of a fractal geometry at smaller ones. Here, D is the fractal dimension, which describes the scaling of the mass in the porous structure of the aerogels. At the smaller scales, the fractal domain is also limited by the granularity associated with dense particles. Here, a second crossover in $I(q)$ is observed. At larger q , the scattering is dominated by the density fluctuations associated with particle surface; again a power law decay of the intensity follows $I(q) \propto q^{-D_s}$ can be observed. D_s is the surface fractal dimension, which equals 2, in the case of a smooth surface, where a decay proportional to q^{-4} is observed known as Porod's law[9]. Small-angle X-ray scattering measurements were performed at room temperature using an apparatus(D/max-RB) with a 0.5mm×0.5mm point focus $\text{CuK}\alpha$ incident beam. Fig.7 is the SAXS result of a base-catalyzed aerogel with a density of 140 kg/m^3 . At small q , one observes the power law characteristic of fractal structure. From the slope, a $D \approx 2.1$ is deduced. The crossover from a q -independent intensity to this power law region at about $q \approx 0.006 \text{ \AA}^{-1}$ denotes the correlation length ξ is about 100nm. At about $q \approx 0.03 \text{ \AA}^{-1}$, a crossover to surface scattering is observed too; the slope is about -4, therefore the surface of the colloidal particles is quite smooth, and their size a is about 20nm. Between ξ and a , the structure is fractal with a fractal dimension of about 2.1.

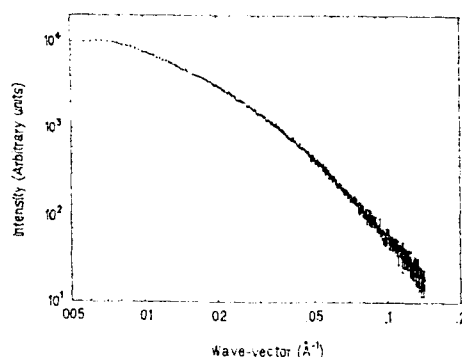


Fig.7 SAXS result of a base-catalyzed aerogel

Furthermore, with the fitness of a computer, the SAXS can give the size distribution of particles (Table 1). This is quite consistent with the TEM results.

The SAXS experiments also show that the extent of the fractal range of the base-catalyzed aerogels decreases with increasing density, and for acid-catalyzed aerogels it

is considerably diminished. Within fractal range the structure looks the same at all lengths $\xi > L > a$. This is called self-similarity or dilation symmetry. This character is typical for base-catalyzed aerogels.

CONCLUSION

Silica aerogels are prepared through sol-gel process from TEOS. The reason why SCD technique should be used is discussed. The nanostructure of aerogels are investigated via BET, SEM and SAXS techniques and a typical fractal structure is found especially for base-catalyzed aerogels. The effects of catalysis and aging on the structure are also investigated and discussed.

ACKNOWLEDGMENTS

This work was supported by the Volkswagen-Stiftung of Germany (contract No. I/68078) and the Natural Science Foundation of China (contract No. 59302020). The authors are very grateful to J. Fricke and the members in his group of Würzburg University for their useful advice.

REFERENCE

1. J. Fricke, ed., *Aerogels*, Springer Proceedings in Physics, **6**, (Springer, Heidelberg, 1986).
2. J. Fricke and A. Emmerling, in *Aerogels-Preparation, Properties, Applications*, edited by R. Reisfeld and C.K. Frgensen, Springer Series Structure and Bonding, **177**, (Springer, Heidelberg, 1992) PP.37-87.
3. E. Courtens, J. Pelous, J. Phalippou, R. Vacher and T. Woignier, Phys. Rev. Lett. **58**, 128 (1987).
4. J. Pelous, R. Vacher, T. Woignier, J.L. Sauvajol and E. Courtens, Phil. Mag. B, **59**, 65 (1989).
5. C.J. Brinber, D.E. Clark and D.R. Ulrich in *Better Ceramics Through Chemistry*, (Mat. Res. Soc. Proc. **32**, North-Holland, New York, 1984) pp. 25-32.
6. J. Phalippou, T. Woignier and M. Prassas, J. Mater. Sci, **25**, 3111 (1990).
7. T. Woignier, J. Phalippou and R. Vacher, J. Mater. Res. **4**, 688 (1989).
8. R. Vacher, T. Woignier, J. Pelous and E. Courtens, Phys. Rev. B, **37**, 6500 (1988).
9. G. Porod, Kolloidz. **124**, 83(1951).

CHARACTERIZATION OF THE INTERACTION OF HYDROGEN WITH IRIDIUM CLUSTERS IN ZEOLITES BY INELASTIC NEUTRON SCATTERING SPECTROSCOPY

J.M. NICOL*, T.J. UDOVIC*, R.R. CAVANAGH*, Z. XU**, S. KAWI**, T. MURE**,
and B.C. GATES**

*National Institute of Standards and Technology, Gaithersburg, MD 20899

**Department of Chemical Engineering, University of Delaware, Newark, DE 19716 and
Department of Chemical Engineering and Materials Science, University of California, Davis,
CA 95616

ABSTRACT

Incoherent inelastic neutron scattering (IINS) measurements of hydrogen bound to Ir₆ clusters in the nanoscale pores of zeolite NaY and similar clusters in KL zeolite are reported. On the basis of hydrogen uptake measurements and the observation of peaks in the IINS spectra, we infer that hydrogen is bound to the metal nanoclusters in the zeolite pores. The IINS data for both zeolites are similar and consistent with the presence of IrH₂ species.

INTRODUCTION

Most catalytic materials used in commercial technology are complex, consisting of multiple components and phases. Noble metals are common catalytic components, generally being present in small amounts (typically, 1 wt%) as highly dispersed particles or clusters on the surface of a porous ceramic material called a support. Because supported metal clusters are sometimes smaller than 1 nm in diameter and nonuniform in size and shape, it has been difficult to understand their structures and thus the relationships between structure and performance. Consequently, researchers have striven to prepare supported metal clusters that are nearly uniform in size and structure, often by attempting to confine the metal clusters in the small cages of molecular sieve zeolites. The research summarized here is an investigation of iridium clusters in the cages of zeolites Y and L utilizing incoherent inelastic neutron scattering (IINS) spectroscopy.

Some of the important unanswered questions about structure of supported metal catalysts have to do with the nature of the hydrogen on their surfaces. Hydrogen is typically present as protons in hydroxyl groups terminating the surfaces of ceramic supports. Furthermore, H₂ adsorbs dissociatively on metal surfaces to give atomic hydrogen species. When the metal particles are large, the maximum ratio of hydrogen to surface metal atoms is often ≤ 1 . However, when the metal is present in clusters as small as 1 nm in diameter, the maximum ratio can become somewhat larger. For example, in the case of Ir, the H:Ir ratio can approach 3 and probably depends on the nature of the support.¹

Because of the nonuniformity of supported metal catalysts and the lack of sensitivity to hydrogen of the commonly used spectroscopic characterization methods, it is difficult to determine the chemical nature of hydrogen associated with highly dispersed metal clusters. Characterization of such materials by extended X-ray adsorption fine structure (EXAFS) spectroscopy² showed that there are typically two metal-oxygen distances in such samples, one

about 0.21 nm and one about 0.26 nm. It has been suggested that the relative amounts of the structures characterized by these two distances are determined by how much hydrogen is present on the metal and at the interface between the metal and the support.²

Our goal was to use IINS measurements to characterize the hydrogen in highly dispersed supported metals. The catalyst samples were iridium supported in zeolites Y and L. Iridium was chosen because the H:Ir ratio is greater than that observed for other supported metals¹ and because earlier work³ indicated that extremely small Ir clusters of nearly uniform size could be prepared in the cages of zeolites.

IINS is well-suited to studies of the dynamics of hydrogen interacting⁴ with solid-state materials such as supported metal catalysts, since the incoherent neutron scattering cross section for hydrogen is ca. 10-30 times that of other nuclei. Thus IINS spectra will favor those vibrational modes associated with displacement of the hydrogen nuclei. Furthermore, in contrast to other photon or electron spectroscopies, there are no dipole, polarizability, surface, or symmetry selection rules, so in principle all modes may be observed. Finally, neutron scattering intensities are proportional to the number of scattering nuclei, allowing estimates of surface coverage, and they are easily calculated, a valuable aid in making mode assignments.

EXPERIMENTAL

The synthesis of Ir clusters in NaY zeolite was performed by a method similar to that described by Kawi et al.³ The synthesis and sample transfers were carried out with exclusion of air and moisture on a double-manifold Schlenk vacuum line and in a N₂-purged glove box. CO (Matheson, UHP grade⁵) was purified by passage through a trap containing particles of activated γ -Al₂O₃ at a temperature >523 K to remove traces of metal carbonyls and through a trap containing activated zeolite to remove traces of moisture. [Ir(CO)₂(acac)] (Strem⁶) was used as received. Hexanes (Aldrich, Reagent Grade⁵) were degassed by purging with N₂ for 30 min before use. NaY zeolite powder (LZY-52, Union Carbide,⁵ unit cell size 2.47 nm, SiO₂/Al₂O₃ ratio 4.74) was evacuated to 0.1 Pa at room temperature before use.

In a 250-mL Schlenk flask, 20 g of NaY zeolite was slurried with 0.16 g of [Ir(CO)₂(acac)] in hexanes. The white zeolite powder became dark brown, and the initially greenish-black solution became clearer after stirring for several hours. The slurry was stirred for three days, and the solution became colorless, indicating the uptake of the [Ir(CO)₂(acac)] by the zeolite. The solvent was removed by evacuation overnight. The zeolite contained 0.8 wt% Ir.

[Ir₆(CO)₁₆] was formed in the zeolite as follows: in the presence of flowing CO (15 mL/min) at atmospheric pressure, the sample was heated to 403 K, held there for 15 h, then cooled back down to room temperature. The infrared spectrum of the zeolite, in agreement with that of Kawi et al.,³ indicates the formation of [Ir₆(CO)₁₆] in the zeolite. The sample was light yellow. Attempts to extract the [Ir₆(CO)₁₆] from the zeolite by contacting the sample with solutions of tetrahydrofuran or bis(triphenylphosphoranylidene) ammonium chloride in tetra-hydrofuran were not successful, consistent with the entrapment of the clusters in the supercages of the zeolite. Further treatments to decarbonylate the clusters were made with the zeolite contained in the IINS sample cell. The sample is referred to in the text as Ir/NaY zeolite.

Ir clusters in KL zeolite were synthesized by an impregnation method similar to that used for NaY zeolite. [Ir(NH₃)₃Cl]Cl₂ was prepared by refluxing K₃[IrCl₆] · 3H₂O with (NH₄)₂CO₃ and NH₄Cl in water under an atmosphere of NH₃. The product was recrystallized and washed with aqueous solutions of HCl and then ethanol. KL zeolite (Union Carbide,⁵ K:Al atomic ratio = 1.03) was washed with water until the pH of the wash solution was 9.5, then dried in air and crushed into a fine powder. [Ir(NH₃)₃Cl]Cl₂ was dissolved in 40 mL of water by heating to 343

K and adding a few drops of HNO_3 . The pH of the solution was adjusted to 7.0 by addition of NH_4OH , and the solution was then added dropwise to the zeolite. The slurry stood for 3 h and the resultant solid was dried overnight at 393 K. The zeolite contained 2 wt% Ir. Further details of similar preparations and reductions are to be reported elsewhere.⁶ Treatments to reduce the Ir-containing KL zeolite were made with the zeolite contained in the IINS sample cell. The sample is referred to as Ir/KL zeolite.

For the IINS studies, between 10-15 g of the Ir-containing zeolite powder was loaded, using a helium filled glove box, into thin-walled aluminum or stainless-steel tubular cells,⁴ in which in-situ sample treatments under flowing gas, evacuation and hydrogen adsorption at elevated temperatures could be performed. He (Air Products,⁷ 99.995%), H_2 (Spectra Gases,⁸ research grade) and D_2 (Matheson,⁹ 97%D) gases used for decarbonylation and hydrogen activation were purified by passage through traps containing particles of Cu_2O and of activated zeolite to remove traces of O_2 and moisture, respectively. IINS scattering data were obtained at the Neutron Beam Split-Core Reactor (NBSR) at the National Institute of Standards and Technology, Gaithersburg, MD, using the BT-4 spectrometer with a liquid-nitrogen-cooled Be filter analyzer. A Cu (220) monochromator with 40" pre- and post-monochromator collimations was used to cover the energy range 31-160 meV (1 meV = 8.065 cm^{-1}). The energy resolution varied from ~ 4 meV at 35 meV to 10 meV at 150 meV. IINS measurements were made with the sample cooled to ca. 10 K. Data were corrected for fast neutron background contributions.

RESULTS

Reduction or decarbonylation of the clusters in both the Ir/KL and Ir/NaY zeolites was done with the samples contained in the IINS cells. After treatment with flowing H_2 , the zeolites were either purged with He for 0.5 h or evacuated to remove gaseous H_2 from the cell, which may contribute to the scattering signal. Data were collected at each stage of treatment, and by comparison of relative scattering intensities, a check could be made on the sample integrity.

The Ir clusters in KL zeolite were reduced by treatment in flowing H_2 at atmospheric pressure by slowly raising the temperature to 573 K, holding there for 1 h, and cooling back down to room temperature. After measurement of the vibrational spectra, the hydrogen-treated clusters were evacuated at 573 K for 2 h, and another vibrational spectrum was taken. Figure 1a shows the spectrum following this evacuation treatment, which was found to desorb H associated with the Ir clusters. For the purpose of background data, the IINS spectrum of dehydrated KL zeolite was measured after heating at 573 K for 1 h and cooling to room temperature, both under flowing H_2 , a treatment identical to that used to reduce the Ir/KL zeolite. The spectra obtained were identical to that obtained for the Ir/KL zeolite after evacuation at 573 K, shown in figure 1a. As a result, the data in figure 1a were used as the 'blank' Ir/KL zeolite spectrum for subsequent data obtained following H_2 adsorption. Additionally, spectra obtained for the hydrogen-treated, dehydrated KL zeolite before and after a He purge to remove gaseous H_2 were indistinguishable, showing that residual H_2 gas in the IINS cell was not contributing to the observed scattering signal.

The scattering features observed for the blank Ir/KL (fig. 1a) and dehydrated KL zeolite are contributions from hydrogen riding on lattice vibrations and from hydroxyl groups present in the zeolite. These hydroxyl groups are associated with the cations and termination sites at the edges of zeolite crystallites. The vibrational features have previously been assigned to the wagging modes of hydroxyl groups and with pore opening modes of the zeolite framework.^{7,8}

The clusters in the blank Ir/KL zeolite were reexposed to H_2 in amounts equivalent to coverages of 1 and 2 H's per Ir. These reexposures were followed by a temperature ramp

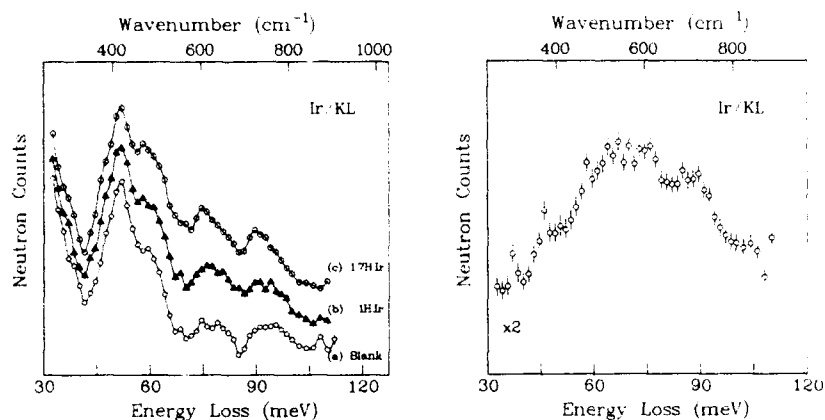


Figure 1 (left). IINS spectra of Ir/KL zeolite (a) after evacuation of cluster-adsorbed hydrogen at 598 K for 2 h, and after H₂ readsorption yielding (b) 1H/Ir and (c) 1.7 H/Ir.

Figure 2 (right). Difference spectrum obtained by subtraction of the blank Ir/KL spectrum (1a) from the spectrum of the sample with 1.7 H's per Ir (1c) revealing scattering contributions due to the cluster-adsorbed hydrogen.

(5 K/min) from room temperature to 473 K and back down to room temperature to ensure equilibrium. The resulting spectra are shown in figure 1 (b) and (c). For the higher exposure of 2H's per Ir, a maximum of 1.7 H's per Ir were actually adsorbed, indicating that a portion of the clusters were larger than Ir₆ or that not all of the Ir atoms were accessible for H adsorption. The vibrational spectra after this rehydrogenation were essentially identical in both intensity and lineshape to that following the original reduction in flowing H₂. The integrity of the samples was found not to diminish to any significant extent by repeated hydrogenation/dehydrogenation cycles. A difference spectrum obtained by subtraction of the Ir/KL blank spectrum from the spectrum of the sample containing 1.7 H atoms per Ir is shown in figure 2. The observed scattering features are due to hydrogen associated with the Ir clusters.

The Ir₆ clusters in NaY zeolite were first decarbonylated by treatment with flowing He, and subsequently treated with flowing H₂, in a similar fashion to that used for Ir/KL zeolite. The maximum hydrogen treatment temperature was 598 K (held for 2 h). In a separate experiment, a wafer of the sample in an infrared cell was treated under similar conditions, and the complete disappearance of the $\nu_{\text{C-O}}$ bands indicated that the decarbonylation was complete. Details of the decarbonylation are to be presented elsewhere.⁸ For Ir/NaY zeolite prepared in the way, EXAFS³ indicates that about 85% of the Ir is in the form of Ir₆ clusters. Again, spectra were measured before and after hydrogenation. The sample was then evacuated at 598 K (fig. 3a), followed by a volumetric adsorption of H₂ (again similar to the treatment of Ir/KL), which yielded a maximum H/Ir ratio of 2.9. One cannot be entirely certain that this large H/Ir ratio reflects only hydrogen bound to the clusters. It is always possible that some spillover of hydrogen onto the zeolite support is occurring. Nonetheless, the resulting hydrogen spectra determined from data taken before and after this readsorption of hydrogen were essentially identical to that derived from the first hydrogen treatment. Moreover, this hydrogen spectrum

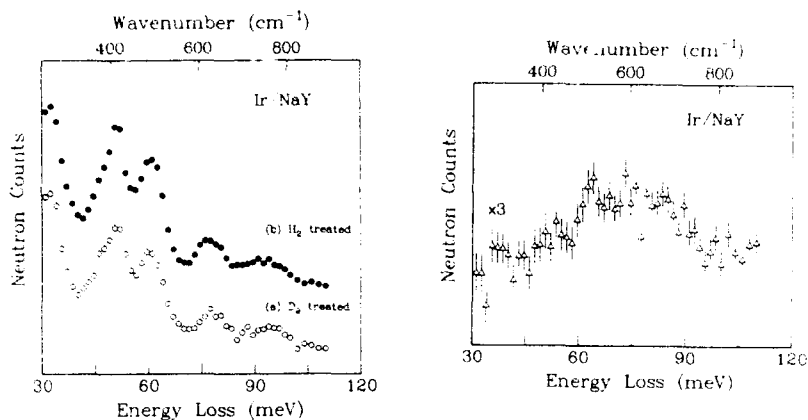


Figure 3. IINS spectra of (a) H_2 - and (b) D_2 -activated Ir/NaY zeolites. Data are normalized and without offset, showing how D_2 activation leads to a reduction in scattering from the zeolite support.

Figure 4. Difference spectrum obtained by subtraction of the spectrum of the D_2 -activated Ir/NaY blank from that of the sample with 2.9 H's per Ir adsorbed on the clusters.

is in good agreement with that for the Ir/KL sample.

Repeating the hydrogen activation cycle at 598 K using D_2 gas led to a reduction in the scattering from the Ir/NaY zeolite, as shown in figure 3. The lower scattering intensity resulting from the D_2 treatment is due to the overall scattering contribution of D being ~ 12 times less than that for H. Thus, residual scattering associated with protons on the catalyst support is reduced by exchange with D, which although chemically similar, has very different neutron scattering properties. Subsequently, hydrogen was volumetrically adsorbed onto the D_2 -activated Ir/NaY zeolite. The spectrum resulting from the subtraction of the D_2 -activated Ir/NaY zeolite from that with adsorbed hydrogen reveals the scattering intensity from the H associated with the Ir clusters (fig. 4). The spectrum is very similar to that observed in the case of Ir/KL zeolite (fig. 2).

DISCUSSION

For both Ir/NaY and Ir/KL zeolites, scattering intensity due to hydrogen adsorbed on the iridium clusters is observed between 60-90 meV, indicating that very similar hydrogen species are present on the iridium clusters, independent of the type of zeolite. The scattering is broad, consisting of a number of components, but the principal intensity is centered around 65 and 85 meV. At the present time, there is insufficient information to establish the precise nature of the hydrogen. However, a number of comments may be made about possible assignments. First, the possible existence of a molecular dihydrogen species can be discounted when a comparison is made to existing data for dihydrogen complexes, including Ir complexes,^{9,10} for which an intense mode due to the H_2 torsion is observed between 30-50 meV. Second, although there is not conclusive evidence, the data are consistent with the bending modes for IrH and IrH₂. In

the Ir complexes with hydride ligands, hydrogen bending modes have been observed in the region of 86-101 meV.¹⁰ There is also the possibility that the lower-energy scattering is due to a wagging or rocking mode of IrH₂. Third, the complexity and broadness of the adsorbed hydrogen spectrum is consistent with the large H/Ir ratio attained for these clusters. The prospect of up to three hydrogens bound to each essentially corner-like Ir atom of a three dimensional Ir₉ cluster suggests the presence of multiple adsorption-site geometries as well as significant H-H lateral interactions. Different site geometries lead to normal mode vibrations with a set of distinct eigenenergies, while H-H interactions result in dispersion (i.e., broadening) of these individual normal mode vibrations. Both effects are potentially present in the measured vibrational spectrum.

CONCLUSION

Hydrogen is bound to the Ir clusters in iridium-loaded NaY and KL zeolites. This is known from our quantitative uptake measurements, and from the existence of extra scattering signal in the IINS data after exposure to H₂. The reproducibility of the IINS data after repeated dehydrogenation/rehydrogenation cycles shows that the Ir clusters in both the Ir/KL and Ir/NaY zeolites are stable under the conditions used. The IINS spectra are consistent with the presence of IrH or IrH₂ species. The loading of 0.8 wt% Ir in NaY zeolite translates into the occupation of 1 in 90 α -cages with an Ir₉ cluster. A higher metal loading as in the case of Ir/KL zeolite will increase the scattering signal and hence help in the interpretation of the data. Moreover, it is hoped that future neutron diffraction experiments aided by the current EXAFS results can provide further insight about the actual geometry of the hydrogenated Ir₉ clusters within the zeolite cages. Such information is needed to more completely characterize the hydrogen dynamics.

ACKNOWLEDGEMENTS

The research at the University of Delaware and University of California, Davis, was supported by U.S. Department of Energy, Office of Energy Research, Office of Basic Energy Sciences (contract No. FG02-87ER13790). The authors would like to thank J. Miller (Amoco Research Center) for preparation of the Ir/KL zeolite sample.

REFERENCES

1. B.J. Kip, F.B.M. Duivenvoorden, D.C. Koningsberger, R. Prins, *J. Catal.*, **105**, 26 (1987).
2. M. Vaarkamp, PhD thesis, Eindhoven University of Technology, The Netherlands, 1993.
3. S. Kawi, J.-R. Chang, B.C. Gates, *J. Am. Chem. Soc.*, **115**, 4830 (1993).
4. J.M. Nicol, *Spectrochimica Acta*, **48A**, 313 (1992).
5. Manufacturers are identified in order to adequately specify the experimental procedure. In no case is this intended as a recommendation or endorsement by NIST.
6. N.D. Triantafyllou, J.T. Miller, B.C. Gates (to be published).
7. T.J. Udovic, R.R. Cavanagh, J.J. Rush, M.J. Wax, G.D. Stucky, G.A. Jones, D.R. Corbin, *J. Phys. Chem.*, **91**, 5968 (1987); J.M. Nicol and T.J. Udovic, (to be published).
8. F.S. Xiao, Z. Xu, O. Alexeev, B.C. Gates (to be published).
9. J. Eckert, *Spectrochimica Acta*, **48A**, 363 (1992).
10. J. Eckert, (private communication).

STUDIES ON NANOSTRUCTURED M50 TYPE STEEL USING X-RAY ABSORPTION SPECTROSCOPY AND NMR

MAHALINGAM BALASUBRAMANIAN *, Y.D. ZHANG **, J.I. BUDNICK **,
K.E. GONSALVES *, AND T.D. XIAO **

* University of Connecticut, Department of Physics, Storrs, CT 06269

** University of Connecticut, Department of Physics and Connecticut Advanced
Technology Center for Precision Manufacturing, Storrs, CT 06269

* University of Connecticut, Polymer Science Program, Institute of Materials Science and
Department of Chemistry, Storrs, CT 06269

** University of Connecticut, Connecticut Advanced Technology Center for Precision
Manufacturing, Storrs, CT 06269

ABSTRACT

We have investigated the local structural and magnetic properties of Fe in nanostructured Fe-Cr-Mo-V-C M50 type steel. Experimental techniques which we used include XAFS and NMR. NMR results on as-synthesized M50 type steel shows that the material contains a small amount of bcc Fe plus some other highly disordered phase(s). XAFS measurements indicate that the near neighbor coordinations around Fe are not simply well ordered bcc or fcc Fe and that the sample doesn't have long range crystalline order. XAFS measurements on the consolidated sample show that Fe is predominantly in the form of bcc Fe with good long range order.

INTRODUCTION

Iron based alloys are technologically important materials and have been widely used in modern industry. Conventional M50 steel has good resistance to tempering, wear and rolling contact fatigue. Hence it has been widely used in the aircraft industry in main-shaft bearings in gas-turbine engines. Conventional M50 steel, which is micro structured, is produced by mixing and melting of the respective metal powders. However, in recent years, much attention has been devoted to the reduction of grain size from the micrometer size to the nanometer regime. Nanostructured materials are anticipated to exhibit technologically attractive properties. We have utilized X-Ray Absorption Fine Structure (XAFS) and Nuclear Magnetic Resonance (NMR), two complementary local probes, to help in studies of the fabrication and processing of nanostructured M50 type steel.

XAFS involves the measurement of the absorption coefficient as a function of the incident X-Ray energy. X-Ray Absorption Near Edge Structure (XANES) contains information about near neighbor bonding geometry, bonding distances, valence states of the absorbing atom and projected unoccupied density of states. The Extended X-Ray Absorption Fine Structure (EXAFS) is determined by the type and number of near neighbor atoms, near neighbor distances, and the degree of order around the absorber. A detailed description of the XAFS technique can be found in Ref. (1). In NMR, nuclear species that occur naturally in a material are used as probes to gain information concerning the atomic structure, electronic structure, and other related interactions on a microscopic scale. The type of NMR used in this study is NMR spectroscopy of magnetic materials. In such an experiment the magnetic field at the nuclear sites arises from the internal hyperfine field and the application of an external field is not required. This is known as "Zero Field"

NMR spectroscopy. In this investigation naturally occurring ^{57}Fe nuclei in the sample were utilized as the probe of structure and magnetism in the material.

EXPERIMENTAL DETAILS

Our samples were prepared from the thermal decomposition of organometallic precursors using a chemical synthesis method. A portion of the as-synthesized powder was consolidated into a bulk sample. Detailed description of the synthesis and characterization using XRD, SEM, TEM, and HRTEM has been earlier reported by Gonsalves, et al.² The material composition obtained was 94.2% Fe, 0.3% Cr, 0.4% Mo, 2.1% V, and with the balance, Carbon. XAFS measurements were carried out at the National Synchrotron Light Source on beam line X-11A using a Si (111) double crystal monochromator. The harmonic contamination was minimized by detuning the incident intensity by 20%. Data at the Fe K edge, were taken using the standard transmission mode at 77K for the as-synthesized sample and using the glancing emergent angle (GEA) fluorescence method (so as to largely eliminate fluorescence distortions) at room temperature for the consolidated sample.³ The data were subsequently normalized, background subtracted and Fourier transformed using standard procedures.¹ Data analysis was performed using the "University of Washington EXAFS Analysis" package. NMR experiments were performed at 4.2 and 1.3 K and at frequencies ranging from 10 to 60 MHz.

RESULTS AND DISCUSSION

Fig. (1) shows the zero field spin echo NMR spectrum of as-synthesized M50 type steel taken at 4.2 K. The spectrum is very broad and the Fe hyperfine fields are distributed over a wide range from 240 to 370 KOe with a broad peak at 314 KOe, 20 KOe lower than

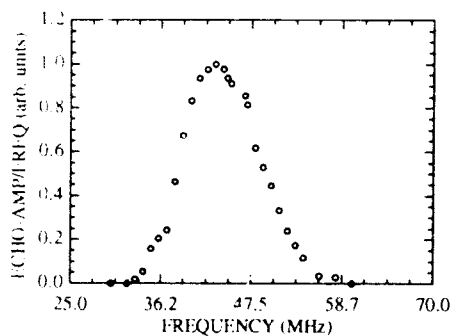


Fig. (1) NMR spectrum of as-synthesized M50 type steel taken at 4.2 K

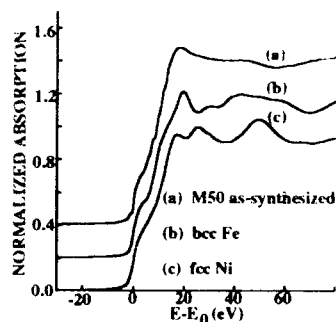


Fig. (2) Fe K edge XANES of as-synthesized M50 type steel compared with the XANES of bcc Fe and fcc Ni

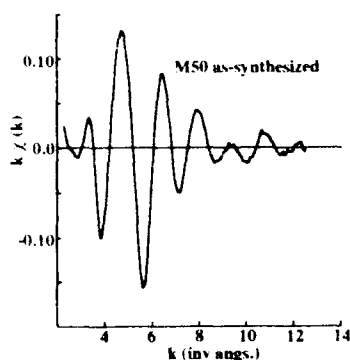


Fig. (3) Fe k edge EXAFS of as-synthesized M50 type steel.

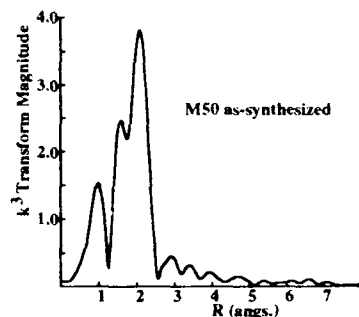


Fig. (4) Fourier Transform magnitude of Fe k edge EXAFS in M50 type steel

bcc Fe. This wide distribution of the hyperfine field is probably due to the presence of a large amount of disorder in the material. Furthermore, a small satellite can also be seen around 334 KOe (46.67 MHz) which is the characteristic frequency of bcc Fe. This indicates that a small amount of bcc Fe is also present.

Particles in the superparamagnetic state will not contribute to the zero field NMR signal due to thermal fluctuations in the direction of magnetization. However, the application of an external field may align some of the moments giving rise to an NMR signal. Hence, if some of the particles are superparamagnetic, an increase in signal intensity could occur with the application of an external field. In order to test for the presence of superparamagnetic particles, an NMR measurement was performed at 1.3K in the presence of an external magnetic field. As the strength of the magnetic field was increased the signal intensity gradually decreased and totally disappeared at a field of 500 Oe. This suggests that most particles are not superparamagnetic in nature.

In Fig. (2), the Fe k edge XANES spectra of as-synthesized M50 type steel is shown in comparison with the XANES of pure bcc Fe and fcc Ni. The energy origin is set at the first inflection point. The structure at the near edge of fcc Fe is similar to that of fcc Ni.⁴ Therefore, for convenience, a fcc Ni spectra has been included to represent fcc Fe. It can be seen that the XANES of the as-synthesized sample is different from that of both bcc Fe and fcc Fe; indicating that the near neighbor environment around the central Fe atom in as-synthesized M50 type steel is distinctly different from that of well ordered bcc or fcc Fe.

Fig. (3) represents the EXAFS spectrum (χ function) of as-synthesized M50 type steel, at the Fe k edge, taken at 77K. We note that the amplitude of the EXAFS wiggles are rather small, when compared to bcc Fe [Fig. (5)]. Further, the EXAFS oscillations die out rapidly towards large k. Fig. (4) shows the Fourier Transform (FT) corresponding to data in Fig. (3). It can be seen that there are no peaks beyond ~ 3 Å in the FT, showing the absence of long range crystalline order. The peak around 2 Å is split into an unresolved doublet indicating the presence of either two close-by shells or two or more phases

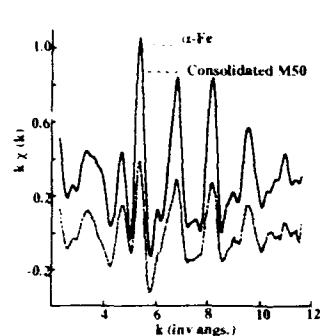


Fig. (5) Fe k edge EXAFS of consolidated M50 type steel compared with bcc Fe

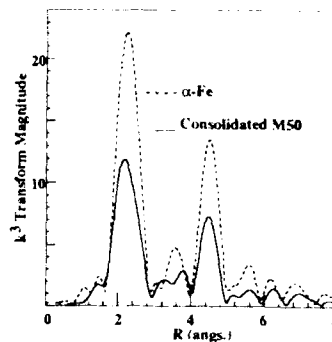


Fig. (6) Fourier Transform magnitude of Fe k edge EXAFS in consolidated M50 type steel compared to bcc Fe.

containing Fe. The peak near 1 Å is probably spurious in nature and can be attributed to poor signal to noise ratio. Detailed analysis of this data to identify the near neighbors and near neighbor distances is in progress.

Fig. (5) shows the Fe k edge χ functions of Fe in consolidated M50 type steel, as well as in pure bcc Fe, both taken at room temperature. The similarity in the χ functions indicates that the Fe in consolidated M50 type steel is predominantly in the form of bcc Fe. However, the EXAFS amplitude is reduced throughout the entire k range. Fig. (6) shows the FTs corresponding to the data shown in Fig. (5). It can be seen from the FTs, that the peaks in the consolidated sample coincide with that of bcc Fe, but are diminished in amplitude. Microscopic techniques indicate that the particle sizes are in the order of several nanometers.² Hence, such a large diminution in the EXAFS amplitude cannot be attributed to particle size effects. Experiments by Haubold et. al, on nanocrystalline Cu and W have shown a reduction in the EXAFS amplitude, which has been attributed to the absence of structural order in the grain boundaries (primarily due to a wide distribution of bond lengths in the grain boundaries).^{5,6} More detailed data analysis and experiments to understand the cause of the amplitude reduction in the EXAFS signal of our sample is in progress.

ACKNOWLEDGEMENTS

We wish to thank Douglas M. Pease and Dale L. Brews for their help in this work. We acknowledge support from the Department of Energy under contract No. DE-A505-80ER10742 and No. DE-F602-90ER45424. This work was also supported by the Department of Energy, by a sub-contract through North Carolina State University, under

contract No. DE-FG05-89ER45384 and by the Precision Manufacturing Center, University of Connecticut.

REFERENCES

1. X-Ray Absorption: Principles, Applications, Techniques of EXAFS, SEXAFS, and XANES, edited by D.C. Koningsberger and R. Prins (John Wiley & Sons, 1988).
2. K.E. Gonsalves, T.D. Xiao, G.M. Chow, C.C. Law, *Nanostructured Mat.*, Vol. 4 (2), 139, 1994.
3. D.L. Brewe, E.C. Bouldin, D.M. Pease, J.I. Budnick, and Z. Tan, *Rev. Sci. Instruments* 63, 3298, 1992.
4. J.I. Budnick, M.H. Choi, G.H. Hayes, D.M. Pease, Z.Tan, E. Klein, and B. Illerhaus, *Journal De Physique, Colloque C8, Supplement au n 12, Tome 47, Decembre 1986*.
5. T. Haubold, R. Birringer, B.Lengeler, and H. Gleiter, *Phys. Lett. A*, Vol. 135, No. 8,9 1989
6. T. Haubold, W. Krauss, and H. Gleiter, *Philo. Mag. Lett.*, Vol. 63, No. 4, 245, 1991.

SONOCHEMICAL SYNTHESIS AND CATALYTIC PROPERTIES OF NANOSTRUCTURED MOLYBDENUM CARBIDE

KENNETH S. SUSLICK*, TAEGHWAN HYEON, MINGMING FANG, and
ANDRZEJ A. CICHOWLAS

School of Chemical Sciences and Materials Research Laboratory, University of Illinois at
Urbana-Champaign, 505 S. Mathews Ave., Urbana, IL 61801

ABSTRACT

Molybdenum hexacarbonyl in hexadecane was irradiated with high intensity ultrasound under argon at 90°C to yield face centered cubic molybdenum carbide, Mo₂C. After thermal treatment, oxygen and excess carbon were removed to give stoichiometric Mo₂C. SEM micrographs showed that the surface was extremely porous. TEM micrographs showed that the solid was an aggregate of particles with diameters of ≈ 2 nm. This material has a very high surface area, 188 m²/g as determined by BET gas adsorption. Catalytic studies have been conducted on the dehydrogenation of cyclohexane and the hydrogenolysis of ethane. The sonochemically prepared Mo₂C shows good catalytic activity for the dehydrogenation of cyclohexane with 100% selectivity for formation of benzene without hydrogenolysis to methane. The material revealed poor catalytic activity for the hydrogenolysis of ethane.

INTRODUCTION

The preparation of nanophase materials has been the focus of intense study in materials science [1,2]. A variety of chemical and physical preparative methods have been applied to produce materials with nanometer structure, including metal evaporation [3], decomposition of organometallic compounds [4], and the reduction of metal salts [5,6]. Sonochemical decomposition of transition metal carbonyl compounds has also been proven to be a useful technique to generate nanophase transition metals [7,8].

Recently, molybdenum and tungsten carbides have been explored as heterogeneous catalysts because of the similarity in activity that these carbides share with Pt and Pd [9,10,11]. For catalytic applications, high surface area materials are generally needed. The preparation of interstitial carbides of molybdenum and tungsten with high surface areas, however, is very difficult. Boudart and Volpe prepared carbides of molybdenum and tungsten with high surface areas by the temperature programmed carburization of the corresponding nitrides [12]. Here we present a simple sonochemical synthesis of nanophase molybdenum carbide from the ultrasonic irradiation of molybdenum hexacarbonyl in hexadecane at low temperature.

EXPERIMENTAL PROCEDURES

All manipulations for the preparation of samples were performed using Schlenk line and inert atmosphere box (Vacuum Atmospheres, < 1 ppm O_2) techniques. Pentane was distilled over sodium-benzophenone and hexadecane was distilled over sodium. Both solvents were degassed by three cycles of freeze-pump-thaw. Ultrasonic irradiation was accomplished with a high intensity ultrasonic probe (Sonic and Materials, model VC-600, 0.5 in Ti horn, 20 kHz, 100 Wcm⁻²).

X-ray powder diffraction data were collected on a Rigaku D-max diffractometer using Cu K α radiation ($\lambda = 1.5418$ Å). Scanning electron micrographs were taken on a Hitachi S800 electron microscope. Transmission electron micrographs were taken on a Phillips CM-12 electron microscope.

Hydrogen (99.99%, Linde), methane (99.97%, Matheson) and ethane (99.0+%, Linde) were further purified through 5 Å molecular sieves and oxy-traps (Alltech). Samples for elemental analysis were submitted in sealed vials without exposure to air. A quartz cell was used for both adsorption and gas-solid catalytic studies. The catalysts were transferred from an inert atmosphere box to the catalytic rig without exposure to air. Surface areas were calculated by applying the BET equation to the N₂ adsorption isotherm measured at 77 K. The gas products obtained during the temperature-programmed desorption (TPD) and temperature-programmed reaction (TPR) experiments were measured by a quadrupole mass spectrometer (Spectra Instruments).

Cyclohexane (99+%, Fischer) was dried over molecular sieves prior to use. A MKS mass flow controller maintained the flow of hydrogen at 27.5 cm³ (STP)/min to carry the cyclohexane vapor at a constant partial pressure of 0.09 atm through the catalyst. The cyclohexane reaction products (benzene and aliphatic hydrocarbons) were analyzed by gas chromatography (Hewlett-Packard 5730A) on a n-octane/Porasil C column with flame ionization detection. The hydrogenolysis of ethane was also examined at 573 K, 5:1 hydrogen to ethane. Products were analyzed by GC and MS.

RESULTS AND DISCUSSION

Sonochemistry

The chemical effects of ultrasound originate from hot spots formed during acoustic cavitation (the formation, growth and collapse of bubbles in a liquid) [13,14]. The temperature reached during bubble collapse is approximately 5000 K with sub-microsecond lifetime [15]. Consequently, the acoustic cavitation produces extraordinary cooling rates above 10¹⁰ Ksec⁻¹.

In order to achieve good sonochemical reaction yields, precursors should be thermally stable and volatile since the primary sonochemical reaction site is the vapor inside the cavitating bubbles [16]. To achieve good sonochemical activity, the vapor pressure of precursors should be roughly 5 torr during sonolysis. The vapor pressure of molybdenum hexacarbonyl is only 0.17 torr at 25°C. In order to increase this vapor pressure of Mo(CO)₆, we need to choose a high boiling solvent, because excess solvent

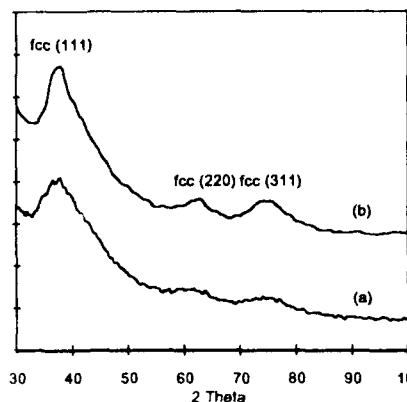


Figure 1. X-ray powder diffraction patterns of sonochemically produced Mo_2C (a) after synthesis, (b) after heat treatment under He, 450°C , 12 hrs.

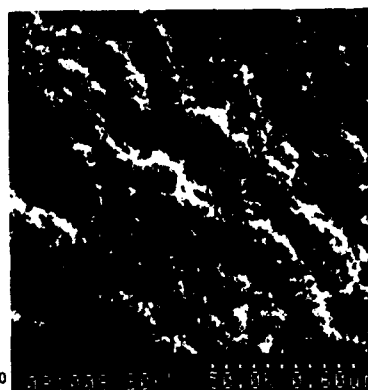


Figure 2. Scanning electron micrograph of sonochemically produced Mo_2C .

vapor inside the bubble would reduce the cavitation temperature during bubble collapse. Hexadecane was chosen because it has very low vapor pressure at 90°C and is relatively inert under sonochemical conditions.

Synthesis and characterization

A slurry of molybdenum hexacarbonyl in hexadecane was sonicated at 90°C for 3 hours under argon to yield a black powder. The powder was filtered inside a dry box, washed several times with purified, degassed pentane, and heated at 100°C under vacuum. X-ray powder diffraction (XRD) showed extremely broad peaks centered at a d spacing of 2.4 Å, 1.5 Å, and 1.3 Å (Figure 1(a)), which do not match body centered cubic (bcc) lines of molybdenum metal [17]. FT-IR spectrum of the material indicated that carbon monoxide was adsorbed on the surface of the powder. Temperature programmed desorption (TPD) under helium showed the desorption of carbon monoxide with maximum temperatures at 430 K and 800 K. TPD also revealed the evolution of carbon dioxide with maximum temperatures at 450 K and 750 K. After the heat treatment at 750 K under helium flow for 12 hours, sharper peaks in the XRD were observed at d spacing values of 2.39 Å, 1.49 Å, and 1.27 Å which match very well with face centered cubic (fcc) molybdenum carbide, Mo_2C (Figure 1(b)). Elemental analysis also confirmed the stoichiometry of Mo_2C . The formation of molybdenum carbide can be explained by the disproportionation of carbon monoxide on the active metal surface to form carbon and carbon dioxide [18].

The SEM at 50,000 magnification showed that the surface is extremely porous (Figure 2). The TEM at 430,000 magnification showed that the particles were aggregates of 2 nm sized particles (Figure 3(a)). The particle size calculated from the line



Figure 3. Transmission electron micrographs of sonochemically produced Mo_2C (a) after synthesis, (b) after thermal treatment under condition of 1:1 CH_4 to H_2 , at 500°C for 48 hours.

broadening of X-ray powder diffraction was 1.6 nm. Surface area, determined by BET gas adsorption isotherms was found to be $188 \text{ m}^2/\text{g}$.

Catalytic studies

Even after heat treatment at 750 K under helium, about 4 weight percent of oxygen was still in the material. Since the presence of oxygen could poison the catalytic activity [19], it was removed before catalytic studies. In order to remove oxygen, the molybdenum carbide powder was heated in a flowing 1:1 CH_4/H_2 mixture at 573 K for 1 h, then at 673 K for 1 h, and finally at 773 K for 48 h. The flow rate of the CH_4/H_2 mixture was 27.5 cm^3 (STP)/min. After the heat treatment, the elemental analysis results showed the sample was pure Mo_2C ; oxygen, excess carbon, and hydrogen had been removed. Electron micrographs showed that the materials was still porous and was composed of particles of 3 nm in diameter (Figure 3(b)). The BET surface area decreased slightly to $130 \text{ m}^2/\text{g}$.

The catalytic activity of the sonochemically produced molybdenum carbide was tested for dehydrogenation of cyclohexane. Figure 4 shows the catalytic activity (in terms of turnover frequency of cyclohexane molecules converted per site per second) as a function of temperature for the sample pretreated under CH_4/H_2 at 500°C for 48 hours and for the sample pretreated under helium at 450°C for 12 hours.

Through all the reaction temperatures, benzene was the only product formed for either sample. No hydrogenolysis products were detected. Compared to the sample heat treated under CH_4/H_2 , the sample heat treated under helium revealed the same selectivity (benzene is the only product), but with somewhat lower activity. These results demonstrate that the sonochemically prepared molybdenum carbide is an excellent dehydrogenation catalyst and a rather poor hydrogenolysis catalyst. This is also confirmed by the lack of activity for ethane hydrogenolysis: during 28 hour reaction at 573 K, no methane was detected by either GC or MS.

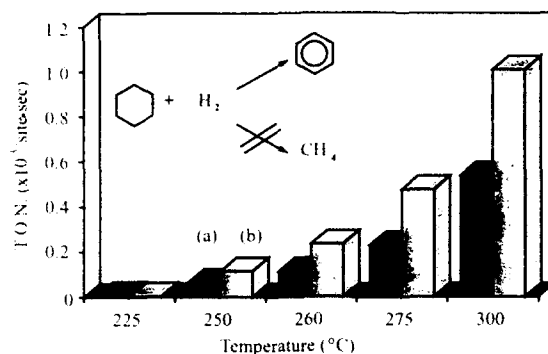


Figure 4. Catalytic activity of sonochemically produced Mo_2C for dehydrogenation of cyclohexane, (a) sample heat treated under helium at 450°C for 12 hours and (b) sample heat treated under CH_4/H_2 at 500°C for 48 hours.

The catalytic properties of Mo_2C (fcc) and Mo_2C (hcp) have been studied intensively in recent years [9,10,11,20,21,22]. Many reactions such as CO hydrogenation [23], olefin hydrogenation [24], isomerization and hydrogenolysis of hydrocarbons have been investigated. However, few reports mention Mo_2C as an active dehydrogenation catalyst. In fact, carburization of Mo is known to temper Mo metal for dehydrogenation of hydrocarbons [25]. Bell *et al.* show there is some catalytic activity for ethane hydrogenolysis using Mo_2C (fcc) prepared by reduction and carburization of MoO_3 under the similar conditions (573 K , $\text{H}_2/\text{C}_2\text{H}_6 = 5$) [9]. It seems the sonochemically prepared Mo_2C (fcc) has different and more selective catalytic behavior compared to the molybdenum carbides generated by the other methods. Surface and catalytic studies to explore the catalytic properties and mechanisms of our sonochemically prepared materials are continuing.

CONCLUSIONS

Sonochemical decomposition of molybdenum hexacarbonyl in hexadecane at 90°C gave nanometer-sized powder of face centered cubic molybdenum carbide. The material was extremely porous with a high surface area and consisted of aggregates of $\approx 2\text{ nm}$ sized particles. The catalytic properties of the sonochemically prepared fcc Mo_2C have been studied on dehydrogenation and hydrogenolysis of cyclohexane and hydrogenolysis of ethane. The catalytic results showed the molybdenum carbide generated by ultrasound was a good dehydrogenation catalyst and a poor hydrogenolysis catalyst.

ACKNOWLEDGMENTS

This work was supported by National Science Foundation. We thank Peggy Mochel, Vania Petrova, and the UIUC Center for Microanalysis of Materials, supported by the US Department of Energy, for their assistance in the electron microscopic studies.

REFERENCES

1. H. Weller, *Adv. Mater.* **5**, 88-95 (1993).
2. G.A. Ozin, *Adv. Mater.* **4**, 612-649 (1992).
3. S.C. Davis and K.J. Klabunde, *Chem. Rev.* **82**, 152-208 (1982).
4. A.S. Lisitsyn, A.V. Golovin, A.L. Chuvilin, V.L. Kuznetsov, A.V. Romanenko, A.F. Danilyuk and Y.I. Yermakov, *Appl. Catal.* **55**, 235-258 (1989).
5. H. Boennemann, W. Brijoux R. Brinkmann and T. Jousen, *Angew. Chem., Int. Ed. Engl.* **129**, 273-275 (1990).
6. K.-L. Tsai, J.L. Dye, *J. Amer. Chem. Soc.* **113**, 1650-1652 (1991).
7. K.S. Suslick, S.B. Choe, A.A. Cichowlas and M.W. Grinstaff, *Nature* **353**, 414-416 (1991).
8. M.W. Grinstaff, M.B. Salamon and K.S. Suslick, *Phys. Rev. B* **48**, 269-273 (1993).
9. G.S. Ranhotra, G.W. Haddix, A.T. Bell and J.A. Reimer, *J. Catal.* **108**, 40-49 (1987).
10. J.S. Lee, S.T. Oyama and M. Boudart, *J. Catal.* **125**, 157-170 (1990).
11. M.J. Ledoux, C. Pham-Huu, Guille, J. and H. Dunlop, **134**, 383-398 (1992).
12. L. Volpe and M. Boudart, *J. Solid State Chem.* **59**, 332-356 (1985).
13. K.S. Suslick, *Science* **247**, 1439-1445 (1990).
14. K.S. Suslick, in Ultrasound: Its Chemical, Physical, and Biological Effects, edited by K.S. Suslick (VCH Press, New York, 1988), pp. 123-163.
15. E.B. Flint and K.S. Suslick, *Science* **253**, 1397-1399 (1991).
16. K.S. Suslick, R.E. Cline and D.A. Hammerton, *J. Amer. Chem. Soc.* **106**, 5641-5642 (1986).
17. Joint Committee on Powder Diffraction Standards, XRD powder diffraction data file (1991).
18. N.M. Rodriguez, M.S. Kim and R.T.K. Baker, *J. Catal.* **144**, 93-108 (1993).
19. R.B. Levy and M. Boudart, *Science* **181**, 547-549 (1973).
20. J.S. Lee, L. Volpe, F.H. Ribeiro and M. Boudart, *J. Catal.* **112**, 44-53 (1988).
21. G.S. Ranhotra, G.W. Haddix, A.T. Bell and J.A. Reimer, *J. Catal.* **108**, 24-39 (1987).
22. C. Pham-Huu, M. Ledoux and J. Guille, *J. Catal.* **143**, 249-261 (1993).
23. E.I. Ko and R.J. Madix, *Surf. Sci. Lett.* **100**, L449 (1980).
24. K. Aika and A. Ozaki, in Catalysis, Science and Technology, edited by R.B. Anderson and M. Boudart (Springer-Verlag, Berlin, 1981), p.87.
25. E.I. Ko and R.J. Madix, *Surf. Sci.* **100**, L449, L505 (1980).

PROCESSING OF NANOSTRUCTURED ZIRCONIA CERAMICS

G. SKANDAN¹, H. HAHN², B. H. KEAR¹, M. RODDY³ AND W. R. CANNON³

¹Dept. of Materials Science and Engineering

³Dept. of Ceramic Engineering

RUTGERS, The State University of New Jersey

P. O. Box 909, Piscataway, NJ 08855, U. S. A

²Technische Hochschule Darmstadt

31 Hilperstr., Darmstadt, Germany

Abstract

The inert gas condensation (IGC) technique was employed to synthesize non-agglomerated nanoparticles of ZrO_2 and Y_2O_3 with different average particle sizes ranging from 4 to 14 nm. The sintering behaviors (in air and vacuum) of single phase $n\text{-ZrO}_2$ (monoclinic crystal structure) and $\text{Y}_2\text{O}_3\text{-ZrO}_2$ mixture (Y-TZP) were studied in terms of densification rate and final sintering temperature. There was a strong correlation between densification characteristics and properties of the starting powder compacts such as average particle size, particle and pore size distributions. $n\text{-ZrO}_2$ was sintered to full density in air at temperatures as low as 1125 °C (0.47 T_m) and in vacuum at 975 °C (0.42 T_m). Although the grain sizes in the fully sintered samples were well below 100 nm, the grains had grown by a factor of 10 as compared to the initial particle size. Therefore, a pressure-assisted sintering technique was employed to further reduce the densification temperature and final grain size. Threshold effects in this process are also discussed.

Introduction

Increasing efforts are being directed towards synthesis of nanostructured metals and ceramics [1 - 3]. Consolidation of loosely agglomerated nanoparticles (less than 10 nm) of ceramic materials is expected to result in significant payoffs in terms of lowering of sintering temperatures, and hence avoidance of the use of sintering aids, decomposition of constituent phases [4] and deleterious interfacial interactions. Moreover, smaller grain sizes should result in improved mechanical properties and superplastic behavior for net shape forming [5].

Currently, a number of production techniques are available for the synthesis of nanoparticles of ceramics. These include, spray pyrolysis [6], laser ablation [7], sol-gel processing, flame pyrolysis and inert gas condensation (IGC). One of the principal concerns in all these techniques is the control of agglomeration. An agglomerated mass of powder is of little benefit during densification as coarsening prevails over sintering. A modified version of the original IGC technique pioneered by Gleiter [8] was employed to synthesize non-agglomerated powders of $n\text{-Y}_2\text{O}_3$ [9] and $n\text{-ZrO}_2$ with average particle sizes less than 15 nm. The process consists of evaporation of either the pure metal or the monoxide in a low pressure atmosphere of helium followed by careful post-oxidation. The details of this process are described elsewhere [10].

This paper describes sintering studies performed on single phase $n\text{-ZrO}_2$ and $n\text{-ZrO}_2$ doped with $n\text{-Y}_2\text{O}_3$. Both the $n\text{-ZrO}_2$ and $n\text{-Y}_2\text{O}_3$ powders were synthesized by the IGC technique. The sintering behavior of nanostructured powders is expected to be significantly different as compared to the commercial powders available today. Densification of pure $n\text{-ZrO}_2$ was carried out in air and in vacuum. In both cases, fully dense samples with a monoclinic crystal structure were obtained. The grain sizes in the fully sintered states were still in the nanoscale regime. Correlations have been drawn between initial powder properties and sintering characteristics. Sinter-forging experiments, performed on single phase $n\text{-ZrO}_2$ are also described in this paper.

Experimental

The powder synthesis process consists of evaporation of zirconium monoxide in a helium atmosphere of 100 to 1500 Pa followed by post-oxidation of the monoxide nanoparticles. As mentioned before, proper control of the latter step is critical to the formation of non-agglomerated powder.

Compacts, 8 mm in diameter and 0.5 mm thick, were made by applying an uniaxial pressure in the range of 200 to 1000 MPa at room temperature. These pellets were sintered in air and in vacuum (4×10^{-4} Pa) at several different temperatures for varying lengths of time. The samples sintered in vacuum were subsequently annealed in flowing oxygen below the sintering temperature to establish stoichiometry. Additionally, sintering was studied in situ by dilatometry on cylindrical samples. The heating rate was 10 °C/min. These samples, with a diameter of 3 mm and a height of 3 to 4 mm, were compacted at 400 MPa at room temperature. Sinter-forging was carried out in a creep rig. Cylindrical pellets, 3 mm in diameter and 2 mm in height were first cold isostatic pressed and then presintered to render rigidity to the samples. Pore size distributions on as pressed samples were measured using Coulter Omnisorb 360. Density of the pellets was measured using Archimedes' principle and from geometry and weight of the specimen.

Y_2O_3 -stabilized tetragonal zirconia was prepared in the following way: a colloidal suspension containing $n\text{-ZrO}_2$ and 3 mole% of $n\text{-Y}_2\text{O}_3$ was formed in deionized water and treated ultrasonically to obtain good mixing. The water was then dried out. After compaction at room temperature, the samples were heated at 995 °C for 40 min. to obtain interdiffusion of the oxides and sintering.

Results and Discussion

Fig. 1 shows a TEM image of as synthesized powder; Fig. 2 shows particle size distribution for the same powder. The average particle size depends on the He-gas pressure during evaporation: it increases from 6 to 12 nm at 100 Pa to 1000 Pa He pressure, respectively. The as prepared powder consists of a phase mixture of tetragonal and monoclinic crystals. The latter is the stable phase at room temperature while the former can be formed by applying high pressures (of the order of several GPa's) at elevated temperatures. The formation of these high pressure phases, which have higher densities, has been explained on the basis of Gibbs-Thomson effect [11], [10]. However, on compaction (even at small uniaxial pressures of the order of 10 MPa), all the tetragonal grains transform to the monoclinic crystal structure.

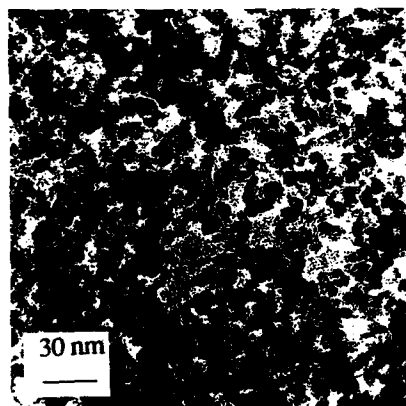


Fig. 1. TEM image of as prepared $n\text{-ZrO}_2$ powder.

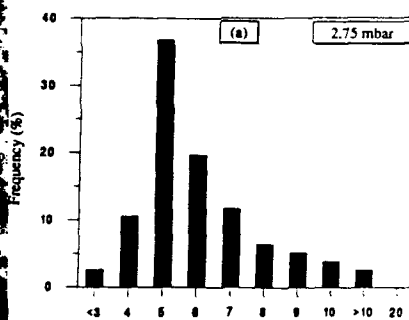


Fig. 2. Particle size distribution of as prepared powder obtained from bright field imaging. The average particle size is about 6 nm.

Green densities in the range 36 to 51% of the theoretical density (ρ_c) of monoclinic zirconia were obtained by compacting at different pressures. High pressures of the order of 400 MPa or so were needed to achieve green densities of about 45% (Fig. 3). The reason is that there is a large frictional resistance between the nanoparticles which must be overcome by compaction. The pore size distribution is shown in Fig. 4. The pore size distribution is narrow and mimics the particle size distribution. This microstructure of the green pellet is desirable for sintering and has been achieved by controlled post-oxidation avoiding exothermic heat release.

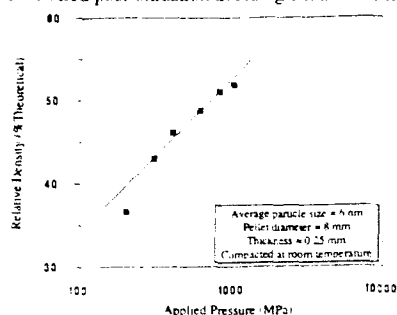


Fig. 3. Green density as a function of compaction pressure. There is no break stress in the range studied.

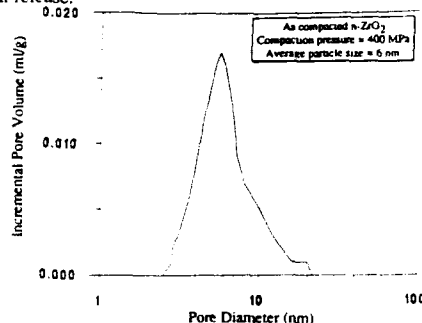


Fig. 4. Pore size distribution in the as compacted state. The bulk densities calculated from the total pore volume and using Archimedes principle match pretty closely signifying that all the pores can be accounted for.

Fig. 5 shows sintering curves of $n\text{-ZrO}_2$ with an average particle size of 9 nm and a commercial Y-stabilized ZrO_2 ceramic (Nippon, 2.6 Y-TZP) measured by dilatometry. Apparently, sintering commences at 600 °C, i. e. $0.3 T_m$, for the nanopowder while there is no densification until 1100 °C for the commercial ceramic. Careful neutron scattering study [13] however revealed that the apparent shrinkage during the intermediate stages of sintering is a consequence of coarsening and particle rearrangement resulting in close packing. There was strong evidence for inter-particle interference suggesting that the bulk consisted of a network of pores equally separated from each other. This is corroborated by the uniform grain size of these samples shown in the micrograph in Fig. 6. It is argued that such a homogeneous microstructure in the intermediate stage is responsible for low temperature sintering. Fig. 7 shows density as a function of time at several different temperatures. Full density can be achieved by sintering in air at 1125 °C for 60 minutes.

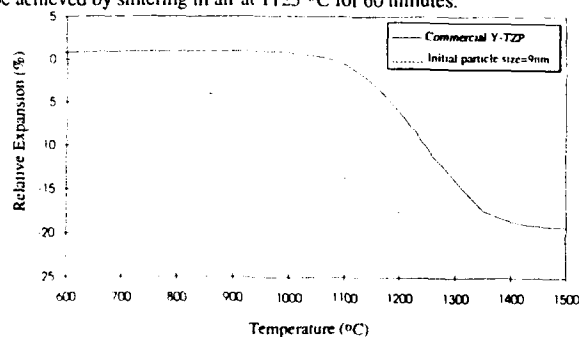


Fig. 5. Sintering curves of $n\text{-ZrO}_2$ and commercial Y-TZP powder.

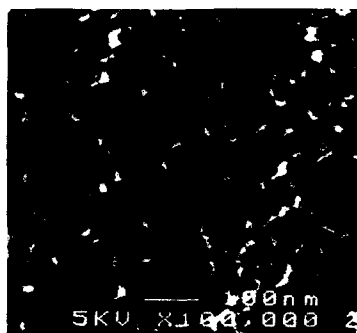


Fig. 6. HRSEM image of a scratched surface showing the uniformity in the grain size in the intermediate stages of sintering.

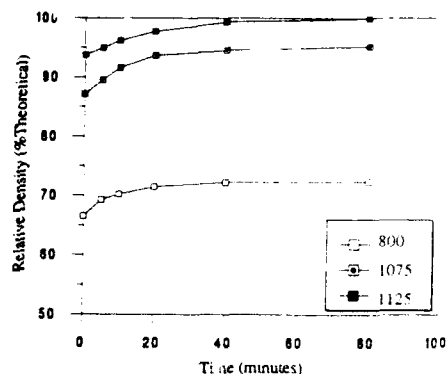


Fig. 7. Relative density (%theoretical) as a function of sintering time at several different temperatures. The sintering atmosphere was air.

The sintering temperature could be further lowered by sintering in vacuum. Near theoretical densities were achieved by sintering at 975 °C for 40 minutes. The reasons for the enhancement of sintering in vacuum compared to air are presently not clear. Avoiding a negative sintering pressure due to the presence of air in the pores and enhancement of diffusivity in non-stoichiometric $n\text{-ZrO}_2$ probably contribute to the observed changes in the densification rates. Since the sintering temperature is well below the monoclinic to tetragonal transformation, no microcracking occurs and theoretical densities are achieved.

Fig. 8 shows grain size as a function of density. Grain growth during densification is inevitable but it should be noted that there is no exaggerated grain growth in the final stages of sintering. The grain sizes, determined from X-ray line broadening agree well with those determined from HRSEM images (Fig. 9). Dense samples sintered in vacuum had a grain size of 60 nm while those sintered in air had an average grain size of 80 nm.

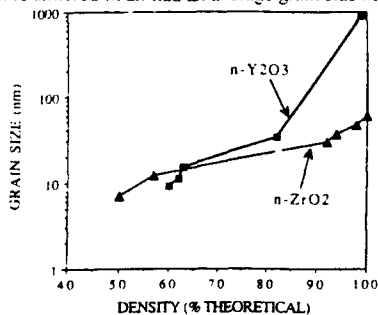


Fig. 8. Grain size as a function of percentage porosity for samples sintered in vacuum. Exaggerated grain growth did not occur at sintering temperatures of 975 °C when full density could be achieved.

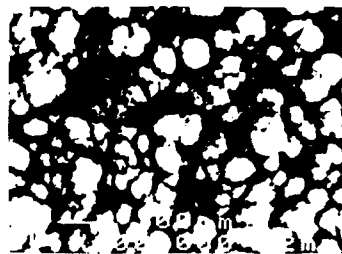


Fig. 9. HRSEM image of a fractured surface of an $n\text{-ZrO}_2$ sample sintered to 95% of theoretical density.

Stable colloids of n-ZrO_2 and $\text{n-Y}_2\text{O}_3$ in deionized water were mixed to obtain 3 mol% $\text{n-Y}_2\text{O}_3$ in n-ZrO_2 . After drying and compacting, the samples were sintered in vacuum at 995°C for 40 minutes to achieve full density. X-ray diffraction showed that complete interdiffusion had occurred, transforming all the monoclinic grains to the tetragonal structure.

The possibility of further reducing the grain size without the addition of any grain growth inhibitor was studied by sinter-forging at temperatures below 1000°C . Sinter-forging of ceramics is a consolidation technique where a partially sintered or a green sample is subjected to an uniaxial load at a certain temperature so that the specimen sinters and deforms simultaneously. Therefore, this process can be employed to obtain fully sintered, net shape components. Sinter-forging was carried out at 950°C for 1 hour at different applied pressures ranging from 10 to 300 MPa. Details of these experiments have been described elsewhere [13]. The behavior of two types of powder was investigated: powder A had an average particle size of 6 nm and a specific surface area of $136\text{ m}^2/\text{g}$; powder B was coarser with an average particle size of 12 nm and a specific surface area of $65\text{ m}^2/\text{g}$. Density as a function of applied pressure is shown in Fig. 10. There is a break in both the curves, called the threshold stress which is lower for the coarser grained sample. This explains why such a break had never been observed in forging experiments from commercial grade powder.

This unique behavior of ultrafine-grained ceramics under an applied stress can be interpreted by considering the driving forces for densification. The total driving force is composed of two components; the intrinsic driving force due to curvature and the extrinsic driving force due to applied stress [14], [15]. Fig. 11 shows a schematic of the total driving force as a function of grain size. At small grain sizes, such as G1, the contribution of the applied stress to the total driving force is far less significant as compared to that due to the curvature. At a grain size G2, the two components are comparable while at G3, stress plays a dominant role. On the basis of this argument, one can expect to have a break in a curve of densification rate versus applied stress. Since the final density is a consequence of the densification rate, the breaks in the curves for the different grain sized materials occur at different stress levels.

A pressure of 300 MPa had to be applied at 950°C to densify pure n-ZrO_2 . The grain size determined from X-ray line broadening was 45 nm.

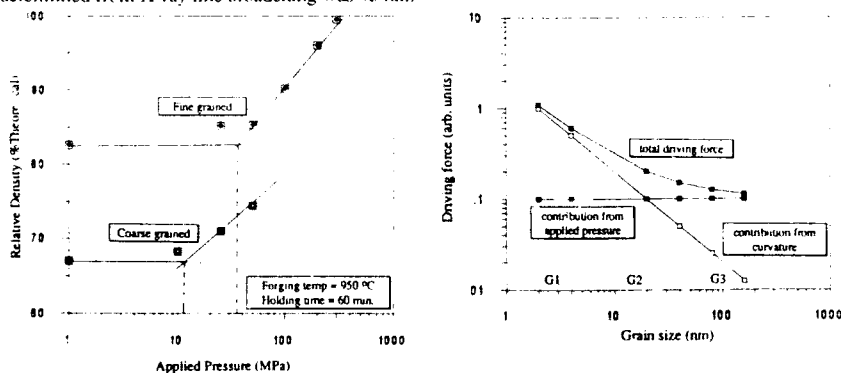


Fig. 10. Relative density as a function of applied pressure during sinter-forging for two powders. Fig. 11. Driving force (arbitrary units) as a function of grain size. There are two components to the driving force, namely, contribution from the applied pressure and contribution from the curvature. The threshold stress, that is the driving force, is different for the two powders.

Conclusions

- (i) Non-agglomerated nanoparticles of $n\text{-ZrO}_2$ and $n\text{-Y}_2\text{O}_3$ in the range 4 to 14 nm in diameter can be synthesized by the inert gas condensation process.
- (ii) The as prepared powder consists of both the stable monoclinic phase and a high pressure tetragonal phase. On compaction the latter transforms to the stable phase.
- (iii) Sintering characteristics largely depend on the initial powder properties and a homogeneous intermediate state is essential for full densification at temperatures below $0.5 T_m$.
- (iv) Full density can be obtained by sintering in air at 1135 °C for 60 min. and the same can be achieved by sintering in vacuum at 975 °C for 40 min. The grain sizes in both cases are well within the nanoscale regime.
- (v) The pressures needed to densify fine grained materials is higher as compared to those applied to sinter commercial ceramics. Unique pressure effects were observed in these fine-grained materials. Pure $n\text{-ZrO}_2$ was densified by applying a pressure of 300 MPa at 950 °C for 1 hour. The grain size was 45 nm.

References

1. H. Gleiter, Progress in Mat. Sci. , **33** (4) (1990).
2. R. Uyeda, Progress in Mat. Sci. , **15** (5) (1991).
3. R. W. Siegel, Nanostructured Materials, **3**, 1 (1993).
4. P. S. Kislyi, Ya. A. Kryl, V. M. Filipenko, Sverkhtrverdye Materialy, **6**, 29-34 (1987).
5. H. Hahn and R. S. Averback, Nanostructured Materials, **1**, 95 (1992).
6. G. Messing, S. Zhang and G. Jayanthi, J. Am. Ceram. Soc. , **76** [11], 2707 (1993).
7. W. R. Cannon and S. C. Danforth, J. of Am. Ceram. Soc. , **65** [7], 324 (1982).
8. R. Birringer, H. Gleiter, H. P. Klein and P. Marquardt, Phy. Lett. **102A**, 365 (1984).
9. G. Skandan, H. Hahn and J. C. Parker, Scripta Met. , **25**, 2389 (1991).
10. G. Skandan, H. Hahn, M. Roddy and W. R. Cannon, J. Am. Ceram. Soc. , in press.
11. G. Skandan, C. M. Foster, H. Frase, M. N. Ali, J. C. Parker and H. Hahn, Nanostructured Materials, **1**, 313 (1992).
12. A. Allen, S. Krueger, G. Long, H. Kerch, J. C. Parker, G. Skandan and H. Hahn, to be published in the proceedings of World Ceramic Congress at Florence, Italy.
13. G. Skandan, H. Hahn, B. H. Kear, M. Roddy and W. R. Cannon, to be published in Mat. Letters.
14. F. B. Swinkels and M. F. Ashby, Acta Metall. , **29** [2] 259 (1981).
15. R. L. Coble, J. of App. Phy. , **41** (12), 4798 (1970).

Acknowledgements

This work was supported in part at Rutgers-The State University of New Jersey by a capital equipment grant to the Laboratory of Nanostructured Materials Research. G. S acknowledges the support given by the Center of Ceramics Research by allowing the use of characterization and processing facilities. Thanks are due to Mr. Robert Woodman for helping with the Nitrogen Adsorption experiments.

CHEMICAL SYNTHESIS AND CHARACTERIZATION OF NANOSTRUCTURED TITANIUM ALUMINIDE

S.T. SCHWAB, P.P. PAUL, Y-M. PAN

Southwest Research Institute, Materials Engineering and Technology Division,
6220 Culebra Road, P. O. Drawer 28510, San Antonio, Texas 78228-0510

ABSTRACT

Although plagued by a lack of ductility, titanium aluminides are among the most promising intermetallics under development. Significant improvements in ductility may be obtained from nanostructured intermetallics. Nanosize particles of TiAl_3 have been prepared by heat-treatment of chemically synthesized precursor (compound I). Nanosized TiAl_3 has been characterized by chemical analysis, XRD, EDS, NMR, and HREM.

INTRODUCTION

Considerable effort has been devoted to the development of intermetallic compounds, such as titanium aluminides, for use in aerospace and automotive applications; however, their acceptance has been hampered by their lack of ductility.¹ Three intermetallic compounds or ordered alloys exist in the Ti-Al system: Ti_3Al , TiAl , and TiAl_3 .^{2,3} Of the three, TiAl_3 exhibits the lowest density and the best oxidation resistance, but is the least ductile.^{2,3} Attempts to increase ductility through micro-⁴ or macro-⁵ alloying have yet to meet with success. The availability of nanostructured materials may be essential to the development of TiAl_3 with acceptable levels of ductility.⁶

While a number of methods are available for the generation of nanosize particles, researchers have traditionally relied on vapor phase or mechanical attrition techniques that are not readily amenable to industrial scale production.⁷ Because of deficiencies in these traditional methods, there is growing interest in chemical techniques of producing nanostructured materials.⁸ We report here the chemical synthesis and characterization of nano-structured TiAl_3 . Although nanosize TiAl has been obtained through metal vapor condensation,⁹ to the best of our knowledge, this is the first report of the chemical synthesis of any titanium aluminide and the first report of nanostructured TiAl_3 .

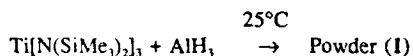
Borohydride reduction has been shown to yield nanosize metals and alloys.^{10,11} Although the tetrahydro-borate adduct of titanium is stable and has been shown to be a useful precursor to titanium diboride,¹² the corresponding tetrahydroaluminate adduct appears

to be unstable.¹³ Co-reduction of metal chlorides with lithium triethylborohydride ("superhydride") has been shown to produce nanosize particles of single phase alloys.¹¹

EXPERIMENTAL

Co-reduction of TiCl_4 and AlCl_3 with superhydride yielded a very reactive solid that, upon heat treatment at 1000°C under inert conditions, converted to microcrystalline Ti_3Al , as observed by X-ray powder diffraction (XRD), with substantial impurities (primarily LiCl) also present.

In an attempt to produce salt-free Ti_3Al , a dilute hexane solution of $\text{Ti}[\text{N}(\text{SiMe}_3)_2]_3$ ¹⁴ was combined with an excess of AlH_3 ¹⁵ at room temperature, according to Equation 1. A very fine, steel-gray powder precipitated from the dark solution after stirring for 16 hours. This pyrophoric powder was washed with ether and dried under vacuum to produce Compound 1 in 60-65% yield, based on Ti.



Compound 1 was pressed into a cylindrical pellet and heated in a quartz crucible under vacuum to 1000°C for 0.5 hour. Upon cooling to room temperature, the fragile pellet was crushed to yield a fine black powder (2).

RESULTS AND DISCUSSION

The solid state ^1H NMR (CRAMPS, 360 MHz) spectrum of 1 consists of resonances at 0.3 ppm and 7.3 ppm, which can be assigned to $-\text{Si}(\text{CH}_3)_3$ and $-\text{NH}$ protons, respectively.¹⁶ The solid state ^{27}Al MAS NMR spectrum (156.4 MHz) of 1 presents absorptions at 60 ppm, 25 ppm, 2 ppm and -492 ppm. While the absorptions seen at 2 ppm, 25 ppm, and 60 ppm are within the normal range of chemical shifts for ^{27}Al , the absorption found at -492 ppm is highly unusual.¹⁷ Not only is this chemical shift far outside the range normally displayed by ^{27}Al , it varies with applied field strength. We believe this unusual behavior may arise from paramagnetic contact shifts.¹⁸ The room temperature X-band ESR spectrum of 1 displays a resonance pattern that indicates the presence of one or more unpaired electrons. While variable temperature ESR experiments to further characterize the spin system are in progress, the presence of an unpaired electron or electrons would be

consistent with the paramagnetic contact shift hypothesis. While the characterization of 1 is not yet complete, we believe it to be a loose cluster of titanium and aluminum atoms that contains relatively few organic functions and a substantial number of "dangling bonds."

Comparison of the XRD pattern obtained from 2 (Figure 1) with that obtained from a sample obtained commercially confirms its identity as TiAl_3 . The XRD pattern also reveals the presence of small amounts of TiO_2 and Ti_3Al . The TiO_2 is probably produced through reaction with the atmosphere, and should be eliminated through strict maintenance of anhydrous and anaerobic conditions. The appearance of Ti_3Al is puzzling, but may be controlled through optimization of the reaction conditions or heat treatment procedure. Analysis of 2 by Energy Dispersive Spectroscopy (EDS) indicated a Ti:Al ratio of 1:3, while chemical analysis of 2 indicated a Ti:Al ratio of 1:2.94. The solid state ^{27}Al MAS NMR spectrum (156.4 MHz) of 2 presents a major absorption at 252 ppm and little indication of the unusual resonance at -492 ppm that dominated the spectrum of 1. The absorption at 252 ppm may be assigned to TiAl_3 ; the solid state ^{27}Al MAS NMR spectrum (156.4 MHz) of the commercial powder consisted of a single resonance at 256 ppm.

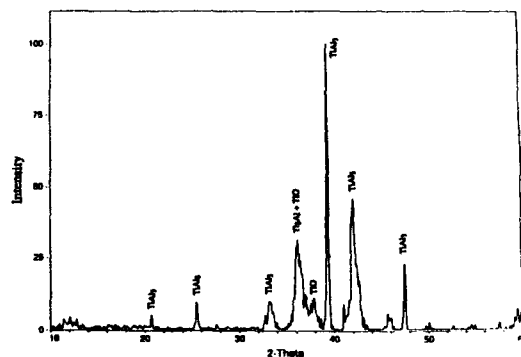


FIGURE 1. Powder X-Ray Diffraction Pattern of Nanosize TiAl_3 (compound 2).

A small portion of 2 was dispersed on holey carbon-coated copper grids for High-Resolution Electron Microscopy (HREM) analyses. Bright field micrograph reveals 2 to be composed of agglomerates of nanosize particles with a size distribution of approximately 5-25 nm (Figure 2). HREM lattice imaging reveals two adjacent nanocrystalline grains

having the same spacing of 0.212 nm, which are consistent with the lattice fringes expected from (004) plane of TiAl_3 (Figure 3). The crystals tend to be equiaxed; their interfaces appear to be sharp at the grain boundaries. EDS microanalysis of 2 using a probe size of about 1 nm further confirms its identity as TiAl_3 .

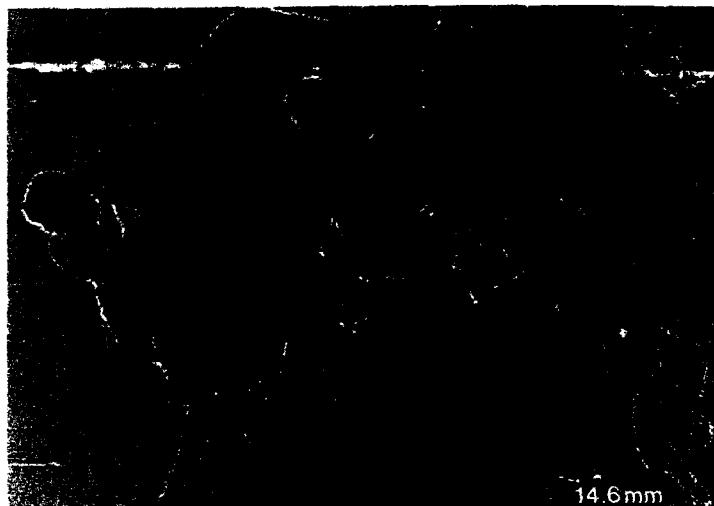


FIGURE 2. Transmission Electron Micrograph of Nanosize TiAl_3 Powder (compound 2).

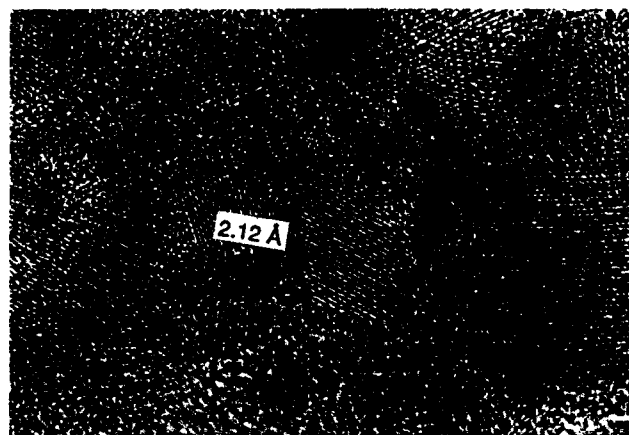


FIGURE 3. High-Resolution Electron Micrograph Lattice Fringes From (004) Plane of Nanosize TiAl_3 (compound 2).

CONCLUSION

Solution chemistry has been used for the first time to produce titanium aluminide, and nanostructured TiAl₃ has been obtained for the first time. While the precursor powder (1) has yet to be fully characterized, it does yield salt-free TiAl₃ when heated. We have demonstrated that chemical methods can be used to produce advanced intermetallics in the nanosize regime. Bulk specimens of this chemically derived TiAl₃ are being produced with which to determine if the promise of novel or improved properties has been realized by this nanostructured material.

Acknowledgment: The authors gratefully acknowledge the financial support of the Office of Naval Research (Contract N00014-91-C-0085). The HREM work reported here was performed at Arizona State University in the Center for High Resolution Electron Microscopy, which is supported by the National Science Foundation (Grant DMR-9115680).

REFERENCES:

1. a) R.L. Fleischer, *J. Mat. Sci.*, **22**, 2281 (1987); b) R.L. Fleischer, D.M. Dimiduk, and H.A. Lipsitt, *Ann. Rev. Mater. Sci.*, **19**, 231 (1989); c) S. Naka, M. Thomas, and T. Khan, *Mater. Sci. Tech.*, **8**, 291 (1992); d) D.M. Dimiduk, D.B. Miracle, and C.H. Ward, *Mater. Sci. Tech.*, **8**, 367 (1992); e) N.S. Stoloff, in High-Temperature Ordered Intermetallic Alloys, edited by C.C. Kirch, C.T. Liu, and N.S. Stoloff, *Mat. Res. Soc. Symp. Proc.*, **39**, Pittsburgh, PA, pp. 3-30 (1985).
2. a) F.H. Froes, C. Suryanarayana, and D. Eliezer, *J. Mat. Sci.*, **27**, 5113 (1992); b) K.S. Kumar, in Structural Intermetallics, edited by R. Darolia, J.J. Lewandowski, C.T. Liu, P.L. Martin, D.B. Miracle, and M.V. Nathal, (The Minerals, Metals & Materials Society: Warrendale, PA, 1993) pp. 87-96; c) Z.L. Wu and D.P. Pope, in Structural Intermetallics, (*op. cit.*), pp 107-116.
3. Y. Umakoshi, M. Yamaguchi, T. Sakagami, and T. Yamane, *J. Mat. Sci.*, **24**, 1599 (1989).
4. K. Aoki and O. Izumi, *J. Jpn. Inst. Met.*, **43**, 358 (1979).
5. T. Liu and H. Inouye, *Metall. Trans. A.*, **10A**, 1515 (1979).

6. R. Bohn, T. Haubold, R. Birringer, and H. Gleiter, *Scripta Met. et Mat.*, **25**, 811 (1991).
7. L.E. Brus and R.W. Siegel, *et. al.*, *J. Mater. Res.*, **4**, 704 (1989).
8. a) G.M. Whitesides, J.P. Mathias, and C.J. Seto, *Science*, **254**, 1312 (1991); b) G.A. Ozin, *Adv. Mater.*, **4**, 612 (1992).
9. a) H. Chang, H.J. Höfler, C.J. Altstetter, and R.S. Averbach, *Scripta Met. et Mat.*, **25**, 1161 (1991); b) H. Chang, C.J. Altstetter, and R.S. Averbach, *J. Mater. Res.*, **11**, 2962 (1992).
10. H. Bonnemann, W. Brijoux, and T. Joussen, *Angew. Chem. Int. Ed. Engl.*, **29**, 273 (1990).
11. D. Zeng and M.J. Hampden-Smith, *Chem. Mater.*, **5**, 681 (1993).
12. J.A. Jensen, J.E. Gozum, D.M. Pollina, and G.S. Girolami, *J. Am. Chem. Soc.*, **110**, 1643 (1988).
13. B.M. Bulychiev, S.E. Tokareva, G.L. Soloveichick, and E.V. Evdokimova, *J. Organomet. Chem.*, **179**, 263 (1979).
14. E.C. Alyea, D.C. Bradley, and R.G. Copperwaite, *J. Chem. Soc., Dalton Trans.*, 1580 (1972).
15. A.E. Finholt, A.C. Bond, and H.I. Schleisinger, *J. Am. Chem. Soc.*, **69**, 1199 (1947).
16. G.E. Maciel, C.E. Bronnimann, and B.L. Hawkins, in Advances in Magnetic Resonance, edited by W.S. Warren (Academic: New York, 1990, Vol. 14) pp 125-150.
17. J.W. Akitt, in Progress in Nuclear Magnetic Resonance, edited by J.W. Emsley, J. Feeney, and L.H. Sutcliffe, (Pergamon: Oxford, U.K., 1989, Vol.21) pp 1-149.
18. J.P. Jesson, in NMR of Paramagnetic Molecules: Principles and Applications, edited by G.N. La Mar, W. DeW Horrocks, Jr., and R.H. Holm, (Academic: New York, 1973) pp. 1-52.

SYNTHESIS AND PROCESSING OF NANOGRAINED Fe - (Fe, Mo)₆C COMPOSITE POWDERS

R. K. SADANGI¹, B. H. KEAR¹, I. E. McCANDLISH²

¹Department of Mechanics and Materials Science
Rutgers- The State University of New Jersey, Piscataway, New Jersey 08855-0909

²Nanodyne Incorporated,
19 Home News Row, New Brunswick, New Jersey 08901

ABSTRACT

Spray Conversion Processing was used to synthesize high volume fractions (0.52 - 0.74) of nanograined (Fe, Mo)₆C carbide dispersions in iron, starting from water soluble precursors. The essential features of the process are, (1) preparation of a chemically homogeneous precursor powder, and (2) thermochemical conversion of the precursor powder to the desired nanostructured composite powder through controlled gas-solid reactions. The thermodynamic and kinetic features of the gas-solid reactions, and the influence of various processing parameters on the structures developed, are discussed. The powders were consolidated to near theoretical density by pressureless sintering and hot pressing. All the consolidated samples had bicontinuous structures. Compared to M2 high speed tool steels, these high volume fraction carbide strengthened iron alloys display superior hardness values up to 500 °C.

INTRODUCTION

Nanostructured materials (polycrystalline materials with grain size less than 100 nm) have generated considerable interest in recent years [1,2]. The synthesis of powder precursors is an essential step in the processing of nanostructured materials. A number of physical methods, such as inert gas condensation and high energy ball milling, chemical methods such as gas phase combustion synthesis, electro-deposition and sol-gel processing, and many colloidal based procedures have been used to synthesize nanostructured powders [3]. Exposure of single phase nanostructured powders to high temperatures during consolidation leads to significant grain growth. Thus it seems imperative to use multiphase alloys to mitigate grain growth during high temperature consolidation of nanostructured powders.

This research was targeted on synthesis and processing of an iron-base alloy, which contained a high volume fraction of nanodispersed M₆C phase (mixed carbide of Fe and Mo, also known as η carbide). Eta carbide (Fe, Mo)₆C (henceforth, η) is a hard, brittle and thermodynamically stable phase in high speed steels, high temperature alloys, such as superalloys and heat-resistant steels. Moreover Fe and η phases have limited mutual solubility and also a favorable low interfacial energy, and comparable thermal expansion coefficients [4].

The conventional method [5] for synthesizing η carbide phase involves are melting of the elements, remelting and long annealing at high temperatures to circumvent the kinetic barrier to obtain the thermodynamically stable phase. In such cases the microstructural scale is coarse (few hundreds of microns), and the interconnectivity of η carbide in a high volume fraction composite makes it inherently brittle. The Fe-Mo-C phase diagram is shown in Figure 1. To produce Fe + η , with different volume fractions of η carbide, the composition of the powder has to be precisely controlled within the narrow two-phase field. None of the methods listed above is suitable for synthesizing the two-phase nanoscale Fe + η structure with varying volume fraction of η carbide. The high volume fraction of nanoscale dispersions, however, can be achieved by utilizing a novel chemical processing method, called Spray Conversion

Processing [6], which has already been exploited to produce prealloyed nanostructured WC-Co powders: the scale of WC particles are typically $\sim 0.02 - 0.1 \mu\text{m}$.

Our basic chemical synthesis method comprises four sequential steps: (1) preparation and mixing of an aqueous starting solution of ammonium heptamolybdate and ferric nitrate in a predetermined ratio, as fixed by the nominal composition of the final product powder, (2) spray drying of the starting solution to form an homogeneous precursor powder with amorphous or microcrystalline structure, (3) reductive decomposition of the precursor powder in flowing hydrogen to yield a high surface area reactive metallic intermediate, and (4) selective carburization of the reactive intermediate to yield the desired two-phase nanograined powder. The structural scale of the final product can be controlled by adjusting the synthesis temperature. The composition and purity of phases are controlled precisely by adjusting the carbon activity of the carburizing gas. Since this process relies on gas-solid reactions, it has good reproducibility and potential for scale-up. Moreover, it is not necessary to resort to blending of powders of individual phases, and energy intensive ball-milling to achieve uniform dispersions.

In this paper, we describe procedures for synthesis of prealloyed Fe- η carbide powders, and for their consolidation by hot pressing and pressureless sintering.

EXPERIMENTAL

1) Preparation of precursor powders

Aqueous solutions of ferric nitrate and ammonium hepta-molybdate were mixed to achieve 52, 60, 68 and 74 vol% dispersions of η carbide in the iron matrix. The nominal compositions were calculated on the assumption of stoichiometric $(\text{Fe}_3\text{Mo}_3)\text{C}$ carbide and x-ray density of carbide. Spray drying of aqueous solutions was carried out in DL-41[®] spray drying unit. The XRD traces of spray dried powders shows patterns characteristic of amorphous compounds (Figure 2), indicating homogeneous mixing of inorganic salts without any phase separation. All the spray dried powders were hygroscopic in nature due to presence of ferric nitrate. The precursor powders were pyrolyzed in argon at 300 °C to get rid of the volatile constituents (ammonium and nitrate ligands, water of crystallization). This reduced the hygroscopicity and eliminated the tendency of the precursor powders to form agglomerates. The XRD traces (Figure 2) of the pyrolyzed powders showed unidentified, poorly defined crystalline peaks. There was no evidence for any pure binary iron or molybdenum oxides. The Fe-Mo-O system contains a family of double oxides, and presumably some kind of mixed oxide is formed. The pyrolyzed powders retained the broken shell morphology of the spray dried powder, varying in size from 2-50 μm .

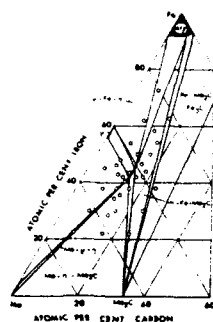


Figure 1 Phase diagram of Fe-Mo-C, isothermal section at 1000 °C [5]

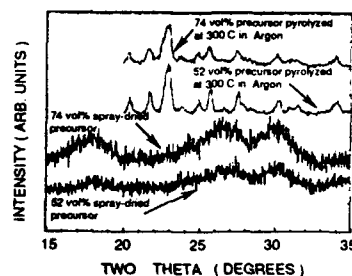


Figure 2 XRD patterns of spray dried and pyrolyzed powders

2) Thermochemical conversion of precursor powders

The thermochemical conversion of precursor powders was monitored in a thermogravimetric analyzer (TGA). Sample weight changes were monitored using a Cahn 1000 microbalance. Reactive gases were supplied from a gas manifold, through Brooks mass flow controllers. Samples were placed in a platinum boat which was suspended in a vertical tube furnace. The reaction temperature, gas flow rate, and the weight change were plotted using a computer program. About 100 mg of sample was taken in each case. Each sample was heated to the reaction temperature at a rate of 15 °C/min. Reduction was carried out in flowing hydrogen and subsequently a carburizing gas mixture was introduced. To evaluate the powder structure, prior to carburization, the reductive decomposition was carried out isothermally at 600, 650, and 700 °C in pure hydrogen. Passivation was done at room temperature to overcome the pyrophoric nature of the fully reduced product. The procedure followed was pure argon for 30 minutes to scavenge the system, followed by 2% O₂/Ar for 30 minutes and 4% O₂/Ar for 30 minutes. Carburization experiments were carried out at 700 °C until the weight in TGA reached a plateau. Carbon activity was varied from 0.1 to 0.9 at 0.1 steps by adjusting gas flow rates of Ar, CO, CO₂ while maintaining the oxygen potential was 5×10^{-23} atm to prevent the formation of MoO₃. XRD analyses of the powder samples were carried out in a Siemens diffractometer using CuK α source and graphite monochromator. Scanning Electron microscopy was carried out using an AMRAY 1200 microscope, operating at 20kV.

DISCUSSION OF RESULTS

A. Powder Synthesis

1. Reductive decomposition of precursor

In the temperature range 600-700 °C, the reduction profiles showed similar trends for all compositions investigated, Figure 3 (a) and (b). Weight loss was gradual and was complete in a single stage. At lower temperatures, the reduction profile is a superposition of rapid weight loss and a gradual weight loss. This can be explained on the basis of the different thermodynamic stabilities of iron and molybdenum oxides and their solid solutions.

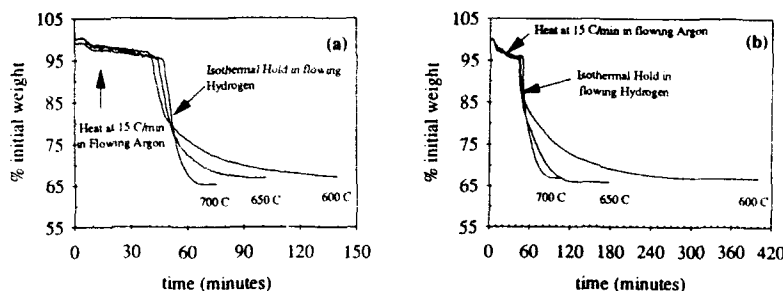


Figure 3 Reduction kinetics of (a) 52 vol% precursor, (b) 74 vol% precursor

XRD patterns of the two compositions (52 and 74 vol%) showed an iron peak and a diffuse, broad peak in the two theta range of 35 to 47 degrees, Figures 4 (a) and (b). The diffuse pattern corresponds to d spacings of Fe₇Mo₆. Such diffuse patterns are signatures of poorly crystalline, or nanocrystalline structures. But in the two compositions, the broad peak is at the same two theta position, suggesting that an identical nanocrystalline phase is formed in both cases. The width of the broad peak is unchanged irrespective of reduction temperature. The fully reduced intermediate is pseudomorphic with the original precursors powder, but with reduced dimensions and with a lot of submicron pores.

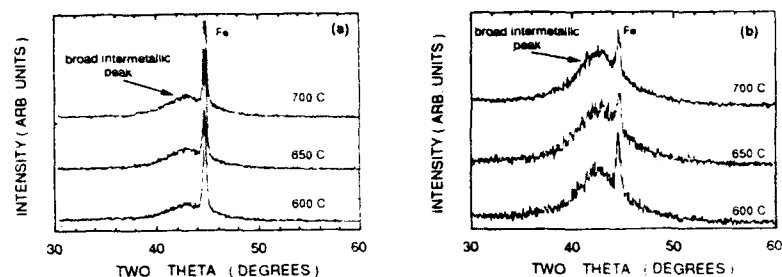


Figure 4 XRD patterns of reduced intermediates (a) 52 vol% precursor, (b) 74 vol% precursor

2) Gas phase carburization of reactive intermediate

a) Thermodynamic considerations

Equilibrium phases that can be obtained by addition of carbon to the reduced intermediate are determined by the Fe-Mo-C phase diagram. At the lower temperature of 700 °C, the established phase diagram at 1000 °C is at best an approximation. The carbon activity of the system, a_c , varies in accordance with the Gibb's phase rule. If the temperature and pressure is kept constant, in the three-component system, there will be variation in the carbon activity in the two phase field, whereas the carbon activity will be invariant in the three phase field.

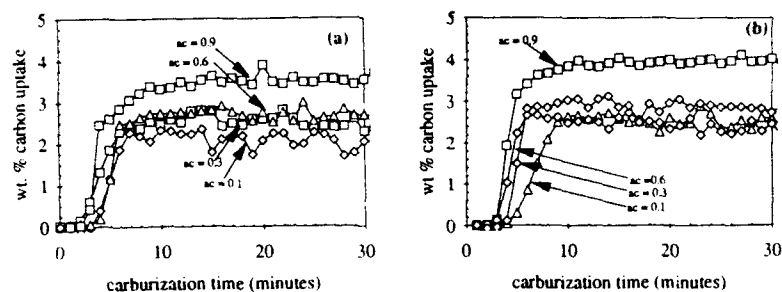


Figure 5 Carburization kinetics of reduced intermediates of (a) 52 vol% precursor, (b) 74 vol% precursor at 700 °C

The XRD traces of the reaction products at four different carbon activities are shown in Figure 6 (a) and (b). It is seen that at carbon activities ≤ 0.1 , we get the equilibrium two phase mixture of iron and eta carbide, for both the extreme compositions investigated. Although the composition variation across the two phase field is small, the carbon activity variation is large. This permits control of both the carbon content and phase purity of the carburized end product.

b) Kinetic Considerations

The rate of any gas-solid reaction can be either diffusion controlled, or interface controlled or mixed mode, depending on the reaction conditions, particle size, and the particular system. In any case, the

overall reaction rate is proportional to the reaction surface area and is maximum when the available surface area is maximum. The high surface area of the nanoporous reaction intermediate permits the carburization to be carried out at lower temperature and minimum time, thereby limiting grain growth of the carbide phase.

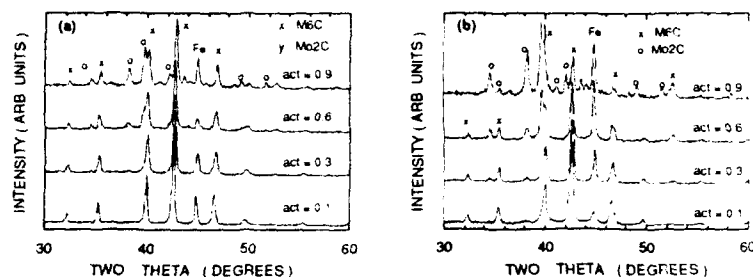


Figure 6 XRD patterns of 700 °C carburized samples of (a) 52 vol% precursor, (b) 74 vol% precursor

Figure 5 (a) and (b) shows the carburization kinetics at 700 °C. In most cases during carburization, Mo_2C is formed as a metastable intermediate. This is indirectly confirmed by an initial weight pick up during carburization at 0.1 carbon activity and slight weight loss (decarburization) to give iron and eta carbide. A lower carburization activity in the gas phase will enhance the decarburization kinetics and thus, carburization was carried out at 0.1 activity to eliminate other products due to kinetic constraints. At higher carbon activities, where Mo_2C is stable, the amount of carbon is high in the case of 74 vol% precursor, which contains higher molybdenum. There has been various schools of thought pertaining to the Mo_2C to M_6C transformation during tempering of molybdenum containing steels. Mo_2C has limited solubility (5 wt%) in iron. It has hexagonal structure and forms as needles due to surface energy anisotropy as a result of its crystal symmetry. The η carbide has FCC structure and tends to form as spheroids. The change from needle to spheroid morphology is triggered by the reduction in surface energy and this occurs *in-situ*. This can occur by (1) nucleation of M_6C at the interface between iron and Mo_2C , with subsequent growth controlled by diffusion in the matrix, (2) nucleation of M_6C inside the Mo_2C particle and diffusion controlled growth of the nucleated phase. In our case, the first mechanism seems to be more probable because of the controlled carbon potential in the gas phase, which ultimately drives the reaction. The rate of transformation is determined by diffusivity of molybdenum, whereas the spheroidization of Mo_2C to M_6C is determined by diffusivity of iron at the synthesis temperature.

The kinetics of carburization of the 74 vol% reactive intermediate is followed at 600, 650 and 700 °C at carbon activity 0.1. The XRD traces of reaction products are given in Figure 7. At 600 °C, even after carburization for 12 hours, there is a mixture of iron and Mo_2C . On the other hand, at 700 °C, complete conversion to iron and M_6C is achieved in one hour. This corroborates the fact that diffusion of molybdenum is the rate determining factor for the Mo_2C to M_6C transformation. There is no significant grain growth due to prolonged annealing at 700 °C. The scanning electron micrograph (Figure 9) of the carburized powder is pseudomorphic with that of the reduced intermediate. The average grain size of both phases is around 50nm. Figure 8 shows the XRD traces of different volume fraction carbide dispersions synthesized at 700 °C. The intensity of carbide peaks increases with increasing content of η carbide, with a corresponding decrease in the intensity of iron peak. The grain sizes of both phases remain more or less unaffected.

B. Powder Consolidation

The powders were consolidated to theoretical density by pressureless sintering [7,9] and hot pressing [8]. In both cases, a bicontinuous structure was obtained. Pressureless sintering resulted in a relatively coarse carbide grain size of 0.6 - 1.5 μm . With hot pressing [8], the grain size of carbide was

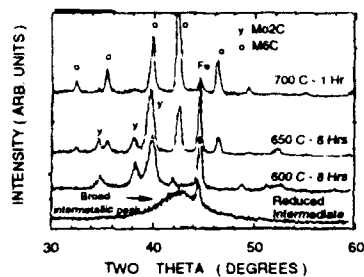


Figure 7 XRD patterns reaction products of 74 vol% precursor at low temperature

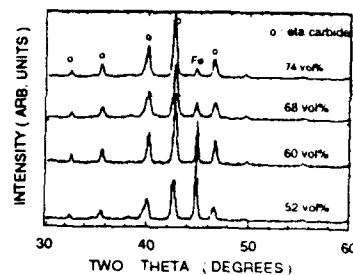


Figure 8 XRD patterns of as-synthesized cermet powders with different volume fractions of carbide phase

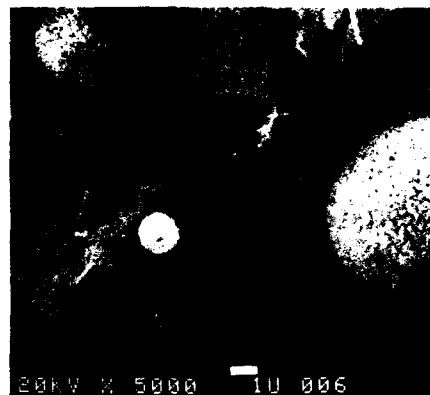


Figure 9 Scanning electron micrograph of carburized end product powders

lowered to 200 - 300 nm. Pressureless sintering of intermediate volume fraction (60 and 68 vol%) η carbide composites yielded submicron-grained structures [9], in contrast to single phase materials which would have yielded structures in tens to hundreds of microns. Thus, two-phase nanograined Fe - η powders with optimal volume fraction (60 - 68 vol% of hard phase) appear to mitigate grain coarsening during sintering. Furthermore, subsequent annealing at higher temperatures caused no further coarsening of the carbide grain size.

C. Hot Hardness

Figures 10 (a) and (b) show temperature dependence of hardness of the consolidated samples. The hardness increases with volume fraction of carbide, for both the pressureless sintered and hot pressed samples. A hardness of 760 kg/mm² is obtained for the pressureless sintered 74 vol% carbide composite and the corresponding value for 52 vol% is 415 kg/mm². There was no visible cracking at the corners of the indentations, even under a load of 30 kg for the 52 vol% composite, but in some cases, wavy cracking

was observed in the 74 vol% composite. This suggests that these bicontinuous composite materials are not inherently brittle. A hardness value of 780 kg/mm^2 is obtained for the hot pressed 52 vol% carbide composite, whereas for the 74 vol% material it is 1020 kg/mm^2 . In all the composites, the hot pressed samples demonstrated higher hardness values.

The hot hardness of these bicontinuous composite materials is relatively insensitive to temperature up to $400 - 500^\circ\text{C}$, depending upon the carbide content. All the samples showed better hot hardness than M2 high speed tool steel. High hardness in M2 tool steel is obtained by dispersion of M_6C carbides in a tempered martensite matrix. So the hardness falls off rapidly at high temperature because martensite loses its strength.

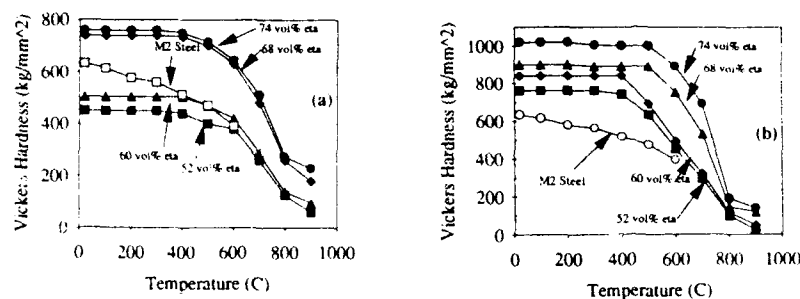


Figure 10 Hot hardness data for (a) pressureless sintered samples, (b) hot pressed samples. Also shown is hardness data for M2 high speed steel

SUMMARY

We have shown that spray conversion processing is a viable means of producing high volume fraction ($> 52 \text{ vol}\%$) of nanograined dispersions of η carbide in iron. From preliminary investigations, these materials can be consolidated to full density, yielding bicontinuous structures that possess acceptable toughness. Experiments are in progress to evaluate high temperature strength and creep properties.

ACKNOWLEDGMENTS

This work was supported by Office of Naval Research under contract # N00014-91-J-1828.

REFERENCES

- 1) H. Gleiter, *Nanostructured Materials*, vol 1, pp 1 - 19, 1992
- 2) H. Gleiter, *Progress in Materials Science*, vol 33, p 1, 1990
- 3) N. P. Louat, *Acta Met.*, vol 33, no 1, pp 59 - 69, 1985
- 4) H. J. Goldschmidt, *Interstitial Alloys*, Butterworth, London, 1967
- 5) A. C. Fraker, H. H. Stadelmaier, *Trans. Met. Soc. AIME* 245, p 847 - 851, 1969
- 6) L. E. McCandlish, B. H. Kear, B. Kim, *Mat. Sc. & Tech.*, vol 6, p 953, 1990
- 7) R. K. Sadangi, B. H. Kear, L. E. McCandlish, *Nanostructured Materials*, vol 2, pp 563 - 569, 1993
- 8) R. K. Sadangi, B. H. Kear, L. E. McCandlish, *Nanostructured Materials*, vol 3 pp 69 - 76, 1993
- 9) R. K. Sadangi, B. H. Kear, L. E. McCandlish, unpublished results

HRTEM ANALYSIS AND MAGNETIC PROPERTIES STUDY OF SURFACE OXIDIZING AND NITRIDING OF NANOCRYSTALLINE PARTICLES

CHI-MING HSU*, HONG-MING LIN*, KUEN-RONG TSAI*, PEE-YEW LEE**

*Department of Materials Engineering, Tatung Institute of Technology, Taipei, Taiwan, R.O.C.

**Graduate Institute of Materials Engineering, National Taiwan Ocean University, Keelung, Taiwan, R.O.C.

ABSTRACT

Nanocrystalline iron powders were produced by means of the gas condensation. Pure nitrogen, or oxygen, or air, was introduced into the as-made powders before they were taken from the chamber. Various atmospheres produced varied layer structures around the iron particles. A high resolution transmission electron microscope was used to analyze the crystal structure and vibrating-sample magnetometer was used to measure the magnetic properties of nanocrystalline iron particles. The results showed that a layer of amorphous or nanocrystalline structure was formed initially on the surface of iron particles. This thin amorphous layer crystallized into Fe_3O_4 after annealing under electron irradiation when the introduced atmosphere was pure oxygen or air. However, it formed a passivated layer of $\zeta\text{-Fe}_2\text{N}$ when nitrogen was introduced. The exchange anisotropy between the iron core and the superficial iron oxide or nitride shell was observed as the sample was cooled in an applied field of 10 kOe from room temperature to 5 K. The shift of the hysteresis loop caused by exchange anisotropy was 16 % for the nitride shell and 8 % for the oxide shell.

INTRODUCTION

Nanocrystalline (NC) materials can be made by various methods including chemical reduction[1], sputter deposition[2], gas-condensation techniques[3-5], and others[6]. The gas-condensation method produces powders with a narrow distribution of sizes.

Nanocrystalline iron powders are chemically active. A passivated layer forms on the surface of powders when a little air or O_2 leaks slowly into the chamber before the powders are removed. Varied structures of the passivated layer are obtained depending on the process. The structure determination of the passivated were achieved with various instruments. These instruments include X-ray diffractometer, Mossbauer spectrometer, high resolution transmission electron microscope (HRTEM), and transmission electron microscope (TEM). Different results were obtained by different groups. Fe_3O_4 or $\gamma\text{-Fe}_2\text{O}_3$ is the most common structure which people agreed[7-15].

Saturation magnetization of fine particles is less than that of bulk materials and decreases with decreasing size of particles. A varied model was built to explain the decrease of saturation of magnetization of fine particle[16-19]. Also the origin of the coercivity of fine particle is different depending on the hypothesis that people made[14,18-22].

The purposes of this work were to determine the structure of the passivated layer and the effect of various passivated layer on the magnetic properties.

EXPERIMENTAL

Ultrafine particles of iron were prepared by means of the gas condensation. Pure iron was placed in a resistively heated tungsten boat. It evaporated and condensed on the surface of a trap cooled with liquid N_2 . Oxygen or air at a flow rate 5 standard cubic centimeter per minute (SCCM) and 900 Pa or nitrogen at a flow rate 100 SCCM and 9000 Pa was introduced to the chamber for one hour to form a passivated layer around the powders before they were removed from the chamber.

A superconducting quantum interference (SQUID) magnetometer was also used to measure the magnetic properties. This task was done by cooling the samples in an applied field of 10 kOe from room temperature to 5 K at which the hysteresis loop was measured.

TEM images were taken with a TEM/STEM (Hitachi 800). Selected area diffraction patterns were used to identify the structure. The HRTEM image was formed with a TEM (JOEL-4000EX) operating at 400 kV. The images from the HRTEM were processed with commercial software (Adobe Photoshop) and the optical diffraction pattern was obtained from a fast Fourier transformation (FFT) program.

RESULTS AND DISCUSSION

Surface Analysis of Nanocrystalline Iron

As the particles made by gas condensation are small, it is not easy to identify the crystal structure of the layer around the iron by X-ray diffractometry. High resolution transmission electron microscopy is an alternative method. As-made powders exposed to pure oxygen before being removed from the chamber show an oxide layer with thickness of 4.5 nm around the iron core (figure 1). High resolution TEM observation of this oxide layer initially indicated no crystalline structure. However, after exposure of the sample to the electron beam about 30 minutes, an island-like crystalline area (figure 2(a) area A) appeared. This small area of crystalline structure is believed to be induced by electron irradiation. In order to identify this crystalline structure, the atomic fringe image was processed (figure 2(b)) and transformed to an optical diffraction pattern through FFT as shown in figure 2(c). The diffraction pattern is indexed as the $[1\bar{1}14]$ zone of a Fe_3O_4 spinel structure. The same procedure was used to examine the formation of oxide layer when the O_2 atmosphere was replaced with air. The results indicate that an air atmosphere also produces a Fe_3O_4 layer.



Figure 1 : TEM image of as-made iron powders exposed to O_2 showing an oxide layer indicated by arrow A.

The nanophase iron powders treated with nitrogen give a different result. A nitride layer was formed on the surface of these powders. Figure 3a shows a small crystalline structure (area A). This area was processed with image analysis (figure 3b) and transformed to the optical diffraction pattern, through the FFT, shown in figure 3c which was indexed as the $[001]$ zone of

ζ -Fe₂N. The crystalline area A is due to exposure to the electron beam about the 30 minutes which caused partial crystallization of amorphous structure.

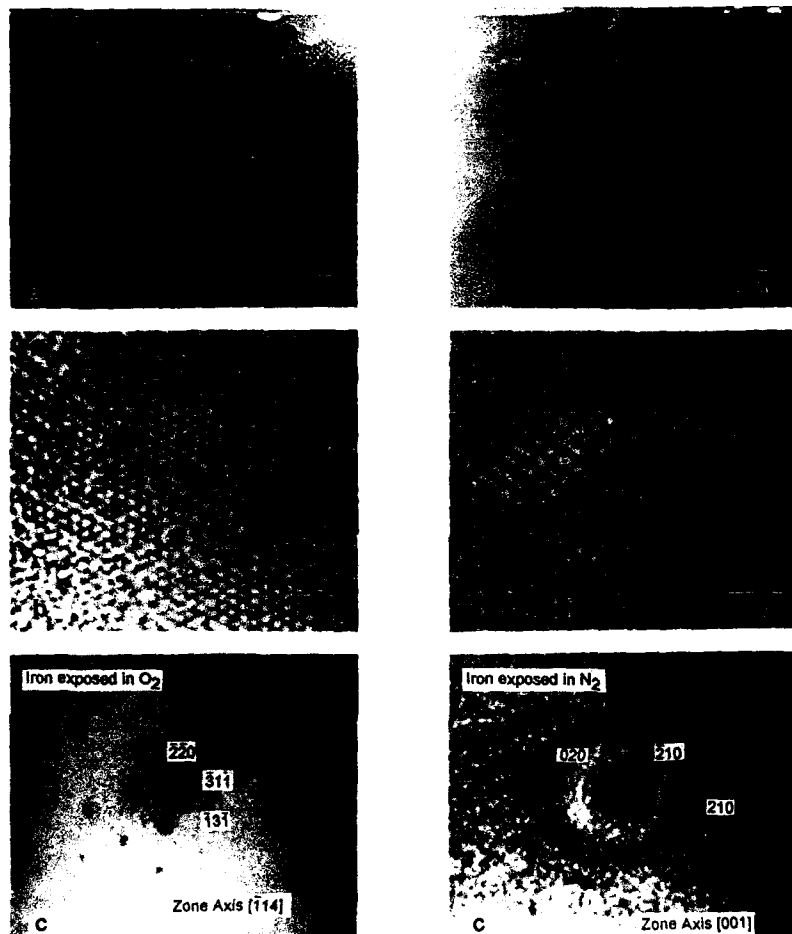


Figure 2 : (a) High resolution image of as-made nanophase iron powders exposed to O₂; (b) processed image of area A; (c) optical diffraction pattern from (b) by means of FFT.

Figure 3 : (a) High resolution image of as-made nanophase iron powders exposed to N₂; (b) processed image of area A; (c) optical diffraction pattern from (b) by means of FFT.

To confirm the result from the HRTEM, we employed the SAD pattern of TEM (figure 5) for nanophase iron particles exposed to O₂, air or N₂. Because the particles are so small, the SAD patterns of these three samples are ring patterns that are a combination of an iron pattern and a diffuse ring at the center (figure 4a & c). In an attempt to confirm that the crystalline area

observed in HRTEM was induced by the electron irradiation, we exposed the samples to the condensed electron beam of TEM for ten minutes. The inner diffuse ring altered to distinct ring spots (figure 4b & d). Hence it is evident that annealing the as-made iron powders with an electron beam causes crystallization of the amorphous oxide or nitride layer. The crystalline structure of the surface layer of nanophase iron particles exposed to O_2 or air was then identified as Fe_3O_4 (figure 4b). The $\zeta\text{-Fe}_2\text{N}$ structure obtained from HRTEM in nanophase iron particles exposed to N_2 was also confirmed again by TEM (figure 4d).

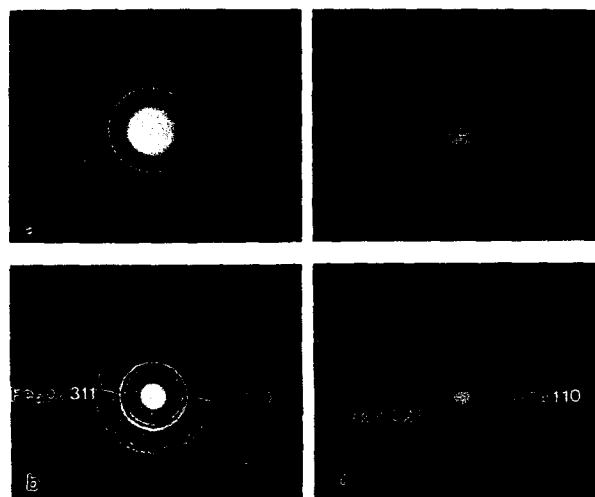


Figure 4 : TEM selected area diffraction pattern of nanophase iron powders exposed to O_2 and air; (a) as-made; (b) after annealing with the electron beam; and nanophase iron powders exposed to N_2 ; (c) as-made (d) after annealing with electron beam.

Surface Anisotropic Effects on Magnetic Properties

The magnetic properties of iron particles with varied outer layers were investigated. Figure 5 shows that the saturation magnetization of oxide- and of nitride- coated particles are almost the same at room temperature. The coercivities of oxide- coated particles at room temperature are slightly larger than that of nitride coated particles when the particle sizes are between 20 and 40 nm (figure 6). If the particle size is less than 20 nm, both samples have almost the same magnitude of coercivity. This result indicates that the interactions between the spins of iron and of iron nitride or iron oxide are similar at room temperature. According to Meiklejohn and Bean[23], this interaction between the spin of the iron core and spin of outer layer is called exchange anisotropy. In their research, they found an exchange anisotropy between an antiferromagnetic and a ferromagnetic material. In order to inspect the effect of exchange anisotropy on the coercivity, we cooled samples in an applied field 10 kOe from room temperature to 5 K and the hysteresis loop was measured at 5 K.

Figure 7 shows the hysteresis loop of field-cooled nitride-coated particles of mean diameter of 13 nm and applied maximum field 55 kOe. The loop is shifted to the left from its symmetrical origin. To emphasize the shift of the loop, the figure shows only the loop with H between -5000 Oe and 5000 Oe, and the amount of shift is defined as $\mu H_c - H_c$, in which μH_c and H_c represent the intrinsic coercive forces in the forward and reverse directions, respectively. As the loop is only slightly asymmetrical, the abc segment in the third and fourth quadrants of the loop is superimposed onto the first and second quadrants of the loop; the amount of shift is 305 Oe with the $\mu H_c = -1845$ Oe and $H_c = 1540$ Oe. The loop was shifted about 16% to the left. This exchange anisotropy was also found between iron and iron oxide layer in nanophase iron particles of mean diameter 14 nm. However, it is not as large as for the nitride-coated iron particles. The loop is shifted about 8% for the oxide-coated iron particles.

According to these results the nitride-coated particles show greater anisotropy at lower temperature. The greater coercivity (1845 Oe) of nitride-coated nanophase iron particles at 5 K is, therefore, due to its larger exchange anisotropy. The magnitude of this exchange anisotropy depends on the material. Meiklejohn and Bean found a large exchange anisotropy between antiferromagnetic and ferromagnetic materials. Here the Fe_3O_4 is ferrimagnetic and iron is ferromagnetic at 5 K. This result indicates that exchange anisotropy also exists between ferromagnetic and ferrimagnetic materials, but it is small. The magnetic type of the nitride layer at 5 K is unclear, but according to the above result its exchange anisotropy appears to be larger than for the oxide-coated particle.

CONCLUSIONS

1. Iron powders made by gas condensation form a passivated layer. This layer with an amorphous or nanocrystalline structure is an

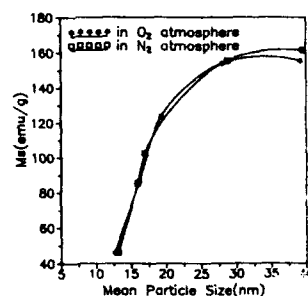


Figure 5 : Saturation magnetization vs. mean particle size at room temperature for nanophase iron particles exposed to O_2 or N_2 atmospheres.

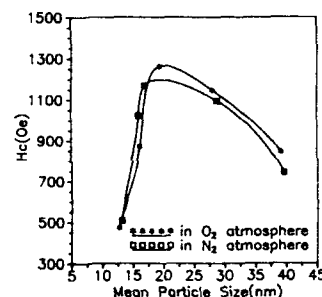


Figure 6 : Coercivity vs. mean particle size at room temperature for nanophase iron particles exposed to O_2 or N_2 .

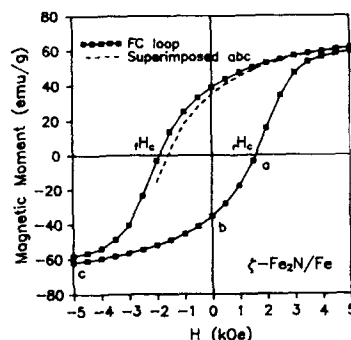


Figure 7 : Hysteresis loop of field-cooled nitride-coated iron powders with mean particle size about 13 nm showing a shift 305 Oe at 5 K.

iron oxide when the powders are exposed to pure oxygen or to air, but an iron nitride if exposed to nitrogen. The oxide amorphous structure transforms to Fe_3O_4 and the nitride amorphous structure transforms to $\zeta\text{-Fe}_2\text{N}$ crystalline structure when they are annealed with an electron beam.

2. The exchange anisotropy exists in both oxide-coated iron particles and nitride-coated iron particles. The amount of shift of the hysteresis loop can reach 305 Oe for the nitride-coated iron particles, and the loop is shifted about 16% to the left. For the oxide-coated iron powders, the amount of shift is 120 Oe, and the loop is shifted about 8%. The greater coercivity of nitride-coated nanophase iron particles at 5 K is caused by a larger exchange anisotropy.

ACKNOWLEDGMENTS

We thank the National Science Council, Republic of China, and Tatung Company Ltd. for financial support through contract number NSC 81-0405-E-036-08 and 81-1706-28, respectively.

REFERENCES

1. L. Yiping, G. C. Hadjipanayis, C. M. Sorensen, and K. L. Klabunde, *J. Mag. Magn. Mat.*, **79**(1989)321.
2. G. Xiao, C. L. Chien, *J. Appl. Phys.*, **51**(1987)1280.
3. K. Kimoto and I. Nishida, *Japan J. Appl. Phys.*, **6**(1967)1047.
4. C. G. Granqvist and R. A. Buhrman, *J. Appl. Phys.*, **47**(1976)2200.
5. Hong-Ming Lin, Shu-Huei Hsieh, Pee-Yew Lee, Ming-Shung Lai and Jie-Shing Wu, *Materials Chemistry and Physics*, **34**(1993)205.
6. F. H. Froes and C. Suryanarayana, *JOM*, June, (1989)12.
7. C. Kaito, K. Fujita and T. Naiki, *Japan J. Appl. Phys.*, **9**(1970)151.
8. C. Kaito, K. Fujita and H. Hashimoto, *Japan J. Appl. Phys.*, **12**(1973)489.
9. K. Haneda & A. H. Morrish., *Nature*, **282**, November, (1979)8.
10. S. Kitahata, M. Kishimoto and M. Amemiya, *IEEE Trans. Magn.*, **MAG-23** (1987)2818.
11. V. Papaefthymious, A. Kostikas, A. Simopoulos, K. Niarchos, S. Gangopadhyay, G. C. Hadjipanayis, C. M. Sorensen and K. J. Klabunde, *J. Appl. Phys.*, **67**(1990)4487.
12. S. Gangopadhyay, G. C. Hadjipanayis, B. Dale, C. M. Sorensen and K. J. Klabunde, *NanoStructured Materials*, **1**(1992)77.
13. Ichiro Tamura and Mitsuhiro Hayashi, *Japan J. Appl. Phys.*, **31**(1992)2540.
14. Wei Gong, Hua Li, Zhongren Zhao and Jinchang Chen, *J. Appl. Phys.*, **69**(1991)5119.
15. C. F. Kerznizan, K. J. Klabunde, C. M. Sorensen, and G. C. Hadjipanayis, *J. Appl. Phys.*, **67**(1990)5897.
16. T. Tanaka and N. Tamagawa, *Japan J. Appl. Phys.*, **6**(1967)1096.
17. Y. W. Du, J. Wu, H. X. Lu, T. X. Wang, Z. O. Qiu, H. Tang and J. C. Walker, *J. Appl. Phys.*, **31**(1992)2540.
18. S. Gangopadhyay, G. C. Hadjipanayis, C. M. Sorensen and K. J. Klabunde, *Mat. Res. Soc. Symp. Proc.*, **206**(1991)55.
19. T. Kaneyoshi, "Introduction to Surface Magnetism", CRC Press, Inc., Boston, (1991)50.
20. Akira Tasaki, Masatoshi Takao and Hideaki Tokunaga, *Japan J. Appl. Phys.*, **13**(1974)271.
21. Katsusi Kusaka, Nobuhiko Wada and Akira Tasaki, *Japan J. Appl. Phys.*, **8**(1969)599.
22. S. U. Jen, C. Y. Lee, Y. D. Yao and K. C. Lee, *J. of Magnetism Materials*, **96**(1991)82.
23. W. H. Meiklejohn and C. P. Bean, *Physical Review*, **105**(3)(1957)904.

SYNTHESIS AND CHARACTERIZATION OF STAR POLYPEPTIDE NONLINEAR OPTICAL MATERIALS

THOMAS M. COOPER*, WEIJIE SU*, ZBIGNIEW TOKARSKI**
AND W.WADE ADAMS*

*Wright Laboratory, WL/MLPJ, 3005 P St. Ste 1, Wright-Patterson AFB, OH 45433

**Science Applications International Corporation, Dayton, OH 45432

ABSTRACT

To develop novel polypeptide-based thin films, a series of star polypeptides modified with nonlinear optical chromophores has been synthesized. Using amino-substituted tetraphenyl porphyrin as an initiator, the N-carboxy anhydride of γ -benzyl L-glutamic acid was polymerized onto the porphyrin at a monomer to initiator ratio 20:1. The resulting four-branch star was modified with a selection of dyes. Dyes that modified both the N-terminus and benzyl side chain were used. We demonstrated feasibility of insertion of a metal ion into the polypeptide porphyrin core. The polypeptide series was characterized by UV/VIS, FTIR, and CD. The UV/VIS data suggested ease of modification of both the N-terminus and side chains. The FTIR and CD data show the resulting polypeptides were α -helical. The results demonstrate the feasibility of modifying the optical properties of a porphyrin by three approaches: insertion of metal, attachment of dye to N-terminus or modification of γ -benzyl L-glutamate side chain.

INTRODUCTION

Polypeptides provide conformations (α -helix, β -sheet, β -turn and coil) useful for construction of supramolecular assemblies. A possible architecture is a multi-branched star[1], with potentially unique colligative and thin film properties. With a porphyrin core, the star has combined porphyrin light sensitivity and polypeptide colligative properties. Recent work on porphyrin-peptide[2]-[4] and porphyrin-chromophore systems[5] demonstrates the feasibility of peptide-chromophore assembly synthesis. Porphyrins are nonlinear absorbers with optical switching and limiting[6] and light harvesting array[7] applications. Insertion of a heavy atom into the porphyrin gives enhanced intersystem crossing rates in reversible saturable absorption experiments[8]. We synthesized a four branch polypeptide star, **I**, by polymerizing γ -benzyl L-glutamic acid N-carboxy anhydride onto tetra-*p*-aminophenyl porphyrin (Fig. 1). This system has three modification sites: the polypeptide N-terminus, the γ -benzyl L-glutamate side chain, and the metal insertion site. The four branch star was modified with NLO and photochromic dyes, both at the star branch N-termini, the γ -benzyl L-glutamate ester side chains and by heavy metal atom (Pb) insertion.

SYNTHESIS METHODS

Stilbenes 1-3, obtained from Dr. Charles Spangler (Dept. of Chemistry, Northern Illinois

University), 1'-(2-carboxyethyl)-6-nitro spiro(2H-1-benzopyran-2,2'-indoline) (COOH-BIPS) (Chroma Chemical, Dayton OH) and all other materials (Aldrich Chemical Co.) were used without further purification

Polypeptide Synthesis of tetra-*p*-aminophenyl porphyrin was by standard methods[9].

γ -Benzyl L-glutamate N-carboxyanhydride (0.008 mole)[10] and tetra-*p*-aminophenyl porphyrin (0.0001 mole) was dissolved in dry dichloromethane, refluxed for 30 min and stirred at room temperature 2 days. The polymer was precipitated with methanol and washed. Two more subsequent dissolution/precipitation cycles were performed to ensure complete removal of monomer.

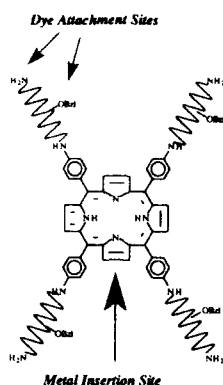


Fig. 1 Four branch polypeptide star(I) with three types of modification site

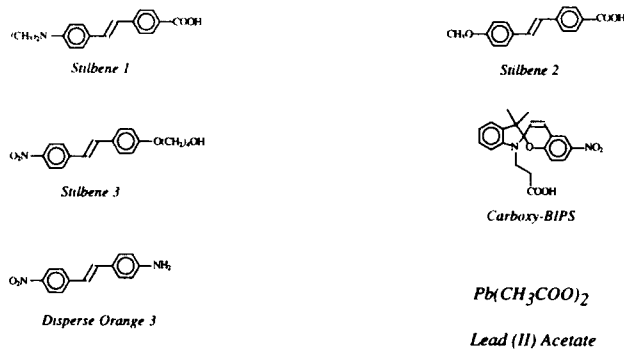


Fig. 2 Compounds used to test polypeptide modification procedures

A series of dyes (Fig. 2) was chosen to test various polypeptide modification procedures. Modification of the N-termini was performed by carbodiimide chemistry (stilbene 1, stilbene 2, carboxy-BIPS). Modification of the γ -benzyl L-glutamate side chain was performed by transesterification (stilbene 3) or ester to amide conversion (disperse orange 3). Lead(II) acetate was used for metal insertion experiments.

Stilbene 1, Stilbene 2, COOH-BIPS (6×10^{-6} mole NH_2), dye (24×10^{-6} mole), diisopropylcarbodiimide (0.001 mole), hydroxybenzotriazole (6×10^{-6} mole) were dissolved in just enough DMF/dioxane to dissolve. The mixture was heated for 2-3 days at 40 °C. Upon cooling, the modified polypeptide was precipitated with chilled methanol followed by methanol wash.

Stilbene 3 (6×10^{-6} mole NH_2): Dye:p-toluene sulfonic acid, 1:5:3 were dissolved in minimum amounts of DMF/dioxane. The mixture was heated at 75 °C for 3 days. Upon cooling, the polymer was precipitated with chilled methanol and washed with methanol.

Disperse Orange 3. (6×10^{-6} mole NH_2), disperse orange 3 (6×10^{-5} mole), KCN (6×10^{-6} mole) was dissolved in 12 drops DMF, then 6 drops MeOH added. The mixture was heated at 40 °C for 3 days. The product was precipitated out in chilled methanol, followed by a methanol wash [11].

Lead(II) Acetate. Lead-modified polypeptide was prepared by standard methods [12].

RESULTS AND DISCUSSION

In the preparation of **I** and its derivatives, we used a monomer to amino group ratio of 20:1, resulting in an average of 20 amino acids per star branch with unknown variation in branch length. Rapid propagation relative to initiation would result in one of the four star branches being significantly longer than the other three. It is feasible to vary the monomer to initiator ratio, with corresponding changes in solubility, processability and optical properties. The circular dichroism spectrum of **I** and all derivatives dissolved in trimethyl phosphate exhibited a negative band at 208 nm (α -helix $\pi\pi^*$ exciton band) and 222 nm (α -helix $n\pi^*$ band). In all the polypeptides, the ellipticity ratio $\theta_{208\text{nm}}/\theta_{222\text{nm}}$ varied from 1:2, characteristic of aggregated α -helices, to 1:1, characteristic of unaggregated α -helices. The ratio varied over time (~1 hr), suggesting aggregation changes while in solution. Similarly, IR spectra of **I** and its derivatives in a KBr pellet showed an amide I band at 1654 cm^{-1} , characteristic of an α -helix.

We used the appearance of dye absorption bands in the UV/VIS spectrum of modified **I** dissolved in trimethyl phosphate as evidence of successful modification (Fig. 3). When attached to **I**, the absorption maximum of stilbene 1 blue shifted from 378 to 326 nm, suggesting the dye was in the *cis* form when attached (Fig 3A). Stilbenes 1-3, COOH-BIPS and disperse orange 3 were successfully attached to **I**. The dye absorption spectra were unchanged upon reaction. Insertion of lead into **I** was straightforward (Fig. 3F), showing the disappearance of Q_x and Q_y band splitting upon change from D_{2h} to D_{4h} symmetry.

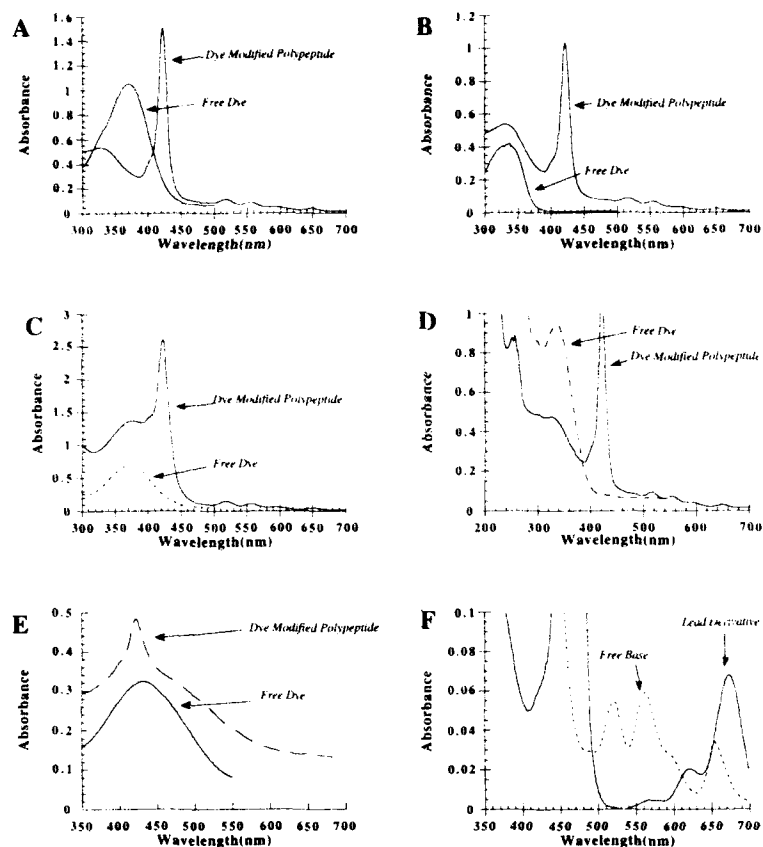


Fig 3. Absorption spectra of dye-modified I and free dye. A: Stilbene 1, B: Stilbene 2, C: Stilbene 3, D: Carboxy-BIPS, E: Disperse Orange 3, F: Lead(II) Acetate

The extent of dye modification was estimated from the absorption spectrum of the dye-polypeptide complex and the expression

$$\frac{n_{\text{dye}}}{n_{\text{porph}}} = \frac{A_{\text{dye}} \epsilon_{\text{porph}}}{A_{\text{porph}} \epsilon_{\text{dye}}} \quad (1)$$

where A is the absorbance corrected for scattering background and ϵ is the extinction coefficient. Modification of N-terminus will give at most 4 dyes/porphyrin. With current synthesis

conditions, modification of γ -benzyl L-glutamate side chains will give at most 80 dyes/porphyrin. Using extinction coefficients for tetraphenylporphyrin[13], [14] Q bands and extinction coefficients for the dyes (measured in our laboratory), relative degree of modification was estimated. The estimated moles dye/mole porphyrin for the N-terminal modifiers were: COOH-BIPS: 4.2, Stilbene 2: 4.0, Stilbene1: 3.5. For modification of the benzyl glutamate side disperse orange 3: 39.5, stilbene3: 3.7. The results suggested successful carbodiimide coupling, transesterification and ester to amide conversion reactions.

Compared to tetraphenyl porphyrin, the UV/VIS spectrum of **1** showed slight red shifting in the Q and B bands. The largest shift, from 646.5 to 655 nm, was observed in the $Q_x(0,0)$ band(Fig. 4). The $Q_x(0,0)$ band(Fig. 4) ranged from 655 nm for **1** to 648-650 nm for dye modified **1**. Dye attachment might shift absorption maxima by changing the phenyl group-porphyrin plane angle or porphyrin ring planarity[9].

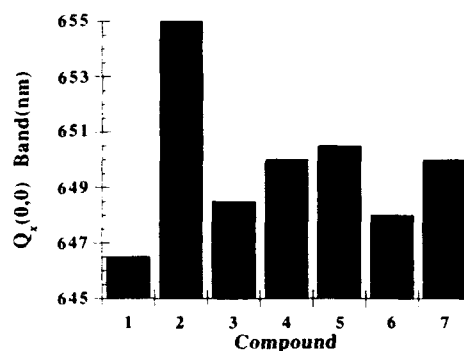


Fig. 4 Bar graph of porphyrin $Q_x(0,0)$ absorption maximum(nm) for porphyrins and dye-modified polypeptides, 1: tetraphenyl porphyrin, 2: **1**, 3: stilbene 1, 4: stilbene2, 5: stilbene 3, 6: carboxy-BIPS, 7: disperse orange 3.

In this work we have demonstrated the synthesis of a porphyrin core, four-armed polypeptide star. Polymerization from *p*-amino tetraphenyl porphyrin resulted in a polypeptide star with a cross shape. The star was modified by three approaches: insertion of metal, attachment of dye to the branch N-termini and attachment to branch side chain by displacement of benzyl alcohol groups. Future dye modifications will focus on enhanced charge and energy transfer with the porphyrin. Current work includes characterization of thin films of **1** and its derivatives by atomic force microscopy and measurement of nonlinear absorption of solutions of this new class of polypeptides.

ACKNOWLEDGEMENT

The authors thank Donna Brandelik(SAIC) for measurement of dye extinction coefficients, Christine Yoon(MLPJ) and David Stitzel(MLPJ) for synthesis assistance and L. V. Natarajan(SAIC) for insightful discussions.

REFERENCES

1. W. H. Daly, D. Poche, P. S. Russo, I. Negulescu, *Polymer Preprints* **33**, 188, (1992).
2. N. Nishino, H. Mihara, H. Kiyota, K. Kobata, T. Fujimoto, *J. Chem. Soc., Chem. Commun.*, 162, (1993).
3. N. Nishino, H. Mihara, R. Hasegawa, T. Yanai, T. Fujimoto, *J. Chem. Soc., Chem. Commun.*, 692, (1992).
4. D. H. Thompson, J. Kim, C. Di Meglio, *SPIE Organic and Biological Optoelectronics* **1853**, 142, (1993).
5. D. Gust, et al., *J. Am. Chem. Soc.* **114**, 3590, (1992).
6. M. M. Devane, *Optics Commun.* **52**, 136, (1984).
7. S. Prathapan, T. E. Johnson, J. S. Lindsey, *J. Am. Chem. Soc.* **115**, 7519, (1993).
8. K. Mansour, et al., *SPIE Organic and Biological Optoelectronics* **1853**, 132, (1993).
9. D. Dolphin, Ed., *The Porphyrins, Vol I, Structure and Synthesis Part A* (Academic Press, New York, 1978).
10. W. H. Daly, D. Poche, *Tetrahedron Lett.* **29**, 5859, (1988).
11. R. C. Larock, *Comprehensive Organic Transformations: A Guide to Functional Group Preparations* (VCH Publishers Inc., New York, 1989).
12. W. J. Buchler, in *The Porphyrins, Vol I, Structure and Synthesis Part A* D. Dolphin, Ed. (Academic Press, New York, 1978) pp. 390.
13. M. Gouterman, in *The Porphyrins* D. Dolphin, Ed. (Academic Press, New York, 1978), vol. III, pp. 1.
14. G. D. Dorrough, J. R. Miller, F. M. Huennekens, *J. Am. Chem. Soc.* **73**, 4315, (1951).

PREPARATION OF POLYPEPTIDE-DYE MULTILAYERS BY AN ELECTROSTATIC ASSEMBLY PROCESS

THOMAS M. COOPER*, ANGELA L. CAMPBELL*, CAROL NOFFSINGER*, JANELLE GUNTHER-GREER**, ROBERT L. CRANE* AND W. WADE ADAMS*

*Wright Laboratory, WL/MLPJ, 3005 P St. Ste. 1, Wright-Patterson Air Force Base, OH 45433

**Department of Materials Science and Engineering, Massachusetts Institute of Technology, Cambridge, MA 02139

ABSTRACT

To develop novel optical thin films, we have prepared self-assembled polypeptide films by an electrostatic process. The films were placed on a glass slide previously silanized by an amino silane and given a positive charge by immersion in aqueous acid. Subsequent immersion of the slide in aqueous anionic solutions of either poly(L-glutamic acid), congo red, copper phthalocyanine tetrasulfonic acid or *p*-nitroaniline-modified poly(L-glutamic acid) resulted in deposition of the anions on the surface. Following anionic immersion, the slides were dipped into a cationic poly(L-lysine) solution. Alternate dipping into anionic and cationic solutions yielded multilayers. The thin films were characterized by optical absorption and circular dichroism. The optical density increased with dipping cycles. Circular dichroism measurements of the thin films showed induced dichroism of the congo red and phthalocyanine-containing films, suggesting formation of a locally ordered dye-polypeptide complex. Solution circular dichroism measurements of the polypeptides indicated a coil conformation, while poly(L-glutamic acid)/poly(L-lysine) complexes showed circular dichroism spectrum characteristic of a β -sheet.

INTRODUCTION

Thin films have been placed on optical surfaces by a variety of techniques, including spin coating[1], dip coating[2] and the Langmuir-Blodgett technique[3]. An alternative approach involves laying down of multilayers of alternate charged species(Fig. 1).

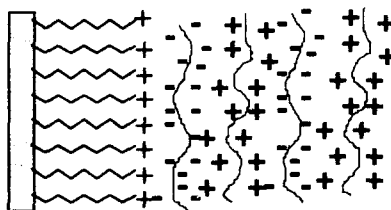


Figure. 1 Schematic of multilayer produced by electrostatic assembly method

Suspensions of highly charged particles form crystalline arrays with applications in laser medicine and laser spectroscopy[4]. Her[5],[6] describes a technique where alternate layers of positively and negatively charged colloidal particles are deposited onto a smooth surface such as

glass, yielding a variety of interference colors. More recently[7], this technique was applied to deposit multilayers of oppositely charged polymers onto an optical surface. We have been exploring the properties of polypeptide thin films, including holograms based on spiropyran-modified poly(L-glutamic acid)[8]. In this work we prepared polypeptide-dye multilayers by the electrostatic assembly(EA) approach. We have prepared multilayers composed of alternately charged polypeptides, a polypeptide and an alternately charged dye, and a polypeptide and an alternately charged chromophore-modified polypeptide. We also performed solution circular dichroism studies of the various complexes to gain information about the structures of these films.

EXPERIMENTAL

Materials Polypeptides(Sigma), dyes and other materials(Aldrich) and N-(4-nitrophenyl)-4-hydroxypiperidine(NHP), (Dr. Steve Pollock, University of Cincinnati) were used without further purification(Fig. 2).

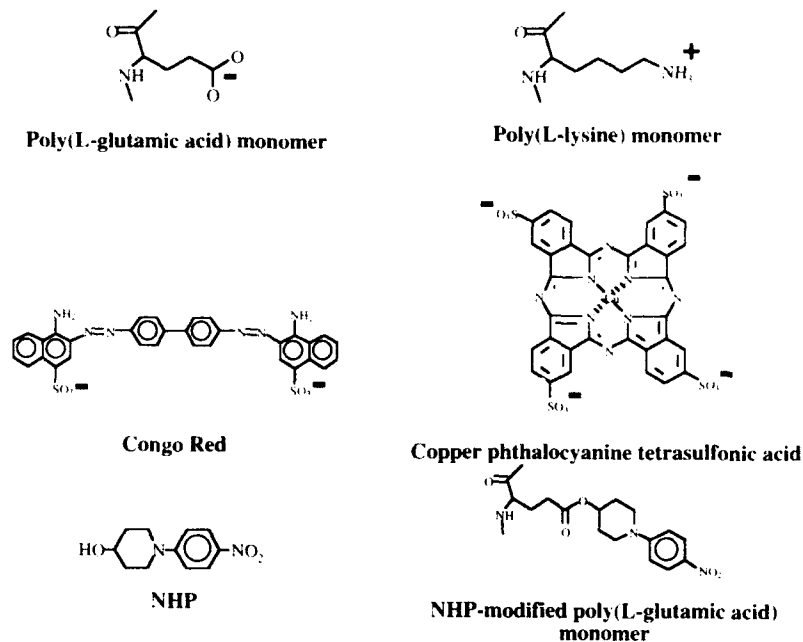


Figure 2 List of materials used in this study

Preparation of dye-modified polypeptide Poly(L-glutamic acid, sodium salt) (0.0045 mol, 0.68 gm), dimethylaminopyridine(0.0045 mole, 0.549 gm, diisopropylcarbodiimide(0.0045 mole, 0.567 gm) and NHP(0.0045 mole, 1 gm) was dissolved in 50 ml dimethylformamide. The esterification reaction was allowed to proceed for five days. The reaction mixture was then concentrated by rotatory evaporation and polypeptide precipitated out by addition of ethanol. Unreacted dye was removed by repeated washing of the polypeptide with ethanol. The extent of

dye attachment(4.1%) was measured from the absorption spectrum of a weighed solution($\epsilon_{\text{max}} = 13,500$ at 381 nm).

Preparation of silanized glass slides[9] Cleaning Solution 1: 280 ml concentrated sulfuric acid mixed with 120 ml 30% hydrogen peroxide. Cleaning Solution 2: 375 ml deionized water, 75 ml 30% hydrogen peroxide, 75 ml concentrated ammonium hydroxide. Fifty microscope slides were placed in solution 1 heated over a hot plate. The slides were then rinsed twice with deionized water. The slides were then treated with solution 2 for 30 minutes at room temperature, rinsed three times with deionized water and allowed to dry overnight. Slides were placed in a silanizing solution(500 ml 2% N-[3-(trimethoxysilyl)-propyl]ethylenediamine in 95% ethanol with gentle stirring for five minutes to allow for hydrolysis and silanol formation. The treated slides were rinsed with ethanol and cured for 10 minutes in a vacuum oven at 110 °C.

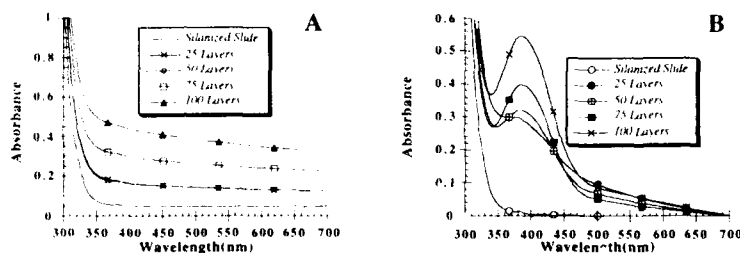
Polypeptide and dye solutions Polypeptide solutions: poly(L-glutamic acid), DP=380, 2mg/ml in deionized water, poly(L-lysine), DP=2300, 2mg/ml in neutral deionized water. NHP-modified poly(L-glutamic acid): The dye modified polypeptide was soluble in pH 12 NaOH solution. For dipping purposes, a 1 mg/ml solution of the polypeptide in pH 12 NaOH solution was acidified to pH7 in deionized water at pH 7. Dye solutions: Congo red 1 mg/ml, copper phthalocyanine tetrasulfonic acid tetrasodium salt 2 mg/ml.

Thin film preparation procedure: Amino groups on the slide surface were protonated by dipping slides in 10 ml 0.01N HCl for 2 minutes. Slide was dipped in anionic electrolyte solution for 2 minutes, rinsed in pH 7 water for 2 minutes, dried with nitrogen stream for 2 minutes, dipped in cationic electrolyte for 2 minutes, followed by a 2 minute rinse. A "layer" is defined to be one anion dip plus one cation dip. Cycle was repeated 25, 50 75 and 100 times.

Characterization: UV/VIS absorption spectra were collected on a Perkin-Elmer Lambda-9 spectrophotometer. Circular dichroism spectra were collected on a Jasco J720 spectropolarimeter.

RESULTS AND DISCUSSION

Figure 3 shows absorption spectra of films obtained from alternately dipping a silanized slide in an anionic and cationic electrolyte. As the number of dipping steps increased, the apparent absorbance increased. The presence of scattering centers in the films(Fig. 3A, 3B) also caused increased optical absorption. It was feasible to prepare films with polypeptide/dye systems(Fig. 3C, 3D) as well as polypeptide/polypeptide systems. Significant optical density was achieved($OD \approx 2$) for both congo red and copper phthalocyanine tetrasulfonic acid systems. This result shows that the EA technique could be used with high molecular weight cations and low molecular weight dyes, as well as polymeric systems.



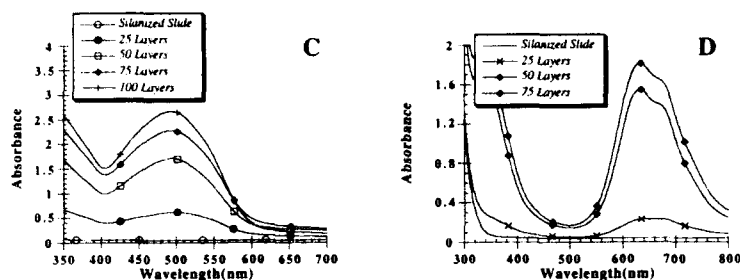


Figure 3 Absorption spectra of films of polypeptide-dye combinations. A: poly(L-lysine)/poly(L-glutamic acid), B: poly(L-lysine)/poly(L-glutamic acid)+NHP, C: poly(L-lysine)/congo red, D: poly(L-lysine)/copper phthalocyanine tetrasulfonic acid

To gain information about the molecular structure of the multilayer thin film, we performed circular dichroism measurements of the conformation of the polypeptides[10] and polypeptide/dye complexes. Poly(L-glutamic acid), poly(L-lysine) and NHP-modified poly(L-glutamic acid) in neutral aqueous solution showed CD spectra characteristic of the coil conformation(Fig. 4). In solution, the poly(L-lysine)/poly(L-glutamic acid) and poly(L-lysine)/NHP-modified poly(L-glutamic acid) complexes were a mixture of β -sheet and coil. The fraction coil was a function of the molar ratio of the two species. When the ratio was one, the soluble complex was β -sheet. Coil content increased with increasing net positive or negative charge.

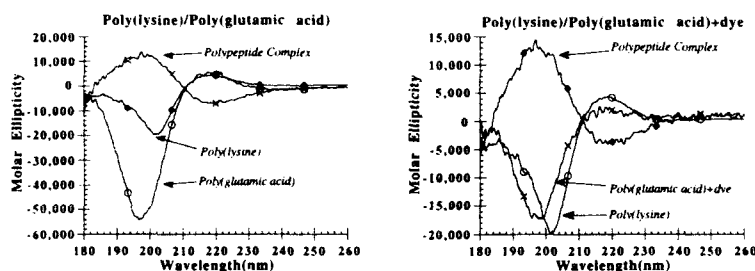


Figure 4 Left: Solution circular dichroism spectra of poly(L-lysine), poly(L-glutamic acid) and poly(L-lysine)/poly(L-glutamic acid) complex. Right: Solution circular dichroism spectra of poly(L-lysine), DHP-modified poly(L-glutamic acid) and poly(L-lysine)/DHP-modified poly(L-glutamic acid) complex. All solutions were at pH 7

Intense induced dichroism was observed associated with the congo red absorption band of the poly(L-lysine)/congo red thin film complex, with a similar induced dichroism observed in solution(Fig 5). Measurement of the intensity of induced dichroism as a function of congo red/L-lysine monomer molar ratio in solution showed the intensity increased until a 1:2 ratio and leveled off thereafter. The 1:2 ratio suggested that each of the two negative charges on congo red was neutralized by one lysine charge and the poly(L-lysine) congo red complex consisted of lysines cross linked by congo red. Poly(L-lysine) was in a coil conformation(Fig. 6, left) both

free and complexed with congo red. The molar ellipticity decreased in the complex, suggesting "tightening" of the coil upon neutralization of side chain charge.

Poly(L-lysine) also retained a coil conformation with "tightening" in the presence of copper phthalocyanine tetrasulfonic acid (Fig. 6, right). No induced dichroism of copper phthalocyanine absorption bands was observed in solution, although weak induced dichroism was observed in the poly(L-lysine)/copper phthalocyanine tetrasulfonic acid film (Fig. 7). The difference in behavior between the congo red and copper phthalocyanine complexes resulted from the difference in dye molecular shape. Congo red has a roughly linear shape, which allows for easy neutralization of lysine charge. Copper phthalocyanine tetrasulfonic acid has four charges arranged in a ring, possibly introducing steric constraints on complex formation.

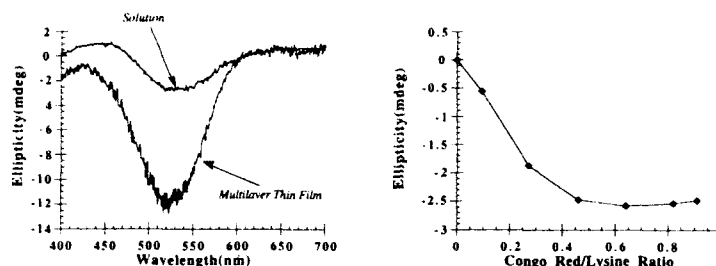


Figure 5 Left: Circular dichroism spectra (400-700 nm) of poly(L-lysine)/congo red complex, both as thin film (100 layers) and in aqueous solution. Right: Intensity of induced dichroism of poly(L-lysine)/congo red complex in solution as a function of congo red/L-lysine monomer ratio.

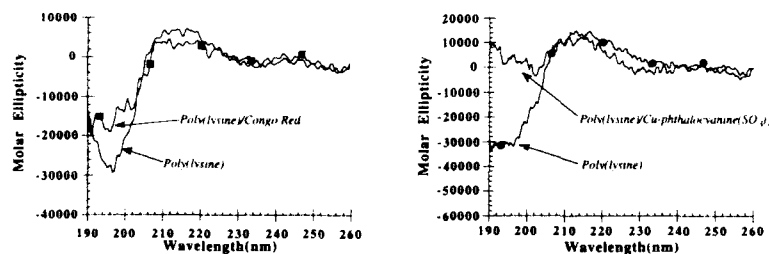


Figure 6 Left: Circular dichroism spectra (190-260 nm) of poly(L-lysine) and poly(L-lysine)/congo red complex, congo red/L-lysine monomer ratio = 2, Right: Poly(L-lysine)/Cu-phthalocyanine tetrasulfonic acid complex, dye/monomer ratio = 2.4

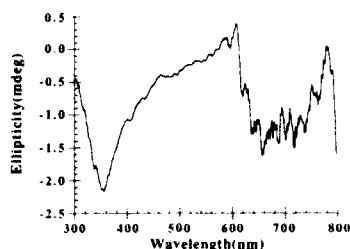


Figure 7 Circular dichroism spectra(300-800 nm) of poly(L-lysine)/Cu-phthalocyanine tetrasulfonic acid thin film complex. Spectrum is average of spectra obtained from 50, 75 and 100 layer films.

We have demonstrated the EA technique for preparation of polypeptide and dye multilayers. Solution circular dichroism measurements show β -sheet formation in poly(L-glutamic acid)/poly(L-lysine) complexes and retention of coil conformation in dye/polypeptide complexes. There is an uncertain relation between polypeptide conformation in solution and in the films. Preliminary FTIR measurements of thin film material embedded in KBr pellets suggest α -helix/ β -sheet mixture for poly(L-glutamic acid)/poly(L-lysine) systems and α -helix in the poly(L-lysine)/dye systems. The data show the importance of environment on polypeptide conformation. The presence of water stabilized the coil, while a dried multilayer stabilized the α -helix and β -sheet conformations.

ACKNOWLEDGEMENT

The authors thank Donna Brandelik(Science Applications International Corporation), Keith Obermeier(MLPJ) for assistance in preparing silanized slides and Mike Rubner(MIT) for introducing us to this technique.

REFERENCES

1. W. A. Levinson, A. Arnold, O. Dehodgins, *Polymer Engineering and Science* **33**, 980, (1993).
2. L. E. Scriven in *Better Ceramics Through Chemistry*, edited by C. J. Brinker, D. E. Clark, D. R. Ulrich. (Mat. Res. Soc., III, Pittsburgh, 1988), vol. III, pp. 717.
3. H. Fuchs, H. Ohst, W. Prass, *Adv. Mater.* **3**, 10, (1991).
4. E. A. Kamenetzky, J. G. Magliocco, H. P. Panzer, *Science* **263**, 207, (1994).
5. R. K. Iler, *J. Colloid and Interface Sci.* **21**, 569, (1966).
6. R. K. Iler, U.S. Patent No. 3 485 658 (Dec. 23, 1969).
7. G. Decher, J. D. Hong, J. Schmitt, *Thin Solid Films* **210**, 831, (1992).
8. T. M. Cooper, et al., *Applied Optics* **32**, 674, (1993).
9. E. P. Plueddemann, *Silane Coupling Agents* (Plenum Press, New York, 1991).
10. R.W. Woody, *The Peptides*, **7**,15, (1985).

BIOMIMETIC PROCESSING OF CALCIUM CARBONATE-CHITOSAN COMPOSITES

SUKUN ZHANG[#] AND K. E. GONSALVES^{#, *}

Institute of Materials Science, Polymer Science Program[#] & Department of Chemistry*,
U-136, University of Connecticut, Storrs, CT 06269, USA

INTRODUCTION

Ceramic-polymer composites produced by natural organisms are known to have properties far beyond those that can be achieved in present technological materials [1]. The mollusk shell, for example, starting with relatively weak structural ingredients calcium carbonate and chitin is one such ceramic-polymer composite. In nacre, the overall composite is more than 95 volume percent calcium carbonate, with the remainder an organic matrix of protein and chitin. The inorganic phase consists of highly oriented aragonite platelets forming the bricks and the organic matrix forming the mortar in between [1]. Even though nacre consists of a high amount of the inorganic component, it has excellent fracture toughness and high strength. Studies have been conducted to understand the factors which control the nucleation and orientation of crystallization [2-4]. However, very limited knowledge about the ceramic polymer interfaces, structure, chemistry and whether the interfacial interaction involves ion-binding is known.

To model nacre we have chosen chitosan, in which free amino groups exist, as a substrate and low molecular weight polyacrylic acid as an additive instead of complex proteins. The crystal growth of calcium carbonate on a chitosan substrate has been achieved from a supersaturated solution of calcium carbonate, at different concentrations of polyacrylic acid. Several techniques have been employed to characterize the systems, such as X-ray diffraction, X-ray photoelectron spectroscopy and attenuated total reflectance infrared spectroscopy. By producing charges, ion-binding involved in the nucleation and crystallization, the interfacial interactions between ceramic and polymer have been investigated.

EXPERIMENTAL

Calcium Carbonate Supersaturated Solution

The supersaturated calcium bicarbonate solution was prepared following the procedure described by Mann [4]. A suspension of CaCO_3 (calcite) with the ratio 0.9/100 (mg/ml) of calcium carbonate to distilled water was first prepared. While stirring, CO_2 was bubbled into the system at room temperature and kept for 6 hours. The suspension was then filtered and the filtrate purged with CO_2 gas for 30 minutes, to dissolve any remaining crystals. The pH of the resulting supersaturated solution was about 6.00.

Chitosan Film

A chitosan film was obtained by casting the 1% (w/w) solution of chitosan in 1% (w/w) acetic acid aqueous solution on a PMMA plate or a glass slide. In a typical preparation of the casting solution, 2 g of chitosan was added in 100 ml of distilled water and stirred for 10 minutes. Then 100 g of 2% (w/w) acetic acid was added and stirred at room temperature for another 30 minutes [5]. A viscous solution was obtained and filtered. The chitosan film made in this way was then neutralized with dilute ammonium hydroxide and washed extensively with water. After air drying, it was further dried under vacuum at room temperature.

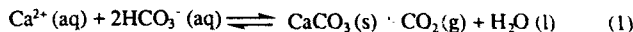
Polyacrylic acid with molecular weight 2,000 was employed as an additive. Various amounts of the polyacrylic acid were weighed and placed into polystyrene (PS) bottles, before adding the calcium carbonate supersaturated solution.

Measurements

The pH of solution was measured by a Fisher pH meter (model 107). Ultrafine CaCO_3 crystallite sizes and morphology were observed under a polarized optical microscope model Nikon Labophot-pol, and scanning electron microscopy (SEM, AMR 1200B). X-ray diffraction (XRD) was carried out to determine the crystallite sizes and phases. The surfaces of chitosan films, with or without soaking in polyacrylic acid solution, were examined by attenuated total reflectance infrared spectroscopy (ATR IR, Mattson Polaris) by using a 60 degree Germanium analyzer. X-ray photoelectron spectroscopy (XPS) was used to detect the surface structures of chitosan films. XPS spectra were collected on a monochromatic spectrometer (Perkin-Elmer, 5300) using Al $K\alpha$ source (600 w, 15 KeV) with the pass energy 37.5 eV. The vacuum was maintained at approximately 1×10^{-9} torr.

RESULTS AND DISCUSSION

Crystallization of CaCO_3 was controlled by the following equilibrium in which carbon dioxide is continually lost:



On the evolution of carbon dioxide gas from the solution, the pH of the supersaturated solution increased. Fig. 1 shows the result of six systems with different concentrations of polyacrylic acid. As the crystallization proceeded, the pH of solution increased and finally leveled off to a plateau. Three such plateaus were obtained. First, in the absence of polyacrylic acid the pH value increased as the crystallization of CaCO_3 proceeded. After 40 hours, it was up to a plateau of about 8.0. Crystallization was complete at a pH of about 8.50, and the XRD pattern showed that calcite was formed [Fig. 3(a)]. The calcium carbonate crystals appeared as a multi-layer habit, precipitating on the chitosan film randomly and sporadically [Fig. 2(a), (d)]. The crystals also occurred on the air/water interface as well as the inner edge of the container in the same formation. In the presence of polyacrylic acid, pH values of the solutions increased as crystallization proceeded and leveled off to different plateau values, depending on the polyacrylic acid concentration. At low concentrations, such as 0.01% (wt) and 0.02% (wt), the pH increased as fast as in the case without polyacrylic acid in the first 30 hours. After that the pH values increased rapidly and leveled off to a plateau of about 9.10. At a concentration of 0.06%, crystallite nucleation and growth were inhibited at the beginning, resulting in a lower pH than that of the lower polyacrylic acid concentrations. Eventually, the pH of the solution went up to 9.25. Since the dissociation constant of polyacrylic acid is 4.5 [6], the acid groups of polyacrylic acid are mostly in the form of $-\text{COO}^-$ carboxylate ions at pH range of 5.8 to 9.25. Thus, for the polyacrylic acid concentration of 0.1%, although its pH eventually got to 9.00, crystallization was mostly inhibited by mobile polyacrylic acid carboxylate ions in the solution, and only a few crystals grew on the chitosan film [Fig. 2(f)]. When the concentration of polyacrylic acid was 0.2%, crystallization was totally inhibited, and the pH of the solution remained at 6.00. In addition, the crystal shapes and habits were different from those obtained without polyacrylic acid. Crystals only appeared on the chitosan film and showed spherical symmetry around a center of nucleation [Fig. 2(b, c)].

In the absence of the polyacrylic acid only calcite appears in the XRD pattern. In the presence of the polyacrylic acid XRD pattern shows that a mixture of calcite and vaterite was formed. The high and sharp peak at 2θ (37.6) and small peak at 2θ (28.8) represent 110 and 104 planes of calcite respectively, the remaining peaks pertain to planes of vaterite.

The crystallite sizes of vaterite phase were calculated from the half-peak width of the XRD according to the following equation [7]:

$$t = 0.9 \lambda / B \cos \theta, \quad B^2 = B_t^2 + B_l^2 \quad (2)$$

where t is average crystallite size, λ is the wavelength of copper (1.54 \AA), B is the width of the half-height peak and θ is the diffraction angle. B is the width measured from x-ray pattern, B_t

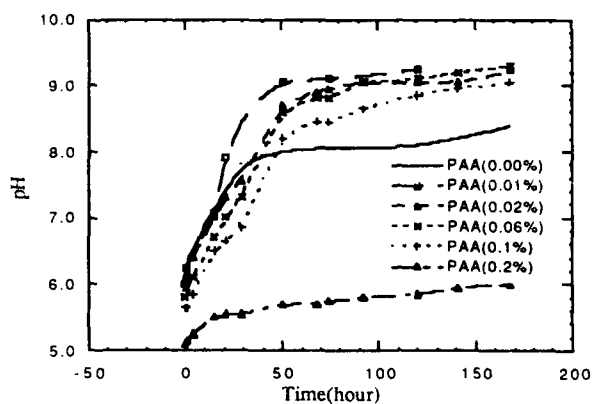


Figure 1 pH of supersaturated calcium carbonate solutions as functions of crystallization time(20°C)

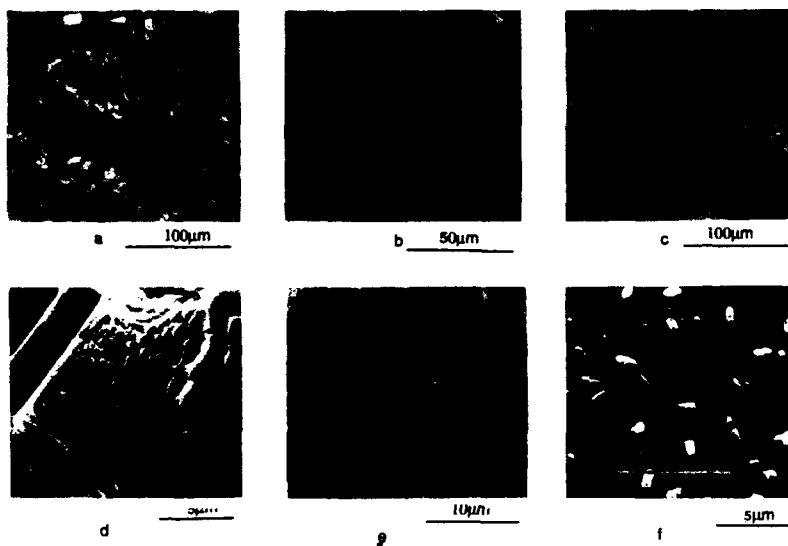


Figure 2 OM and SEM pictures of calcium carbonate crystals on chitosan films
 (a) 0.00% PAA (OM) (b) 0.02% PAA(OM) (c) thinner film 0.02% PAA(OM)
 (d) 0.00%PAA(SEM) (e) 0.02% PAA(SEM) (f) 0.1% PAA(SEM)

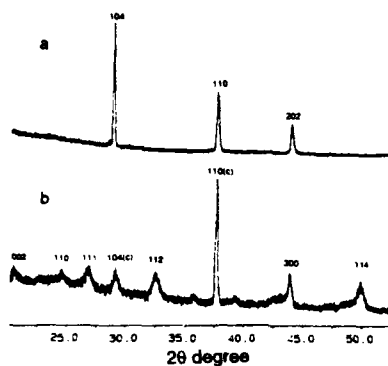


Figure 3 X-Ray patterns of calcium carbonate
(a) with 0.00% PAA in the system
(b) with 0.02% PAA in the system

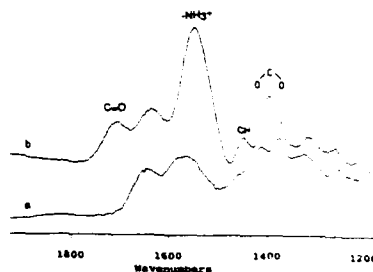


Figure 4 ATR spectra of chitosan surface
(a) without polyacrylic acid
(b) soaking in 0.2% PAA 3 hours

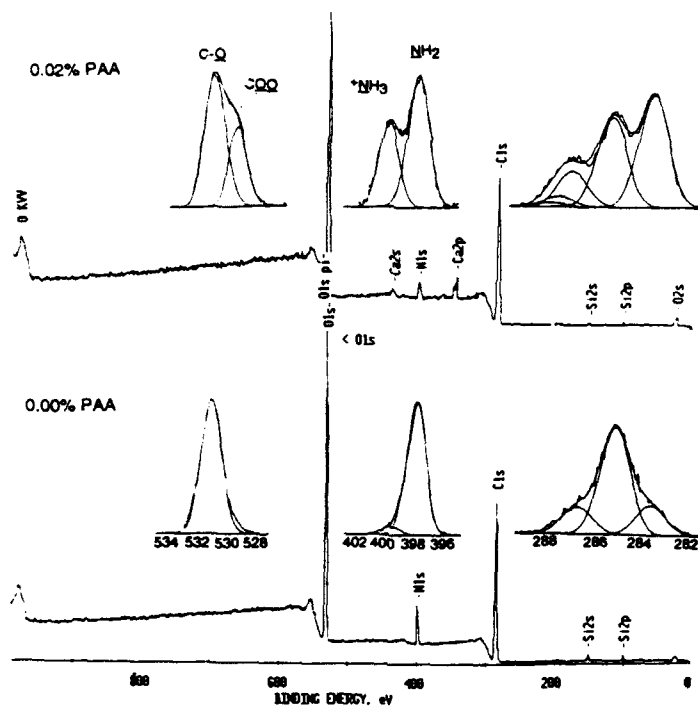


Figure 5 XPS wide scan and core-level spectra of chitosan-film surface after soaking in supersaturated calcium carbonate aqueous solution at different concentrations of polyacrylic acid.

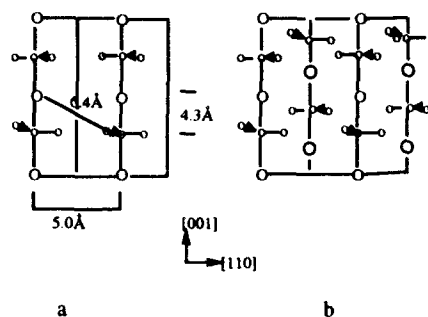


Figure 6 Cell projections for calcite (a) parallel to the (110) axis only coplanar atoms in the (110) face (b) parallel to the (110) axis with additional non-coplanar atoms [4]

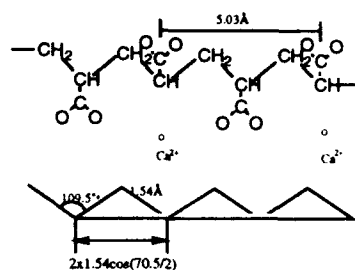


Figure 7 Scheme for the conformation of polyacrylic acid on the chitosan film

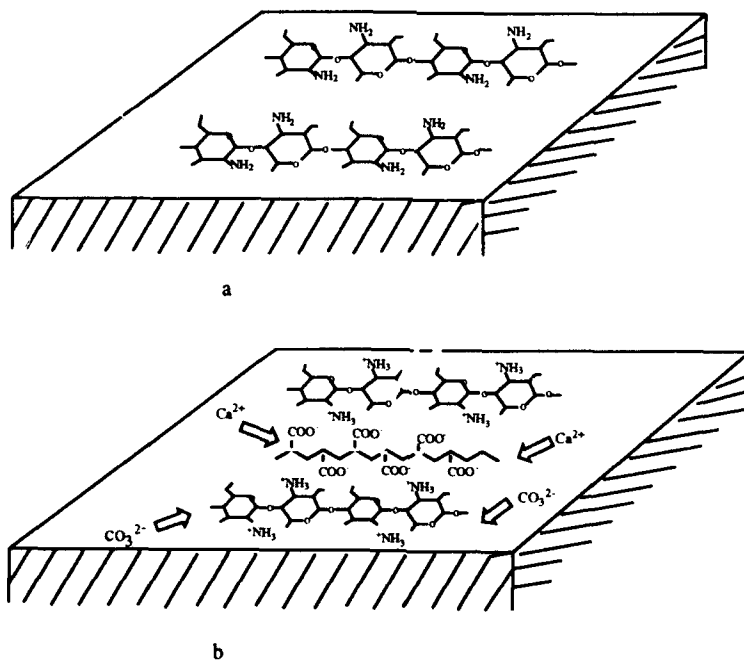


Figure 8 Scheme for the structure of chitosan-film surface (a) in the absence of polyacrylic acid, (b) in the presence of polyacrylic acid

is the actual width of a sample and B_i is the width caused by the instrument. Since the peak of calcite 110 plane is very sharp, it was considered to be the width caused by the instrument. By picking several vaterite peaks, the average crystallite size of vaterite was calculated using equation (2). As a result, the average crystallite size t of vaterite was about of 15 nm. Also, in the presence of polyacrylic acid, as the crystallization proceeded, the crystallites covered the whole chitosan film [Fig. 3(d)].

The ATR spectra of chitosan-film surfaces are shown in Fig. 4. Sample A is the one without soaking in the polyacrylic acid aqueous solution and sample B is soaked in a 0.2% polyacrylic acid aqueous solution for three hours. A new band at 1707 cm^{-1} appearing in sample B corresponds to the carbonyl C=O stretching absorption of the carboxyl group in polyacrylic acid. The band appearing at 1550 cm^{-1} in the spectrum can be assigned to a symmetric -NH_3^+ deformation, and broad bands appearing at 2500 cm^{-1} and 1900 cm^{-1} confirm the presence of -NH_3^+ on the chitosan film [8]. Another new band at 1400 cm^{-1} represents the carboxylate ion. Thus, the negatively charged carboxylate ion and positively charged -NH_3^+ coexist on the chitosan-film surface in the presence of polyacrylic acid. This was also confirmed by XPS analysis.

Figure 5 shows a series of XPS 0-1000 eV wide scan and core-level spectra of the chitosan-film surfaces after being soaked in supersaturated calcium carbonate aqueous solution for four hours under a series of concentrations of polyacrylic acid. In the absence of polyacrylic acid, only one kind of nitrogen and oxygen appears. Three types of carbon detected in this case represent O-C-O, C-C-O and C-N respectively [9-11], their area ratio is 1:4:1, which matches the ratio of the chitosan repeat unit. The absence of calcium element in this situation indicates that no calcium carbonate nuclei formed at the beginning of the crystallization. In the presence of polyacrylic acid, on the other hand, two peaks occurred at binding energies about 400 eV and 398 eV, which represent protonated nitrogen and free base nitrogen respectively. The other two peaks detected at binding energies about 531 eV and 530 eV pertain to the oxygen of -C-O-C of chitosan and -C=O of polyacrylic acid respectively. The appearance of calcium element in the XPS spectra, results from the nucleation of calcium carbonate on the chitosan-film surface in the presence of polyacrylic acid. In this case, the positive and the negative charges occur on the chitosan film.

The crystallographic orientation can be estimated by an atomic matching at the interface of the organic matrix and inorganic minerals. The Ca-Ca distance of calcite is about 5.0 Å on the 110 plane [Fig. 6] [4]. In the zig-zag conformation, the distance of two carboxylate ions in polyacrylic acid is 5.03 Å [Fig. 7, 8], which matches the lattice of the 110 plane of calcite. Thus, Ca-binding to negatively charged carboxylate ions in polyacrylic acid results in the nucleation of the (110) plane of calcite.

REFERENCES

- [1] M. Sarikaya and I. A. Aksay, Structure, Cellular Synthesis and Assembly of Biopolymers (Springer-Verlag, Amsterdam, 1992) Chapt. 1, S. Case(ed) 1-25
- [2] S. Weiner and L. Addadi, Trends in Biochemical Science vol. 16 iss 7 pp. 252-256 (1988)
- [3] A. Berman, Science **259**, 5 February 1993
- [4] S. Mann, Nature **334** 692-695 (1988); Structure and Bonding **54** 125-174 (1983), J.Chem. Soc. Faraday **86**, 1873-1880 (1990)
- [5] P. R. Austin and D. Wilmington US Pat. 4,309,534 (1982)
- [6] S. Chibowski, J. Colloid & Interface Sci. **140** No.2 pp. 444-449 (1990)
- [7] B. D. Cullity, Elements of X-ray Diffraction (Reading, Mass., Addison-Wesley) (1956)
- [8] F. G. Pearson, J. Polym. Sci. **XLIII**, 101-116 (1960)
- [9] C. D. Wagner, Handbook of X-ray Photoelectron Spectroscopy, Perkin-Elmer (1979)
- [10] J. D. Andrade, Surface and Interfacial Aspects of Biomedical Polymers vol.1 Chapt. 5 (1985)
- [11] D. T. Clark, Polymer Surfaces Edited by D.T. Clark and W. J. Feast (Wiley & Sons) New York, Chapt.6 (1978)

SURFACE CHEMISTRY OF NANOCRYSTALLINE CERIUM OXIDE

ANDREAS TSCHÖPE*, J.Y. YING*, K. AMONLIRDVIMAN*, AND M. L. TRUDEAU**

*Massachusetts Institute of Technology, Department of Chemical Engineering, Cambridge, MA, 02139

**Hydro-Québec Research Institute, Materials Technology Department, Varennes, Québec, J3X-1S1, Canada.

ABSTRACT

Nanocrystalline cerium oxide was synthesized by magnetron sputtering of a metallic target, followed by controlled post-oxidation. The resulting cerium oxide clusters were <10 nm in size, and highly non-stoichiometric in nature. The oxygen deficiency of such materials was associated with the unusual catalytic activity in oxidation and redox reactions. This paper compares the surface chemistry of nanocrystalline CeO_{2-x} with stoichiometric CeO_2 . It further explores the promoting effect of Cu-doping on surface reduction and oxidation.

The oxidation states of metal cations were examined with X-ray photoelectron spectroscopy after various oxidizing and reducing heat treatments in a connected reaction chamber. Isothermal pulsed reduction and oxidation of the samples were investigated by thermogravimetric analysis. Reduction properties of the different materials are discussed in terms of their microstructure, oxygen deficiency and chemical composition. These studies will help to understand the importance of bulk defects and synergistic effects in multicomponent and multiphase materials for high surface reactivity.

INTRODUCTION

Cerium oxide has attracted much attention in catalysis for its excellent properties as a transient oxygen storage material in automobile catalytic converters [1,2] and for its activity in catalytic redox reactions such as SO_2 reduction by CO [3-5], CO oxidation and methane oxidation [6]. Functionality in these reactions is related to properties such as (i) large deviation from stoichiometric composition in reducing atmospheres at high temperatures and (ii) high oxygen vacancy mobility. Upon reduction, oxygen vacancies are created which are doubly ionized at the beginning and singly ionized or neutral at larger oxygen deficiency. The electrons of the extracted O^{2-} anions are localized at Ce cations changing their oxidation state from +4 to +3. Since each Ce^{4+} is a potential host, these electrons are moderately mobile by a hopping process, and the reduced CeO_{2-x} is a mixed ionic/electronic conductor [7]. Temperature-programmed reduction (TPR) [1], electron-spin resonance (ESR) [8], and Fourier-transform infrared spectroscopy (FT-IR) [9] revealed the existence of different types of surface oxygen species: (i) lattice-type oxygen tetrahedrally bonded to two Ce^{4+} cations, (ii) surface capping oxygen octahedrally bonded to one Ce^{4+} cation, and (iii) superoxide species O_2^- adsorbed on the reduced CeO_{2-x} surface. TPR measurements also indicated that stability of these species against reduction is in the order superoxide < capping oxygen < lattice oxygen. Reduction of the ceria surface can be promoted by supported precious metals such as Pt or Pd [1,10]. Recent studies on mixed Pr-Ce oxide with supported precious metals also indicated that reduction in the temperature range 200°C - 600°C is not limited to surface species but can be extended to bulk reduction [2].

In this paper, we report our studies on reduction and oxidation properties of pure and doped nanocrystalline CeO_{2-x} materials. Inert gas condensation was used to synthesize unsupported oxygen-deficient nanoclusters. We have shown recently that these materials are excellent catalysts for selective catalytic reduction of SO_2 by CO, with higher activity than stoichiometric ceria prepared by chemical precipitation and calcination [4]. The purpose of the present work is focussed on understanding the reduction properties of pure and doped nanocrystalline CeO_{2-x} . The effects of bulk oxygen-deficiency and Cu-doping on surface reduction

are investigated. Cu-doping would be of considerable interest if synergistic effects can be achieved between the dopant and the oxide matrix. Such effects usually involve expensive precious metals finely dispersed on an oxide support in a supported catalyst system. Synthesis of Cu-doped CeO_{2-x} by inert gas condensation is a novel approach towards establishing an ultrahigh dispersion for Cu/ CeO_{2-x} catalyst [11]. A nanocrystalline alloy of Cu-Ce was generated from a mixed metal target. Through controlled oxidation, Cu was forced to segregate to the surface of CeO_{2-x} since the two elements lost their solubility in their respective oxide forms. When annealed above 500 °C, a second phase of copper oxide was formed by migration and coalescence of Cu. By this method, we started from a homogeneous solid solution, and induced unique forms of intimate dispersion of two oxides through thermal treatments.

EXPERIMENTAL AND RESULTS

Nanocrystalline materials may be generated with Joule-heating of dc-/rf-magnetron sputtering by inert gas condensation [12-14]. In this study, a metallic cerium target (99.99%) was vaporized by dc-magnetron sputtering in 25 Pa argon [4,11]. The metal vapor became rapidly supersaturated by thermalization with the inert gas resulting in nucleation and growth of nanometer-sized clusters. The clusters were collected on a liquid nitrogen-cooled ground shield as shown in Fig. 1 [11]. After deposition for 20 min, the sputtering process was stopped and the ultrahigh vacuum chamber was evacuated and oxygen was slowly introduced until a pressure of 100 Pa was reached. The nanocrystalline clusters were scraped off from the ground shield and consolidated to pellets at room temperature under a pressure of 0.5 GPa. This pressure provided a substantial residual porosity and surface area in the green compact. For Cu-doped CeO_{2-x} , samples were produced from sputtering a mixed metal target of 15 at% Cu/ 85 at% Ce [11].

Microcrystalline CeO_2 (99.9965%, Alfa) with grain size of 1-2 μm was used as a reference material for bulk ceria. This powder was compacted into a pellet and then annealed at 1400 °C for 1 hour in 15% O_2 /He. A second reference material was CeO_2 synthesized by chemical precipitation of $\text{Ce}_2(\text{CO}_3)_3$ from an aqueous solution of $\text{Ce}(\text{NO}_3)_3$ and $(\text{NH}_4)_2\text{CO}_3$. The precipitate was washed, dried and calcined at 650 °C in air. Ultrafine CeO_2 was used as a standard for high

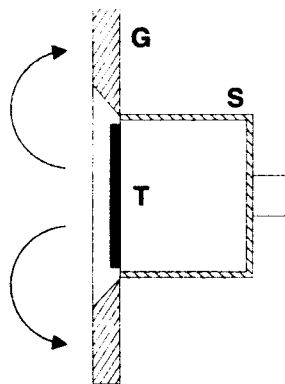


Fig. 1 Schematic of the sputter gun and substrate geometry for synthesis of nanocrystalline materials by inert gas condensation. Magnetron sputtering gun S with metallic target T, and LN2-cooled ground shield substrate G [11].

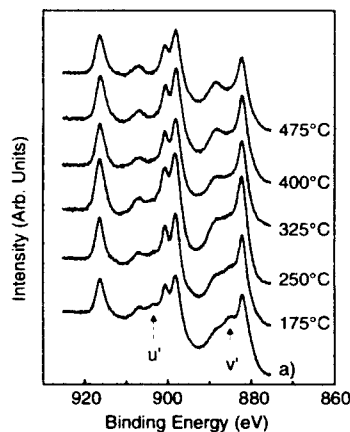


Fig. 2 Ce-3d core-level spectrum measured by XPS for nanocrystalline CeO_{2-x} (a) after synthesis and (b) after annealing at increasing temperature in 1000 Pa of 1% CO_2 /He.

surface area stoichiometric ceria. By comparing the properties of the nanocrystalline CeO_{2-x} with the precipitated ultrafine CeO_2 , the effect of oxygen-deficiency on surface reduction and oxidation can be determined.

The initial oxidation state of nanocrystalline CeO_{2-x} after preparation was determined by X-ray photoelectron spectroscopy (XPS) using a PHI-5500 XPS spectrometer using monochromatic Al-K_{α} radiation. The instrument was connected to a reaction chamber which allowed *in situ* heat treatment of the samples. Due to the insulating state of these materials, electronic surface compensation was necessary. The setting of the electron flood gun was varied for each sample in order to minimize the peak widths. Fig. 2 illustrates the cerium 3d core-level spectra for the as-prepared sample and after it has been annealed in 1000 Pa of 1% CO_2/He atmosphere at increasing temperatures. In addition to the typical 6-line spectrum of stoichiometric CeO_2 , the as-prepared nanocrystalline CeO_{2-x} has two distinct peaks denoted v' and u' , associated with Ce^{3+} . Deconvolution of the spectrum using Lorentzian-Gaussian distributions and Shirley-type background was used to obtain the percentage of Ce^{3+} after oxidation treatment at different temperatures [15,16] (Fig. 3).

Thermogravimetric analysis was performed in a Perkin Elmer TGA-7. All samples were annealed at 550 °C in 15% O_2/He for 20 hours before the analysis, except the nanocrystalline Cu-doped CeO_{2-x} which was not pretreated. Preannealing allowed all spontaneous changes in the microstructure that are thermally activated at 550 °C to occur. Since all following measurements were made at lower temperatures, the microstructure is assumed to be invariant for the time of the experiment. Measurements were done isothermally at temperatures between 200 °C and 500 °C. The samples were first equilibrated in 15% O_2/He for several hours (Fig. 4: region I) after which the purge gas was changed to 2% CO/He (at point A). We measured the weight change as a function of time for a period of 500 min (region II). The purge gas was switched back to 15% O_2/He at point B and we continued the measurement for 500 min to re-equilibrate the sample (region III). When CO is introduced two super-imposed processes were detected, CO adsorption and reduction of the sample. Since CO desorption is slow, as indicated by the gradual weight loss in region III, we assume that the amount of adsorbed CO right before and after the gas change from CO to O_2 (at point B) is the same. Therefore, the weight increase Δ (arrow) is attributed

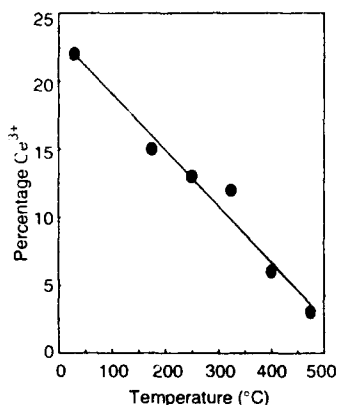


Fig. 3 Decrease of the Ce^{3+} concentration in nanocrystalline CeO_{2-x} as the sample is oxidized in 1 kPa of 1% CO_2/He at increasing temperatures, determined by the v' and u' component in XPS Ce-3d core level spectra.

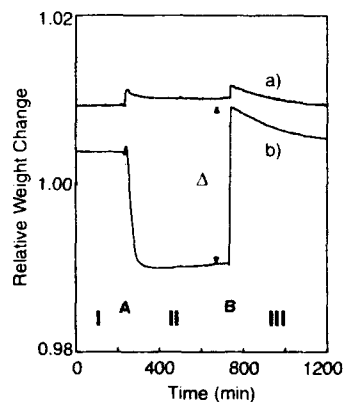


Fig. 4 Sample weight in an isothermal thermogravimetric measurement at 207 °C for (a) pure and (b) Cu-doped nanocrystalline CeO_{2-x} . Gas composition in region I (15% O_2/He), II (2% CO/He), and III (15% O_2/He).

to oxidation only, and represents the degree of reduction achieved when CO was used as the purge gas.

Four different samples were studied by thermogravimetric analysis at different temperatures (Fig. 5). Reduction of microcrystalline CeO_2 did not occur below 500 °C. Since this sample has negligible surface area ($<1 \text{ m}^2/\text{g}$), its reducibility represents that of the bulk phase of CeO_2 . Reduction of the other samples at temperatures below 500 °C is attributed to the large surface area. A possible change in bulk reduction behavior due to small crystal size is not considered in this work. The effect of non-stoichiometry on surface reduction is revealed by the difference between the nanocrystalline CeO_{2-x} and the precipitated ultrafine CeO_2 powder. Nanocrystalline CeO_{2-x} was reduced at temperatures as low as 150 °C and could be reduced to a larger overall extent than precipitated high surface area CeO_2 . The greatest reducibility was demonstrated by the nanocrystalline Cu-doped material. In order to compare the different samples on a surface area basis, we normalized the weight change with the B.E.T. surface area of each sample (Fig. 6). The reducibility of Cu-doped CeO_{2-x} sample between 200 °C and 400 °C was independent of temperature and increased above 400 °C. The weight loss of 0.38 mg/m^2 at 200 °C corresponds to $560 \mu\text{mol O}_2/\text{g}$ or 1.4×10^{19} oxygen atoms/ m^2 , which is on the order of magnitude for one monolayer of oxygen on ceria [2]. The reduction of metal cations in Cu-doped CeO_{2-x} was studied by XPS. A sample was oxidized in an atmosphere of 1000 Pa of 1% CO_2/He at 250 °C, and the XPS spectrum showed the presence of primarily Ce^{4+} with a mixture of Cu^{2+} and Cu^{+} (Fig. 7(a)). Then the sample was degassed in vacuum at room temperature for 72 hours which resulted in considerable reduction of the surface. After this reduction, Cu was in oxidation state +1, determined from the 2p binding energy of 932.2 eV and the LMM Auger kinetic energy of 916.4 eV [17]. Ce was strongly reduced as indicated by the distinct v' and u' lines corresponding to Ce^{3+} .

DISCUSSION

Cerium is well known as a highly pyrophoric metal. However, TPR measurements showed that complete oxidation to stoichiometric CeO_2 is a thermally activated process which requires temperatures as high as 850-900 °C [1,10]. Therefore, metallic cerium oxidizes completely when

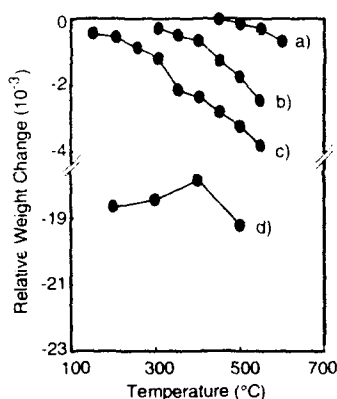


Fig. 5 Reduction of cerium oxide samples as a function of temperature for (a) microcrystalline CeO_2 , (b) precipitated ultrafine CeO_2 , (c) nanocrystalline CeO_{2-x} , and (d) Cu-doped nanocrystalline CeO_{2-x} .

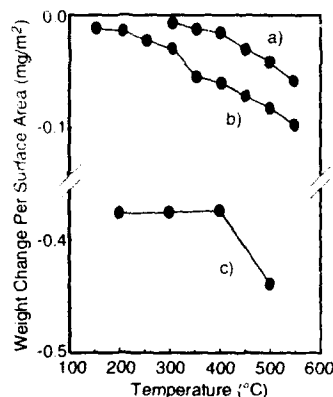


Fig. 6 Reduction of cerium oxide samples normalized to the total surface area for (a) precipitated CeO_2 , (b) nanocrystalline CeO_{2-x} , and (c) Cu-doped nanocrystalline CeO_{2-x} .

suddenly exposed to air due to the heat release by this exothermic process. Through slow oxidation, a residual oxygen deficiency can be preserved even under an oxidizing atmosphere and temperatures as high as 600°C. XPS measurements showed that 22% of the Ce cations have a oxidation state +3 in nanocrystalline CeO_{2-x} . After oxidation at 550 °C in CO_2/He , this component was reduced to the resolution limit of XPS-measurements, indicating a re-oxidation at least at the surface. Residual oxygen deficiency inside the cluster volume might not be detected by a surface-sensitive method like XPS. Superoxide species O_2^- are adsorbed on Ce^{3+} surface defects which are presumably formed by electron donation from the reduced CeO_{2-x} . Since superoxide is desorbing at lower temperatures than capping oxygen ions, the surface of oxygen-deficient CeO_{2-x} can be reduced more easily than a capping oxygen layer for stoichiometric CeO_2 . This effect is shown in thermogravimetric measurements by comparing the nanocrystalline material with the precipitated material.

Cu-doped nanocrystalline CeO_{2-x} exhibited the greatest reducibility. From the result that the extent of reduction is independent of temperature between 200 °C and 400 °C and the information on weight loss due to the amount of extracted oxygen, we suggest that one monolayer was removed from the surface at 200 °C - 400 °C, and reduction of the first lattice layer started at 500°C. XPS measurements showed that both Cu and Ce cations are reduced indicating a promotional effect of Cu on CeO_{2-x} reduction. This can be the result of: (i) spill-over of CO onto CeO_{2-x} after adsorbing on Cu, or (ii) electronic effects. Since reduction of CeO_2 involves the transfer of electrons to localized Ce-4f^1 states close to the valence band, doping of CeO_2 with Cu might affect the enthalpy of formation for ionized vacancies. We found evidence for this kind of interaction in the low-binding energy part of XPS spectra (Fig. 8). The valence band of stoichiometric CeO_2 is shown at the bottom as a reference. Pure but reduced CeO_{2-x} showed an additional peak above the valence band edge, marked by an arrow. This peak corresponds to the Ce-4f^1 final states of reduced CeO_{2-x} . This peak is not so distinct in Cu-doped CeO_{2-x} , which is caused by a larger overlapping with the valence band shifted by about 0.5 eV. We assume that this shift is qualitatively due to the mixing of a 2.5 eV band gap semiconductor (Cu_2O) in a 5.5 eV band gap semiconductor (CeO_2) [18].

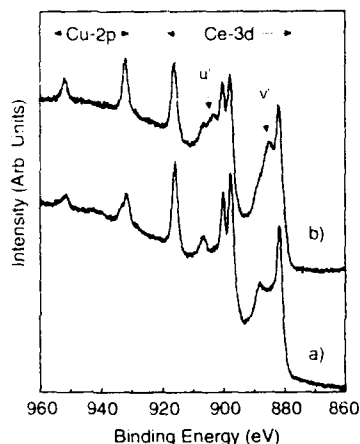


Fig. 7 XPS Cu-2p and Ce-3d core level spectra for nanocrystalline Cu-doped CeO_{2-x} , (a) after oxidation in 1000 Pa of 1% CO_2/He at 250°C, and (b) after degassing in vacuum for 72 hours at room temperature.

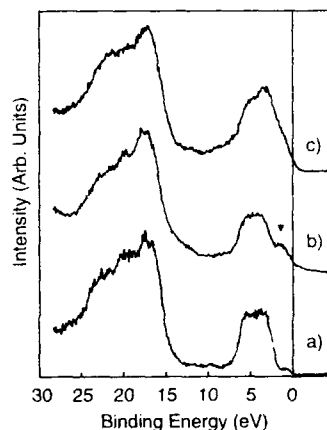


Fig. 8 Density-of-states below the Fermi energy as measured by XPS for (a) stoichiometric CeO_2 , (b) partly reduced nanocrystalline CeO_{2-x} , (c) nanocrystalline Cu-doped CeO_{2-x} , partly reduced in vacuum.

Our TGA measurements showed that reduction starts at about 500 °C for bulk CeO_2 , at 300 °C for capping oxygen surface ions, and 150 °C for superoxide species O_2^- .

SUMMARY

Unsupported oxygen deficient CeO_{2-x} was synthesized by inert gas condensation, and its reduction and oxidation properties were compared with precipitated ultrafine CeO_2 as well as microcrystalline CeO_2 . Oxygen deficiency of the nanocrystalline CeO_{2-x} increased the reducibility of the surface as compared to stoichiometric CeO_2 . Cu-doping was found to promote surface reduction allowing complete removal of one monolayer of oxygen at temperatures as low as 200 °C. This effect might be related to a shift in the valence band of this material.

ACKNOWLEDGMENT

This project is sponsored by National Science Foundation (CTS-9257223 and DMR-9022933) and Sloan Fund. A. Tschöpe acknowledges the BASF Fellowship of the German National Scholarship Foundation.

REFERENCES

1. H.C. Yao and Y.F. Yu Yao, *J. Catalysis* **86**, 254 (1984).
2. A.D. Logan and M. Shelef, *J. Mater. Res.* **9** [2], 468 (1994).
3. W. Liu and M. Flytzani-Stephanopoulos, ACS Symposium Series 552, ed. by J. Armor, Ch. 31, pp 375-392, 1994.
4. A. Tschöpe and J.Y. Ying in Nanophase Materials: Synthesis-Properties-Applications, edited by G.C. Hadjipanayis and R.W. Siegel (Kluwer, Netherlands, 1994).
5. A. Tschöpe, J.Y. Ying, W. Liu, and M. Flytzani-Stephanopoulos in Materials and Processes for Environmental Protection, presented at the 1994 MRS Spring Meeting, San Francisco, CA, April 1994.
6. W. Liu, A.F. Sarofim, and M. Flytzani-Stephanopoulos in Materials and Processes for Environmental Protection, presented at the MRS spring meeting, San Francisco, CA, 1994).
7. H.L. Tuller and A.S. Nowick, *J. Electrochem. Soc.* **126** [2], 209 (1979).
8. M. Che, J.F.J. Kibblewhite, A.J. Tench, M. Dufaux, and C. Naccache, *J. Chem. Soc. Faraday Trans.* **69**, 857 (1973).
9. C. Li, K. Doran, K. Maruya, and T. Onishi, *J. Am. Chem. Soc.* **111**, 7683 (1989).
10. T. Yamada, K. Kayano, and M. Funabiki, in New Aspects Of Spillover Effect In Catalysis, edited by T. Inui, K. Fujimoto, T. Uchijima, and M. Masai, (Elsevier, 1993).
11. A.S. Tschöpe and J.Y. Ying, submitted to *Nanostr. Mater.*
12. H. Gleiter, *Prog. Mater. Sci.* **33** [4], 223 (1989).
13. R. Birringer, U. Herr, and H. Gleiter, *Trans. Jpn. Inst. Met.* **27** suppl., 43 (1987).
14. J.Y. Ying, *J. Aerosol Sci.* **24** [3], 315 (1993).
15. A. Laachir, V. Perrichon, A. Badri, J. Lamotte, E. Catherine, J.C. Lavalley, I. El Fallah, L. Hilaire, F. Le Normand, E. Quemere, G.N. Sauvion, and O. Touret, *J. Chem. Soc. Faraday Trans.* **87**, 1601 (1991).
16. M.L. Trudeau, A. Tschöpe, and J.Y. Ying, to be published in *Surf. Interf. Anal.*
17. *Handbook of X-ray Photoelectron Spectroscopy*, Perkin Elmer Corp., p. 203.
18. W.H. Strehlow and E.L. Cook, *J. Phys. Ref. Data* **2** [1], 163 (1973).

ORGANIC/INORGANIC SUPERLATTICES : STRUCTURAL AND OPTICAL PROPERTIES

SHIZUO TOKITO, J. SAKATA AND Y. TAGA

Toyota Central Research & Development Laboratories Inc., 41-1, Aza Yokomichi, Oaza Nagakute, Nagakute-cho, Aichi-gun, Aichi 480-11, Japan

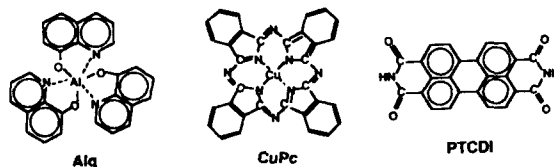
ABSTRACT

A new class of superlattices consisting of alternating layers of organic and inorganic materials has been prepared from 8-hydroxyquinoline aluminium (Alq), copper phthalocyanine (CuPc), 3,4,9,10-perylenetetracarboxylic diimide (PTCDI) and MgF₂ by molecular beam deposition. Small-angle x-ray diffraction data and cross-sectional transmission electron micrograph of the superlattices reveal that the superlattices have layered structure throughout the entire stack. From comparison of the x-ray diffraction patterns, it is found that the interface roughness between organic and MgF₂ layers depends on the materials for organic layers. High-angle x-ray diffraction data indicate that there is a structural ordering in the CuPc and PTCDI layers. From the optical absorption and photoluminescence measurements, it is found that the exciton energy of Alq shifts to higher energy with decreasing Alq layer thickness.

INTRODUCTION

Artificial multilayers have attracted great attention because of their unusual physical properties. In particular, magnetic properties of metallic superlattices consisting of magnetic and nonmagnetic layers [1,2] and optoelectronic properties of semiconductor superlattices consisting of two kinds of semiconducting layers [3,4] have been studied intensively. Many novel device concepts have been developed. Recently, Unique combination of organic materials with inorganic ones has been tried for the superlattices [5-7]. The unique combination brings out novel possibility for the creation of new type of optoelectronic materials, because organic materials have prominent properties such as large photoconductivity [8], electroluminescence [9] and nonlinear optical effects [10], and a wide variation of the combination of materials. Furthermore, higher chemical and structural stability in the superlattice structure rather than an organic single layer is expected.

In this paper we report structural properties of organic/inorganic superlattices which were fabricated from alternating layers of organic and inorganic materials. Large aromatic molecules, Alq, CuPc and PTCDI, which are well-known organic semiconductors [9,11,12], were chosen for the organic layers. MgF₂ was used for the inorganic layer, because this material has a wide transmission region from 200 to 5000 nm [13]. The layered structures and intra-layer structures of the superlattices are characterized by small-angle, high-angle x-ray diffraction experiments, and a transmission electron microscopy (TEM). Optical properties of well-fabricated Alq/MgF₂ superlattices will be also shown.



EXPERIMENTAL

Commercially available powders of Alq, CuPc and PTCDI, and MgF₂(99.99%) were used in this study. All of the organic materials were purified by a train sublimation method [14], before

the uses as the molecular beam sources. The organic/inorganic multilayered films with artificial superstructure were prepared using a multi-source type molecular beam deposition system. The alternating layered structures were fabricated on polished Si(100) wafers and glass substrates (Corning 7059) using shutters, for each crucible, controlled by a microcomputer. The temperature of the substrates during deposition was at around room temperature. The typical deposition rate was 20 Å/min. The thicknesses of the organic layer and the MgF₂ layer were designed to be 50 Å and 30 Å, respectively, as measured by a quartz crystal thickness monitor (INFICON XTC). The base pressure of the deposition system was 8×10^{-8} Torr, and the pressure during deposition was 1×10^{-7} Torr.

Small-angle and high-angle x-ray diffraction experiments were carried out using a diffractometer (Rigaku RAD-2B) with CuK α radiation. Cross-sectional TEM observation was performed with a JEOL JEM-2000EX operated at 200 keV. Optical absorption and photoluminescence were measured with a spectrophotometer (Hitachi 330) and an intensified multi-channel photodetector (Otsuka Electronics IMUC-7000).

RESULTS AND DISCUSSION

Structures

Fig.1 shows small-angle x-ray diffraction patterns of superlattices with 30 periods. In the diffraction patterns, Bragg reflection peaks were observed at small angles corresponding to artificial superlattice period. The designed period is the sum of single organic layer thickness,

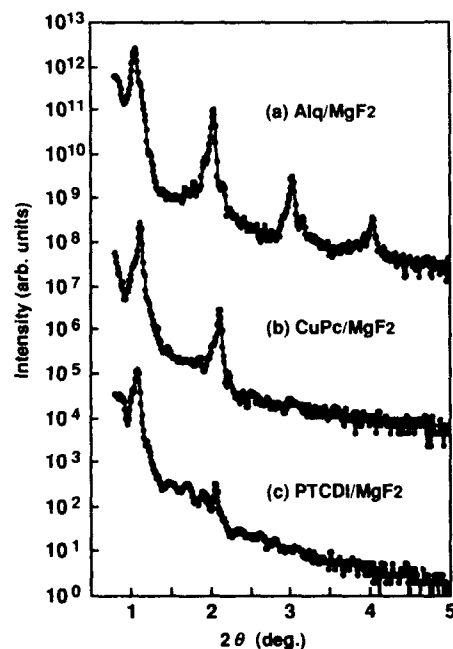


Fig.1 Small-angle x-ray diffraction patterns for (a) Alq(50Å)/MgF₂(30Å), (b) CuPc(50Å)/MgF₂(30Å) and (c) PTCDI(50Å)/MgF₂(30Å) superlattices.

50Å, and single MgF₂ layer thickness, 30Å, determined from the thickness monitor. The observed periods from first-order Bragg peaks were in very good agreement with the designed period (80Å) (Table 1). These results indicate that the three superlattices have periodically layered structure throughout the entire stack. The Alq/MgF₂ superlattice exhibits higher-order Bragg peaks and they are fairly sharp. Even in the pattern for the superlattice with Alq layer thickness of 10Å, strong first-order peak was observed [7]. The CuPc/MgF₂ superlattice exhibits strong first- and second-order diffraction peaks and weak third-order diffraction. The PTCDI/MgF₂ superlattice exhibits strong first-order diffraction peak, but the second-order diffraction is not strong and the third-order is absent. It is known that the interface roughness between two layers gives rise to broadening of Bragg peaks as well as in damping of higher-order peak intensity [15,16]. Comparison of the diffraction patterns indicates that the interface roughness in the Alq/MgF₂ superlattice is smaller than that in the CuPc/MgF₂ and PTCDI/MgF₂ superlattices.

Table 1 Comparison of "designed" and "observed" periods in superlattices. Designed periods were determined from the thickness monitor and observed ones were obtained from x-ray diffraction.

Superlattice	Periods (Å)	
	"Designed"	"Observed"
Alq/MgF ₂	80	82
CuPc/MgF ₂	80	79
PTCDI/MgF ₂	80	82

We have tried to get direct images of the cross-section and succeeded in the observation in the CuPc/MgF₂ superlattice. Fig.2 shows the TEM image of the CuPc/MgF₂ superlattice. In the image, periodic bright and dark layers are observed. The dark layers which are thinner than bright layers should be MgF₂ as a result of its higher density. The observed image is consistent with the structure predicted from the small-angle x-ray diffraction data, showing the superlattice exactly consists of alternating layers of CuPc and MgF₂. Interface roughness is also observable in the image. However, there might be some parts damaged in preparing the specimen for the TEM observation.

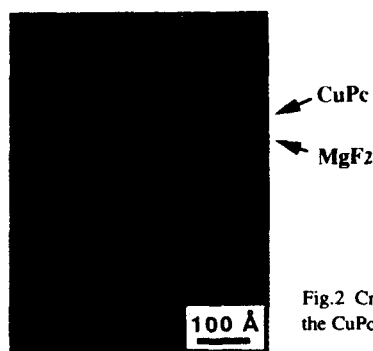


Fig.2 Cross-sectional TEM image of the CuPc(50Å)/MgF₂(30Å) superlattice.

High-angle x-ray diffraction can give intra-layer structural information. Any diffraction peaks had not been observed in the diffraction pattern of the Alq/MgF₂ superlattice. This suggests that the Alq and MgF₂ layers have no structural ordering. Small interface roughness in the Alq/MgF₂ superlattices is probably due to amorphous structure of each layers. On the other hand, the CuPc/MgF₂ and PTCDI/MgF₂ superlattices exhibited diffraction peaks in the diffraction patterns. Fig.3(a) shows the high-angle x-ray diffraction pattern of the CuPc/MgF₂ superlattice. For comparison, the diffraction pattern of a single layer (1000Å) of CuPc is also shown. A significant diffraction peak was observed at the same angle as the corresponding peak for the single layer. The diffraction peak at around 7° is attributable to the crystal plane of α or β -phase crystals [17], indicating that the CuPc layers in the superlattice have an uniaxial ordering of the crystallites. The PTCDI/MgF₂ superlattice exhibits two broad diffraction peaks at 25 and 27°, which is also similar to that of a PTCDI single layer (1000Å) as shown in Fig.3(b). These patterns are much different from that of the PTCDI powder [18], indicating that the PTCDI layers in the superlattice have an ordering of the crystallites as well as the single layer. Thus, crystalline ordering can be retained even in the ultra-thin organic layers between amorphous MgF₂ layers.

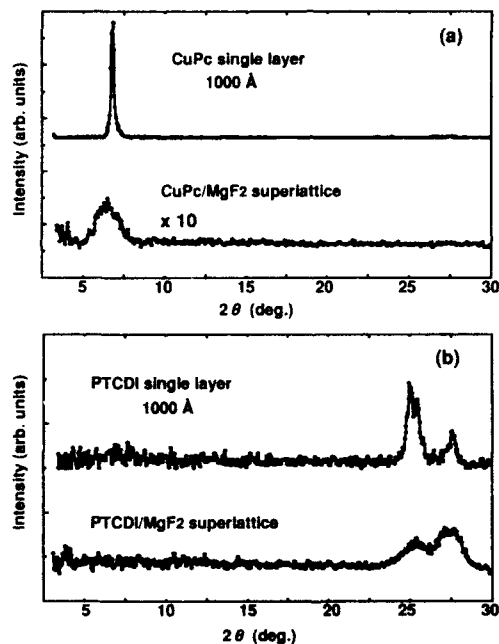


Fig.3 High-angle x-ray diffraction patterns of (a) CuPc single layer (1000Å) and CuPc/MgF₂ superlattice, and (b) PTCDI single layer (1000Å) and PTCDI/MgF₂ superlattice.

Optical Properties

Here, we show the optical properties for the well-fabricated Alq/MgF₂ superlattices. Fig.4 shows the optical absorption and photoluminescence spectra. The absorption and photoluminescence peaks are located at 390 nm and 520 nm, respectively, which are almost

identical with that of a single layer films (ca. 500Å) previously reported [9]. However, we have found that the absorption and photoluminescence peaks shift to shorter wavelength (higher energy) region as the Alq layer thickness decreases. The dependences of the energies for such peaks on Alq layer thickness are shown in Fig.5. The results in Fig.5 show that the blueshifts occur in the Alq layer thickness less than about 50 Å. The absorption and photoluminescence peaks are attributable to the exciton in the Alq layers, because MgF₂ is transparent in this wavelength region and to excitation light, 365 nm.

From the lowest-energy cutoff of the absorption spectrum, the "energy gap" is estimated to be about 2.7 eV for Alq. Since MgF₂ is completely insulating material with an extremely large energy gap over 8 eV, the exciton in the Alq layer is isolated by MgF₂ layers. The blueshifts in the absorption and the photoluminescence lead us to consider a simple quantum mechanical model based on exciton confinement in two dimensional layer, in which the energy shifts could be interpreted as the change of exciton binding energy owing to quantum confinement. Similar explanation has been reported in the blueshifts of optical absorption in organic multiple quantum well consisting of 3, 4, 7, 8-naphthalenetetracarboxylic dianhydride (NTCDA) and PTCDA [19], and Alq and aromatic diamine [20].

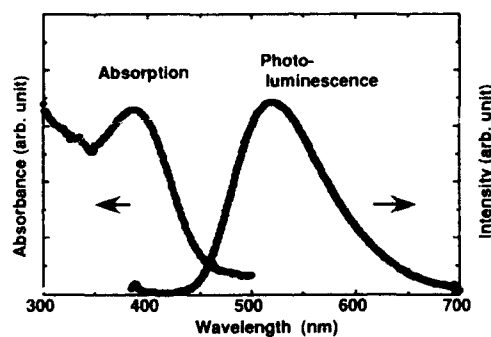


Fig.4 Optical absorption and photoluminescence spectra of the Alq(50Å)/MgF₂(30Å) superlattice.

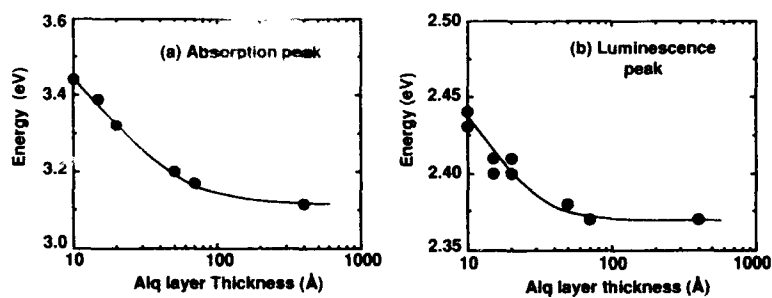


Fig.5 Energies of absorption and photoluminescence peaks of Alq/MgF₂ superlattices with various Alq layer thicknesses.

CONCLUSIONS

We have succeeded in fabrication of the high-quality superlattices consisting of alternating layers of organic materials and MgF₂. From the small-angle x-ray diffraction studies and the direct image of cross-section, the periodically layered structures with organic layers and MgF₂ layers have been confirmed. The interface roughness in the Alq/MgF₂ superlattice is smaller than that in the CuPc/MgF₂ and PTCDI/MgF₂ superlattices. The high-angle x-ray diffraction data showed that the Alq layers have no structural order, but the CuPc and PTCDI layers have a high degree of crystalline ordering. Small interface roughness in the Alq/MgF₂ superlattices is attributable to the amorphous structure of each layers. The blueshifts in the optical absorption and photoluminescence spectra were observed in the well-fabricated Alq/MgF₂ superlattices. The energy shifts could be interpreted as the effect of exciton confinement.

ACKNOWLEDGEMENTS

We would like to thank N. Suzuki for cross-sectional TEM observation of the superlattice. We also thank H. Fujikawa for computer programming for shutter control in sample preparation, and Dr. K. Seno and M. Suzuki for their helpful discussions.

REFERENCES

- (1) M. N. Baibich, J. M. Broto, A. Fert, F. Nguyen van Dau, F. Petroff, P. Etienne, G. Creuzet, A. Friederich and J. Chazelas, *Phys. Rev. Lett.*, **61**, 2472(1988).
- (2) S. S. P. Parkin, R. Bhadra and K. P. Roche, *Phys. Rev. Lett.*, **66**, 2152(1991).
- (3) P. Voisin, G. Bastard, C. E. T. Goncalves da Silva and M. Voos, L. L. Chang and L. Esaki, *Solid State Commun.*, **39**, 79(1981).
- (4) B. Abeles and T. Tiedje, *Phys. Rev. Lett.*, **51**, 2003(1983).
- (5) K. Orihara, *Thin Solid Films*, **219**, 236(1992).
- (6) J. Takada, H. Awaji, M. Koshioka, A. Nakajima and A. Nevin, *Appl. Phys. Lett.*, **61**, 2184(1992).
- (7) S. Tokito, J. Sakata, and Y. Taga, *Appl. Phys. Lett.*, **64**, 1353(1994).
- (8) Z. D. Popovic, R. O. Loutfy and Ah-M. Hor, *Can. J. Chem.*, **63**, 134(1985).
- (9) C. W. Tang and S. A. VanSlyke, *Appl. Phys. Lett.*, **51**, 913(1987).
- (10) D.S. Chemla and J. Zyss, *Nonlinear Optical Properties of Organic Molecules and Crystals* (Academic Press Inc., 1987).
- (11) R. O. Loutfy, A. M. Hor, P. Kazmaler, and M. Tam, *J. Image. Sci.*, **33**, 151(1989).
- (12) E. A. Silinsh, *Organic Molecular Crystals* (Springer-Verlag, Heideberg, 1980).
- (13) H. K. Pulker, *Applied Optics*, **18**, 1969(1979).
- (14) H. J. Wanger, R. O. Loutfy and C-K. Hsiao, *J. Mater. Sci.*, **17**, 2781(1982).
- (15) Y. Huai, R. W. Cochrane and M. Sutton, *Phys. Rev. B*, **48**, 2568(1993).
- (16) S. Tamada, Y. Tsuchiya, N. Nakayama, K. Kosuge, S. Nagata, and S. Tamaguchi, *J. Mag. Mag. Mater.*, **126**, 164(1993).
- (17) M. K. Debe, and K. K. Kam, *Thin Solid Films*, **186**, 289(1990).
- (18) S. Tokito, J. Sakata, and Y. Taga, (private communication).
- (19) F. F. So, S. R. Forrest, Y. Q. Shi and W. H. Steier, *Appl. Phys. Lett.*, **56**, 674(1990).
- (20) Y. Ohmori, A. Fujii, M. Uchida, C. Morishita, and K. Yoshino, *Appl. Phys. Lett.*, **62**, 3250(1993).

MOLECULAR SIEVE BASED CHEMICAL SENSORS

LAURA J. SOTTILE*, KENNETH J. BALKUS, JR.*, SCOTT J. RILEY*
AND BRUCE E. GNADE**

*University of Texas at Dallas, Department of Chemistry,
Richardson, TX 75083-0688

**Materials Science Laboratory, Semiconductor Research and Development,
Texas Instruments, Inc., Dallas, TX 75265

ABSTRACT

By virtue of their shape selectivity and stability, molecular sieves are ideal components for discriminating chemical sensors. In this paper we report the preparation of capacitance type sensors based on aluminum phosphate molecular sieves. Thin films of the molecular sieves $\text{AlPO}_4\text{-5}$, $\text{AlPO}_4\text{-H3}$ and $\text{AlPO}_4\text{-H1}$, which cover a range of pore dimensions, were deposited on titanium nitride coated silicon wafers by laser ablation. A subsequent hydrothermal treatment followed by a Pd/Au coating and the application of standard photoresist/masking techniques were used to generate the capacitors. The molecular sieves exhibit significant changes in capacitance upon exposure to target molecules, including CO_2 , CO, N_2 , H_2O and toluene.

INTRODUCTION

Aluminum phosphate (AlPO_4) molecular sieves belong to a family of low density crystalline metal oxides having well defined pore and channel systems [1]. Zeolites and related molecular sieves are attractive as components for chemical sensors because of the shape selective adsorption of molecules which is a consequence of having uniform pore dimensions. Additionally, molecular sieves are chemically and thermally robust. Zeolite molecular sieves have been incorporated into piezoelectric devices such as surface acoustic wave (SAW) [2] and quartz crystal microgravimetric (QCM) type sensors [3-5]. These chemical sensors, which essentially rely on a weight change, have shown promise in selectively detecting organic molecules. However, it is not clear how discriminating such sensors would be for molecules of similar size and shape. Ideally the adsorption of an analyte molecule would affect some signature change in the molecular sieve properties that could then be quantified. For example, the dense phase aluminum phosphate berlinite exhibits a small increase in dielectric constant

when hydrated [6]. We might expect such a change in dielectric constant to be amplified in an AlPO_4 molecular sieve where the surface area is several orders of magnitude greater. Shape selectively adsorbed molecules with dissimilar polarities should illicit different responses. A version of this concept has been realized in an interdigitized capacitor employing a Y type zeolite coating as the dielectric phase [7,8]. Changes in zeolite capacitance upon adsorption of different molecules were recorded in the picofarad range. This rather poor capacitance is probably the result of the device configuration where it appears that bulk zeolite crystals are packed between the electrodes. Since Capacitance, $C = A \epsilon / d$ (where A is the plate area and d is the distance between them) the thinner the dielectric phase the more measurable the capacitance. The higher the capacitance the greater the changes in C are expected to be. Of course there will ultimately be a trade off with leakage current but nevertheless one would prefer the thinnest molecular sieve film possible. The preparation of thin films has been a major challenge for all the molecular sieve based devices so far. However, we have found that continuous AlPO_4 molecular sieve films in the nanometer range can be obtained via laser ablation [9]. Aluminum phosphate molecular sieves are not ionic conductors and therefore, are preferred over aluminosilicate zeolites as dielectric materials.

In this paper, we describe the preparation of capacitance type chemical sensors based on ablated films of AlPO_4 molecular sieves on TiN. The AlPO_4 molecular sieves in this study, $\text{AlPO}_4\text{-H3}$ ($3.5 \times 3.7 \text{ \AA}$), $\text{AlPO}_4\text{-5}$ (7.4 \AA) and $\text{AlPO}_4\text{-H1}$ (12 \AA), cover a range of pore sizes. The capacitance of these molecular sieves should reflect the shape selective adsorption of different molecules. For example, the kinetic diameter of CO (3.8 \AA) is too large for $\text{AlPO}_4\text{-H3}$, while H_2O (2.65 \AA) should readily be adsorbed. Therefore, the dielectric constant of $\text{AlPO}_4\text{-H3}$ should be unaffected by the presence of CO but is expected to change dramatically upon exposure to water. $\text{AlPO}_4\text{-5}$ should discriminate against larger hydrocarbons, whereas $\text{AlPO}_4\text{-H1}$ is expected to be sensitive to such molecules. One could imagine a microarray of several different molecular sieves that could selectively sense distinct molecules in a mixture such as a combustion gas stream. In this preliminary account the results for the detection of N_2 , CO_2 , CO, H_2O and toluene are presented.

EXPERIMENTAL

The laser ablation and hydrothermal treatment of the AlPO_4 molecular sieve films will be described elsewhere [9]. The capacitors were prepared from TiN coated (100 nm) silicon wafers with <200 nm thick ablated AlPO_4 molecular sieve films. Titanium nitride was selected because of oxidative resistance and used in semiconductor processing. The TiN served

as one electrode, while the other electrode was generated by the vapor deposition of a Au/Pd alloy to a thickness of approximately 1 μm on top of the molecular sieve layer. The capacitors were defined using standard photolithography. The metal exposed in the development process was etched away with aqua regia. The capacitor was then washed with acetone to remove the remaining photoresist and dried in a vacuum oven (20 Torr) at 50°C.

Capacitance and current measurements were performed on a custom probe station. The probe chamber was equipped with four active and one ground probe controlled by micrometers. Capacitance and current data were collected using a Hewlett Packard 4284A Precision LCR Meter and a Keithly 237 High voltage source. The probe station was equipped with a microscope for viewing the probe tip placement and a gas manifold for controlling the atmosphere.

All capacitance measurements were taken from the standpoint of having a capacitor in series with a resistor (Cs-RSV). This approach is reasonable since the titanium nitride coating has a conductivity of 50 to 100 $\Omega\cdot\text{cm}^{-1}$ as opposed to that of gold ($4.09\times 10^5 \Omega\cdot\text{cm}^{-1}$) or palladium ($9.26\times 10^4 \Omega\cdot\text{cm}^{-1}$). The typical voltage range was set at -0.5V to +0.5V. The voltage range employed was divided so as to produce 21 data points during the measurement. The AC frequency of the current applied to the capacitor, either varied logarithmically during a measurement (typically from 0.005kHz to 100MHz) or was static at a specific oscillation frequency (0.001kHz to 100kHz). All measurements were made at room temperature and atmospheric pressure. Capacitance or current data from the five readings were averaged for each voltage point taken with a margin of error <3%.

Current measurements were taken to find the leakage current and the breakdown voltage. The current was set at 0.1 Ampere. The breakdown voltage of capacitors was determined by scanning the voltage from 0V to 10V. For leakage current measurements the voltage range was set equal to that of the capacitance measurement being made (-0.5V to +0.5V). The voltage range was divided so as to produce 11 data points.

RESULTS AND DISCUSSION

Capacitance type sensors were prepared from hydrothermally treated laser ablated AlPO_4 molecular sieve thin films (dielectric phase). The electrodes were the TiN substrate and Au/Pd pads (area= $1.39\text{E}-3\text{cm}^2$) deposited on top of the dielectric phase using standard mask and etch techniques. Figure 1 shows a schematic view of such a capacitor. The capacitors were heated under vacuum to remove template and adsorbed water then transferred to the probe chamber. Pure, dry analyte gases were introduced via a gas manifold. A nitrogen atmosphere generally produced the

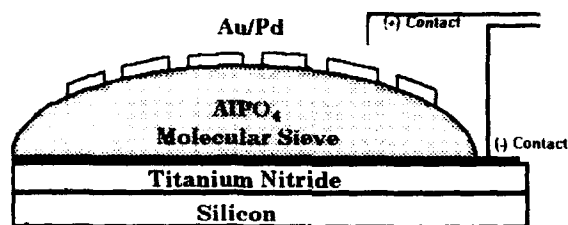


Figure 1. Side view of molecular sieve based capacitance type sensor.

lowest capacitance which varied with thickness. Figure 2 shows a plot of capacitance per square meter for a 47.5 nm thick $\text{AlPO}_4\text{-5}$ molecular sieve measured at +0.3 volts and an oscillator frequency 100 kHz. The nitrogen response is ~100 times greater than the instrument noise level (10^{-13} farads). Upon exposure to pure atmospheres of carbon dioxide or toluene the capacitance increases nearly 1000 times. The response to CO is almost 10 times greater than CO_2 at this voltage. This is consistent with the highly

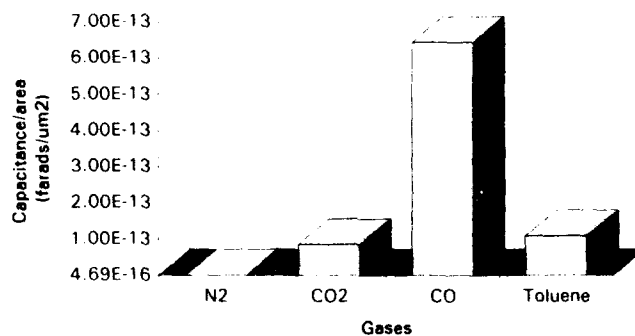


Figure 2. Capacitance per m^2 after adsorption of N_2 , CO_2 , CO or toluene $\text{AlPO}_4\text{-5}$ ($V=+0.3$, Leakage Current $1/\mu\text{m}^2=7.19\text{E-}19$)

polar CO molecule strongly adsorbing in the molecular sieve. This suggests that it may be possible to discriminate between CO_2 and CO. All these changes are reversible with temperature or pressure adjustments.

Figure 3 shows the capacitance per square meter measured between -0.5 and +0.5 volts for a 70.3 nm thick $\text{AlPO}_4\text{-5}$ sensor. The breakdown voltage for these capacitors is typically in the range of 1 volt. Current versus voltage plots are routinely made in order to evaluate leakage current. However, leakage would also be characterized by a sharp increase in capacitance, especially at the higher voltages. Such leakage is not apparent for this sensor.

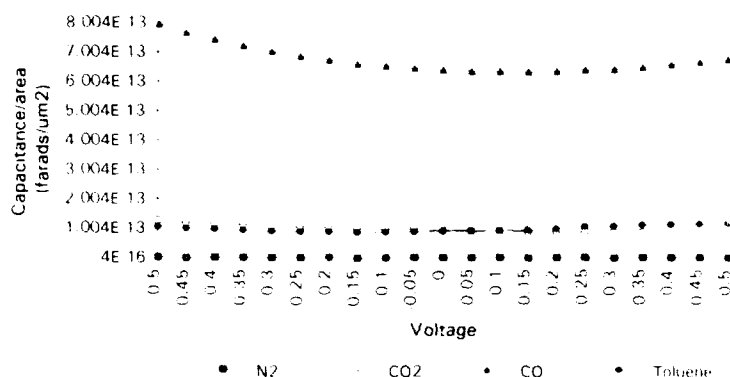


Figure 3. Plot of capacitance/ μm^2 versus voltage for an $\text{AlPO}_4\text{-5}$ sensor

The sensitivity of these sensors is still being evaluated. The selectivity is remarkably different between the different types of molecular sieves which presumably reflects the different pore dimensions. Figure 4 illustrates this point in a plot of capacitance ratios for the detection of CO_2 versus N_2 by ablated $\text{AlPO}_4\text{-H1}$, $\text{AlPO}_4\text{-H3}$ and $\text{AlPO}_4\text{-5}$ (~100nm). The largest pore molecular sieve $\text{AlPO}_4\text{-H1}$ exhibits the highest sensitivity for detection of CO_2 . The smaller (3.3Å) and more polar CO_2 apparently interacts to a greater extent with the $\text{AlPO}_4\text{-H1}$ channels. Although, CO_2 easily fits in $\text{AlPO}_4\text{-5}$ the amount of CO_2 is probably smaller. The small pore $\text{AlPO}_4\text{-H3}$ shows no significant change in capacitance when exposed to CO_2 relative to N_2 . However, $\text{AlPO}_4\text{-H3}$ exhibits large changes in capacitance when exposed to moisture which reflects the smaller kinetic diameter of water (2.65Å).

In conclusion we have shown that a capacitance type chemical sensor can be generated from laser ablated AlPO_4 molecular sieves. $\text{AlPO}_4\text{-5}$ appears to be selective for CO while $\text{AlPO}_4\text{-H1}$ is selective for CO_2 . Shape selectivity is apparent in the case of $\text{AlPO}_4\text{-H3}$ which is sensitive to the presence of moisture but does not discriminate between N_2 and CO_2 .

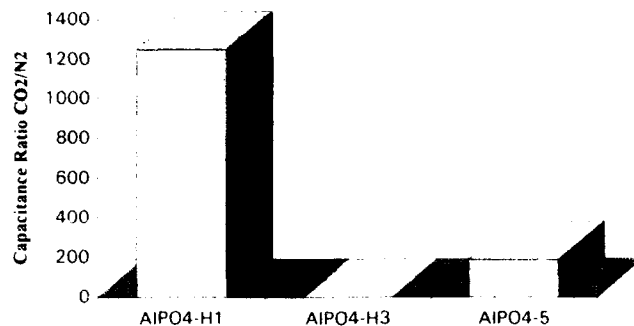


Figure 4. Capacitance ratio of CO₂/N₂ for AIPO₄-H1, AIPO₄-H3 and AIPO₄-5 (V=+0.3 and I/μm²=7.19E-19)

ACKNOWLEDGMENTS

We wish to thank the National Science Foundation (CHE-9157014) and Texas Instruments, Inc. for financial support of this work.

REFERENCES

1. R. Szostak, Molecular Sieves, (Van Nostrand Reinhold, New York, 1982).
2. K. Brown, T. Bein, G.C. Frye and C.J. Brinker, *J. Am. Chem. Soc.* **111**, 7640 (1989).
3. Y. Yan and T. Bein, *Mater. Res. Soc. Symp. Proceed.* **233**, 175 (1991).
4. Y. Yan, and T. Bein, *J. Phys. Chem.* **96**, 9387 (1992).
5. Y. Yan and T. Bein, *Chem. Mater.* **4**, 975 (1992).
6. R. D. Shannon, A. J. Vega, B. H. T. Chai and G.R. Rossman, *J. Phys. D: Appl. Phys.* **26**, 93 (1993).
7. K. Alberti, J. Haas, L. C. Plog, and F. Fetting, *Catal. Today* **8**, 509 (1991).
8. J. Haas, C. Plog and E. Obermeier, *Eur. Patent No.* 426,989 A1 (1991).
9. K. J. Balkus, Jr., S. J. Riley and B. E. Gnade, *Mater. Res. Soc. Symp. Proceed.*, submitted.

SELF-ASSEMBLY OF ORIENTED METAL BISPHOSPHONATE MULTILAYERS WITH POTENTIAL NONLINEAR OPTICAL PROPERTIES

GRACE ANN NEFF, ASTRID C. ZEPPENFELD, BETHANY KLOPFENSTEIN and CATHERINE J. PAGE

University of Oregon, Department of Chemistry, Eugene, Oregon 97403

ABSTRACT

We are investigating a method for synthesizing oriented layered thin film structures that exhibit nonlinear optical properties. This method involves self-assembly of metal bisphosphonate multilayers on gold and silicon substrates. Multilayers are characterized via optical ellipsometry, diffuse reflectance and attenuated total reflectance FTIR, and grazing angle X-ray diffraction.

To incorporate nonlinear optical activity into self-assembled films, we use α,ω bisphosphonates containing aromatic π systems sandwiched between donor and acceptor groups. In order to maximize the overall polarizability of the film, the polarizable bisphosphonate molecules must preferentially bind in only one orientation. To accomplish this, one of the terminal phosphonate groups of the molecule is protected (in ester form). After binding the free phosphonic acid end, the terminal ester is converted to a phosphonic acid group by hydrolysis with bromotrimethylsilane (BTMS). Layering is continued by binding a metal layer and repeating the cycle. Films prepared via this route do exhibit second harmonic generation, but apparently incomplete deprotection of each layer leads to increasing disorder with increasing number of layers.

INTRODUCTION

The method of self-assembly involves the spontaneous adsorption of an ordered monolayer from solution onto a substrate. Multilayer assemblies can be built up as well, if the first self-assembled layer presents surface groups which are reactive or which can be functionalized to bind a second chemical species. The system under investigation involves Hf- α,ω bisphosphonate films, which are structurally analogous to the prototype zirconium bisphosphonate systems developed by Mallouk and coworkers.¹ One advantage to this system is the fact that it can accommodate a wide variety of organic groups within the bisphosphonate layer.^{1,2} Many possibilities exist for incorporation of nonlinear optical properties, via chromophores, into these materials, as has been demonstrated by Katz et al.³ In the present study, the chromophore is incorporated into a bisphosphonic acid/ester molecule, shown below in Figure 1.

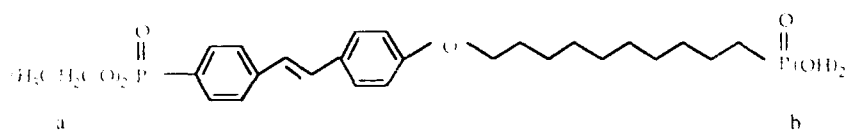


FIGURE 1 (4)-p-Diethylphosphonate-trans Stilbene-10-decylphosphonic Acid Ether

Directional polarizability of the molecule is provided by the extended π system which is sandwiched between an electron donor (ether linkage) and an electron acceptor (phosphonate ester (a)). The polarizability affects the magnitude of the nonlinear optical effect. As shown, (I) has a phosphonate ester on one end (a), and is functionalized on the other end by a phosphonic acid (b). This allows us to orient the molecule during self-assembly, as only the phosphonic acid will bind to Hf metal on the surface.⁴ The molecules within each layer must be oriented such that the bulk film has no inversion symmetry in order for even-order nonlinear optical effects to be observed.⁵

The reaction sequence involved in self-assembly of (I) onto a hafnium-functionalized surface and subsequent deprotection is shown in Figure 2. The terminal ester group is converted to a phosphonic acid by gentle hydrolysis with bromotrimethylsilane (BTMS).⁶ Following deprotection, a layer of hafnium ions is adsorbed, and the process is repeated to build multilayers.

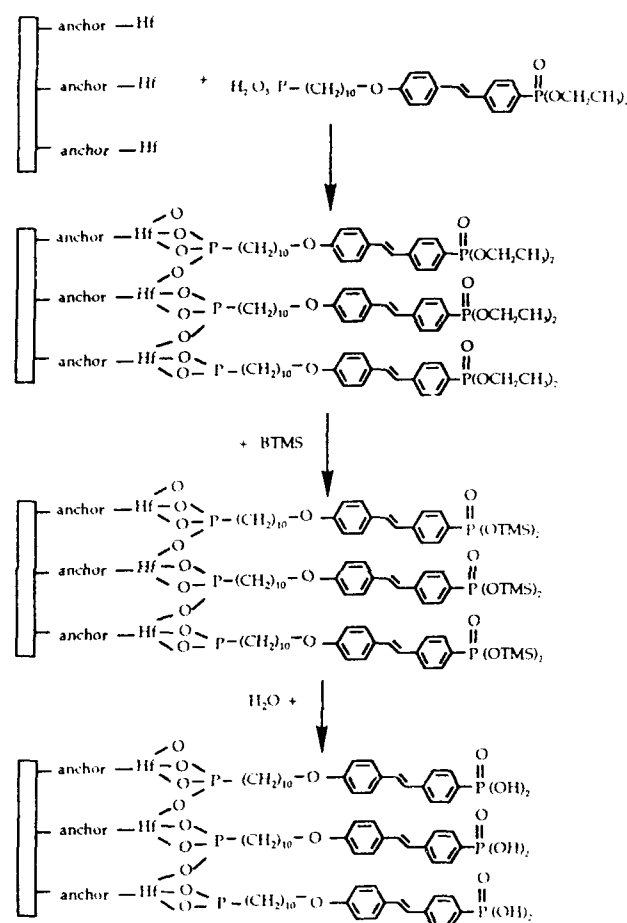


FIGURE 2 Reaction sequence for self-assembly of layers of Hf-(I)

A problem we have anticipated with this reaction sequence is the possibility that the steric bulk of the surface phosphonate esters (and of the trimethylsilane groups) may result in a less efficient deprotection than is normally obtained in solution. To maximize the extent of deprotection, we adopted a practice of sequentially deprotecting surface layers twice, rinsing in water between BTMS immersions.

EXPERIMENTAL

Materials

Hafnium oxychloride octahydrate was used as received from Teledyne Wah Chang Albany, Inc. 4-mercaptobutylphosphonic acid was provided by Prof. Thomas E. Mallouk (Penn. State Univ.). (I) was prepared by a several step reaction.⁷ 3-mercaptopropylsilane was used as received from Aldrich. In all preparations of multilayers and solutions, deionized water purified to a resistivity of 18 M Ω -cm with a Barnstead Nanopure II was used.

Substrates and surface functionalization

Gold substrates were prepared by evaporation of ~ 2000 Å of 99.99% pure gold wire (DF Goldsmith) onto single crystal silicon (100) wafers (Silicon Quest International). Prior to functionalization, silicon wafers were rinsed sequentially with trichloroethylene, 2-propanol and ultrapure water, each for 15 min. Prior to gold deposition, the Si wafers were pretreated with 3-mercaptopropylsilane, which acts as a molecular adhesive.⁸ After gold deposition, wafers were cleaned with a 3:1 H₂SO₄:H₂O₂ solution and rinsed with copious amounts of ultrapure water. To bind the 'anchor' layer, wafers were immersed in a 4:1 water/methanol solution of ~ 1 mM mercaptobutylphosphonic acid for over 24 h, then rinsed sequentially in methanol and water.

The silicon substrates utilized for ATR measurements are Si ATR crystals, of dimensions 50 x 10 x 3 mm, spp 45 degrees (Part # EE3132, Harrick Scientific Corp). These are first degreased as above, rinsed with water and dried in a stream of nitrogen. An anchor layer of Hf is deposited by immersion of the crystal in 5 mM HfOCl₂·8H₂O at 45° C for 48 hours,⁹ followed by rinsing with copious amounts of water and drying under flowing nitrogen.

Instrumentation and measurements

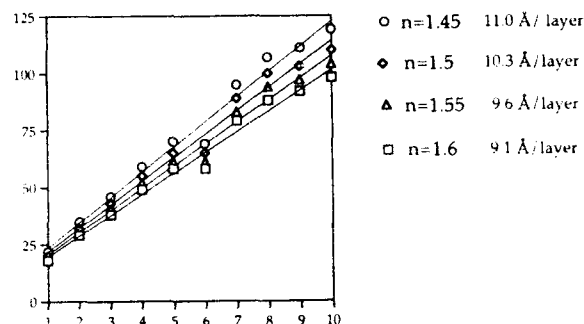
Ellipsometry measurements were taken on a Rudolph Research Thin Film Ellipsometer, Type 43702-200E, using a tungsten filament light source filtered to exclude all but 6328 Å light, at an incident angle of 70 degrees. Measurements were taken after deposition of (I) and after the deprotection steps. The measured parameters delta (Δ) and psi (Ψ) are used, along with various indices of refraction for the layered materials, to calculate layer thickness on DAFIBM, a program provided by Rudolph Research. The refractive indices of the gold substrate are calculated using Δ and Ψ values for the bare gold substrate and equations given in ref. 10. Diffuse reflectance FTIR spectra were taken on a Nicolet Magna-IR 550 Spectrophotometer with a Spectra Tech Inc. FT 80 Specular Reflectance 0014-305 attachment and OMNIC software. All spectra are the average of 1024 scans, with 4 cm⁻¹ resolution. The spectra are taken relative to a background of a bare gold prepared similarly to the wafer used for layering. These measurements were also recorded after deposition of (I) and deprotection steps. The spectra are baseline corrected with the OMNIC software to align all spectra to the same zero baseline. The attenuated total reflectance FTIR were taken on the same instrument with a Harrick Scientific Corporation Twin Parallel Mirror Attachment, Variable Angle Unit. The spectra shown are the average of 256 or 512 scans with 4 cm⁻¹ resolution, taken relative to a background scan from the bare crystal. They too are baseline corrected.

RESULTS

Shown below in Figure 3 are plots of calculated total layer thickness vs. number of deposited layers on a functionalized gold substrate. The values of refractive indices utilized to obtain these thicknesses have been chosen to include the range generally accepted for metal bisphosphonate

films, $1.55 < n < 1.45$.^{1,11} Individual layer thickness is given as the slope of calculated fits to this data.

FIGURE 3 Total Thickness vs. # of Layers



As can be seen from the slope of these plots, layering appears to be quite regular for the first five layers, and then appears to stop at step 6 (as layer thickness is the same for layers 5 and 6), and then to continue again at step 7 at roughly the same slope. We cannot be certain what is occurring here, but suggest that at step 6, little or no material adsorbs as a new layer but merely fills in gaps in the previous layer. Subsequent layering then resumes at the same rate. This also appears to occur at step 9, although to a lesser extent.

Also, the calculated layer thickness is much smaller than our estimate of ~ 30 Å for a layer in which the bisphosphonate (I) is oriented perpendicular to the substrate surface. We suggest that deprotection of the first (and probably subsequent) layer (s) is incomplete. Subsequent layers are then also incomplete and can tilt over at a much larger angle than would a densely packed layer. This would result in smaller layer thicknesses.

Figure 4 shows the diffuse reflectance FTIR spectra for up to 10 layers of Hf-(I) on gold for protected (a) and deprotected (b) layers. The region shown is that where characteristic C-H stretches occur. We assign the peak at ~ 2929 cm^{-1} as the asymmetric methylene stretch ($\nu_a \text{CH}_2$) and that at ~ 2855 cm^{-1} as the symmetric methylene ($\nu_s \text{CH}_2$). These peaks are shifted to higher energies, relative to location of such peaks for crystalline structures. Such a shift is characteristic of liquid-like structures.^{12,13} Note the fact that intensity level decreases upon deprotection, most notably in layer 7. This could support what was seen in the ellipsometry data, i.e. that no new material went down in step 6. Thus step 7 would be the deposition of layer 6 and IR spectrum intensity would increase over that of layer 5 only slightly. It is odd, however, that this seems to have "recovered" by layer 10, as also seen in ellipsometry.

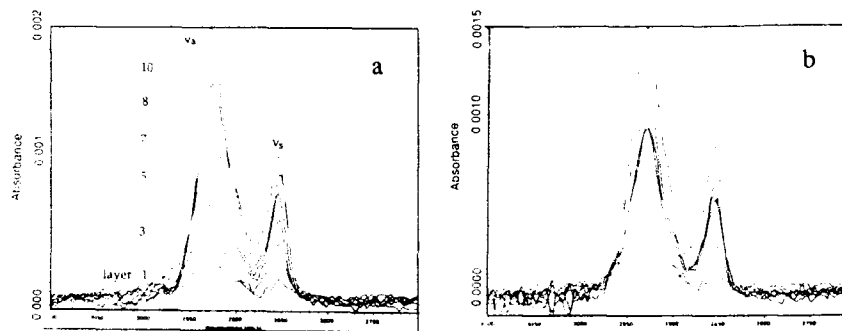


FIGURE 4 Diffuse Reflectance FTIR for layers of Hf-(I) on gold

Unfortunately no peaks from a methyl (CH_3) group were observed in this region. The methyl ester is the only group specific to the protected molecule (I) (see Figure 1). Inability to detect a distinct CH_3 stretch is probably due to this low intensity peak being obscured by the stronger, shifted CH_2 stretches.

We also were unable to observe a peak from the CH_3 rocking vibration at lower energies. This vibration was probably masked by the stronger stretches associated with P-O and P-O-C bonds. The region $800\text{--}1800\text{ cm}^{-1}$ where these peaks are expected is quite crowded and we could not reliably resolve or assign any peaks in this region.¹⁴

Figure 5 shows the Attenuated Total Reflectance FTIR spectra from two layers of Hf-(I) on a Si ATR crystal. The signal to noise is much higher with this method, and the spectra are much cleaner than those taken via diffuse reflectance. The small shoulder at $\sim 2980\text{ cm}^{-1}$ in the spectrum of the protected layer is probably due to a methyl stretch, since it is nearly absent in the spectrum of the deprotected layer. If this assignment is correct, this vibration will aid in assessing the deprotection process.

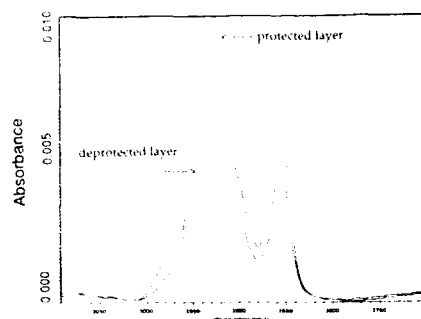


FIGURE 5
ATR FTIR for layers of
Hf-(I)

DISCUSSION

It is apparent from both ellipsometry and FTIR data that sequential deposition of Hf-(I) layers onto gold surfaces is occurring to some extent. Preliminary results indicate that these films do exhibit SHG¹⁵, confirming net polar orientation of (I) in the films. It also appears from ellipsometry, however, that these layers are quite thin. While thicknesses determined by ellipsometry are subject to several sources of error, the use of reasonable refractive indices for these films suggests the average layer spacing is $9.6\text{--}11.0\text{ \AA}$, which is significantly smaller than the length of (I), which we estimate to be 28.9 \AA .

We suggest that the deprotection of layers of (I) is incomplete as we currently perform the procedure. This is likely due to the steric bulk of both the phosphonate ester 'surface' in each layer and the trimethylsilane deprotection reagents. If this is the case, subsequent deposition would form incomplete layers, and films would become increasingly disordered as the number of layers increases. The apparently small layer thickness could be explained by a large tilt angle of the bisphosphonate molecules with respect to the surface normal, possibly resulting from a low density of bisphosphonate molecules in the organic layer. This data not only points to the necessity of a better deprotection method, but also indicates the need for another method of determining layer thickness. For this, we have attempted to observe grazing angle x-ray diffraction. However, we have been unable to detect any x-ray interference peaks from thin films on gold substrates. For multilayer films on silicon substrates, grazing angle diffraction generally gives an interference pattern from x-rays reflected off the front and back of the film, enabling an accurate determination of film thickness.¹¹ The inability to observe this for multilayers on gold is most likely a consequence of the positioning of the total reflectance peak from the gold, which tails to relatively high angles ($2\theta \sim 1.1^\circ$) and obscures any peaks from our films.

The FTIR data obtained using diffuse reflectance methods does tell us we are layering onto our substrates, but we were unable to obtain information confirming deprotection. For this reason

and because we were unable to obtain diffraction data from gold substrates, we began layering on silicon substrates and utilizing attenuated total reflectance FTIR. The spectra obtained thus far are somewhat encouraging. We believe we can detect at least one methyl peak. We expect to observe grazing angle x-ray diffraction from films with three or more layers, on the basis of experiments performed on similar thin films on silicon substrates.¹¹ The two layers we have assembled so far are still too thin to see by diffraction.

In order to improve the efficiency of the deprotection reaction, we are exploring the use of iodide salts to increase the rate of reaction in the BTMS deprotection.¹⁶ Other methods of hydrolysis, such as acid hydrolysis, will also be explored.

In summary, we have investigated the incorporation of 'asymmetric' bisphosphonate nonlinear optical chromophores into metal bisphosphonate multilayers. The approach we have taken shows promise, but more efficient deprotection strategies need to be developed for the asymmetric molecules employed in this study in order to make highly ordered multilayers with optimized nonlinear optical properties.

REFERENCES

1. a) H. Lee, L.J. Kepley, H.-G. Hong, T.E. Mallouk, J. Am. Chem. Soc. **110**, 618-620 (1988) b) H. Lee, L.J. Kepley, H.-G. Hong, S. Akhter, T.E. Mallouk, J. Phys. Chem., **92**, 2597-2601 (1988).
2. M.B. Dines, P.M. DiGiacomo, Inorg. Chem., **20**, 92-97 (1981)
3. H.E. Karz, G. Scheller, T.M. Putvinski, M.L. Schilling, W.L. Wilson, C.E.D. Chidsey, Science, **254**, 1485-1487 (1991)
4. G.A. Neff, unpublished results.
5. a) E. G. J. Staring, G. L. J. A. Rikken, C. J. E. Seppen, S. Nijhuis, and A. H. J. Venhuizen, Adv. Mat., **3**, 401 (1991) b) D. F. Eaton, G. R. Meredith, and J. S. Miller, Adv. Mat., **3**, 564 (1991) c) Wenjiang Nie, Adv. Mat., **5**, 520 (1993).
6. T. Morita, Y. Okamoto, and H. Sakurai, Bull. Chem. Soc. Japan, **51**, 2169-2170 (1978)
7. B. Klopfenstein and C.J. Page, in press.
8. C.A. Goss, D.H. Charych, and M. Majda, Anal. Chem. **63**, 85 (1991).
9. H.-G. Hong, D.D. Sackett, T.E. Mallouk, Chem. Mater., **3**, 521-527 (1991)
10. H.L. Tompkins, A User's Guide to Ellipsometry, (Academic Press, Inc., San Diego, CA, 1993), p. 36.
11. A.C. Zeppenfeld and C.J. Page, in press.
12. B.L. Frey, D.G. Hanken, and R.M. Corn, Langmuir, **9**, 1815-1820 (1993).
13. M.D. Porter, T. B. Bright, D. L. Allara, and C.E.D. Chidsey, J. Am. Chem. Soc., **109**, 3559-3568 (1987)
14. H.C. Yang, K. Aoki, H. Hong, D.D. Sackett, M.F. Rendt, S. Yau, C.M. Bell, and T.E. Mallouk, J. Am. Chem. Soc., **115**, 11855-11862 (1993).
15. We have observed SHG from these films, but experimental details and substrate inconsistencies limit our quantification of signal at this time.
16. T. Morita, Y. Okamoto, and H. Sakurai, Bull. Chem. Soc. Jpn., **54**, 267-273 (1981)

CHARACTERIZATION OF SILICON NANOPARTICLES PREPARED FROM POROUS SILICON

RICHARD A. BLEY*, SUSAN M. KAUZLARICH*, HOWARD W. H. LEE†, JEFFREY E. DAVIS‡

* Department of Chemistry, University of California, Davis, CA 95616

† Lawrence Livermore National Laboratory, Livermore, CA 94550

‡ Department of Applied Science, University of California, Davis, CA 95616

ABSTRACT

Nanometer sized silicon particles have been produced by ultrasonic dispersion of thin sections of porous silicon in organic solvents. High resolution TEM and FTIR have been used to establish the size range and surface structure/composition of these particles. The larger particles, which range in size from 20 to 50 nm, are made up of a conglomeration of smaller particles with a diameter of a few nanometers. The HRTEM shows an amorphous layer on the surface of many of the clusters. FTIR data suggest this amorphous layer is silicon-dioxide which may also have organic constituents.

INTRODUCTION

Production of luminescent colloidal suspensions of Si from porous silicon (PS) by ultrasonic fracture [1,2] provides an opportunity to investigate the mechanism involved in the luminescence of PS. It is still unclear whether this is due to quantum confinement of the electron and its respective hole, the so-called particle in a box condition, or if this is due to some other silicon compound such as siloxene ($\text{Si}_6\text{O}_3\text{H}_6$) [3,4,5]. Characterization should also help establish whether the existence of a surface layer of SiO_2 is necessary for high efficiency luminescence to occur as has been suggested [6,7]. Until recently, Si semiconductor nanocluster synthesis has not been pursued as vigorously as other semiconductor nanoclusters such as the II-VI and III-V materials. This is most likely due to the difficulties involved in synthesizing discrete Si clusters. However, in 1990, when Canham [8] first pointed out the importance of visible photoluminescence in PS and suggested that this may be the result of a quantum confinement effect, interest in nanometer sized silicon clusters greatly increased. Some of the methods which have been used to synthesize Si nanoclusters include thermal pyrolysis [9], evaporation and laser ablation into an inert atmosphere [10,11,12,13], and high pressure solution phase synthesis [14]. Generally a wide size range is obtained with these methods including the technique of ultrasonic fracturing [1]. To date the technique which has produced Si nanoclusters of the most uniform size involves a high temperature pyrolysis where the Si clusters are prepared as an ethylene glycol colloid [7].

In our continuing investigation of the production of nanometer sized Si clusters from colloidal suspensions of PS, we have broadened the parameters under which we had previously carried out these experiments [2]. By using ethanol in the anodization solution, and increasing the anodization times, it is hoped that smaller, more uniform crystallites can be obtained. This paper describes the FTIR and HRTEM characterization results of Si colloids produced under several different conditions. The photoluminescence spectroscopy of these materials will be reported elsewhere in this publication [15].

EXPERIMENTAL

The PS samples were formed by anodizing p-type (B-doped) (100) oriented silicon wafers with resistivity of 14 - 22 Ωcm in 20% HF solutions. Parameters used in the synthesis of the clusters are given in table I. Anodization took place over 20 or 180 minutes with a constant

Table I. Parameters Used to Prepare Colloidal Si From PS.

HF (%)	Ethanol (%)	Current Density (mA/cm ²)	Anodization Time (min.)	Colloid Solvent	Sonification Time (days)
20	0	20	20	acetonitrile	1
20	0	20	20	acetonitrile	2
20	0	20	20	acetonitrile	5
20	0	20	20	acetonitrile	7
20	10	20	20	acetonitrile	7
20	10	20	20	toluene	7
20	30	20	20	acetonitrile	7
20	30	20	20	toluene	7
20	30	5	180	acetonitrile	7
20	30	7.5	180	acetonitrile	7
20	60	5	180	acetonitrile	7

current density of 5, 7.5 or 20 mA/cm². The 20% HF solutions contained 0, 10, 30 or 60% ethanol by weight with a corresponding amount of water making up the remainder of the solution. With some samples a second electrochemical etch was performed using a 1% HF solution of HF/H₂O with a current density of 160 mA/cm² for one minute to separate the anodized PS layer from the Si substrate.

The samples were then rinsed with deionized water and dried under a stream of N₂ gas and placed in a vacuum chamber. The chamber was evacuated to 70 mtorr for several hours to help facilitate the removal of water and the samples were brought into a solvent-free drybox. The PS was mechanically removed from the Si substrate. The resulting material was collected in a side arm shlenke flask. Approximately 10 ml of solvent (acetonitrile or toluene) which had been dried over calcium hydride, distilled and degassed, was added to the flask containing the P. The mixture was placed in a Branson Ultrasonic bath for up to 7 days. Upon removal from the ultrasonic bath the solution was allowed to settle and the resulting supernatant was removed for study.

UV-Vis spectra were obtained of the solutions several times during their sonication with a Hewlett-Packard 8450A diode-array spectrophotometer. FTIR spectra were collected for the PS powders before sonication by combining the powder with KBr for making a KBr pellet. An equal mass of KBr was used as a reference. IR spectra of the colloid solutions were obtained both by evaporation of the colloid solvent on a CsI salt plate and from a solution cell made of two KBr salt plates. All of these spectra were collected on a Mattson Galaxy series FTIR 3000.

HRTEM samples were prepared by evaporation of the colloid solution on lacy carbon-coated electron microscope grids. The high resolution transmission electron microscope (HRTEM) was a 200CX HREM which operated with an accelerating voltage of 200 kV.

RESULTS AND DISCUSSION

An expansion of our experimental parameters from previous work was purposely undertaken in order to determine the most appropriate conditions for creating the PS colloid with the most uniform structure and smallest size range distribution. Table I shows the parameters used in the preparation of the PS colloid. The addition of ethanol to our anodic solution and the increase in anodization times over our previously reported work was performed in hopes of making more uniform crystallites with a greater proportion in the smaller size range where the crystallite diameter does not exceed the exciton diameter of silicon (about 10 nm). HRTEM studies carried out on the PS colloid samples made only with HF and water showed a wide range of particle sizes (20 - 50 nm) and shapes with few particles in the smaller ranges. The samples prepared with ethanol in the anodization step, however, have produced a significant fraction of the smaller nanometer-sized particles with sizes ranging from 7 and 40 nm. Even smaller

particles have been observed in the electron microscope from these samples made in ethanol but the lattice fringes have not been resolved. These particles range in size from 2 to 10 nm and seem to occur only in the presence of other larger crystallites. Because the crystallites seem to adhere to the grid only in areas absent of holes, the lattice fringes and diffraction patterns of these smaller particles have not been obtained.

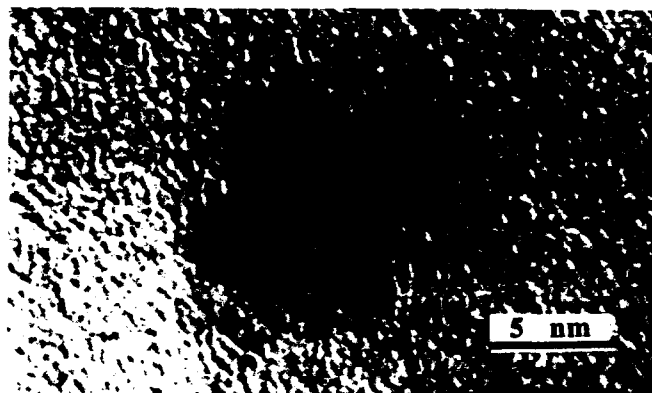


Figure 1. High-resolution TEM micrograph of a Si nanocluster. The lattice spacing of 0.31 nm indicates this is a view down a $\langle 110 \rangle$ axis showing the $\{111\}$ interplanar spacings.

Figure 1 shows an electron micrograph of a particle around 8 nm. This was obtained from a colloid solution made with 60% ethanol in the anodization solution, a current density of 5 mA/cm², and an anodization time of 180 minutes. Its diffraction pattern and lattice spacing of 0.31 nm suggest that the $\{111\}$ planes are responsible for the visible fringes in the micrograph. Figure 2 shows a much larger particle of around 40 nm from the same colloid solution.

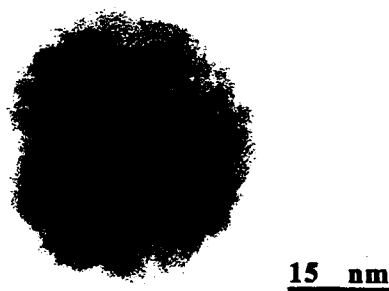


Figure 2. High-resolution TEM micrograph showing a conglomeration of individual Si crystallites. An amorphous layer of between 3 to 4 nm surrounds the entire structure.

The lattice fringes suggest that this is not a single particle, but a conglomeration of several smaller particles. The electron diffraction pattern for this cluster shows diffraction spots and can be interpreted as arising from several crystallites of different orientations. The smaller particles making up the cluster are around 7 to 11 nm. This picture typifies the general structure of the larger clusters in that they are made up of smaller crystallites which have conglomerated together. Whether it is chemical bonding or Van der Waals forces holding the crystallites together is not known. As can be seen from the micrograph in figure 2 an amorphous layer surrounds the entire structure demonstrating that a separate morphology exists at its surface. Whether this layer is only on the surface of the conglomeration or is also present around the entire surfaces of the individual crystallites can not be determined from the micrograph.

Detailed IR experiments on the different PS samples were carried out before and after ultrasonification to help determine the composition of the amorphous surface layer. The PS, removed from the wafer, was mixed with ground KBr and pressed into a pellet. Figure 3 shows the IR of a PS sample made from an anodic HF solution having 30% ethanol, a current density of 5 mA/cm², and an anodization time of 180 minutes.

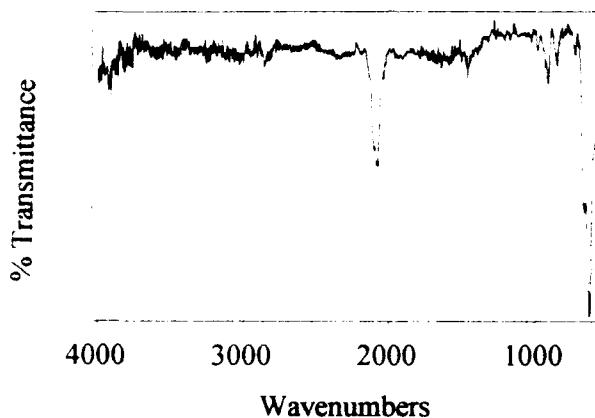


Figure 3. FTIR spectra of PS sample made with 30% ethanol in the HF solution. A current density of 5 mA/cm² was used with an anodization time of 180 min.

This spectra was taken after the sample was in a solvent free drybox for 24 hours. The three prominent features of this spectra are the Si-H stretching at 2073 cm⁻¹ and the Si-H bending and wagging modes at 902 and 661 cm⁻¹ respectively [16].

Figure 4 shows a typical IR of the sonicated colloidal Si suspension after evaporation of the solvent on a CsI salt plate. The Si-H peaks have disappeared completely and new peaks arise in the hydrocarbon region of the spectrum around 2958, 2927 and 2856 cm⁻¹. In addition, a Si-O stretching peak at 1087 cm⁻¹ is present. It has been suggested that the hydrocarbon peaks which often appear in IR spectra of PS samples are due to alcohol (generally ETOH) residue left by the anodization solution [17]. As can be seen in Figure 3, no such peaks are present for the PS sample prepared with HF/ ETOH. These peaks are present in our PS samples made only with HF and water after brief periods of exposure to air. This suggests that the presence of the hydrocarbon constituents is not due to the use of alcohol in the anodization step. We have found that after brief exposure to air the PS samples show hydrocarbon contamination, even when

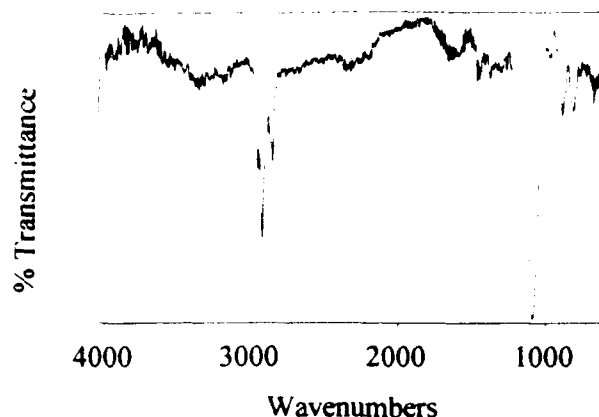


Figure 4. FTIR spectra of colloidal Si suspension after evaporation of solvent.

alcohol is not used in the anodization process. The appearance of these hydrocarbon peaks is greatly slowed if the PS sample is kept in a solvent free drybox under N_2 . However, these peaks begin to appear even under solvent free conditions. This pattern of Si-H peak disappearance along with Si-CH₃ and Si-O peak appearance is seen for all PS samples regardless of the anodization conditions. The samples were monitored by IR over time and intermediate spectra where both sets of peaks are present were collected. IR spectra of the acetonitrile colloid showed an -OH stretch in addition to the Si-CH_x ($x = 1$ to 3) and Si-O peaks. This alcohol must be produced in the colloid solution during the sonication step. At the present time, it appears that even under rigorously dry anaerobic conditions O_2 is still present in large enough amounts to form Si-O on the nanoclusters and the alcohol in the colloid solution. Further studies are underway to better characterize the Si colloid solutions prepared from PS.

ACKNOWLEDGMENT

We thank R. L. Smith for the use of the Potentiostat/Galvanostat. Thanks also to R. L. Smith, J. Penczek, and M. L. S. Olsen for useful discussion. We thank C. Nelson and F. Ross of the National Center for Electron Microscopy, Lawrence Berkeley Laboratory, for their assistance with the HRTEM. This work was supported by the National Science Foundation (DMR-9201041), and performed under the auspices of the U. S. Department of Energy by Lawrence Livermore National Laboratory under contract No. W-7405-ENG-48.

REFERENCES

1. J.L. Heinrich, C.L. Curtis, G.M. Credo, K.L. Kavanagh, M.J. Sailor, *Science* **255**, 66 (1992).
2. S. Berhane, S.M. Kauzlarich, K. Nishimura, R. L. Smith, J.E. Davis, H. W. H. Lee, M. L. S. Olsen, L. L. Chase, *Mat. Res. Soc. Symp. Proc.* **298**, 99 (1993).
3. S.M. Prokes, *J. Appl. Phys.* **73**, 407 (1993).

4. H.D. Fuchs, M.S. Brandt, M. Stutzmann, J. Weber, *Mat. Res. Soc. Symp. Proc.* **256**, 159 (1992).
5. M.J. Sailor, K.L. Kavanagh, *Adv. Mater.* **4**, 432 (1992).
6. S.M. Pillai, Z.Y. Xu, M. Gal, R. Glaisher, M. Phillips, D. Cockayne, *Jpn. J. Appl. Phys.* **31**, L1702 (1992).
7. K.A. Littau, P.J. Szajowshki, A.J. Muller, A.R. Kortan, L.E. Brus, *J. Phys. Chem.* **97**, 1224 (1993).
8. L.T. Canham, *Appl. Phys. Lett.* **57**, 1046 (1990).
9. J.J. Wu, R.C. Flagan, *J. Appl. Phys.* **61**, 1365 (1987).
10. S. Hayashi, S. Tanimoto, K. Yamamoto, *J. Appl. Phys.* **68**, 5300 (1990).
11. R. Okada, S. Ijima, *Appl. Phys. Lett.* **58**, 1662 (1991).
12. S. Ijima, *Jpn. J. Appl. Phys.* **26**, 357 (1987).
13. Y. Saito, *J. Cryst. Growth* **47**, 61 (1979).
14. J.R. Heath, *Science* **258**, 1131 (1992).
15. H. W. H. Lee, J. E. Davis, M. L. Olsen, S. M. Kauzlarich, R. A. Bley, S. Risbud, D. Duval, *Mat. Res. Soc. Symp. Pro.* This volume.
16. P. Gupta, V. L. Colvin, S. M. George, *Phys. Rev. B* **37**, 8234 (1988).
17. A. Borghesi, A. Sassella, B. Pivac, L. Pavesi, *Solid State Commun.* **87**, 1 (1993)

SYNTHESIS OF LOW DENSITY MICROCELLULAR ACTIVATED CARBON SUPPORTED NANOPHASE Pt AND Pd PARTICLES AND STUDY OF ITS CATALYTIC PROPERTIES

HONG-MING LIN, CHING-SHUNG HUANG, CHI-MING HSU

Department of Materials Engineering, Tatung Institute of Technology, Taipei, Taiwan, R O C.

ABSTRACT

The use of activated low density microcellular carbon (LDMC) as a catalysis supporter for nanophase Pt or Pd particles has been successfully developed in this study. The good dispersion and interfacial properties of nanophase Pt or Pd particles on activated LDMC are formed by using an impregnation and sintering process. The interfacial structures are examined by TEM, HRTEM and an image analyst system. No preferred orientation of interfacial bonding has been found between nanophase Pt and activated LDMC. The activated LDMC supported Pt or Pd catalysts have the high reactivity which can complete hydrogenation and oxidation of CO gas at low temperatures (<453 K). The catalytic activity of CO hydrogenation is increased as the size of the nanophase Pt and Pd particles decreases.

INTRODUCTION

Nanocrystalline (NC) catalysts have limitations in actual applications. NC particles will sinter or weld from the heat released in a chemical reaction without a good supporter. At the same time, they do not have enough mechanical strength to fight against environmental failure. A suitable supporter is therefore necessary for NC catalytic particles [1, 2].

Low density microcellular materials (LDMM) were developed by the U.S. Department of Energy (DOE) National Laboratories [3]. Because of its low atomic number, good chemical corrosion resistance, low thermal expansion and great carrying areas properties, the activated low density microcellular carbon (LDMC) is used as a precursor for NC catalyst particles in this study. Carbon supported catalysts were found to be more active than the silica, molybdenum oxide and alumina supported catalysts in the low temperature range ($T < 473$ K) [4-7]. In the past, alumina supported metal halide catalysts were used by Todo et al. [8], carbon supported copper oxide catalysts were employed by Nozaki et al. [9], and a catalyst contained vanadium on both activated carbon and titania/carbon was developed by Kasaoka et al. for low temperature applications [10].

Although carbon, especially in the form of activated carbon, had been used in many studies as supporter for noble metal catalysts, there has not been any study on the effects of the activated LDMC structure on the dispersion and activity of NC Pt and Pd particles and on the selective catalytic oxidation or hydrogenation of CO. We therefore report the results of such a study here.

EXPERIMENTAL

The pure platinum and palladium particles with diameters of less than 20 nm, have been produced by gas-evaporation in a helium atmosphere [11]. The size of these NC particles are controlled by changing the different helium pressure, evaporation rates of the metals, and the distance between the evaporated tungsten boat and the collecting cold trap.

Two kinds of solutions are used as precursors to synthesize LDMC. One is a resorcinol/formaldehyde (RF) solution, and the other is a styrene/divinylbenzene (PS) solution. The volume ratio of RF to PS is fixed at one and the acetone used is kept between a range of 30 to 60 vol% to induce inverse emulsion and cross linking polymerization. The maleic anhydride and benzoylperoxide are used as catalysts for polymerization. The pre-LDMC polymers are carbonized in N_2 gas at 1173 K for two hours. LDMC is then activated in carbon dioxide at 1173 K for 9 hours to form activated LDMC.

To combine the NC Pt or Pd particles with activated LDMC supporter, the pores of LDMC by acetone solvent are impregnated into the NC particles. The NC particles are then trapped on the wall of pores by small electrostatic forces or van der Waals forces. A suitable sintering temperature (873K) and three different sintering times 30, 60, and 90 minutes are used to form a good bond between the NC particles and supporters.

The morphology and structure of the NC particles are examined using TEM image and diffraction patterns. The interfacial properties and dispersion of Pt and Pd, which are supported on activated LDMC, are analyzed using a JEOL 4000-EX HRTEM and the Image Analyst System MATROX MVP-AT + IPPLUS.

The catalytic behavior of the hydrogenation or oxidation of CO is studied at 0.03 MPa in a small plug-flow column reactor under different reaction conditions. A 206 SCCM flow rate with a volume ratio of H_2 :CO equal to 3:6:1 or 200 SCCM flow rate of 1% CO is passed through the sample. After 2 minutes of reaction, the products are periodically analyzed using SHIMADZU GC-6MA gas chromatography to measure the amount of unreacted CO. The data are used to determine the activity of the Pt/activated LDMC catalyst or Pd/activated LDMC catalyst.

RESULTS AND DISCUSSION

A. Structures and Sizes of Nanocrystalline Particles

TEM micrograph of NC Pt particles produced in different helium pressures are shown in Figure 1. The images indicate that the shape of NC Pt particles are almost spherical with a clean particle surface. The particle size of Pt becomes larger as the helium pressure increases. The helium pressure in this study was kept in a range from 1 mbar to 100 mbar. Under the same helium pressures, NC Pd always has a greater mean particle size than that of Pt. This result is due to the higher evaporation rate of Pd than that of Pt at the same temperature.

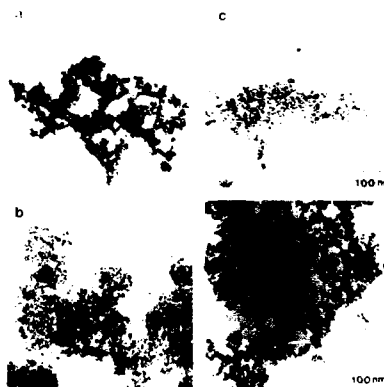


Figure 1: TEM images of NC Pt produced under helium pressure of (a) 1 mbar, (b) 10 mbar, (c) 50 mbar and (d) 100 mbar.

B. Characterization of LDMC Supports

The pore morphologies in pre-LDMC polymer are quite different from different viscosities. In this study, the viscosities vary by the vol% of acetone in the mixed solution of RF/PS. The results indicate that adding 40 vol% acetone polymerization will produce 72% porosity and 0.19 g/cm³ bulk density, which would indicate that LDMC is a good supporter. The variation of physical properties when changing the vol% of solvent is shown in Figure 2. Although adding 50 vol% of acetone will create a better porosity, its mean pore size measured by using SEM images, is too large to be a good catalysts supporter.

The LDMC40 (synthesized by adding 40 vol% acetone during polymerization) has the lowest bulk density, but not than the highest porosity. This is due to the fact that close pores still exist in LDMC40. The porous morphologies of various LDMC are shown in Figure 3. When the solvent is increased to 60 vol% during the polymerization, the spherical porous

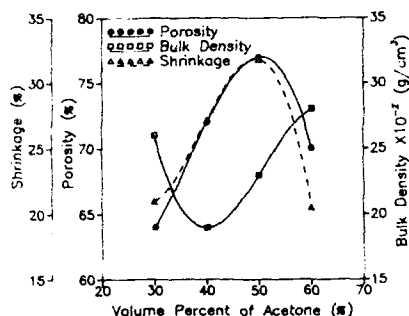


Figure 2 : Physical properties of activated LDMC with different vol% of acetone.

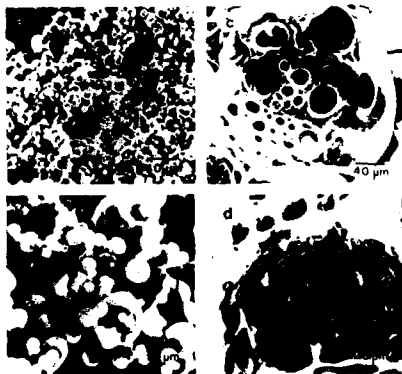


Figure 3 : The porous morphologies of activated LDMC produced by adding (a) 30 vol%, (b) 40 vol%, (c) 50 vol%, (d) 60 vol% of acetone.

structure is destroyed completely and a close-packed sheet structure is formed. This result in a lower porosity and higher bulk density for LDMC60.

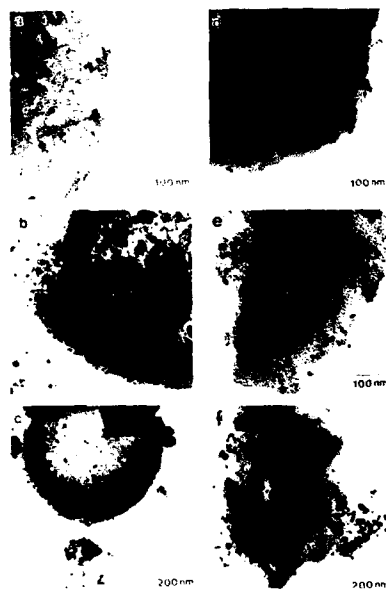


Figure 4 : TEM images of Pt/LDMC under sintering time of, (a) 30 minutes, (b) 60 minutes, and (c) 90 minutes at 873 K and TEM images of Pd/LDMC under sintering time of, (d) 30 minutes, (e) 60 minutes, and (f) 90 minutes at 873 K.

The chemical adsorption ability of LDMC will be improved and increased by activation. According to the activation process, many micropores and mesopores are created on the surface of LDMC, and the inside surface of inside activated LDMC increases quickly. The specific surface area ($1095.79 \text{ m}^2/\text{g}$) of activated LDMC which is measured by BET is thirty five times that of non-activated LDMC.

C. Sintering Effects

A sintering process is used to bond the NC Pt or Pd particles to the activated LDMC supporter. The interfacial bonding between the impregnated nanosize particles and supporter is formed in the sintering process. The strength of the bonding increases with an increase of the sintering time at 873K . But in order to avoid dispersion reduction, activity and selectivity of the catalyst as well as the conditions of sintering are carefully selected. In this study, a persistent and high dispersion supported catalysts was produced. Figure 4 shows the morphologies of NC Pt and Pd particles coated on the activated LDMC supporter having different sintering times.

D. Interfacial Analysis

The interfaces formed between the nanosize Pt catalyst and activated LDMC supporter were studied. Using JEOL 4000-EX HRTEM, the lattice fringe image of NC Pt particles were obtained and are shown in Figure 5. When the NC Pt particles are bound to an amorphous activated LDMC supporter, the interfaces form at different Pt planes. The diffraction pattern at the corner of Figure 5 was obtained from the Fourier transformation of the lattice image by Image Analyst System. For nanosize Pt particles, the atoms can slip more easily during surface diffusion

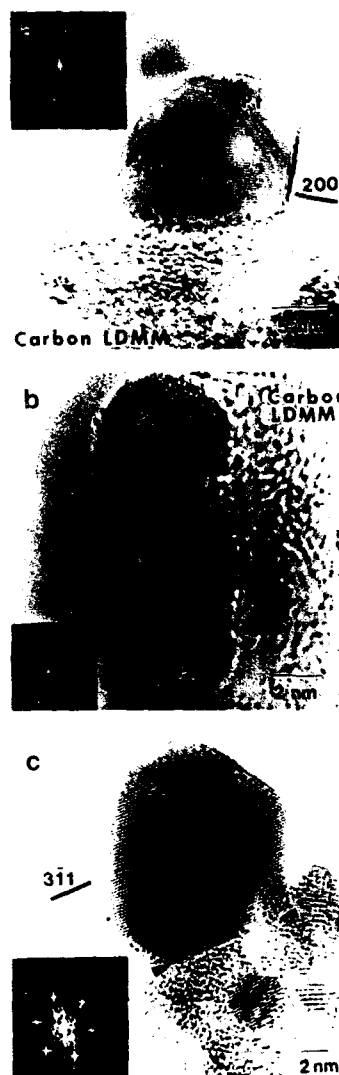


Figure 5 : Three different interfaces between NC Pt particles and activated LDMC supporter observed by HRTEM.

and form bonds more easily with the amorphous structure of activated LDMC using a low sintering temperature in different lattice planes. No preferred orientation of interfacial bonding have been found in Pt/LDMC material. The atomic image in Figure 6 indicates that the sintered NC Pt particles have many steps on the surface which will increase the catalytic activity.

E. Characterization of the Catalysts

The catalytic activity and selectivity of nanosize Pt and Pd particles supported on low density microcellular activated carbon are examined by gas chromatography. The dependence of catalytic activity for the CO hydrogenation on the particle size of Pt or Pd is shown in Figure 7 and 8. The catalytic activity for CO hydrogenation increases with decreasing particle size of Pt or Pd. This means that the low density microcellular activated carbon supported NC Pt or Pd catalyst activity for the CO hydrogenation reaction is sensitive to structure

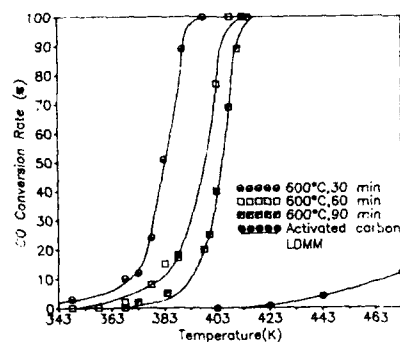


Figure 7 : CO conversion rates as the function of the reaction temperature for CO hydrogenation of Pt/activated LDMC catalysts under different sintering time at 873 K.

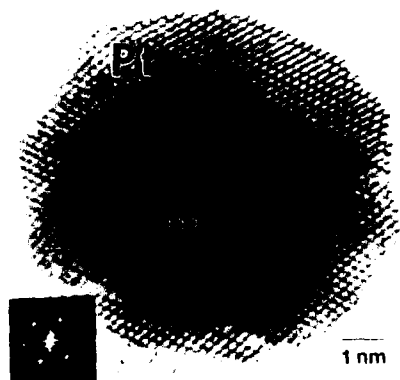


Figure 6 : HRTEM observation of a sintered NC Pt particles (873 K, 60 minutes) with step structure on the surface.

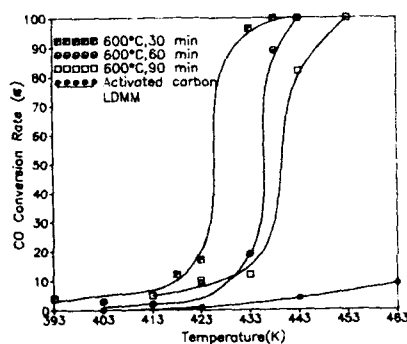


Figure 8 : CO conversion rates as a function of the reaction temperatures for CO hydrogenation of Pd/activated LDMC catalysts under different sintering time at 873 K.

CONCLUSIONS

The results of this study are summarized as follows.

1. NC Pt or Pd mean particle size and size distribution are increased and broadened, respectively, with increasing helium pressure during evaporation.
2. The pore structures of LDMC are changed by adding acetone in polymerization process. The best porous structure, which has 72% porosity and 0.19 g/cm³ low density, is obtained by adding 10vol% acetone during polymerization. Activation of LDMC will create micropores and mesopores on the surface of carbon.
3. Nanosize Pt and Pd particles bond to the activated LDMC supporter at low sintering temperature. No preferred orientation between Pt and activated LDMC is formed.
4. The structure sensitive reaction of NC Pt/activated LDMC catalyst for CO by $\text{CO} + \text{H}_2 \rightarrow \text{CH}_4 + \text{H}_2\text{O}$ indicated that a smaller particle will have a higher catalytic activity and similar behavior also occurs in NC Pd/activated LDMC catalyst. In this study, the reactivity of NC Pt and Pd/activated LDMC catalysts were much higher than that of conventional materials. Also, the 100% CO conversion rate is achieved below 453 K.

ACKNOWLEDGMENTS

We would like to thank the National Science Council, Republic of China for financial support through Contract Number NSC 82-0405-E-036-032.

REFERENCES

1. G. A. Somorjai, *Catal. Rev.*, **7** (1972) 87.
2. Y. Takasu, R. Unwin, B. Tesche, A. M. Bradshaw and M. Grunze, *Surf. Sci.*, **77**(1978)219.
3. J. D. Lemay, R. W. Hopper, L. W. Hrubesh, and R. W. Pekala, *MRS Bulletin/December*, (1990) 19-41.
4. H-J Jung, P. L. Walker Jr. and M. A. Vannice, *J. Catal.*, **75** (1982) 416.
5. F. Rodriguez-Reinoso, I. Rodriguez-Ramos, A. Guerrero-Ruiz, and J. D. Lopez-Gonzalez, *Appl. Catal.*, **21** (1986) 251.
6. H-J Jung, M. A. Vannice, L. N. Mulay, R. M. Stanfield, and W. N. Delgass, *J. Catal.*, **76** (1982) 208.
7. J. J. Venter, M. Kaminsky, G. L. Geofroy, and M. A. Vannice, *J. Catal.*, **103** (1987) 450.
8. N. Todo, N. Nishijima, A. Ueno, M. Kurita, H. Hagiwara, T. Sato and Y. Kiyozumi, *Chem. Lett.*, (1976) 897.
9. S. Kasaoka, E. Sasaoka and H. Iwasaki, *Bull. Chem. Soc. Jpn.*, **62** (1989) 1226.
10. A. A. Chen, M. A. Vannice, and J. Phillips, *J. Phys. Chem.*, **91** (1987) 6257.
11. Hong-Ming Lin, Shu-Huei Hsieh, Pee-Yew Lee, Ming-Shung Lai and Jie-Shing Wu, *Materials Chemistry and Physics*, **34** (1993) 205-213.

EXFOLIATION OF MoS₂ CATALYSTS: STRUCTURAL AND CATALYTIC CHANGES

M. DEL VALLE*, M. AVALOS-BORJA**, J. CRUZ*** AND S. FUENTES**

*Centro de Investigación Científica y de Educación Superior de Ensenada, Ensenada, B. C., Mexico, and UABC, Department of Chemistry, Tijuana, B. C., México.

**Instituto de Física-UNAM, Apdo. Postal 2681, Ensenada, B. C., 22800, México

***UABC, Department of Chemistry, Tijuana, B. C., México

ABSTRACT

A study of the microstructural differences between exfoliated and non-exfoliated MoS₂-based materials is presented, relating them to differences in their catalytic activity. Both commercial (crystalline) MoS₂ and molybdenum sulfide catalysts prepared by thiosalt decomposition are subjected to chemical exfoliation reported to separate MoS₂ monolayers from the original structure. Electron microscopy results show that the chemical treatment yields non-typical MoS₂ nanostructures. Average surface area is also modified by exfoliation. The thiophene HDS activity of commercial MoS₂ increases after exfoliation, while it decreases after exfoliation in the case of MoS₂ catalysts.

INTRODUCTION

Over the years, molybdenum disulfide-based catalysts have proven to be of the utmost importance in industrial hydrotreating processes. However, a clear picture of the structure-activity relationship in these catalysts remains elusive. The main difficulty in this regard has been the anisotropic structure of these materials. Fundamental research studies have already recognized important features related to the chemical reactivity of edge planes [1-3], which contrast with the demonstrated inertness of basal planes [4,5]. The edge planes have been identified as the active sites for several reactions, including hydrodesulfurization [6], hydrogenation [7], isomerization [8] and hydrodenitrogenation [9]. Recently, Eijsbouts et al. [10] have shown that the hydrodesulfurization and hydrodenitrogenation activities of molybdenum disulfide promoted catalysts are proportional to the degree of dispersion of MoS₂ and that, consequently, the loss of activity with time on stream is due to a loss of dispersion.

Divilgapitiya et al. [11] have developed a method of exfoliation that allows the dispersion of molybdenum disulfide crystallites leading to single-layer materials. Chemical exfoliation of crystalline MoS₂ was first reported by Joensen et al. [12]. Since significant structural modification occurs as a result of the exfoliation procedure, we decided to study its effect on the HDS behavior of the crystalline MoS₂ as compared with that of exfoliated molybdenum sulfide catalysts.

Observed changes in structure and activity could then be related to the broader question of the HDS reaction mechanism in MoS₂ catalysts.

EXPERIMENTAL

Unsupported molybdenum sulfide catalysts were obtained by thermal decomposition of ammonium thiomolibdate (ATM), according to a known method [13]

Samples of commercial MoS₂ crystalline powder (Johnson-Matthey, 97%+) and the molybdenum sulfide catalysts were treated according to the exfoliation procedure outlined by Joensen et al. [12]. First, a solution of n-Butyllithium in hexane (50% molar excess) was added under inert atmosphere to a given amount of the molybdenum sulfide, initiating a vigorous exothermic reaction. After 48 h, the lithium-intercalated material was filtered and washed of excess reagent, then made to react with water to yield the exfoliation product, which was recovered by filtration and left to dry in the glovebox. In the case of the commercial MoS₂, after reaction with water the samples were centrifuged at 3500 rpm for 10 min, thus obtaining a "light" fraction in the supernatant and a "heavy" fraction in the sediment, which were then separated, filtered and dried.

All the HDS catalytic activities of the samples were obtained in a high-pressure flow microreactor, under differential reactor conditions. A thiophene/H₂ mix was fed through the reactor at a flow rate of 100 mL/min, under 2067 kPa and reactor temperature of 453-483 K; typical sample loads were 0.15 g. Rate constants were calculated from the consumption of thiophene, which was followed using a Varian 5000 gas chromatograph with a Chromosil 330 packed column and Spectra-Physics Integrator.

The microstructure and electron diffraction patterns of the exfoliated and non-exfoliated MoS₂ samples were observed using a JEOL 100C transmission electron microscope. Standard multipoint BET specific area measurements were done on a Gemini 2060 surface analyzer, using nitrogen as adsorbate. Samples were degassed at 473 K with argon flow for 2 h prior to analysis.

RESULTS

A typical view of MoS₂ crystals under high resolution conditions is shown in Fig. 1. The lattice resolution of (002) planes in a large crystal is clearly identified and shows the characteristic layered structure of the MoS₂-2H structure (hcp). At the border of the crystal, the formation of a step due to a stacking fault is observed. This kind of defect is very common in MoS₂ crystals, as reported earlier [14].

High resolution images of the samples of exfoliated crystals after sedimentation are shown in Fig. 2 and 3a. In the first image we observe a wide view of the sediment. The remains of a large crystal are shown in the center of the picture, where some (002) lattice planes are still evident, but in general a great deal of disorder prevails in the material. The presence of black spots over the entire image suggests the presence of small crystallites offering different orientations with respect to the electron beam. Fig. 3a shows a bright field image of the product of exfoliation found in the supernatant after centrifugation. It is formed mainly by small crystallites with a nearly spherical shape, their typical sizes ranging between 5-25 nm. The dark field image taken under

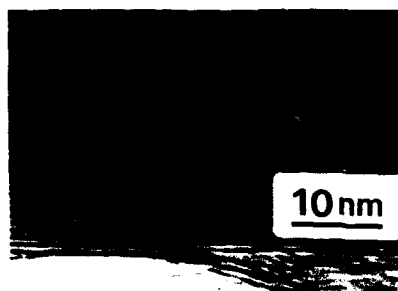


Fig. 1. High resolution bright field image of crystalline MoS_2 showing (002) planes.



Fig. 2. Bright-field image of the sediment of exfoliated MoS_2 showing the remains of a large crystal.

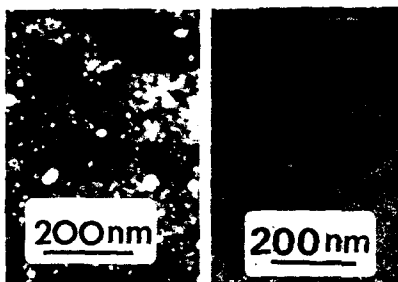


Fig. 3a and 3b. Bright-field and dark-field images of the "particulated phase" separated by centrifugation after exfoliation.

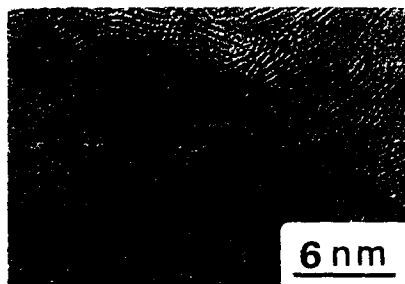


Fig. 4. High-resolution bright-field image of the MoS_2 catalyst obtained by ATM decomposition showing the "poorly crystalline" structure.

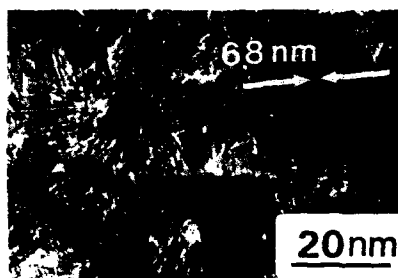


Fig. 5. High-resolution bright-field image of the exfoliated MoS_2 catalyst.

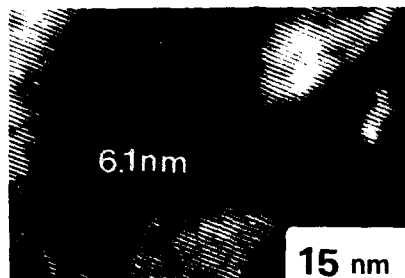


Fig. 6. High-resolution dark-field image of a particle obtained after exfoliation of the MoS_2 catalyst showing (002) planes.

weak beam conditions [15] allows the identification of thickness fringes, which suggest that most of the particles are three-dimensional (Fig. 3b).

Figure 4 is a bright field image of the catalyst obtained by decomposition of ATM under a gas mixture $\text{H}_2\text{S}(15\%) / \text{H}_2$. The image shows a very irregular structure with stacks of (002) planes in all directions. This structure has been called the "poorly crystalline" phase of molybdenum disulfide because it gives very weak and broad lined X-ray spectra [16] and a multiple ring pattern by electron diffraction [17]. The bright field images typical of the exfoliated catalyst are shown in Fig. 5 and 6, corresponding to the sediment and supernatant, respectively. The sediment in Fig. 5 still has the "poorly crystalline" structure, although in some zones of this sample the distance separating (002) planes was 0.68 nm, suggesting that lithium remains intercalated between them. The "light" fraction is mainly composed of particles similar to that of Fig. 6. The particles are crystalline, with (002) planes running all across the particle.

The results of surface area and catalytic activity are shown in Table I. It is observed for the commercial MoS_2 that the surface area remains almost unchanged by the exfoliation treatment. The catalytic activity on the other hand, increases substantially by a factor of 3.5. Both samples have similar surface areas before and after the reaction. For the catalyst, the surface area decreases very strongly both by the exfoliation or the reaction test, reflecting a high instability of the catalyst. The catalytic activity of the original sample is higher than that of the exfoliated catalyst and it was necessary to measure it at lower temperatures in order to make a comparison. The exfoliated catalyst requires a temperature about 30 degrees higher to have an activity similar to that of the original catalyst.

Table I.- Experimental surface area and catalytic activity measurements.

(a) $T = 483 \text{ K}$, (b) $T = 453 \text{ K}$

Sample	BET area (m^2/g) before	BET area (m^2/g) after	Increase in BET area (m^2/g)	Rate constant (10^{-8} mol/s g)
Commercial MoS_2	11.65	10.25	-1.40	7.70 (a)
Commercial MoS_2 after exfoliation	13.61	12.04	-1.57	26.95 (a)
MoS_2 Catalyst	41.53	8.11	-33.42	16.94 (b)
MoS_2 Catalyst after exfoliation	5.85	3.78	-2.07	10.78 (a)

DISCUSSION

The exfoliation method has proven very promising in the synthesis of new materials with very interesting properties in optics [18], composites [19], magnetic storage materials [20], etc.

The main characteristic of this method is the claimed dispersion of molybdenum disulfide crystals into single layer materials. The evidence shown by HREM confirms the redispersion of MoS_2 crystals. Two different structures have been identified in the exfoliation product after centrifugation, one found in the sediment and the other in the supernatant. The "highly disordered" phase which is characteristic of the sediment shows large particles where (002) planes are disordered between different zones of the same particle. This phase is very similar to the "poorly crystalline" phase observed in molybdenum disulfides obtained at low temperatures and which are commonly used as catalysts [16]. The "particulated" or "highly dispersed" phase which is characteristic of the supernatant is mainly formed by small particles in the range of 5 to 25 nm. This phase has never before been observed by electron microscopy, yet it probably constitutes a by-product of the chemical exfoliation that yields the "single layer" material reported by Joensen et al. [12].

The catalytic activity for the HDS of thiophene is noticeably increased by the exfoliation procedure in the case of the commercial (crystalline) MoS_2 . This catalytic effect is obtained with no appreciable variation in BET surface area of the sample, as shown in Table I. Therefore, this result may be explained by an increase of the edge sites that occurs due to the process of fragmentation (redispersion) from large to small particles. Edge sites are held to be the active sites for HDS reactions in MoS_2 -based catalysts.

Entirely different catalytic results are found for the exfoliated MoS_2 catalyst. In this case, even though there is evidence of redispersion owing to formation of particles like the ones in Fig. 6, both the catalytic activity and the surface area are drastically reduced, suggesting that microporosity plays an important role in the behavior of this catalyst.

These results show a contrary effect of the exfoliation depending on the type of MoS_2 that is being used. A positive effect of exfoliation in the catalytic activity of crystalline MoS_2 , and a negative effect on the catalytic activity of poorly crystalline MoS_2 .

CONCLUSIONS

The exfoliation treatment of commercial (crystalline) molybdenum disulfide is shown to disperse or fragment large crystals into small crystallites. This dispersion occurs with no appreciable change in the surface area of the sample. No conclusive evidence of single layer structures was found by TEM. Catalytic activity of commercial MoS_2 is substantially increased by the exfoliation treatment, suggesting that the dispersion or fragmentation process augments the number of catalytically active edge sites.

ACKNOWLEDGEMENTS

The authors acknowledge funding for this research by the DGAPA-UNAM, through grant No. IN-102692. Acknowledgement is also due to F. Ruiz for valuable technical assistance. M. Del Valle acknowledges fellowship support from CONACYT.

REFERENCES

1. K. Tanaka and T. Okuhara, Proc. III Int. Conf. on the Chem. and Uses of Molybdenum, Ed. Climax Molybdenum, p. 170, 1979.
2. O.P. Bahl, L. Evans and J.M. Thomas, Proc. Roy. Soc. A, **53**, 306 (1983).
3. C.B. Roxlo, M. Daage, A.F. Rupert and R.R. Chianelli, J. Catal., **100**, 176 (1986).
4. M. Salmeron, G.A. Somorjai, A. Wold, R.R. Chianelli and K.S. Liang, Chem. Phys. Lett., **90**, 105 (1983).
5. M.H. Farias, A.J. Gelman, R.R. Chianelli and K.S. Liang, Surf. Sci., **181**, 140 (1984).
6. S.J. Tauster, T.A. Pecoraro and R.R. Chianelli, J. Catal., **63**, 515 (1980).
7. A. Wambecke, L. Jelowiecki, S. Kasztelan, J. Grimblot and J.P. Bonnelle, J. Catal., **109**, 320 (1988).
8. S. Kasztelan, H. Toulheat, J. Grimblot and J.P. Bonnelle, Bull. Soc. Chim. Belg., **93**, 807 (1984).
9. R.A. Kemp, R.C. Ryan and J.A. Smegal in "Proc. IX Int. Congr. on Catalysis", edited by M.J. Phillips and M. Ternan, The Chemical Institute of Canada, vol. 1, Ottawa, 1988, p. 74.
10. S. Eijssbouts, J.J.L. Heinerman and H.J.W. Elzerman, Appl. Catal. A, **105**, 53 (1993).
11. W.M.R. Divigalpitiya, R.F. Frindt and S.R. Morrison, Appl. Surf. Sci., **48**, 572 (1991).
12. P. Joensen, R.F. Frindt and S.R. Morrison, Mat. Res. Bull., **21**, 457 (1986).
13. O. Weisser and S. Landa, in "Sulfide Catalyst: Their Properties and Applications", Pergamon, Oxford, 1973.
14. A. Vazquez, J.M. Dominguez, C. Piña, A. Jaidar and S. Fuentes, J. Mat. Sci. Lett., **9**, 712 (1990).
15. M.J. Yacamán and T. Ocaña, Phys. Stat. Sol. A, **42**, 571 (1977).
16. K.S. Liang, R.R. Chianelli, F.Z. Chien and S.C. Moss, J. non Cryst. Sol., **79**, 251 (1981).
17. J. Cruz-Reyes, M. Avalos-Borja, M.H. Farias and S. Fuentes, J. Catal., **137**, 232 (1992).
18. W.M.R. Divigalpitiya, S.R. Morrison and R.F. Frindt, Thin Solid Films, **186**, 177 (1990).
19. W.M.R. Divigalpitiya, R.F. Frindt and S.R. Morrison, J. Mat. Res., **6**, 1103 (1991).
20. R.F. Frindt, A.S. Arrott, A.E. Curzon, B. Heinrich, S.R. Morrison, T.L. Templeton, W.M.R. Divigalpitiya, M.A. Gee, P. Joensen, P.J. Schurer and J.L. Lacombe, J. Appl. Phys., **70**, 6224 (1991).

A LOW TEMPERATURE, SOLUTION PHASE SYNTHESIS OF III-V SEMICONDUCTOR NANOCRYSTALS

SUREYAS S. KHER AND RICHARD L. WELLS

Department of Chemistry, Paul M. Gross Chemical Laboratories, Duke University,
Durham, North Carolina 27708, U.S.A.

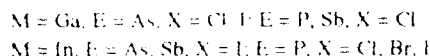
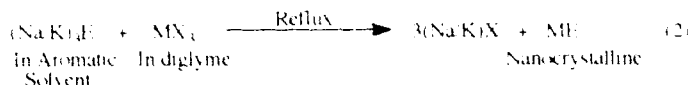
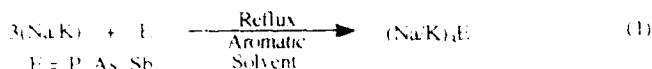
ABSTRACT

Nanocrystalline materials have been intensely investigated in the recent past due to the novel properties associated with size-quantized particles. We have developed a new method for high yield, solution phase synthesis of nanocrystalline III-V semiconductors which eliminates the use of substituted or unsubstituted Group V hydrides and Group III alkyls. Our approach consists of *in situ* syntheses of $(\text{NaK})_3\text{E}$ ($\text{E} = \text{P}, \text{As}, \text{Sb}$) in aromatic solvents and subsequent reactions of these pnictides with Group III halide solutions in coordinating solvents. The nanocrystalline III-V semiconductors GaP, GaAs, GaSb, InP, InAs and InSb are readily prepared in a wide range of particle sizes (4-36 nm) and in high yields. The resultant III-V materials have been characterized by XRD, EDXA, TEM and elemental analyses.

Introduction

Semiconductor nanocrystals are potentially useful materials due to their novel physical properties markedly different from those of the bulk solids. Although a variety of synthetic methods are reported for obtaining nanocrystalline materials, those for synthesizing III-V nanocrystals in solution have mainly focused [1] on the reaction of GaCl_3 and $\text{As}(\text{SiMe}_3)_3$ in organic solvents, one of the dehalosilylation reactions, developed by Wells and co-workers [2]. In addition, Uchida *et al.* reported the synthesis of GaAs and InAs nanocrystals from $\text{Ga}(\text{acac})_3$ and $\text{In}(\text{acac})_3$, respectively by reactions with $\text{As}(\text{SiMe}_3)_3$, however, formation of other by-products or the fate of the acetylacetonate ligands were not reported [3]. The reported previous methods use the toxic and air-sensitive $\text{As}(\text{SiMe}_3)_3$ or $\text{P}(\text{SiMe}_3)_3$ [2d] as starting materials. Thus, an alternative route to the nanocrystalline III-V semiconductors is desirable. Recently Kaner and co-workers reported a general method involving solid state metathesis (SSM) to synthesize binary III-V semiconductors by reacting sodium pnictides with Group III halides either in bombs or sealed glass ampules at high temperatures. These exothermic reactions generate enough heat to melt the sodium halide product and yield polycrystalline III-V semiconductors often contaminated with starting materials and by-products [4]. It has also been reported that this method produces III-V compound semiconductors containing considerable amounts of non-removable halide inclusions and the rapid exothermic SSM reactions introduce high defect concentration and lattice strain in resulting semiconductors [4d]. However, an important aspect of Kaner's work involved controlling the particle size by adding inert materials as heat sinks to the SSM reaction mixtures. The particle size of MoS_2 synthesized from the SSM reaction between MoCl_5 and Na_2S was altered by the amount of NaCl added to the reactants. The larger the amount of NaCl , the smaller the particle size of MoS_2 obtained [4e]. The SSM route involves rather severe reaction conditions and high temperatures; thus, we investigated fundamentally similar reactions to that described by Kaner and co-workers but carrying out the reactions in organic solvents. The solid state reactions are diffusion controlled; whereas, due to the ease of stirring, a better control can be achieved in the solution phase chemistry. This should also result in solvents acting as better heat sinks and refluxing rather than the observed [4b, c] meltdown of the reaction flux in the SSM reactions. Although the use of solvents resulted in reduced particle size, we discovered that a further reduction in the particle

size could be achieved by employing co-ordinating solvents. Herein, we report [5] the first account of the solution phase synthesis of nanocrystalline III-V semiconductors which does not utilize substituted or unsubstituted phosphine, arsine or stibine (eqs. 1 and 2).



Experimental

The synthesis of $(\text{Na/K})_3\text{E}$ ($\text{E} = \text{P, As, Sb}$) was adapted from a similar procedure described by Peterson *et al.* [6] for the synthesis of $(\text{Na/K})_3\text{P}$ in benzene. In a typical experiment, $(\text{Na/K})_3\text{E}$ ($\text{E} = \text{P, As, Sb}$) was synthesized *in situ* by reacting sodium-potassium alloy with excess arsenic powder or excess (at least 30%) white phosphorus or a stoichiometric amount of antimony powder in refluxing toluene (for $\text{E} = \text{P, As}$) or in xylene (for $\text{E} = \text{Sb}$) for two days. The reaction flask containing finely divided black pnictide was then cooled to 0°C and to this was added MX_3 solution in diglyme, followed by refluxing the mixture for 1-2 days. On cooling the reaction mixture to room temperature, deionized water was added to the reaction mixture to dissolve alkali halide by-products and to destroy remaining trace amounts of unreacted pnictide, if any. Ethanol or methanol can also be substituted for deionized water. The resulting suspension was then vacuum filtered in air and the solid residue on the filter paper was washed with copious amounts of deionized water followed by washing with acetone and air drying. The resultant dry solid was then heated to 350°C under dynamic vacuum in a sublimator for 2-3 hours to remove any volatile materials. In case of the phosphides and arsenides, the excess Group V element readily sublimates but antimony does not and remained as an impurity in the antimonides. The resultant phosphides and arsenides are light to dark brown whereas the antimonides are dark grey materials. The yields of the reactions ranged from 53-95%. The elemental analyses of these materials showed that desired III-V constituents were present and the halogen concentrations were typically less than 0.01%. Small amounts of carbon and hydrogen were also detected.

Results and Discussion

The semiconductor powders thus produced were characterized by XRD, TEM, EDXA and elemental analysis. From the XRD patterns, the approximate average particle sizes were calculated to be 4-36 nm using the Scherrer equation [7]. Figure 1 shows the XRD patterns of the various nanocrystalline III-V materials synthesized using the new procedure. Effect of solvent on the resultant particle size is evident in Figures 1A and 1B. When the aforementioned reaction was carried out with GaCl₃ dissolved in toluene, crystallites of approximately 36 nm average particle size resulted. However, reaction of GaCl₃ solution in diglyme with (Na/K)₃As in toluene resulted in approximately 10 nm GaAs nanocrystals. In some of the XRD patterns, there seemed to be a broad hump near 35 degrees two-theta angle. The origin of this feature is yet unknown but is likely to be due to amorphous oxides of gallium and arsenic as suggested later. The elemental analysis of GaAs powders indicated that there was a slight excess of gallium in the samples giving the Ga:As ratio of 5.1:4.0. Fitzmaurice and co-workers [1c] and

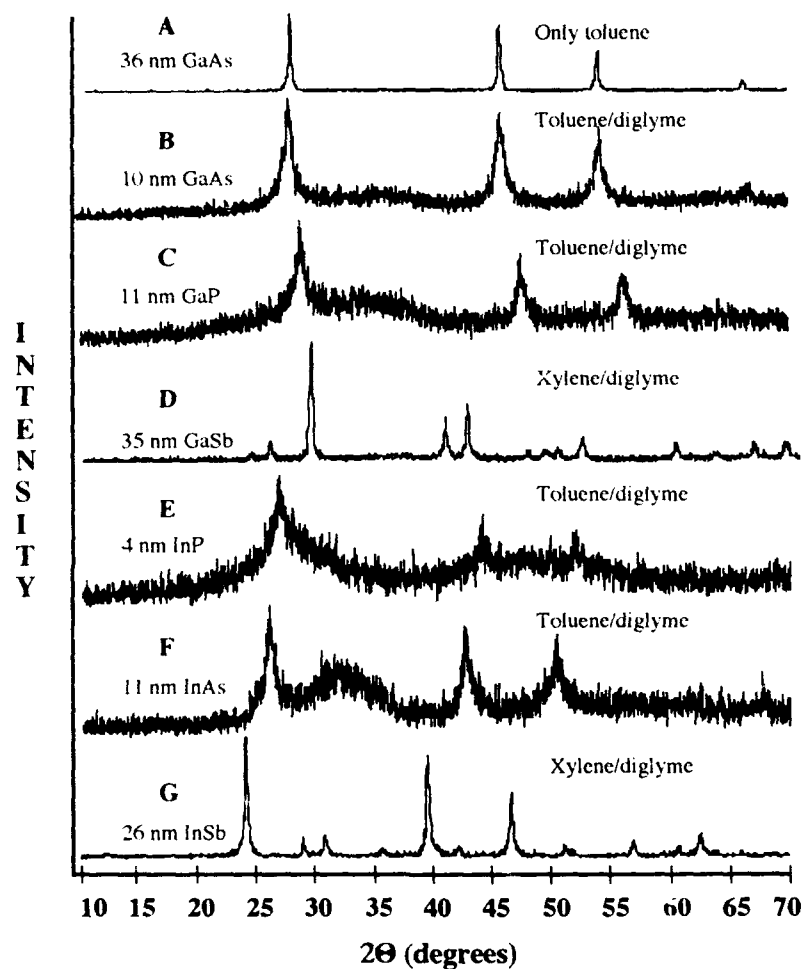


Figure 1. XRD Patterns of III-V nanocrystalline semiconductors synthesized from the new method. The approximate average particle size for each specimen was calculated from the XRD pattern. (A) 36 nm GaAs obtained from reaction of GaCl_3 solution in toluene and $(\text{Na/K})_3\text{As}$ in toluene. For all the other reactions, MX_3 solutions in diglyme were allowed to react with $(\text{Na/K})_3\text{E}$ in either toluene ($\text{E} = \text{P, As}$) or xylene ($\text{E} = \text{Sb}$) (B) 10 nm GaAs obtained from GaCl_3 , (C) 11 nm GaP obtained from GaCl_3 , (D) 35 nm GaSb resulted from GaCl_3 , (E) 4 nm InP obtained from InI_3 , (F) 11 nm InAs synthesized from InI_3 , (G) 26 nm InSb resulted from InI_3 .

Alivisatos and co-workers [1a] have observed similar excess of gallium (Ga:As ratio 5:4) in nanocrystalline GaAs prepared from GaCl_3 and $\text{As}(\text{SiMe}_3)_3$. Sandroff *et al.* reported surface oxidation of nanocrystalline GaAs exposed to air resulted in 1-1.5 nm layers of Ga_2O_3 and As_2O_3 [8a]. The surface oxidation of all the III-V semiconductors is well documented and is a common phenomenon [8b]. The depth of the layers of these oxides may be quite significant with decreasing particle size of gallium arsenide. As_2O_3 is known to sublime at 193 °C [9] and would do so during the vacuum sublimation carried out at 350 °C to remove excess arsenic. This would effectively increase the amount of gallium in the specimen relative to arsenic. Figure 2a shows the fringe pattern resulting from the lattice planes of a 7 nm GaAs crystallite. The image was obtained on a transmission electron microscope (TEM). Similar to GaAs, the reaction of GaCl_3 solution in toluene with $(\text{Na/K})_3\text{P}$ in toluene gave GaP powder with approximate average particle size of 21 nm while carrying out the same reaction using GaCl_3 solution in diglyme resulted in 11 nm GaP nanocrystals (Figure 1C). Elemental analysis of a typical GaP sample gave the Ga:P ratio of 1.1:1.0. The XRD pattern of GaSb synthesized from *in situ* reaction of GaCl_3 solution in diglyme with $(\text{Na/K})_3\text{Sb}$ in xylene gave 35 nm GaSb particles (Figure 1D). The elemental analysis of the powder indicated Ga:Sb ratio 1.0:1.0. The reaction of InI_3 solution in diglyme with $(\text{Na/K})_3\text{P}$ in toluene resulted in approximately 4 nm InP crystallites as calculated from the XRD pattern (Figure 1E). The elemental analysis of a typical InP sample thus synthesized indicated In:P ratio to be 1.0:1.0. The Energy Dispersive X-Ray Analysis (EDXA) of nanocrystalline InP is shown in Figure 2b. In addition to the signals due to indium and phosphorus, no other signals, including alkali metal or halide impurities, were observed. The iron and cobalt signals originated from the TEM pole piece and the copper signals originated from the specimen grid were detected. Standardless quantitative elemental analysis indicated In:P ratio to be 1:1 within experimental error.

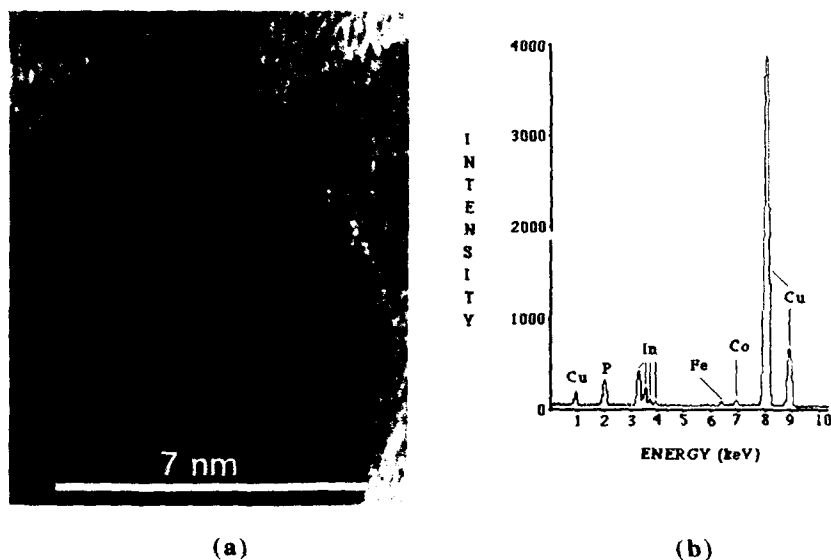


Figure 2. (a) TEM image of the lattice planes of a 7 nm GaAs nanocrystal. (b) Energy Dispersive X-Ray Analysis of approximately 4 nm InP prepared from the reaction of InI_3 solution in diglyme with $(\text{Na/K})_3\text{P}$ in toluene.

During the InP synthesis, it was observed that the reactions involving stoichiometric amounts of sodium-potassium alloy and white phosphorus led to InP containing free indium metal and, occasionally, indium and trace amounts of InI_2 both were observed in the XRD pattern besides the reflections due to InP. However, the use of at least 30% excess white phosphorus for the $(\text{Na/K})_3\text{P}$ synthesis consistently resulted in InP nanocrystals devoid of any by-products due to the reduction of InI_3 . Employing less than 30% excess white phosphorus again resulted in the undesirable indium containing impurities. An earlier report [10a] suggested that reactions involving stoichiometric amounts of an alkali metal and phosphorus gave products containing less alkali metal than the desired stoichiometric 3:1 phosphide, M_3P . This implies that in stoichiometric reactions, some alkali metal may remain unreacted which would reduce InI_3 leading to indium containing impurities. Finely divided alkali metal is also essential for the formation of M_3P , chunks of the metal are known to cause incomplete reactions leading to complex polyphosphides [6]. White phosphorus is light sensitive and readily transforms to the red allotrope [10b]; thus, it is likely that the white phosphorus used in our reactions may contain an unknown amount of the red allotrope. However, a minimum of 30% excess seemed to provide sufficient white phosphorus to form the stoichiometric $(\text{Na/K})_3\text{P}$. In light of the preceding discussion, the suggestion by Kaner and co-workers [4a] that the reduction of In^{3+} by P^3 as a leading cause for presence of the free indium metal in InP seems unlikely. They eliminated indium containing by-products by adding excess phosphorus to the reaction mixture containing Na_3P and InI_3 rather than using excess phosphorus for the synthesis of Na_3P . Under their reaction conditions ($>600^\circ\text{C}$), the possibility exists for the formation of InP from excess phosphorus and indium resulting from the reduction of InI_3 as the high temperature reaction of the elements is known to form InP at temperatures as low as 420°C [11]. However, under our reaction conditions it is unlikely that any InP is formed due to the reaction of the elements.

InAs of approximately 11 nm average particle size was obtained from the reaction of InI_3 solution in diglyme with $(\text{Na/K})_3\text{As}$ in toluene (Figure 1F). The XRD pattern showed a broad hump, likely to be due to surface oxides present on the nanocrystals as a result of the exposure to air. The elemental analysis indicated the In:As ratio to be close to 3:2. The loss of arsenic from the sample is probably due to sublimation of As_2O_3 which could result due to surface oxidation [8b], similar to the oxidation of air-exposed GaAs nanocrystals. The XRD pattern of approximately 26 nm InSb resulted from the *in situ* reaction of InI_3 solution in diglyme with $(\text{Na/K})_3\text{Sb}$ suspension in xylene is shown in Figure 1G. The elemental analysis of InSb showed the In:Sb ratio to be 1:1.

The role of diglyme is not yet clear, although the fact that ether solvents form adducts with Group III compounds is well documented [12]. Group III halides, in general, exist as dimers due to the Lewis acidity of the Group III metal atom; however, Nöth and co-workers reported that the glyme solvents tend to break up the dimeric structures of these halides and form ionic coordination complexes by expanding the coordination sphere of the metal center [13]. It seems reasonable to suggest that these ionic complexes may play an important role in the mechanism to limit the growth of particles/clusters beyond a certain size. This aspect remains to be investigated. It was also discovered that only dimeric Group III halides (GaCl_3 , GaI_3 and InI_3) were able to produce nanocrystalline III-V compounds. For example, the oligomeric InX_3 ($\text{X} = \text{Cl}, \text{Br}$) yielded semiconductors with larger particle sizes (22-26 nm InP). These halides may not form adducts readily with diglyme and this may be a contributing factor to the observed particle sizes.

Acknowledgement

The financial support for this work was provided by the Air Force Office of Scientific Research (AFOSR).

References

1. (a) M. A. Olshavsky, A. N. Goldstein, A. P. Alivisatos, *J. Am. Chem. Soc.* **112**, 9438 (1990); (b) H. Uchida, C. J. Curtis, A. J. Nozik, *J. Phys. Chem.* **95**, 5382 (1991); (c) L. Butler, G. Redmond, D. Fitzmaurice, *J. Phys. Chem.* **97**, 10750 (1993).
2. (a) R. L. Wells, C. G. Pitt, A. T. McPhail, A. P. Purdy, S. Shafieezad, R. B. Hallock, *Chem. Mater.* **1**, 4 (1989); *Mater. Res. Soc. Symp. Proc.* **131**, 45 (1989); (b) R. L. Wells, R. B. Hallock, A. T. McPhail, C. G. Pitt, J. D. Johansen, *Chem. Mater.* **3**, 382 (1991); (c) R. L. Wells, M. F. Self, A. T. McPhail, S. R. Aubuchon, R. C. Woudenberg, J. P. Jasinski, *Organometallics* **12**, 2832 (1993); (d) S. R. Aubuchon, A. T. McPhail, R. L. Wells, J. A. Giambra, J. R. Bowser, *Chem. Mater.* **6**, 82 (1994).
3. (a) H. Uchida, C. J. Curtis, P. V. Kamat, K. M. Jones, A. J. Nozik, *J. Phys. Chem.* **96**, 1156 (1992); (b) H. Uchida, T. Matsunaga, H. Yoneyama, T. Sakata, H. Mori, T. Sasaki, *Chem. Mater.* **5**, 716 (1993).
4. (a) R. E. Treece, G. S. Macala, L. Rao, D. Franke, H. Eckert, R. B. Kaner, *Inorg. Chem.* **32**, 2745 (1993); (b) R. E. Treece, E. G. Gillan, R. M. Jacubinas, J. B. Wiley, R. B. Kaner, *Mater. Res. Soc. Symp. Proc.* **271**, 169 (1991); (c) R. E. Treece, G. S. Macala, R. B. Kaner, *Chem. Mater.* **4**, 9 (1992); (d) D. Franke, H. Eckert, R. B. Kaner, R. E. Treece, *Anal. Chim. Acta* **283**, 987 (1993); (e) J. B. Wiley, R. B. Kaner, *Science* **255**, 1093 (1992).
5. S. S. Kher and R. L. Wells, U.S. Patent Application Serial No. 08/189, 232 (filed on January 31, 1994).
6. D. J. Peterson, T. J. Logan, *J. Inorg. Nucl. Chem.* **28**, 53 (1966).
7. H. P. Klug, L. E. Alexander, *X-Ray Diffraction Procedures* (John Wiley & Sons, Inc., New York, 1962) p. 491.
8. (a) C. J. Sandroff, J. P. Harbison, R. Ramesh, M. J. Andrejco, M. S. Hegde, D. M. Hwang, C. C. Chang, E. M. Vogel, *Science* **245**, 391 (1989); (b) C. W. Wilmsen, *J. Vac. Sci. Technol.* **19**, 279 (1981) and references therein.
9. *CRC Handbook of Chemistry and Physics*, edited by R. C. Weast, (CRC Press, Inc., Boca Raton, volume **66**, 1985), p. B-74.
10. (a) J. R. Van Wazer, *Phosphorus and its Compounds, Volume I: Chemistry*, (Interscience Publishers, Inc., New York, 1958) p. 133; (b) *ibid.*, p. 113.
11. E. P. Trifanova, Zheleva, N. N., D. B. Kushev, *Mat. Res. Bull.* **23**, 779 (1988).
12. *Comprehensive Coordination Chemistry, Volume 3*, edited by G. Wilkinson, (Pergamon Press, Oxford, 1987) Chapters 24-25.
13. (a) S. Böck, H. Nöth, A. Wietelmann, *Z. Naturforsch.* **45b**, 979 (1990); (b) H. Nöth, R. Rurländer, P. Wolfgardt, *Z. Naturforsch.* **37b**, 29 (1981).

METAL CLUSTER OXIDATION: STICKING PROBABILITIES AND IONIZATION POTENTIAL SHIFTS

MATS ANDERSSON, LOTTA HOLMGREN, JOHN L. PERSSON, THORBJÖRN ÅKLINT
AND ARNE ROSÉN

Department of Physics, Chalmers University of Technology and University of Göteborg,
S-412 96 Göteborg, Sweden.

ABSTRACT

This study deals with the initial oxidation of some 3d metal clusters in gas phase. In the experiments neutral metal clusters in a supersonic beam are made to collide with one or a few oxygen molecules in a reaction cell. The reaction products are detected with photoionization and mass spectrometry. By comparing the abundance of unreacted and reacted clusters, absolute sticking probabilities (S) can be determined. Transition metals with open d shells, e.g. Ni, have high, almost constant S for O_2 on clusters containing more than 20 atoms. The size evolution of S for Cu, on the other hand, shows repeated minima and maxima. Cluster sizes which have high ionization potentials (IPs) and closed electronic shells, according to the spherical jellium model, are the ones with the lowest S . The IPs of Cu_nO_2 clusters have also been investigated. Compared with the IPs of the pure Cu clusters, the IPs of the oxidized clusters are generally higher and the large drops at the shell openings are less distinct.

INTRODUCTION

Today, ultrafine particles can be produced in macroscopic quantities and are finding their way into many interesting applications [1]. The technical development of materials built up of small clusters with diameters ≤ 1 nm has, on the other hand, not yet reached very far. Much fundamental research remains to be done both on characterization of properties and development of production techniques. There is, however, no doubt that the understanding of the physical and chemical properties of clusters will be of vital interest for many applied areas of science.

In small clusters a comparatively large number of atoms are located at the surface. Thus, properties governed by surface atoms, such as reactivity, adhesion, etc. are expected to be even more significant for small clusters than for ultrafine particles. For many future applications of clusters the reactivity towards oxygen will be of great importance, since this will influence the stability in various environments and especially in ambient atmosphere. In certain applications, such as catalysis, the reactivity will definitely be a property that determines the materials characteristics and performance.

We have recently started to investigate the reactive and catalytic properties of metal clusters and in our first experiments we have studied the reactivity and, especially, the initial oxidation of some 3d metals [2,3]. The reactions have been performed under single-collision-like conditions and by comparing the number of reactive collisions with the total number of collisions absolute sticking probabilities have been determined. This experiment is primarily a test on the outcome of a cluster-molecule collision, whether a stable product is formed or not. Another aspect of the reactivity investigations is to characterize properties such as geometry, electronic structure and stability of the product clusters. One way to get a clue about the electronic structure of neutral clusters is to measure the ionization potential (IP) and we have initiated such a study on oxidized copper clusters. Also theoretical calculations are made in our group to increase the understanding of metal cluster reactivity and, especially, copper cluster oxidation [4,5].

In this paper we will discuss the oxidation of some 3d metal clusters with focus on the difference between metals with open d shells, here represented by Ni, and the coinage metal Cu. We will also describe some preliminary indications of how the IP shifts upon oxidation for the copper clusters.

EXPERIMENTAL METHODS

The experimental set-up consists of two vacuum chambers, one for the production of clusters and one for the detection, as shown in fig. 1. A pulsed beam of neutral clusters in He carrier gas is produced in a laser vaporization source. Each pulse contains a wide size distribution of metal clusters, ranging from individual atoms to clusters of several hundred atoms. The cluster beam enters the second chamber through a 1 mm diameter skimmer and then passes through a 50 mm long reaction cell. A reactive gas is leaked through the gas cell to keep a pressure of 10^{-4} - 10^{-2} mbar in the cell, and due to the small apertures (1 mm diameter) a pressure ratio of > 1000 can be maintained between the cell and the surrounding chamber. The number of collisions experienced by the clusters in the reaction cell is Poisson distributed, with an average ranging from less than one up to ten in this pressure interval. Finally, the clusters are ionized with pulsed laser light of low intensity and short wavelength (~ 0.3 mJ/cm² at 193 nm) and detected in a linear time-of-flight mass spectrometer.

In the mass spectra peaks appear for all cluster sizes as well as for all reaction products, as can be seen in fig. 2. Thus, the relative abundance of pure and reacted clusters can be determined for each reaction cell pressure. Using a hard sphere model for the molecules and clusters, the average number of collisions can be determined for every cell pressure, i. e. for every average number of collisions. Now the product abundance vs. number of collision data can be fitted to a first-order kinetic model with the sticking probabilities (*S*) as fitting parameters. The kinetic model involves the successive addition reactions: $M_n + O_2 \rightarrow M_nO_2$, $M_nO_2 + O_2 \rightarrow M_nO_4$ etc. and, in principle, the sticking probability of also the second, third etc. molecule could be determined.

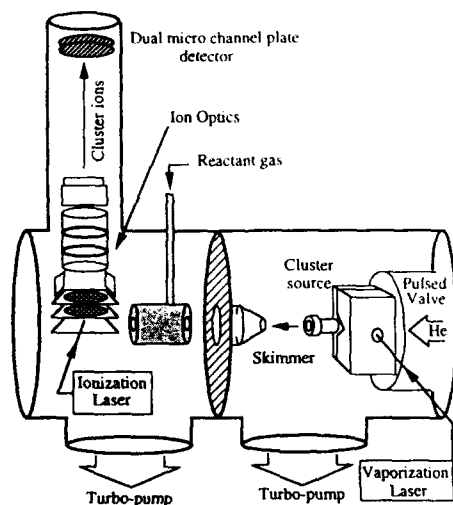


Fig. 1. The experimental set-up: cluster source, reaction cell and time-of-flight mass spectrometer.

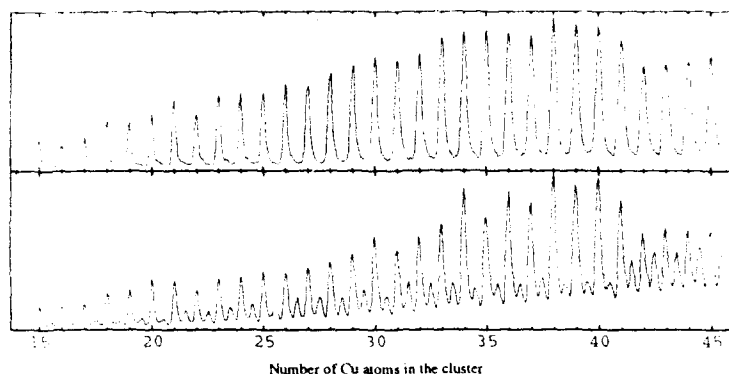


Fig. 2. Mass spectra of Cu clusters of size 15-45. The top spectrum has been recorded without oxygen in the reaction cell. The lower spectrum has been recorded at an oxygen pressure of $1.5 \cdot 10^{-3}$ mbar.

In the experiments for measuring the ionization potentials of copper oxides a constant oxygen pressure of $1.5 \cdot 10^{-3}$ mbar was maintained in the reaction cell to produce a reasonable fraction of Cu_nO_2 products, but still very few Cu_nO_4 . Actually, we cannot include the Cu_nO_4 in the evaluation, neither in reactivity nor in IP determinations, because of a mass interference with Cu_{n+1} .

Two lasers were used for ionization. The frequency doubled light from a tuneable dye laser was used to measure the photoionization efficiency in the 206-240 nm wavelength region, corresponding to photon energies of 5.2-6.0 eV. For normalization of these measurements mass spectra were simultaneously recorded using the 193 nm light from the ArF excimer laser. The two lasers were fired alternating on every other cluster pulse, and the signals were accordingly switched into one of the two channels of a digital storage oscilloscope. Mass spectra were recorded at 1 or 0.5 nm wavelength intervals and by dividing the peak intensities in the dye laser spectrum with the intensities in the corresponding excimer laser spectrum, the relative photoionization cross section at that wavelength could be determined for each Cu_nO_2 as well as each Cu_n cluster.

RESULTS AND DISCUSSION

In the way described above the reactivity of various transition and noble metal clusters (Fe, Co, Ni, and Cu) towards O_2 has been studied. Fig. 3 shows the sticking probabilities for the first oxygen molecule on Ni_n and Cu_n . Ni_n shows a rather simple S vs n dependence with an almost monotone increase as n goes from 10 to 20 and then S seems to be constant for $n > 20$. Here S is not shown for $n > 30$, but the trend is definitely that $S = 0.5$ also for the larger clusters. Qualitatively the same size dependence has been observed for the O_2 sticking on Fe_n and Co_n [3], but these metals have a somewhat higher S for the larger cluster sizes: 0.7 and 1.0, respectively. The O_2 sticking on Cu_n is distinctly different both quantitatively and qualitatively. There are repeated maxima and minima in the S vs. n curve and even the most reactive sizes have $S < 0.25$.

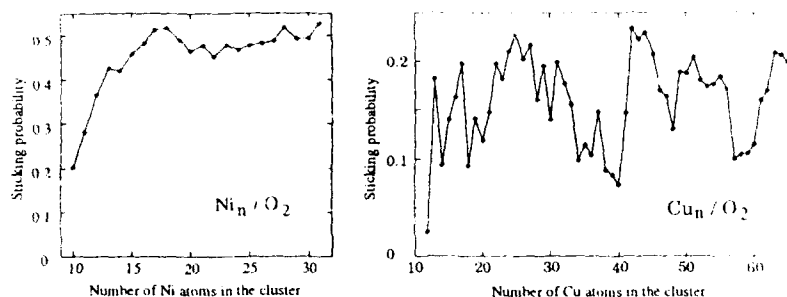


Fig. 3. Sticking probabilities of oxygen molecules on Ni_n (left) and Cu_n (right). The error estimate for the sticking probability is ± 0.05 .

These results show that the oxygen reactivity is very much dependent on the electronic structure of the metal clusters. Bulk surfaces of Ni and other metals with unfilled d electron bands have high initial sticking probabilities for O_2 , usually $S=0.5-1.0$, and form strong metal oxygen bonds [6]. This seems to be the case also for transition metal clusters, at least if the clusters contain 20 atoms or more. Smaller clusters may appear less reactive in this type of experiment, where no buffer gas is present in the reaction cell to thermalize the reaction products. Smaller clusters with fewer vibrational degrees of freedom will then have a lower ability to form stable oxide products. Another possible explanation is that the oxidation involves electron transfer from the cluster to the oxygen and since smaller clusters often have higher IPs they might be less reactive. However, the latter does not fit very well for Ni_n since the IPs show very little variation for $n=11-22$ [7].

The electronic properties of bulk Cu is dominated by the 4s valence electrons, and this is definitely the case also for Cu clusters. The size dependence of several measured properties, such as stability [8], ionization potentials [9], electron affinities and photoelectron spectra [10,11], has shown that the Cu clusters can be well described by the jellium model. In this model [12,13] the valence electrons, one 4s electron per Cu atom, are delocalized over the cluster and the positive charge of the remaining ionic cores is modeled to constitute a uniform potential for the delocalized electrons. In this potential well there will be quantized electronic levels ordered in shells. Closed shells are predicted to appear for clusters with 8, 18, 20, 34, 40, 58, etc. electrons and clusters with this number of electrons are found to be more stable or to have a higher electron binding energy. This corresponds very well with the measured S for O_2 . Local minima in S appear for clusters having closed shells and/or local maxima in IP. High reactivity is regained at a few sizes above a closed shell, which might indicate that more than one Cu 4s electron is needed for efficiently binding an O_2 molecule. The low oxygen reactivity for clusters with closed electronic shells has earlier been observed for Cu_n [14] as well as for Al_n [15] and Na_n [16].

After seeing that the jellium model quite well describes several properties of the copper clusters, including the O_2 reactivity, the next question is what the electronic structure of the copper oxide reaction products will be like. We have started to measure the relative photoionization cross sections for Cu_nO_2 . The analysis work is in progress and the assigned IP values will be published elsewhere [17]. Here we will describe the general trends and compare the IPs of the Cu_nO_2 with the IPs of the pure Cu clusters for $n=19-48$. The IPs of Cu_n [9] are characterized by the large drops in the IP at the shell openings, but also by an even-odd variation over wide size ranges. The latter is thought to be an effect of that clusters without closed shells may

be deformed to an ellipsoidal shape. Energy levels that are degenerate in a spherical symmetry are then splitted into two-electron levels in a geometrically deformed cluster.

For the Cu_nO_2 there are no obvious shell openings (i.e. a local maximum in the IP followed by a local minimum for the next size) but the even-odd variation is significant throughout the studied size region. This indicates that in the Cu_nO_2 , as well as in the Cu_n , there is a number of delocalized electrons populating two-electron orbitals. On the other hand, the absolute number of delocalized electrons is difficult to determine, since there is no obvious shell structure pointing out clusters with 20/21, 34/35 or 40/41 electrons. Thus, a definite number for the charge transfer in the Cu_nO_2 formation is not possible to determine only from this IP measurement.

For most clusters in this size range the IP increases upon oxidation with an average shift of 0.1-0.2 eV. Only for a few cluster sizes the IP is maintained or even lowered. This is the case for clusters with closed electronic shells and specifically high IP as pure clusters, e. g. for $n=34, 40$.

ACKNOWLEDGEMENTS

We gratefully acknowledge financial support from the NUTEK/NFR Materials Science Consortium "Clusters and Ultrafine Particles", the Swedish Research Council for Engineering Sciences (TFR) and the Swedish Council for Planning and Coordination of Research (FRN).

REFERENCES

1. R.W. Siegel, *Nanostr. Mater.* **4**, 121 (1994)
2. J. L. Persson, M. Andersson and A. Rosén, *Z. Phys. D* **26**, 334 (1993)
3. M. Andersson, J.L. Persson and A. Rosén, *Nanostr. Mater.* **3**, 337 (1993)
4. H. Grönbeck and A. Rosén, *Comp. Mater. Sci.*, accepted
5. H. Grönbeck, M. Andersson and A. Rosén, this volume
6. The Chemical Physics of Solid Surfaces and Heterogeneous Catalysis, vol. 2-3, edited by D.A. King and D.P. Woodruff, (Elsevier, Amsterdam 1984/1990)
7. M.B. Knickelbein, S. Yang and S.J. Riley, *J. Chem. Phys.* **93**, 94 (1990)
8. I. Katakuse, T. Ichihara, Y. Fujita, Matsuo, T. Sakurai and H. Matsuda, *Int. J. Mass. Spectrom. Ion Processes* **67**, 229 (1985), *ibid.*, **74**, 33 (1986)
9. M.B. Knickelbein, *Chem. Phys. Lett.* **192**, 129 (1992)
10. C.L. Pettiette, S.H. Yang, M.J. Craycraft, J. Conceicao, R.T. Laaksonen, O. Cheshnovsky and R.E. Smalley, *J. Chem. Phys.* **88**, 5377 (1988)
11. C.-Y. Cha, G. Ganteför and W. Eberhart, *J. Chem. Phys.* **99**, 6308 (1993)
12. W.A. de Heer, *Rev. Mod. Phys.* **65**, 611 (1993)

13. M. Brack, *Rev. Mod. Phys.* **65**, 677 (1993)
14. E. ...ter, E.K. Parks and S.J. Riley, *J. Chem. Phys.* **94**, 8618 (1991)
15. ...uchner, A.C. Harms and A.W. Castleman Jr., *J. Chem. Phys.* **94**, 1093 (1991)
16. ...oge, H. Göhlich, U. Näher and T.P. Martin, *Chem. Phys. Lett.* **192**, 544 (1992)
17. M. Andersson, J. L. Persson, L. Holmgren, T. Åklint and A. Rosén, to be published

FORMATION AND PROPERTIES OF SILANE MONOLAYERS ON
IRON AND ALUMINUM SURFACES,

Maxim A. Petrunin and Andrey P. Nazarov,

Institute of Physical Chemistry, Russian Academy of Sciences, 31
Leninsky prosp., Moscow 117915, Russia.

ABSTRACT

The adsorption of ethoxysilanes $\text{RSi}(\text{OEt})_3$ on the Fe and Al surfaces from the vapor phase, water and toluene solutions was studied by the piezoquartz nanobalance and ellipsometry. The values of the "landing sites" and the energy of the interaction for different silanes were calculated. The self-assembling silane monolayers with good adhesion to the Al surface (due to the covalent bonds Al-O-Si) was shown to form during adsorption from dilute water solution. The influence of silane monolayers on the H_2O adsorption and wetting of the surface was studied. The silane layers have considerably hydrophobic effect and prevent the growth of hydroxide film on the Al. The synthesis of charged silane nanophases was carried out by the addition of the acid (sulfo-, imidodiacetate-) and the basic (amino-) groups into the epoxysilane molecule. The effect of the charge density and the surface potential on the ion adsorption at the interface metal/electrolyte was investigated.

INTRODUCTION

Organic silanes have found wide use as promoters of the adhesion and water resistance of polymer coatings on mineral substrata [1]. However, despite the intensive studies the mechanism of the silane adsorption, the structure and properties of the surface compounds forming during modification of metals and the interphase bonds nature are still not clear. The presence of silane nanophases on metal surfaces may considerably change the properties of surface. Surfaces of oxide metals may be modified with monolayers of silanes to make them hydrophobic or hydrophilic; and neutral, cationic, or anionic. Thus, the use of silanes of different structure allows to control the physical chemical processes occurred on the metal surface. Such control should be useful for the development of surface chemistry, gas-liquid chromatography, theory of heterogeneous catalysis etc. In addition, the electrochemistry of metals with attached thin organosilicon films is a perspective direction of a surface chemistry as the application thin siloxane layers with ionic groups changes the double electric layer structure and character of interface interactions [2]. The goal of the present work was a study of the mechanism of the formation of silane monolayers on the Al and Fe surfaces (including the synthesis of charged silane nanophases) and influence of silane films on physical chemical processes at the interfaces metal-gas and metal-electrolyte.

EXPERIMENTAL PROCEDURE

The adsorption of silanes on the Al surface was studied by the

piezoquartz nanobalance [3] and ellipsometry techniques. A vacuum cell for this experiments was used. A 100 nm thick Al (A999, pure) and Fe (pure) films were deposited by thermal sputtering on the quartz surface. The accuracy of the mass measurements was 10^{-9} g/cm². "The true surface area" of the metal was measured by the use of the BET method [4] and it was taken into account in each of the experiments.

Electrochemical experiments were made by the potentiodynamic method with the potential sweep speed equal to 1 mV/sec.

The trimethylethoxysilane $(\text{CH}_3)_3\text{-Si}(\text{OC}_2\text{H}_5)$ (MS) and triethoxysilanes of structure formula $\text{RSi}(\text{OEt})_3$, where R:

$\text{CH}_2=\text{CH-}$ (VS), $\text{C}_6\text{H}_5\text{-}$ (PS), $\text{NH}_2(\text{CH}_2)_3\text{-}$ (APS), $\text{CH}_2=\text{CH-CH}_2\text{O}(\text{CH}_2)_3\text{-}$ (GPS), $[(\text{C}_2\text{H}_5)_3\text{N}(\text{CH}_2)_2]\text{-}$ (DA), $\text{J}[(\text{C}_2\text{H}_5)_3\text{N}^+(\text{CH}_2)_3]\text{-}$ (TA), $(\text{CH}_2\text{COOH})_2\text{NCH}_2\text{-CH}(\text{OH})\text{-CH}_2\text{-O}(\text{CH}_2)_3\text{-}$ (IDC), $\text{C}_8\text{H}_{17}\text{-}$ (ootil), $\text{SO}_2\text{CH}_2\text{-CH}(\text{OH})\text{-CH}_2\text{-O}(\text{CH}_2)_3\text{-}$ (SUL) were used.

RESULTS AND DISCUSSION

The piezoquartz nanobalance study of adsorption of silanes on Al from a vapor phase has shown both reversible and irreversible adsorption for mono- (MS) and triethoxysilanes (VS, PS, APS). Alkoxysilanes are physically adsorbed on the aluminum surface as 1.4-3 mono layers (MS - 3, VS - 3, APS - 1.5, PS - 1.4 mono layer). The amount of the irreversible adsorbed silane in all the cases is about one statistic mono layer. The adsorption isotherms of silanes are described by the Langmuir and BET equations. The values of the "landing sites" of silane molecules (S) have been calculated (Table I). There is the vertical location for APS and MS. The relatively high values S for VS and PS may point to their plane orientation with regard to the metal due to additional interactions of the organic radicals with the surface.

Table I. Values of the "landing sites" and the adsorption heats of the ethoxysilane molecules.

Adsorbate	S, nm ² /mol		Adsorption heat kcal/mol
	BET equation	Langmuire eqn.	
VS	0.77	0.65	1.75
APS	0.40	0.35	2.31
PS	0.94	0.52	1.86
MS	0.33	0.31	1.66

According to the BET equation [4] the energy of interaction of adsorbate with the surface was evaluated (Table I). The low adsorption heat values indicate the presence of weak Van-der-Vaals interactions (of H-bonds), arising during adsorption of silanes on the aluminum from the vapor phase.

We have investigated the effect of $\text{H}_2\text{O}_{\text{ads}}$ on the interactions between surface and silane molecules during adsorption. For this, Al sputtered on piezoquartz was kept in H_2O vapour (at different humidities). Then the physically adsorbed water was removed, and

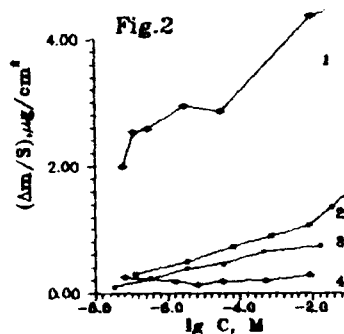
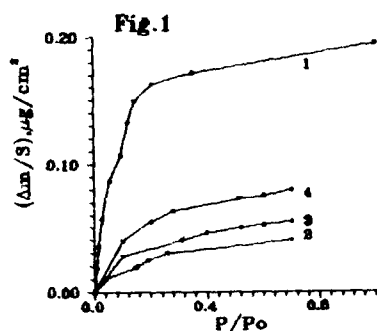


Fig. 1. Isotherms of irreversible adsorption of MS on Al preliminary kept in H_2O vapour for p/p_{OH_2O} : 1-0; 2-0.1; 3-0.2; 4-0.5.

Fig. 2. Isotherms of adsorption of silanes on Al from water solution 1-VS, 2-APS, 3-MS, 4-PS.

the adsorption of silanes was measured. It was established that the preliminary adsorption of small quantities of water ($p/p_{OH_2O}=0.1$) decreases appreciably adsorption of MS (Fig. 1) and

VS. This effect may be due to the blocking of active adsorption places of the surface by water. Increasing the water content in the range of $p/p_{OH_2O}=0.2-0.5$ led to a proportional increase in the amount of adsorbed silane. In the case of excess of H_2O_{ads} (75-100% humidity) VS and APS during adsorption destroy the structure of the phase film of water on the surface and displace H_2O_{ads} to the vapor phase.

The experiments have shown, that a necessary condition of the formation of the covalent bonding of silane molecules with the surface (Al-O-Si bonds) is the presence of H_2O_{ads} . One may suppose that the mechanism of silane chemisorption includes hydrolysis to form silanol: $(EtO)_3SiR + H_2O \rightarrow (OH)_3SiR$ (1), and the condensation with hydroxyl groups of the surface: $=Al-OH + (OH)_3SiR \rightarrow =Al-O-Si(OH)_2R + H_2O$ (2).

The increase in the amount of adsorbed water leads to an rise in the surface concentration of silanol molecules and consequently, in the amount of the chemisorbate. Molecules silane displaces water from the surface during competing adsorption. That is confirmed by the experiments on the study of water adsorption on the silyl-coated metal surface. It was shown by the piezoquartz nanobalance that vinyl- and methyl-siloxane films decrease the

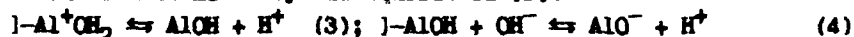
adsorption of water by a factor of 3 with regard to unmodified aluminum. No water condensation occurred on iron surfaces with ordered Langmuir-Blodgett siloxane films at 100% humidity.

The studies of the silane adsorption on the Al and Fe surfaces from solution were carried out. It was established by means of ellipsometry that VS adsorbed on the surface of Al and Fe as a polymolecular layer with thickness about 20 nm both from toluene and water solution. A quartz nanobalance study showed (Fig. 2) that during adsorption in aqueous solutions the coverage of surface arrive at 10, 5 and 3 molecular layers for VS, PS and APS respectively. The first monolayer is covalently bonded with Al surface (Al-O-Si bonds). On other hand, GPS has adsorbed on the aluminum surface with surface occupancy being close to a monolayer (from 0.4 to 3.3 mol/nm² as the GPS concentration from increased from 9 μM to 5 mM). Then surface occupancy did not change (up to 50 mM. MS, incapable of the reaction of polycondensation, is adsorbed on metal as a monolayer.

In order to evaluate the stability and the adhesion of silane layers on aluminum surface, the interactions at the interface aluminum/water have been studied. One monolayer silane was chemisorbed on the aluminum surface, after that it was kept in distilled water, and the hydration rate of Al₂O₃ was evaluated (Fig.3). The data obtained indicate that the presence of monolayer of chemisorbed silane can decrease by 1.5-2 times the rate of interaction between the aluminum and water. According to the degree of the hydration inhibition of the oxide film the silanes may be arranged in the following series :VS>PS>APS>MS.

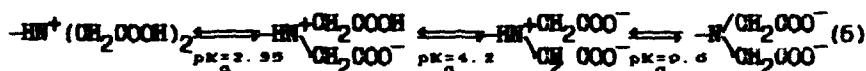
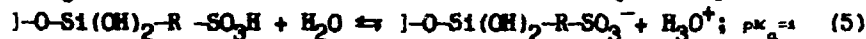
Thus, silane self assembling monolayers with good adhesion to the aluminum and iron surfaces (due to the covalent bonds Me-O-Si) form during adsorption from dilute water solution. The silane during chemisorption destroys the phase water film on the metal surface, forms stable surface layer having considerably hydrophobic effect, and prevents the hydration of Al₂O₃.

The presence of silane layers may change the charge of metal surface. The charge of a nonmodified aluminum surface in aqueous media is determined by the equilibria [2]:



For solution pH below the isoelectric point (IEPS=8.5) the surface is positively charged.

The formation on the surface siloxane layers leads to the changing of sign or density of charge in dependance of nature of silane [2]. To control surface charge densities we modified surfaces of Al by silanes with ionogenic groups. The charge of the silane molecules was changed by opening the oxyrane cycle in GPS to form sulfate-, iminodiacetate- and quarternary ammonium groups. The experimental occupancy of surface by a silane was evaluated by quartz balance and ellipsometry (Table II). The charge of the modified surface is determined by the equilibria:



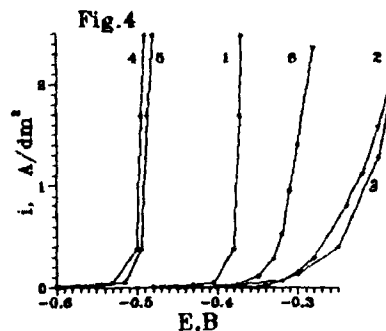
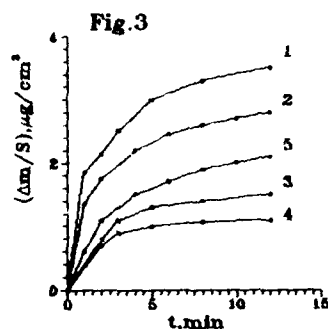
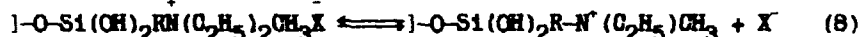
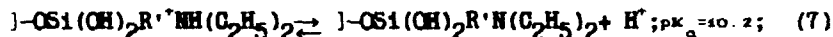


Fig. 3. Kinetic of hydration of oxide film on Al modified by silanes (1 monolayer from vapour phase) in distilled water. 1.- Al; 2.- MS; 3.- APS; 4.- VS; 5.-PS.

Fig. 4. Anodic polarization curves of (1) Al and Al modified by (2) SUL, (3) IDA, (4) DA, (5) TA and (6) GPS in 0.1M NaCl solution, 1-3, 5, 6 - pH 10.1; 4 - pH 6.1..



where $R = (CH_2)_3-O-CH_2CH(OH)CH_2$; $X = Cl, I$. It is evidence that

the metal surface may be charged both positively and negatively by changing a silane structure and pH of solution. Charge density will be determined by the coverage of surface by silane.

We studied electrochemical behavior of Al with grafted siloxane layers. Anodic polarization curves were obtained (Fig. 4). The surface of Al covers by passive film under usual conditions. In the presence of Cl^- ions in background solution the aluminum dissolves anodically on the local mechanism with breakdown of passivity (depasivation) through some small active parts of surface (so called pits). The process local dissolution is often called a pitting formation. The basic value characterized the pitting formation on a metal is the critical potential of pitting formation (E_p). E_p is a potential at which the pits begin to form on a metal surface. We have determined E_p magnitudes for all of silane used. Potentiodynamic polarization curves (Fig. 4) show that adsorption of GPS containing no ion-generating groups increases aluminum-anodic polarizability (the inhibition of pitting formation). The introduction of sulfate or iminodiacetate groups into silane radical amplifies this effect, whereas amino and ammonium radicals stimulate electrode depassivation.

In neutral and weakly alkaline electrolytes the surface has the properties of anion-exchangers. There is competing adsorption between Cl^- depassivator anion and some inhibitor ion on

anion-exchange centers M-OH_2^+ . The presence of negatively charged groups changes the sign of the surface charge from the positive to negative one. The latter leads to a decrease of the surface activity of Cl^- (Eq. 9) and an increase of E_p (Eq. 10)

$a_{\text{Cl}}^- = a_{\text{Cl}}^- \exp(-zF\psi'/RT)$ (9); $E_p = E_{\text{Al/AlCl}_3}^\circ - RT/F \ln a_{\text{Cl}}^- + \eta_{\text{Al}}$ (10), where a_{Cl}^- , a_{Cl}^- are a surface and bulk activity of Cl^- , $E_{\text{Al/AlCl}_3}^\circ$ is the standard potential of formation AlCl_3 , η_{Al} - overvoltage of a pitting formation, ψ' - surface potential, T - temperature, R , F - constant. The increase in the positive charge leads to an increase in the sorption properties on the surface and a decrease of E_p . Substitution of Eq. 9 into 10 elucidates the dependencies of the E_p from the surface potential: $\Delta E_p = -\Delta\psi'$ (11).

ΔE_p is a difference between E_p of modified and unmodified Al. We have calculated the charge generated on the metal surface by different siloxane layers (Table II). Based on charged densities one may calculate the potential (ψ') in the adsorbed charges. Because specific interactions is mostly absent between ion-generating silane radicals and electrolyte ions, we used the Gouy-Chapman model for calculating. ψ' potential in the model is determined by the surface charge:

$\psi' = 2RT/F \text{arcsinh}[q/2A(a_{\text{Cl}}^-)^{1/2}]$ (12), where $A = (\epsilon RT/2\pi)^{1/2}$, ϵ is the dielectric constant and q is the charge density (C/m^2). The theoretical values of ψ' -potential and experimental E_p is

a good agreement (Table II). Some deviations deals with the defects in the adsorption silane layers.

Thus, the formation of siloxane monolayers with ion-generated group in organic radicals allows to control effectively electrochemical processes at the interface Al/electrolyte.

Table II. The values of surface occupancy, calculated surface charge and potential, and experimental E_p for various silanes.

Silan	pH	$\theta, \text{mol/nm}^2$	$q, \text{C/m}^2$	$\Delta\psi, \text{mV}$	$\Delta E_p, \text{mV}$
SUL	10.1	3.183	-0.8	-0.194	0.17
IDA	10.1	5.73	-0.91	-0.2	0.172
DA	6.1	2.9	0.42	0.16	-0.08
TA	10.1	3.01	0.48	0.167	-0.11

References

1. E.P. Pluddemann, Silane coupling agents (Plenum Press, New York, 1982) p. 11.
2. A.P. Nazarov, M.A. Petrunin, Yu.N. Mikhailovsky, *Zashchita metallov*. 28, 970 (1992) [Protection of metals 28, 432 (1992)].
3. Strekalov P.V., Mikhailov A.A., Yu.N. Mikhailovsky, *ibid.*, 19, 179 (1983).
4. S. Brumauer, L. Couplend, D. Cantro in The solid-gas interface. edited by E.A. Flood (Marcel Dekker Inc., New York, 1967) p. 347.

MAGNETIC PROPERTIES OF NANOSIZE IRON CLUSTERS

E. L. VENTURINI, J. P. WILCOXON and P. P. NEWCOMER
Sandia National Laboratories, MS 0345, Albuquerque, NM 87185-0345

ABSTRACT

Isolated, monodisperse α -Fe clusters between 1.4 and 15 nm in diameter were prepared inside inverse micelles using an oil-continuous, nonaqueous system. The magnetic properties of these clusters were studied in a SQUID magnetometer as a function of cluster size, temperature and applied magnetic field. The blocking temperature, coercive field and remanent moment of 12.5 nm Fe clusters in inverse micelles are significantly lower than those reported for clusters of similar α -Fe core size but with a surface oxide. The novel synthesis technique may yield metallic clusters with essentially intrinsic magnetic properties.

INTRODUCTION

The properties of nm-sized magnetic particles have been studied both experimentally and theoretically for more than sixty years.[1-4] Interest in these materials has remained high because of their use in numerous practical applications in catalysis, magnetic recording, magnetic fluids and permanent magnets. In addition, there are fundamental research questions concerning the development of long-range magnetic order and associated hysteretic properties such as coercivity and remanence as the cluster size increases from a few atoms with all atoms at the surface to a large cluster with predominantly interior atoms.

Cluster synthesis and experimental handling play crucial roles in understanding the magnetic properties, particularly in separating the intrinsic properties from the effects of a surface layer [5-8] (such as a thin oxide shell) or particle-particle interactions due to agglomeration [8]. Here, we report initial studies on the magnetic properties of α -Fe clusters prepared by a novel synthesis technique which yields monodisperse particles and, we believe, mitigates both surface layer and agglomeration effects. Following are synthesis, microscopy and experimental details, presentation of the magnetic properties and concluding remarks placing our results in context.

EXPERIMENTAL DETAILS

Size-selected nanosize Fe clusters were grown by a process which is described in detail elsewhere.[9-11] Controlled nucleation and growth of metal clusters occurs in the interior of surfactant aggregates called inverse micelles. In our process an ionic salt (e.g., FeCl_3) is dissolved in the hydrophilic interior of the micelles while the surrounding continuous hydrophobic oil limits nucleation and growth to the micelle interior volume. We emphasize that the anhydrous salt is dissolved to form a transparent "ionic" solution but with a complete absence of water; in a sense the salt is "hydrated" by the micelle. The absence of water allows extremely novel and aggressive chemistry to be used in the reduction and growth process.[9,10] Encapsulation of the ionic salt solely in the micelle interior ensures spatial homogeneity during the nucleation process while the growth kinetics are determined by the rate of reduction of the metal salt and the diffusion of the micelles themselves (not the Fe atoms!). In this sense our synthetic method for size-selected clusters is fundamentally different than other cluster growth processes which occur in a continuous medium (e.g., gas or liquid phase growth) and which for fundamental reasons result in a power-law (i.e., log-normal) cluster size distribution.

Three conditions can be used to control the final cluster size: the micelle size, intermicellar interactions (e.g., phase boundaries which determine micelle diffusion rates) and reaction chemistry. To provide a constant magnetic background independent of cluster size, we have employed a single type of surfactant and solvent and varied the reduction chemistry to control the final iron cluster size for the experiments described here. We varied the strength of the nonaqueous reducing agents used to reduce the Fe(III) to Fe(0) so that the most rapid reduction kinetics produced the smallest final iron clusters. Size-selected α -Fe metallic clusters with diameters between 1.4 and 15 nm were produced. Spectroscopy was used to demonstrate 100% reduction of the Fe(III) to the final Fe(0) cluster form.[11]

All reactions took place in anaerobic conditions in a Vacuum Atmospheres dry box with continuous oxygen and moisture removal and appropriate sensors. Typical oxygen levels were 0.1 to 1 ppm and moisture levels were 0.5 to 3 ppm in the dry box. All solvents and surfactants used were hplc grade and were completely dust free. The latter is critical to prevent inhomogeneous nucleation. Magnetization samples were weighed to determine total iron concentration and transferred to capped NMR tubes in the dry box to minimize oxygen exposure. The capped tubes were then removed from the dry box and transferred to the commercial SQUID magnetometer (Quantum Design MPMS) for magnetic characterization.

The inverse micelle system used in these experiments was DTAC (dodecyltrimethyl ammonium chloride) in hexadecane with hexanol used as a cosurfactant. Previous small-angle neutron scattering [9] has shown that this system provides stable growth in the cluster size range of 1 to ~18 nm which was well suited to the present investigation. After growth occurs, the resulting clusters are fully dispersed and stable in a variety of oils and their magnetic properties may be investigated as a function of cluster size. The stability against agglomeration is due to the presence of the surfactant on the cluster surface.

Fig. 1 is a bright field transmission electron micrograph (diffraction contrast) taken on a JEOL 1200EX at 120 kV showing the isolated, monodisperse 12.5 ± 0.5 nm Fe particles formed in one synthesis (the scale is indicated by the 20 nm bar). Selected area electron diffraction confirmed that these particles are the bcc α -Fe phase. Other monodisperse Fe clusters produced by this surfactant/solvent process ranged from 1.4 ± 0.1 to 15.0 ± 0.5 nm, all below the maximum size of 16.4 nm [12] for single magnetic domain Fe.



Fig. 1. TEM photograph showing monodisperse, 12.5 ± 0.5 nm Fe clusters.

MAGNETIC MEASUREMENTS

Fig. 2 compares the response to an applied magnetic field at 5 K for the dissolved FeCl_3 salt (Fe^{+3} ions in a frozen solution) before adding the reducing agent (open triangles) to that of 12.5 nm Fe clusters after reduction (solid triangles). The dashed line is a Brillouin function fit to the Fe^{+3} ion data using a g-factor of 2 and an angular momentum of 2.5. The agreement confirms the presence of isolated Fe^{+3} ; further, the low-field slope (susceptibility) decreases by a factor of 2 between 5 and 10 K, suggesting negligible magnetic interactions between the ions. In contrast, the Fe clusters show a distinct saturation in their response for fields above 1 tesla, consistent with ferromagnetic or superparamagnetic behavior characteristic of strong magnetic interactions within the clusters. Note the qualitative difference between the isolated ions and the clusters: the isolated Fe^{+3} ions exhibit a linear response to applied field at low fields and a nonlinear response at high fields while the 3.7 nm Fe clusters show a nonlinear response (and a larger moment per gram) at low fields but saturate to a constant moment in moderate fields.

Fig. 3 shows isothermal hysteresis data (moment M versus applied magnetic field H) measured at 5 K following zero-field cooling. The open circles denote the initial response to an increasing field, the solid triangles for a decreasing field, and the open triangles for an increasing field. The data are shown between -0.25 and $+0.25$ tesla, but the actual hysteresis measurement used field strengths to ± 2 tesla. These 12.5 nm α -Fe clusters are ferromagnetic at 5 K with the data approaching saturation and exhibiting reversibility at high field strengths. There is a substantial remanent moment M_{rem} at zero field and a moderate coercive field H_{coer} (where the moment crosses through zero following saturation). The saturation moment for these particles at 5 K, determined by plotting M versus $1/H$ and extrapolating to infinite field, is 2.2×10^{-3} emu or ≈ 25 emu/g for the 88 μg of Fe in this sample; the saturation moment for bulk α -Fe is 220 emu/g at low temperatures [12]. The total diamagnetic (negative) signal from the surfactant, solvent, glass NMR tube and reducing agent salts (measured in a separate experiment) is linear in applied field and -6.8×10^{-4} emu in 1 tesla at 5 K; all data have been corrected for this diamagnetism. Although this correction is small at the fields strengths in Fig. 3, it is large at 5 tesla for the dilute Fe samples studied here. Since the Fe sample plus surfactant/solvent/reducing agent is measured independently from the diamagnetic correction, there is considerable uncertainty in the determination of a saturation value by plotting the corrected moment versus $1/H$ due to the dominance of the correction term.

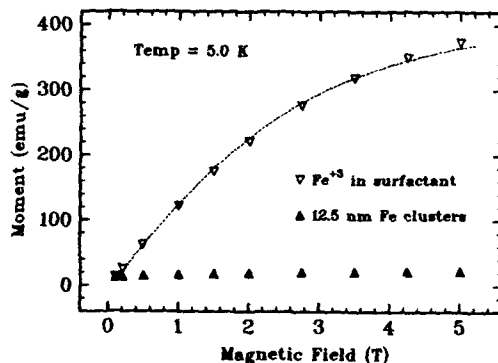


Fig. 2. Moment versus field at 5 K before and after reduction to Fe clusters.

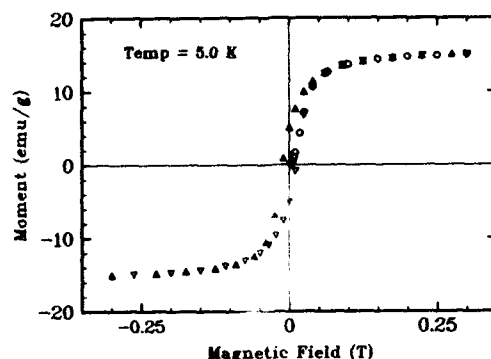


Fig. 3. Hysteresis at 5 K for 12.5 nm α -Fe clusters.

The magnetic moment of each Fe particle in a frozen solution will exhibit random rotations driven by thermal fluctuations.[13] Opposing these fluctuations is the magnetic anisotropy energy $E_{\text{anis}} = KV$ where K is the anisotropy energy per unit volume and V is the volume of the particle. An assembly of such particles will relax to equilibrium through thermal fluctuations on a time scale τ given by

$$\tau = \tau_0 \exp[KV/kT] \quad (1)$$

where τ_0 is a characteristic time on the order of 10^{-9} seconds, k is the Boltzmann constant and T the absolute temperature.[14]

One of the distinguishing features of small, single domain magnetic particles is the appearance of a blocking temperature T_B defined as the temperature where the relaxation time τ in Eq. (1) becomes comparable to the experimental time of 100 seconds. For temperatures above T_B , the magnetization versus applied magnetic field is reversible due to thermal fluctuations, i.e., the sample exhibits no remanence or coercivity in a hysteresis measurement.[14] Fe has cubic anisotropy with an anisotropy energy K_{Fe} of 4.6×10^5 ergs/cm³; the easy direction for magnetization is one of the [100] axes. For spherical Fe particles with cubic anisotropy, the K in Eq. (1) must be replaced by $K/4$. [14] Using Eq. (1) for the 12.5 nm Fe particles and $\tau_0 = 10^{-9}$ seconds, we predict $T_B \approx 34$ K for a thermal relaxation time of 100 seconds (the calculated relaxation time is 3×10^9 sec at 20 K and 18 nsec at room temperature).

An experimental blocking temperature can be determined from isothermal hysteresis measurements using the vanishing of remanence and coercivity. Fig. 4 shows the remanent moment and coercivity versus temperature for the 12.5 nm particles; both vanish between 50 and 60 K. This experimental T_B is only 50% higher than the calculated value and the latter is extremely sensitive to particle size and morphology. For example, 14 nm particles have a predicted T_B of 47 K which would agree with our experimental result. In addition, various improvements to Eq. (1) have been suggested.[15] We have also studied a sample with 3.7 nm α -Fe particles and found an experimental T_B of 15 K. The volume of these particles is only 2.6% of that for the 12.5 nm clusters, and Eq. (1) predicts a blocking temperature of 0.9 K. The cause of this large disagreement between simple theory and experiment for these 3.7 nm clusters is not understood. It may be that the assumptions of spherical particles and bulk magnetic anisotropy are not valid for very small cluster sizes.

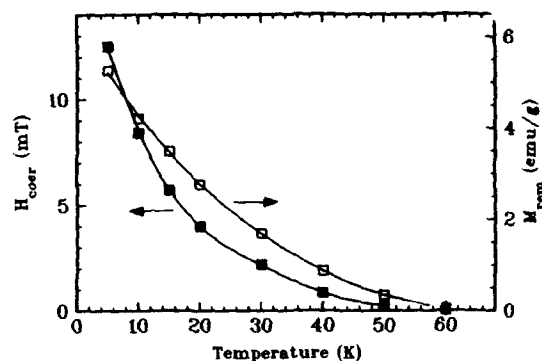


Fig. 4. Coercive field and remanent moment versus temperature for 12.5 nm α -Fe clusters.

DISCUSSION AND CONCLUSIONS

Nanometer-sized particles of Fe, Co or Ni are promising for applications requiring a high saturation magnetization and large coercivity. We have developed a novel synthetic procedure for size-selected clusters between 1 and ~18 nm in diameter. The nonaqueous synthesis under anaerobic conditions produces clusters which are individually isolated within inverse micelles and thus stabilized against agglomeration. Careful sample handling permits studies with minimal exposure to oxygen or moisture. Magnetic data for the saturation magnetization M_{sat} , remanent moment M_{rem} , coercivity H_{coer} and superparamagnetic blocking temperature T_B of a sample with 12.5 ± 0.5 nm α -Fe clusters differ considerably from literature values.

M_{sat} is ≈ 25 emu/g at 5 K from extrapolation of magnetization versus $1/H$ or roughly 10% of the 220 emu/g for bulk α -Fe. Literature values range from 20% of bulk Fe for ~10 nm particles [5,8] to the bulk value for Fe clusters with 500 to 700 atoms [16] (~2.5 nm diameter). However, the 10 nm particles were oxidized [5,8] and the effects of an oxide shell on the measured M_{sat} of the α -Fe core are not clear. M_{rem} is ≈ 5 emu/g at 5 K and vanishes between 50 and 60 K for the 12.5 nm Fe clusters in inverse micelles compared to 30 emu/g at both 220 and 300 K for oxidized Fe particles with a 3.3 nm diameter metallic core [5]. Again, oxidation of the Fe clusters appears to drastically alter the superparamagnetic transition and remanence.

Coercivity varies strongly with particle size, reaching a maximum for ~15 nm particles of Fe and Co.[17] However, the origin of the coercivity is poorly understood, particularly the effect of surface oxide. The maximum calculated H_{coer} for single domain Fe particles is 50 mT due to magnetic anisotropy while measured values are twice as large.[17] Oxidized α -Fe can have H_{coer} up to 340 mT at 10 K for 6 nm particles [5] and 160 mT for 13 nm particles [6]. The latter is a factor of 20 larger than $H_{coer} \approx 8$ mT at 10 K for the 12.5 nm α -Fe particles studied here (Fig. 4). More importantly, oxidized Fe particles with α -Fe core diameters between 8.4 and 14 nm exhibited strong coercivities of 40 to 110 mT at room temperature [5], while the coercivity of our 12.5 nm α -Fe particles decreases rapidly with increasing temperature and vanishes between 50 and 60 K, i.e., at T_B (Fig. 4). In one experiment, Fe particles between 6 and 22.7 nm in diameter were synthesized by gas evaporation, collected on a Ag film and covered by a second Ag film inside the evaporation chamber to minimize oxidation.[5] These samples exhibited large, nearly temperature-independent H_{coer} [5], strikingly different from the behavior of the present Fe clusters.

Superparamagnetic blocking temperatures were 50-60 K for 12.5 nm clusters and 15 K for 3.7 nm clusters in inverse micelles. The former value agrees reasonably well with the calculated T_B based on cluster size and the magnetic anisotropy of bulk Fe while the latter value is considerably above the calculated T_B . Reported values ranged from 230 K for 5.3 nm Fe cores to 120 K for 2.5 nm cores of oxidized clusters.[5] Granular films with 3 to 9 nm α -Fe particles in a BN host matrix had a field-dependent blocking temperature between 35 and 40 K.[7] However, particle interactions were evident in the strong dependence of coercivity on Fe concentration [7] and these interactions may affect the measured T_B .

Our novel synthesis technique for isolated, size-selected α -Fe clusters in the 1 to 18 nm range provides an opportunity to test various predictions for coercivity, remanence and saturation magnetization as a function of particle size and temperature. The same synthesis has been used for preparing size-selected Co and Ni clusters. The magnetic behavior of these particles should identify the separate roles of thermal energy, magnetic anisotropy and surface versus "bulk" atoms as the cluster size approaches a few unit cells, thus improving our understanding of magnetic phenomena in this size range.

ACKNOWLEDGEMENTS

The assistance of Sharon Craft in cluster synthesis is gratefully acknowledged. This work was performed at Sandia National Laboratories and was supported by U.S. Department of Energy, Office of Basic Energy Sciences, under Contract No. DE-AC04-94AL85000.

REFERENCES

1. I.S. Jacobs and C.P. Bean in *Magnetism*, edited by G. T. Rado and H. Suhl (Academic Press, New York, 1963), Vol. III, pp. 271-350, and references therein.
2. W.F. Brown, Jr., *Micromagnetics* (Wiley Interscience, New York, 1963).
3. E.P. Wohlfarth in *Magnetism*, edited by G. T. Rado and H. Suhl (Academic Press, New York, 1963), Vol. III, pp. 351-393.
4. E. Kneller in *Magnetism and Metallurgy*, edited by A. Berkowitz and E. Kneller (Academic Press, New York, 1969), Vol. 1, pp. 365-471 and references therein.
5. S. Gangopadhyay, G.C. Hadjipanayis, S.I. Shah, C.M. Sorensen, K.J. Kablunde, V. Papaefthymiou, A. Kostikas, J. Appl. Phys. **70**, 5888 (1991).
6. S. Gangopadhyay, G.C. Hadjipanayis, B. Dale, C.M. Sorensen, K.J. Kablunde, V. Papaefthymiou, A. Kostikas, Phys. Rev. B **45**, 9778 (1992).
7. A. Tsoukatos, H. Wan, G.C. Hadjipanayis, V. Papaefthymiou, A. Kostikas, A. Simopoulos, J. Appl. Phys. **73**, 6967 (1993).
8. A. Tasaki, S. Tomiyama, S. Iida, N. Wada, R. Uyeda, Jpn. J. Appl. Phys. **4**, 707 (1965).
9. J.P. Wilcoxon, R.L. Williamson, R.J. Baughman, J. Chem. Phys. **98**, 9933 (1993).
10. J.P. Wilcoxon, U.S. Patent No. 5,147,841, "Method for the Preparation of Metal Colloids in Inverse Micelles and Product preferred by the method", issued 15 September 1992.
11. A. Martino, J.P. Wilcoxon, J. Kawola, Energy and Fuels, in press.
12. B.M. Berkovsky, V.F. Medvedev, M.S. Krakov, *Magnetic Fluids: Engineering Applications* (Oxford Univ. Press, Oxford, 1993), p. 12.
13. L. Néel, Compt. Rend. **228**, 664 (1949).
14. C.P. Bean and J.D. Livingston, J. Appl. Phys. **30** (supplement), 120S (1959).
15. For example, W.F. Brown, Jr., J. Appl. Phys. **30** (supplement), 130S (1959).
16. I.M. Billas, J.A. Becker, A. Châtelain, W.A. de Heer, Phys. Rev. Lett. **71**, 4067 (1993).
17. F.E. Luborsky, J. Appl. Phys. **32** (supplement), 171S (1961) and references therein.

PART IV

Characterization and Modelling

SMALL ANGLE NEUTRON SCATTERING FROM NANOCRYSTALLINE Pd AND Cu COMPACTED AT ELEVATED TEMPERATURES

P.G. SANDERS*, J.R. WEERTMAN*, J.G. BARKER†, and R.W. SIEGEL‡

*Northwestern University, Materials Science and Engineering Department, Evanston, IL 60208

†National Institute of Standards and Technology (NIST), Cold Neutron Research Facility,
Gaithersburg, MD 20899

‡Argonne National Laboratory, Materials Science Division, Argonne, IL 60439

ABSTRACT

Nanocrystalline (n-) Cu and Pd, prepared by inert gas condensation (IGC) and *in situ* room temperature (RT) and elevated temperature (warm) compactions, have been studied by small angle neutron scattering (SANS). Previous work [1] on room temperature compacted and subsequently annealed n-Pd seemed to show that all the scattering could be accounted for by a distribution of pores. Analysis of more extensive SANS measurements, together with the results of prompt gamma activation analysis (PGAA), indicates that the SANS can be explained by the presence of pores and hydrogen. Warm compaction reduces the hydrogen impurity level, while increasing the bulk density and decreasing the pore size. This can lead to a dramatic hardness increase in these materials.

INTRODUCTION

The presence of impurities and a variety of defects can have a strong influence on the mechanical properties of n-metals [2]. In an effort to obtain and study the intrinsic properties of these materials, an investigation has been undertaken to quantify the types of existing imperfections, as well as to identify methods to reduce their prevalence. This paper reports preliminary findings on the presence of hydrogen (H) and oxygen (O) impurities and their influence on porosity and hardness.

PROCEDURE

The n-Pd and n-Cu were produced by IGC and compaction at Argonne National Laboratory [3]. High purity (~99.999%) Pd wire or Cu shot was evaporated in 600 Pa of high purity (~99.999%) He, and the resulting powder was compacted in vacuum for 10 min under 1.4 GPa of pressure at temperatures ranging from 20 to 300°C to form disks 9 mm in diameter and ~0.2 mm thick. One of the Pd samples was electro-discharge machined into quarters, with one quarter receiving no further treatment, while the other 3 were annealed at 100, 300, or 800°C for 100 min in high purity (~99.999%) flowing argon. The bulk density was measured using Archimedes principle. Grain size was determined from broadening of the 111 and 222 x-ray peaks using the Warren-Averbach method [4]. The H level was measured by PGAA in the Cold Neutron Research Facility at NIST [5], while the O concentration was found by fast neutron activation analysis (FNAA) performed in the Department of Chemistry at the University of Kentucky [6]. (PGAA and FNAA give no information on the chemical state of the

contaminants.) The SANS measurements were performed on the 30 m NSF SANS instrument at NIST [7] over a q -range from 0.01 to 5.7 nm⁻¹. (The magnitude of the scattering vector q is $(4\pi/\lambda)\sin \theta$, where λ is the neutron wavelength and 2θ is the scattering angle.) The reported Vickers microhardness values were an average of ten measurements made with a 100 g load and a dwell time of 20 s.

RESULTS

PGAA and FNAA measurements were carried out to determine the H and O impurity levels in n-Cu and n-Pd. Interest in these measurements was heightened by the observation of a pressure rise in the chamber just prior to warm compaction, possibly indicating that adsorbed gases were being liberated. Also, recent SANS measurements extended out to large q values had a high, constant background thought to originate from incoherent scattering from H. (H has a very large incoherent scattering cross-section, while that of O is much lower.) The H and O concentrations from PGAA and FNAA analysis, as well as the H content calculated from the SANS background level, are shown in Table I. The good agreement between the H level obtained by PGAA and SANS shows that the SANS background can be attributed to incoherent scattering by H. Tschöpe and Birringer [8] reported 3.9 at% H and 3.0 at% O in n-Pt made by IGC and compacted at 80°C, values that are in the same range as those found in n-Pd and n-Cu.

Table I. Impurities and Grain Size as a Function of Compaction Temperature

	Temp.	at% O	at% H (PGAA)	at% H (SANS)	Grain Size (nm)
Pd	20°C			7.5	5.7 ± 0.5
Pd	100°C	0.8 ± 0.3	4.5 ± 1.3	5.2	6.6 ± 0.5
Pd	300°C		< 2.1	0.4	12 ± 0.6
Pd*	200°C	1.2 ± 0.2	< 1.1		9.2 ± 0.3
Pd†	800°C			0.5	59 ± 5
Cu	20°C			7.7	7.7 ± 0.3
Cu	100°C	4.1 ± 0.5	6.3 ± 0.6	5.7	8.9 ± 0.4
Cu	150°C		4.8 ± 0.9	6.5	11 ± 1

*powder warmed by heat lamp prior to 200°C compaction

†RT compaction followed by 800°C anneal

The SANS data were found to be dominated by Porod scattering, with some incoherent scattering visible at high q , as mentioned above. The behavior predicted by Porod [9] is:

$$I(q) = \frac{2\pi(\Delta\rho)^2}{q^4} \frac{S}{V} + I_{inc}, \quad (1)$$

where $I(q)$ is the differential scattering cross section, $\Delta\rho$ is the difference in scattering length density between the matrix and the scattering defect, S/V is the total surface area per unit sample volume of scatterers, and I_{inc} is the incoherent background level. Equation 1 is valid for $qR \geq$ about 3, where R is the radius of the scattering entity. In a plot of Iq^4 vs q^4 , the slope yields the incoherent scattering cross-section (I_{inc}) and the intercept is the Porod constant C_p ($C_p = 2\pi(\Delta\rho)^2 S/V$). A plot of this type for Cu is shown in Fig. 1, where it can be seen that the fits are very good. Figure 2 is a plot of $\ln I$ vs $\ln q$ for the n-Pd data after subtracting the background. The portion of the curve with a slope of -4 corresponds to the Porod region.

The invariant Q was used to calculate the volume fraction of scatterers (V_v) [9] where

$$Q = \int_0^\infty q^2 I(q) dq \text{ and } V_v(1 - V_v) = \frac{Q}{2\pi^2(\Delta\rho)^2}. \quad (2)$$

The data were extrapolated to $q = 0$ and $q = \infty$ using the Guinier relation [9] and Porod relation, respectively. Based on the work of Schaefer [10], where voids in n-metals were identified using positron annihilation, it was assumed that voids are the primary scattering entity in the SANS experiments. Using $\Delta\rho = \rho_{Pd}$ or ρ_{Cu} , good correlation was found between the density obtained by the invariant and that measured by Archimedes principle (Fig. 3a and b).

Using both the S/V ratio from C_p and the V_v from Q , a characteristic void radius R_v can be obtained ($R_v = 3V_v/(S/V)$). The results of this calculation are shown in Fig. 4a and b. The pore size in the RT-compacted samples seems to scale with the grain size. These pores are in the same size range as Schaefer's [10] "missing grain" voids. The number density can also be obtained from this method, and it tends to scale with the number of grains in the RT-compacted samples.

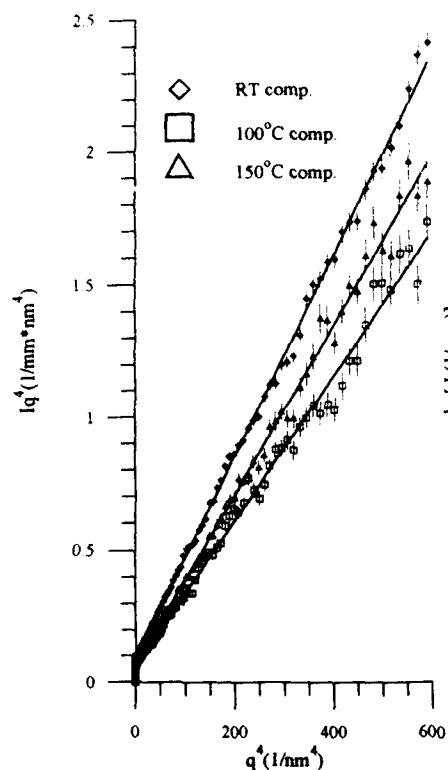


Fig. 1. Determination of I_{inc} and C_p for n-Cu.

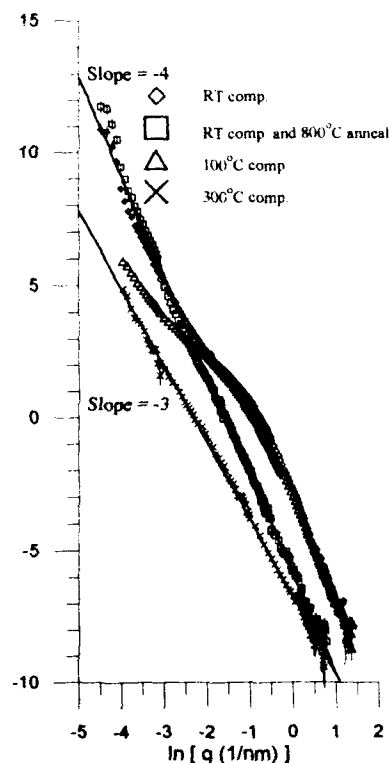


Fig. 2. SANS data for n-Pd.

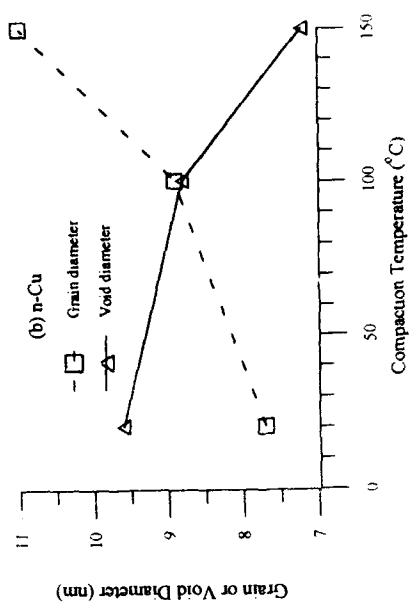
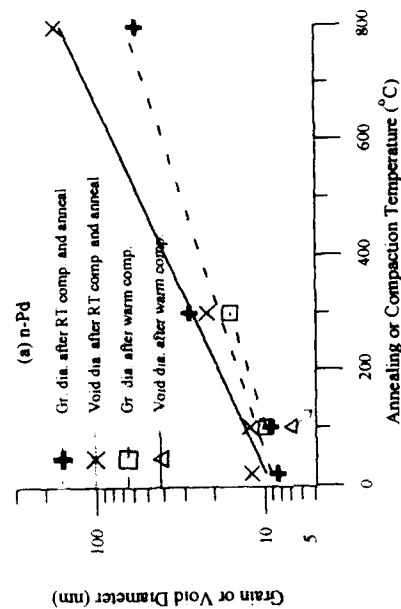


Fig. 4 Grain or void diameter in n-Pd (a) and n-Cu (b).

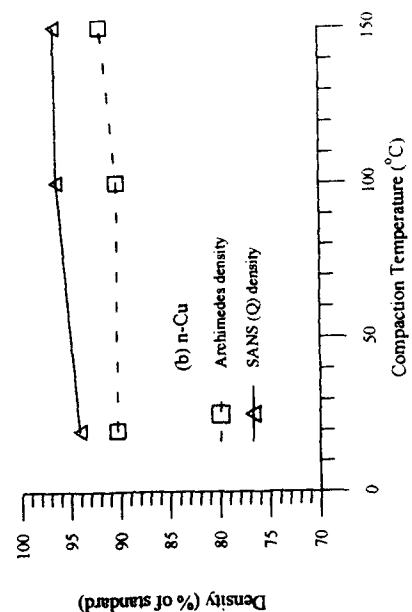
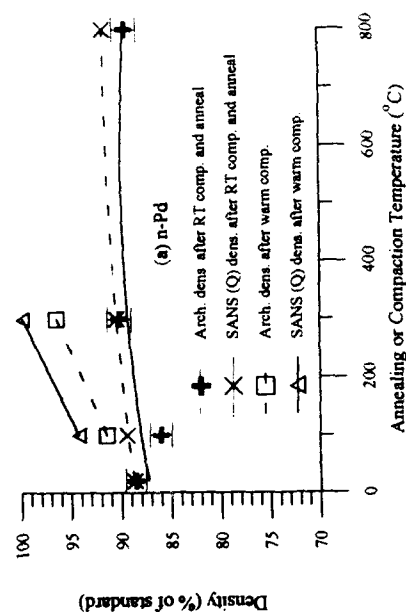


Fig. 3. Density of n-Pd (a) and n-Cu (b).

DISCUSSION

The H and O contamination discussed above could result from the adsorption of water vapor on the small crystallites after they are collected by the cold finger. Even though there is a cold trap in the synthesis chamber, the cold finger can act like an additional cold trap during the evaporation, a time when the system is not actively pumped. The data in Table I suggest (within experimental uncertainties) that water vapor is driven off by warming the powder. This hypothesis is supported by the order of magnitude lower H levels in the n-Pd sample compacted at elevated temperatures. (The O data are too limited to verify this trend.) For the 300°C compaction, where the powder was allowed to outgas in the hot die prior to insertion of the piston, a H level of 0.4 at% was achieved (Table I). Another sample, compacted at 200°C after warming the powder in front of a bakeout lamp, had a H content even lower than that of the 300°C compaction with a smaller increase in grain size (Table I).

The H concentration can also be greatly reduced by annealing, but at the expense of extensive grain growth. This is demonstrated by the quarter annealed at 800°C, where the H level measured by SANS decreased from 7.5 to 0.5 at% while the grains grew from 5.7 to 59 nm (Table I). Samples annealed at 100 and 300°C produced proportionately smaller reductions in the H level, along with decreased grain growth.

The small discrepancy between the density as measured by Archimedes principle and SANS may be the result of either a few large pores or surface roughness. The presence of very large scatterers ($> 0.1 \mu\text{m}$ for the q-range used in this experiment) can lead to substantial errors in the volume fraction calculated from Q [11], since the scattering from these defects may be hidden by the beamstop. A few 1-5 μm voids, elongated perpendicular to the compression axis, have been observed in fracture surfaces of RT-compacted n-Pd by scanning electron microscopy (SEM). On the other hand, small surface flaws unable to be wetted by the fluid (ethyl phthalate) used to make the density measurements could make the Archimedes density too low. High resolution SEM images of the surface of warm compacted n-Cu and n-Pd reveal valleys and holes between clusters in the range of 10 to 100 nm, as well as surface roughness in the micrometer range.

Warm compaction produces increased bulk densities compared to RT-compaction and annealing. At this time it is not clear if the reduction in gaseous impurities or the improved sintering between particles is the main reason for the improvement. Despite the uncertainty in mechanism, the pores in n-Pd compacted at 100°C are approximately half the grain size, while in the sample which was RT compacted and annealed at 100°C the pores are larger than the grain size (Fig. 4a). As shown in Fig. 2, the slope for the sample compacted at 300°C changes from -4 to -3, while the intensity is much lower. Perhaps the pores are no longer the dominant scatterers (this is depicted in Fig. 4a by a downward sloping line from the 100°C compaction), and scattering from another defect type (e.g. grain boundaries) has become detectable. The behavior of the n-Cu clearly shows (Fig. 4b) the pore size decreasing with increasing compaction temperature.

Preliminary results indicate that warm compaction can produce significantly higher hardness in n-Pd. The sample compacted at 300°C had a density of 96.4 %, a H level of 0.4 at%, and a hardness of 5.8 GPa. This is more than 1 GPa higher than other reported values for n-Pd. Small amounts of elasticity (the sample has been reversibly bent slightly without breaking) has also been observed. More work is necessary to confirm these results and isolate the causes.

CONCLUSIONS

Hydrogen and oxygen contamination can be a significant problem in n-materials made by IGC and compaction, but this contamination can be reduced by warming powders prior to compaction, or by subsequent annealing. Voids on the order of the grain size have been identified in n-Pd and n-Cu by SANS. The size of the voids decrease (both absolutely and relative to the grain size) with increasing compaction temperature. Preliminary results indicate that warm compaction is much more effective for porosity reduction than room temperature compaction followed by annealing. Lower H concentrations (possibly due to desorption of water vapor) and higher densities produced by warm compaction may lead to large increases in hardness.

ACKNOWLEDGEMENTS

This work was supported by the U.S. Department of Energy (DOE), Grant DE-FG02-86ER45229, at Northwestern University, by the U.S. DOE, Office of Basic Energy Sciences, Contract W-31-109-Eng-38, at Argonne National Laboratory, and by the National Science Foundation, Agreement DMR-9122444, at the National Institute of Standards and Technology. The authors would like to thank Richard Lindstrom and William Ehmann for doing the PGAA and FNAA, respectively.

REFERENCES

1. P.G. Sanders, J.R. Weertman, J.G. Barker, and R.W. Siegel, *Scripta Metall. et Mat.* **29**, 91 (1993).
2. G.W. Nieman, J.R. Weertman, and R.W. Siegel, *J. Mat. Res.* **6**, 1012 (1991).
3. R.W. Siegel, S. Ramasamy, H. Hahn, Z. Li, T. Lu, and R. Gronsky, *J. Mat. Res.* **2**, 1367 (1988).
4. B.E. Warren, *X-ray Diffraction* (Addison-Wesley, Reading, 1969), pp. 251-314.
5. R.M. Lindstrom, *J. Res. NIST* **98**, 127 (1993).
6. W.D. Ehmann and B.F. Ni, *J. Radioanal. Nucl. Chem.* **160**, 169 (1992).
7. B. Hammouda, S. Krueger, and C.J. Glinka, *J. Res. NIST* **98**, 31 (1993).
8. A. Tschöpe and R. Birringer, *Phil. Mag. B* **68**, 223 (1993).
9. G. Porod, in *Small Angle X-ray Scattering*, edited by O. Glatter and O. Kratky, (Academic, London, 1982) pp. 17-51.
10. H.-E. Schaefer, in *Mechanical Properties and Deformation Behavior of Materials Having Ultra-Fine Microstructures*, edited by M.A. Nastasi, D.M. Parkin, and H. Gleiter (Proc. NATO Advanced Study Inst., Kluwer Academic, Dordrecht, 1993) pp. 81-106.
11. J.G. Barker and J.R. Weertman, *Scripta Metall. et Mat.* **24**, 227 (1990).

INTERFACIAL STRUCTURE OF ELECTRICALLY CONDUCTING ADSORBED MULTILAYERS

G. J. KELLOGG*, A.M. MAYES*, W. B. STOCKTON*, M. FERREIRA*, M.F. RUBNER* AND S.K. SATIJA**

*Department of Materials Science and Engineering, M.I.T., Cambridge, MA 02139

**Reactor Radiation Division, Natl. Institute of Standards and Technology, Gaithersburg, MD 20899

ABSTRACT

The multilayer organization of sulfonated polyaniline/polyallylamine (SPAN/PAH) films was investigated by neutron reflectivity. Films were prepared by sequential adsorption of polycations and polyanions from dilute solution. Scattering contrast was achieved by selective deuteration of blocks of bilayers at varying intervals along the films. The internal organization of the multilayer structure was found to decay significantly with increasing number of bilayer depositions. In addition, a high degree of roughness was determined at the free surfaces of the films. Together, these results suggest that both conformal and nonconformal roughness are present in the films, i.e., defects introduced during individual layer depositions are to some degree transferred to the surface of subsequently deposited layers.

INTRODUCTION

Molecular-scale processing techniques hold great promise for next-generation optoelectronic device fabrication. Waveguides, light emitting diodes and anisotropic conductors have been prepared via Langmuir-Blodgett and other molecular assembly schemes. Employing the sequential adsorption method first developed by Decher¹, Rubner and coworkers² have fabricated electrically conducting multilayer (ML) films using highly conjugated polyelectrolytes. The technique involves dipping a surface-modified glass or silicon substrate alternately into dilute polycation and polyanion solutions, depositing in each dip a monolayer of charged material which serves as an attractive surface for the subsequent layer of opposite charge. A schematic illustration of the system investigated is shown in Fig. 1. This comparatively simple method of molecular-level assembly offers a novel means to fabricate complex thin film structures with tunable optical/electronic properties. For example, the conductivity of multilayer thin films of the materials used in this study were previously measured³ to be $\sim 10^{-3}$ S/cm. However, little is known about the uniformity or the extent of interpenetration of the deposited bilayers, structural features which ultimately influence device performance. The aim of the current study was to investigate layer organization as a function of film depth in conducting polyelectrolyte multilayers assembled by sequential adsorption. Here we report results of neutron reflectivity studies from a set of 40 bilayer films of sulfonated polyaniline/polyallylamine, SPAN/PAH, each selectively labelled at different depths with 8 bilayer blocks of SPAN-d₇/PAH. The technique of neutron reflectivity is highly sensitive to gradients in the scattering length density normal to the film surface, thus allowing for a quantitative evaluation of the internal layer organization when such a labelling scheme is employed.

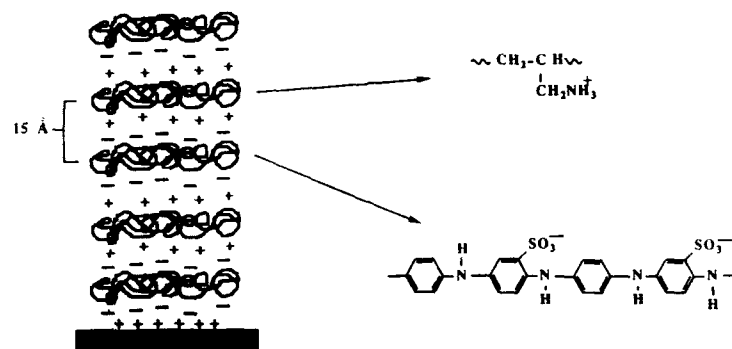


Figure 1. Schematic illustration of SPAN/PAH ML film prepared by sequential adsorption technique.

EXPERIMENTAL PROCEDURE

Polished silicon substrates 10 cm in diameter and 0.25 cm thick with (100) planes parallel to the surface were purchased from Semiconductor Processing Co. A series of films consisting of alternating layers of the polyanion sulfonated polyaniline (SPAN) and the polycation polyallylamine (PAH) were adsorbed onto the surface of the silicon substrates to produce films ~600 Å thick composed of 40 bilayers. Prior to the first monolayer deposition, the substrates were immersed in a bath of $\text{H}_2\text{SO}_4/\text{H}_2\text{O}_2$ for 30 minutes, rinsed with deionized water and placed immediately in a bath of boiling $\text{H}_2\text{O}/\text{NH}_4\text{OH}/\text{H}_2\text{O}_2$ for 1 hour. Afterwards, substrates were rinsed thoroughly and left to soak in deionized water until used. This surface treatment closely follows the procedure of Decher et al.¹ Adhesion to the silicon oxide surface was promoted through modification with the monofunctional coupling agent, 4-amino butyl dimethyl methoxy-silane, prior to the first polyelectrolyte deposition.

To investigate the multilayer organization, 8-bilayer blocks were selectively contrasted at varying depths within the separate films by substituting SPAN- d_7 for SPAN. In total, four 40-bilayer systems were investigated with the following labelling schemes: 8D/32H (A), 16H/8D/16H (B), 32H/8D (C), 8D/8H/8D/8H/8D (D), where D denotes bilayers containing isotopically labelled SPAN and H represents the unlabelled bilayers. Sample D integrates the labelled regions of the three other samples into a single film, and serves to test the reproducibility of the film structure and consistency of our analysis. The periodic spacing of the labelled blocks should additionally give rise to observable Bragg reflections in the measured reflectivity, if the film is sufficiently ordered.

Neutron reflectivity measurements were performed on the BT-7 instrument at the National

Institute of Standards and Technology (NIST) in Gaithersburg, Maryland. The experimental setup and sample alignment procedure are described in previous publications.^{4,5} A graphite monochromator delivers neutrons of wavelength $\lambda = 2.37 \text{ \AA}$ and resolution $\Delta\lambda/\lambda \approx 0.01$ to the sample surface. Reflectivity profiles are generated by rotating the sample θ and the detector 2θ degrees with reference to the incident beam. Data points were taken in steps of 0.01° in θ out to 0.8° or 0.07 \AA^{-1} in neutron momentum, $q_z = 4\pi \sin \theta / \lambda$, with an angle-dependent resolution of $\Delta\theta/\theta \approx 0.02$ at the highest angles sampled. Background intensities were obtained by offsetting 2θ by $+0.25^\circ$. After background subtraction, the reflectivity was obtained by normalizing the net intensity by the main beam intensity for identical slit conditions.

To fit the reflectivity data, scattering length density (b/v) profiles were generated by modeling the films as adjacent layers of an assumed thickness and b/v value, with finite interfaces ($a_i = (2\pi\sigma^2)^{1/2}$, where σ is the rms roughness) between layers. The theoretical reflectivity was then derived from the model b/v profile and evaluated against the experimental data. Model parameters (thickness, b/v , a_i) were modified iteratively until a best fit to the data was achieved.

RESULTS AND DISCUSSION

Figure 2a shows the measured reflectivity as a function of q_z from sample A, which contains an 8 bilayer block of SPAN-d7/PAH adjacent to the silicon surface (a schematic illustration of the labelling scheme is inset in Fig. 2b). Oscillations in the reflectivity data arise from interferences between neutrons reflected from the surface of the film and the internal interfaces created by incorporating the isotopically labelled block. The oscillations are seen to decay rapidly as a function of increasing angle θ . Qualitatively this result implies that a high degree of roughness is present at the film surface. The solid line in Fig. 2a represents the best fit to the data, corresponding to the scattering length density profile shown in Fig. 1b. A number of important observations can be made on examining this result. First, the deuterated block is clearly distinguishable as a region of high contrast next to the substrate. (Note that a thin oxide layer has been incorporated into the profile at the Si surface.) However, the interface between this region

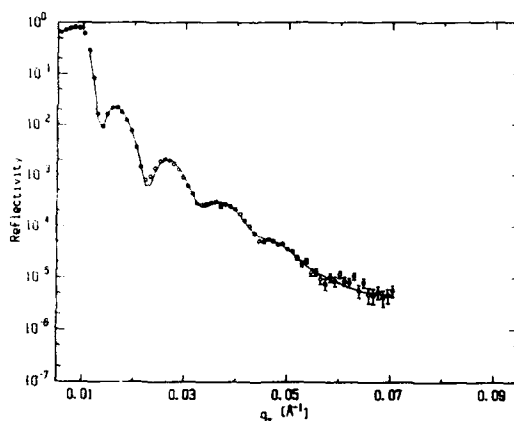


Fig. 2a. Fitted reflectivity for SPAN/PAH ML film with 8 labelled bilayers adjacent to substrate.

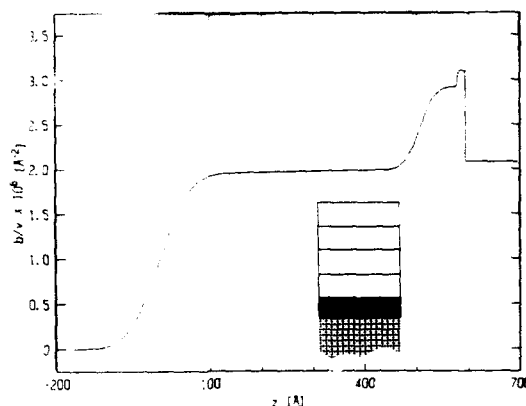


Fig. 2b. Model scattering length density profile yielding the best fit to the reflectivity data. Inset shows a schematic illustration of labelling scheme in the film.

and the unlabelled portion of the film is quite broad, $a_i \approx 45 \text{ \AA}$. At least two interpretations can be made of the observed interfacial width. Since the average bilayer thickness is approx. 15 \AA , the broad interfacial region could suggest the interdiffusion of chains over several bilayers. Alternatively, the broad interface could indicate a highly corrugated or irregular interface between the labelled and unlabelled bilayers. Since the roughness at the silicon surface is expected to be no greater than 5 \AA , this internal roughness would have been introduced through uneven bilayer depositions. The high degree of surface roughness apparent for this film ($a_i \approx 95 \text{ \AA}$) would support this latter interpretation.

The conclusion that the surface roughness increases with increasing number of bilayer depositions is supported by the reflectivity results on samples labelled at other positions along the film. Figure 3 shows results for sample *D*, in which the labelled bilayer blocks are spaced periodically within the film. The measured reflectivity (Fig. 3a) has a broad first order Bragg reflection at $q_z \approx 0.026 \text{ \AA}^{-1}$, indicating that the multilayer structure induced by alternately depositing 8-bilayer blocks of deuterated and hydrogenated SPAN with PAH is to some extent preserved. The oscillations in this profile are notably weak, however, and again decay rapidly as a function of increasing q_z . Fig. 3b shows the b/v profile which yields the fit to the reflectivity data represented by the solid line in Fig. 3a. With increasing number of deposited layers, certain trends are evident in the b/v profile. A continuous increase in the interfacial width is noted between labelled and unlabelled portions of the film on moving up from the substrate. After 32 bilayer depositions the interfacial width between D and H blocks is found to be $> 60 \text{ \AA}$. Moreover, the scattering length density of the deuterated blocks is seen to decrease substantially from the substrate to the surface. The width of the polymer/air interface is again on the order of 90 \AA for this system. This large surface roughness, coupled with the decay of the internal ML organization, suggests that defects introduced by the deposition process are transferred conformally to the film surface during subsequent layer depositions.

These observations are consistent with atomic-force microscopy (AFM) measurements

performed on films prepared concurrently with the neutron reflectivity samples. For 32 bilayer films of SPAN/PAH, AFM reveals an extremely rough top surface (~ 80 Å). The lateral length scale of the surface corrugations appears to be 100-200 Å.

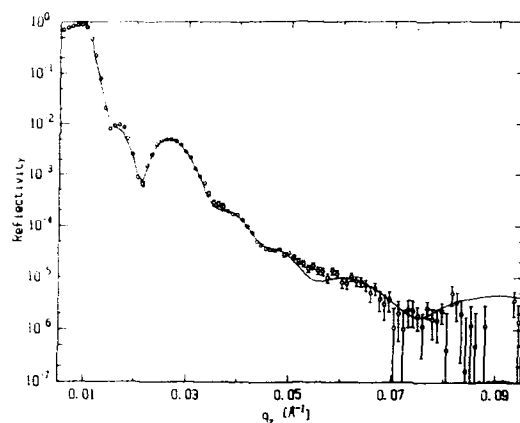


Fig. 3a. Fitted reflectivity for 40 bilayer SPAN/PAH ML film with blocks of 8 labelled bilayers spaced periodically along the film.

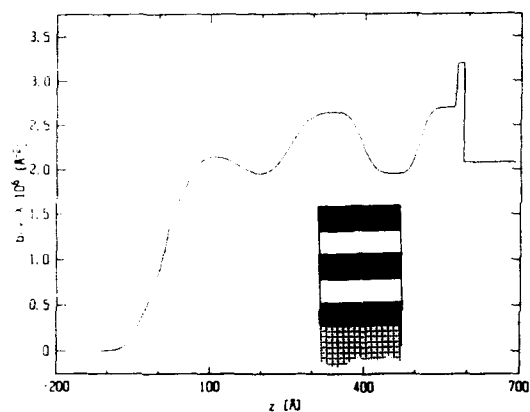


Fig. 3b. Model scattering length density profile yielding the best fit to the reflectivity data. Inset shows a schematic illustration of labelling scheme in the film.

We can compare our results to those of Schmitt, *et al.*⁶, who used x-ray and neutron reflectivity to characterize self-assembled multilayer films of sulfonated polystyrene/polyallylamine (SPS/PAH) on silicon, using a slightly different contrast method. The widths of internal interfaces were found to be about 48 Å, while at the free surface they reported $a_i \approx 33$ -38 Å. It should be noted that x-ray reflectivity measurements of their films exhibited up to 25 thickness oscillations (Kiessig fringes) for films 1200 Å thick, while preliminary x-ray studies of our SPAN/PAH films exhibited at most two such oscillations. These observations are consistent with the neutron data which suggest that the SPAN/PAH films display a much rougher surface than the SPS/PAH system, perhaps due to the relative stiffness of the highly conjugated SPAN component.

Finally, the total thicknesses of the films investigated here were nearly identical (580-590 Å), showing that while layer adsorption may introduce surface irregularities, the average amount of material deposited in each layer is very reproducible. Furthermore, the b/v values of the H blocks are consistent ($b/v \sim 2.0 \times 10^{-6} \text{ Å}^{-2}$) for the four films. However, these values are nearly twice that calculated from the molecular structures of SPAN and PAH. It is possible that unknown concentrations of counterions present in the films from the polyelectrolyte solutions significantly enhance the b/v values in both the H and D blocks. We hope to address the issue of counterion concentration in future investigations through optical and x-ray frequency absorption experiments.

ACKNOWLEDGMENT

This work was supported by the Center for Materials Science and Engineering under NSF grant #DMR90-22933.

REFERENCES

1. G. Decher, J.D. Hong and J. Schmitt, *Thin Solid Films* **210**, 831 (1992).
2. M. Ferreira, J.H. Cheung, W. Scruggs and M.F. Rubner, "Molecular self-assembly of conducting polymers: a new process for fabricating electrically conducting thin films", *SPE Proc.*, New Orleans, LA 1993.
3. M. Ferreira, J.H. Cheung and M.F. Rubner, "Molecular self-assembly of conjugated polyions: a new process for fabricating multilayer thin film heterostructures", *Thin Solid Films* (in press).
4. S.H. Anastasiadis, T.P. Russell, S.K. Satija and C.F. Majkrzak, *J. Chem. Phys.* **92**, 5677 (1990).
5. A.M. Mayes, T.P. Russell, S.K. Satija and C.F. Majkrzak, *Macromolecules* **25**, 6523 (1992).
6. J. Schmitt, T. Grunewald, G. Decher, P.S. Pershan, K. Kjaer, and M. Losche, *Macromolecules* **26**, 7058 (1993).

DETERMINATION OF THE BOND STRENGTH BETWEEN NANOSIZED PARTICLES

ALFRED P. WEBER and SHELDON K. FRIEDLANDER
Department of Chemical Engineering, University of California, Los Angeles, 405 Hilgard Ave., Los Angeles, CA 90024

ABSTRACT

A method has been developed for determining the bond energies between nanosized particles from the kinetics of the rearrangement of aerosol agglomerates. The method of calculation is based on the change in Gibbs' free energy during restructuring. For Ag and Cu agglomerates, bond energies between the nanosized particles are of the order of magnitude calculated from bulk Hamaker constants.

INTRODUCTION

Agglomerates of nanometer particles formed in collision processes are held together by bonds between the primary particles. Such bonds may range from van der Waals attraction to stronger bonds such as ionic or covalent. Strong bonds between the primary particles may make powders of these agglomerates more difficult to process in the fabrication of ceramic materials. Aerosol processing can for instance be done by heat transfer (sintering). There are two extreme types of sintering processes. On the one hand agglomerates of very strongly bonded particles (e.g. solid state bridges) retain their general topology (expressed by the fractal-like dimension) during sintering. In this case, the size of the agglomerates is decreasing while the mean size of the subunits (e.g. thickness of the dendrites or primary particle size) increases during sintering [1].

On the other hand, agglomerates of weakly bonded primary particles tend to collapse first at low temperature during heat transfer. Solid state diffusion between primary particles in close contact starts at much higher temperatures [2]. The studies described in this paper were conducted at much below this temperature. A model for the kinetics of rearrangement is discussed and tested for silver and copper agglomerates. The main goal of this work was to establish a method for the in situ measurement of the bond energies between nanometer particles.

KINETICS OF REARRANGEMENT

The arrangement of non-coalescing particles within a certain gas volume has two limiting cases: the particles can be fully dispersed within the volume, subject to the Brownian motion and non-interacting (see Fig. 1a). In this state which we will call "gaseous" state in analogy to a gaseous species within another carrier gas, the Gibbs' free energy is maximum and the number of bonds is zero.

On the other hand, the arrangement with minimum Gibbs' free energy for attractive particles is the closed packed structure shown in Fig. 1c. Again, by analogy to the condensation of a gas, this state will be called the "condensed" state. From the condensation of noble gases, the coordination number c_N (number of nearest neighbors) is expected to lie between 8 and 11 [3]. The theoretically possible coordination number, about 12, for the close packed structures in 3 dimensions [4]

has not been observed for aerosol agglomerates. However, the upper limit of c_N can be determined when better data are available. For our model only the relative change in the coordination number is of importance and the influence of the upper limit of c_N on the resulting bond energy was found to be small.

In between these extreme states an intermediate state exists where the particles are bonded, but the excess Gibbs' free energy drives the agglomerates to restructure towards the condensed state. In the final stages of decay to the condensed state, the change in c_N is assumed to follow a linear relationship :

$$\frac{dc_N}{dt} = -L \cdot (G - G_{eq}) \quad (1)$$

where c_N : coordination number, G : Gibbs' free energy of the agglomerate, G_{eq} : minimum Gibbs' free energy (condensed state) and L : phenomenological coefficient which depends on the temperature..

The Gibbs' free energy can be related to the coordination number by $G = \epsilon \cdot c_N$, where ϵ is the bond energy between two primary particles. Combining this relation with eq. (1) gives a differential equation for c_N . The bonds between the particles represent an energy barrier that has to be overcome for rearrangement. In the analysis which follows, we assume (a) that the probability that a particle overcomes a certain activation energy is of an Arrhenius form ($L = e^{-\epsilon/kT}$) [5] and (b) the activation energy for the rearrangement of the agglomerate measured in this way is equal to the bond energy. The Arrhenius form assumption can be tested as follows.

Integrating eq. (1) from 0 to t and rearranging gives:

$$\ln \left(\frac{1}{t} \cdot \ln \left(\frac{c_{N0} - c_{Neq}}{c_N(t) - c_{Neq}} \right) \right) \sim \epsilon / kT \quad (2)$$

where the time $t=0$ corresponds to the initial unsintered agglomerate. This means that it is

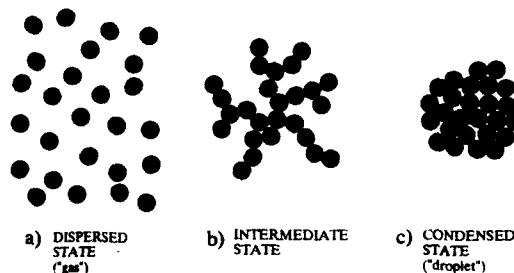


Fig. 1: Different states of primary particles.

possible to calculate the bond energy ϵ from the knowledge of $c_N(t, T)$ during sintering. To relate c_N to a measurable agglomerate parameter, the concept of fractals is used; there is a power law relationship between the average number N of primary particles per agglomerate and the agglomerate diameter d_p (e.g. mobility equivalent diameter):

$$N = A \cdot \left(\frac{d_p}{d_0} \right)^{D_f} \quad (3)$$

where A : proportionality constant, d_0 : primary particle diameter and D_f : fractal-like dimension.

For $D_f = 1$ the agglomerate is string-like and the average number of bonds per primary particle is 2 (neglecting the two particles at the end of the string). In the other limiting case, for $D_f = 3$ the agglomerate is sphere-like. As mentioned above, the coordination number is expected to be between 8 and 11. Eq. (3) applies to agglomerates only over a limited size range and only in a statistical sense. This power law is considered to be an empirical relation between agglomerate size and volume, and does not have to be a fractal in a mathematical sense. However, in experiments it was found that eq. (3) holds down to only a few primary particles [2]. This makes it possible to relate D_f and c_N by scaling eq. (3) down to a distance equal to twice the primary particle radius. Then, every particle that centers within this volume counts as a nearest neighbor and the average number of bonds per primary particle is obtained by subtracting the particle placed in the origin:

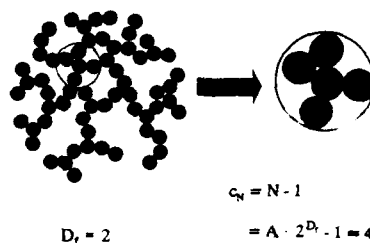


Fig. 2: Concept of fractal-like dimension.

$$c_N = N - 1 \quad (4)$$

where for $D_f = 1$ the condition $c_N = 2$, and for $D_f = 3$ the condition $c_N = 8$ have to be fulfilled. Therefore, A must also be a function of D_f , but a weak one: $A(1) = 1.5$ and $A(3) = 1.125$. In the following, it is assumed that A is a linear function of D_f which fits the two end conditions.

EXPERIMENTAL SETUP

A schematic diagram of the experimental setup is shown in Fig. 3. Copper and silver particles are produced by heating a ceramic boat containing the material of interest in a tube furnace. The metals are evaporated at temperatures of 1200 °C for Cu and 1050 °C for Ag. Then, during cooling the vapor condenses to form spherical primary particles. At the end of the furnace a sharp

temperature decrease is maintained by reflecting the heat radiation from the furnace and by cooling the quartz tube by a fan. Nitrogen of different purities was used as a carrier gas at flow rates varying from 3 to 5 lpm. The primary particles agglomerated in a coagulation tube with average gas residence times from 70 to 110 s.

To obtain agglomerates with $D_f \geq 2$, a preheater is installed after the agglomeration section. In addition, samples for transmission electron microscopy (TEM) are taken from an aerosol sidestream.

After a bipolar charging of the agglomerates in a ^{85}Kr source (2.5 mCi), a certain size class is selected by a differential mobility analyzer (DMA) by applying an electric field perpendicular to the direction of the gas flow. The selected agglomerates, negatively charged and uniform in size, are conducted through a heating section. While the gas flow rate is kept constant at 0.6 lpm, the heating time and temperature are varied. Then, the change in agglomerate mobility due to rearrangement is detected with a second DMA in combination with a condensation particle counter (CPC).

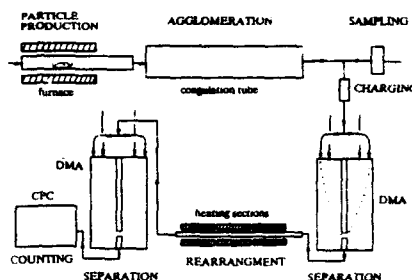


Fig. 3: Experimental setup.

RESULTS AND DISCUSSION

The mobility equivalent diameter d_p of Ag agglomerates is shown in Fig. 4 as a function of the sintering temperature for four different initial size classes. A steep decrease occurs at 70 °C and ends at 300 °C. For higher temperatures the size stays constant in agreement with the results by Schmidt-Ott [2], who showed by TEM micrographs that at 300 °C the agglomerates reached a close-packed state with $D_f = 3$. In the following, the diameter of the close-packed clusters will be called d_c . Assuming that the total number of primary particles per agglomerate N does not change during the rearrangement (mass conservation per agglomerate), eq. (3) can be used to relate the condensed state of the agglomerate to any lower density arrangement.

According to eq. (3), the slope in a double logarithmic plot of d_p vs. d_c gives $3/D_f$. Values of D_f for Ag agglomerates are shown in Fig. 5 as a function of the temperature for a sintering time of 5.28 s at room temperature. Using eqs. (2) and (4), the natural logarithm of the relative change in the coordination number is calculated and shown in Fig. 6 as a function of $1/kT$ for Ag agglomerates. The slope of the curve gives the bond energy. The good correlation of the data with a straight line is consistent with assumption (a) above. Data for Ag agglomerates which differ only in the sintering time, fall on the same curve within the experimental error. This result was also found for Cu agglomerates with different sintering times, consistent with our model. Using the same procedure, the data for Ag and Cu agglomerates produced with a tube furnace at various conditions were evaluated, and the results are shown in Table I. The size distributions of the primary particles were determined from image analysis of TEM micrographs. Geometric

standard deviations for Cu and Ag particles were 1.03 and 1.10, respectively. The diameters given in Table I correspond to the count median diameter of the size distributions.

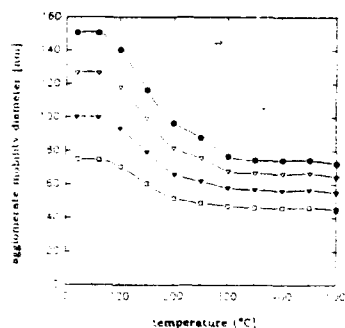


Fig. 4: Mobility diameter of silver agglomerates as a function of the sintering temperature for four different size classes.

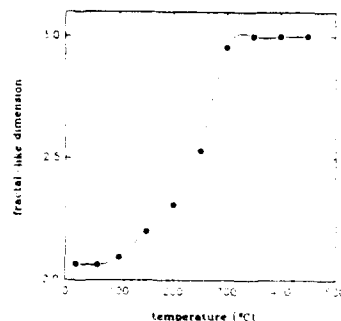


Fig. 5: Fractal-like dimension of silver agglomerates as a function of sintering temperature.

The results for Ag agglomerates produced by spark discharges [6] and for Ag agglomerates [2] are also shown in Table I. Although the particles were produced by different techniques, for nearly equal primary particle sizes the bond energies agree within a few percent. No significant differences between the bond energies of Cu particles produced in high purity N_2 (99.999%) and in industrial N_2 (99.7%) were found. We are currently studying the effects of trace gas concentrations and particle size on the bond energy. It is interesting to note that the agglomerate size (or the number of primary particles per agglomerate) did not affect the bond energies. This is consistent with the assumption of short range interaction forces. The values for the bond energies are of the order of magnitude expected from the Hamaker constant for bulk Ag and Cu. This is consistent with assumption (b) above. However, for silver, experiments showing enhanced coagulation rates for small silver particles, indicate that attractive energies are at least four orders of magnitude higher than expected from the bulk behavior [7,8]. Further experiments are needed to determine the cause of these disagreements.

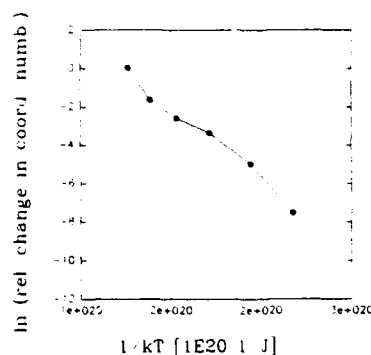


Fig. 6: Natural logarithm of the relative change in the coordination number vs. $1/kT$ for silver agglomerates.

Table I: Bond energies and primary particle diameters for Cu and Ag particles. The three temperatures correspond to the three heating zones of the furnace.

material	gas (purity [%])	T _{furnace} [°C]	d _p [nm]	ε _{bond} [10 ⁻²⁰ J]
Cu	N ₂ (99.999)	1146/1200/1200	10.8	- 8.0
Cu	N ₂ (99.7)	1138/1200/1148	6.3	- 5.0
Ag	N ₂ (99.7)	644/1050/ 1050	15.6	- 10.6
Ag [2]	N ₂	1000	15.0	- 11.0
Ag [6]	Ar (99.999)	spark discharges	8.5	- 5.7

CONCLUSIONS

An experimental method of determining in situ the bond energy between nanosized particles has been developed and tested on Ag and Cu agglomerates. The experimental results are consistent with a theoretical analysis of the kinetics of rearrangement. For both materials the calculated bond energy is of the order of magnitude expected from Hamaker constant of the bulk material. This means that the restructuring of weakly bonded primary particles is adequately described by our method.

Acknowledgement

This work was supported by the Swiss National Science Foundation and U.S. National Science Foundation Grant CTS 92-18222.

References

1. R. Sempéré, D. Bourret, T. Woignier, J. Phalippou and R. Jullien, *Phys. Rev. Lett.* **71**, 3307 (1993).
2. A. Schmidt-Ott, *J. Aerosol Sci.* **19**, 553 (1988).
3. I.Z. Fisher, *Statistical Theory of Liquids*, 2nd ed. (The University of Chicago Press, Chicago and London, 1964), pp. 69-96.
4. N.J.A. Sloane, *Scientific American* **250** (1), 116 (1984).
5. S. Chandrasekhar, *Rev. Modern Phys.* **15**, 1 (1943).
6. A.P. Weber, *Characterization of the Geometrical Properties of Agglomerated Aerosol Particles* (Ph. D. Thesis, Paul Scherrer Institute report 129, ISSN 1019-0643, 1992) pp. 47-67.
7. H. Burtscher and A. Schmidt-Ott, *Phys. Rev. Lett.* **48**, 1734 (1982).
8. A. Majorewicz, K.P. Smidowich, G.P. Reischl, W.W. Szymanski and P.E. Wagner, *J. Aerosol Sci.* **22**, S47 (1991).

GRAIN BOUNDARIES IN NANOPHASE MATERIALS AND CONVENTIONAL POLYCRYSTALS - ARE THEY DISTINCT?

S. C. Mehta and D. A. Smith, Department of Materials Science and Engineering,
Stevens Institute of Technology, Hoboken, NJ-07030
U. Erb, Department of Materials and Metallurgical Engineering, Queen's University,
Kingston, Canada K7L 3N6

ABSTRACT

Nanograined materials, with grain sizes in the range of 1-20 nm, exhibit significant enhancement of grain boundary dependent properties such as yield strength, intergranular fracture toughness, grain boundary diffusivity, specific heat and thermal expansion coefficient. Measurements by indirect techniques suggest that the grain boundaries in nanophase materials are structurally different from the boundaries in their conventional polycrystal counterparts. Exploratory HRTEM observations, on the other hand, indicate that the grain boundary structure in nanophase materials is the same as that found in grain boundaries in conventional polycrystals. This paper reports an HRTEM investigation of the microstructure in electrodeposited nanocrystalline (nc) Ni-1wt.%P alloy. These observations reveal the presence of about 8-10 vol. % porosity in the microstructure. There is also evidence for the presence of an amorphous phase at some grain boundaries and triple junctions. A comparison of grain boundary structures with boundaries in conventional materials suggests that grain boundaries in the nc Ni-P alloy are, for the most part, normal.

INTRODUCTION

Nanograined materials exhibit enhanced or novel mechanical and physical properties such as yield strength [1], intergranular fracture toughness [2], superplasticity [3,4], grain boundary diffusivity [5,6], optical [7,8] and magnetic properties [8-10]. The non-equilibrium nature of the processing of these materials allows formation of supersaturated solid solution and even alloying among normally immiscible components [11-18]. Thus a wide range of solid solution alloys which cannot be produced by conventional routes can be made in nanocrystalline form. Besides being technologically important, these materials are also of great academic interest. Their desirable properties have generated research interest in exploring the microstructure/chemical composition/processing/property relationships of these novel materials.

Various direct and indirect techniques of characterization have been used in previous work to probe the microstructure of nanocrystalline materials. Indirect techniques include X-ray diffraction [19], Positron Annihilation Spectroscopy (PAS) [20], Mossbauer spectroscopy [21], Small Angle Neutron Scattering (SANS) [22] and Extended X-ray Absorption Fine Structure (EXAFS) [23]. The results of these indirect studies suggest that the nanocrystalline microstructure consists of small grains of

conventional crystalline material embedded in a large volume fraction of completely disordered (lacking even short range order) material (fig. 1).

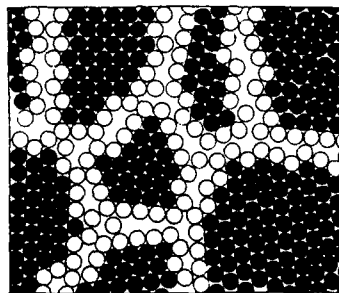


Fig. 1 Two dimensional atomic model of the structure of a nanocrystalline material. The atoms in the centers of the crystal are indicated in black. The ones in the boundary core regions are represented by open circles [4].

However, direct microstructural studies by lattice imaging using the High Resolution Electron Microscope (HREM) are very few in number [24, 25] and inconsistent. The HRTEM studies of Wunderlich et al. [24] on as-prepared nc-Pd, produced by the inert gas condensation technique, suggest a highly non-equilibrium microstructure with large internal stresses as manifested by a large density of dislocations ($10^{15}/\text{m}^2$), twins, low angle grain boundaries and extended grain boundaries. The low density of nc-Pd was attributed to the residual porosity in the microstructure even after processing and to the extended grain boundary structure. However, upon annealing, the low angle grain boundaries completely vanished and therefore the dislocation density decreased. This explains the one possible role of processing and post-process treatment in influencing the microstructure and therefore the structure dependent properties in nanograined materials. The HRTEM results of Thomas et al. [25] on nc-Pd, also prepared by the inert gas condensation technique, are contrary to the previous observations [24]. Their study [25] suggests that there is completely normal, relaxed grain boundary structure in nc-Pd. The microstructure was also found to be free of dislocations or any residual elastic strain.

Further evidence for the non-equilibrium nature of microstructure in materials produced by the inert gas condensation technique is available from the work of Tschope et al. [26]. Their calorimetric measurements on as-prepared nc-Pt suggest the presence of unrelaxed grain boundaries and/or internal strains in the microstructure in agreement with the HRTEM results of Wunderlich et al. [24]. There is still a lack of understanding as to how the different structural features such as non-equilibrium nature of grain boundaries, residual strain, porosity, solute segregation, texture etc. influence the properties. In most cases, the microstructural characterization is not performed on the

same material which is used for property tests thus further complicating the task of gaining fundamental understanding. As a result, ambiguities among the mechanical/physical property data are prevalent and the structure-property-processing relationship in nanograined materials is still far from complete. There is also a dearth of data on microstructural characterization and property measurements in nanograined materials produced by other techniques.

This paper reports HRTEM observations of microstructural features in nc Ni-1wt.%P, produced by electrodeposition.

EXPERIMENTAL

The nc Ni-1wt.%P samples used in this study were made by electrodeposition. The thin TEM foils of these samples were prepared using the twin jet electropolishing technique at a temperature of -20 C. A solution of nitric acid and methanol mixed in 1:2 ratio was used as an electrolyte. The microscopy work was performed using a 300 keV, Philips CM30 High Resolution TEM.

RESULTS

Fig. 2(a) is a low magnification micrograph providing an overview of the microstructural inhomogeneities present in nc Ni-1wt.%P alloy.

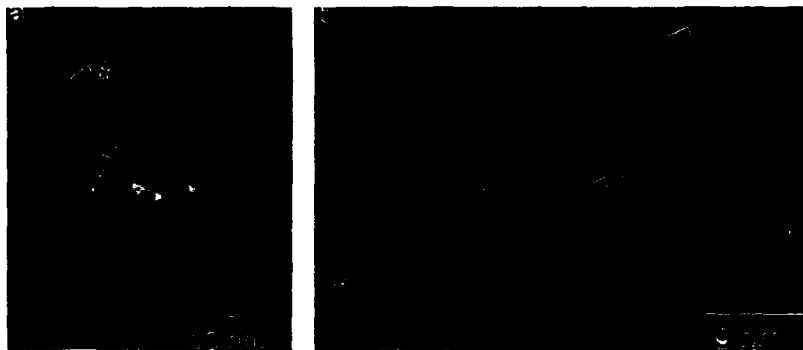


Fig. 2 (a) Microstructural inhomogeneities in nc Ni-1wt.%P showing contrast features, marked as S, which may be voids or amorphous inclusions, and a pocket of amorphous phase embedded in the triple junction, marked as T. (b) An enlarged view of the inset in fig. 2(a).

The microstructure has a granularity with a length scale of the order of 5nm. It consists of crystalline regions showing lattice fringes, and other contrast modulations. These contrast modulations such as that marked S are round in shape and could be open porosity or more likely regions of amorphous phase. These contrast features occupy between about 8 to 10% of the microstructure of the nanocrystalline material. Also

shown in the micrograph is a pocket of amorphous phase embedded in the triple junction marked T. Fig. 2(b) shows an enlarged view of the region T marked in the fig. 2(a). It has been found that small pockets of amorphous phase randomly dispersed in the microstructure are commonplace in this material.

Fig. 3 (a-d) show the HRTEM images of a variety of grain boundary structures in nc Ni-1 wt. % P alloy.

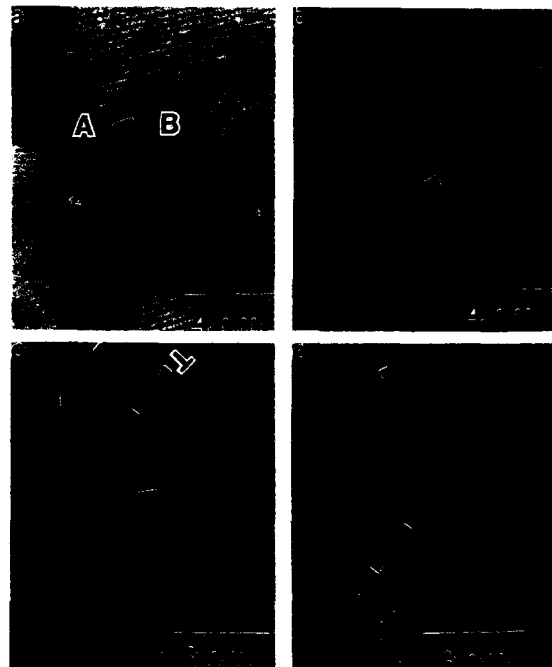


Fig. 3(a-d) HRTEM micrographs of grain boundaries in nc Ni-1wt.%P.

Micrograph 3(a) shows two grains (labelled as A and B respectively) separated by a low angle grain boundary. A set of (111) planes is imaged; these are misoriented by about 9 degrees. The electron beam direction is close to $\langle 110 \rangle$ in both grains. It can be seen that the (111) lattice fringes in both grains extend all the way upto the edges of the grain with an abrupt change of orientation across the grain boundary. There is no direct evidence for an extended grain boundary region. Fig. 3(b) from a thicker region of the sample shows a $\Sigma 9/(221)$ symmetrical tilt grain boundary (shown by an arrow). The parallel fringes observed in the adjacent grains are from the (111) planes. The micrograph also shows several sets of moiré fringes due to the overlap of grains along the beam direction. Fig. 3(c) is an HRTEM micrograph showing several low angle grain

boundaries and the associated dislocations. Micrograph 3(d) shows a lattice dislocation and fringe bending arising from the displacement field associated with it.

The average grain size of Ni-1wt.%P alloy as measured by the linear intercept method was about 10 nm. However, a significant degree of inhomogeneity in the grain size was observed. Grain sizes ranged from 5 nm upto 20 nm. The diffraction pattern of Ni-1wt.%P gave sharp rings of the f.c.c. Ni. The absence of diffraction rings corresponding to Ni_3P reflections suggests that phosphorus is present either in the solid solution form in the nickel or resides in segregated form along grain boundaries. The equilibrium solid solubility of phosphorus in nickel at room temperature is less than 0.01 wt. %. A simple calculation indicates that segregation of a monolayer of phosphorus along the grain boundary in 10 nm average grain size material would accommodate phosphorus level of only 0.3 atomic percent. It therefore appears that most of the phosphorus exists in supersaturated solid solution.

DISCUSSION

The observations described above show that a wide variety of features are various kinds of microstructural inhomogeneities in the Ni-1wt.%P alloy. The existence of porosity and/or amorphous phase along grain boundaries and triple junctions are likely to affect significantly the grain boundary dependent material properties such as yield strength, fracture toughness, creep and grain boundary sliding.

HRTEM observations show an abundance of low angle grain boundaries in the microstructure of nc Ni-1wt.%P. These have the dislocation structure expected from the Read-Shockley model. This is also consistent with the HRTEM observations of Wunderlich et al. [24]. The $\Sigma 9/(221)$ symmetrical tilt grain boundary appears structurally very similar to coincidence related boundaries in conventional polycrystals [27]. There is no evidence for an extended region of decreased coordination in the grain boundary region as was observed in a previous study [24]. The observation of a lattice dislocation within a grain is potentially significant since it has sometimes been argued that in nanocrystalline material the grains are too small for lattice dislocations to be present. The investigation of the mobility of the observed dislocation remains an important issue. Also shown in fig. 3(d) is a small facet of (111) coherent twin boundary. There is a perfect matching of atoms along the twin plane as expected. Multiple twins were also occasionally observed. Such multiple twins are common in isolated icosahedral islands but unusual in continuous solid films. Thus, apart from microstructural inhomogeneities such as porosity and the presence of an amorphous phase, the grain boundary structure in nc Ni-1wt.%P is perfectly normal.

CONCLUSION

The HRTEM observations showed contrast features suggesting the existence of amorphous inclusions and/or porosity in the microstructure. Pockets of amorphous phase along grain boundaries and triple junctions in the microstructure of Ni-1wt.%P alloy

were also observed. The presence of low angle grain boundaries and lattice dislocations indicate a normal mode of relaxation. The HRTEM study of grain boundaries in nc Ni-1wt.%P suggests that grain boundaries in nanophase and conventional material are not distinct apart from the presence of amorphous films at some triple junctions and coating some boundaries.

REFERENCES

1. J. R. Weertman, *Mater. Sci. and Engg. A* **166**, 161, 1993.
2. H. Gleiter, *Phase Transition* **24-26**, 15, 1990.
3. R. W. Siegel, *Annu. Rev. Mater. Sci.* **21**, 559, 1991.
4. H. Gleiter, *Prog. Mater. Sci.*, **33**, 223, 1989.
5. J. Howarth, R. Birringer and H. Gleiter, *Sol. State Comm.* **62(5)**, 319, 1989.
6. S. Schumacher, R. Birringer, R. Strauss and H. Gleiter, *Acta Metall.* **37**, 2585, 1989.
7. S. Veprck, Z. Iqbal, H. R. Oswald and A. P. Webb, *J. Phys.*, **C14**, 195, 1981.
8. R. Dagani, *C & EN*, 18, Nov. 1992.
9. W. Wagner, A. Wiedenmann, W. Petry, A. Geibel and H. Gleiter, *J. Mater. Res.*, **6(11)**, 2305, 1991.
10. J. A. Cowen, B. Stolzman, R. S. Averback and H. Hahn, *J. Appl. Phys.*, **61(8)**, 3317, 1987.
11. B. Huang, N. Tokinaze, K. N. Ishihara, P. Shingu and S. Nasu, *J. of Non Cryst. Sol.* **117/118**, 688, 1990.
12. T. Mutschele and R. Kirchheim, *Scripta Metall.* **21**, 135, 1987.
13. T. Mutschele and R. Kirchheim, *Scripta Metall.* **21**, 1101, 1987.
14. E. Ivanov, *Mater. Sci. Forum* **88-90**, 475, 1992.
15. J. Eckert, J. C. Holzer and W. L. Johnson, *Scripta Metall. et Mater.*, **27**, 1105, 1992.
16. Y. R. Abe, J. C. Holzer and W. L. Johnson, 1991 MRS Fall Meeting, Boston, MA, Dec. 2-6, 1992.
17. R. Birringer, H. Hahn, H. Hofler, J. Karch and H. Gleiter, *Defect and Diffusion Forum* **59**, 17, 1988.
18. H. Gleiter, *Nanostructured Materials* **1**, 1, 1992.
19. X. Zhu, R. Birringer, U. Herr and H. Gleiter, *Phys. Rev.* **35(17)**, 9085, 1987.
20. R. Wurschum, M. Scheytt and H. E. Schaefer, *Phys. Stat. Solidi A* **102**, 119, 1987.
21. U. Herr, J. Jing, R. Birringer, U. Gonser and H. Gleiter, *Appl. Phys. Lett.* **50(8)**, 472, 1987.
22. E. Jorra, H. Franz, J. Piesl, G. Wallner, W. Petry, R. Birringer, H. Gleiter and T. Haubold, *Phil. Mag. B* **60(2)**, 159, 1989.
23. T. Haubold, R. Birringer, B. Lengeler and H. Gleiter, *Phys. Lett. A* **135(8,9)**, 461, 1989.
24. W. Wunderlich, Y. Ishida and R. Maurer, *Scripta Metall. et Mater.* **24**, 403, 1990.
25. G. J. Thomas, R. W. Siegel and J. A. Eastman, *Scripta Metall. et Mater.* **24**, 201, 1990.
26. A. Tschöpe, R. Birringer and H. Gleiter, *J. Appl. Phys.*, **71(11)**, 5391, 1992.
27. W. Krakow, J. T. Weitzel and D. A. Smith, *Phil. Mag. A* **53**, 739, 1986.

ATOMISTIC SIMULATION OF VAPOR-PHASE NANOPARTICLE FORMATION.

Michael R. Zachariah and **Michael J. Carrier**, National Institute of Standards and Technology, Gaithersburg, Md; and **Estela Blaisten-Barojas**, George Mason University, Fairfax, Va

Abstract

In order to understand from a fundamental view how nanoparticles form and grow, classical molecular dynamics simulations of cluster growth and energy accommodation processes have been conducted for clusters of silicon (< 1000 atoms), over a wide temperature range. Simulations involved solution of the classical equations of motion constrained with the three body Stillinger-Weber potential. The results show the large heat release and resulting cluster heating during a cluster-cluster collision event, and the corresponding time evolution of the internal energy to a more stable state. Dynamic effects associated with the temperature of the cluster and the impact parameter are also clearly evident. In particular, clusters show a large sensitivity to temperature in the rate of coalescence, particularly at low temperature. Calculated diffusion coefficients are significantly larger than surface diffusion constants stated in the literature. Phonon density of states spectra do not seem to show size effects.

Introduction

Nano-scale materials have the potential for accessing material properties that can be varied through control of particle size. One of the limitations in rapid use of such materials is an understanding of the size dependent properties such materials have. The other limitation is the relative difficulty in the characterization of very small clusters and the ability to control their growth. Vapor phase growth of small clusters is perhaps the most robust method of producing bulk quantities of such materials [1-4]. However, many questions and challenges remain, including control of growth, and a knowledge of chemical reactivity and transport properties.

Computation Method

The approach used in this work is to apply an atomistic simulation using classical molecular dynamics (MD) methods [5-7]. Computations were conducted using the three body formulation of the silicon potential proposed by Stillinger and Weber (SW) [8]. The three body formulation provides the mechanism by which the directional nature of the bonding can be realistically simulated. While many potentials are available to simulate silicon, the SW potential was chosen because it accurately predicts bulk melting characteristics. Because most cluster formation processes occur at high temperatures, liquid like characteristics should play an important role in any description of cluster growth. Classical MD was conducted by solving the Newtonian equations of motion with a time step of 5.7×10^{-4} ps. All simulations were started by first equilibrating the appropriate size cluster to a specified temperature prior to cluster collision. Each cluster was then given a bulk cluster velocity so that the collision kinetic energy along the line of centers of the clusters corresponds to twice the thermal energy. Both head-on and large impact parameter collisions were included.

Bulk vs Surface Properties

The size dependent properties of clusters can be thought to arise as a result of the rapid change in the surface to volume ratio. The cluster energy can be fit to an expression that involves a bulk and a surface contribution to the total energy, E_T .

$$E_T = \sum_{i=1-N} (\text{Potential} + \text{Kinetic Energy}) \quad (1)$$

$$E_T = -E_b N + E_s N^{2/3} \quad (2)$$

Fig 1. shows the result of fitting the total energy to a bulk and surface energy contribution as expressed in equation 2. The results clearly show that the calculated results can be fit quite nicely to such an expression. The bulk energy term becomes more negative as the cluster size is increased (becoming more stable) while the surface term shows a shallow positive term. The ratio of bulk to surface energy for the two temperatures indicates the relative importance as a function of both temperature and cluster size. The results show that increasing temperature causes a decrease in the $E(\text{Bulk})/E(\text{Surf})$ as average bond length increases and results in an increase in the bulk energy (potential energy). Increasing cluster size decreases the surface to volume ratio and results in a decrease in the relative importance of the surface energy. Under all conditions calculated here $E_i < 0$, which implies the cluster was always stable. Extrapolating the 2000 K results to $E_T = 0$ occurs at $N < 1$; i.e all cluster sizes below at least 2000 K are unconditionally stable.

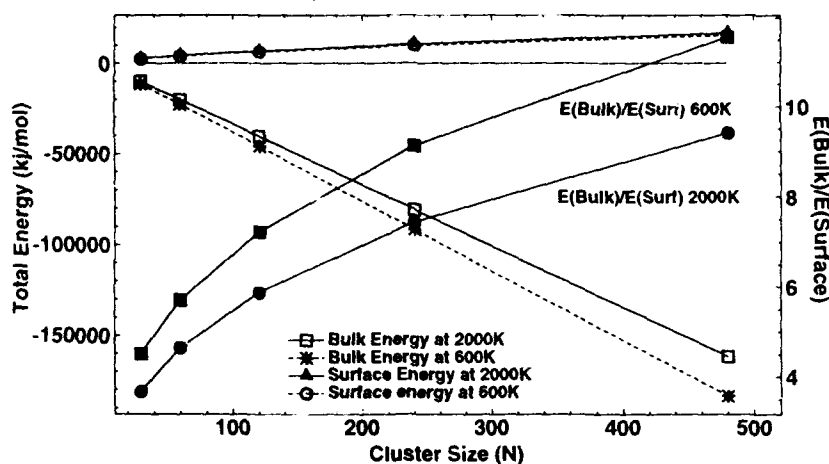


Fig. 1 Contribution of bulk and surface energy terms to the total cluster energy at 600 K and 2000 K

The approach to bulk behavior is one of the most interesting aspects to the understanding of nanostructured materials. These would include mechanical, optical, and chemical properties. One aspect of this approach to bulk behavior is the average binding energy of atoms as a function of particle size. Fig 2. shows the approach to bulk behavior as the derivative of the potential energy per atom with respect to cluster size. This effectively gives a measure of the incremental increase in binding energy upon addition of an atom to the cluster. As seen in Fig. 2 the atomic binding energy in the cluster rapidly reaches an asymptotic behavior by 1000 atoms. This is one measure of the approach to bulk behavior.

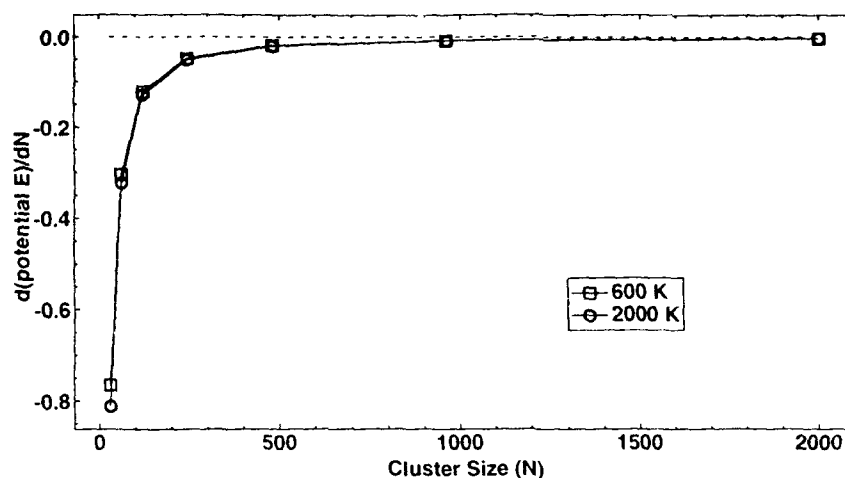


Fig 2. Approach to bulk binding energy

Fig 3. shows the phonon density of states as a function of cluster size at a temperature of 2000 K. The spectra show the two dominant modes found in bulk silicon (acoustic - 150cm^{-1} ; optical - 400cm^{-1}). However, we do not observe any size dependent structure and in fact the spectra basically track what is observed for bulk silicon. In contrast, some of our prior calculations on temperature dependence have shown a softening of the modes to lower frequencies as temperature increases [7].

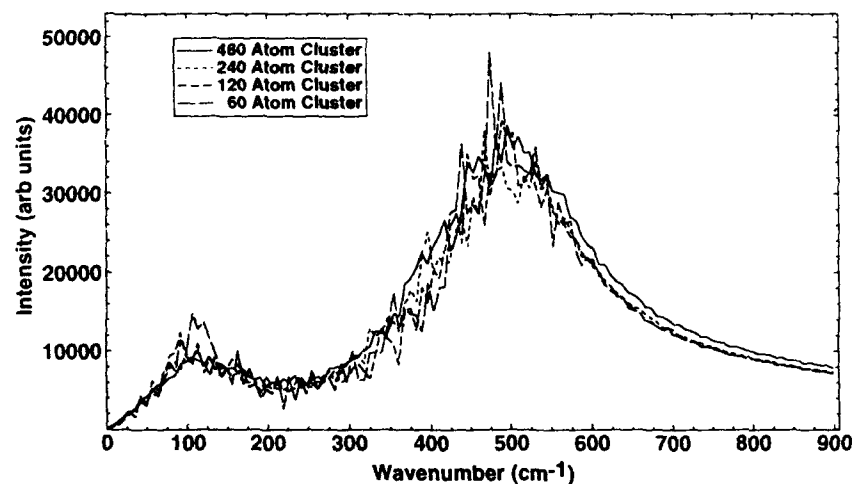


Fig 3. Phonon density of states for various cluster sizes at 2000 K

Cluster Growth

Cluster aggregation processes have been investigated by colliding equilibrated clusters at various temperatures and sizes ($15 < N < 480$; $600 < T < 2000$ K). Cluster collisions were conducted under thermal energy collision conditions, i.e. clusters were given relative collision energies commensurate with the temperature of the cluster. The result of a cluster-cluster collision is the formation of new bonds for surface atoms. The decrease in the number of surface dangling bonds lowers the potential energy and through conservation of energy, results in heating of the cluster (increase in thermal energy of the atoms). The extent of cluster heating is shown for different cluster sizes as a function of initial cluster temperature in Fig 4. The general trends observed are that smaller clusters have greater heat release resulting from a higher fraction of unsatisfied dangling bonds. Clusters with higher initial temperature have greater heat release. This is probably due to the higher energy state of the surface atoms in a hotter cluster. Grazing collisions result in smaller heat release as some of the energy goes into the angular momentum of the resulting cluster. In all cases, the collisions were reactive; i.e. sticking coefficient = 1. This is in contrast to small cluster nucleation which can show nucleation kinetics that are well below gas kinetic collision rates [9].

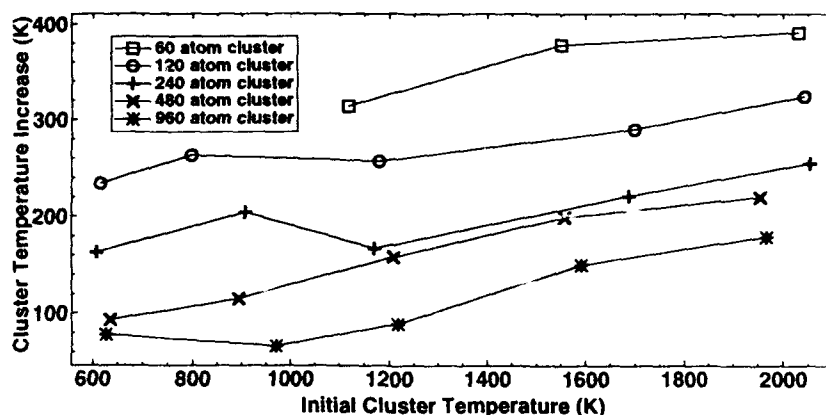


Fig. 4 Cluster temperature rise during cluster growth; head on encounter

One of the most important issues facing vapor phase growth of nano-particles is the problem of aggregate formation. The most desirable morphologies are spherical or soft agglomerates. Since coalescence (sintering) processes are ongoing during nucleation and growth, control requires an understanding of the time scales and basic physics behind sintering of nanoparticles. Our dynamic simulations can track the evolution of particle morphology during a cluster-cluster encounter. The results can be expressed in many forms. For the purposes here we show in Fig. 5 the time required for two clusters to coalesce, as a function of particle size and initial temperature. The results clearly indicate that cluster coalescence is very temperature sensitive. Coalescence times at the lower temperatures are very size sensitive, with the larger clusters showing the slowest coalescence rates. At higher temperatures (above 1200 K) cluster coalescence times are independent of size. In general, melted or near melted clusters coalesce spontaneously. While not shown here, calculations show that the melting temperature is well below the bulk value.

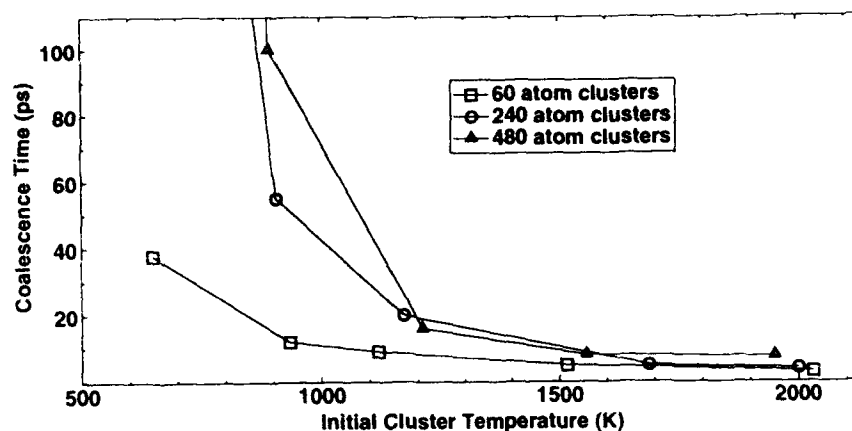


Fig. 5 Cluster coalescence times as various cluster sizes and initial temperature.

Cluster morphology changes resulting from sintering processes can be thought of as occurring through movement of atoms via atomic diffusion. Molecular dynamics computations lend themselves naturally to the calculation of diffusion constants. Figure 6 shows calculations of the mean square displacement (MSD) of atoms in a 480 atom cluster (at 600, 1200 and 2000 K) as a function of time. The diffusion coefficient can then be calculated from the initial slope of the MSD curves by the usual Einstein relation (eq. 4).

$$\text{MSD} = \langle |r_i(t) - r_i(0)|^2 \rangle \quad (3)$$

$$D = 1/6 [\text{initial slope of MSD}] \quad (4)$$

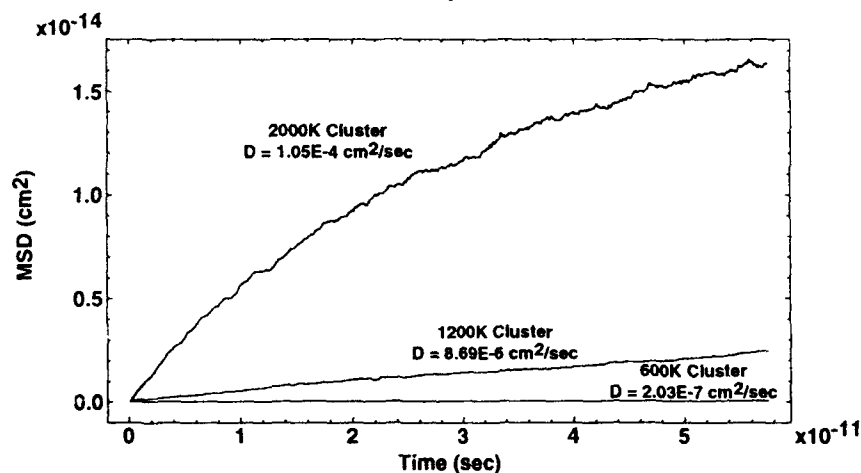


Fig. 6 Mean square displacement of atoms as a function of time; $D = \text{slope}/6$

Because clusters of this size are essentially composed of surface rather than volume type atoms, comparison with experiment is most appropriate with surface self-diffusion data. Unfortunately such data is scarce and of questionable accuracy. The most direct measurement has been made by Makowiecki and Holt [10] who reported a silicon surface diffusion constant of $4 \times 10^{-8} \text{ cm}^2/\text{s}$ at 1000 K. A curve fit of our data showed a diffusion constant at 1000 K of $5 \times 10^{-6} \text{ cm}^2/\text{s}$ which is significantly larger than the experimental results. At this time there is no obvious way to access this discrepancy. Certainly, it is well known that the Stillinger-Weber potential under predicts the binding energy in bulk silicon. This would tend to decrease the computed surface diffusion coefficient constant.

Conclusion

Atomistic simulations utilizing classical MD methods have been used to characterize the characteristics of equilibrium and kinetic properties of large silicon clusters undergoing growth via cluster-cluster collisions. The results show that the binding energy of clusters increases with cluster size and decreases with cluster temperature. Phonon density of states for liquid silicon clusters were found to be insensitive to size and similar to the bulk. Cluster kinetics indicate that significant heat release occurs as a result of new bond formation. Cluster morphology effects similar to those observed in nanophase particle processing are also evident. In particular, cluster coalescence is very sensitive to temperature below 1000 K. Mean square displacement calculations have been used to deduce diffusion constants, a comparison of which with experimental results for surface diffusion shows considerable discrepancy. Future work will be aimed at correlating these observations to scaling laws that can be applied to phenomenological models of particle growth.

References

1. Zachariah, M.R., Chin, D., Semerjian, H.G., and Katz, J.L., *Combustion and Flame* **78**, 287 (1989)
2. Zachariah, M.R., and Huzarewicz, S., *J. Mat Res.* **6**, 264 (1991)
3. Zachariah, M.R., M. I. Aquino, R.D. Shull, and E. Steel, "Formation of Superparamagnetic nanocomposites from Vapor Phase Condensation in a Flame" Submitted to *J. Nano Struct. Mat.*
4. Zachariah, M.R., and Semerjian, H.G., *AIChE. J.*, **35**, 2003 (1989)
5. Blasiten-Barojas, E. and Levesque D., *Phys. Rev. B*, **34**, 3910 (1986)
6. Blasiten-Barojas, E. and Zachariah, M.R., *Phys. Rev. B*, **45**, 4403 (1992)
7. Zachariah, M.R., Carrier, M.J., and Blasiten-Barojas, E. to appear in *Gas-Phase and Surface Chemistry in Electronic Materials Processing*, (1994)
8. Stillinger, F.H. and Weber, T.S., *Phys. Rev. B*, **31**, 5262 (1985)
9. Zachariah, M.R., and Tsang, W., *Aeros. Sci. Tech.*, 499 (1993)
10. Makowiecki, D.M., and Holt, J.B., *Sintering Processes*, Mater. Sci., Res. (ed. G.C. Kuczynski), **13**, 279 (1979)

STRUCTURE AND PROPERTIES OF STRAINED CRYSTALLINE MULTILAYERS

J. HOEKSTRA*, H. YAN*, G. KALONJI* AND H. JONSSON†

*Department of Materials Science and Engineering, FB-10

†Department of Chemistry, BG-10

University of Washington, Seattle, Washington 98195, U.S.A

ABSTRACT

We present a computer simulation study of thin crystalline multilayers constructed from two FCC solids with differing lattice constants and binding energies. Both materials are described by Lennard-Jones interatomic potentials and initially have the same orientation and coherent interfaces. We have studied systems in which interfaces are perpendicular to the common [100] and [111] directions, respectively. A novel technique for analyzing local atomic ordering, Common Neighbor Analysis, is used to identify structural characteristics in these systems. We have found several structural changes in the layers of smaller atoms, including an FCC to HCP transition. In a system with (111) texture, a coherent interface to incoherent interface transformation is observed. Calculations of elastic constants of these multilayer structures show that elastic anomalies are associated with the structural variations.

INTRODUCTION

Recent investigations of possible enhancement of mechanical, electrical and magnetic properties of composition-modulated superlattices, including the so-called "super-modulus effect" [1-6], have generated a great deal of interest in metallic multilayers. Due to the small size and complicated geometry, experimental study of the structural properties of these materials is difficult. The nanoscale dimensions of these systems, however, provide an excellent opportunity for applying computer simulation methods such as molecular dynamics which, due to the large amount of computation involved, have to be used on systems that are either naturally or artificially reduced to a manageable size.

Structural phase transitions in single crystals due to external stress have been studied extensively [7-10]. When two different crystalline materials with different lattice constants are brought together to form an interface, a certain amount of strain exists to accommodate the different sizes of these two atomic structures. This strain can affect, or even alter, the structure and properties of the layered materials. This is, to some degree, similar to the structural phase transitions in single crystals subject to external stresses. The characteristics of layered materials, however, are intimately related to the planar geometry and nanoscale dimensions of the interfaces. Experimentally, Pizzini et al. [11] have found that, for a Co/Cu (111) textured multilayer system, as the modulation wavelength is increased past about 70 Å the initially ordered FCC structure of the smaller Co atoms begins to develop stacking faults and associated local HCP structures. For a Co-Cr superlattice, Vavra et al. [12] found an abrupt structural transition from a close-packed structure to BCC in the Cr layers. When Co is layered with Pt, at a thickness of greater than 4 Å, it transforms to an HCP structure and lattice coherence between layers is lost with a great number of defects in the layers. The lattice mismatch in this case is about 11% [13]. A considerable amount of work has been done to elucidate the relationship between structural properties and elastic anomalies in metallic superlattices [14,15].

Computer studies involving an embedded-atom empirical potential (EAM) for a Au/Ni alternating layer system with a lattice mismatch of 13% have shown that the Ni layer undergoes a

structural transformation from its normal FCC structure to an HCP structure [16]. A Cu/Ni layered system with a 2.7% lattice mismatch, however, shows no such structural anomaly. In order to elucidate the effects of lattice mismatch on the structure and elastic properties of multilayers in a systematic manner, we have carried out molecular dynamics simulations of model multilayer systems using a generic Lennard-Jones-type pair potential and monitored our systems through a range of lattice mismatches from 0% to 20%. For the systems with (100) texture, we are able to identify several significant structural changes involving creation of stacking faults at zero temperature in the layers of smaller atoms for mismatches ranging from 9% to 13%. Around 14% mismatch, a transition to HCP associated with a dramatic relief of strain is observed in the material of smaller lattice parameters. In a system with (111) texture, on the other hand, we have observed a transition from coherent interfaces to incoherent ones with significant disordering in the layers of smaller atoms. The calculated elastic constants of these systems also directly reflect these structural variations.

THE SYSTEMS

The multilayer system in our simulation of the (100) texture consists of 1152 atoms arranged in an FCC configuration consisting of 36 layers with 32 atoms per layer. Alternating materials 24 and 12 atomic layers thick, hereafter referred to as materials A and B respectively, are assembled with no relative crystallographic misorientation. The interfaces are perpendicular to the common [100] directions. Periodic boundary conditions are used in all three dimensions. For the study of (111) textured multilayers, two systems are used. The first is a system of 36 atomic planes with 40 atoms per layer. Again, the alternating materials were of 24 and 12 atomic layers thick. The second had 27 atomic planes, each having 50 atoms. The thickness ratio of the alternating layers is also 2:1. Both systems are assembled with the interfaces perpendicular to the common [111] direction.

For the Lennard-Jones potential we have used, the cutoff radius, r_c , is chosen to be 2.3σ . The value of the energy parameter $\epsilon(AA)$ is chosen to be twice that of $\epsilon(BB)$ to ensure that material A, the material with the larger lattice constant, remains solid at the elevated temperatures in our study [17], although only results for zero temperature are reported here. The lattice mismatch between the two materials is created by increasing the length parameter $\sigma(AA)$ up to 20% with a 1% increment while holding $\sigma(BB)$ constant at a reduced value of 1.0. This approach allows us to study systematically the effect of lattice mismatch on the two materials. The length parameter of the unlike interaction, $\sigma(AB)$, is chosen as the average of $\sigma(AA)$ and $\sigma(BB)$.

RESULTS AND DISCUSSION

Structural Variations and Elastic Properties of (100) Textured Multilayers

For the system with the interfaces perpendicular to the [100] orientation, with a lattice mismatch between layers less than 8%, the structure remains characteristically unchanged despite an increase in the strain energy of the system. However, when the mismatch is greater than 8%, there is a significant variation in both total energy and volume of the system, indicating a structural change in the layers. Using the Common Neighbor (CN) analysis [18], we are able to identify the structural change corresponding to generation of stacking faults in the layers of B atoms.

The creation of stacking faults is well demonstrated in Figure 1 for the system with a 9% mismatch. Because layer A maintains its original FCC structure, for a better illustration only the structure of layer B is shown, viewed in the original [101] direction. Atoms with different local

coordinations as indicated by the CN analysis are represented in different shades and solid lines correspond to the stretched bonds identified by a subpeak in the radial distribution function (RDF) of the system. This is a structure with periodic stacking faults, whose stacking sequence may be described as $\cdots ABCA^{\wedge}CABC^{\wedge}BCAB \cdots$, where \wedge represents a fault. We have verified that the formation of this structure is not size dependent.

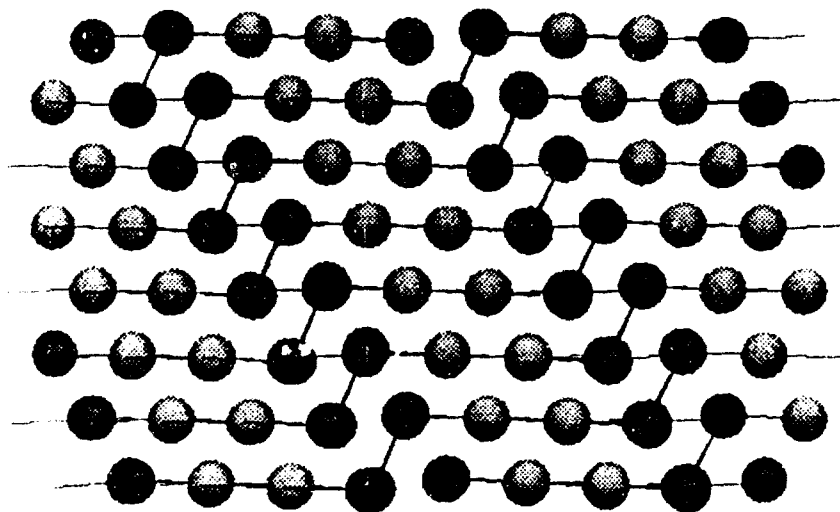


Figure 1 - Illustration of the B layer in the system at 9% mismatch, viewed in the [101] direction. Black spheres represent atoms identified by the CN analysis as in an HCP environment and gray ones are those in an FCC environment.

As the mismatch is further increased, more stacking faults are created until the stacking sequence is $\cdots AB^{\wedge}AB^{\wedge}AB^{\wedge}AB^{\wedge} \cdots$, which is an HCP stacking, though much distorted, with its basal plane along the original [111] direction. Then around 14% mismatch, the layer undergoes a dramatic transformation. Figure 2 shows the atomic configuration of the system at 14% mismatch viewed in the [010] direction of the untransformed FCC layer A. The structure of the layer B has clearly changed its orientation such that the basal plane (0001) is now parallel to the FCC (010) plane, and the (2 $\bar{1}$ 10) plane to the (100) plane of the A layer. Accompanying this orientational change is also a significant drop in volume and energy of the system.

A similar structural phase transformation in the layers of smaller atoms has also been observed in a previous computer simulation of a Au/Ni multilayer system (with 13% mismatch) using the many-body EAM potential [16]. In that study, the Ni layer was found to have changed to an HCP structure when its thickness was increased beyond four monolayers, while the Au layer maintained its FCC structure. Correspondingly, the elastic constants, such as C_{11} and Young's modulus, were also found to increase dramatically while C_{44} weakened once the structural change of the Ni layer took place.

In this study, we have also calculated C_{11} of the system using a finite strain method. The results are plotted in Figure 3 as a function of mismatch. Initially, as the mismatch increases, C_{11} decreases. Then corresponding to the generation of stacking faults at mismatches greater than 8%, C_{11} increases and fluctuates due to the structural variations in this regime. Beyond the 14%

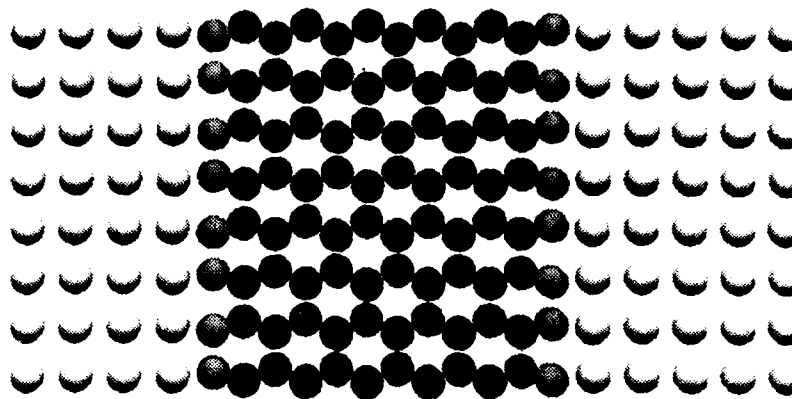


Figure 2 - Illustration of the system at 14% mismatch. The B atoms in the center layer which are identified as HCP atoms are in black, the A atoms are white. Viewed in $[001]$ direction of the FCC structure.

mismatch where the layer B has transformed to an HCP structure, the elastic constant has a steady increase, indicating a strengthening of C_{11} .

We point out that such calculations of C_{11} were carried out earlier for a similar Lennard-Jones system by Phillpot and Wolf [2] in a study of the "supermodulus effect" of metallic multilayers. They also found similar behavior of the elastic constant as lattice mismatch changes, which had a turnabout around 12.5%. Although no structural correlation was shown and discussed in that study, this phenomenon is consistent with what we have observed in our simulations. Further evidence for the relationship between structural variations and elastic anomalies has been found in experimental studies [14,15].

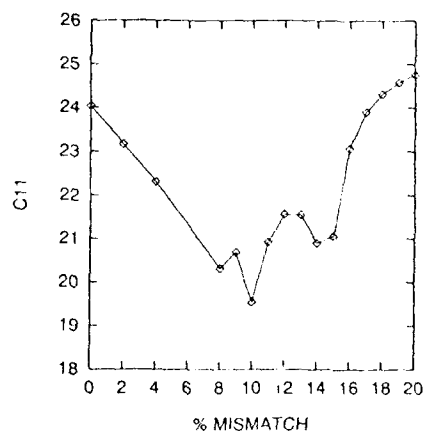


Figure 3 - C_{11} vs % mismatch for (100) textured multilayers

Structural Variations and Elastic Properties of (111) Textured Multilayers

For a (111) textured multilayer system with an initial 5×8 planar atomic arrangement and the B layer 12 monolayers thick, there is a structural transformation that occurs in the layers of smaller atoms for mismatches larger than 11%. Figure 4 shows the structure of a system at 15%

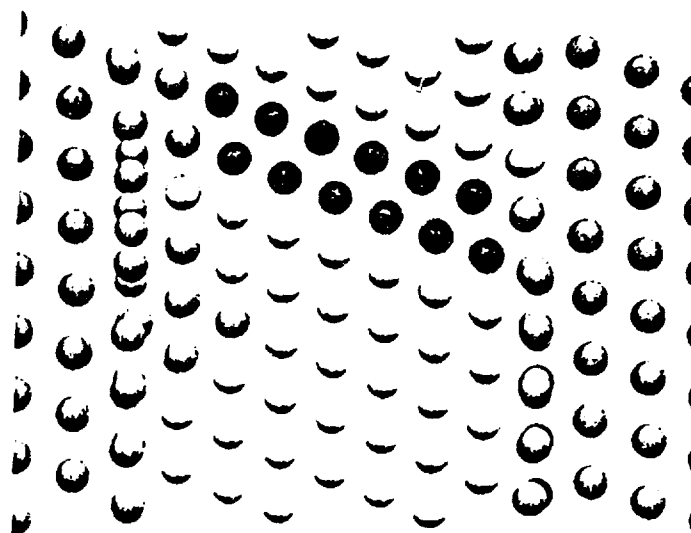


Figure 4 - Illustration of system with interface perpendicular to the $[111]$ direction at 15% mismatch. Figure shows incoherent interface along with stacking faults and local disorder within the B material. Black spheres represent local HCP structure, white FCC, and gray disordered interfacial structure.

mismatch. The initially coherent interface now becomes incoherent with considerable atomic disorder in the region. Within the bulk of the B layer, there are stacking faults generated, similar to those discussed above. We note that associated with this characteristic structural change beginning at around 11% mismatch is a dramatic drop in the energy of the system.

Figure 5 shows the effect that the coherent to incoherent interface transition has on the mechanical properties of the system. Here, C_{11} , shown as a function of mismatch, has a qualitative change of behavior when the transformation occurs at 11% mismatch. This indicates that the incoherency and disorder in the interface region contribute to the elastic strengthening of the multilayer, consistent with earlier studies [4,15].

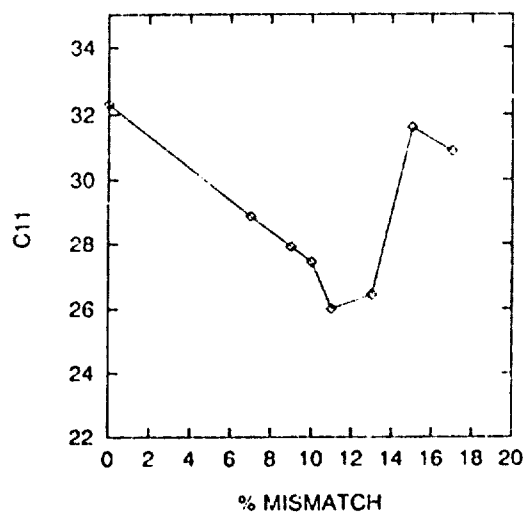


Figure 5 - C_{11} vs % mismatch for (111) textured multilayers

However, this structural change is not unique. It is dependent on the atomic arrangement and system size. In our simulation of a different system with 15% mismatch where the B layer is 9 atomic planes thick and the initial planar arrangement as 5×10 , an HCP structure is formed for the B layer, similar to what we have observed above for (100) textured multilayers at mismatches larger than 14%. The basal plane is now parallel to the FCC $(2\bar{1}\bar{1})$.

SUMMARY

In this work we have carried out a study of the structure and elastic properties of nanoscale multilayered systems. We used a Lennard-Jones system with differing sets of parameters for the two materials to demonstrate systematically the generic effects of lattice mismatches on the layer structure and corresponding elastic responses.

For the (100) textured multilayer systems, we have seen stacking faults developing in the layers of smaller atoms, which eventually transformed into an HCP structure at even larger mismatches. For the (111) textured multilayer systems, we have found in one system a transition around 11% mismatch from a coherent interface to an incoherent interface, together with the creation of stacking faults and disorder, while in another system of different sizes, a transition from FCC to HCP in the layers of smaller atoms, which is associated with considerable shearing of the whole system.

Accompanying these structural changes, there is generally a strengthening in the elastic constant, C_{11} , of these materials. Calculations of more elastic constants using a lattice dynamics method are currently underway in order to obtain more comprehensive knowledge of these elastic responses. Further studies will continue to provide insight into the relationship between structural variations and elastic anomalies in metallic multilayers.

ACKNOWLEDGMENT

This work is supported in part by a contribution from the Kyocera Corporation and by NSF grant CHE-9217774.

REFERENCES

- [1] A. Jankowski, and T. Tsakalakos, *Mater. Sci. Eng. B*, **6**, 87 (1990).
- [2] S.R. Phillpot and D. Wolf, *Scripta Metall. Mater.*, **24**, 1109 (1990).
- [3] J. A. Jaszcak, S. R. Phillpot, and D. Wolf, *J. Appl. Phys.*, **68**, 4573 (1990).
- [4] J. A. Jaszcak, and D. Wolf, *J. Mater. Res.*, **6**, 1207 (1991).
- [5] R. S. Jones, J. A. Slotwinski and J. W. Mintmire, *Phys. Rev. B*, **45**, 13624 (1992).
- [6] M. Imafuku, Y. Sasajima, R. Yamamoto and M. Doyama, *J. Phys. F*, **16**, 823 (1986).
- [7] F. Milstein and B. Farber, *Phys. Rev. Lett.*, **44**, 277 (1980).
- [8] M. Parrinello and A. Rahman, *J. Appl. Phys.*, **52**, 7182 (1981).
- [9] K.P. Thakur, *Phys. Rev. B*, **26**, 3001 (1982).
- [10] K. Seyoum, K. P. Thakur and D. Jha, *Phys. Stat. Sol.*, **167**, 495 (1991).
- [11] S. Pizzini, F. Baudalet and A. Fontaine, *Phys. Rev. B*, **47**, 8754 (1993).
- [12] W. Vavra, D. Barlett, S. Elagoz, C. Uher, and R. Clarke, *Phys. Rev. B*, **47**, 5500 (1992).
- [13] Z. G. Li, P. F. Carcia and Y. Cheng, *J. Appl. Phys.*, **73**, 2433 (1992).
- [14] E.E. Fullerton, I.K. Schuller, F.T. Parker, K.A. Svinarich, G.L. Eesley, R. Bhadra and M. Grimsditch, *J. Appl. Phys.*, **73**, 7370 (1993).
- [15] G. Carlotti, A. Montone, C. Petrillo and M.V. Antisari, *J. Phys.: Condens. Matter*, **5**, 4611 (1993).
- [16] A. Taiwo, H. Yan and G. Kalonji, in "Materials Theory and Modelling", ed. by P.D. Bristowe, J. Broughton and J.M. Newsam (Materials Research Society, 1993).
- [17] J. Hoekstra, H. Yan, G. Kalonji and H. Jonsson, to be published in *J. Mater. Res.*
- [18] A. S. Clarke and H. Jonsson, *Phys. Rev. E*, **47**, 3975 (1993); D. Faken and H. Jonsson, *Comp. Mater. Sci.*, (in press).

APPLICATION OF FRACTALS AND KINETIC EQUATION IN MODELLING CLUSTER AND ULTRAFINE PARTICLE SIZE DISTRIBUTIONS

J. CHAIKEN* AND JERRY GOODISMAN

Department of Chemistry and the Solid State Science and Technology Program, Syracuse
University, Syracuse, New York 13244-4100

ABSTRACT

We briefly describe a model which seems to be applicable to a variety of coalescence growth systems. Spanning cluster growth, particle growth and hillock formation in thin metal films, this model is based on the Smoluchowski kinetic equations and fractals. We describe how this model has been able to suggest the effect of translational to internal energy conversion in coalescing systems in determining the shape of particle size distributions. We also suggest how this model can be employed to account for the behavior of hillocks in supersaturated alloy films under thermal annealing conditions.

INTRODUCTION

One of the more enticing materials science oriented applications of laser chemistry is the synthesis of cluster and ultrafine particles using organometallic [1] precursors. Clusters and ultrafine particles are predicted [2,3] to have a variety of unique electrical and optical properties which allow revealing investigations of the scaling of fundamental properties and could also allow important applications. Models [4,5] exist which connect the distribution of cluster sizes present in a bulk sample, and the microscopic properties of the clusters, to the electrical, mechanical and optical properties of the bulk material. A model [6] is needed to connect a particular distribution produced to the particular set of reaction conditions used to synthesize those clusters. Although numerical treatments [7,8] have been in existence for some years we desire an analytic model which may be of intuitive value in addition to empirical value. The problem is complex because of the importance of multiple kinetic pathways in the synthesis of any cluster containing more than a few monomers. We report progress in exploring the utility of a model based on the Smoluchowski equations. As an illustration of its potential generality, we also mention recent progress in exploring the applicability of the same model to hillock formation and growth in thin metal films.

The model is presented in detail elsewhere [9] so only the general concepts will be described here. The basic idea is contained in the Smoluchowski equations (1) which were introduced [10] in the context of colloidal aggregation and solved in the limit of cluster/particle growth in

$$\frac{dn_k}{dt} = \frac{1}{2} \sum_{j=1}^{k-1} K_{j,k-j} n_j n_{k-j} - n_k \sum_{j=1}^{\infty} K_{j,k} n_j \quad (1)$$

chemical solutions in 1916. Only binary collisions are considered and reaction rates are calculated as collision frequencies using number densities and cross sections, or in the particular language of fractal coalescence studies, number densities and "kernels". These kernels have the form of second order rate constants which connect the number densities of the different cluster sizes to the rate of coalescence of the clusters per unit time. A given cluster size is only formed by the coalescence of smaller clusters and is destroyed only by its coalescence with other clusters to form still larger ones. This is a mean-field type treatment in that no spatial correlation is presumed to exist between different cluster sizes.

The information mediating the various interactions involved in aggregation chemistry is contained in these kernels. There are essentially three analytical approaches which have been applied to cluster and particle formation. Each leads to a theory which relies on basic input parameters taken

from one limit in the problem. Using a thermodynamic approach (e.g. the Kelvin equation) [11] and employing homogeneous nucleation theory [12], in which aggregation occurs by addition of monomers, one bases the parameters of the model on the energetics of bulk materials. Alternatively, one can begin in the opposite limit and attempt to approach understanding the kernels based on the properties of the individual monomers [8,13,14] which are calculated and extrapolated using quantum chemical calculations. The third approach, our approach, is to focus on the scaling of the properties of the clusters and particles and the reacting system from the microscopic regime to the bulk regime.

To illustrate the physical content of scaling, we refer to the following example. In some agglomerating systems, the so-called "ballistic" regime, the clusters' mean free path is long compared to their own size. As the number of monomers in a cluster is increased, the cluster's size increases. In our model of this case, the probability per unit time that a particular cluster will interact with, and agglomerate with, another cluster increases with size because the amount of space explored per unit time increases with increasing size. However, for a constant temperature system, the more monomers in a cluster, the greater its mass and the slower it moves, thereby exploring less space per unit time in the reaction medium for coalescence partners. Do the rate constants, i.e. kernels, increase with increasing sizes or decrease due to the competing tendencies?

Which tendency prevails in a particular agglomerating system depends on the shape, i.e. represented in terms of the fractal dimension, of the growing particles. A particle can grow in various ways such that its average crosssectional area increases in correspondingly different ways. Which tendency prevails also depends on how quickly the clusters slow down with increasing size. Exothermicity or endothermicity of agglomeration, evaporation effects, as well as the efficiency of conversion of center of mass translational energy and angular momentum into internal energy and angular momentum can affect the distribution of velocities and thereby, mass transfer rates. Thus, the *scaling* of the kernels with increasing cluster size, i.e. number of monomers in the cluster, is the issue in our model. The actual values of the kernels [15] are important for connecting a particular simulation or analytic result based on (1) to a particular set of reaction conditions.

Rigorous calculations in the ballistic or diffusion-limited mass transfer regime suggest that the scaling of kernels should be represented as (2).

$$K_{\lambda_i, \lambda_j} = \lambda^2 \omega K_{ij} \quad (2)$$

There is an implicit assumption in the literature that the scaling varies smoothly as reaction conditions are changed from the ballistic to the diffusive regimes. Using (3), which is equivalent to (2), absolute values for all kernels can be calculated within a single constant multiplicative factor from the number of monomers in each of the interacting clusters and the scaling parameter, ω . We have already described [15] how to obtain this constant factor from appropriate experimental measurements.

$$K_{i,j} = K_{1,1}(ij) \omega \quad (3)$$

We have showed how to determine ω from experimental data.

When (2) is obeyed, the kernels are said to be homogeneous. For homogeneous kernels, Jullien [16] found an asymptotic solution for the Smoluchowski equations, (4). Here, $a = -2\omega$ and b depends on τ .

$$n_k \rightarrow A k^a e^{-bk} \quad (4)$$

Jullien's solution (4) and the well-known lognormal distribution function are very similar. Using a Taylor's series expansion of (4) about the most probable cluster size, it is possible to show [9] that (4) and the lognormal distribution are nearly identical. The lognormal distribution has long been associated with coalescence growth [6] but the only mathematical justification has involved random numbers and the Central Limit Theorem.

There have been many empirical uses of the lognormal distribution over the last century and a half [17] including particle size distributions relating to objects created by breaking down larger objects. For this, the Rosin-Rammler probability density distribution function [18] has also been used extensively. Both of these distributions can be seen to resemble Jullien's rigorous solution to the Smoluchowski equations. In the case of breaking down phenomena producing particle size, i.e. fragment size, distributions, we suggest that coalescence growth is again the ultimate cause. In this case we suggest that a substantial portion of the net breakdown process occurs at grain boundaries. These boundaries are mostly determined by the process mediating the growth of the grains.

Determination of the ω corresponding to a particular set of cluster or particle size data can be accomplished in a variety of ways. For experiments involving mass spectrometric determination of cluster size distributions or others for which a set of non-zero populations exist, equation (5) is advantageous. A plot of $\ln(n_k)$ can be fit to a bilinear form in k and $\ln k$, and thereby yield a and b directly. Data from other sources is often represented using "bins" to produce histograms.

$$\ln(n_k) = \ln A + \ln k - b_k \quad (5)$$

$$\frac{\langle k \rangle}{k_m} = \frac{a+1}{b} = \frac{2\omega+1}{2\omega} \quad (6)$$

When some of the bins contain zero observations of a given cluster size or size range, fitting the cumulative distribution is advantageous. This can be fit to also give a and b directly which is tantamount to knowledge of ω . Earlier [9] we employed the lognormal distribution to estimate the average cluster size, $\langle k \rangle$, and the most probable cluster size, k_m , for a particular set of data. Given these values and (6) we calculated ω .

We have calculated and compared values of ω from a set of nozzle beam expansion-produced cluster size distributions. We have since recalculated ω values from the data which are somewhat different from those earlier published values [9]. Since the value of ω depends on reaction conditions in addition to the nature of the monomer, comparability across various experiments is not immediately assured. It was observed, however, that its value is usually more negative than anticipated by the theory. Simulations show that significant loss of all coalescing species from the reacting system, e.g. by diffusion out of the reacting volume, leads to size distributions having more negative values of ω . Alternatively, this general observation may suggest that all clusters slow down faster with increasing cluster size than predicted based on the kinematics of the conversion of center of mass translational energy to internal energy. Based on this idea it was possible to rationalize the values of ω obtained based on the position of the monomer in the periodic table.

Simulations [9,22] based on integrating (1) suggest that the value of ω obtained from a particular size distribution is not affected if only a subset of kernels is arbitrarily changed from the homogeneous values. The existence of a "magic number" cluster would seem to affect only a

subset of the total set of kernels whereas evaporation or diffusion could directly affect the populations of *all* cluster sizes. When all sizes are affected, the perturbation is "global" and a different ω is manifest. Based on the ability of a homogeneous set of kernels to represent actual data and the existence of multiple kinetic pathways for producing any cluster with more than a few monomers, all clusters which are not magic number clusters probably exist in a range of different structures that for the purposes of kinetics are indistinguishable. Magic number clusters are the only ones with unique structures and in all likelihood have coalescence kernels which are smaller than that predicted by homogeneity.

Depending on deposition conditions, e.g. substrate temperature and deposition rate, metal films can be deposited which possess structures known as "hillocks" because of their appearance in electron micrographs [19]. Backscattered and secondary electron studies at variable angles of incidence can be used to study these objects and determine their morphology and locations in the films. It is thought that material at grain boundaries moves under the influence of compressive strain and participates in some type of coalescence growth. This leads to a temporal variation in the distribution of hillock sizes. We have attempted to apply our coalescence model to the formation and growth of hillocks using the published data of Vook [20] and coworkers. Although this particular study involved hillock chemistry stimulated by thermal annealing, we hope to extend this approach to electromigration [21] induced hillock chemistry.

Although this study will be described in detail in a separate publication [22], certain conclusions are forthcoming. One test of the model is to show that Jullien's solution is better than other functional forms in representing the data for pure metal. In fact, no other form is better at representing it although very similar forms, e.g. the lognormal distribution, represent the data equally well. The data for one alloy film is slightly better represented using the lognormal distribution although it should be noted that our model is applicable only to pure clusters, particles or hillocks. Another aspect of the model involves the time evolution of the b parameter. While it is expected that b should vary in time so as to be proportional to $t^{1/(2\omega-1)}$, a is expected to be time independent. Application to Vook's data gives a value of ω that does vary in time.

Notwithstanding this discrepancy, if one uses the average value of ω obtained over the time series, it is true that the b parameter varies more or less as expected.

We are encouraged by these observations in so far as the experiment was not designed to isolate the types of comparisons we have attempted. The particular alloy being used for the time evolution experiment was supersaturated in one component with respect to other so that a precipitate was being formed which could affect the value of ω . The experiment was not able to clearly observe the smallest objects contributing to hillock growth and Vook pointed out that these smallest entities were important. Observations on the largest spatial scales are also limited. Given these potential sources of experimental artifacts and competing physical processes not contained in the Smoluchowski treatment, it seems remarkable that the model discovers any order in the data at all. This study suggests that a study can be designed which could unequivocally discern whether the model is uniquely suited to modelling hillock formation and growth. As a practical matter, the model already suggests that the interpretation of the effect of background gases on the formation of hillocks during deposition needs to be reexamined.

References

- * author to whom correspondence should be addressed.
- 1. see various chapters in Laser Chemistry of Organometallics, edited by J. Chaiken ACS Symposium Series Vol. 530, (American Chemical Society, Washington, D.C. 1993) or see J. Chaiken, M. J. Casey, M. Villarica, J. Phys. Chem. **96**, (1992)3183-3186.
- 2. Purna Das and H. Metiu, J. Phys. Chem., **89**, 4680-4687(1985).
- 3. A. E. Neeves and Meyer H. Birnboim, Opt. Lett., **13**, 1087-1089(1988), Eiichi Hanamura, Phys. Rev. B. **37**, 1273-1279(1988).

4. D. E. Aspnes, *Thin Solid Films*, **89**, 249-262(1982).
5. S. Mader, *Thin Solid Films*, **2**, 35-41(1964), S. Mader, H. Widmer, F. M. d'Heurle and A. S. Nowick, *Appl. Phys. Lett.*, **3**, 201(1963).
6. R. A. Buhrman and C. G. Granqvist *J. Appl. Phys.* **47**, 2220-2222(1976), C. G. Granqvist and R. A. Buhrman, *Solid State Commun.* **18**, 123-126(1976) and *J. Catal.* **42**, 477-479(1976).
7. W. R. Cannon, S.C. Danforth, J. H. Flint, J. S. Haggarty and R. A. Marra, *J. Am. Cer. Soc.* **65**, 324-329(1982), W. R. Cannon, S.C. Danforth, J. H. Flint, J. S. Haggarty and R. A. Marra, *J. Am. Cer. Soc.* **65**, 329-335(1982).
8. W. H. Zurek and William C. Schieve, *J. Chem. Phys.* **68**, 840-846(1978), W. H. Zurek and William C. Schieve, *J. Phys. Chem.* **84**, 1479-1482(1980).
9. M. Villarica, M. J. Casey, J. Goodisman, J. Chaiken, *J. Chem. Phys.* **98** (1993) 4610-4625.
10. M. V. Smoluchowski, *Phys. Z.* **17**, 557(1916).
11. H. J. Freund and S. H. Bauer, *J. Phys. Chem.* **81**, 994-1000(1977), D. J. Fruip and S. H. Bauer, *J. Phys. Chem.* **81**, 1001-1006(1977), D. J. Fruip and S. H. Bauer, *J. Phys. Chem.* **81**, 1007-1015(1977), D. J. Fruip and S. H. Bauer, *J. Phys. Chem.* **81**, 1015-1024(1977).
12. B. Nowakowski, E. Ruckenstein, *J. Chem. Phys.* **94**, 8487-8492(1991).
13. for Na see W. D. Knight, Keith Clemenger, Walt A. de Heer, Winston Saunders, M. Y. Chou and Marvin L. Cohen, *Phys. Rev Lett.* **52**, 2141-2143(1984).
14. John W. Brady, Jimmie D. Doll, Donald L. Thompson, *J. Chem. Phys.* **71**, 2467-2472(1979), John W. Brady, Jimmie D. Doll, Donald L. Thompson, *J. Chem. Phys.* **73**, 2767-2772(1980), John W. Brady, Jimmie D. Doll, Donald L. Thompson, *J. Chem. Phys.* **74**, 1026-1028(1981).
15. J. Chaiken and Jerry Goodisman, *J. Photosci. Photobio. A* in press.
16. R. Jullien, *New J. Chem.* **14**, 239-253(1990) and R. Botet and R. Jullien, *J. Phys. A.* **17**, 2517-2530(1984).
17. D. B. Siano, *J. Chem. Ed.* **49**, 755-757(1972), J. Aitchison, J. A. C. Brown, *The Lognormal Distribution* (Cambridge Press, Cambridge, 1957).
18. see Terrance Allen, *Particle Size Measurement*, 3rd ed. (Chapman and Hall, New York, 1981), p. 139.
19. C.Y. Chang and R. W. Vook, *J. Vac. Sci. Technol.* **A9**, 559-562(1991).
20. S. Aceto, C. Y. Chang, R. W. Vook, *Thin Solid Films* **219**, 80-86(1992).
21. C. Y. Chang and R. W. Vook, *Thin Solid Films* **223**, 23-30(1993), C. Y. Chang and R. W. Vook, *Materials Chemistry and Physics*, **36**, 199-216(1994).
22. J. Chaiken and Jerry Goodisman, manuscript in preparation.

PART V

Vapor Deposition and Si Particles

CHEMICAL VAPOR SYNTHESIS OF NANOSTRUCTURED CERAMICS

W. CHANG*, G. SKANDAN*, H. HAHN**, S. C. DANFORTH*** AND B. KEAR*

*Rutgers University, Department of Materials Science, Piscataway, NJ 08854

**Technical University of Darmstadt, Department of Materials Science, Germany

***Rutgers University, Department of Ceramic Engineering, Piscataway, NJ 08854

ABSTRACT

A modification of the conventional inert gas condensation apparatus for making nanostructured powders, wherein an evaporative source is replaced by a chemical source, is described. The new chemical synthetic process, called chemical vapor condensation (CVC), combines rapid thermal decomposition and expansion of a precursor/carrier gas stream in a hot tubular reactor with rapid condensation of the product particle species on a cold substrate under a reduced inert gas pressure of 1-50 mbar. The process has been used to synthesize loosely agglomerated nanoparticles (6 to 10 nm) of n-SiC_xN_y, starting from hexamethyldisilazane (HMDS) as precursor compound. The phase, morphology, and composition of n-SiC_xN_y powders can be modified by heat treatment. β -SiC particles with grain size less than 10 nm form after annealing at 1300°C in flowing Ar. In a 1:1 NH₃/H₂ mixture n-SiC_xN_y powders transform into α -Si₃N₄ whiskers, with [100] growth direction.

INTRODUCTION

Nanostructured materials with average grain size or other structural domain size less than 100 nm have shown different properties from, and often superior to, those of conventional materials that have grain structures on a larger size scale.¹ A variety of synthetic techniques have been developed in recent years to synthesize nanostructured materials.² Among those methods inert gas condensation (IGC) is the most applicable method for the synthesis of loosely agglomerated metal or ceramic nanoparticles with uniform size, size distribution, and low impurities.^{3,4} In most gas condensation systems, an evaporative source is used to generate ultrafine particles which are convectively transported to and condensed on a cold substrate. The key to the formation of non-agglomerated nanoparticles is the reduced chamber pressure and rapid quenching of the gaseous species. Meanwhile the challenge of scaling-up the inert gas condensation process is being addressed, using a forced convective flow system for continuous processing of powders, and a multi-kilowatt electron beam for achieving high evaporation rates. However, many useful ceramics and low vapor pressure metals cannot easily be produced by such an evaporation method, so some other approach is needed. In the present study, we have taken a conventional IGC system and adapted it for the purpose of synthesizing nanostructured ceramic particles from metalorganic precursors.⁵ In this new process, called chemical vapor condensation (CVC), a heated tubular reactor decomposes the precursor to form a stream of clusters or nanoparticles entrained in a carrier gas.

Hexamethyldisilazane (HMDS) is used as the precursor compound to synthesize silicon-base nanostructured ceramics because it is chemically stable and nontoxic. By selecting different carrier gases, the pyrolyzed product can be SiC, Si₃N₄ or SiC/Si₃N₄ composite.⁶

A wide range of metalorganic precursors is available commercially, all of which can, in principle, be utilized in this new process. Thus, it appears that, by appropriate choice of precursor compound and carrier gas, the CVC method can be used to synthesize nanostructured powders of oxides, carbides, nitrides, borides, and their composites.

EXPERIMENTAL METHOD

Powder synthesis

A schematic of the CVC apparatus is shown in Figure 1. It consists essentially of two separate components: a reaction chamber that is maintained at a pressure of 1-20 mbar by high speed pumping, and a precursor delivery system operating at ambient pressure. The two components are connected via a needle valve, which continuously monitors and controls the flow rate of the precursor/carrier gas stream from the gas delivery system into the reaction chamber. A Mo-wound furnace tube of high purity Al₂O₃ provides a heat source for controlled decomposition of the precursor. During the short residence time of the precursor in the heated tube, the HMDS precursor decomposes to form small clusters or nanoparticles. At the outlet of the furnace, rapid expansion of the particles formed in the gas stream serves to mitigate particle growth and agglomeration. Finally, the particles condense out on a liquid nitrogen cooled rotating substrate from which the particles can be scraped off and collected.

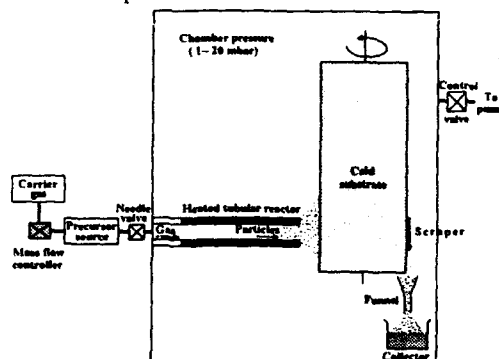


Figure 1. Schematic of the chemical vapor condensation (CVC) processing apparatus

The characteristics of the powder product will depend on the carrier gas, the precursor concentration in the gas stream, and the residence time of the precursor compound in the tubular furnace, i.e. the flow rate of the gas stream, chamber pressure, and pyrolysis temperature. In a series of experiments He was used as the carrier gas with flow rate fixed at 8.55×10^{-3} mole/min by means of a MKS mass flow controller and the leak rate was fixed to maintain a constant operation pressure in the chamber. Under these

conditions the HMDS concentration was about 16.5 mole% in the gas stream. The furnace temperature was varied over the range 1100 to 1400°C in 100°C steps and the chamber pressure was varied over the range 3 to 12 torr in 3 torr steps. The stand-off distance of the cold substrate from the hot reactor tube was set at about 2", in order to ensure rapid quenching of the particles.

Post-annealing treatment

Different gas atmospheres, such as Ar, NH₃, and H₂ were used for post-annealing of as-synthesized powders. Samples were annealed at temperature in the range 400 to 1500 °C in the flowing gas streams.

Sample characterization

X-ray diffraction (CuK α radiation) was used to study the phases present in the as-synthesized and annealed samples. Density of the powder was determined by He-pycnometry. Specific surface area of as-synthesized and annealed samples was measured by single point BET. Scanning electronic microscopy, TEM, and HREM were used to characterize the microstructure and morphology of as-synthesized and annealed samples. To prepare the TEM samples, powders were first dispersed in methyl alcohol to form a solution by ultrasonic vibration. Then, a copper grid coated with a holy-carbon film was dipped into the dispersed solution and dried in air immediately. Chemical compositions were determined using Rutherford backscattering spectroscopy with 2 MeV He-ions. The experimental composition profiles were fitted using computer program RUMP.

Table 1. Some properties of as-synthesized SiC_xN_y powder

Sample name	Reactor Temperature (C)	Powder density* (g/cm ³)	Powder appearance	Surface area** (m ² /g)	Particle size from BET (nm)	Particle size from TEM (nm)
S-1	1100	2.614	brown	568	4	10
S-2	1200	2.737	dark-brown	555	4	10
S-3	1300	2.781	brown-black	360	6	8
S-4	1400	2.783	jet-black	272	8	6

RESULTS AND DISCUSSION

The residence time calculated from the gas flow rate, pyrolysis temperature, and chamber pressure is less than 0.1 second. In a deposition time of 30 minutes 2-3 grams of powder was collected. X-ray diffraction analysis showed that all the as-synthesized powders were amorphous. A waxy powder product with light-brown color and polymer-like properties forms at pyrolysis temperatures < 1000°C. By increasing the pyrolysis temperature the color of the powder deposits change from brown to black (see Table 1), clearly indicating different degrees of pyrolysis during the short residence time of the precursor in the heated tube. The average particle size from TEM range from 6-10 nm with the smallest particle size corresponding to the highest pyrolysis temperature. In contrast the measured particle size from BET increased with the reaction temperature over the range 4-8 nm. This suggests that the particles determined by TEM, at least at the lower pyrolysis temperature, are actually composed of small clusters. In this case it is not

easy to resolve the clusters in the 10 nm particles by TEM because of the low contrast of the amorphous structures.

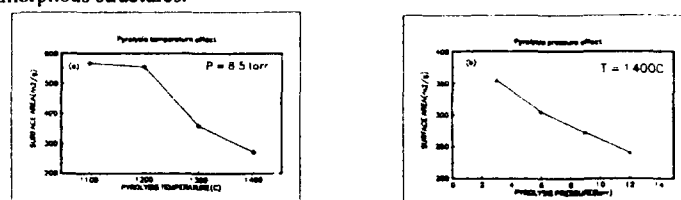


Figure 2. Specific surface area of as-synthesized $n\text{-SiC}_x\text{N}_y$ powder
(a) effect of pyrolysis temperature (b) effect of pyrolysis pressure

Figure 2 shows that the specific surface area of as-synthesized powders range from 270-570 m^2/g with increasing pyrolysis temperature and pressure. The density of the nanoparticles, shown in Figure 3, increases with increasing reaction temperature and pressure. The surface area and density data at the lowest reaction temperature are consistent with the formation of nanoparticles composed of aggregates of very high surface area clusters. All the density of the particles increases with the reaction temperature and pressure, which probably reflects the higher degree of precursor pyrolysis, i.e. conversion of the precursor to SiC_xN_y phase.

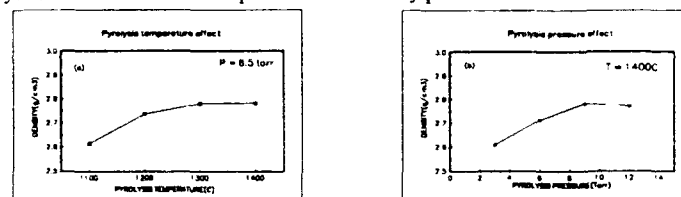


Figure 3. Density of as-synthesized $n\text{-SiC}_x\text{N}_y$ powder
(a) effect of pyrolysis temperature (b) effect of pyrolysis pressure

The effect of annealing in flowing Ar at temperatures in the range 1000-1500°C is shown in Figure 4. As-synthesized $n\text{-SiC}_x\text{N}_y$ powders start crystallizing at temperatures higher than 1200°C and $\beta\text{-SiC}$ particles with grain size less than 10 nm are formed at 1300°C. There is a little change on the surface area of the powder annealed at 1400°C (Figure 5). The particle size measured from BET is close to the grain size calculated from the X-ray line broadening. It is believed that the presence of excess carbon in the crystallized powders inhibits grain growth.⁵

Figure 6 shows the effect of heat treating amorphous $n\text{-SiC}_x\text{N}_y$ powder in flowing NH_3/H_2 (1:1 mixture) at temperatures in the range 800-1400°C for 5 min. Crystallization into hexagonal $\alpha\text{-Si}_3\text{N}_4$ occurs at 1400°C. The $\alpha\text{-Si}_3\text{N}_4$, shown in Figure 7, is in the form of nanowhiskers with diameters varying from 30 to 60 nm and aspect ratio as high as 500:1. As HREM image of the whisker shows a high degree of single crystal perfection, Figure 8. The growth direction of the whisker is [100].

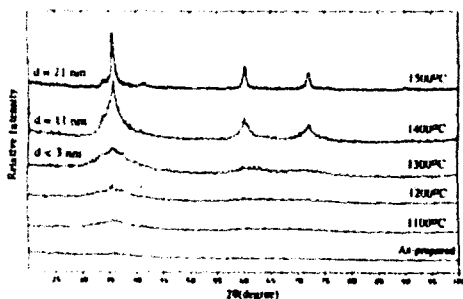


Figure 4 XRD pattern of $n\text{-SiC}_x\text{N}_y$ powder annealed in flowing Ar

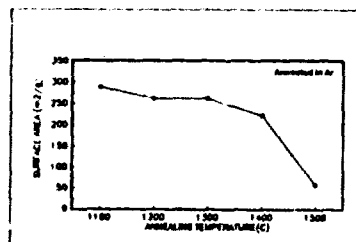


Figure 5. Specific surface area of $n\text{-SiC}_x\text{N}_y$ powder annealed in flowing Ar

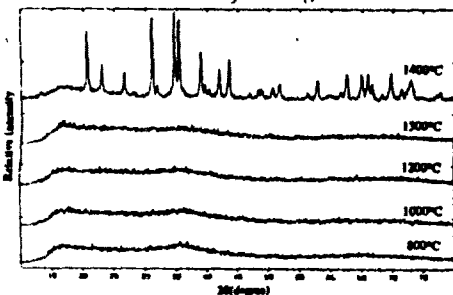


Figure 6. XRD pattern of $n\text{-SiC}_x\text{N}_y$ powder annealed in flowing NH_3/H_2

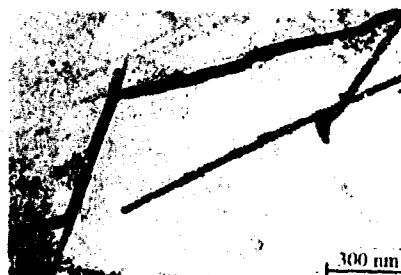


Figure 7. TEM image of $\alpha\text{-Si}_3\text{N}_4$ nano-whisker

It is not clear at this time what exactly leads to the transformation of these whiskers, on the basis of our most recent results, the possible mechanism being envisaged is that ultrafine droplets of liquid silicon are formed by reductive decomposition of $n\text{-SiC}_x\text{N}_y$ particles in the powder bed, and these droplets are responsible for the growth of single crystal $\alpha\text{-Si}_3\text{N}_4$ nanowhisker.⁷ Apparently, the liquid silicon droplets migrate through the powder bed, dissolving amorphous $n\text{-SiC}_x\text{N}_y$ powders in their path and leaving crystalline whiskers in their wake, Figure 9. Coalescence of liquid silicon droplets formed in a powder agglomerate can also give rise to larger silicon droplets, which in turn can generate larger diameter whiskers, Figure 10. Table 2 gives the composition data of samples annealed in flowing NH_3/H_2 . There is a systematic change in the composition with the annealing temperature. At 1400°C a sharp reduction in oxygen content and a corresponding enrichment in nitrogen occurs, which probably exerts an important influence on the whisker formation at this temperature.

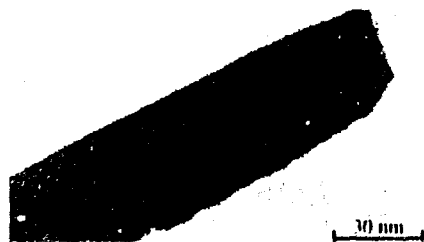


Figure 8. HREM image of $\alpha\text{-Si}_3\text{N}_4$ nano-whisker

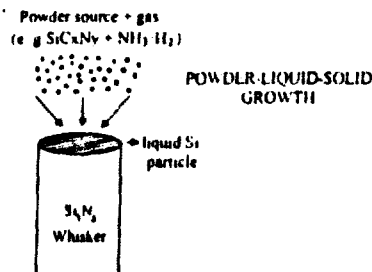


Figure 9. A schematic of the proposed nano-whisker growth mechanism

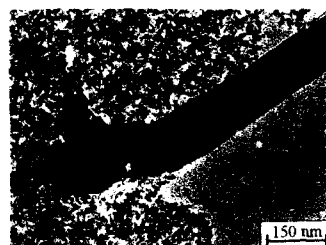


Figure 10. TEM image of thick α - Si_3N_4 whisker

Table 2 Chemical composition for samples annealed in NH_3/H_2

Sample name	Annealing Temperature (°C)	$\text{Si}_x\text{C}_y\text{N}_z\text{O}_w$		
		X	Y	Z
NH-1	400	1.86	0.46	0.23
NH-2	800	1.53	0.57	0.23
NH-3	900	1.23	0.77	0.33
NH-4	1000	0.91	0.69	0.53
NH-5	1200	0.97	0.82	0.24
NH-6	1400	0.73	1.22	0.09

CONCLUSIONS

- (1) Nanostructured amorphous SiC_xN_y powders with particle size less than 10 nm can be synthesized by the chemical vapor condensation method.
- (2) Critical to success of the chemical vapor condensation method are: (i) low concentration of precursor in the carrier gas; (ii) rapid expansion of the gas stream through an heated tubular reactor in a reduced pressure, and (iii) rapid quenching of the gas phase nucleated clusters or nanoparticles as they exit from the reactor tube.
- (3) The surface area of as-synthesized powders was in the range of 240 to 570 m^2/g , which is higher than values reported in the literature.
- (4) By annealing in Ar, n- SiC_xN_y powders transform into β - SiC particles with grain size less than 30 nm. In flowing NH_3/H_2 (1:1 mixture) α - Si_3N_4 nanowhisker with high aspect ratio are formed. The growth direction of the whisker is [100].

ACKNOWLEDGMENT

Support for this research has been provided by the Office of Naval Research under grant number N00014-91-J-1828. An equipment grant from the Advanced Technology Center for Surface Engineering Materials and Center for Ceramic Research in Rutgers University are also gratefully acknowledged.

REFERENCE

- ¹R. W. Siegel, *Nanostructured Materials*, 3, 1 (1993)
- ²H. Glitter, *Progress in Materials Science*, 33 (1990)
- ³H. Hahn, J. A. Eastern and R. W. Siegel, *Ceramic Transactions 1B: Ceramic Powder Science*, 1115 (1988)
- ⁴H. Hahn and R. S. Averback, *J. Appl. Phys.*, 67, 1113 (1990)
- ⁵W. Chang, G. Skandan, H. Hahn, S. C. Danforth, and B. Kear, *Nanostructured Materials*, 4, No1 (1994)
- ⁶A. Samaguchi, K. Ioda, and K. Niihara, *J. Am. Ceram. Soc.*, 74 [5] 1142-44 (1991)
- ⁷W. Chang, H. Hahn, and B. Kear (to be published)

Characterization of Nanoscale Particles Produced by Laser Vaporization / Condensation in a Diffusion Cloud Chamber

M. Samy El-Shall, W. Slack, D. Hanley and D. Kane
Department of Chemistry, Virginia Commonwealth University
Richmond, VA 23284-2006

ABSTRACT

Nanoscale metal oxide particles have been synthesized by using a novel method which combines laser vaporization of metal targets with controlled condensation in a diffusion cloud chamber. The following oxides have been synthesized: ZnO, SiO₂, Fe₂O₃, Bi₂O₃, PdO, NiO, AgO, TeO, Sb₂O₃, TiO₂, ZrO₂, Al₂O₃, CuO, In₂O₃, SnO₂, V₂O₅ and MgO. With this method, the size of the particles can be conveniently controlled by careful control of the degree of supersaturation which is accomplished by adjusting the temperature gradient, total pressure, and partial pressure of the metal vapor generated by laser vaporization in a diffusion cloud chamber. The microscale structures of the SiO₂ and Al₂O₃ particles exhibit interesting web-like matrices with a significant volume of vacancies. These materials may have special applications in catalysis and as reinforcing agents for liquid polymers.

INTRODUCTION

Nanoscale particles possess several unique properties such as large surface areas, unusual adsorptive properties, surface defects and fast diffusivities [1-3]. The characterization of these properties can ultimately lead to identifying many potential uses, particularly in the field of catalysis [4]. For example, nanoparticles of metal oxides and mixed oxides such as SiO₂/TiO₂ exhibit unusual acidic properties and are used as acidic catalysts [5]. Recently we described a novel technique to synthesize nanoparticles of controlled size and composition [6]. Our technique combines the advantages of pulsed laser vaporization with controlled condensation in a diffusion cloud chamber under well defined conditions of temperature and pressure. The present work demonstrates the advantages of this method in controlling the composition and the properties of the nanoscale metal oxide particles.

EXPERIMENTAL

In the experiments, a modified upward thermal diffusion cloud chamber is used for the synthesis of the nanoscale particles. This chamber has been commonly used for the production of steady state supersaturated vapors for the measurements of homogeneous and photo-induced nucleation rates of a variety of substances [7,8]. A sketch of the diffusion cloud chamber with its relevant components is shown in Figure 1-a. The chamber consists of two, horizontal, circular stainless steel plates, separated by a circular glass ring. A metal target of interest sets on the lower plate, and the chamber is filled with a carrier gas such as He or Ar containing a known composition of the reactant gas (e.g. O₂ in case of oxides, N₂ or NH₃ for nitrides, CH₄ or C₂H₄ for carbides, etc.). The metal target and the lower plate are maintained at a temperature higher than that of the upper one (temperatures are controlled by circulating fluids). The top plate can be cooled to less than 120 K by circulating liquid nitrogen. Nichrome heater wires are wrapped around the glass ring and provide sufficient heat to prevent condensation and fogging. The large temperature gradient between the bottom

and top plates results in a steady convection current which can be enhanced by using a heavy carrier gas such as Ar or Kr under high pressure conditions ($1-10^3$ torr). The metal vapor is generated by pulsed laser vaporization using the second harmonic (532 nm) of a Nd-YAG laser (15-30 mJ/pulse). Laser vaporization typically releases more than 10^{14} metal atoms per pulse (2×10^{-8} s). The hot metal atoms react with O_2 (in the case of oxides syntheses) to form vapor phase metal oxide molecules which undergo several collisions with the carrier gas thus resulting in efficient cooling via collisional energy loss. Under the total pressure employed in these experiments (100 - 800 torr), it is expected that the metal atoms and the oxide molecules approach the thermal energy of the ambient gas within several hundred microns from the vaporization target. The unreacted metal atoms and the less volatile metal oxide molecules are carried by convection to the nucleation zone near the top plate of the chamber. The temperature T , partial pressure P of diffusant, saturation pressure P_e , and supersaturation, $S = P/P_e$ vary with elevation in the chamber in the manner demonstrated in Figure 1-b. By controlling the temperature gradient, the total pressure and the laser power (which determines the number density of the metal atoms released in the vapor phase), it is possible to control the size of the condensing particles. This is the basic principle of our method.

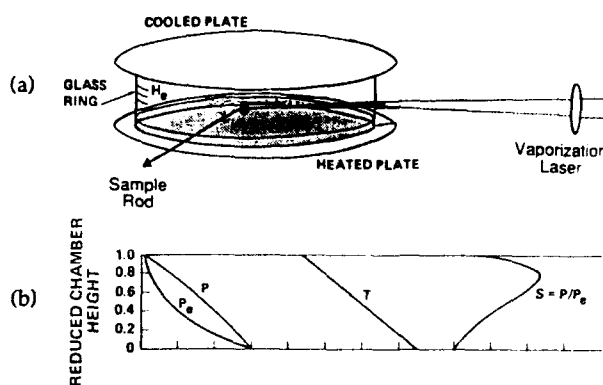


Figure 1 (a) : Sketch of diffusion cloud chamber with relevant components indicated.

(b) : Typical courses of diffusant partial pressure P , saturation pressure P_e , temperature T , and supersaturation S in a diffusion cloud chamber.

RESULTS AND DISCUSSION

Figure 2 displays SEM micrographs obtained for ZnO and Al_2O_3 particles synthesized using 20% O_2 in He at a total pressure of 800 torr and top and bottom plate temperatures of $-100^\circ C$ and $20^\circ C$, respectively. It is clear that the particles exhibit a unique agglomerate pattern which appears as a web-like matrix. Based on the TEM analyses of these, individual particle's sizes are estimated between 10-20 nm.



Figure 2 (a) : SEM micrograph of ZnO particles.

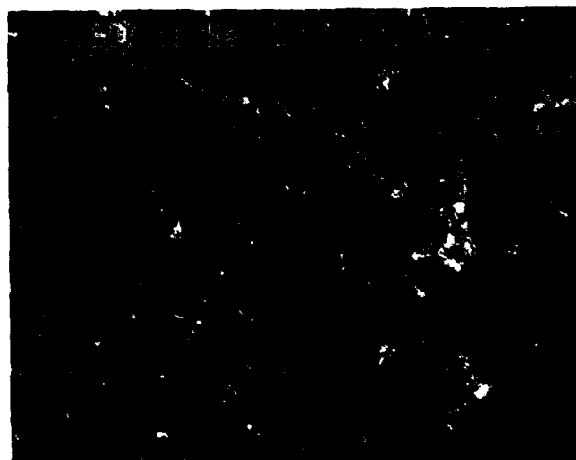


Figure 2 (b) : SEM micrograph of Al₂O₃ particles.

The Raman spectrum of the TiO₂ nanoparticles synthesized in Ar (shown in Figure 3) exhibits the characteristic peaks of the nanoscale anatase phase of TiO₂ (the low temperature phase) [9, 10]. By varying the experimental conditions such as the partial pressure of O₂ and the carrier gas we were able to synthesize both the rutile and anatase phases of TiO₂ [6].

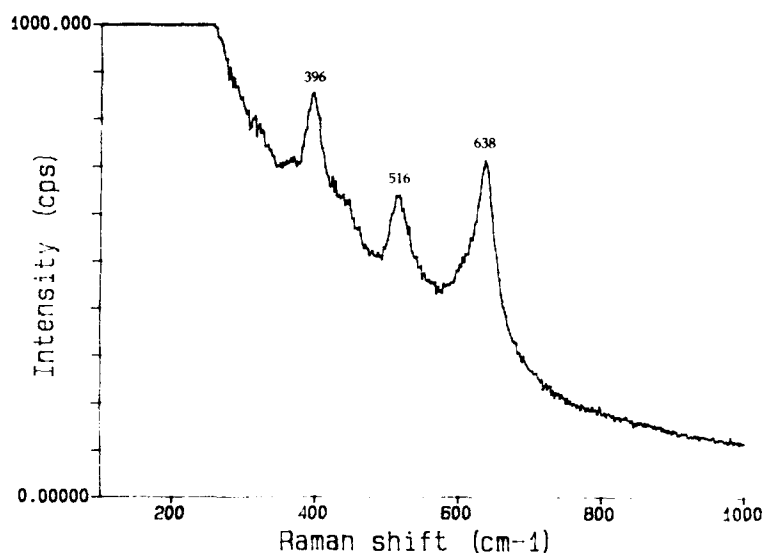


Figure 3 : Raman spectra of TiO₂ particles synthesized in O₂/Ar mixture.

To illustrate the effect of the O₂ / carrier gas mixture on the ratio of the oxidized-to-nonoxidized metal particles, we measured the x-ray photoelectron spectra (XPS) of the particles prepared under different experimental conditions. Figure 4 illustrates the results for SiO₂ particles synthesized using different concentrations of O₂ in He. By decreasing the O₂ concentration in the carrier gas the Si 2p peak (≈ 99.5 eV) is enhanced due to the unoxidized Si particles. From the data presented in Figure 4 (a, b, c), the SiO₂ / Si ratios are estimated as 0.99, 0.76 and 0.60, respectively. Therefore, the data demonstrates the control of the compositions of the nanoparticles. The oxide / metal ratio in the nanoparticles also depends on the type of the carrier gas as well as on the O₂ concentration. By using different carrier gases containing different concentrations of O₂, it was possible to affect the efficiency of the oxidation process. In this way, nanoparticles containing more than 99% oxide molecules or more than 60% unoxidized metal have been synthesized.

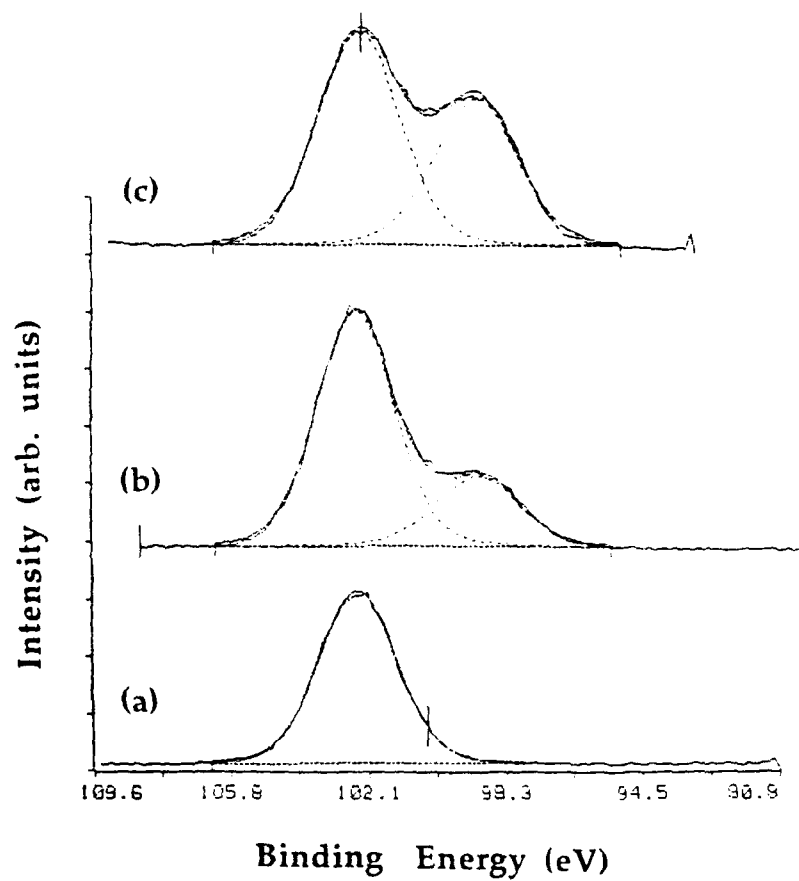


Figure 4 : XPS spectra of SiO_2 particles synthesized using : (a) 30% O_2 in He, (b) 7% O_2 in He, (c) 2% O_2 in He.

CONCLUSIONS

The results of this study appear to demonstrate the feasibility and the promise of the laser

vaporization / condensation method in the synthesis of nanoparticles with well defined properties. The combination of the laser synthetic approach and the spectroscopic characterizations of the bulk and surface properties of the nanoparticles will lead to significant results particularly in two areas: (i) the synthesis of specific catalysts (e.g. metal/metal oxide systems) of controlled sizes and compositions and (ii) the design of new nanomaterials such as mixed oxides/nitrides or carbides/nitrides and other refractive, semiconductor and superconductor materials.

ACKNOWLEDGEMENTS

The authors gratefully acknowledge financial support from NSF Grants DMR 9207433 and CHE 9311643. Acknowledgement is also made to the Exxon Education Foundation and Kate Miller Jeffress Memorial Trust for the partial support of this research. We thank Dr. Daniel Graiver (Dow Corning) for the SEM micrographs, Dr. Ismat Shah (du Pont) for the XPS measurements and Professor James Turner (VCU) for the Raman spectra.

REFERENCES

- [1] See for example: "Frontiers in Materials Science", Science 255, 1049 (1992).
- [2] R. W. Siegel, Annu. Rev. Mater. Sci. 21, 559, 1991.
- [3] R. Pool, Science 248, 1186 (1990).
- [4] M. Che, C. O. Bennett, "The Influence of Particle Size on the Catalytic Properties of Supported Metals", Adv. in Catalysis 36, 55 (1989).
- [5] A. Stakheev, Yu., E. S. Shapiro, J. Apijok, J. Phys. Chem. 97, 5668, 1993;
- [6] M. S. El-Shall, W. Slack, W. Vann, D. Kane, D. Hanley, J. Phys. Chem. 98, xx (1994).
- [7] D. Wright, R. Caldwell, C. Moxely, M. S. El-Shall, J. Chem. Phys. 98, 3356, 1993;
- [8] M. S. El-Shall, H. M. Rabeony, H. Reiss, J. Chem. Phys. 91, 7925, 1989.
- [9] J. C. Parker, R. W. Siegel, J. Mater. Res. 5, 1246, 1990.
- [10] R. J. Capwell, F. Spagnolo, M. A. DeSesa, Appl. Spectrosc. 26, 537, 1972.

GRAIN-SIZE STABILITY AND MICROHARDNESS OF COPPER-FULLERENE NANOCOMPOSITES

R.L. HOLTZ*, E.V. BARRERA**, J. MILLIKEN***, AND V. PROVENZANO****

*Geo-Centers, Inc., 10903 Indian Head Hwy., Ft. Washington, MD 20744

**Department of Materials Science, Rice University, Houston, TX 77251

***Chemistry Division, Code 6120, Naval Research Laboratory, Washington, DC 20375

****Materials Science and Technology Division, Code 6370, Naval Research Laboratory, Washington, DC 20375

ABSTRACT

Nanocomposites of copper with low concentrations of dispersed fullerenes were synthesized by simultaneous sputtering of copper and sublimation of fullerenes. Post deposition heat treatments at 400 and 800°C were performed to assess the thermal stability of the microstructure and the effect on the Vicker's microhardness. The as-deposited copper-fullerene composite has submicron-scale granularity, in contrast to pure copper which has conventional columnar growth. Grain growth in the heat-treated fullerene-containing specimens is suppressed and the microhardness enhanced relative to pure copper.

INTRODUCTION

One possible application of buckminsterfullerene is as a reinforcement in structural materials. Fullerenes dispersed in a metal matrix, for example, could result in dispersion strengthening via the Orowan mechanism¹, and because a fullerene molecule is of nanometer size, with the carbon molecules on a 0.7 nm diameter in the case of C₆₀, they could be more effective reinforcements than conventional micron-scale dispersoids. Additionally, fullerenes could act as grain-boundary pinning centers, thereby inhibiting thermally-activated grain growth², which causes loss of strength by increases in grain size according to the empirical Hall-Petch relation³. Furthermore, since fullerenes are hollow, with a 0.35 nm diameter open interior volume, they also could be used to reduce density of a composite, yielding important strength to weight ratio advantages.

The principal argument against the large-scale application of fullerenes as structural reinforcement has been a common notion that fullerenes are much too expensive for such uses. While the very first commercially available fullerenes were quite expensive, the cost of fullerene extract, the C₆₀ + C₇₀ mixture, has dropped from \$ 3000 per gram a few years ago to around \$ 80 per gram currently. New continuous-mode processing methods are being developed⁴ which promise to be higher-yield and higher-throughput than the labor-intensive, batch-mode research-scale carbon-arc method. These new manufacturing-compatible fullerene production methods are expected⁵ to lower the cost of fullerenes to \$ 15 per gram by 1996, and to under \$1 per gram by 1998. If a viable, large-scale practical application for fullerenes could be demonstrated, that would drive further development of manufacturing-compatible fullerene production, and could lower the cost to the point where fullerenes are competitive with other structural reinforcement materials. It is with these issues in mind that the present study of metal-fullerene structural nanocomposites has been initiated.

The simplest way to make a composite of fullerenes and a metal is by conventional powder metallurgy methods. However, in work done thus far on fullerene-metal composites by powder metallurgy processes,^{6,7,8} it has been found that, due to the very strong van der Waals bonding between fullerene molecules, they tend to agglomerate and cannot be dispersed in the metal, regardless of various mixing and slurry methods that have been tried.

Codeposition via sublimation of fullerenes⁹ and evaporation or sputtering of a metal is a processing route that does allow homogeneous dispersion of fullerenes. It has been shown that fullerenes can be dispersed in thin films of copper and tin⁸ by this method.

To obtain "bulk" pellets of dispersed copper-fullerene composites for the present work, sublimated fullerenes and DC sputtered copper were codeposited onto a large, rotating, liquid-nitrogen cooled substrate, shown schematically in Fig. 1. Fullerenes were sublimated from a ceramic coated, resistively heated boat at 600°C after high-temperature vacuum degassing. To avoid "spitting" of the powder during degassing, the fullerene extract was pressed into small pellets. The substrate is scraped following deposition, and the material, in the form of a fine powder consisting of small flakes of thin film, is collected, transported in-situ to a uniaxial cold press, and compacted under pressures of about 500 MPa to make solid pellets. The pellets are typically 80 % of theoretical density. This deposition system and the procedure is described in more detail elsewhere.^{8,10}

RESULTS AND DISCUSSION

As described above, the as-deposited material is a powder consisting of small flakes of thin film; consequently, the pressed pellets consist of a compact of these thin film flakes. For

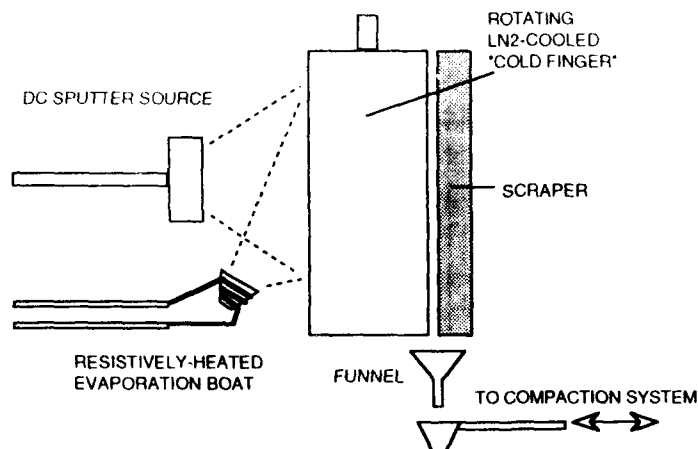


Figure 1. Schematic diagram of the codeposition system used for the physical vapor deposition of copper-fullerene composites.

both the codeposited copper-fullerene and for pure copper samples, the large-scale microstructure of the flakes is that of columnar thin-film growth, as expected. However, high-magnification scanning electron microscopy (SEM) reveals, as shown in Fig. 2, that in the codeposited material, the columnar growth possesses a submicron granular substructure, with average particle sizes of 50 nm. No carbon agglomerates are visible, which suggests that the fullerenes did in fact disperse uniformly on length scales less than the resolution of the SEM.

Energy-dispersive spectrometry (EDS) in the SEM was used to confirm that carbon is present in the granular structure of Fig. 2(a), but not in the pure copper Fig. 2(b). The total carbon concentration detected is approximately 1 wt.%, which corresponds to approximately 4 vol % if present as isolated fullerenes. That fullerenes are present in this codeposited material was confirmed by hot toluene extraction performed on some uncompacted powder. When fullerenes are dissolved in toluene, the solution takes on a deep red color. Since the molar absorptivity of fullerenes in toluene is very high, this simple test is quite sensitive. The solution also was analyzed by Fourier Transform Infrared Spectrometry (FTIR), further confirming the presence of fullerenes by the presence of C60 absorption lines at 527 and 577 cm^{-1} .

Pieces of the copper-fullerene and pure copper specimens were annealed in one atmosphere of flowing hydrogen for 2 hours at 400 and 800°C to determine the thermal stability of the microstructure. For the 400°C annealed specimens, shown in Fig. 3, the submicron granularity of the copper-fullerene composite has disappeared. However, the flakes in the copper-fullerene have not sintered and coarsened to the same degree as those in the pure copper. Although the submicron scale granularity is not stable, the presence of the small concentration of fullerenes inhibited micron-scale thermal grain growth to some degree.

After annealing at 800°C, the flakes have all sintered and the microstructure densified in both the copper-fullerene and the pure copper specimens as shown in Fig. 4. The average grain sizes are smaller in the annealed copper-fullerene (1.2 μm) than in the pure copper (2.4 μm), again indicating grain growth suppression.

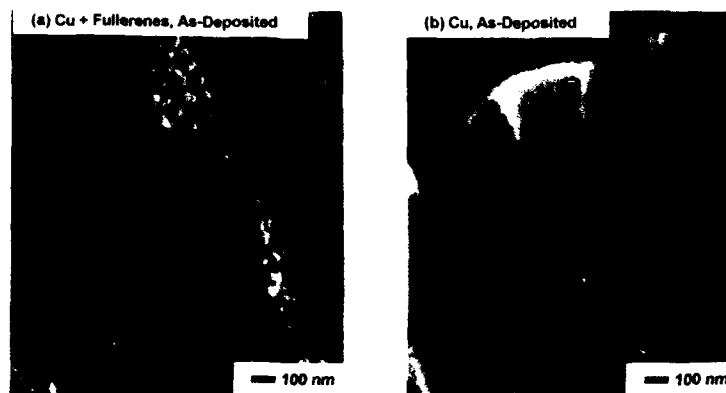


Figure 2. Scanning electron micrographs of copper-fullerene and pure copper in the as-deposited condition.

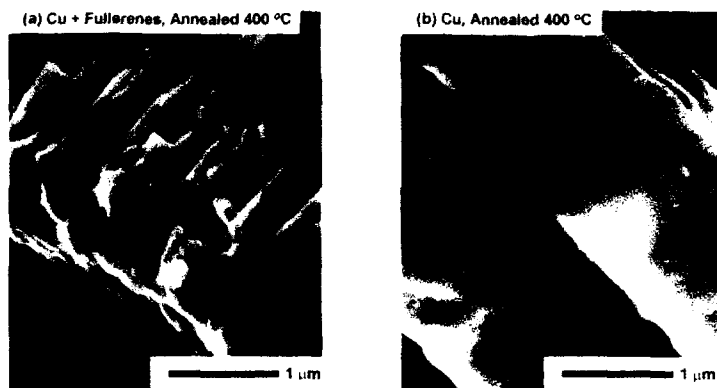


Figure 3 Scanning electron micrographs of copper-fullerene and pure copper after annealing in hydrogen at 400°C for 2 hours

SEM/EDS measurements confirm that carbon is present in the 400°C annealed specimen at about the same concentration as that in the as-deposited specimen. In the 800°C specimen, however, no carbon EDS signal significantly above background levels could be found. Fullerenes could not be detected in the annealed samples by the toluene extraction and FTIR methods, but it's likely that fullerenes embedded in and surrounded by a copper matrix could not dissolve in the toluene.

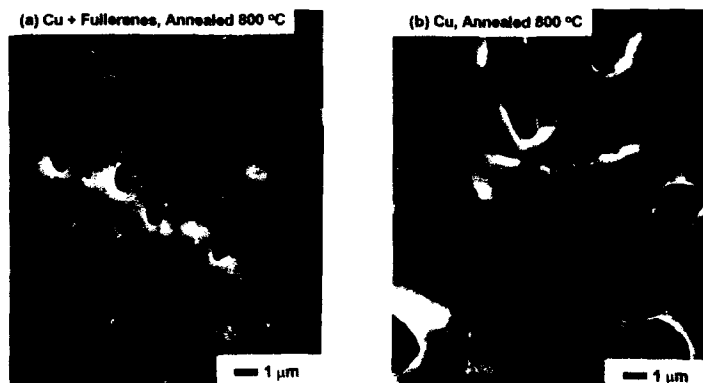


Figure 4 Scanning electron micrographs of copper-fullerene and pure copper after annealing in hydrogen at 800°C for 2 hours.

Wavelength-dispersive spectrometry with an electron microprobe was used to confirm the presence of fullerenes in the codeposited copper-fullerene specimens¹¹, both as-deposited and heat-treated to 400°C. High-resolution transmission electron microscopy could, in principle, be used to examine the fullerene dispersion directly, however, this technique is not useful for characterization of bulk materials, which is the key issue in the present case. Clearly, new and improved methods of detecting and measuring fullerenes embedded in metals will be needed to completely characterize bulk metal-fullerene composites.

Tests with loose fullerene powder indicate that fullerenes are stable when annealed in hydrogen at 400°C, but sublime at a very high rate above 600°C and decompose¹² at 800°C. This is consistent with the FDS results. As the specimen temperature is increased to 800°C, any fullerenes present that could escape due to the porosity of the specimens would sublime and be carried away in the hydrogen stream. Any that remain would likely decompose. No carbon compounds were evident in x-ray diffractometer scans, although a small amount of carbide reaction with the copper can not be ruled out.

The Vicker's microhardness of the specimens is shown in Fig. 5. The codeposited copper-fullerene specimens are harder than the pure copper in all conditions. The hardness enhancement in the as-deposited condition is about 10%, for a fullerene content estimated to be around 4 vol.%. Because of the porosity of the samples, meaningful comparisons to dispersion-hardening theory or to the Hall-Petch relation are not possible, but these results do qualitatively demonstrate reinforcement of metals with fullerenes. The hardness enhancement of the codeposited material relative to copper is more pronounced for the heat-treated conditions. For 400°C annealing, the codeposited material is 50% harder than pure copper, while for 800°C annealing, it is 80% higher than pure copper. For the 800°C annealed specimens, for which distinct grain sizes could be measured for both specimens via SEM, the difference in hardness

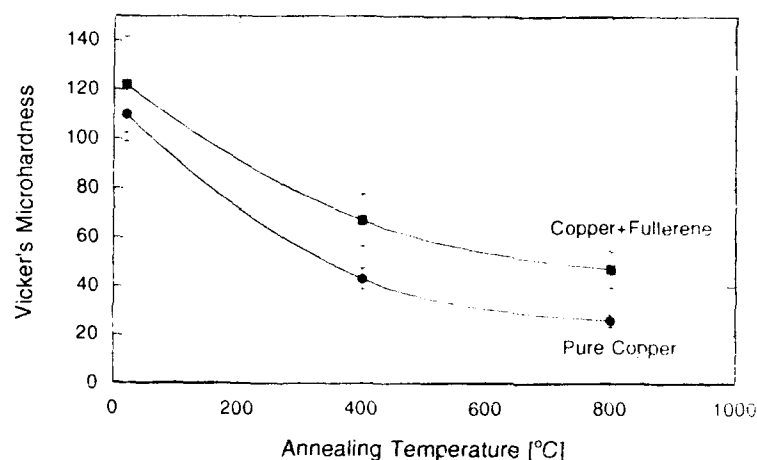


Figure 5 Vicker's microhardness of copper-fullerene and pure copper versus annealing temperature.

is nearly three times greater than is expected on the basis of Hall-Petch behavior alone³ although it's possible that this enhancement is due to dispersion hardening by carbides if decomposition of the fullerenes occurred at 800°C.

CONCLUSIONS

Codeposition of fullerenes with copper yields a submicron granular microstructure. Upon annealing, grain growth is suppressed and the microhardness is enhanced compared to pure copper. Improved methods of characterizing fullerenes embedded in metals are needed.

ACKNOWLEDGEMENTS

The authors acknowledge the work of J. Stevens, a Science and Engineering Apprenticeship Program (SEAP) participant at the Naval Research Laboratory during 1993, who performed the toluene extraction and FTIR tests, and P. Pehrsson, D. Vestyk, and L. Troilo of the Chemistry Division of the Naval Research Laboratory who performed preliminary Raman spectroscopy on some of the specimens. R. L. Holtz is under contract to the Materials Science and Technology Division of the Naval Research Laboratory.

REFERENCES

- ¹M.F. Ashby, in *Physics of Strength and Plasticity*, edited by Ali S. Argon, (Massachusetts Institute of Technology, 1969), pp. 113-131.
- ²P.R. Rios, *Acta Metall.* **35**, 2805 (1987), E. Nes, N. Ryum, and O. Hunderi, *ibid.* **33**, 11 (1985), O. Hunderi, E. Nes, and N. Ryum, *ibid.* **37**, 129 (1989).
- ³E. O. Hall, *Yield Point Phenomena in Metals and Alloys*, (Plenum Press, New York, 1970), pp. 36-49.
- ⁴High-Tech Materials Alert, **11** (2), 1 (1994), *ibid.* **10** (3), 2 (1993), *ibid.* **10** (8), 2 (1993).
- ⁵M. Yadav, Materials & Electrochemical Research Corporation, Tucson, Arizona (private communication).
- ⁶G. Zong *et al.*, (unpublished, submitted to Mat. Sci. & Eng.)
- ⁷H.-S. Min and J.C.M. Li, *Nanostruct. Mat.* **2**, 311 (1993).
- ⁸E. V. Barrera, J. Sims, D.L. Callahan, V. Provenzano, J. Milliken, and R.L. Holtz, (accepted for publication in *J. Mat. Res.*, March 1994).
- ⁹I. Abrefah, D.R. Olander, M. Balooch, and W.J. Siekhaus, *Appl. Phys. Lett.* **60**, 1313 (1992).
- ¹⁰R.L. Holtz and V. Provenzano, (accepted for publication in *Nanostruct. Mat.*, March 1994).
- ¹¹M. Wasz and E. V. Barrera, (submitted to *Scripta Metall.*, March 1994).
- ¹²C.S. Sundar, A. Bharathi, Y. Hariharan, J. Janaki, V. Sankara Sastry, and T.S. Radhakrishnan, *Solid State Commun.* **84**, 823 (1992).

FT-IR CHARACTERIZATION AND AB INITIO STUDY OF THE SURFACE SPECIES OF A NANOSIZED SiC POWDER

MARIE-ISABELLE BARATON*, SYLVETTE BESNAINOU** AND LHADI MERHARI*

*I.M.C.T.S., URA 320 CNRS, Faculty of Science, 123 Av. A. Thomas, F-87060 Limoges, France

**Lab. Physical Chemistry, URA 176 CNRS, 11 r. P. et M. Curie, F-75231 Paris Cedex 05, France

ABSTRACT

The $\nu(\text{SiH})$ stretching absorption band is known to be sensitive to the local environment of the silicon atom. The presence of SiH groups on silicon carbide surface can be taken advantage of to evaluate the oxidation degree of this ceramic powder.

The surface analysis of a SiC nanosized powder was performed by FT-IR spectrometry. The evolution of the $\nu(\text{SiH})$ absorption band, followed *in situ* under controlled temperatures and oxygen pressures, consists in a frequency shift toward higher wavenumbers when oxidation proceeds. The resolution of the SiH absorption range into four subbands corresponding to the $\text{HSiO}_x\text{C}_{3-x}$ possible surface groups showed the relative evolution of the different species. *Ab initio* SCF MO calculations on molecular models gave evidence of the charge transfer to the more electronegative oxygen atom, making the silicon atom more positive and seemingly strengthening the SiH bond and thus inducing an upward shift of the $\nu(\text{SiH})$ frequency.

INTRODUCTION

Silicon carbide is widely known for its chemical inertness, heat resistance and hardness. Although the silicon carbide surface can easily oxidize, its oxidation leads to the formation of a protective layer of silica. However, the presence of oxygen in silicon carbide-carbon composites may drastically weaken their mechanical properties¹. On another hand, the thermal stability of silicon carbide which is better than the alumina's one, makes this material a preferential catalyst support. For this latter application, the superficial oxygen content plays a major part in the optimization of the metal particles dispersion². Therefore, the determination of the oxygen content in the very first atomic layers of a silicon carbide surface is of critical importance for the different required properties of this ceramic.

The Fourier transform infrared (FT-IR) spectrometry is a powerful method to learn about surface species provided that the specific surface area of the powder is high enough.

The goal of this work was to get a thorough knowledge of the chemical composition of the first atomic layer by using the frequency variations of the $\nu(\text{SiH})$ stretching vibration in the SiH surface species. Indeed, according to Low³, the $\nu(\text{SiH})$ absorption band can serve as a probe of the local environment.

In the experimental approach, we performed a controlled superficial oxidation of the powder. The variations of the infrared spectrum were followed *in situ* versus temperature, oxygen pressure and oxidation time. Then, in order to discriminate between the $\text{H-SiO}_x\text{C}_{3-x}$ surface species contributions, we resolved the $\nu(\text{SiH})$ stretching range into four subbands. *Ab initio* calculation, using the self-consistent-field molecular orbital theory (SCF-MO), gave the quantum mechanical aspect of the $\nu(\text{SiH})$ evolution.

EXPERIMENTAL

The silicon carbide powder was prepared by laser driven reaction from a $\text{SiH}_4/\text{C}_2\text{H}_2$ mixture following the method previously reported⁴. The specific surface area, $62 \text{ m}^2\text{g}^{-1}$, was determined by BET measurements. The powder was slightly non-stoichiometric with silicon in excess ($\text{C}/\text{Si}=0.85$). The oxygen content was determined to be 2.2 wt% by chemical analysis.

The infrared spectra were recorded using a Nicolet 5DX spectrometer in the $4000\text{--}400 \text{ cm}^{-1}$ range with a 4 cm^{-1} resolution.

The powder slightly pressed into a self-supported pellet, was placed inside a vacuum cell described elsewhere⁵. This cell allowed to analyze a sample at different temperatures and under controlled pressures of gases. Prior to start an experiment, the SiC pellet was activated. The activation consisted in heating the sample at 870K under dynamic vacuum (10^{-5} mbar) for two hours and in cooling it down to room temperature while kept under vacuum. This activation made the sample surface free of all pollution. The evolution of the IR spectrum was followed *in situ* while the sample was submitted to different oxygen pressures at 670, 770 and 870K.

INFRARED DATA

In figure 1, the infrared spectra of the activated SiC surface are compared before and after oxidation. A previously reported analysis of the oxidation pointed out the strong increase of the 3747 cm^{-1} band assigned to the $\nu(\text{OH})$ stretching vibration in Si-OH species on silica-like surfaces along with the appearance of CO_2 in the gas phase⁶. In the following, the discussion will deal with the $\nu(\text{SiH})$ absorption range, namely $2400\text{--}2000 \text{ cm}^{-1}$.

Figure 2 shows the $\nu(\text{SiH})$ absorption range at two different temperatures for the same oxygen pressure, whereas figure 3 compares the effect of two different oxygen pressures for the same temperature. In both figures, spectra are given versus oxidation times.

Prior to oxygen addition, two bands are located at 2262 and 2142 cm^{-1} . This latter band has already been assigned to the $\nu(\text{SiH})$ stretching vibration in the SiH_x surface species on free silicon particles⁷ whose presence is confirmed by the C/Si ratio in the present sample.

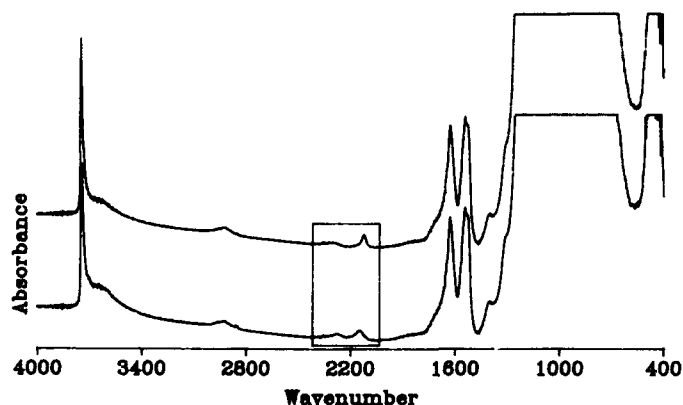


Figure 1. Infrared spectra of the silicon carbide surface: activated (bottom) then oxidized (top) at 770 K, under 80 mbar O_2 during 5 h.

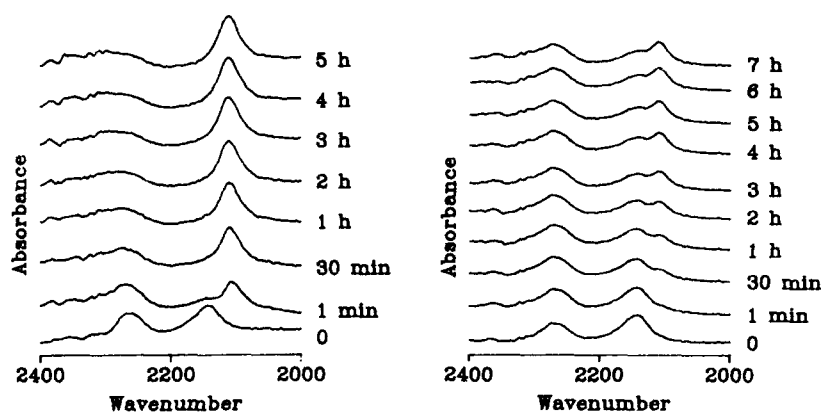


Figure 2. Infrared spectra of Si-H absorption range versus oxidation time. Oxidation under 48 mbar O₂ at 870 K (left) and 670 K (right).

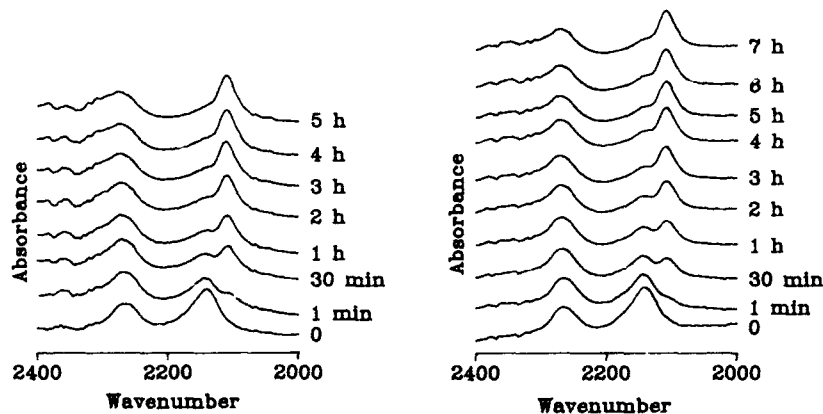


Figure 3. Infrared spectra of the Si-H absorption range versus oxidation time. Oxidation at 770 K under 48 mbar O₂ (left) and 10 mbar O₂ (right).

The oxygen action makes this 2142 cm⁻¹ band shift downward to 2110 cm⁻¹. This latter frequency can be assigned to the $\nu(\text{SiH})$ vibration in monohydride SiH surface groups on silicon particles. This is probably connected to the formation of Si-OH surface species as above mentioned^{6,7} (Fig. 1).

The 2262 cm⁻¹ has been assigned to the $\nu(\text{SiH})$ vibration in $\text{H-SiO}_x\text{C}_{3-x}$ surface groups⁷. Under oxygen, its absorption maximum shifts toward higher wavenumbers (for example, up to 2297 cm⁻¹ at 870K, 48 mbar O₂, 5h). We can relate this evolution to the effect observed by Lucovsky *et al.*⁸ in SiO_x-H alloys. Indeed, those authors showed that the $\nu(\text{SiH})$ frequency depends on the local electronegativity around the Si atom. As a result, different environments of the silicon atom imply distinct SiH stretching bands.

Considering the SiH chemical species in the present sample, the silicon atom is bonded to carbon atoms from the bulk. When oxidation occurs, those carbon atoms are steadily replaced by oxygen atoms leading to the formation of $\text{H-SiO}_x\text{C}_{3-x}$ mixed species ($x=1, 2$ or 3) whose $\nu(\text{SiH})$ frequencies vary versus x values. The greater electronegativity of oxygen compared with the carbon one should result in an increase of the $\nu(\text{SiH})$ absorption wavenumber.

SIMULATION ANALYSIS: RESOLUTION OF THE 2270 cm^{-1} BAND

Each $\text{H-SiO}_x\text{C}_{3-x}$ species ($x=0, 1, 2$ or 3) contributes to the $\sim 2270 \text{ cm}^{-1}$ band. Therefore, we intended to resolve it into four subbands corresponding to each $\text{H-SiO}_x\text{C}_{3-x}$.

The analysis was performed by using the FOCAS program (Full Optimization Curve Analysis Software, from Nicolet Inc.). In agreement with literature data^{8,9}, we assumed a Gaussian shape for all the subbands with a bandwidth fixed at 50 cm^{-1} which is roughly the width at half maximum absorbance of a $\nu(\text{SiH})$ band in similar compounds¹⁰. During the first step, the frequencies of the four absorption maxima were estimated in order to get on average the best fit for all the experimental bands. Then, the calculation was run keeping those frequencies constant. The intensities of the subbands varied so as to fit the $\sim 2270 \text{ cm}^{-1}$ band at best.

In this way, the SiH absorption range was resolved into four components at 2232, 2268, 2300 and 2317 cm^{-1} , corresponding respectively to $\text{H-SiO}_x\text{C}_{3-x}$ species with $x=0, 1, 2$ or 3 . As an example, the relative intensities of those bands are given in Table I for several oxidation degrees. Figure 4 compares the evolution of the experimental spectra with the one of the modelled spectra reconstructed from the four subbands.

Table I. Resolution of the $\sim 2270 \text{ cm}^{-1}$ band into four subbands.
The relative area (A) of each subband is given versus oxidation time, for an oxygen pressure of 48 mbar at 770K.

oxidation time	0	1-5 min	30 min	1 h	2 h	3 h	5 h
A (2317 cm^{-1})	8	23	31	30	28	31	32
A (2300 cm^{-1})	3	8	1	1	5	6	11
A (2268 cm^{-1})	86	60	59	64	60	58	54
A (2232 cm^{-1})	3	8	9	4	7	5	4

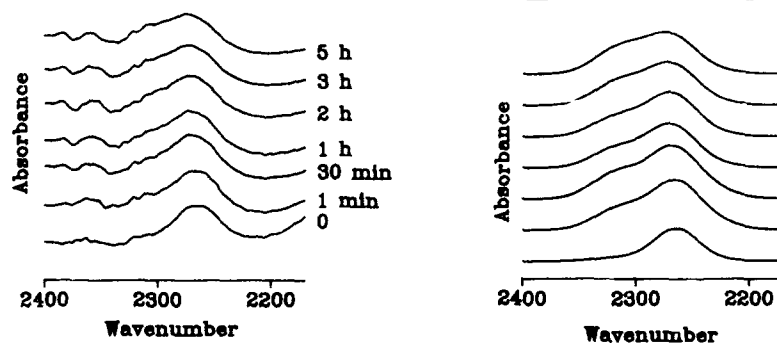


Figure 4. Comparison of the evolutions of Si-H absorption range under oxidation: experimental spectra (left) and reconstructed spectra from the four subbands (right).

The concomitant increase of the 2317 cm^{-1} band corresponding to the H-SiO_3 species with the decrease of the 2268 cm^{-1} band ($\text{H-SiC}_2\text{O}$ species) proves the superficial oxidation. As for the other two species, it is hard to find a precise evolution due to their weak intensities. However, a fact is worth mentioning, prior to any oxidation, the predominant species are not the H-SiC_3 ones, but the $\text{H-SiC}_2\text{O}$ ones. This could be related to the presence of oxygen in the raw SiC powder. Moreover, the intensity of the 2232 cm^{-1} band assigned to those scarce H-SiC_3 species does not seem to decrease. An attempt of explanation could be that those species would not be on the surface but inside the bulk instead, which would be consistent with the fact that the H/D isotopic exchange on the SiH species does not reach completion.

AB INITIO CALCULATIONS.

The $\nu(\text{SiH})$ frequencies depending on the number of oxygen atoms bonded to silicon were calculated using the *ab initio* SCF-MO method with the restricted Hartree-Fock (RHF) 3-21G basis set (GAUSSIAN 92 package¹¹). Since a model representing the surface species had to be chosen, pseudo-molecules were constructed based on the trimethylsilane molecular geometry¹² and literature data¹³. Geometries were optimized in order to get the equilibrium energies under the restraining condition of frozen CH_3 groups, given that the rotation of those groups should hardly influence the $\nu(\text{SiH})$ frequencies.

In those above-defined systems, results show that the $\nu(\text{SiH})$ stretching vibration is clearly isolated from all other vibrational modes of the pseudo-molecules. In Table II are reported the $\nu(\text{SiH})$ frequencies along with summarized results regarding the corresponding Si and H atoms.

Table II. Summarized results of the 3-21G calculations

Pseudo-molecule	$(\text{CH}_3)_3\text{Si-H}$	$(\text{CH}_3)_2(\text{OH})\text{Si-H}$	$(\text{CH}_3)(\text{OH})_2\text{Si-H}$	$(\text{OH})_3\text{Si-H}$
Symmetry	C_{3v}	C_s	C_1	C_3
Frequency $\nu(\text{SiH})$ (cm^{-1})	2216 (A_1)	2306 (A')	2351 (A)	2467 (A)
SiH force constant ($\text{mdyn } \text{\AA}^{-1}$)	3.008	3.263	3.392	3.739
SiH bond length (\AA)	1.497	1.482	1.476	1.458
H atomic charge	-0.230	-0.250	-0.288	-0.295
Si atomic charge	+1.494	+1.600	+1.681	+1.763

It is well known that this method of calculation overestimates the frequencies¹². If we consider the experimental $\nu(\text{SiH})$ frequency in trimethylsilane¹⁴, namely 2116 cm^{-1} , as a reference, the resulting scale factor is 0.955. Applying this scale factor to the other frequencies, we obtain the following corrected ones: 2202, 2249 and 2355 cm^{-1} . The striking feature among these results is the negative charge on the hydrogen atom on one hand, and on the other hand the positive charge on the Si atom which greatly increases with the number of neighboring oxygens. An explanation can be found in the higher electronegativity of the oxygen atoms which draw charge away from silicon when substituted to carbon⁸. The strong increase of the silicon charge along with the shortening of the SiH bond length are consistent with the Sanderson's model¹⁵ quoted by Hasegawa *et al.* in $\text{SiO}_x\text{-H}$ alloys analysis¹⁶. As a consequence, the SiH force constant increases as the $\nu(\text{SiH})$ stretching frequency does. This increase of the calculated frequencies is strong compared with the experimental values. Indeed, the calculations, performed on isolated pseudo-molecules, do not take into account silicon's second-neighbor

atoms which should reduce the electron transfer. Nevertheless, these results clearly show the charge transfer caused by the carbon-oxygen substitution.

CONCLUSION

The investigation of the $\nu(\text{SiH})$ absorption range by FT-IR spectrometry along with simulation analysis and *ab initio* SCF-MO calculations prove the $\nu(\text{SiH})$ stretching frequency to be a good sensor of the oxidation degree of the silicon carbide surface.

Under controlled oxidation, oxygen steadily replaces carbon in the $\text{H-SiO}_x\text{C}_{1-x}$ surface mixed species. The greater electronegativity of oxygen causes a charge transfer resulting in a more positive silicon atom, a shortened SiH bond length, a stronger SiH force constant and thus a higher $\nu(\text{SiH})$ frequency. Consequently, the frequency of the maximum absorption of the $\nu(\text{SiH})$ band allows us to identify the nearest neighbors, oxygen or carbon, of the silicon atoms on the surface.

ACKNOWLEDGEMENTS

The authors are indebted to Dr. M. Cauchetier (CEA, Saclay, France) for providing them with silicon carbide powder.

REFERENCES

1. C. Vix-Guterl, J. Lahaye and P. Ehrburger, *Carbon* **31**, 629 (1993).
2. M. Boutonnet-Kizling, P. Stenius, S. Andersson and A. Frestad, *Appl. Catalysis B* **1**, 149 (1992).
3. M.J.D. Low and A.G. Severdia, *J. Mol. Struct.* **80**, 209 (1982).
4. M. Cauchetier, O. Croix, M. Luce, M. Michon, J. Paris and S. Tistchenko, *Ceram. Intern.* **13**, 13 (1987).
5. M.I. Baraton, *J. High Temp. Chem. Proc.* (1994), in press.
6. G. Ramis, G. Busca, V. Lorenzelli, M.I. Baraton, T. Merle and P. Quintard in *Surfaces and Interfaces Analysis*, edited by L.C. Dufour (Kluwer Academic Publishers, Dordrecht, 1989) pp. 173-184.
7. P. Quintard, G. Ramis, M. Cauchetier, G. Busca and V. Lorenzelli, *J. Mol. Struct.* **174**, 369 (1988).
8. D.V. Tsu, G. Lucovsky and B.N. Davidson, *Phys. Rev. B* **40**, 1795 (1989).
9. R.R. Koropec, F. Alvarez and R. Arce, *J. Appl. Phys.* **69**, 7805 (1991).
10. D.V. Tsu and G. Lucovsky, *J. Non-Cryst. Solids* **114**, 501 (1989).
11. Gaussian 92, Revision E.1, M.J. Frisch, G.W. Trucks, M. Head-Gordon, P.M.W. Gill, M.W. Wong, J.B. Foresman, B.G. Johnson, H.B. Schlegel, M.A. Robb, E.S. Replogle, R. Gomperts, J.L. Andres, K. Raghavachari, J.S. Binkley, C. Gonzalez, R.L. Martin, D.J. Fox, D.J. Defrees, J. Baker, J.J.P. Stewart and J.A. Pople, Gaussian, Inc., Pittsburgh PA, 1992.
12. W.J. Hehre, L. Radom, P.v.R. Schleyer and J.A. Pople, *Ab initio Molecular Orbital Theory* (J. Wiley Publishers, New-York, 1986) pp. 133-344.
13. A.G. Pelmenchikov, G. Morosi and A. Gamba, *J. Phys. Chem.* **96**, 7422 (1992).
14. G.J. Janz and Y. Mikawa, *Bull. Chem. Soc. Japan* **34**, 1495 (1961).
15. R.T. Sanderson, *Chemical Bonds and Bond Energy* (Academic, New-York, 1976) p. 77.
16. L. He, Y. Kurata, T. Inokuma and S. Hasegawa, *Appl. Phys. Lett.* **63**, 162 (1993).

CATALYTIC PROPERTIES OF NANOCRYSTALLINE WO_{3-x} , $\text{Pt}/\text{WO}_{3-x}$ AND $\text{Pd}/\text{WO}_{3-x}$ PARTICLES

CHIUN-YEN TUNG*, HONG-MING LIN*, CHI-MING HSU* and CHAO-CHENG YANG**

*Department of Materials Engineering, Tatung Institute of Technology, Taipei, Taiwan, R.O.C.

**Department of Humanities and Sciences, Chemistry Division, National Yunlin Institute of Technology, Yunlin County, Taiwan, R.O.C.

ABSTRACT

The gas-condensation technique is used to produce the nanocrystalline WO_{3-x} , $\text{Pt}/\text{WO}_{3-x}$ and $\text{Pd}/\text{WO}_{3-x}$ powders under different atmospheres and pressures. High resolution electron microscope shows there exists well bonded interface between Pt or Pd and WO_{3-x} . The WO_{3-x} , $\text{Pt}/\text{WO}_{3-x}$ and $\text{Pd}/\text{WO}_{3-x}$ nanocrystals grow into needle shape with plate inside when these as-evaporated powders are compacted and sintered at 900 °C for two hours. The plate grows preferentially in $\{2\bar{2}0\}$ plane along $\langle 00\bar{1} \rangle$ direction. However, the mean particle size of nanophase Pt and Pd only increases from less than 10 nm to 30 nm and 50 nm, respectively. The gas chromatography results show that nanophase $\text{Pt}/\text{WO}_{3-x}$ powders have better catalytic effects in converting CO to CO_2 than nanophase WO_{3-x} and $\text{Pd}/\text{WO}_{3-x}$ powders.

INTRODUCTION

The rate of product formation in a catalytic reaction depends on extrinsic parameters (which can be varied for a given catalyst) such as partial pressures, temperature, flow rate, etc., as well as on 'intrinsic' parameters which are defined by the nature of the catalyst itself. The steady-state rate of catalytic reaction is in general a consequence of a rather complex series of elementary steps consisting of adsorption, desorption, surface reaction, and migration processes. The reaction mechanisms of catalysis were well discussed and many models were proposed in many papers [1-22].

In the absence of diffusion limitation, the rate of a catalytic reaction should be proportional to the surface area of the active sites. To maximize the surface area, it is necessary to make the particles as small as possible, i.e. to maximize the fraction of the atoms that are on the surfaces. This is particularly important with the noble metals of Group VIII which are expensive but of high catalytic activity.

In this investigation, gas-condensation technique [23] was used to produce the nanocrystalline Pt or Pd coated nanophase tungsten oxide (WO_{3-x}) powders. The advantages of having the nanocrystalline (NC) metal particles on the support are as follows:

- (1) They make the handle of catalyst easier and safer.
- (2) They may be used in a variety of reactors.
- (3) They may be recovered by filtration, when used in a liquid medium.
- (4) They are hard to grow by sintering when heated to high temperature because the particles are well separated from each other.
- (5) They provide a means of bringing promoters into close contact with the metal.

The objectives of this study are first, to study the interfacial properties between nanocrystalline metal and oxides so as to evaluate the performance of the applications, and second, to study the catalytic activities of compacting nanocrystalline WO_{3-x} , $\text{Pt}/\text{WO}_{3-x}$ and $\text{Pd}/\text{WO}_{3-x}$ powders for CO oxidation.

EXPERIMENTAL

The gas-condensation system consists of a high vacuum chamber with a pressure of about 3×10^{-5} mbar[23]. The starting materials are evaporated using conventional methods but kept in a constant high purity oxygen (or mixed with helium) pressure. During the evaporation in the oxygen (or mixed with helium) atmosphere, the particles are carried by convective gas flow from the resistance-heated source to a cold trap where the particles are collected. The size of nanocrystalline particles can be controlled by setting different chamber pressures. The pure tungsten was evaporated in O_2 atmosphere of 10 mbar to produce the nanophase WO_{3-x} powders first. The resulting nanophase tungsten oxides were deposited on a rotary cold trap with a diameter less than 100 nm. Then, the pure Pt or Pd was directly evaporated under He atmosphere of 3×10^{-5} mbar and nanophase particles were formed with diameters of less than 10 nm onto the surface of nanophase tungsten oxides.

Hitachi 800 TEM/STEM images of as-evaporated powders are used to determine the mean particle size. Interfacial properties of nanocrystalline Pt (or Pd) and tungsten oxide are examined by JEOL 4000EX high resolution transmission electron microscopy (HRTEM). Those powders are compacted with polyvinyl alcohol (PVA) into a disc shape of 4 mm in diameter and 0.5 mm in thickness under 1.5 GPa pressure. Then the compacted specimens are sintered at 600 °C, 750 °C, and 900 °C, separately, for 2 hours in an argon atmosphere of 0.5 atm to obtain different structures and grain sizes.

The surface morphologies of these sintered samples are analyzed by Akashi Beam Technology ABT-55 scanning electron microscope (SEM). The composition and the noble metal distribution of $\text{Pt}/\text{WO}_{3-x}$ or $\text{Pd}/\text{WO}_{3-x}$ were analyzed by energy dispersive X-ray spectrometer in ABT-55 SEM. Gas chromatography is used to analyze the carbon monoxide conversion rate of compacting nanocrystalline WO_{3-x} , $\text{Pt}/\text{WO}_{3-x}$ and $\text{Pd}/\text{WO}_{3-x}$ powders at various temperatures in a space velocity of 12000 ml h^{-1} and 10000 ppm CO/Air atmosphere.

RESULTS AND DISCUSSION

Figure 1 shows TEM images and diffraction patterns of as-evaporated WO_{3-x} , NC Pt-coated, and NC Pd-coated NC WO_{3-x} particles separately. The particle size of WO_{3-x} is about 100 nm or less and the shapes are spherical, rhombic, and hexagonal. The diffraction patterns indicate that the crystal structure of NC WO_{3-x} is tetragonal. Image also shows that the doped NC Pt and Pd have mean particle size of less than 10 nm and that they are well dispersed on the surface of NC WO_{3-x} .

Interfacial bonding of metal with oxide is a preliminary requirement for WO_{3-x} supported Pt or Pd catalysis. HRTEM images in figure 2 show that a good interfacial bonding between the nanocrystalline Pt or Pd and nanocrystalline WO_{3-x} is achieved. This demonstrates the possibility of synthesizing the nanocrystalline metal/nanocrystalline oxide particles by the gas-condensation technique with good metal/oxide interfacial bonding.

Sintered NC Pt/WO_{3-x} particles present an interesting phenomenon. Figure 3 indicates that the particle size does not change too much at low sintering temperature such as 600 °C or 750 °C. However, for sintering at higher temperature, the particle size and shape as shown in figure 3 would change dramatically. When sintering temperature reaches 900 °C, the particles grow into a needle shape with crystal plates inside. Streak lines can be seen in the diffraction spots. Streak lines in diffraction patterns arise from the crystal plates lying parallel to the electron beam. This indicates that the plate shape has a preferential growth plane and direction. The electron diffraction pattern is effectively a cross-section of reciprocal space. The overall effect is to produce either streaks or satellites. When the deviation parameter S is equal to zero, the precipitate streaks in the plane of Ewald sphere are visible in the diffraction pattern. However, when $S \neq 0$ the Ewald sphere cuts the precipitate streaks at an angle and forms satellites. The results of diffraction pattern and image of NC Pt/WO_{3-x} indicate that the crystal plates are in the $\{2\bar{2}0\}$ plane along $\langle 00\bar{1} \rangle$ direction. Sintered NC WO_{3-x} or Pd-doped WO_{3-x} particles also show the similar results as the NC Pt/WO_{3-x} ones.

Nanophase Pt or Pd particles did not grow into a thin film or big particles at high temperature such as 900 °C. Actually, the growth of nanophase Pt or Pd particles on the surface of WO_{3-x} is not very significant. The mean particle sizes of nanophase Pt and Pd particles are only increased to around 30 nm and 50 nm respectively after being sintered at 900 °C for two hours. It is believed that the minor growth of nanophase Pt or Pd particles is due to good dispersion of nanophase Pt or Pd particles on the surface of WO_{3-x} particles.

SEM images of surface morphology of WO_{3-x} in figure 4 indicated that lower sintering temperature causes less porosity. No pore structures are observed when sintering temperature is below 750 °C, whereas clear pores of network structure appear when the sintering temperature reaches 900 °C. The presence of a network structure is due to the fact that the WO_{3-x} grows into needle shapes and large pores form as sintering temperature is 900 °C. When WO_{3-x} is doped with Pt or Pd, the same results are obtained as shown in figure 4. This indicates that even at sintering temperature as high as 900 °C, the NC Pt or Pd is not sintered. The good dispersion of Pt or Pd prevents the growth of small Pt or Pd particles. The results of SEM observation prove

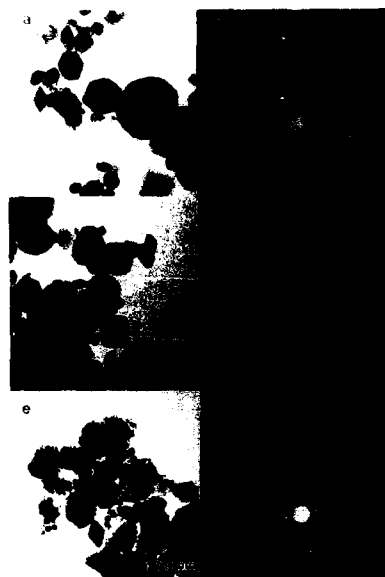


Figure 1 : (a) and (b) are TEM image and selected area diffraction pattern of NC WO_{3-x}, respectively, (c) and (d) are TEM image and selected area diffraction pattern of NC Pt/WO_{3-x}, respectively, and (e) and (f) are TEM image and selected area diffraction pattern of NC Pd/WO_{3-x}, respectively.

this speculation. X-ray mapping of Pt and Pd shows that NC Pt and Pd particles are homogeneously dispersed on the surface of WO_{3-x} . Measurement of the amounts of Pt and Pd doping by EDS shows that they are 5.3 wt% and 8.5 wt%, respectively.

Figure 5 shows the CO conversion rate of WO_{3-x} , Pt/ WO_{3-x} , Pd/ WO_{3-x} and filler at different reaction temperatures with a space velocity of 12000 ml h^{-1} , 10000 ppm CO. It is obvious that the CO conversion rate of Pt/ WO_{3-x} catalysis is better than the one of Pd/ WO_{3-x} . This is probably due to the particle size effect. As the particle size of Pd gets bigger than the one of Pt after being

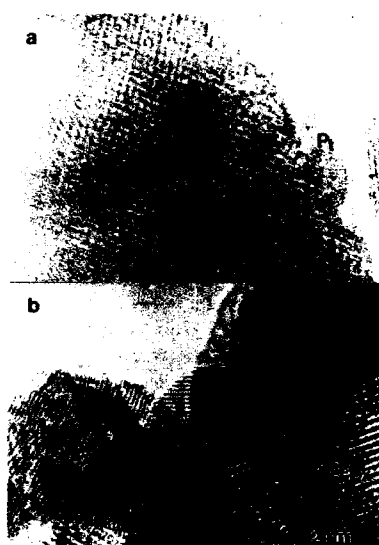


Figure 2 : (a) HRTEM images of nanophase Pt/ WO_{3-x} (b) HRTEM images of nanophase Pd/ WO_{3-x} .

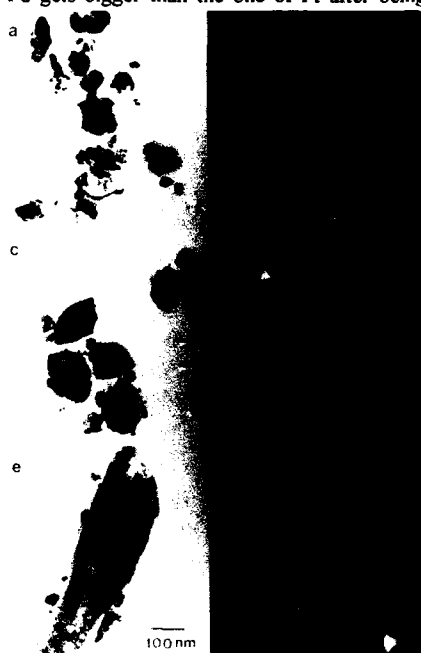


Figure 3 : (a) and (b) are TEM image and selected area diffraction pattern of NC Pt/ WO_{3-x} sintered at 600°C for 2 hours, respectively, (c) and (d) are TEM image and selected area diffraction pattern of NC Pt/ WO_{3-x} sintered at 750°C for 2 hours, respectively, and (e) and (f) are TEM image and selected area diffraction pattern of NC Pt/ WO_{3-x} sintered at 900°C for 2 hours, respectively.

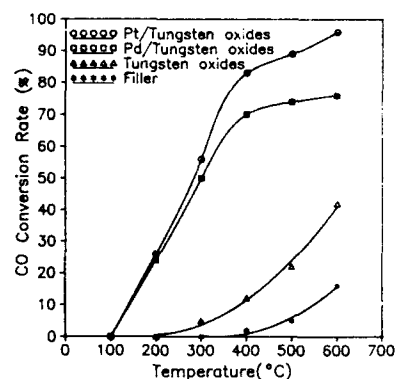


Figure 5 : Catalytic activities of CO oxidation for WO_{3-x} , Pt/ WO_{3-x} , and Pd/ WO_{3-x} catalysts.

sintered, the number of active sites of Pd decreases. Also, the catalytic activity of Pt is better than the one of Pd in CO conversion. The activity of a catalyst is expressed by T_X , where T_X is the temperature for which the conversion level is X%. The catalytic activities of $\text{Pt}/\text{WO}_{3-X}$, $\text{Pd}/\text{WO}_{3-X}$, and WO_{3-X} are shown in table 1. For the same catalytic activity, the $\text{Pt}/\text{WO}_{3-X}$ always shows a lower reaction temperature. The lower reaction temperature of $\text{Pt}/\text{WO}_{3-X}$ is attributed to the smaller size of NC Pt particles.

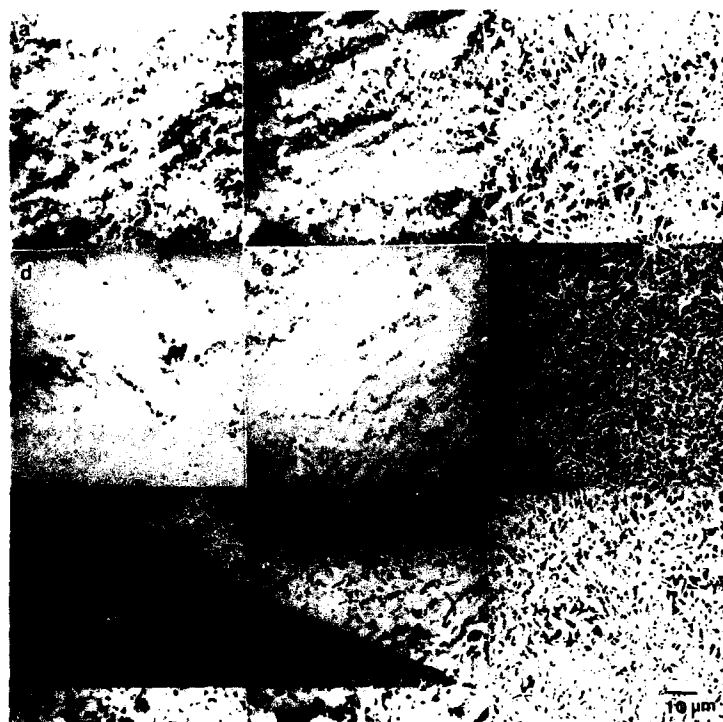


Figure 4 : SEM micrographs of WO_{3-X} sintered for 2 hours at (a) 600°C, (b) 750°C and (c) 900°C, SEM micrographs of $\text{Pt}/\text{WO}_{3-X}$ sintered for 2 hours at (d) 600°C, (e) 750°C and (f) 900°C, and SEM micrographs of $\text{Pd}/\text{WO}_{3-X}$ sintered for 2 hours at (g) 600°C (h) 750°C and (i) 900°C.

Table 1: Activities of WO_{3-X} , $\text{Pd}/\text{WO}_{3-X}$ and $\text{Pt}/\text{WO}_{3-X}$ catalysts

	T_{10}	T_{50}	T_{90}
WO_{3-X}	380°C	>600°C	>>600°C
$\text{Pd}/\text{WO}_{3-X}$	120°C	300°C	>600°C
$\text{Pt}/\text{WO}_{3-X}$	100°C	280°C	500°C

CONCLUSIONS

Nanocrystalline WO_{3-x} , $\text{Pt}/\text{WO}_{3-x}$ and $\text{Pd}/\text{WO}_{3-x}$ catalysts are synthesized by gas evaporation method. The results show a good interfacial bonding between the Pt or Pd and WO_{3-x} particles. Sintered at 900°C , the NC WO_{3-x} particles grow into a needle shape with the plate structure inside while a network structure is formed. The plate grows preferentially in the $\{220\}$ plane along $\langle 001 \rangle$ direction. NC Pt or Pd doped WO_{3-x} possesses the same feature due to the fact that the NC Pt or Pd is well dispersed on the surface of WO_{3-x} . NC Pt or Pd particles do not grow dramatically even when sintered at 900°C . This is an advantage of NC Pt or Pd doped oxide. NC $\text{Pt}/\text{WO}_{3-x}$ shows better CO conversion rate than NC $\text{Pd}/\text{WO}_{3-x}$. However for the same conversion rate, the $\text{Pt}/\text{WO}_{3-x}$ has a lower reaction temperature.

ACKNOWLEDGMENTS

We would like to thank the National Science Council, Republic of China, and Tatung Company Ltd. for financial support through Contract Number NSC 81-0405-E-036-08 and 81-1706-30 respectively.

REFERENCES

1. T. Engle, G. Ertl, In: *The Chemical Physics of Surfaces and Heterogeneous Catalysis*, P. Woodruff and D. A. King, eds., **4** (1982) 73.
2. R. J. Behm, G. Ertl, K. Christmann, M. A. Van Hove, *J. Chem. Phys.*, **73** (1980) 2984.
3. A. M. Baro, H. Ibach, *J. Chem. Phys.*, **71** (1979) 4812.
4. J. L. Gland, *Surface Sci.*, **93** (1980) 487.
5. C. T. Campbell, G. Ertl, H. Kuipers, Segner, *J. Surface Sci.*, **107** (1981) 220.
6. J. L. Gland, B. A. Sexton, G. B. Fischer, *Surface Sci.*, **95** (1980) 587.
7. T. Engle, G. Ertl, *J. Chem. Phys.*, **69** (1978) 1267.
8. T. Matsushima, *J. Catalysis* **55**, (1978) 337; *Surf. Sci.*, **79** (1979) 63.
9. J. L. Taylor, D. E. Ibbotson, W. H. Weinberg, *J. Catalysis*, **62** (1980) 1.
10. G. Ertl, J. Koch, *Proc. Vth Int. Congr. on Catalysis, Palm Beach.*, (1972) 969.
11. H. Hopster, H. Ibach, G. Comsa, *J. Catalysis*, **46** (1977) 37.
12. S. Ladas, H. Poppa, M. Boudart, *Surface Sci.*, **102** (1981) 151.
13. N. W. Cant, P. C. Hicks, B. S. Lennon, *J. Catalysis*, **54** (1978) 372.
14. M. Humenik, and W. D. F. Kingery, *Amer. Ceram. Soc.*, **37** (1954) 18.
15. W. D. F. Kingery, *Amer. Ceram. Soc.*, **37** (1954) 42.
16. R. M. Pilliar and Nutting, *J. Phil. Mag.*, **16** (1967) 181.
17. C. Weaver, *Chem. and Indust.*, (1965) 370.
18. H. J. de Bruin, A. F. Moodie, and C. E. F. Warble, *Materials Sci.*, **7** (1972) 909.
19. R. C. Baetzold, *Surface Sci.*, **36** (1972) 123.
20. C. S. Nicolau and H. G. Thom, *Z. Anorg. Allgem. Chem.*, **303** (1960) 133.
21. G. M. Schwab, *Surface Sci.*, **13** (1969) 198.
22. G. M. Schwab and H. Zettler, *Chimia*, **23** (1969) 489.
23. Hong-Ming Lin, Shu-Huei Hsieh, Pee-Yew Lee, Ming-Shung Lai and Jie-Shing Wu, *Material Chemistry and Physics*, **34** (1993) 205-213.

FACET FORMATION OF LINESHAPED SILICON MESAS GROWN WITH MICRO SHADOW MASKS

H. GOSSNER, G. FEHLAUER, W. KIUNKE, I. EISELE, M. STOLZ*, M. HINTERMAIER*
and E. KNAPEK*

Institute of Physics, Faculty of Electric Engineering, Universität der Bundeswehr München,
D-85577 Neubiberg, FRG

* Siemens AG, Research Laboratories, Otto-Hahn-Ring 6, D-81739 München, FRG

ABSTRACT

As reported previously, perfect facets can be achieved at the side walls of submicron silicon mesa structures grown by molecular beam epitaxy (MBE) with micro shadow masks [1]. An essentially self organizing, three-dimensional growth was observed. In this paper we present the results of the epitaxial growth on (001) substrates using long ($\geq 1 \mu\text{m}$), lineshaped mask apertures, which put constraints on the formation of facets. At a growth temperature of 500°C {111} facet formation is observed for lineshaped mesas oriented along the $\langle 110 \rangle$ direction of the substrate. Side walls with a length of $1 \mu\text{m}$ are perfectly plane, while mesas with a length of $10 \mu\text{m}$ and more show rough sidewalls. This is explained by a limited silicon adatom diffusion on the facet. For higher flux rates the facet formation is suppressed. This can be understood in terms of a reduced adatom diffusion.

A crossover from {111} to {113} facet formation is observed at growth temperatures above 500°C . A model for the temperature dependent formation of {111} and {113} facets is given.

INTRODUCTION

Nonplanar epitaxial growth allows the fabrication of extremely small, low-dimensional electronic devices without high resolution lithography [2,3,4]. Various methods are reported in the literature on how to achieve controlled facet formation. In III-V materials epitaxial growth on vicinal substrates [5] and on patterned substrates has been investigated [3,6]. Facet formation of silicon has been observed for selective epitaxial growth on silicon dioxide patterned silicon substrates [7] and for local epitaxial growth with micro shadow masks [1]. Both ultra high vacuum chemical vapor deposition (UHV-CVD) and molecular beam epitaxy (MBE) have been utilized for epitaxial growth. UHV-CVD has different growth rates on different surface orientations due to different reaction rates for the decomposition of silane or disilane. On the other hand for MBE the sticking coefficient of silicon is equal to one, independent of surface orientation. However, a local variation of growth rates at a mesa surface can be achieved by geometrical means such as shadow masks. Different growth rates of different facets lead to changes in the size of the facets. The slowest growing facet is preferred at convex edges, while at concave edges the fastest growing facet is formed. Simulations based on these assumptions agree with growth experiments on nonplanar GaAs substrates [8].

As opposed to other techniques, the concept of micro shadow masks allows to grow freestanding mesas with crystalline perfect surfaces. Epitaxial growth with micro shadow masks at a low growth rate ($\sim 0.1 \text{ nm/s}$) and a growth temperature of 470°C leads to {111} facet formation [1]. For square mask apertures with a side length of 350 nm the mesas take the shape of a pyramid with a tip radius of less than 10 nm . The base lines of the pyramid are oriented parallel to the $\langle 110 \rangle$ axes of the substrate, independent of the orientation of the mask

aperture. In this case both shape and orientation of the mesa are determined by the orientation of the substrate and not by the mask.

To determine the limits of such selforganizing growth, we investigate here facet formation of lineshaped mesas depending on the length and orientation of the mask aperture. We also show the influence of flux rate and growth temperature on the facet formation.

EXPERIMENT

The growth experiments were performed in an indigenous MBE system. The base pressure was $3 \cdot 10^{-10}$ mbar rising to $2 \cdot 10^{-9}$ mbar during evaporation. Before MBE growth a micro shadow mask was built up on the substrate [9]. (001) Si substrates were thermally oxidized at 1050°C up to $1 \mu\text{m}$ oxide thickness. In an LPCVD process a 100 nm thick silicon nitride layer was deposited at 700°C onto the oxide layer. Electron beam lithography in combination with CF_4 -plasma etching was used to pattern the nitride film. After the etching the PMMA was removed with boiling acetone and the oxide was etched by hydrofluoric acid. By underetching the nitride layer the shadow mask was formed. After a final RCA clean the substrates were transferred to the MBE system. The natural oxide was desorbed at 900°C for 5 minutes. For most of the experiments a growth rate of 0.08 nm/s was chosen. The growth rate relates to the poly silicon layer on top of the nitride. The growth temperature was varied between 500°C and 730°C . The temperature was determined by pyrometry.

For the investigation of the mesa growth SEM analysis was performed at cleaved edges.

RESULTS AND DISCUSSION

By depositing silicon atoms through the mask aperture of the shadow mask, mesa structures grow locally on the (001) substrate. Among the possible facets, which can be formed on the surface of the mesa, the {111} facet (Fig. 1) is preferred due to its lowest surface energy of 1.23 J/m^2 [10]. For {100}, {113} and {110} facets this energy amounts to 1.36 J/m^2 , 1.38 J/m^2 and 1.43 J/m^2 . However, as MBE growth works in supersaturation, equilibrium properties like the formation of a thermodynamically stable surface do not necessarily occur.

At first we investigate mesa structures aligned along the $\langle 110 \rangle$ direction. $1 \mu\text{m}$ long, lineshaped mesas grown at 500°C essentially exhibit {111} facets at the side walls and a (001) surface on top (Fig. 2a). Although the mask aperture has a roughness of 50 nm due to overgrown poly silicon grains, the side walls are perfectly plane. Mesa structures with a length of $10 \mu\text{m}$ (Fig. 2b) and more show rough side walls, which consist of many, small sections of {111} facets. Slight misorientation of the mask towards the $\langle 110 \rangle$ direction of the substrate, defects and contamination at the substrate surface or locally varying growth rates due to fluctuations

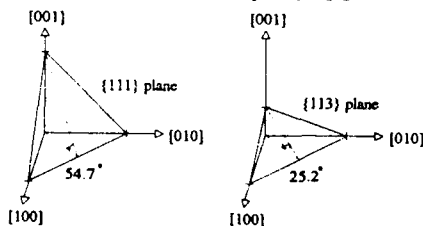


Fig. 1: inclination angles of the {113} and {111} crystallographic planes

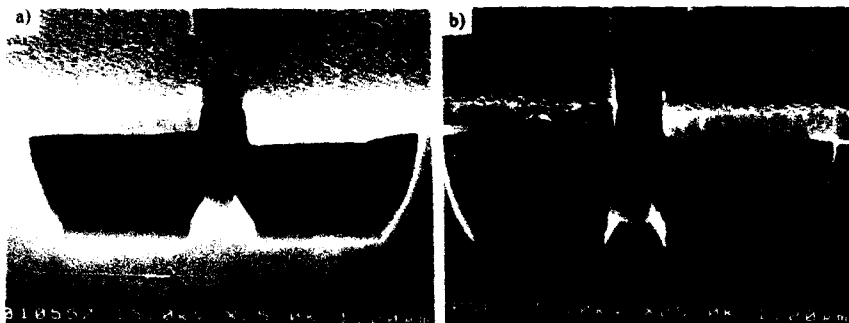


Fig. 2: SEM micrographs of cleaved micro shadow masks oriented along the $\langle 110 \rangle$ direction of the (001) Si substrate. The a) 1 μm and b) 10 μm long mesas were grown at 500°C.

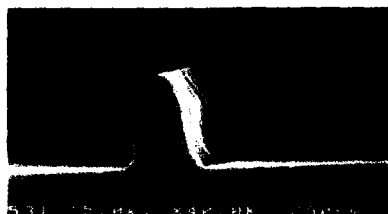


Fig. 3: SEM micrograph of a cleaved Si mesa. Mask aperture oriented along $\langle 100 \rangle$. Growth temperature: 500°C, Growth rate: 0.08 nm/s.



Fig. 4: SEM micrograph of a cleaved Si mesa. Mask aperture oriented along $\langle 100 \rangle$. Growth temperature: 500°C, growth rate: 0.27 nm/s.

in the mask aperture width can lead to this roughness. For small structures diffusion of the adatoms obviously smooths out any steps at the side walls. Structures exceeding the diffusion length for adatoms in the direction of the mesa orientation will in general not show a single-facet side wall. Even long, lineshaped mesas oriented along the $\langle 100 \rangle$ axes of the substrate exhibit $\{111\}$ facets (Fig. 3), which again proves the preference of the $\{111\}$ surfaces. However, the different orientation of mesa and facet leads to a very ragged side wall.

The facet formation can be suppressed by a higher growth rate of 0.27 nm/s (Fig. 4). This indicates the importance of a relaxation time for the facet formation. We discuss this by the following model for the mesa growth with micro shadow masks including diffusion of adatoms under the shadow mask.

In the initial growth stage of the first few monolayers the deposited Si atoms will experience a rather rough substrate surface due to the previous HF-dip or a slight miscut of the (001) substrate ($\pm 1^\circ$). They will immediately be built in at steps of the substrate and a further diffusion is suppressed. The initial width of the mesa should be close to the width of the mask aperture. Determining the ratio of the growth rates of the (001) top surface layer and the $\{111\}$ facet to 3.8 from figures 5a and 5b, the initial width of the mesa can be estimated to be 330 nm. This agrees well with the measured width of the mask aperture of 310 nm. The edges of the mesa are located under the shadow mask. Thus the growth of the $\{111\}$ facet depends on the Si adatoms diffusing from their place of deposition to the edge of the mesa. This will in general be a slow process, which enables the side wall to form a thermodynamically stable



Fig. 5. SEM micrographs of cleaved Si mesas grown with a 310 nm wide micro shadow mask at a growth temperature of 500°C. The growth is stopped at different stages.

{111} facet. At a growth temperature of 500°C the low diffusion-limited flux of adatoms also leads to the smaller growth rate of the {111} facet. Thus the extension of the {111} facet increases relative to the (001) surface while growth proceeds (Fig. 5b). At a mature growth stage of the mesa the {111} facet will extend from an area underneath the shadow mask into the window of the mask (Fig. 2a). Still the growth rate of the side wall facet is lower compared to the top surface, because Si atoms deposited on the part of the facet inside the mask aperture have to provide the material for the growth of the whole facet. Finally the (001) top surface of the mesa vanishes and a sharp ridge is formed (Fig. 5c). If the part of the facet underneath the shadow mask equals the diffusion length for Si adatoms in the direction to the mesa basis, no mass transport can occur beyond this length at the {111} facet. A steep wall appears at the bottom of the mesa side wall.

The prerequisite for such an evolution of the mesa is a sufficient flux of Si adatoms under the shadow mask by diffusion. The grown surfaces seem to be smooth enough to allow a transport of adatoms on the {111} facet up to a distance of 100 nm beyond the edge of the mask aperture. However, at higher flux rates of impinging Si atoms a fast nucleation of adatoms can occur near the place, where they have been deposited. These atoms are bound in dimers on the (001) top surface [11] and do not contribute to the diffusing adatoms forming the side wall facet. Facet formation is suppressed and steep side walls as a projection of the mask are formed. Thus both facets and steep side walls can be fabricated depending on growth rate and, by the diffusivity, on growth temperature.

The temperature dependence of facet formation is studied for 1 μm long mesas. It shows a crossover from {111} facets to {113} facets at a temperature of about 570°C (Fig. 6). At 500°C only the {111} facet is detected. The kinks at the edges of the (001) top surface layer are due to surface diffusion [8]. For higher temperatures the extension of the {113} facet increases, while the {111} facet vanishes. From the equilibrium point of view the vanishing of the {111} facet as the surface orientation with the lowest surface energy, is unexpected. An exclusive {113} facet formation has also been observed for UHV-CVD selective epitaxial growth at $T=550^\circ\text{C}$ in oxide windows [7]. Although the growth rate of the {111} facet was determined to be about a factor 2.5 lower than the growth rate of the {113} surface, no {111} facet formation was detected. Hirayama et al. explained the dominance of the {113} facet by a reconstruction at the (001) terrace edges minimizing the formation energy of the tilted side walls [12]. However, in our experiment the shape giving parameter seems to be neither the surface energy nor the formation energy. As the surface energy of a {111} facet is lower compared to the {113} facet, the disappearance of {111} facets (Fig. 6d) contradicts a hypothesis of a dominating influence of the surface energy on the shape of the mesa for our growth conditions. On the other hand, if the formation energy determines the facet formation at the

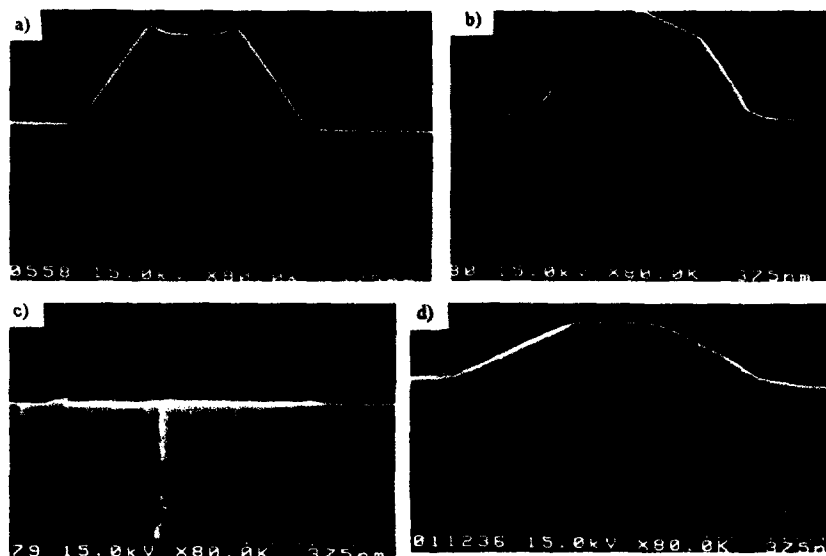


Fig. 6: SEM micrographs of cleaved Si mesas grown with a 400 nm wide micro shadow mask oriented along the $\langle 110 \rangle$ axis of the (001) Si substrate. The growth temperatures were a) 500°C, b) 570°C, c) 630°C and d) 730°C.

side walls, the size of the $\{113\}$ facets should increase with decreasing temperature, because at lower growth temperatures the metastable state of a formation energy minimum can more easily be frozen in. However, the opposite is observed.

We propose a model for the simultaneous appearance of $\{113\}$ and $\{111\}$ facets during epitaxial growth in micro shadow masks, based on a temperature dependent growth rate of the facets. As discussed previously, the $\{111\}$ facet is formed underneath the shadow mask. Initially its growth depends on Si adatoms diffusing from the projected edge of the mask aperture to the edge of the (001) top surface of the mesa. As temperature is increased the diffusivity of the Si adatoms is increased, too. More adatoms will reach the $\{111\}$ facet. Thus the $\{111\}$ facet will grow faster. At the same time these adatoms are missing for the growth of

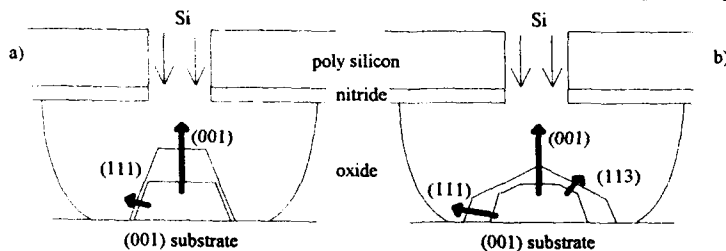


Fig. 7: growth model for MBE growth with micro shadow masks at a) low and b) high temperatures

the top layer, especially in the area close to the mesa edge. A {113} facet can be formed between the {111} facet and the (001) layer, growing slower than the (001) top surface (Fig.7). The higher the temperature the higher the growth rate of the {111} facet. Thus rising temperature will decrease the {111} and increase the {113} facet. The base width of the mesa will also increase (Fig. 6 a-d). In a situation, where the growth rates of {111} and {113} facets are comparable ($T=630^{\circ}\text{C}$), random fluctuation in the facet length can occur (Fig. 6c).

SUMMARY

We have investigated the growth kinetics of lineshaped, submicron wide mesas in micro shadow masks. Mesas with a length up to $1\text{ }\mu\text{m}$ exhibit plane side walls formed by a single facet. Longer mesas show rough side walls. These observations may be explained by diffusion of Si adatoms on the facets, smoothing out growth irregularities.

For MBE growth with micro shadow masks a facet formation at the side walls of free-standing mesas can only occur when Si adatoms can diffuse under the shadow mask. High flux rates suppress the facet formation by reducing the amount of freely diffusing Si adatoms. It is suggested that diffusion plays the essential role for the transition from {113} to {111} facet formation, too. Higher temperatures lead to a higher flux of adatoms under the shadow mask. This modifies the growth rates of the different facets and thus their extension.

It has been shown that by adjusting the growth parameters flux and temperature, steep side walls as well as perfect facets can be achieved. Thus MBE growth with micro shadow masks offers a chance for the construction of zero- and one-dimensional electronic devices without high resolution lithography.

ACKNOWLEDGEMENTS

This work was supported by the Bundesministerium für Forschung und Technologie (NT 2409).

REFERENCES

1. H.Gossner, H.Baumgaertner, E.Hammerl, F.Wittmann, I.Eisele, T.Heinzel, H.Lorenz, *Jpn.J.Appl.Phys.* 33,447 (1994).
2. R.Nötzel and K.H.Ploog, *Adv.Mater.* 5, 22 (1993).
3. K.Eberl, P.Grambow, A.Lehmann, A.Kurtenbach, K.v.Klitzing, D.Heitmann, M.Dilger, M.Hohenstein, *Appl.Phys.Lett.* 63, 1059 (1993).
4. K.C.Rajkumar, K.Kaviani, P.Chen, A.Madhukar, K.Rammohan, D.H.Rich, *J.Cryst.Growth* 127, 863 (1993).
5. M.Krishnamurthy, M.Wassermeier, D.R.M.Williams, P.M.Petroff, *Appl.Phys.Lett.* 62, 1922 (1993).
6. Y.D.Galeuchet and P.Roentgen, *J.Cryst.Growth* 107, 147 (1991).
7. H.Hirayama, M.Hiroi, T.Ide, *PRB* 48, 17331 (1993).
8. M.Ohtsuka and A.Suzuki, *J.Appl.Phys.* 73, 7358 (1993).
9. E.Hammerl and I.Eisele, *Appl.Phys.Lett.* 62, 2221 (1993).
10. D.J.Eaglesham, A.E.White, L.C.Feldman, N.Moriya, D.C.Jacobson, *PRL* 70, 1643 (1993).
11. Y.-W. Mo, B.S.Swartzentruber, R.Kariotis, M.B.Webb, M.G. Lagally, *PRL* 63 (1989).
12. D.J. Chadi, *PRL* 59, 1691 (1987).

BLUE LIGHT EMISSION FROM SILICON ULTRAFINE PARTICLES

SHINJI NOZAKI, S. SATO, H. ONO AND H. MORISAKI

The University of Electro-Communications, Department of Communications and Systems,
1-5-1 Chofugaoka, Chofu-shi, Tokyo 182, Japan

ABSTRACT

The oxygen-containing silicon (Si) ultrafine particles have been deposited onto Si and SiO₂ substrates by evaporation of Si powder in an oxygen-containing argon atmosphere. The as-deposited Si ultrafine particles exposed to the ultraviolet light emit blue light, which is strong enough to be seen with the naked eye. The blue light emission is associated with a broad photoluminescence (PL) peak at 2.7 eV, which is attributed to radiative recombination via a radiative recombination center. The proposed model with one radiative and two nonradiative recombination centers well explains the temperature-dependent PL peak intensity.

INTRODUCTION

The recent discovery of visible light luminescence from porous Si by Canham [1] has attracted wide attention because of their potential application to Si light emitting devices. Although he proposed an ultrafine quantum wire structure to explain visible light emission, it is now widely understood that crystalline Si ultrafine particles remaining in the texture of the porous layer are the origin of the light emission [2]. The detailed mechanism still remains obscure. It is, however, clear that the Si nanostructures possess electrical and optical properties different from those of bulk Si.

We reported orange-red light emission from the ultrafine particles deposited by evaporation of Si powder in an argon atmosphere and associated the luminescence with the quantum size effect [3]. The atmosphere during the deposition was found to affect the size of Si particles and then the luminescence color. In this paper, we report blue light emission from the Si ultrafine particles deposited by evaporation of Si powder in an oxygen-containing argon atmosphere and discuss the mechanism of the blue light emission.

EXPERIMENTAL

A conventional gas-evaporation technique was used to deposit Si ultrafine particles onto Si or SiO₂ substrates. As shown in Fig. 1, after evacuating the chamber, argon gas containing 1 % oxygen was introduced into the chamber. When the total gas pressure reached 6 torr, high-purity Si powder or small pieces cut from Si substrates in a boron-nitride (BN) boat was heated in an oxygen-containing argon atmosphere. The total pressure of the atmosphere was kept constant at 6 torr during evaporation. A typical film thickness was about 0.5 μm after 5 minute evaporation.

A sample for transmission electron microscopy (TEM) was prepared by collecting the Si ultrafine particles scratched off from the substrate onto a mesh. A JEOL-2000 FX electron microscope operating at 200 kV was used for TEM studies.

Photoluminescence (PL) measurements were carried out with a mercury lamp as an excitation source from 20 to 292 K.

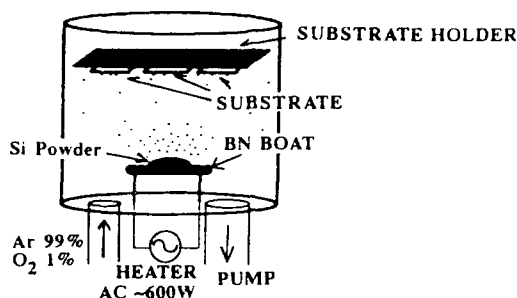


Fig. 1 Gas-evaporation apparatus to deposit the oxygen-containing Si ultrafine particles.

RESULTS AND DISCUSSION

The TEM micrograph in Fig. 2 shows intertwined chain-like nanostructures containing spherical particles. A similar structure was reported for the oxidized Si microcrystalline particles by Kawaguchi and Miyazima [4]. None of Si crystalline particles has been detected in the sample as shown in the Si2p ESCA (electron spectroscopy for chemical analysis) spectrum in Fig. 3. The spectrum shows only SiO_x . Nevertheless, the ESCA result is not a conclusive evidence for absence of microcrystalline Si. The detailed microstructure in the Si ultrafine particles to exhibit blue light emission is under study and will be published elsewhere.

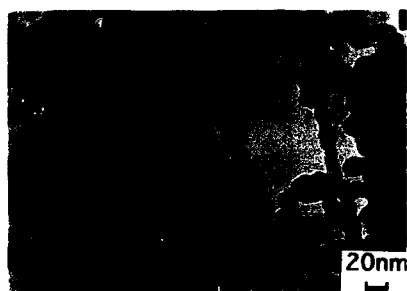


Fig. 2. TEM micrograph of the oxygen-containing Si ultrafine particles.

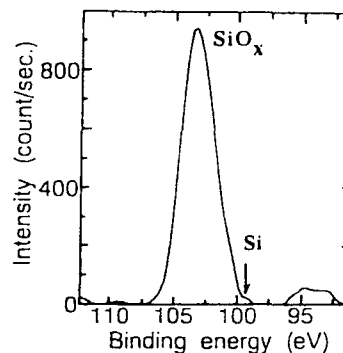


Fig. 3. Si2p ESCA spectrum of the oxygen-containing Si ultrafine particles.

Figure 4 shows two PL spectra measured at 20 and 292 K. It is interesting to note that the PL peak energy and the half width at half maximum are almost the same. Both PL spectra are well fitted to Gaussian curves shown in solid curves in Fig. 4. The broad peak at 2.7 eV contributes to the blue light emission. The above features in the PL spectra are true for all temperatures from 20 to 292 K. Similar temperature-insensitive peak position and linewidth were observed in the PL spectra of chalcogenide glasses [5]. The luminescence intensity, however, strongly depends on temperature as shown in Fig. 5. The temperature dependence originates from a nonradiative process with rate p_{nr} , which is competitive with the radiative recombination, according to

$$I_r = Ap_r/(p_r + p_{nr}), \quad (1)$$

where A is a constant, and p_r is the radiative recombination rate. The observed blue light emission from the Si ultrafine particles is hard to be explained by the quantum size effect because a diameter of 10 nm in the microstructure shown in Fig. 2 is considerably greater than the particle size required for blue light emission by the quantum size effect [6]. Therefore, the blue light emission is more likely to be associated with radiative recombination via a radiative recombination center.

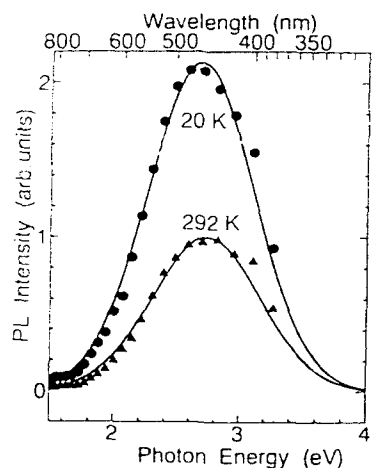


Fig. 4. PL spectra of the Si oxygen-containing Si ultrafine particles at 20 and 292 K.

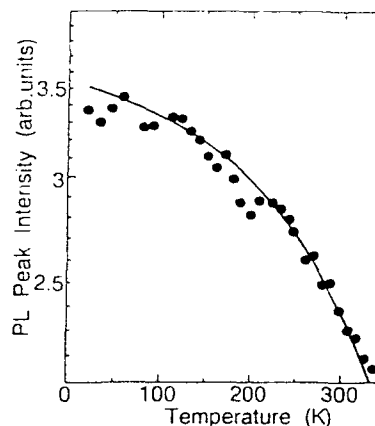


Fig. 5. Temperature-dependence of PL peak intensity at 2.7 eV.

We use the same model to describe recombination in amorphous materials, originally proposed by Street [7]. As illustrated in Fig. 6, we assume one radiative and two nonradiative recombination centers and the escape of a portion of the trapped electrons from the radiative center to the nonradiative centers by one-directional tunneling. These assumptions are reasonable if the nonradiative recombination centers are deep-level centers and the nonradiative recombination rates, p_{nr1} and p_{nr2} , are larger than the radiative recombination rate p_r . Following the tunneling theory between two recombination centers by Street, the transition rate from a radiative to a nonradiative center via tunneling is given by

$$p_w = p_o \exp(T/T_o) \quad (2)$$

with

$$p_o = v_{ph} \exp(-2aR_o) \quad (3)$$

and

$$T_o = (4a^2\gamma^2k)^{-1}, \quad (4)$$

where v_{ph} is a frequency of order 10^{12} sec^{-1} , a the tunneling parameter, R_o the spatial separation of two centers, γ the shape of the parabola, and k the Boltzmann constant [7].

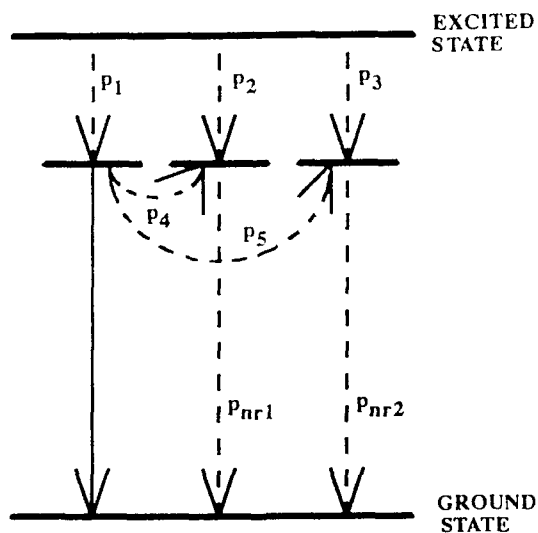


Fig. 6. Model of the recombination process.

Applying eq. (2) to the model in Fig. 6, the transition rates from the radiative to the nonradiative recombination centers via tunneling, p_4 and p_5 , are given by

$$p_4 = p_{40} \exp(T/T_{40}) \quad (5)$$

and

$$p_5 = p_{50} \exp(T/T_{50}). \quad (6)$$

The excited electrons can be trapped either by the radiative or the nonradiative recombination centers. The number of electrons at the excited state trapped by the radiative recombination center n_1 is then given by

$$n_1 = Ap_1/(p_1 + p_2 + p_3), \quad (7)$$

where A is a constant. Since a portion of the electrons trapped by the radiative recombination center may escape to the nonradiative recombination centers via tunneling, the total number of electrons contributing to luminescence is now

$$n_2 = Ap_1/(p_1 + p_2 + p_3) \cdot p_1/(p_1 + p_4 + p_5). \quad (8)$$

Here we make assumptions: (1) a direct transition from the excited state to the ground state is neglected; (2) the energy levels of all recombination centers are about the same; and (3) p_1 is much less than p_4 or p_5 . The first assumption is made because the direct transition from the excited state to the ground state is temperature independent and should not affect the observed temperature dependence of the PL peak intensity. The second is reasonable by considering tunneling between the centers. The last is justified by a low luminescence efficiency. Then, eq. (8) will be simplified to show the temperature dependence using eqs. (5) and (6):

$$I_t = I_0 \{ p_{40} \exp(T/T_{40}) + p_{50} \exp(T/T_{50}) \}, \quad (9)$$

where I_0 is a constant. Note that p_1 is temperature independent.

The obtained temperature dependent PL peak intensity is best fitted to eq. (9) by setting the adjusting parameters, p_{40} , p_{50} , T_{40} , and T_{50} , to

$$p_{50}/p_{40} = 0.015, \quad (10)$$

$$T_{40} = 3000 \text{ K}, \quad (11)$$

and

$$T_{50} = 90 \text{ K}. \quad (12)$$

In our analysis, we also considered the model with one radiative and one nonradiative recombination center, but the experimental data could not be well fitted to the model. Therefore, we conclude that the model requires one radiative and at least two nonradiative recombination centers for the best fit between the experiment and the theory. We, however, admit that the model empirically explains the experimental data and that there is no physical explanation for the nature of the recombination centers. Further study is needed to identify these recombination centers.

CONCLUSIONS

We have fabricated the Si ultrafine particles by evaporation of Si in an oxygen-containing argon atmosphere and observed blue light emission. The TEM study reveals that the sample consists of chain-like nanostructures with a mean diameter of 10 nm. The blue light emission is associated with the broad peak at 2.7 eV. The peak cannot be simply explained by the quantum size effect because the size of the nanostructure is too large.

The temperature-dependent PL intensity was best described by the model with one radiative and two nonradiative recombination centers based on the tunneling theory between two centers proposed by Street [7]. The nature of these centers is not well understood. One may have better physical understanding of the centers by studying dynamics of tunneling by time-resolved photoluminescence measurements.

REFERENCES

1. L. T. Canham, *Appl. Phys. Lett.* **57**, 1046 (1990).
2. E. A. Fitzgeralds, J. M. Macauley and T. D. Harris, *J. Appl. Phys.* **71**, 2403 (1992).
3. H. Morisaki, F. W. Ping, H. Ono and K. Yazawa, *J. Appl. Phys.* **70**, 1869 (1991).
4. T. Kawaguchi and S. Miyazima, *Jpn. J. Appl. Phys.* **32**, L215 (1993).
5. B. T. Kolomiets, T. N. Mamoxtova, E. A. Smorgonskaya and A. A. Babaev, *Phys. Stat. Sol.* **A11**, 441 (1972).
6. H. Morisaki, *Nanotechnology* **3**, 196 (1992).
7. R. A. Street, *Advances in Physics* **25**, 397 (1976).

IR-VISIBLE PHOTOLUMINESCENCE STUDY OF NANOMETER-SIZE AMORPHOUS SILICON POWDER PRODUCED BY SQUARE-WAVE-MODULATED RF GLOW DISCHARGE.

J. COSTA, P. ROURA, G. SARDIN, J. R. MORANTE, E. BERTRAN.
Departament de Física Aplicada i Electrònica, Universitat de Barcelona.
Av. Diagonal 647, E08028 Barcelona, Catalonia (Spain).

ABSTRACT

Amorphous silicon powder exhibiting microstructural properties such as nanometer size, large presence of silicon-hydride groups and high surface/volume ratio has been produced in a plasma enhanced chemical vapor deposition (PECVD) reactor using pure silane gas and low frequency square-wave-modulated (SQWM) rf power (13.56 MHz). The possible crystallinity of nanometer-size domains embedded in the amorphous network was studied with Raman spectroscopy and electron diffraction analysis.

Photoluminescence (PL) in the near IR-VIS region was excited by an Ar laser. The PL intensity exhibits very unusual properties: a supralinear dependence on excitation power and an exponential decrease with pressure (below 50 Pa). The analysis of PL dynamics led us to propose a mathematical model of excitation of the PL. This model involves the existence of an intermediate step, with an extremely long lifetime, that controls the PL dynamics.

INTRODUCTION

The formation of silicon powders (pwd-Si) during PECVD processes has stimulated many reports^{1,2} due to its involvement as a contaminant during hydrogenated amorphous silicon, a-Si:H, thin film deposition or etching. Furthermore, pwd-Si produced by PECVD is a promising new material for sintering ceramics, for making nanoscale filters or supports for catalytic surfaces.

The special characteristics of powder obtained by PECVD are its nanometer-size, microstructure, high purity, its chemical reactivity and the possibility of preparing alloys by mixing precursor gases. Some of these characteristics, such as size, composition and microstructure can be controlled by the technological parameters of the plasma processing.^{3,4,5} One of the relations between the discharge parameters and the microstructural properties of the Si powders has shown the dependence of powder size on plasma-on periods (when the square-wave-modulation, SQWM, of the rf power was used).^{5,6} Compactness and hydrogen concentration of the samples can also be controlled by the SQWM frequency of the incident power and by the gas residence time in the reaction chamber.^{3,6}

Photoluminescence (PL) of Si nanostructures has attracted much interest in recent years because it lies in the visible region. PL of porous silicon (PS)^{7,8} and other silicon structures like small crystallites produced by sputtering⁹, skeleton clusters¹⁰, evaporated particles¹¹, or siloxene

compounds¹², have been the object of many reports. Although there is no clear evidence that the PL is due to the same cause in all these materials, there are two main explanations: the increase of the optical gap due to the quantum confinement of the electrons¹, and the presence of siloxene-type compounds¹². In spite of the strong microstructural similarity between the Si powder produced by PECVD and the structures described above, we report unusual PL properties of Si powder.

In a previous study¹¹ we showed the visible PL emission of Si powders and the dependence of PL intensity, I_{PL} , on both laser intensity and gas pressure inside the cryostat, at pressures below 50 Pa. In that case we found an exponential decrease of I_{PL} when we increased the pressure ($I_{PL} = I_0 \exp(-p/p_0)$, where p_0 was of about 1.5 Pa). A gas pressure increase from 1 to 15 Pa decreased I_{PL} by four orders of magnitude. The dependence on laser power, Φ , was strongly supralinear ($I_{PL} \propto \Phi^m$, where m ranged between 4 and 6).

In this paper we report the preliminary results of a more extensive study of the PL of Si powder, which includes the determination of the near IR-VIS PL spectra at different laser intensities and the study of rise, τ_{exc} , and decay, τ_{PL} , lifetimes. Extraordinarily long lifetimes, of about several hundred ms are shown for both rise and decay. The PL is modeled as an excitation process of at least two steps, one of which is responsible for the unusually long lifetimes.

Furthermore, in order to elucidate the existence of small crystals in the Si powder, which might be responsible for the PL emission, we performed Raman spectroscopy and electron nanodiffraction analysis.

EXPERIMENTAL

Silicon powder was produced inside the reaction chamber of a capacitively coupled rf reactor.¹³ The reactor was kept at room temperature, the silane plasma was modulated at low frequency (0.1 Hz) with 50% duty cycle; the SiH_4 gas flow was 20 sccm, the pressure 65 Pa and the rf power density, 200 mW/cm². The sample was kept under the atmosphere for about three months.

The PL was excited by the 488 nm line of an Ar laser which produces a spot of about 4 mm² on the sample surface. The incident laser intensity ranged between .5 and 5 mW. A 0.5 m monochromator was used to obtain the spectral feature of PL. The emitted light was detected by an InAs photodiode cooled to 77°K, and analyzed with a 0.5 m monochromator. The reported spectra were corrected by the transfer system function. Samples were mounted inside a closed-circuit helium cryostat, where the surrounding gas pressure was held at 10⁻² Pa. All PL measurements described here were carried out at room temperature and under vacuum.

Micro-Raman analysis was performed with the 488 nm line of an Ar laser that produced a spot of about 2 μm in diameter on the Si powder sample. We used a weak laser power, 1.2 mW measured on the sample, in order to avoid the laser annealing of the particles.

Electron nanodiffraction analysis was carried out with a Hitachi HT-800-NA microscope. The electron spot used was 2 nm in diameter.

RESULTS AND DISCUSSION

Previous transmission electron microscopy studies of Si powder were used to deduce particle sizes ranging between 10 and 200 nm.⁴ The Si-H bond configuration was estimated from the Fourier transform infrared (FTIR) spectra. The FTIR analysis revealed the predominance of SiH₃ groups (2100 cm⁻¹), in front of Si-H (2000 cm⁻¹) bonds, in a highly polymeric form (850 and 890 cm⁻¹).¹ The appearance of both 2180 and 2250 cm⁻¹ peaks indicated the spontaneous oxidation of the samples exposed to the atmosphere.¹⁵ Thermal desorption spectrometry, TDS,

showed the predominant presence of weakly bonded hydrogen, which evolves at about 300 °C, and the large hydrogen content of the silicon powder particles (above 30%).¹⁵

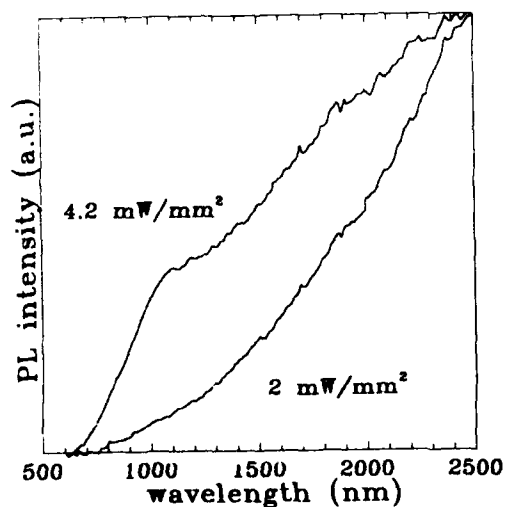


Figure 2. PL spectra of the Si powder for two laser intensities.

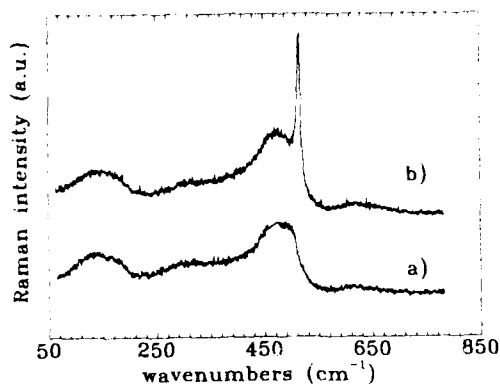


Figure.1 Micro-Raman spectra of Si powder. Totally amorphous, a); and with crystalline evidences, b).

X-ray diffraction showed no crystallinity of the samples. Furthermore, micro-Raman spectroscopy indicated the amorphous character of the powder in almost every measurement (Figure 1.a). Only in few cases did sample zones produce a Raman spectrum with evidence of crystallinity (Figure 1.b). Then, the c-Si peak, usually centered at 520 cm⁻¹, appeared superposed to the amorphous curve, and it was shifted to shorter wavenumbers (510 cm⁻¹) indicating the small size of these ordered regions. Electron nanodiffraction never produced any diffraction image, giving clear proof of the absence of crystals larger than the electron spot (2 nm). We can conclude

from these two analyses that the Si powder is mainly amorphous. Moreover, the PL dynamics study we describe here rules out the possibility of electron quantum confinement as the cause of PL in this material.

Figure 2 shows the normalized PL spectra of Si powder, for two different incident laser intensities. In both cases, PL emission starts in the visible region (600 nm) and rises continuously until 2500 nm. Unfortunately, we are not able yet to correct the spectrum to the detector limit (3.1 μm), but our measurements show that the PL emission continues beyond this limit. The structureless shape of PL spectra and the fact that the emission at higher energies increases for the sample illuminated at higher power, suggest that the PL emission is caused by a multiplicity of electron states.

The study of transient phenomena, excitation (τ_{ex}) and decay (τ_{PL}) lifetime, as well as the PL intensity (I_{PL}) dependence on laser intensity (Φ), were obtained by integrating the PL emission between 1.9 and 3.1 μm .

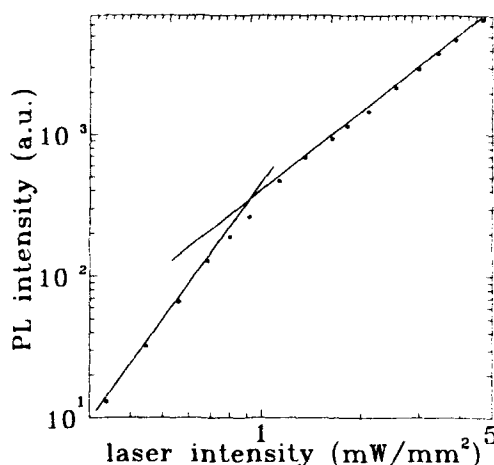


Figure 3. Supra-linear dependence of PL intensity on incident laser intensity.

The I_{PL} dependence on Φ is non-linear. In Figure 3 we can see that it varies with the incident light power following a supra-linear dependence, $I_{\text{PL}} = \Phi^m$, where m ranges between 2 and 3. Below 0.8 μm this exponent is greater ($m = 4 - 6$)¹³. This fact is consistent with the evolution of the spectral shape with laser intensity shown in figure 2, where the PL intensity increases with laser power, faster at lower wavelengths.

Figure 4 shows the time response of PL of Si powder to a laser pulse. Although there is no pure exponential rise or decay, but a distribution of lifetimes, we can estimate the rise time, of about 400 ms, which is longer than the decay time, around 50 ms. The PL we observe does not have any faster contribution. Both the rise and decay times are about four orders of magnitude longer than the longest times reported for porous silicon¹⁶⁻¹⁸.

The key of the PL dynamics analysis is the fact that the PL emission has a null derivative close to $t = 0$ as shown in the inset of Figure 4. This behavior cannot be explained according to the usual direct excitation from a ground state, where the dynamics would be described by the following equation:

$$\frac{dn_{\text{PL}}}{dt} = \sigma n_0 \Phi - \frac{n_{\text{PL}}}{\tau_{\text{PL}}} \quad (1)$$

where n_0 is the population of the ground state, σ is the optical cross section, Φ the laser photon

flux and τ_{PL} , the lifetime of the excited state. As I_{PL} is proportional to the luminescent state population (n_{PL}), from eq.1 it is clear that at $t=0$ the PL emission derivative should be proportional to $\sigma n_0 \Phi$. Thus the null derivative implies that n_0 must be 0. This leads us to propose a multiple step model which assumes the presence of intermediate states, whose occupation increment is caused by the light excitation of the preceding state.

We can describe the process as follows:

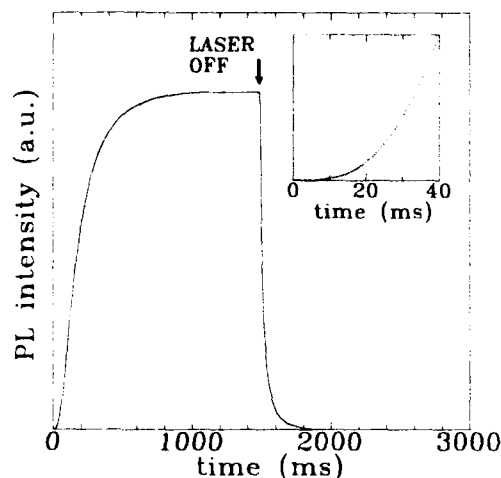
$$\frac{dn_1}{dt} = n_0 \sigma_0 \Phi - \frac{n_1}{\tau_1}$$

$$\frac{dn_2}{dt} = n_1 \sigma_1 \Phi - \frac{n_2}{\tau_2}$$

.

.

$$\frac{dn_{PL}}{dt} = n_{PL-1} \sigma_{PL-1} \Phi - \frac{n_{PL}}{\tau_{PL}}$$



A more detailed study of

the model, to be published, gives the following results: a) The exponent m (from the $I_{PL} \propto \Phi^m$ dependence) is a lower value of the number of steps needed to reach the luminescent state, and b) While the PL emission decay depends on the effective lifetime of the luminescent state, τ_{PL} , the excitation, τ_{exc} , is dominated by the slowest intermediate transition, leading to the difference between τ_{PL} and τ_{exc} ($\tau_{PL} < \tau_{exc}$). According to this model, our experimental results imply that the states emitting at $2 \mu m$ occupy at least the third level of the sequence ($m = 3$), whereas the PL emission near the visible region corresponds to a level $m \geq 6$. These findings reinforce the hypothesis of many different states contributing to the PL spectrum.

Figure 4. PL response to a laser excitation pulse. The first 40 ms of the curve is shown in the inset. Excitation and decay lifetimes are about 400 and 50 ms respectively.

Concerning the possible causes of the Si powder PL, the amorphous character of the samples and the long PL lifetimes rule out the electron quantum confinement hypothesis in small crystallites. Although siloxene-type compounds may be present in our Si powder samples as its spontaneous oxidation might allow, the investigations of Ch. Hollenstein and coworkers on *in situ* PL measurements in dusty silane discharges,¹⁹ where no oxygen is present, also rule out this possibility. The multiple step excitation process and the unusual PL dependences on gas pressure and power indicate that we are faced with a qualitatively different PL emission.

REFERENCES

- [1] *Proceedings of the 39th National Symposium of the American Vacuum Society, Part II*, J. Vac. Sci. Technol. A, **11** 119-1141 (1994).
- [2] *Proceedings of the NATO advanced research workshop: "Formation, Transport and Consequences of Particles in Plasmas"*, Plasma Sources Sci. Technol., (in press).
- [3] J. Costa, G. Sardin, J. Campmany, J. L. Andújar, A. Canillas, E. Bertran, Mater. Res. Soc. Symp. Proc., **286** 155 (1993).
- [4] E. Bertran, J. Costa, G. Sardin, J. Campmany, J. L. Andújar, Plasma Source Sci. Technol. (in press)
- [5] L. Boufendi, A. Plain, J. Ph. Blondeau, A. Bouchule, C. Laure, M. Toogood, Appl. Phys. Lett., **60** 169 (1992).
- [6] J. Costa, G. Sardin, J. Campmany, E. Bertran, Vacuum (in press).
- [7] L. T. Canham, Appl. Phys. Lett., **57** 1046 (1990).
- [8] C. Tsai, K. H. Li, D. S. Kinosky, R. Z. Qian, T. C. Hsu, J. T. Irby, S. K. Banerjee, A. F. Tasch, J. C. Campbell, B. K. Hance, J. M. White, Appl. Phys. Lett., **60** 1700 (1992).
- [9] S. Furukawa, T. Miyasato, Phys. Rev. B, **36** 5726 (1988); Jpn. J. Appl. Phys., **27** L2207 (1988).
- [10] Y. Kanemitsu, K. Suzuki, H. Uto, Y. Masumoto, T. Matsumoto, S. Kyushin, K. Higuchi, H. Matsumoto, Appl. Phys. Lett., **61** 2446 (1992).
- [11] H. Morisaki, F.W. Ping, H. Ono, K. Yazawa, J. Appl. Phys., **70** 1869 (1991).
- [12] M. S. Brandt, H. D. Fuchs, M. Stutzman, J. Weber, M. Cardona, Solid State Commun., **81** 307 (1992).
- [13] J. Costa, P. Roura, G. Sardin, J. R. Morante, E. Bertran, Appl. Phys. Lett., **64** 463 (1994).
- [14] J. L. Andújar, E. Bertran, A. Canillas, J. Esteve, J. Andreu, J. L. Morenza, Vacuum, **39** 795 (1989).
- [15] J. Costa, G. Sardin, J. Campmany, J. L. Anújar, A. Canillas, E. Bertran, Mat. Res. Symp. Proc., **297** 1031 (1993).
- [16] T. P. Pearsall, J. C. Adams, J. E. Wu, B. Z. Nosho, Ch. Aw, J. C. Patton, J. Appl. Phys., **71** 4470 (1992).
- [17] L. R. Tessler, F. Alvarez, O. Teschke, Appl. Phys. Lett., **62** 2381 (1993).
- [18] K. Wang, D. Han, M. Kemp, M. Silver, Appl. Phys. Lett., **62** 157 (1992).
- [19] Ch. Hollenstein *et al.*, Plasma Sources Sci. Technol., (in press).

PART VI

Synthesis and Properties III

STRUCTURAL CHARACTERIZATION OF ORDERED PHASES IN HYDROCARBON DENDRIMERS

Christopher J. Buchko*, Atisa Sioshansi*, Zhifu Xu†, Jeffrey S. Moore**,
and David C. Martin*††

*Materials Science and Engineering, University of Michigan, Ann Arbor, MI 48109-2136

†Department of Chemistry, University of Michigan, Ann Arbor, MI 48109

**Department of Chemistry, Roger Adams Lab, University of Illinois, Urbana, IL 61801

††Macromolecular Science and Engineering Center, University of Michigan, Ann Arbor, MI 48109

ABSTRACT

Structural characterization of phenylacetylene dendrimers (PADs) makes it possible to explore the relationship between molecular architecture and condensed phase organization. The size and geometry of the PAD series is precisely controlled, with phenylacetylene units emanating from a central phenylene in the manner of a tridendron. The branched molecule rapidly increases in size with each synthetic generation. The "shape-persistent" nature of the phenylacetylene molecule makes it ideal for use in the construction of self-assembling supramolecular systems.

Transmission electron microscopy (TEM) has been used to identify the crystal structure of lower generation PADs, and wide-angle X-ray studies confirm the decrease in crystallinity with size. Hot stage optical microscopy studies of thermal transitions reveal melting points for lower generation PADs, and an apparent glass transition for the amorphous higher generations. This type of structural information is essential to the rational design of self-assembling materials.

INTRODUCTION

The design of engineering materials has traditionally relied on the interactions of either individual atoms, often inorganics, or high molecular-weight organic macromolecules. However, fabrication of nanoscale structures from an atomistic level can be unwieldy and time-intensive, especially so with complex macromolecules. Modular, "shape-persistent" units of tens to hundreds of atoms provide a middle ground for the construction of larger molecular assemblies. Strong covalent bonds maintain the rigid architecture of these molecules, while weaker forces like hydrogen bonds and van der Waals interactions can result in large-scale molecular organization. The phenyl ring and the acetylene rod are two such rigid units that can be used in molecular engineering, and together they comprise the phenylacetylene dendrimers (PADs) used in this study.

Dendrimers are a specific class of molecules identifiable by their highly branched topology. The first dendrimers were flexible, branched polymers like the "starburst" poly(amidoamines) [1] of Tomalia et al. Chemical routes for various flexible dendrimers have been developed by other groups [2-5] and recent advances in the large scale synthesis of poly(propyleneimine) dendrimers [6] portend the widespread commercial use of these materials. The PAD molecules differ from the aforementioned dendrimers in that the rigid nature of the substituent units is retained throughout the structure, creating a well-defined architecture. Additionally, the synthesis of these dendrimers involves a repetitive scheme that can produce high molecular weight molecules in relatively few steps [7]. Generations of the PAD molecule branch out from a seed phenylene, and contain tertiary butyl groups on the periphery of the molecule to enhance solubility. PAD-4, named for the number of phenyl rings, is the base member of the PAD family (Figure 1).

† Current Address: PPG Industries Inc., Advanced Research Center,
4325 Rosanna Dr., Allison Park, PA 15101

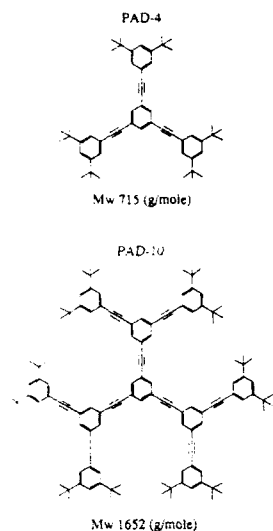


Fig.1 Schematics of lower generation PADs

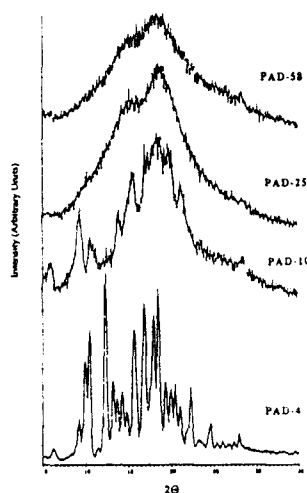


Fig. 2 Powder X-ray diffraction

EXPERIMENTAL

The synthesis of the PAD family, like that of most new organic molecules, is a time consuming process that yields small amounts of material. Synthesis of PAD-4 and PAD-10 follows a convergent route, meaning that the three arms of the molecules are synthesized as wedges, and then coupled to a central core. For PAD-4 and PAD-10, the central core is a 1,3,5-tribromobenzene. Higher generation PADs follow this same convergent scheme, with varied leaving groups on the core phenylene. Although not used in this study, high molecular weight PADs have been prepared using a modified convergent method in which the central core has up to seven phenylenes [7].

Samples for TEM consisted of crystallites nucleated out of a dilute solution or microtomed bulk crystals. A dilute solution of PAD molecules in a 50 w/o toluene-NMP (1-methyl-2-pyrrolidinone) was deposited on amorphous carbon coated mica sheets and allowed to dry under room conditions. Toluene is a better solvent for the PADs than NMP, but its low boiling point made the addition of the less volatile NMP necessary in order to grow larger crystallites. The carbon film and the crystallite layer was floated off the mica substrate in deionized water and collected on copper grids. Gold was evaporated onto the samples as a calibration standard for electron diffraction and to improve contrast at intermediate magnifications. Samples for high resolution imaging were left uncoated. Cross-section samples of PAD-4 crystals were prepared by nucleating crystallites from dilute solution onto a glass slide. These crystallites were embedded in an epoxy droplet that was then cut and positioned in a larger epoxy block suitable for microtomy using a Reichert-Jung UltraCut E.

Low dose electron microscopy techniques allow imaging of these organic samples despite their sensitivity to the high voltage electron beam. The total end point dose (TEPD), J_e , is defined as the dose required for a diffraction spot to disappear as monitored visually, and can be given in terms of the operating parameters of a microscope by:

$$J_e = j_s M^2 t \quad (1)$$

where j_s is the current density at the screen (pA cm^{-2}), M is the magnification, and t (sec) is the time it takes for a diffraction spot to fade. The TEPD was measured for all samples by observing the time required for a particular reflection to become diffuse and indistinguishable from the amorphous scattering of the carbon film (Table I). In general, the dose rate was kept below 85% of the TEPD. Diffraction patterns and intermediate magnification images of PAD-4 were collected on a Philips EM 420, operating at 120 kV. Diffraction patterns of PAD-10 were obtained on a JEOL 4000 EX at 400 kV by searching the sample grid at a low dose rate, as measured at the screen (approximately $10^{-5} \text{ C cm}^{-2} \text{ sec}^{-1}$) while recording the session on VHS tape through a YAG-video system [8] used with an image intensifier and video camera. Patterns recorded on tape were then digitized with a SCION LG-3 frame grabber and analyzed with IMAGE 1.54 on a Macintosh Quadra 700. High resolution imaging was performed on the JEOL 4000 using magnifications from 25 kX to 35 kX. The larger lattice spacings of the PAD molecules, on the order of 2.0 nm, made high resolution imaging possible at these lower magnifications. Additionally, qualitative observations of thermal transitions were made using a GATAN hot stage and a JEOL 2000 FX at 200 kV, which is also equipped with a video imaging system.

RESULTS

The powder X-ray diffraction data in Figure 2 indicates a trend of decreasing crystalline order with increasing generation. Observation of thermal transitions using a Linkham TH1500 hot stage on a Leitz Ortholux II optical microscope indicate melting points for the PAD-4 and PAD-10 molecules and "softening" points for all higher order dendrimers (Table I). Softening is defined as the visible relaxation of surface roughness on the solid molecular aggregates. All generations of the PAD family undergo a thermal degradation above 300°C , even in a dry nitrogen atmosphere, indicated by a color change to orange-brown. The lower generation PADs will not recrystallize when cooled from this point. The crystallites of PAD-4, shown in Figure 3, can have aspect ratios as high as 40:1, and appear to have a roughly rectangular cross-section. PAD-10 crystallites grown from solution in conditions identical to those of PAD-4 are generally smaller, 10 microns long as compared to 50 microns for the PAD-4 crystals. They retain the same general morphology as PAD-4, with aspect ratios of 8:1 (Figure 4).

Hot stage TEM of the thermal transitions of PAD-4 and PAD-10 show the crystallites dissociating laterally only slightly as they melt, while losing the majority of their length rapidly before they enter the liquid phase. The larger crystallites of PAD-4 consist of individual, smaller rod-like crystals bound together laterally. The first step in melting is the separation of these smaller crystals. These crystals then melt at a rate of approximately $2.5 \mu\text{m/sec}$ along the long axis, compared to a rate of $0.02 \mu\text{m/sec}$ in the lateral direction.

Electron diffraction of the PAD-4 crystallites (Figure 5) show characteristic spacings in the long direction of the crystal of 0.64 nm, and a lateral dimension, perpendicular to the long direction, of 2.05 nm. Diffraction patterns obtained from a microtomed cross-section of a PAD-4 crystallite (Figure 6) show spacings of 2.05 nm and 1.91 nm, with an included angle of 90° . There are no observable systematic absences in either of these patterns. Electron diffraction patterns of PAD-10 show a spacing in the long direction of the crystal of 0.62 nm, and a lateral dimension of 1.6 nm (Figure 7). High resolution microscopy of PAD-10 (Figure 8) reveals lattice fringes of $1.6 \pm 0.2 \text{ nm}$.

Table I
Physical Properties

	TEPD (C cm^{-2})	T_M ($^\circ\text{C}$)
PAD-4	1.3×10^{-2}	220
PAD-10	1.2×10^{-3}	180

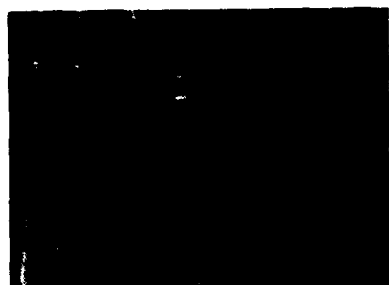


Fig. 3 Optical micrograph of PAD-4 crystals

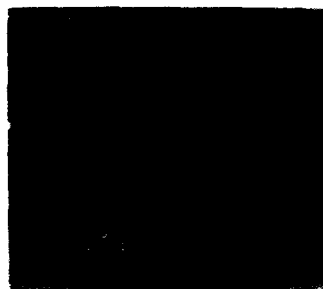


Fig. 4 Optical micrograph of PAD-10 crystals

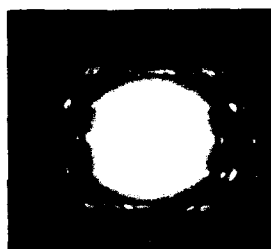


Fig. 5 (010) Zone Axis of PAD-4



Fig. 6 (001) Zone Axis of PAD-4

DISCUSSION

Molecular simulations [9] of individual PAD-4 and PAD-10 molecules indicate that these two lowest generation members of the PAD family maintain a planar conformation. This planarity is lost on the higher generation molecules, as they adopt more spherical conformations, with a large excluded volume in the center of the molecule. Despite the rigid nature of the phenyl rings and acetylene rods, there is a considerable amount of rotational motion about the covalent bond available to the outer branches of the larger molecule. This is evident from the many low energy conformations that the outer arms of the molecules can adopt during minimizations, depending upon the initial configuration of the molecule. Thus, crystallinity decreases as a function of generation due, at least in part, to the potential non-uniformity of the higher-order PADs.

The crystal structure of PAD-4 can be solved using the data collected from the diffraction patterns and molecular simulations. The lack of systematic absences and the 90° angles lead to an orthorhombic unit cell. The positions of the molecules inside the unit cell can be refined by comparing the relative intensities of simulated diffraction patterns with the collected data. Table II is a summary of the proposed unit cell for PAD-4, in which $a = 2.05$ nm, $b = 1.91$ nm, $c = 0.64$ nm, $\alpha = \beta = \gamma = 90^\circ$. A geometrical evaluation of the unit cell predicts that the molecules can take on various low energy configurations, but the only one that replicates the weak reflections along the (001) axis in the experimental patterns is one in which the geometric axis of each PAD-4 is tilted at approximately 66° with respect to the c axis. The PAD-4 molecules take on a motif

resembling stacks of tilted, interdigitated molecules when the energy of the unit cell is minimized (Figure 9). Support for this configuration comes from the strong (501) reflections in Figure 6, which correspond to a real space dimension of 0.35 nm. This is the distance of closest approach of the central phenylene ring of one PAD-4 with the planar core of the next PAD-4, as shown in an off-axis projection of a stack of PAD-4 molecules (Figure 10).

Just as PAD-10 crystallites are morphologically similar to PAD-4, the electron diffraction patterns of PAD-10 (Figure 7) show a geometric similarity to those of PAD-4. In both patterns, the scattering vector perpendicular to the long axis of the crystal, k_1 , extends farther out in reciprocal space than its counterpart along the axis, k_2 . The ratio $k_2/k_1 = 0.6$ indicates greater order perpendicular to the long axis of the crystal between the interdigitated molecules. This is corroborated by observation of the melting of these crystals in the hot stage TEM. Thus, disorder in the c direction of the crystal can be associated with the high energy of the (001) crystal faces, and the subsequent preferential melting along that axis. The lattice fringes in the HREM of PAD-10 appear to curve around defects, indicating that the lateral direction can accommodate imperfections more readily. However, the lower TEPD and fewer reflections for PAD-10 support the thesis of decreasing crystallinity with increasing molecular size.

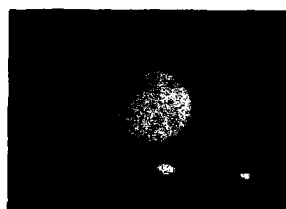


Fig. 7 (010) Zone Axis of PAD-10, captured using video system.

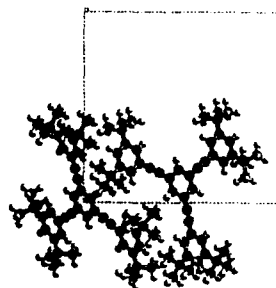


Fig. 8 (001) projection of PAD-4 unit cell



Fig. 9 HREM of PAD-10



Fig. 10 0.35 nm separation of stacked PAD-4

Table II
Proposed PAD-4 Unit Cell

crystal system	orthorhombic
space group	P 2 ₁ 2 ₁ 2 ₁
a	2.05 nm
b	1.91 nm
c	0.64 nm
$\alpha=\beta=\gamma$	90°

CONCLUSIONS

Structural analysis of the lower molecular weight generations of the PAD family provide some insight into the use of the rigid phenyl and acetylene molecules as modular units in the construction of macromolecules. Identification of an orthorhombic unit cell for PAD-4 in which the molecules are oriented as tilted stacks of planar molecules with interpenetrating arms reveals a distance of closest approach for the face-to-face packing of the molecules of 0.35 nm. Although the molecules themselves are planar, they associate more strongly with one another by the interlocking of their arms than by stacking. The higher generation PADs, with various potential conformations of their peripheral branches, cannot take advantage of this spatial arrangement, making condensed phase organization difficult. Substitution of charged groups on the periphery of the molecules could enhance the interaction of the dendrimer arms, and make self-assembly more likely.

ACKNOWLEDGMENTS

DCM and JSM would like to thank the NSF for National Young Investigator Awards. This work is sponsored by NSF grant DMR92-12054 and the Petroleum Research Fund.

REFERENCES

1. Tomalia, D. A., Baker, H., Dewald, J., Hall, M., Kallos, G., Martin, S., Roeck, J., Ryder, J., Smith, P., *Polymer Journal*, Vol. 17, No.1, 117-132 (1985).
2. Newkome, G. R., Yao, Z., Baker, G. R., Gupta, V. K., *J. Org. Chem.*, (1985), **50**, 2003.
3. Hawker, C. J., Frechet, J. M. J., *J. Chem. Soc. Chem. Commun.*, (1990), 1010.
4. Meikelburger, H. B., Jaworek, W., Voegtli, F., *Angew. Chem.*, Int. Ed. Engl., (1992), **31**(12), 1571-1576.
5. Zhou, L. L., Roovers, J., *Macromolecules*, (1993), **26**(5), 963-968.
6. de Brabander-van den Berg, E. M. M., Meijer, E. W., *Angew. Chemie*, Int. Ed. Engl., (1993), **32**(9), 1308-11.
7. Xu, Z., Moore, J. S., *Angew. Chemie*, Int. Ed. Engl., (1993), **32**(2), 246-248.
8. Liao, J., Martin, D. C., *Science*, (1993), **260**, 1489-1491.
9. CERIU 3.2, Molecular Simulations Inc., Burlington, MA., 1993

A MOLECULAR APPROACH TO ULTRATHIN MULTILAYERED FILMS OF TITANIUM DIOXIDE

ELAINE R. KLEINFELD AND GREGORY S. FERGUSON*
Department of Chemistry, Lehigh University, Bethlehem, PA 18015

ABSTRACT

We have used solution-phase inorganic chemistry to form ultrathin, covalently bonded layers of TiO_2 on silicon wafers. Ellipsometry and x-ray photoelectron spectroscopy (XPS) were used to monitor the growth of the films. The ellipsometric thickness of the TiO_2 films increased linearly with the number of reaction cycles, the first absorption cycle resulting in about 3–4 Å of growth, and subsequent cycles resulting in about 1 Å of growth. We attribute this limited growth to the limited number of reactive sites on the surface.

INTRODUCTION

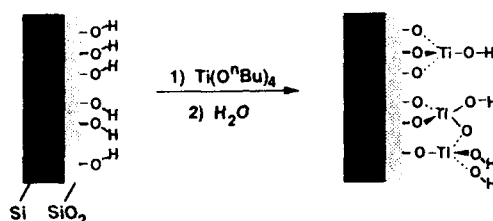
Synthetic inorganic chemistry offers a wide variety of solution-phase reactions that can, in principle, be used to build molecular structure at solid-solution interfaces. An example of remarkable success in this area is the use of coordination chemistry at surfaces to form self-assembled monolayers (SAMs) on inorganic substrates.¹ The two best characterized of these systems are formed by adsorption of alkyltrichloro- (or trialkoxy-) silanes on the native oxide of silicon, or by adsorption of organosulfur compounds on gold surfaces. Three features that distinguish SAMs from other surface coatings are: (1) the molecular adsorbates are densely packed, approaching crystalline-like order; (2) only one layer of these adsorbates is formed at a time; and (3) the adsorbates may contain reactive functionality that can be used in a subsequent, separate adsorption step. These features, in turn, result from two key characteristics of the adsorption processes in these systems: strong bonding of the adsorbate to the surface, which leads to high packing densities; and the finite number of adsorption sites available at the surface, which limits the growth per reaction cycle to one monolayer. In the work reported here, we have used these two characteristics as design principles for building mono- and multilayers of titanium dioxide.

Ultrathin films composed of purely inorganic components are of interest for microelectronics applications,² in catalysis^{3,4} and as components for nonlinear and vacuum ultraviolet/soft x-ray optics.⁵ In addition to physical deposition methods,^{5,6} chemical approaches to the formation of such films have included vacuum methods such as atomic layer epitaxy^{7,8} and chemical vapor deposition,⁹ as well as solution-phase methods.^{3,4} Several groups have reported that a single atomic layer of titanium dioxide can be formed by the reaction of a titanium (IV) alkoxide (from the vapor phase¹⁰ or from solution⁴) at the surface of hydrated silica gel, via a reaction similar to that used for the production of relatively thick films by the sol-gel method.^{11,12} We have investigated the adsorption of ultrathin layers of TiO_2 by forming them on well-defined substrates, polished silicon wafers. The native oxide on a silicon wafer, while not possessing the high surface area of silica gel, does display similar surface chemistry. These substrates also allow characterization of overlayers by various techniques that do not lend themselves to analysis of high-surface-area substrates, such as optical ellipsometry, angle-resolved XPS, and x-ray reflectivity. Films of

oxides formed on silicon wafers can therefore aid in the thorough characterization of surfaces of catalytic interest. In addition, methods developed to form ultrathin films on single crystal silicon substrates may be adaptable to allow preparation of multilayers incorporating more than one type of material, which could potentially serve as components for nonlinear and vacuum ultraviolet/soft x-ray optics.

SAMPLE PREPARATION

Titanium dioxide films were prepared as follows. Clean silicon wafers were imported into a glovebox containing a dry nitrogen atmosphere. They were immersed for 30 s in ~5 mM solutions of titanium (IV) tetra-*n*-butoxide in dry toluene (distilled from sodium), and subsequently rinsed with dry toluene. The wafers were then exported from the glovebox and again rinsed with dry toluene. The samples were rinsed with purified water both to aid in hydrolysis of any unreacted butoxy groups and to remove any adsorbed water-soluble contaminants. Second and subsequent layers were adsorbed by repeating this procedure (Scheme 1).



Scheme 1. Schematic illustration of the two steps in the adsorption cycle used to form an ultrathin film of TiO₂. This cycle was repeated to form multilayers of TiO₂.

CHARACTERIZATION AND DISCUSSION

The thickness of the titanium dioxide films was measured by optical ellipsometry (Rudolph Auto-EL III), assuming a refractive index of 1.76.¹³ (If this number was varied to as high a value as 2.1, ellipsometric thicknesses decreased by less than 0.2 Å, so the exact index used was not critical.) Initial adsorptions onto clean silicon wafers yielded films with thicknesses of approximately 3–4 Å. This layer thickness was independent of the amount of time that the substrate spent in the adsorbate solution, over the range that we measured (30 seconds to 4 days), indicating that the limiting reagent is the hydroxyl groups on the surface of the wafer (silanols and adsorbed water), and not residual water in the solvent. Consistent with the proposed reaction scheme, no adsorption occurred on wafers that had been pre-coated with a SAM by treatment with octadecyltrichlorosilane¹⁴ to provide an unreactive, low-free-energy surface.

As repeated adsorptions were performed on the same wafer, ellipsometric measurements indicated that the TiO₂ thickness increased linearly. Figure 1 shows that the thickness of the first layer and the slope of thickness vs. number of adsorptions were not perfectly consistent from day to day, though they were highly consistent for different wafers prepared on a particular day. This variability could perhaps be linked to variations in temperature or residual water vapor in the glovebox. The intercepts of these least-squares lines were always non-zero (~2–3 Å), implying that a greater amount of TiO₂ was adsorbed in the first cycle than in subsequent cycles (slopes ~1

Å/cycle). Alternatively, the non-zero intercepts could be due to a layer of adventitious contamination adsorbed at the outer surface of the TiO_2 due to its high surface free energy. Control wafers that were treated with the same rinsing procedure as the experimental wafers—but not immersed in a titanium butoxide solution—did not adsorb sufficient contamination to account for the non-zero intercepts. The expected thickness of a TiO_2 monolayer, calculated assuming tetrahedral coordination of each titanium atom to four oxygen atoms and using tabulated covalent radii:¹⁵ is 3.35 Å. Our results thus indicate that, whereas we may have obtained a full monolayer in the first cycle, less than a monolayer of material was adsorbed in subsequent cycles.

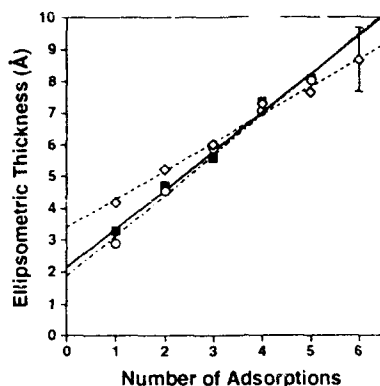


Figure 1. Ellipsometric thickness of a TiO_2 overlayer as a function of the number of adsorption cycles performed. Each symbol represents the average of layer thicknesses measured on three separate samples treated side-by-side. Different shapes (and the corresponding best-fit lines) represent experiments performed on different days. The error bar represents the largest range in data observed across the three samples treated on a single day; a typical range was 50–75% of the one shown.

We expected the TiO_2 layers to be have an amorphous network structure, because they were formed at low temperatures via surface alcoholysis, involving nearly thermoneutral exchange of one oxygen ligand for another. Two experimental results were consistent with this expectation. First, no peaks associated with known phases of crystalline TiO_2 were present in x-ray diffractograms of these samples. The absence of peaks, however, could be due to low signal-to-noise for such a thin sample rather than a lack of order in the film. Second, the layers dissolved in isopropanol, indicating that the titanium atoms were accessible to nucleophiles. Amorphous films of TiO_2 prepared by ALE⁸ were found to undergo transitions to the crystalline phases anatase and rutile upon heating to 350 and 550 °C respectively; we expect similar densification and crystallization of the amorphous networks formed by our method upon annealing, an avenue of inquiry that we have not yet explored.

The elemental composition of the adsorbed films was determined by XPS (Scienta ESCA-300). Spectra of wafers with 1–5 TiO_2 layers contained peaks due to titanium as well as silicon, oxygen, and carbon; some of the wafers also showed trace amounts of contamination by fluorine (most likely from the fluoropolymer tweezers and reaction vessels used) and nitrogen. The expected intensity of the Ti photoemission from the overlayer is given by equation (1):¹⁶

$$I(\text{Ti}) = I_{\infty}(\text{Ti}) (1 - e^{-d/\lambda \cos \theta}) \quad (1)$$

where $I(\text{Ti})$ is observed intensity; $I_{\infty}(\text{Ti})$ is the intensity that would be observed for an infinitely thick sample of TiO_2 ; d is the thickness of the TiO_2 overlayer; λ is the inelastic electron mean free path (assumed to be 25 Å);¹⁷ and θ is the detector angle, with 0° defined as the surface normal. Similarly, the substrate photoemission, that from elemental and oxidized silicon, should be attenuated exponentially by the TiO_2 overlayer as shown in equation (2):

$$I(\text{Si}) = I_s(\text{Si}) e^{-d/\lambda \cos \theta} \quad (2)$$

where $I_s(\text{Si})$ is the intensity that would be observed in the absence of the overlayer. Either signal may in addition be attenuated exponentially by an overlayer of contamination. Figure 2a shows the intensity of the Ti 2p photoemission vs. number of adsorption cycles. The photoemission increased monotonically with the number of adsorption cycles, but was difficult to fit meaningfully to equation (1). Figure 2b shows the attenuation of the oxidized and non-oxidized silicon peaks with the number of TiO_2 overlayers. The observed attenuation indicates that the layers are approximately 1 Å in thickness, but does not indicate that the initial adsorption is thicker than any subsequent adsorption.

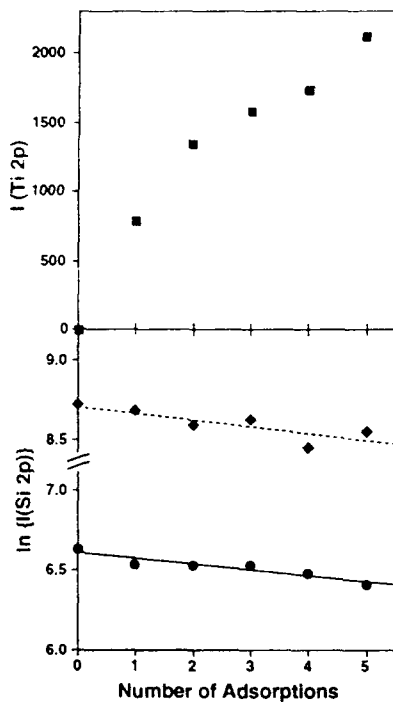


Figure 2. a) Intensity of the Ti 2p photoemission as a function of the number of adsorption cycles on a sample. b) Natural logarithm of the intensity of Si 2p photoemission from oxidized (circles) and elemental (diamonds) silicon as a function of the number of adsorption cycles on a sample. The intensities of the Si signals decreased exponentially as the TiO_2 overlayer grew thicker.

We made angle-resolved XPS measurements in an attempt to investigate whether the TiO_2 formed islands or gave smooth coverage of the substrate after one cycle.^{16,18} A simple analysis, however, did not yield interpretable results; theoretical fits to the data for 100% and 70% coverage are shown in Figure 3. Despite simultaneous optimization of several parameters—the inelastic electron mean free path (for such a thin layer, varying this parameter within reasonable limits made almost no difference), the thickness of an overlayer of carbon contamination, the thickness of the TiO_2 monolayer itself, and the fractional coverage of the overlayer—in no case could we satisfactorily fit the data for detector angles between 50° and 65° from the surface normal. The theoretical lines shown in Figure 3 indicate that for films as thin as ours, variations in coverage have little effect on the fit to the data; consequently, although the best fit to the data was obtained for 100% coverage, we cannot conclude that full coverage was in fact obtained.

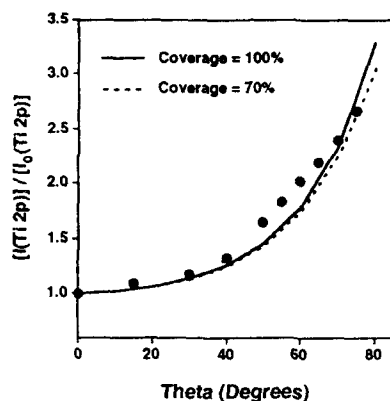


Figure 3. Normalized intensity of the Ti 2p photoemission as a function of the angle between the surface normal and the detector. Lines shown are optimized fits to the data, assuming the inelastic electron mean free path (λ) to be 25 Å. Results indicate that the TiO_2 overlayer thickness is 2 Å, and that it is covered with a layer of contamination that is 2 Å in thickness. Lines for 100% and 70% coverage are shown to illustrate the insensitivity of this analysis to the surface coverage for such a thin overlayer.

CONCLUSIONS

In summary, we have demonstrated that films of titanium dioxide can be grown layer-by-layer on silicon wafers via chemical methods that form strong bonds between the TiO_2 overlayer and the substrate. The limited number of reactive sites (surface hydroxyls) restricts growth to one monolayer or less per adsorption cycle. Ellipsometry and photoemission from titanium indicate that the first adsorbed layer is thicker than subsequent layers, but that thickness increases linearly as more layers are adsorbed.

ACKNOWLEDGMENTS

We gratefully acknowledge a donation of silicon wafers by Wafernet, Inc. We further acknowledge Lehigh University for support of the Scienta ESCA-300 facility, and A.C. Miller and D.H. Carey for assistance with the XPS analyses.

REFERENCES

1. For reviews, see: L.H. Dubois and R.G. Nuzzo, *Annu. Rev. Phys. Chem.* **43**, 437 (1992); G.M. Whitesides and P.E. Laibinis, *Langmuir* **6**, 87 (1990); A. Ulman, *An Introduction to Ultrathin Organic Films: From Langmuir Blodgett to Self-Assembly* (Academic, New York, 1991); G. Cao, H.-G. Hong, and T.E. Mallouk, *Acc. Chem. Res.* **25**, 420 (1992).
2. H.E. Katz and M.L. Schilling, *Chem. Mater.* **5**, 1162 (1993).
3. H.E. Fischer, S.A. King, J.B. Miller, J.Y. Ying, J.B. Benziger, and J. Schwartz, *Inorg. Chem.* **30**, 4403 (1991).
4. S. Srinivasan, A.K. Datye, M. Hampden-Smith, I.E. Wachs, G. Deo, J.M. Jehng, A.M. Turek, and C.H.F. Peden, *J. Catal.* **131**, 260 (1991).
5. E. D'Anna, M.L. De Giorgi, S. Luby, A. Luches, E. Majkova, and M. Martino, *Thin Solid Films* **228**, 145 (1993).
6. T. Nakayama, *J. Electrochem. Soc.* **141**, 237 (1994).
7. E.-L. Lakomaa, S. Haukka, and T. Suntola, *Appl. Surf. Sci.* **60/61**, 742 (1992).
8. S. Haukka, E.-L. Lakomaa, O. Jylhä, J. Vilhunen, and S. Hornytzkyj, *Langmuir* **9**, 3497 (1993).
9. N. Rausch and E.P. Barte, *J. Electrochem. Soc.* **140**, 145 (1993).
10. K. Asakura, J. Inukai, and Y. Iwasawa, *J. Phys. Chem.* **96**, 829 (1992).
11. K. Jurek, M. Guglielmi, G. Kuncová, O. Renner, F. Lukes, M. Navrátil, E. Krousky, V. Vorlíček, and K. Kokesova, *J. Mat. Sci.* **27**, 2549 (1992).
12. U. Selvaraj, A.V. Prasadara, S. Komarneni, and R. Roy, *J. Am. Ceram. Soc.* **75**, 1167 (1992).
13. G.J. Exarhos and N.J. Hess in *Crystallization and Related Phenomena in Amorphous Materials*, edited by M. Libera, T.E. Haynes, P. Cebe, and J.E. Dickinson, Jr. (Mater. Res. Soc. Proc. **321**, 1994) p. 393.
14. D.L. Angst and G.W. Simmons, *Langmuir* **7**, 2236 (1991).
15. Glen E. Rodgers, *Introduction to Coordination, Solid State, and Descriptive Inorganic Chemistry* (McGraw-Hill, Inc., New York, 1994), p. 164.
16. C.S. Fadley, *J. Electron Spect. Rel. Phenom.* **5**, 725 (1974).
17. M.P. Seah and W.A. Dench, *Surf. and Interface Anal.* **1**, 2 (1979).
18. J. Brunner and H. Zogg, *J. Electron Spect. Rel. Phenom.* **5**, 911 (1974).

A NEW PROCESS FOR PREPARING NANOSIZE CERAMIC POWDERS

YONG S. ZHEN, KENNETH E. HRDINA AND ROBERT J. REMICK
Institute of Gas Technology, 3424 South State Street, Chicago, IL 60616

ABSTRACT

We have developed a new poly-foam process for the cost effective preparation of ceramic nanoparticles. The process utilizes the chemistry of polyurethane reactions and is proven to be effective for forming nanometer size ceramic powders of a great variety of single metal oxides and mixed metal oxides. In general, ceramic powders can be prepared by this process having a range of average particle size between 3 to 50 nm, with very narrow particle size distribution. They are free of hard agglomerates, are chemically pure and uniform, and are essentially spherical in shape.

INTRODUCTION

Because of their extremely fine particle size, nanoparticulate ceramic materials (particle size less than 100 nm) exhibit novel combinations of physical, mechanical, and magnetic properties¹. However, traditional ceramic processes such as milling, grinding, and chemical precipitation are not capable of producing ceramic nanoparticles. Significant advances have been made in recent years in developing more sophisticated processes to fabricate ceramic nanoparticles.

The sol-gel process has been used to prepare fine ceramic powder for many years². In one typical procedure, a metal is reacted with an alcohol to form a metal alkoxide. The metal alkoxide then is dissolved in an alcohol. Next, water is added to cause the alkoxide to hydrolyze. After the pH of the solution is adjusted, the materials polymerizes to form a gel which consists of loosely bonded materials and the solvents, water and alcohol. The conversion of the gel to a finely divided metal oxide powder with a very fine particle size is achieved by hypercritical evacuation of the solvent, water and alcohol. Unfortunately, the sol-gel process requires the formation of a metal alkoxide, which is expensive, is air sensitive, and is difficult to control.

The controlled production of ultrafine ceramic particles such as Al_2O_3 and ZrO_2 by gas condensation has recently been refined³. The generation of atom clusters *via* gas condensation proceeds by evaporating a precursor material such as a metal element or volatile metallic compound, in a gas maintained at low pressure, and by the *in-situ* consolidation of the clusters under vacuum conditions. The fine metal clusters can then be collected and oxidized to form the desired metal oxide. The broad application of this process, however, has been hindered by the limited availability of high volatility metal containing precursors and by the inability of the process to produce stoichiometric mixed metal oxides.

A glycine nitrate process has recently been developed for preparing ceramic oxide nanoparticles⁴. This process involves the dissolution of metal nitrates in H_2O and adding glycine to form a metalorganic precursor. The precursor is then heated until it ignites. Combustion takes place at temperatures as high as 1450°C. This process holds promise for producing fine ceramic particles if materials loss due to the high temperature combustion can be minimized and the high reaction temperatures can be controlled to prevent the formation of hard particle agglomerates.

In summary, up-scale production of ceramic nanoparticles remains technically difficult and cost intensive. Until ceramic nanoparticles can be made widely available, we will be unable to utilize their unique properties for a wide range of potential applications. In this paper, we report a new poly-foam process⁵ for preparing ceramic nanoparticles which we believe to have great potential for inexpensive manufacture of high quality ceramic nanometer size powders. Over twenty different ceramic oxides and metal powders have been synthesized using the poly-foam process. The resulting powders are ultrafine (3 to 50 nm in diameter), uniform in size, high purity, and free of hard agglomerates.

THE POLY-FOAM PROCESS

The poly-foam process has four basic steps:

1. Metal cation salts such as nitrates, acetates, oxalates, carbonates, chlorides and mixtures thereof are dissolved in a solvent system such as H₂O, acetone, and alcohol,
2. A polymer foaming reactant such as a mixture of polyols, organic surfactants and catalysts is mixed with the solution containing the dissolved metal salts,
3. Another polymeric foaming reactant, e.g. an isocyanate, is added to the above system and a foam is produced,
4. The polymeric foam comprising the metal cations homogeneously incorporated within the foam cell structure is hardened and heated to decompose the organics, producing nanometer size metal oxide particles.

EXPERIMENTAL METHODS AND RESULTS

The poly-foam process is very flexible and can be used to prepare a wide range of ceramic powders of single metal oxides or mixed metal oxides. We have successfully prepared over 20 different ceramic nano-powders. The following are some of the examples

Stabilized Zirconia

The starting materials used were ZrO(NO₃)₂·xH₂O and Y(NO₃)₃·5H₂O. About 50 grams of the nitrates, in a stoichiometric ratio required to obtain Zr_{0.84}Y_{0.16}O_{1.92} was dissolved in approximately 40 grams of distilled water. The nitrate solution was mixed in a 600 milliliter glass beaker with 200 ml of a mixture of polyols, organic surfactants and catalysts for approximately five minutes. Polymeric isocyanates (200 ml) were added to the mixture and mixed for approximately 30 seconds and the resulting chemical mixture was transferred to two 2 L size porcelain dishes where rapid foaming occurred. The foam containing the metal ions hardened after about thirty minutes and was fired in air at 750°C for three hours with a heating rate of 8°C/min to decompose the organic compounds.

The powder obtained appears to be very fluffy. A powder bulk density of about 0.02 g/cc was measured. Phase studies using X-ray diffraction indicated that a single cubic zirconia phase was obtained.

BET surface area measurement was carried out on the powder sample, a surface area of 96 m²/g was obtained.

The powder was then examined using a Transmission Electron Microscope (TEM), Figure 1. It is noted that the powder has an average particle size of about 20 nm, has a very narrow particle

size distribution, and is essentially spherical in shape. It is also noted that the particle-particle association in the powder follows the pattern of the polymeric foam structure.

In a modification of the procedure described above, the solvent system used contained ethanol and acetone in a one to one ratio. The resulting Y-ZrO₂ powder has a BET surface area of 104 m²/g. This result indicates that the solvent system used to dissolve the metal salts has no significant effect on the characteristics of the final powders.

In yet another modification of the procedure described above, the total nitrates used were 25 g instead of 50 g. The particle size distribution listed in Table I for the resulting powder was measured from TEM micrographs, Figure 2. It is significant to note that the average particle size is only about 7 nm and the particle size distribution is very narrow with the largest particle smaller than 20 nm in diameter. This observation suggests that the average particle size of the nanoparticles can be reduced by reducing the metal loading in the metal ions/polymer precursor.

Table I. Statistical Summary for Crystalline Size Measurements of Y-ZrO₂ Powder

Mean	7.7 nm
Standard Deviation	3.2
Range	16.4
Minimum	2.8
Maximum	19.2
Number of Count	560

Alumina

A similar procedure as above was used to prepare Al₂O₃ nanoparticles. The powder thus obtained has a BET surface area of about 118 m²/g. This corresponds to an average particle diameter of about 13 nm.

Oxide Catalyst

Mixed oxides CuO.Cr₂O₃.Al₂O₃ are used as catalyst type materials. Nanoparticles of these oxides were prepared following a similar procedure to that described above. The resulting powder was found to have a BET surface area of about 81 m²/g.

Other Oxide Ceramics

Other ceramic oxide nano-powders prepared using the poly-foam process include doped barium cerate, lithium ferrite, zinc oxide, yttrium oxide, doped lanthanum chromate, 123-superconductor, nickel oxide, and iron oxide.

DISCUSSIONS

It is significant to note that the poly-foam process can be employed to prepare ceramic nanoparticles for a large number of metal oxides. We believe that the ability of the poly-foam process for forming ceramic nanoparticles relies on two important properties of polymeric foams such as polyurethane foams. The first property is the formation of a vastly expanded three

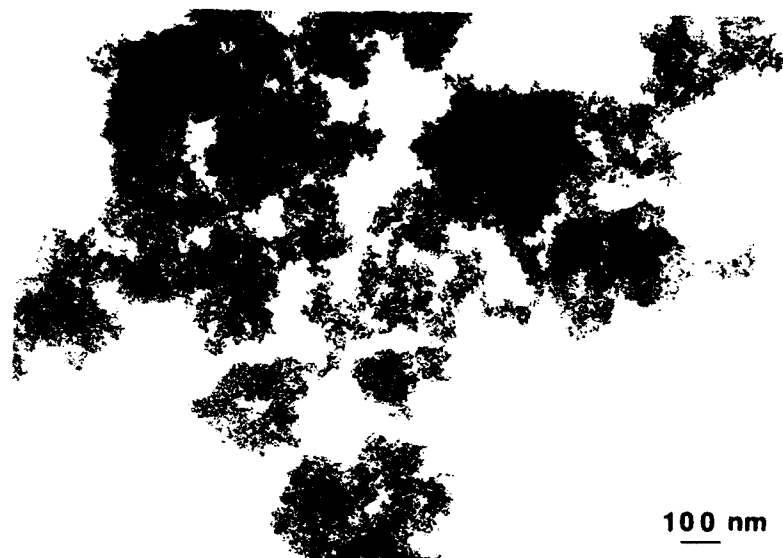


Figure 1 TEM Photograph of Y-ZrO₂ Nanopowder Prepared Using the Poly-Foam Process

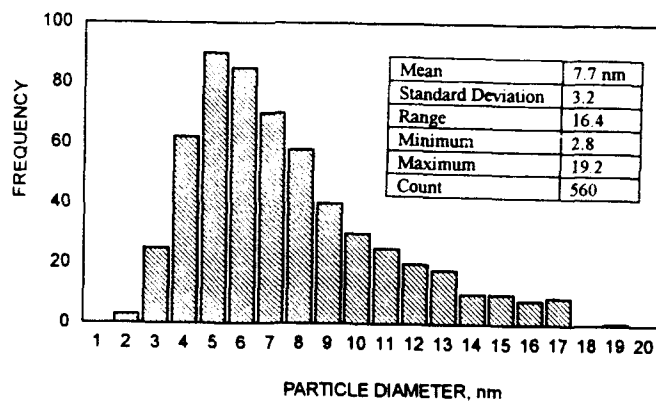
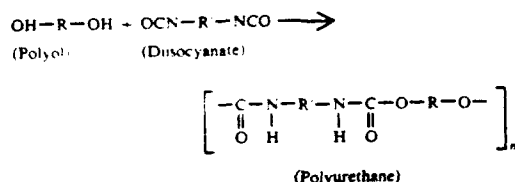


Figure 2 Particle Size Distribution Determined by TEM Analysis of Y-ZrO₂ Nanopowder

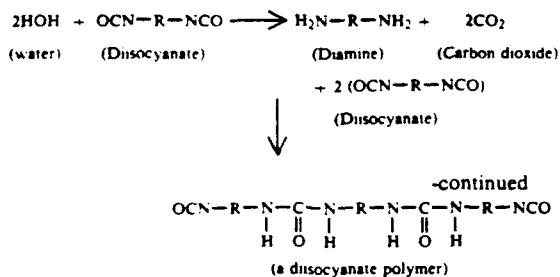
dimensional cellular structure which help to separate metal ions during decomposition and calcination. The second property is the reaction of hydrogen-containing compounds such as water with isocyanate (e.g., forming diamine and carbon dioxide blowing gas), which effectively removes solvent and water that would otherwise be removed by hypercritical evacuation as in the sol-gel process, or by heating as in other wet chemistry processes.

Polyurethanes are chemically complex polymeric materials, usually formed by the reactions of liquid isocyanate components with liquid polyol resin components. The fundamental addition polymerization reaction of diisocyanates with alcohol to produce high polymers was discovered in 1937 by Bayer and his co-workers⁶

Polyurethanes are addition polymers formed by the exothermic reaction of di- or polyisocyanates with polyols in accordance with the following general reaction



After reaction with the polyols, the next most important reaction of isocyanates is with water to yield a substituted urea and carbon dioxide which provides the principal source of gas for blowing in the forming of low density foams. This reaction proceeds in accordance with the following general formula.



It is important to note that water in the system is utilized in the polymerization reactions and, thus, not have to be removed by an extra drying process.

To promote the chemical reaction and permit better control of the foam structure, other chemicals, such as surfactants and catalysts, may be added.

When metal salt solution is added to the polyurethane system, a series of new chemical reactions will occur, which, however, are not fully understood. Nevertheless, it is expected that all hydrogen-containing compounds such as H₂O and alcohol in the metal salt solution will react rapidly with isocyanates. This may explain the fact that the properties of the final powder do not depend significantly on the solvent system. The metal ions, however, could either be chemically bonded to the cross-linked polymeric chains or remained as isolated precipitates physically frozen within the rapidly harden and vastly expanded cellular structure.

It is known that polyurethane foams contain various polyphases⁷. There are discrete hard polymer domains dispersed within a continues soft polymer phase if the water level is low, and

there are also agglomerated polyurea precipitates (polyurea balls) if the water level is high. If the metal ions are not chemically bonded to the polymer chains, they may form groups of precipitates that will be separated by the hard polymer domains and by the agglomerated polyurea precipitates. If this assumption is valid, it is expected that the particle size of the metal oxide nanoparticles will depend on the population of metal ion precipitates in each discrete group.

The hard polymer domains are evenly spaced; the distance is about 65-125 Angstroms. The polyurea balls are also evenly distributed with a separation distance of about 3,000 Angstroms. From these comparative spacing for the morphological feature of polyurethane foam, the particle size of the final powders (between 3 nm and 50 nm) is well anticipated. This hypothesis also suggest that because the hard polymer domains and polyurea balls are evenly distributed in the foam, as a result, the nanoparticles will have a very narrow size distribution. This is indeed observed in our study. It is also clear that if the metal ion loading is low, the population of metal ion precipitates in each discrete group will be small, and thus the final particle size will consequently be small. This is also observed in our experiments.

CONCLUSIONS

A new process has been developed for preparing ceramic nanoparticles. The process utilizes the chemistry of polyurethane reactions and was proven to be effective for preparing nanometer ceramic powders of a great number of single metal oxides and mixed metal oxides. In general, powders prepared by this process have average particle size ranging from 3 to 50 nm, have very narrow particle size distribution, are free of hard agglomeration, are chemically pure and uniform, and are essentially spherical in shape.

ACKNOWLEDGMENT

The authors wish to thank Dr. Y.L. Chen of Lehigh University for her valuable contributions.

REFERENCES

1. R. Dagani, C&EN, November 23, 1992, pp 18-24
2. Brinker, C.J and Scherer, G.W., Sol-Gel Science: The Physics and Chemistry of Sol-Gel Processing, Academic, Boston, 1990.
3. R. W. Siegel, H. Hahn and J.A. Eastman, U.S. Patent No. 5, 128,081 (July 7, 1992).
4. L.A. Chick et al., in Proceedings of the First International Symposium on Solid Oxide Fuel Cells, Vol. 89-11, pp. 171-187.
5. Y.S. Zhen and K.E. Hrdina, U.S. Patent No 5,240,493 (August 31, 1993).
6. O. Bayer, Mod. Plast. 1947, 24, 149-152, 250-262
7. R. Herrington & Kathy Hock eds, in Flexible Polyurethane Foams, Dow Plastics, 1991

THERMAL CONDUCTIVITY REDUCTIONS IN SiGe VIA ADDITION OF NANOPHASE PARTICLES

NANCY SCOVILLE, CLARA BAJGER, JON ROLFE* AND JAN VANDERSANDE**

*ThermoTrex Corporation, Thermoelectrics Department, 74 West Street, Waltham, MA 02254

**Jet Propulsion Laboratory, Thermoelectrics Department, 2800 Oak Grove Drive, Pasadena, CA 91109

ABSTRACT

Transport models have predicted that the thermal conductivity of SiGe alloys could be appreciably reduced by incorporating a discrete 40Å particles with the SiGe grains. Such a thermal conductivity reduction would lead to substantial improvements in the figure-of-merit of thermoelectric materials. This paper reports on recent results on adding 40Å particles to SiGe via a spark erosion process. Thermal conductivity reductions consistent with the transport models have been achieved, however, the improvement in figure-of-merit has not been as large as predicted.

INTRODUCTION

Devices based on the thermoelectric effect have been widely used for power generation in space applications, from the very successful Voyager programs through the current Cassini mission. The performance of thermoelectric materials is quantified in the figure-of-merit, $Z = S^2/\lambda\rho$ where S = Seebeck coefficient, λ = thermal conductivity and ρ = electrical resistivity.

These parameters are interdependent as they are all functions of the carrier concentration; this relationship is illustrated qualitatively in Figure 1. The highest figures-of-merit are achieved for highly doped semiconductors with carrier concentrations in the range of 10^{18} - 10^{21} carriers/cm³. The thermoelectric material most widely used in power generation applications is the high-temperature SiGe alloys. This material can be doped sufficiently and since n- and p- type dopants are available device fabrication is simplified.

Efforts to improve the figure-of-merit have typically focussed on two areas; increasing the electrical power factor (S^2/ρ) by increasing the carrier concentration and decreasing the thermal conductivity by scattering thermal phonons. The thermal conductivity of heavily-doped semiconductors can be separated into two parts, lattice and electronic. The lattice conductivity can be modified by scattering the phonons which transport the heat. In fact, the thermal conductivity of SiGe is appreciably reduced compared to elemental Si and Ge because the mass difference distorts the crystal lattice and scatters short wavelength phonons. Grain boundaries and free carriers are effective at scattering long wavelength phonons. Therefore most of the heat in SiGe alloys is carried by intermediate wavelength phonons. Transport models have predicted that thermal conductivities could be reduced by 40% by adding appropriately sized particles to act as scattering centers for these phonons¹. These particles should be about 50 Å in diameter and the concentration should be close to 10^{16} cm⁻³. These particles must be inside the individual SiGe grains, and not located at the grain boundary. In addition, the SiGe grains must be large

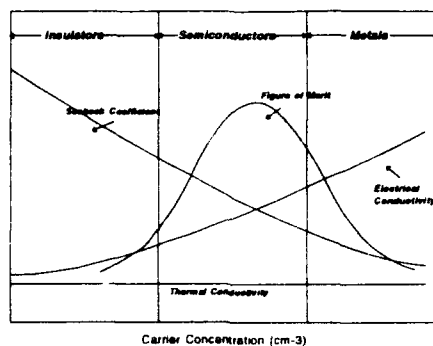


Figure 1. Dependence of Thermoelectric Properties on carrier concentration

enough so that electrons are not scattered by the grain boundaries. The electrons will not be scattered by the 50 Å inclusions located within the grain as a result of their small size relative to the electron mean free path.

In order for the particulate inclusion to be effective the inclusion must be chemically stable in the boron-doped SiGe matrix and thermally stable at 1000C, the maximum use temperature of the thermoelectric device. A variety of materials were evaluated² and BN and B₄C were found to be the most stable. Recent results of these material systems will be the subject of this paper.

EXPERIMENTAL

Nanophase powders of both SiGe and the inert scattering center were fabricated by a spark erosion technique. The spark erosion apparatus has been discussed elsewhere³. The powders were then blended and hot-pressed to form compacts containing 2-10 v/o of the inert particles. High temperature heat treatments were used to grow the SiGe grains to 2 μm while leaving the inert second phase at the initial size. Alternatively, electrodes were first fabricated from a mixture of SiGe and the inert addition. The electrode would then be eroded to produce the powder blend in one step. The powder was then hot-pressed and heat treated.

Seebeck coefficient and electrical resistivity were measured simultaneously from room temperature to 1000C Thermal conductivity was measured using a flash diffusivity technique to measure both diffusivity and heat capacity⁴.

RESULTS AND DISCUSSION

SiGe samples were prepared with 2-6 v/o BN. The boron nitride was prepared by eroding polycrystalline boron rods in a nitrogen atmosphere. Heat treating at 1275C for a minimum of 200 hrs was required to grow the SiGe grains to more than 2 μm. The BN particles did not grow

and were well distributed in the SiGe grains as shown by the TEM micrograph in Figure 2. The concentration of BN particles in this sample was about 2 v/o. The thermal conductivity was reduced without degradation of the power factor resulting in an increase in the average Z , integrated over 600 - 1000C, of 20% over baseline material. The Seebeck coefficient, electrical resistivity, thermal conductivity and figure-of-merit are shown plotted in Figure 3 as a function of temperature with baseline values³ plotted for comparison.

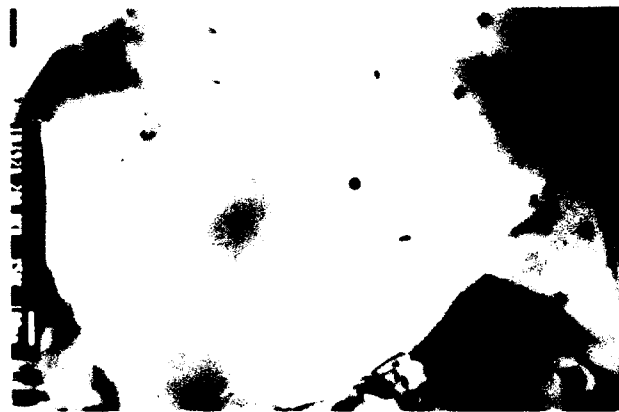


Figure 2. TEM micrograph of SiGe grain containing BN inclusions (dark spots in photo)

While these results were intriguing, attempts to add higher concentrations of BN resulted in samples with low mobility and low figure-of-merit. In these samples, the SiGe grains did not grow to sufficient size even after extensive heat treatment. It was believed that this may have either been due to unreacted or incompletely reacted boron acting to pin the SiGe grain boundaries or to agglomeration of the BN prior to incorporation in the SiGe matrix.

Boron carbide was chosen to as an alternative to boron nitride. Boron carbide would be stable in the SiGe matrix and since it's semi-metallic, the boron carbide could be incorporated into the SiGe electrode so that the matrix and inclusion could be eroded together and separation of the two components minimized.

While evaluating this material system, significant discrepancies were found in the room temperature electrical resistivity relative to the pressing direction. Because this difference was larger than could be expected from just high temperature quenching effects (boron exhibits retrograde solid solubility in SiGe), it appeared as if the sample was geometrically anisotropic. Subsequent examination of the microstructure revealed a highly anisotropic structure with very long and narrow grains similar to stacked plates observed in the perpendicular directions as shown in Figure 4.

This geometrical anisotropy of an otherwise isotropic material leads to a significantly higher mobility and lower electrical resistivity in the perpendicular direction. This anisotropy has only been observed with samples fabricated from spark-eroded powder. Conventional SiGe alloys as well as fine-grained mechanically-alloyed SiGe exhibit a isotropic crystalline morphology.

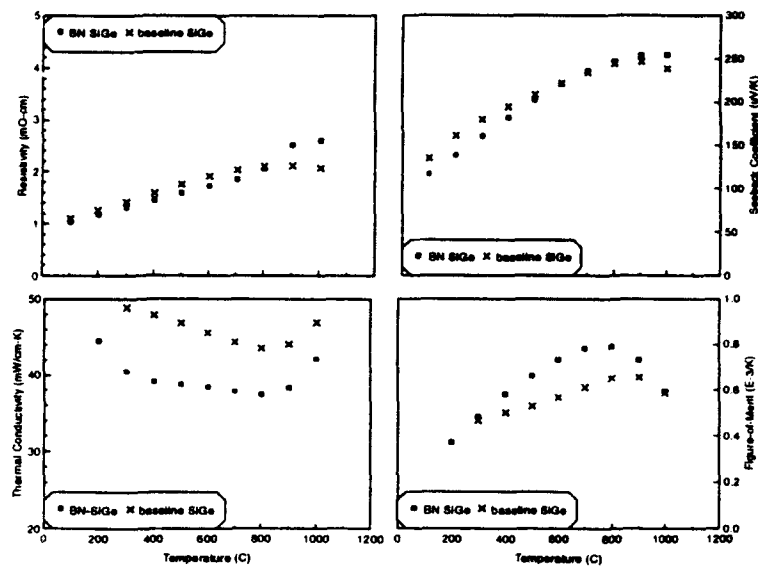


Figure 3. Thermoelectric properties of BN-SiGe sample compared to conventional SiGe material

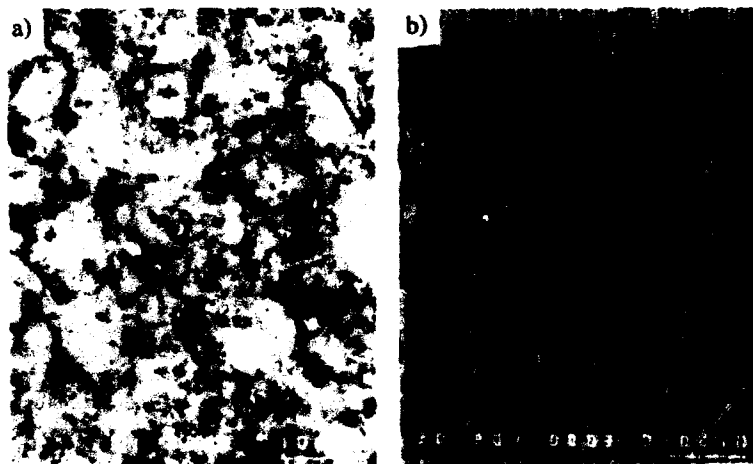


Figure 4. SEM micrographs of B_4C SiGe showing structural anisotropy (a) parallel; (b) perpendicular

Because the mobility is the main transport property affected by the anisotropy, the ratio between electrical resistivities in the parallel and perpendicular directions is translated almost directly into the figure-of-merit. While this result is encouraging and suggests that improvements may be made by taking advantage of this anisotropy in device fabrication, the overall performance of the boron carbide system was not as high as the best BN-SiGe samples. Figure 5 illustrates the resulting relative increase in Z for a typical boron carbide sample. The maximum Z increased from $0.4 \times 10^{-3} \text{ K}^{-1}$ to $0.57 \times 10^{-3} \text{ K}^{-1}$. The low figure-of-merit could be attributed to reduced mobility even in the perpendicular direction when compared to standard SiGe.

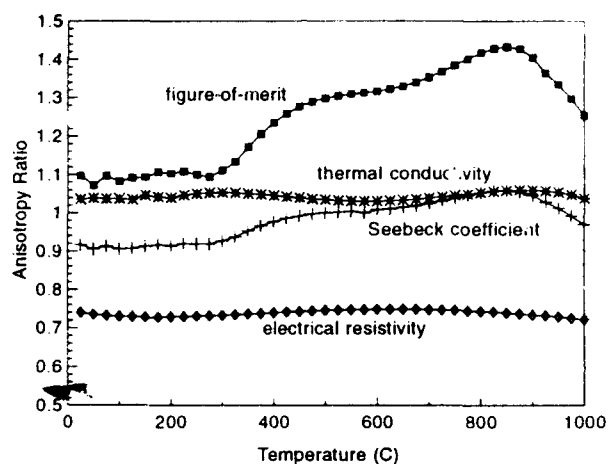


Figure 5. Perpendicular to parallel anisotropy ratio for as-pressed B_4C -SiGe sample

These results prompted a re-evaluation of the BN system. Samples were fabricated using the blended electrode technique developed for the B_4C system. The thermoelectric properties for an as-pressed BN-SiGe sample measured in the perpendicular direction is shown in Figure 6. The integrated average value of $0.58 \times 10^{-3} \text{ K}^{-1}$ is comparable to the baseline material. However, the thermal conductivity is appreciably reduced compared to standard size, hot pressed material. Since this result is for as-pressed material, further improvements can be expected after the sample is annealed and the grain size is increased.

CONCLUSION

Systematic and theoretical studies have resulted in reproducible improvements in the figure-of-merit of p-type SiGe. Several scattering centers have been shown to be effective in reducing the

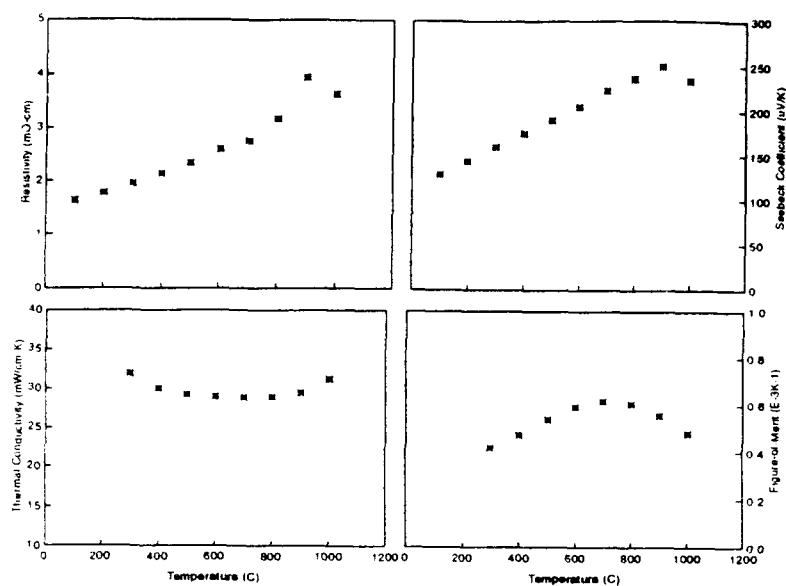


Figure 6. Thermoelectric properties for as-pressed BN-SiGe sample measured perpendicular to pressing direction

thermal conductivity. Addition of nanophase BN has succeeded in increasing the integrated average figure-of-merit to $0.7 \times 10^{-3} \text{ K}^{-1}$. The unexpected occurrence of geometrical anisotropy

in these systems suggests that higher Z's may be obtained when the processing parameters have been fully defined.

ACKNOWLEDGEMENTS

The authors would like to thank P. G. Klemens for many helpful discussions. Part of this work was performed at the Jet Propulsion Laboratory under contract with NASA. Work at TTC was supported by NASA/DoE under the SP-100 program.

REFERENCES

1. Klemens, Paul G., Mar. Res. Soc. Symp. Proc., **434**, 87 (1991).
2. Scoville, N., Bajgar, C., Rolfe, J., Fleuriel, J-P, and Vandersande, J., Proc. XIth Symp. Space Nucl. Power Systems, Albuquerque, NM, **2**, 505 (1994).
3. Beaty, J.S., Rolfe, J.L. and Vandersande, J.W., Proc. of 25th Int. Energy Conv. Eng. Conf., Reno, NV, (2) 379 (1990).
4. Vandersande, J.W., Zoltan, Al, and Wood, C., Int'l J. Thermophys. **10**, 251 (1989).
5. Bajgar, C., Masters, R., Scoville, N., and Vandersande, J., Proc. 8th Symp. Space Nucl. Sys., Albuquerque, N.M., **1**, 440 (1991).

MOLECULAR SIEVE THIN FILMS VIA LASER ABLATION

KENNETH J. BALKUS, JR. *, SCOTT J. RILEY* AND BRUCE E. GNADE**

*University of Texas at Dallas, Department of Chemistry,
Richardson, TX 75083-0688

**Materials Science Laboratory, Semiconductor Research and Development,
Texas Instruments, Inc., Dallas, TX 75265

ABSTRACT

Laser ablation has become widely recognized as an effective technique for the preparation of thin solid films. We have employed an excimer laser (KrF, 248 nm) to deposit well dispersed thin films of aluminum phosphate molecular sieves on a titanium nitride substrate. Results for the ablation of $\text{AlPO}_4\text{-5}$, $\text{AlPO}_4\text{-H3}$ and $\text{AlPO}_4\text{-H1}$ molecular sieve targets are presented. The laser power and repetition rate as well as substrate distance and temperature affect the thin film formation. A subsequent hydrothermal post treatment of the ablated films was found to enhance the surface crystallinity. The molecular sieve thin films were characterized by XRD, SEM, XRF, and FT-IR spectroscopy.

INTRODUCTION

Molecular sieves constitute a special class of low density crystalline metal oxides having well defined micropores [1]. These materials are attractive as the adsorbing phase in chemical sensors because of the shape selectivity imparted by the uniform pore systems. Zeolite molecular sieve based surface acoustic wave (SAW) devices [2] as well as piezoelectric quartz crystal microgravimetric type sensors [3-5] have shown promise in selectively detecting organic molecules. In these cases, thin film configuration is generally a ceramic composite or the zeolites are tethered to the electrode surface via organic linkages. The sensing ability of these devices depends on a weight change. A measure of the change in zeolite electronic properties upon adsorption of target molecules might prove more selective. An interdigitized capacitor type sensor which employed a thin Y type zeolite coating as the dielectric has been reported [6,7]. A change in zeolite dielectric constant was measured upon adsorption of different molecules. Unfortunately, the sensitivity of this device was rather poor. This is not too surprising since capacitance depends inversely on the distance between the electrodes which suggests that exceptionally thin dielectric films would be

required to register large capacitance changes. Additionally, zeolites are ionic conductors and consequently poor dielectrics. We proposed that very thin films of a neutral lattice molecular sieve such as an aluminum phosphate, might form the basis for a sensitive and selective capacitance type chemical sensor. Therefore, we initiated an effort to develop different strategies towards the preparation of uniform AlPO_4 molecular sieve thin films in the nanometer range.

Zeolites have been crystallized onto various metal substrates during synthesis [8-10] where the zeolites reportedly stick to the surfaces quite well. We explored the deposition of AlPO_4 molecular sieves onto a titanium nitride surface during crystallization. The resulting crystals adhered well to the TiN but were too large and not evenly dispersed. It quickly became apparent that we could not control thickness or surface coverage by this method.

The growth of thin films by laser induced evaporation or ablation has been well established for high density metal oxides [11]. Depending upon the deposition conditions this technique may involve equilibrium and/or non-equilibrium processes. Laser ablation offers many advantages over evaporation and sputtering methods. Although, laser ablation has not been applied to low density phases, we felt it might be possible to deposit a continuous film of molecular sieve with a controlled thickness by this technique. In this paper, we report our preliminary results for the laser ablation of AlPO_4 molecular sieves onto a TiN substrate. The nature of the ablated films was found to vary with laser pulse repetition rate, substrate temperature and chamber atmosphere. Partially crystalline films with a thickness of 20nm to $>1\mu\text{m}$ were prepared from AlPO_4 -5, AlPO_4 -H1 and AlPO_4 -H3. The films were characterized by XRD, XRF, SEM and IR spectroscopy. It was discovered that a brief hydrothermal treatment after ablation dramatically improved the surface crystallinity. We propose that the ablated surface is composed largely of molecular sieve fragments that reorganize under hydrothermal conditions that would not normally result in bulk crystals.

EXPERIMENTAL

Molecular sieve AlPO_4 -5 was prepared using tripropylamine as a template under conditions previously published [1]. Molecular sieves AlPO_4 -H1 and AlPO_4 -H3 were prepared without an organic structure directing agent as previously described [12]. AlPO_4 targets for laser ablation were prepared by pressing ~1 gram of molecular sieve in a 1" die. The set up for laser ablation of the molecular sieves is shown schematically in figure 1. A Questek 2000 KrF (248 nm) excimer laser generated a beam with a power density of 10^6 W cm^{-2} . Laser pulse energies of 50mJ to 400 mJ with pulse repetition rates of from 1 to 80 pulses sec⁻¹ were employed in this study. The

beam was reduced to a diameter of 1.7 cm before it was reflected off a computer controlled rastering mirror. The rastering mirror allowed us to move the beam across the target instead of ablating material from a single spot. The beam was reduced further by a 10" focal length convex lens to a 1mm size spot on the target (power density = 10^8 Wcm^{-2}). The beam enters the vacuum chamber through a quartz window and contacts the target mounted at an angle of 35° relative to the beam. The substrate (TiN (100nm) coated silicon wafer) was mounted on a heated stage below the target at varying distances. Substrate temperatures over the range of 150 to 350C were studied. Ablation of the target molecular sieves generated a visible plume of material that varied in size, shape and color depending upon the experimental conditions. The vacuum chamber was also equipped with a gas manifold and pressure gauge.

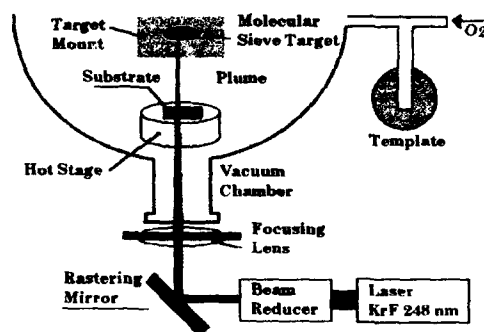


Figure 1. Over head view of setup for laser ablation experiments.

X-ray diffraction patterns were recorded using a Scintag XDS 2000 diffractometer with a scan rate of 1 deg min^{-1} and a chopper increment of 0.01. Scanning electron micrographs were obtained using a JEOL JSM 840A SEM. Diffuse reflectance infrared spectra were measured with a Nicolet FT-IR equipped with a Nic Plan IR microscope. Thickness and Al/P ratios were determined from XRF data using a Rigaku 3550 WD XRF spectrometer.

RESULTS AND DISCUSSION

We previously observed the laser ablation of dense phase $\text{AlPO}_4\text{-H4}$ resulted in partially crystalline thin films of AlPO_4 tridymite and orthorhombic AlPO_4 [13]. It was encouraging that the ablated films exhibited crystallinity which is probably not the result of splatter since the thin film phases were different than the target. Therefore, we initiated a series of

ablation studies using the low density molecular sieve $\text{AlPO}_4\text{-5}$ as the target material. Figure 2 shows a typical SEM of a $\text{AlPO}_4\text{-5}$ film ~500nm thick that was prepared with a laser pulse energy of 350 mJ and a repetition rate of 4 pulses sec^{-1} . Although, the surface morphology lacks any well defined edges the XRD pattern indicates the presence of $\text{AlPO}_4\text{-5}$. This film is most likely composed of molecular sieve fragments that are aluminum rich. The Al/P weight ratio of the ablated surface is typically in the range of 1.4 to 1.8 as determined by XRF and is fairly independent of laser energy (150-350mJ) or



Figure 2. Scanning electron micrograph of an ablated $\text{AlPO}_4\text{-5}$ film.

pulse rate (1-16). The thickness increases only slightly with pulse energy but dramatically increases with increasing pulse repetition rate. This is expected since at higher pulse rates the beam heats up a more localized area which in turns generate more fragments. Low repetition rates (1-4 pulses sec^{-1}) generally result in partial crystallinity for the $\text{AlPO}_4\text{-5}$ surface, whereas higher repetition rates result in formation of tridymite or amorphous films. The thickness also increases with ablation time and decreases with target distance. The film shown in Figure 2 was prepared after 5 minutes at a distance of 1.3 cm. The addition of O_2 (0.08 torr) to the chamber during ablation increases the deposition of material. This effect has been noted before in the ablation of metal oxides, such as superconductors [14]. In contrast, the addition of tripropylamine (template) to the TiN substrate totally inhibits deposition while TPA vapor hinders film growth. The FT-IR spectra of $\text{AlPO}_4\text{-5}$ ablated material indicate the presence of TPA template whenever the substrate temperature was $<250^\circ\text{C}$. Higher substrate temperatures decompose the amine. The presence of template inside the molecular sieve does not appear to have an impact on the ablation process.

In order to enhance the surface crystallinity the ablated films were subjected to a post hydrothermal treatment. Figure 3 shows the SEM for a

100 nm film (prepared at a pulse energy of 250 mJ and a repetition rate of 1 pulse sec^{-1} for 4 min) that was heated at 150C for 24 hours in a teflon lined bomb containing an AlPO_4 gel mixture designed to prepare $\text{AlPO}_4\text{-5}$ ($\text{Al}_2\text{O}_3\text{:P}_2\text{O}_5\text{:H}_2\text{O:TPA}=1\text{:1:40:1}$). During this period the morphology changes from amorphous looking spheres to a crater like relief with edges that are much more apparent. The XRD pattern indicates a highly crystalline pure phase $\text{AlPO}_4\text{-5}$ with an Al/P weight ratio of 0.68. The thickness of this film is

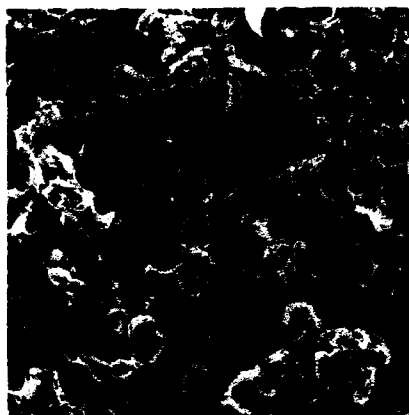


Figure 3. Scanning electron micrograph of ablated $\text{AlPO}_4\text{-5}$ after hydrothermal treatment in an AlPO_4 gel for 24 hours.

971 nm which is much too thick for the sensor application. However, thickness can be controlled by shortening the reaction time.

The nature of the initial target is quite important for the behaviour of the ablated films during hydrothermal treatment. For example, an ablated film prepared from $\text{AlPO}_4\text{-H3}$, was heated in a gel designed for $\text{AlPO}_4\text{-5}$ for 4 hours resulting in a highly crystalline $\text{AlPO}_4\text{-H3}$ surface. In contrast, an ablated film made from an amorphous AlPO_4 target, treated under the same conditions, was converted to an $\text{AlPO}_4\text{-5}$ and $\text{AlPO}_4\text{-H1}$ surface. In both cases, the bulk gels produced a mixture of phases. This implies that the ablated molecular sieve film that is largely amorphous to XRD, seeds the surface and reorganizes under hydrothermal conditions that might not otherwise produce that phase. This is supported further by the fact that blank TiN substrates treated under the same conditions are amorphous after 4 hours. Additionally, ablated films from calcined $\text{AlPO}_4\text{-5}$ targets (i.e. template free) treated in the same $\text{AlPO}_4\text{-5}$ gel results in films composed of at least 4 different phases. This can be compared with ablated films containing TPA template where only pure phase $\text{AlPO}_4\text{-5}$ is observed after hydrothermal

treatment. $\text{AlPO}_4\text{-H3}$ and -H1 do not require a template to form such that at extended heating times lead to mixtures of these two phases. However, at short times (<2 hours) pure phase $\text{AlPO}_4\text{-H1}$ or H3 can be generated from the corresponding ablated films while the bulk remains amorphous.

In conclusion, it appears that laser ablation is a viable method for the deposition of partially crystalline AlPO_4 molecular sieve thin films. Hydrothermal treatment of the ablated films lead to enhanced crystallinity. This suggests the ablated surfaces composed largely of molecular sieve fragments reorganize and seed the gel mixtures. A report of a "memory" associated with the reactivity of amorphous films obtained from sputtered zeolites is consistent with our observations [15]. Laser ablation appears to be a viable method for the preparation of molecular sieve thin films that have potential applications as chemical sensors, membranes and catalysts.

ACKNOWLEDGMENTS

We wish to thank the National Science Foundation (CHE-9157014) and Texas Instruments, Inc. for financial support of this work.

REFERENCES

1. R. Szostak, *Molecular Sieves*, (Van Nostrand Reinhold, NY, (1992).
2. K. Brown, T. Bein, G.C. Frye and C.J.Brinker, *J. Am. Chem. Soc.* **111**, 7640 (1989).
3. Y.Yan and T. Bein, *Mater. Res. Soc. Symp. Proceed.* **233**, 175 (1991).
4. Y.Yan, and T. Bein, *J. Phys. Chem.* **96**, 9387 (1992).
5. Y.Yan and T. Bein, *Chem. Mater.* **4**, 975 (1992).
6. K. Alberti, J. Haas, L. C. Plog and F. Fetting, *Catal. Today* **8**, 509 (1991).
7. J. Haas, C. Plog and E. Obermeier, *Eur. Patent No.* 426,989 A1 (1991).
8. S. P. Davis, E. V. R. Borgstedt, S. L. Suib, S. Chun, C. Jinghui, X. Wenyang and X. Feng., *Chem. Mater.* **2**, 712 (1990).
9. K. E. Creasy, Y. P. Deng, J. Park, E. V. R. Borgstedt, S. P. Davis, S. L. Suib and B. R. Shaw, *Mater. Res. Soc. Symp. Proceed.* **233**, 157 (1991).
10. L. Jianquan, D. Jinxiang, L. Guanghuan, S. Yanjun, C. Jinghui, X. Wenyang and W. Feng., *React. Kinet. Catal. Lett.* **47**, 287 (1992).
11. J.T. Cheung and H. Sankur, *CRC Crit. Rev. Solid State Mater. Sci.* **5**, 63 (1989) and references there in.
12. B. Duncan, M. Stocker, D. Gwinup, R. Szostak and K. Vinje, *Bull. Soc. Chim. Fr.* **129**, 98 (1992).
13. K. J. Balkus, Jr., S. J. Riley and B. E. Gnade, manuscript in prep.
14. L. Lynds, B.R. Weiberger, T.M.Potrepka, G.G.Peterson and M.P.Lindsay, *Physica C* **159**, 61 (1989).
15. I. Boszormenyi, T. Nakayama, B. McIntyre and G. A. Somorjai, *Catal. Lett.* **10**, 343 (1991).

NANOSTRUCTURED Fe-Co CATALYSTS GENERATED BY ULTRASOUND

KENNETH S. SUSLICK*, MINGMING FANG, TAEGHWAN HYEON,
AND ANDRZEJ A. CICHOWLAS

School of Chemical Sciences and Materials Research Laboratory,
University of Illinois at Urbana-Champaign, 505 S. Mathews Ave., Urbana, IL 61801

ABSTRACT

Bimetallic catalysts have been studied intensively because of their unique activity and selectivity. Unsupported alloy catalysts, however, are usually of limited value due to their very small surface areas. We have now developed a sonochemical synthesis of bimetallic alloys that provides both high surface areas and high catalytic activity. We have produced Fe-Co alloys by ultrasonic irradiation of mixed solutions of $\text{Fe}(\text{CO})_5$ and $\text{Co}(\text{CO})_2(\text{NO})$ in hydrocarbon solvents. The alloy composition can be controlled simply by changing the ratio of precursor concentrations. After treatment at 673K under H_2 flow for 2 hours, we obtain nearly pure alloys. BET results show that the surface areas of these alloys are large (10-30 m^2/g). TEM and SEM show that the alloy particles are porous agglomerates of particles with diameters of 10-20 nm. Sonochemically prepared Fe, Co, and Fe-Co powders have very high catalytic activity for dehydrogenation and hydrogenolysis of cyclohexane. Furthermore, sonochemically prepared Fe-Co alloys show high catalytic selectivity for dehydrogenation of cyclohexane to benzene; the 1:1 ratio alloy has much higher selectivity for dehydrogenation over hydrogenolysis than either pure metal.

INTRODUCTION

In recent years, numerous researchers have explored the use of bimetallic catalysts for heterogeneous catalytic processes [1-3]. Bimetallic iron-containing alloys have held special interest because of their industrial applications. Most of the studies in this area have been done on oxide-supported bimetallic catalysts because the usual methods of preparation do not give sufficient surface areas to be effective catalysts. Several studies show that supported Fe-Co catalysts have greater activity and different selectivity for CO hydrogenation [4-5]. We have developed a new technique for the synthesis of high surface area metal alloys, and we have examined the catalytic activity Fe-Co alloys for alkane reforming.

High intensity ultrasound is a new tool for the synthesis of nanostructured metals and alloys through the sonochemical decomposition of volatile organometallic precursors (e.g., $\text{Fe}(\text{CO})_5$, $\text{Co}(\text{CO})_2(\text{NO})$) [6-8]. The chemical effects of ultrasound originate from hot spots formed during acoustic cavitation (the formation, growth, and collapse of bubbles in a liquid) [9-10]. Sonochemically prepared Fe, Co, and Fe-Co alloys have high surface areas even after heat treatment by H_2 at high temperatures, and they are therefore suitable for heterogeneous catalytic studies. We chose to examine the reforming reactions of cyclohexane in order to test the catalytic properties of these Fe-Co alloys on surface-structure sensitive catalytic reactions: i.e., dehydrogenation versus hydrogenolysis.

EXPERIMENTAL

Iron pentacarbonyl was used as received from Strem Chemicals without further purification. Tricarbonylnitrosylcobalt was synthesized by the reaction of dicobalt octacarbonyl with *in situ* generated nitrogen monoxide [11]. Pentane was distilled over sodium-benzophenone, decane was distilled over sodium, and both were stored inside an inert atmosphere box (Vacuum Atmospheres, < 1 ppm O₂). A solution of Fe(CO)₅ and Co(CO)₃(NO) in dry decane was irradiated at 273K with a high-intensity ultrasonic probe (Sonics & Materials, Model VC-600, 0.5 in. Ti horn, 20 kHz, 100 W/cm²) for 3 hours under argon. After irradiation, a black powder was formed, which was filtered and washed with dry pentane in the glove box.

X-ray powder diffraction (XRD) data was collected on a Rigaku D-Max diffractometer using monochromatic Cu K_α radiation. Scanning electron micrographs (SEM) were taken on a Hitachi S800 electron microscope. Transmission electron micrographs (TEM) and energy-dispersive analysis of X-ray spectroscopy (EDX) were taken on a Phillips EM 400T electron microscope. Surface compositions of the catalysts were determined with a Perkin-Elmer Phi 5400 X-ray photoelectron spectrometer (XPS) using a magnesium K_α X-ray source. All sample preparations and transfers for XRD, TEM-EDX, and XPS measurements were done without exposure to air.

The Fe-Co alloys prepared by ultrasound initially contain some carbon, hydrogen, nitrogen and oxygen, which most likely arise from the decomposition of the alkane solvent and carbon monoxide and nitrogen monoxide during ultrasonic irradiation [12-13]. Hydrogen (99.99%, Linde) was further purified through 5A molecular sieves and an oxy-trap (Alltech). The original Fe, Co, and Fe-Co alloys were heated under a H₂ flow at 673K for 2 hours. After the heat treatment, elemental analysis results showed that essentially pure Fe, Co and Fe-Co alloys were prepared. All results and discussions are based on the samples after heat treatment unless otherwise specified.

A specially designed gas-solid microreactor capable of both static manometric and flow GC/MS analyses was used for both adsorption and catalytic studies. The catalysts were transferred from an inert gas box to the catalysis rig without exposure to air. Surface areas were calculated by applying the BET equation to the N₂ adsorption isotherm measured at 77 K.

The cyclohexane (99+%, Fisher) was dried over molecular sieves prior to use. A MKS mass flow controller maintained a flow of hydrogen (27.5 cm³(STP)/min) to carry cyclohexane vapor at a constant partial pressure of 0.09 atm through the catalyst bed. The cyclohexane reaction products (benzene and aliphatic hydrocarbons) were analyzed with a gas chromatograph (Hewlett-Packard 5730A) equipped with a n-octane/Porasil C column and a flame ionization detector.

RESULTS AND DISCUSSION

Synthesis and characterization

Because the sonochemical reactions take place mostly inside the cavitation bubbles in a liquid [9-10], a good precursor should have a substantial vapor pressure. Fe(CO)₅ and Co(CO)₃(NO) were chosen because of their high vapor pressures at modest bulk solution temperatures where they are still thermally stable. The composition of the Fe-Co alloys can be controlled simply by changing the ratio of solution concentrations of the precursors. All composition ranges can be produced by this method. The plot of Fe-Co product composition versus precursor composition is shown in Figure 1.

The solid-solution nature of the alloys was confirmed by TEM-EDX results, which were made on different spots of the polycrystalline alloy powders. The EDX results show that the alloys are homogeneous on a nanometer scale.

The original Fe, Co, and Fe-Co alloys produced by ultrasound are amorphous, as described elsewhere [6-8]. After heat treatment under H₂ gas flow at 673K for 2 hours, all samples underwent crystallization.

The XRD results (Figure 2) show no peaks attributable to iron/cobalt oxide, iron/cobalt carbide or other iron/cobalt impurity phases. Pure Fe crystallizes to cubic (bcc) structure, pure Co crystallizes to cubic (fcc) and hexagonal (hcp) mixed structures. All the alloys that we have tested so far crystallize in the bcc structure. These XRD results are consistent with the known Fe-Co equilibrium phase diagram [14].

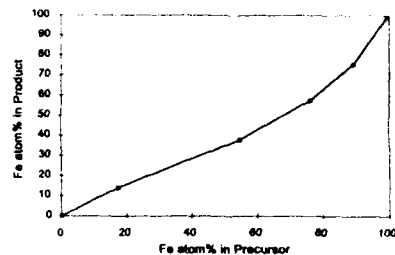


Figure 1. Sonochemical preparation of Fe-Co alloys. Composition of alloy versus solution precursor concentrations.

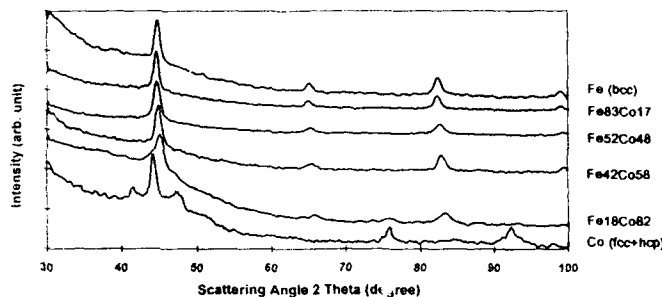


Figure 2. The X-ray diffraction patterns of sonochemically prepared Fe, Co, and Fe-Co alloys after heat treatment and crystallization (673K, H₂, 2 hrs).

The surface areas of the metals and alloys after heat treatment are summarized in Table 1. After the heat treatment under H₂ gas flow at 673K for 2 hours, the sonochemically prepared Fe-Co alloys still have large surface areas. Elemental analysis results show that nearly pure metal and alloys are produced. SEM at high magnification indicates that these materials are porous aggregates of small clusters of 10-20 nm particles.

Table 1. Surface areas of Fe, Co, and Fe-Co alloys (after heat treatment).

Sample	BET(m ² /g)
Fe	12.1
Fe ₈₃ Co ₁₇	22.2
Fe ₅₂ Co ₄₈	30.6
Fe ₄₂ Co ₅₈	24.0
Fe ₁₈ Co ₈₂	21.3
Co	12.6

Table 2. Surface and bulk Fe/Co ratio (after heat treatment).

Sample	Fe/Co (Bulk)	Fe/Co (Surface)
Fe ₈₃ Co ₁₇	4.88	5.32
Fe ₅₂ Co ₄₈	1.22	1.45
Fe ₄₂ Co ₅₈	0.724	0.757
Fe ₁₈ Co ₈₂	0.220	0.254

Surface electronic structures and surface compositions of the sonochemically prepared Fe-Co alloys were also examined by using x-ray photoelectron spectroscopy (XPS). The XPS measurements have been performed on heat treated samples before catalytic reactions. The electronic structures of these samples appear to be the same as the pure metals (Fe^0 or Co^0 on the surfaces). The surface compositions of the alloys demonstrate some enrichment of Fe over Co (Table 2). Similar trends towards an iron-enriched surface have been reported by other researchers with other preparations using coprecipitation methods [15].

Catalytic studies

The cyclohexane dehydrogenation and hydrogenolysis reactions were carried out in a continuous flow system. All catalysts were treated under H_2 gas flow at 673K for 2 hours before the catalytic studies. The catalytic activity (in terms of turnover frequency of cyclohexane molecules converted to benzene per surface Fe/Co atom per second) as a function of temperature is shown in Figure 3. Two kinds of products were formed during the cyclohexane reaction: benzene is the only dehydrogenation reaction product and aliphatic hydrocarbons (mostly methane) are the hydrogenolysis reaction products. The catalytic selectivity (in terms of the percentage of benzene among all the reaction products) as a function of temperature is shown in Figure 4.

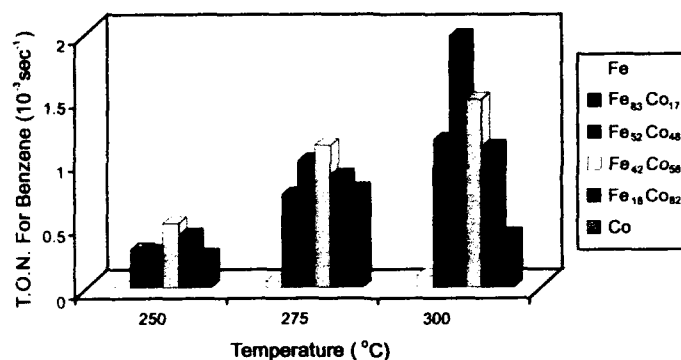


Figure 3. The catalytic activity of Fe, Co, and FeCo alloys for dehydrogenation of cyclohexane to benzene as a function of temperature.

The catalytic properties of the sonochemically prepared Fe, Co and Fe-Co alloys in the cyclohexane reaction exhibit interesting trends. First, they are all active catalysts for cyclohexane conversion: pure Co has the highest activity (albeit primarily for hydrogenolysis), pure Fe has the lowest activity, and Fe-Co alloys have intermediate activity between pure Fe and pure Co. Second, Fe-Co alloys generate much more dehydrogenation product (benzene) than pure Fe or Co. Third, the 1:1 ratio alloys have both much higher dehydrogenation activities and selectivities at all reaction temperatures (250 $^{\circ}\text{C}$ to 300 $^{\circ}\text{C}$) than the other alloys or pure metals. In the best cases, the selectivity for dehydrogenation approaches 100%.

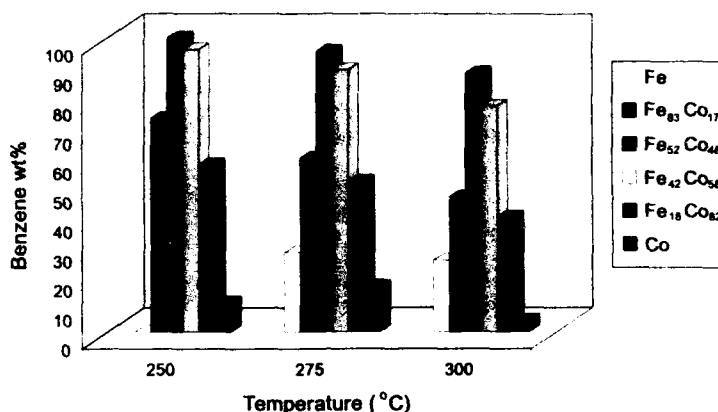


Figure 4. The catalytic selectivity of Fe, Co, and Fe-Co alloys for dehydrogenation versus hydrogenolysis of cyclohexane as a function of temperature.

It is generally assumed that geometric (or ensemble) and electronic (or ligand) effects are decisive factors in controlling the catalytic properties of alloys [1, 16]. The 'electronic effect' concept is based on the assumption that the nature and the strength of a chemical bond between an adsorbate atom and a surface atom (one kind of metal) are influenced by the neighbors (another kind of metal) of that surface atom. There are only a few examples known of bimetallic catalysts where ligand effects dominate selectivity. For all the sonochemically prepared Fe-Co alloys, the XPS results show that the surface electronic states are indistinguishable between the alloys and pure Fe or Co. The XRD results also show that the Fe-Co alloys have the same bulk crystalline structure. It seems likely that the 'ensemble effect' is responsible for the high selectivity of the 1:1 ratio alloys. Further experiments using chemisorption and temperature-programmed desorption are underway to probe such mechanistic questions.

CONCLUSIONS

We have developed a new and effective way to generate nanostructured metal (Fe and Co) and alloys (Fe-Co) by using high intensity ultrasound to decompose volatile organometallic precursors ($\text{Fe}(\text{CO})_5$ and $\text{Co}(\text{CO})_3(\text{NO})$). The sonochemically prepared Fe-Co alloys have large surface areas relative to bulk metal even after heat treatment. We find very high catalytic activity for these Fe, Co, and Fe-Co powders for the dehydrogenation and hydrogenolysis of cyclohexane. The sonochemically prepared Fe-Co alloys show high catalytic activity for the dehydrogenation of cyclohexane to benzene, with 1:1 ratio Fe-Co alloys having selectivities as high as 100%.

ACKNOWLEDGMENTS

This work was supported by National Science Foundation. We thank Ms. Peggy Mochel, Dr. Richard T. Haasch, and the UIUC Center for Microanalysis of Materials, supported by The US Department of Energy, for their assistance in the TEM and XPS studies.

REFERENCES

1. J. H. Sinfelt, in Metal-Metal Bonds and Clusters in Chemistry and Catalysis, edited by J. P. Fackler, Jr. (Plenum Press, New York, 1990), p.103. J. H. Sinfelt, Bimetallic Catalysts: Discoveries, Concepts, and Applications (Wiley, New York, 1983).
2. I. Guzzi, *Res. Chem. Intermediates* **15**, 199 (1991).
3. I. Khomenko, N. Kutyreva, A. Kadushin, Y. Maksimov, and V. Matveev, *J. Mol. Catal.* **56**, 61 (1989).
4. K. B. Arcuri, L. H. Schwartz, R. D. Piotrowski, and J. B. Butt, *J. Catal.* **85**, 349 (1984).
5. T. Ishihara, K. Eguchi, and H. Arai, *Appl. Catal.* **30**, 225 (1987).
6. K. S. Suslick, M. W. Grinstaff, A. A. Cichowlas, and S. B. Choe, *Nature* **353**, 414 (1991); *Ultrasonics* **30**, 168 (1992).
7. M. W. Grinstaff, M. B. Salaman, K. S. Suslick, *Phys. Rev. B* **48**, 269 (1993).
8. M. W. Grinstaff, A. A. Cichowlas, S. B. Choe, K. S. Suslick, *Ultrasonics* **30**, 168 (1992).
9. K. S. Suslick, *Science* **253**, 1397 (1991).
10. K. S. Suslick, Ed. *Ultrasound: Its Chemical, Physical, and Biological Effects*, VCH Press, New York, 1988.
11. R. Job, J. Rovang, *J. Syn. React. Inorg. Metal-Org. Chem.* **6**, 367 (1976).
12. E. B. Flint, K. S. Suslick, *J. Am. Chem. Soc.* **111**, 6987 (1989).
13. K. S. Suslick, J. W. Gawienowski, P. F. Schubert, and H. H. Wang, *J. Phys. Chem.* **87**, 2299 (1983).
14. T. Nishizawa, K. Ishida, *Bull. Alloy Phase Diagrams* **5**, 250 (1984).
15. M. Nakamura, B. J. Wood, P. Y. Hou, and H. Wise in Proceedings, 7th International Congress on Catalysis, Tokyo, (Kodansha Ltd., Tokyo, 1981), p.432.
16. W. M. H. Sachtleir, *J. Mol. Catal.* **25**, 1 (1984).

SUBWAVELENGTH LOCALIZATION OF OPTICAL MODES IN FRACTALS

VLADIMIR SHALAEV*, R. BOTET**, M. MOSKOVITS***

*Department of Physics, New Mexico State University, Las Cruces, New Mexico 88003

**Laboratoire de Physique des Solides, Université Paris-Sud, Centre d'Orsay,
91405 Orsay CEDEX, France

***Ontario Laser and Lightwave Research Centre, and Department of Chemistry, University of
Toronto, M5S 1A1 Canada

ABSTRACT

Resonant optical excitation of fractal clusters generates dipolar eigenmodes which are extremely localized within areas much smaller than the wavelength. The localization occurs due to the fractal morphology and accounts for the very high local fields leading to the huge enhancement of various optical effects. In particular, Rayleigh and Raman light scattering and, especially, nonlinear optical processes, such as 2-photon photoemission and degenerate four-wave mixing, are strongly enhanced in fractal clusters. The spatial distribution of the modes shows the frequency and polarization selectivity.

The localization of dipolar eigenmodes can lead to a dramatic enhancement of many optical effects in fractals [1]. The scaling theory of collective dipole excitations developed in Refs. [2-7] predicts, in particular, that there are extremely localized modes in fractal clusters which concentrate electrical energy in regions smaller than the wavelength [2,3]. Such the localization occurs due to the fractality and is not found in non-fractal solids. It is this localization of optical excitations in fractal clusters that account for the very high local fields leading to the huge enhancement of resonant Rayleigh, Raman and, especially, of nonlinear light scattering [5,6]. In addition to the localization of light-induced dipole excitations fractality can result in the localization (trapping) of the light itself within a range of the order of a wavelength [7]. An important property of the interaction of light with fractals is the very strong frequency and polarization dependence of the spatial location of the light-induced dipole modes. In this paper we present numerical simulations of the localized optical modes. Our direct experimental observations of the optical modes on silver colloid fractal clusters with subwavelength resolution will be published elsewhere [8].

If the polarizability χ_0 (note, we use notation χ for the polarizability rather than for the susceptibility) of particles forming a cluster possesses a resonance at ω_0 , then at laser frequency ω close to ω_0 , a strong interaction between light-induced dipolar moments of the particles occurs. This requires consideration of collective dipolar modes in a fractal cluster. The total cluster polarizability can be presented in this case as follows [2,4]

$$\chi_{\alpha\beta} = \sum_i \chi_{i,\alpha\beta} = \sum_n a_{n\alpha} \chi_{n,\beta}, \quad \chi_{n,\alpha} = a_{n,\alpha} [(v_n - X) - i\delta]^{-1}, \quad a_{n\alpha} = \sum_i (i\alpha | n). \quad (1)$$

where v_n and $|n\rangle$ are the eigenvalues and eigenfunctions of the operator of dipole-dipole interaction \hat{V} among particles, $\chi_{n,\alpha}$ is the polarizability associated with the n -th mode that contributes to the total polarizability with the weight $a_{n\alpha}$ and $i = 1, 2, 3, \dots, N$. Here $N = (R_c/R_n)^D$ is the number

of particles in a fractal cluster, D is the fractal dimension, R_c and R_0 are the radius of gyration and a typical separation between nearest neighbour particles in the cluster, respectively. In Eq. (1), $X \equiv -R_c \chi_0^{-1}$ is the "frequency" parameter (in the vicinity of the resonance $X \propto (\omega - \omega_0)$), and $\delta \equiv -Im\chi_0^{-1}$ is the decay constant, which is small for a resonance with high quality-factor $Q = (R_0^3 \delta)^{-1}$. As follows from Eq. (1), when the frequency variable X is close to one of the eigenvalues e_n of the interaction operator, the corresponding mode gives the resonant contribution to the polarizability.

The interaction \hat{V} includes in general the near-zone (nonradiative), transitional and far-zone (radiative) terms of the dipole field. However, it was shown in [5] that if $R_0^3|X| \gg (R_0/\lambda)^{3-D}$ for $D < 2$ and if $R_0^3|X| \gg (R_0/\lambda)X^{1-2/D}$ for $D > 2$, then particles positioned at distances $r_{ij} \sim \lambda$ and $r_{ij} \gg \lambda$ from a given monomer, i , contribute negligibly to the local field acting on this monomer. In this case one can reduce \hat{V} to the Hermitian near-zone dipole-dipole interaction operator [5]

$$(i\alpha|\hat{V}|j\beta) = \begin{cases} \{\delta_{\alpha\beta} - 3n_{\alpha}^{(i)}n_{\beta}^{(j)}\}r_{ij}^{-3}, & \text{if } kr_{ij} < 1, i \neq j, \\ 0, & \text{otherwise.} \end{cases} \quad (2)$$

As was shown in [2,4] the dipole eigenmodes are localized on fractals within correlation length L_X given by

$$L_X \sim R_0(R_0^3|X|)^{(d-1)/(3-D)} \quad (3)$$

where d is an index called the optical spectral dimension ($0 < d < 1$) [2]. Formula (3) was obtained by assuming that collective excitations of coherence length L_X are invariant with respect to the scale transformation $R_0 \rightarrow R'_0$ due to the self-similarity [2]. In accordance with Eq. (3) there are non-contained and weakly-localized modes in the vicinity of the center of the absorption contour (small values of $R_0^3|X|$) and there are also strongly localized modes which are located towards the wings ($R_0^3|X| \sim 1$). For the most strongly localized modes $L_X \sim R_0 \ll \lambda$ (R_0 is of an order of the size of the particles forming a cluster and typically it is much less than the wavelength λ).

Note, that the localization of dipole excitations on fractals is a nontrivial fact. Since the dipole-dipole interaction for compact aggregates ($D \rightarrow 3$) is long range, dipole modes are generally delocalized over the entire cluster in non-fractal solids.

Below we present numerical simulations of local fields due to excitation of the localized dipole modes on fractal clusters. These modes have been recently observed by means of photon scanning tunneling microscopy (PSTM) [8]. By operating in the near-zone of the dipole fields PSTM can overcome the traditional diffraction limit thereby imaging details smaller than the wavelength [9].

We will calculate the squared modulus of the local field (the intensity) which is the sum of the external field of amplitude $E_{\alpha}^{(0)}$ and the fields of the dipoles with amplitudes $d_{\alpha}^{(i)} = \chi_{\alpha\beta}^{(i)} E_{\beta}^{(0)}$ induced in the particles forming the cluster. The intensity is given by:

$$I = |E_{\alpha}^{(0)} + \sum_j V_{\alpha\beta}^{(i)} \chi_{\beta\gamma}^{(j)} E_{\gamma}^{(0)}|^2. \quad (4)$$

The results of our numerical simulation of the intensity distribution, $I(x, y, z = z_0)$, of local fields due to the excitation of dipole eigenmodes on fractal aggregates are shown in Figure 1.

A 3-dimensional cluster with $N = 512$ was generated assuming cluster-cluster aggregation [10] ($D \approx 1.78$). The 3-D cluster was collapsed to its 2-dimensional projection simulating closely the experimental situation of the PSTM imaging [8]. The dipole excitations and local fields values were calculated using equations (1)-(2) and (4), and assuming the following parameter

values: $\delta = 0.01$, ($R_0 \approx 1$), $z_0/R_m = 2$ where R_m is the radius of particles and $\lambda/R_m = 50$.

The figure shows $I(x, y)$ at two values of the light frequency and for both, s and p , polarizations. Note that the intensity of local fields strongly fluctuates and it is significantly larger than the external field in spatially localized regions of the cluster.

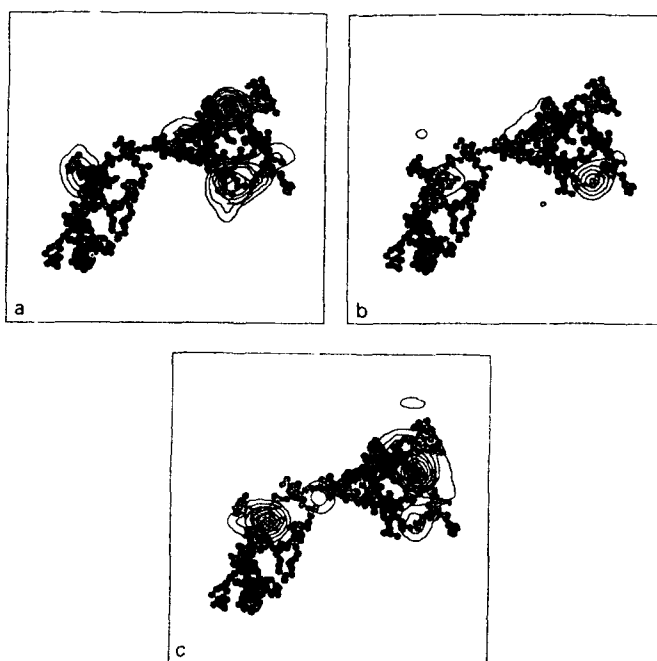


Fig. 1:

Local field intensity, $I(x, y)$, of the light-induced dipole modes calculated for a fractal aggregate.

A) and B): $X = -0.1$, s - and p -polarizations, respectively; C): $X = -0.25$, s -polarization.

The linear dimension of the high-local-field regions in Fig. 1 varies from mode to mode. On average a mode spans several hundred \AA when $R_m = 100\text{\AA}$. The frequency and polarization sensitivity of the mode localization is evident in Figure 1: a change of either light frequency (parameter X) or polarization results in the excitation of new resonant modes with different spatial locations and intensities.

Fractal clusters resulting from cluster-cluster aggregation of colloid particles are random. Their scale-invariance is statistical. Spatial localization of light-induced dipole modes and their sensitivity to polarization and frequency should also be observed on geometrically ordered fractals. Fig. 2 shows $I(x, y)$ for Vicsek cluster, using parameters similar to those used previously to

generate Fig.1 except that $\lambda/R_m = 25$. Again, strong localization of the optical excitations is evident.

Interestingly, there is no symmetry in the positions of the light-induced eigenmodes despite the high symmetry of the Vicsek fractal. The symmetry breaking results from the incommensurate structure of the light field with respect to that of the cluster. Specifically it is the introduction of the two vectors, $\vec{E}^{(0)}$ and \vec{k} , together with the tensor character of the dipole-dipole interaction that breaks symmetry

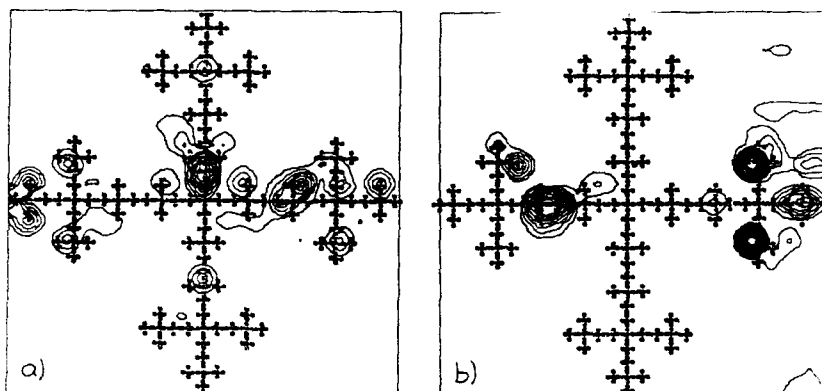


Fig. 2: Local field intensity, $I(x, y)$, of the light-induced dipole modes on a Vicsek fractal. A) and B): s-polarization, $X = -0.1$ and $X = -0.25$, respectively.

As was shown above dipole eigenmodes on fractals "produce" small regions of very high energy density and therefore, they act in some sense similar to optical lenses. Since the modes on fractals are mostly due to the dipole-dipole interaction in the near-zone the localization length is significantly, smaller than the wavelength. Thus the excitation of the resonant modes should lead to extremely high local fields resulting in its turn in giant enhancement of many optical processes on fractals.

Local fields, E_l , of the resonant modes exceed the external one, $E^{(0)}$, by quality-factor Q which, for example, for silver colloid clusters is $\sim 10^2$. The fraction of monomers involved into resonant excitation is small, $\sim Q^{-1}$, and therefore, linear optical processes are not ultimately enhanced (note, however, that for metal aggregates this conclusion is restricted to the visible and the near-infrared portion of the spectrum when one can neglect the Ohmic current in comparison with the displacement current). For nonlinear optical process, $\propto |E|^n$, one obtains [1,6]

$$\langle |E_l/E^{(0)}|^n \rangle \sim Q^n \times Q^{-1} \sim Q^{n-1} \gg 1 \quad (5)$$

where the angle brackets denote averaging over ensemble of clusters. The estimation (5) is valid, in general, for systems with inhomogeneous broadening. In the case of fractals inhomogeneous broadening occurs due to the spatial localization of modes in small areas of a cluster which have different local structures and therefore are characterized by different eigenfrequencies. Thus, the localization of dipolar modes, inhomogeneous broadening of the spectrum and the enhancement of optical processes in fractals are mutually connected properties in optics of fractals.

The enhancement, G , of optical processes due to aggregation of initially isolated particles into fractal cluster can be presented in general as

$$G \sim Q^m F(R_0^3|X|) \quad (6)$$

where m is an integer and F is a function of dimensionless parameter $R_0^3|X|$. Using the model of randomly decimated (diluted) fractals [2] it was shown that F has power-law dependence [5]:

$$G \sim Q^m (R_0^3|X|)^{d_0+m} \quad (7)$$

for Rayleigh ($m = 1$) and Raman ($m = 3$) scattering. For the cluster-cluster aggregation the optical spectral dimension d_0 is 0.3 [5]. In particular, formula (8) describes well the experimentally observed spectral dependence of surface-enhanced Raman scattering (SERS) on silver colloid aggregates [5]. The largest enhancement is expected for nonlinear light scattering like degenerate four-wave mixing (DFWM). In this case one obtains [5]:

$$G \sim Q^6 (R_X^3|X|)^{2d_0+6}. \quad (8)$$

The experimentally observed enhancement of DFWM on silver fractal colloids [6] is in qualitative agreement with that predicted by (8).

To conclude, in agreement with the theoretical predictions our numerical simulations demonstrate the strong spatial localization of the resonant eigenmodes in a fractal cluster and their frequency and polarization selectivity. The results of the simulations are similar to our experimentally observed PST images (which will be published elsewhere [8]) of the localized modes in silver fractal colloid clusters. This verifies the main concept predicted for the resonant optics of fractals [1-7] and explains the giant enhancement of optical processes in fractals.

REFERENCES

- [1] V.M.Shalaev, M.I.Stockman, Zh.Eksp.Teor.Fiz. **92**, 509 (1987) [Sov.Phys.JETP **65**, 287 (1987); Z.Phys.D-Atoms, Molecules and Clusters **10**, 71 (1988); A.V.Butenko, V.M.Shalaev, M.I.Stockman, Zh.Eksp.Teor.Fiz. **94**, 107 (1988) [Sov.Phys.JETP **67**, 60 (1988)]; Z.Phys.D-Atoms, Molecules and Clusters **10**, 81 (1988).
- [2] V.A.Markel, L.S.Muratov, M.I.Stockman, Zh. Eksp. Teor. Fiz. **98**, 819 (1990) [Sov. Phys. JETP **71**, 455 (1990)]; V.A.Markel, L.S.Muratov, M.I.Stockman, & T.F.George, Phys. Rev. B **43**, 8183 (1991).
- [3] F.Claro, R.Fuchs, Phys.Rev.B **44**, 4109 (1991); K.Ghosh, R.Fuchs, Phys.Rev.B **44**, 7330 (1991); I.H.Zabel & D.Stroud, Phys.Rev.B **46**, 8132 (1992).
- [4] M.I.Stockman, T.F.George, & V.M.Shalaev, Phys. Rev. B **44**, 115 (1991); V.M.Shalaev, R.Botet, A.V.Butenko, Phys.Rev. B **48**, 6662 (1993).
- [5] V.M.Shalaev, R.Botet, & R.Jullien, Phys. Rev. B **44**, 12216 (1991); **45**, 7592(E) (1992); M.I.Stockman, V.M.Shalaev, M.Moskovits, R.Botet, & T.F.George, Phys. Rev. B **46**, 2821 (1992); V.M.Shalaev, M.I.Stockman, & R.Botet, Physica A **185**, 181 (1992).
- [6] S. G. Rautian, V. P. Safonov, P. A. Chubakov, V. M. Shalaev, M. I. Stockman, Pis'ma Zh. Eksp. Teor. Fiz. **47**, 243 (1988) [JETP Lett. **47**, 243 (1988)]; A. V. Butenko, P. A. Chubakov, Yu. E. Danilova, S. V. Karpov, A. K. Popov, S. G. Rautian, V. P. Safonov, V. V. Slabko, V. M. Shalaev, M. I. Stockman, Z. Phys. D Atoms, Molecules and Clusters **17**, 283 (1990).
- [7] V.M.Shalaev, M.Moskovits, A.A.Golubentsev, & S.John, Physica A **191**, 352 (1992).
- [8] D. P. Tsai, J. Kovacs, Martin Moskovits, Vladimir Shalaev, J. S. Suh, and R. Botet, Phys. Rev. Lett., submitted.
- [9] E.Betzig & J.K.Trautman, Science **257**, 189 (1992).
- [10] R.Jullien & R.Botet, Aggregation and Fractal Aggregates (World Scientific, Singapore, 1987).

DEVELOPMENT AND CHARACTERIZATION OF ARTIFICIAL MICROSTRUCTURES IN LONG LENGTHS OF SUPERCONDUCTING WIRE

P. D. Jablonski†, P. J. Lee, and D. C. Larbalestier†

Applied Superconductivity Center and †Department of Materials Science and Engineering, University of Wisconsin-Madison, 1500 Johnson Drive, Madison, Wisconsin 53706.

ABSTRACT

Conventional Nb-Ti superconductors are optimized by thermal and mechanical treatments which ultimately produce a nanostructure consisting of 1-2nm thick ribbons of α -Ti dispersed in a matrix of β -Nb-Ti. Several groups are now investigating artificial dispersions of second phase in Nb-Ti which may develop stronger flux pinning nanostructures. However, these new methods generally require true strains of 30 or more. We avoid these large strains (and their associated problems) by forming our composites from a mixture of $\sim 50\mu\text{m}$ size Nb and Nb-Ti powders, thus permitting the desired nanostructure to be produced with strains of order 12. Nb pinning particles were found to develop an irregular shape, tending to nanometer thick ribbons at large strains. The final size nanostructure resembles conventional Nb-Ti, except that the "second" phase is Nb rather than α -Ti. The critical current density (J_c) was found to increase by over two orders of magnitude to peak values of 5490 and 1980 A/mm² at 2 and 5T as the particle thickness was reduced.

INTRODUCTION

The level of critical current density (J_c) in conventionally processed niobium-titanium is dependent upon the amount of second phase that can be produced [1]. Unfortunately, thermodynamic and kinetic restrictions limit the amount of second phase attainable to $\sim 20\text{vol}\%$. Several investigators [2-6] have attempted to introduce the second phase artificially to overcome these limitations (thus these conductors are described as artificial pinning center (APC) conductors). In the majority of these conductors, handling considerations require that the second phase be quite large (a few mm dia.) at billet assembly. Unfortunately, this means that the composite requires a large fabrication strain ($\epsilon = 2 \ln(D_o/D_f)$, where D_o and D_f are the initial and final diameters respectively) in order to reduce the second phase to its optimum size which is comparable to or less than the superconducting coherence length (ξ), $\sim 5\text{nm}$. Typically strains on the order of 30 are required for a hand-assembled APC conductor, versus about 12 to optimize conventional Nb-Ti. In fact, most attempts at developing APC conductors have experienced fabrication problems, largely as a result of the extreme mechanical deformation required. However, if the initial size of the second phase is on the order of tens of microns, then the strain needed is only on the order of 12-16, and some of the fabrication difficulties should be avoided. Powder Metallurgy (PM) is one way to introduce a micron-sized second phase.

EXPERIMENTAL DETAILS

Many of the details of the billet fabrication are contained in our U.S. patent [7], and only the variations specific to this work will be given here. A 20vol%Nb billet was fabricated from 15g Nb and 40g Nb-55wt%Ti powders which were blended and pressed into a $15.9 \times 12.7\text{mm}$

Table I: Powder chemical analysis.

Powder	Analyzed values (ppm)			
	H	N	O	C
Nb-55wt%Ti	8	220	1120	80
Nb	8	30	670	< 30

(OD×ID) copper extrusion can. The billet was evacuated to $< 10^{-5}$ Pa, sealed and hydrostatically extruded at 250C with an area reduction ratio of 25. The composite rod was drawn into 1.5mm diameter wire and cut into 85 pieces. The copper was etched off before rebundling the filaments into a second extrusion can. This bundled filament conductor was re-extruded and then drawn into wire having diameters down to 80 μ m.

The microstructure was characterized in transverse cross section using SEM secondary electron and backscatter imaging techniques; TEM techniques were used on the finer scale structures. Transparencies were placed on 200×250mm prints; tracings were made of the Nb particle outline and these were scanned into a computer-based image analysis system in order to determine Nb particle area, perimeter and thickness, as outlined below. The superconducting critical current density (J_c) measurements were made on wires from the original monofilament, as well as from the bundled (85) filament conductor. A resistivity criterion of $10^{-14}\Omega m$ was used to determine the critical current (I_c), and the voltage taps were set 33cm apart[8]. The superconducting area was found by a weigh and etch technique: both the Nb pinning centers and the Nb-Ti matrix were included in the area which was used to calculate J_c from I_c .

RESULTS

Two different types of starting powders were used; PREP (Plasma Rotating Electrode Process) Nb-55wt%Ti for the matrix and hydride-grind-dehydride (HGD) Nb for the pinning center. The starting powder shapes are quite different due to their different fabrication. Being melted to shape[9], the matrix powder (Figure 1) was slightly rough but spherical. Cross sections revealed a dendritic structure with perhaps some unmelted regions. The individual PREP powder particles are apparently single grained. The HGD Nb pinning center powder was angular in shape (Figure 1) owing to the mechanical grinding used to powder the material. The Nb powder was polycrystalline, typically containing a few grains per particle. According to Table I, the oxygen content of Nb-55wt%Ti powder was 1120ppm, within the range common for Nb-55wt%Ti ingots. However, the 670ppm seen in the Nb is about an order of magnitude higher than normally obtained in ingot Nb. The oxygen content did not appear to adversely affect the drawability of the composite.

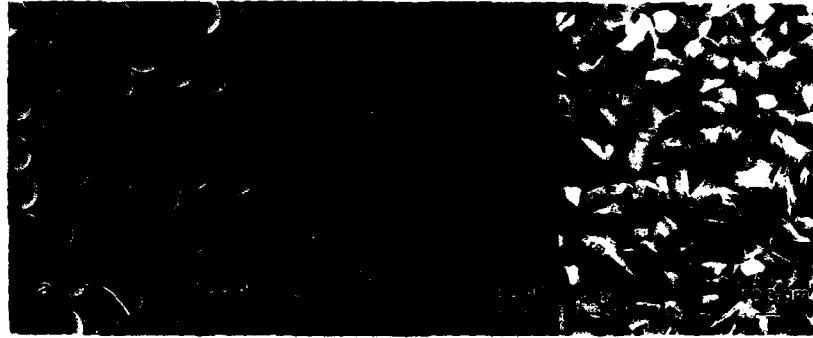


Figure 1: Secondary electron image of the PREP Nb-55wt%Ti powder used as matrix material (a), backscatter electron image of a PREP powder cross section after etching lightly (b), and secondary electron image of the hydride-grind-dehydride Nb powder used for the pinning centers (c).

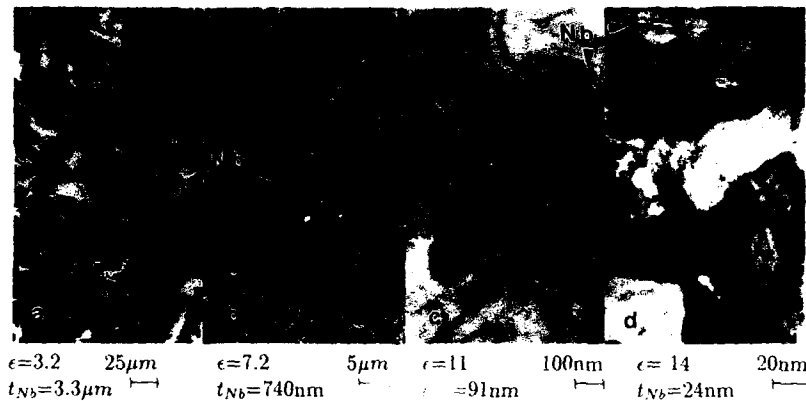


Figure 2: Secondary electron SEM micrographs (a and b) and TEM images (c and d) showing the change of size and shape of the 20vol%Nb APC conductor as a function of strain.

Figure 2 shows the microstructure as a function of strain. At a strain of $\epsilon \sim 3.22$, the Nb particles have developed a highly aspected ribbon morphology and are quite variable in size (Nb particle cross sections ranged from $7\text{-}720\mu\text{m}^2$), especially when compared to the starting powder (Figure 1, $\sim 90\%$ of the powder was $45\text{-}75\mu\text{m}$). The Nb particles became more uniform in size and the ribbon shape more pronounced as wire drawing strain increased (Figure 2b). Beyond $\epsilon \sim 7$ the Nb particles were no longer fully resolvable in our SEM. Figure 2c and 2d show TEM images of the nanostructure at strains of ~ 11 and ~ 14 . An interesting feature of the final nanostructure is that grain boundaries are not constrained to either the Nb or Nb-Ti and can pass from one to another.

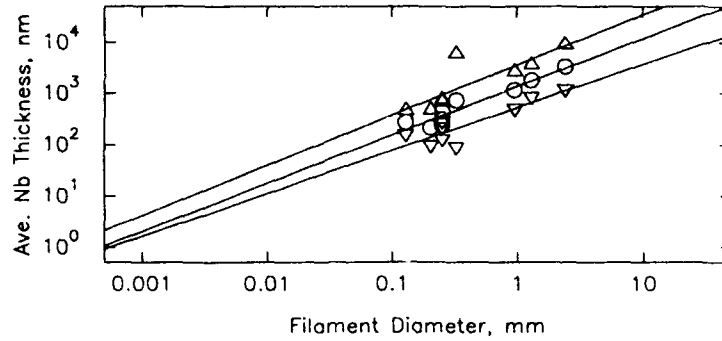


Figure 3: Calculated Nb particle thickness (t_{Nb}) vs. filament diameter for the Nb55wt%Ti + 20vol%Nb conductor.

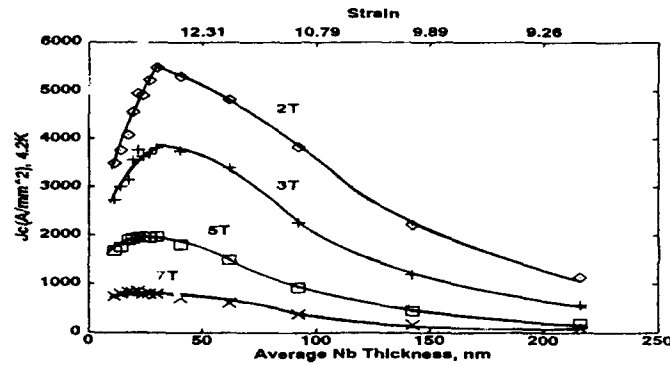


Figure 4: Critical current density vs. calculated Nb pinning center thickness and measured fabrication strain.

Figure 3 plots the average Nb particle thickness (t_{Nb}) vs. the superconducting filament diameter (d , which is based on the original monofilament diameter). The thickness was calculated from the measured Nb particle areas (A) and perimeters (p) using a rectangular model for the particles. This model is equivalent to performing a shape transform on the irregular Nb ribbons. Such a calculation returns the *average* thickness of the particles and is similar to several standard characterization techniques [10]. The average particle thickness is calculated from:

$$t = \frac{p - \sqrt{p^2 - 16A}}{4} \quad (1)$$

A linear (log-log) extrapolation was made to estimate t_{Nb} as the composite reached peak J_c because direct SEM measurements were not possible due to the nanometer scale microstructure.

The superconducting critical current density as a function of ϵ and t_{Nb} is given in Figure 4. Peak J_c values were reached within a strain of about 13.5 ($t_{Nb} \sim 30$ nm) with a

$J_{c,max}$ at 2T of 5490 A/mm² and a $J_{c,max}$ at 5T of 1980 A/mm². A sharp peak in J_c vs. strain was observed at 2T; however, a gradual "softening" of this peak occurred as the field was increased, until a peak was barely observable at 7T.

DISCUSSION

By using the PM approach we have been able to produce a nanometer scale artificial pinning center microstructure in a reduced strain space. The intrinsic superconducting properties of these conductors are strongly related to their microstructure [11]. Both Nb-Ti and Nb are bcc metals which develop a (110) texture during extrusion and wire drawing. Unfortunately, the (110) texture provides only 2 active slip directions during wire drawing, and individual grain deformation must occur in a plane strain, rather than axisymmetric mode [12, 13]. As a result, grains become highly aspected and inter-curl in order to provide a macroscopically uniform deformation (see Figure 2). Heussner et al. [14] showed that the initial grain size plays a major role in controlling the shape instability of Nb-foil-wrapped Nb-Ti rods, and Cooley et al. [15] showed that the overall particle shape could be maintained, at least down to 100nm diameter, in a gunbarrel drilled Nb-Ti/Nb APC composite by starting with fine grained materials. Indeed, it was shown that the pinning center shape in Cooley's composite could be *destroyed* within a strain of 1-2 after a recrystallization heat treatment if the resulting grain size was too large [16]. Consequently, grain size is a critical factor in determining the particle shape that results from axisymmetric deformation of Nb-Ti/Nb composites.

Unlike an earlier PM APC composite [17] containing 40vol%Nb in which the J_c values were compromised by broken filaments, the present conductor showed no sign of broken filaments, or of longitudinal filament irregularity (sausaging). Thus the present results represent an opportunity to determine the "intrinsic" flux pinning characteristics in Nb-Ti. While good superconducting properties were obtained, it does appear that further improvements are possible. One factor which may control the properties is the breadth of the distribution of Nb pinning center thicknesses which results in a similar breadth in the elementary pinning forces (f_p) between the individual vortices and pins. The $t_{Nb} \pm 2\sigma$ values varied by nearly a factor of 5 at the optimized J_c wire size (Figure 3). As Cooley et al. [18] showed, a broad distribution in f_p results in increased flux pinning at low fields at the expense of flux pinning at high fields. This is consistent with the behavior observed: the high field J_c for this alloy is in any case less than that in Nb-47wt%Ti because the upper critical field is $\sim 2T$ lower. Thus further improvement in high field J_c can be obtained by minimizing the distribution in t_{Nb} and increasing the upper critical field to that comparable to Nb-47wt%Ti.

Acknowledgments: This work has been supported by the Department of Energy - Office of High Energy Physics. Special thanks to F. Fox of Naples Research and Manufacturing for advice on hydrostatic extrusion and to P. Roberts and I. Donahue of Nuclear Metals, Inc. for donating the Nb-55wt%Ti powder.

REFERENCES

- [1] P. J. Lee, J. C. McKinnell, and D. C. Larbalestier, *Adv. Cryo. Eng. (Materials)* **36** 287 (1989).
- [2] G. L. Dorofeyev, F. Y. Klimenko, S. V. Frolov, E. V. Nikulenkov, E. I. Plashkin, N. I. Salunin, and V. Y. Filkin, in *Proc. of 9th Inter. Conf. on Magnet Technology*, ed. by C. Marinucci and P. Weymuth, pp 564-566, 1985.
- [3] K. Matsumoto, H. Takewaki, Y. Tanaka, O. Miura, K. Yamafuji, K. Funaki, M. Iwakuma, and T. Matsushita, *Appl. Phys. Lett.* **64** 115 (1994).
- [4] J. M. Seuntjens and D. C. Larbalestier, *IEEE Trans MAG* **27** 1120 (1990).
- [5] B. Zeitlin, M. Walker and L. Motowidlo, US Patent No. 4,803,310, (February 7, 1989).
- [6] R. M. Scanlan, A. Lietzke, J. Royet, A. Wandesforde, C. E. Taylor, J. Wong and M. K. Rudziak. To appear in *Proc. of 13th Inter. Conf. on Magnet Technology* (1993).
- [7] P. D. Jablonski and D. C. Larbalestier, US Patent No. 5,226,947, (July 13, 1993).
- [8] C. Meingast, and D. C. Larbalestier, *J. Appl. Phys.* **66** 5971 (1989).
- [9] A. R. Kaufmann, US Patent No. 3099041 (July 30, 1963), and US Patent No. 3802816 (April 9, 1974).
- [10] J. C. Russ, *Computer-Assisted Microscopy: The Measurement and Analysis of Images*, (Plenum Press, NY), 175-218 (1990).
- [11] C. Meingast, P. J. Lee, and D. C. Larbalestier, *J. Appl. Phys.* **66** 5962 (1989).
- [12] W. F. Hosford Jr., *Trans. AIME* **12** 12 (1964).
- [13] J. C. Malzahn-Kampe and T. H. Courtney, *Scripta Met.* **23** 141-145 (1989).
- [14] R. W. Heussner, P. D. Jablonski, P. J. Lee, and D. C. Larbalestier, to appear in *Adv. Cry. Eng.* **40** (1994).
- [15] L. D. Cooley, P. J. Lee, P. O'Leary, D. C. Larbalestier, *Appl. Phys. Lett.* **64** 1298 (1994).
- [16] L. D. Cooley, and P. D. Jablonski, unpublished work UW-Madison, (1991).
- [17] P. D. Jablonski, P. J. Lee, and D. C. Larbalestier, *Appl. Phys. Lett.* (1994) (submitted).
- [18] L. D. Cooley, G. Stejic, and D. C. Larbalestier, *Phys. Rev. B* **46** 2964 (1992).

Author Index

- Abrazov, M., 43
 Adams, W. Wade, 233, 239
 Andow, Mark, 97
 Akelah, A., 91, 163
 Åklint, Thorbjörn, 299
 Amonlirdviman, K., 251
 Andersson, Mats, 15, 299
 Ansell, Michael A., 171
 Avalos-Borja, M., 287

 Baer, E., 91, 163
 Bajger, Clara, 431
 Balasubramanian, Mahalingam, 195
 Balkus, Jr., Kenneth J., 263, 437
 Baraton, Marie-Isabelle, 381
 Barker, J.G., 319
 Barrera, E.V., 375
 Bertran, E., 405
 Bescher, Eric P., 135
 Besnainou, Sylvette, 381
 Blaisten-Barojas, Estela, 343
 Bley, Richard A., 129, 275
 Bonnemant, Helmut, 3
 Botet, R., 449
 Brioux, Werner, 3
 Buchko, Christopher, 413
 Budnick, J.L., 195
 Burdon, Jeremy, 103
 Burnam, Kimberly J., 21

 Calvert, Paul, 103
 Campbell, Angela L., 239
 Cannon, W.R., 207
 Carpenter, Joseph P., 21
 Carrier, Michael J., 343
 Cavanagh, R.R., 189
 Chaiken, J., 355
 Chang, W., 363
 Chen, Junghuei, 57
 Chow, Gan Moog, 67, 109
 Cichowlas, Andrzej A., 201, 443
 Cooper, Thomas M., 233, 239
 Costa, J., 405
 Costa, Necessio, 97
 Coster, Dominique J., 157
 Crane, Robert L., 239
 Cruz, J., 287

 Dantorth, S.C., 363
 Davis, Jeffrey E., 129, 275
 Day, Victor W., 177
 Del Valle, M., 287
 Dortman, B., 43
 Du, Shou Ming, 57
 Duvail, David J., 129

 Eberspacher, Todd A., 177
 Eisele, I., 393
 El-Shall, M. Samy, 369

 Erb, U., 337

 Fang, Mingming, 201, 443
 Fehlaue, G., 393
 Ferguson, Gregory S., 419
 Ferreira, M., 325
 Freihaut, James D., 147
 Friedlander, Sheldon K., 331
 Fripiat, Jose J., 157
 Fuentes, S., 287

 Galasso, Francis S., 147
 Gale, W., 9
 Gates, B.C., 189
 Gelman, A., 109
 Glosner, R., 21
 Gnade, Bruce E., 263, 437
 Gonsalves, K.E., 195, 245
 Goodisman, Jerry, 355
 Görsman, Claus, 141
 Gossner, H., 393
 Grönbeck, Henrik, 15
 Grow, J., 43
 Gunther-Green, Janelle, 239

 Hahn, H., 207, 363
 Ham, William K., 171
 Hanley, D., 369
 Harlow, Richard L., 31
 Healy, Matthew D., 49
 Heinrich, Thomas, 141
 Herron, Norman, 31
 Hiltner, A., 91, 163
 Hintermaier, M., 393
 Hnatyszyn, H.J., 109
 Hoekstra, J., 349
 Holmgren, Lotta, 299
 Holtz, R.L., 375
 Hrdina, Kenneth E., 425
 Hsu, Chi-Ming, 227, 281, 387
 Huang, Ching-Shung, 281
 Huang, Z.-Y., 9
 Hyeon, Taeghwan, 201, 443

 Jablonski, P.D., 455
 Jones, Bobby D., 21
 Jonsson, H., 349

 Kaiser, Andreas, 141
 Kalonji, G., 349
 Kane, D., 369
 Kanis, David R., 119
 Kauzlarich, Susan M., 129, 275
 Kawi, S., 189
 Kear, B., 207, 219, 363
 Kellogg, G.J., 325
 Kher, Shreyas S., 293
 Kiunke, W., 393
 Kleinfeld, Elaine R., 419

- Klemperer, Walter G., 177
 Klopfenstein, Bethany, 269
 Knappek, E., 393
 Kossovsky, Nir, 109
- Larbalestier, D.C., 455
 Laurich, Bernhard K., 49
 Lee, Howard W.H., 129, 275
 Lee, P.J., 455
 Lee, Pee-Yew, 227
 Lemmon, John P., 8
 Lerner, Michael M., 83
 Levitz, Pierre, 157
 Levy, R., 43
 Liang, Shurong, 177
 Lin, Hong-Ming, 227, 281, 387
 Lin, Weiping, 119
 Liu, Bing, 57
 Lukehart, Charles M., 21
 Lundquist, Paul M., 119
- Ma, Ying, 147
 Mackenzie, John D., 135
 Markowitz, Michael, 67
 Marks, Tobin J., 119
 Marquis, Peter M., 97
 Martin, David C., 413
 Mayes, A.M., 325
 McCandlish, L.E., 219
 Mehta, S.C., 337
 Merhari, Lhadi, 381
 Milliken, J., 375
 Mills, G., 9
 Milne, Stephen B., 21
 Moet, A., 91, 163
 Moore, Jeffrey S., 413
 Morante, J.R., 405
 Morisaki, H., 399
 Moskovits, M., 449
 Mueller, John E., 57
 Mure, T., 189
- Nazarov, Andrey P., 305
 Neff, Grace Ann, 269
 Newcomer, P.P., 311
 Nicol, J.M., 189
 Noffsinger, Carol, 239
 Nozaki, Shinji, 399
- Ohtsuki, Tomoko, 135
 Olsen, Margaret L., 129
 Ono, H., 399
- Page, Catherine J., 77, 171, 269
 Pan, Y.-M., 213
 Paul, P.P., 213
 Persson, John L., 299
 Petrunin, Maxim A., 305
 Peyghambarian, Nasser, 135
 Pollak, Fred H., 43
 Provenzano, V., 375
 Pypkin, B., 43
- Qi, Jing, 57
 Quinn, M., 9
- Ratner, Mark A., 119
 Remick, Robert J., 425
 Riley, Scott J., 263, 437
 Rishud, Subhash H., 129
 Roddy, M., 207
 Rolfe, Jon, 431
 Rosén, Arne, 15, 299
 Roura, P., 405
 Rubner, M.F., 325
- Sadangi, R.K., 219
 Sakata, J., 257
 Salahuddin, N., 163
 Sanders, P.G., 319
 Sardin, G., 405
 Sattja, S.K., 325
 Sato, S., 399
 Schubert, Ulrich, 141
 Schwab, S.T., 213
 Scoville, Nancy, 431
 Seeman, Nadrian C., 57
 Shalaev, Vladimir, 449
 Shen, Jun, 183
 Shen, Lu, 147
 Siegel, P.W., 319
 Singh, Alok, 67
 Sioshansi, Atisa, 413
 Skandan, G., 207, 363
 Slack, W., 369
 Smith, D.A., 337
 Smith, David C., 49
 Sottile, Laura J., 263
 Sponsler, E., 109
 Stock, S.R., 21
 Stockton, W.B., 325
 Stolz, M., 393
 Strongin, M., 43
 Su, Weijie, 233
 Suib, Steven L., 147
 Suslick, Kenneth S., 201, 443
 Szmania, Jeffrey, 103
- Taga, Y., 257
 Tewinkel, Stefan, 141
 Thorn, David L., 31
 Tokarski, Zbigniew, 233
 Tokito, Shizuo, 257
 Trudeau, M.L., 251
 Tsai, Kuen-Rong, 227
 Tschöpe, Andreas, 251
 Tung, Chiun-Yen, 387
- Udovic, T.J., 189
- Vandersande, Jan, 431
 Venturini, E.L., 311
- Wang, Hui, 57
 Wang, Jue, 183
 Wang, Yinli, 57

Weber, Alfred P., 331
Weertman, J.R., 319
Wells, Richard L., 293
Wilcoxon, J.P., 311
Wong, George K., 119
Wu, Jinghe, 83
Wu, Weidong, 183

Xiao, T.D., 195
Xiao, Youming, 147
Xu, Z., 189
Xu, Zhitu, 413

Yan, D., 43
Yan, H., 349
Yang, Chao-Cheng, 387
Yang, X.-Q., 43
Ying, J.Y., 251
Yitzchaik, Shlomo, 119

Zachariah, Michael R., 343
Zeppentfeld, Astrid C., 77, 171, 269
Zhang, Sukun, 245
Zhang, Y.D., 195
Zhang, Yuwen, 57
Zhen, Yong S., 425
Zhou, Bin, 183

Subject Index

- ab initio calculation, 381
- aerogels, 189
- aerosol agglomerates, 331
- none, 77
- catalysts, 31, 201, 281, 287, 387, 443
- chemical vapor deposition, 147, 405
- colloids, 3, 67, 129
- computer simulations, 343, 349
- diamond-like materials, 43
- DNA, 119
- facet formation, 393
- fractals, 189, 355, 449
- fullerenes, 369
- grain boundaries, 337
- hydrodesulfurization, 287
- interfacial properties, 281, 325
- intermetallics, 213
- helium, 15
- Langmuir-Blodgett films, 83
- laser ablation, 363, 437
- light emission, 399
- magnetic properties, 195, 227
- mechanical properties, 337, 349, 369
- MO-LCAO calculations, 15
- molecular
 - beam epitaxy, 393
 - precursors, 31
 - sieves, 263, 437
- multilayer films, 103, 177, 325, 349, 419
- nanoclusters, 49, 91, 171, 207, 355
- nanocomposites, 21, 43, 91, 97, 135, 171, 245, 369
- nanocrystalline materials, 129, 227, 251, 293, 319, 387
- optical
 - parametric amplification, 57
 - properties, 9, 129, 233, 257, 375, 459
- oxidation, 299
- photoluminescence, 399, 405
- poly-foam process, 425
- polypeptide films, 227, 239
- porous
 - materials, 163, 189
 - silicon, 275
- quantum confinement, 49
- self-assembly, 57, 67, 103, 177, 239, 269, 305, 413
- sol-gel, 141, 183, 189
- solution phase synthesis, 293
- spontaneous reduction, 9
- spark erosion, 431
- spray conversion process, 219
- steel, 201
- superconducting wire, 455
- superlattices, 257
- thermal properties, 431
- thermogravimetric analysis, 251
- topology, 119
- ultrasound, 201
- whiskers, 147
- zirconia, 207